Uniaxial Extensional Behavior of A–B–A Thermoplastic Elastomers: Structure-Properties Relationship and Modeling

A DISSERTATION
SUBMITTED TO THE FACULTY OF THE
UNIVERSITY OF MINNESOTA
BY

Luca Martinetti

IN PARTIAL FULFILLMENT OF THE REQUIREMENTS
FOR THE DEGREE OF
DOCTOR OF PHILOSOPHY

Christopher W. Macosko, Frank S. Bates

May 2015

Acknowledgements

I owe my deepest gratitude to my loving parents and sister, who have always stood by my side, supported my decisions, sacrificed themselves to help me pursue a higher education, and provided the ideal environment for writing this thesis. A special thank you goes to my little niece Giulia, for lighting up my heart and making me smile just when I needed it the most. I also want to thank Jenny, with whom this adventure began, for having been my source of true happiness and strength for many years.

I am deeply grateful to my advisors, for their guidance, patience, and support. I would also like to express my gratitude to David Morse, for a valuable teaching experience and many engaging discussions, and to Marc Hillmyer and Timothy Lodge for their insightful comments and suggestions.

My heartfelt appreciation goes to Julie Prince and David Giles, for their warm friendship and constant help throughout this journey. They are the most likable, amiable, and compassionate persons I have had the fortune to meet at the University of Minnesota. Incidentally, David has also patiently taught me a great deal about rheometers, fueled my passion for biking, and provided a place for me to stay when I came back to Minnesota. I am also indebted to all the CEMS staff – especially Teresa Bredahl, Mary Nissen, Jim Pirie, Daniel Williams, Jo Belvedere, and William Gruhlke – for their kindness and dedication.

I thank my numerous lab mates, colleagues, and friends for their support and encouragement during my struggles. I am particularly grateful to Carlos Lopez-Barron, Randy Ewoldt, Milana Trifkovic, Mark Martello, Hyunwoo Kim, Jie Song, Zaifei Wang, Han Zhang, Sangwon Kim, Carmelo Declet-Perez, Jingwen Zhang, Intaek Lee, Hsu Chiang, Nan Zhang, and my best friend, Marilena Di Pietro.

I have also greatly benefited from conversations with Hiroshi Watanabe and Gareth McKinley. Their advice has been a great help in understanding the viscoelastic behavior of block copolymers and in appreciating the value of fractional calculus.

To my parents, Alfonsa Pizzo and Leonardo Martinetti,
and my sister Laura.

"per aspera ad astra"

Abstract

At service temperatures, A–B–A thermoplastic elastomers (TPEs) behave similarly to filled (and often entangled) B-rich rubbers since B block ends are anchored on rigid A domains. Therefore, their viscoelastic behavior is largely dictated by chain mobility of the B block rather than by microstructural order. Relating the small- and large-strain response of undiluted A–B–A triblocks to molecular parameters is a prerequisite for designing associated TPE-based systems that can meet the desired linear and nonlinear rheological criteria.

This dissertation was aimed at connecting the chemical and topological structure of A–B–A TPEs with their viscoelastic properties, both in the linear and in the nonlinear regime. Since extensional deformations are relevant for the processing and often the end-use applications of thermoplastic elastomers, the behavior was investigated predominantly in uniaxial extension. The conceptual basis of the theories underlying each topical area was explained while the emphasis was kept on fundamental principles and the molecular viewpoint. The analysis herein is independent from the specific choice of the constituent blocks and thus applies to any microphase-segregated thermoplastic elastomer of the A–B–A type.

The unperturbed size of polymer coils is one of the most fundamental properties in polymer physics, affecting both the thermodynamics of macromolecules and their viscoelastic properties. Literature results on poly(D,L-lactide) (PLA) unperturbed chain dimensions, plateau modulus, and critical molar mass for entanglement effect in viscosity were reviewed and discussed in the framework of the coil packing model. Self-consistency between experimental estimates of melt chain dimensions and viscoelastic properties was discussed, and the scaling behaviors predicted by the coil packing model were identified. Contrary to the widespread belief that amorphous polylactide must be intrinsically stiff, the coil packing model and accurate experimental measurements undoubtedly support the flexible nature of PLA. The apparent brittleness of PLA in

mechanical testing was attributed to a potentially severe physical aging occurring at room temperature and to the limited extensibility of the PLA tube statistical segment.

The linear viscoelastic response of A–B–A TPEs was first examined at temperatures where the A domains are glassy. Characteristic length scales and tube model parameters were determined, and the role of the glassy A domains on the entangled rubbery B network was assessed. Thermo-rheological complexity, observed near and below $T_{g,A}$, was attributed to augmented motional freedom of the B block ends at the corresponding A/B interfaces, in harmony with the theoretical treatment of thermo-rheological complexity for two-phase materials developed by Fesko and Tschoegl. When the magnitude of the steepness index was taken into account, the shift behavior was analogous to the response measured for pure B melts. Building upon the procedure proposed by Ferry and co-workers for entangled and unfilled polymer melts, a new method was developed to extract the matrix monomeric friction coefficient ζ_0 from the linear response behavior of a filled system in the rubber-glass transition region, and to estimate the size of Gaussian submolecules. Stress relaxation beyond the path equilibration time was found qualitatively and quantitatively compatible with dynamically undiluted arm retraction dynamics of entangled dangling structures (originating either from a fraction of triblock chains having one end residing outside A domains or from diblock impurities). By employing tube models and rubber elasticity theories, suitably modified to account for microphase-segregation, the linear elastic behavior across the rubbery plateau and up to the entanglement time was modeled, and a simple analytical expression relating the Langley trapping factor with the fraction of entangled and unentangled dangling structures of the material was obtained.

The critical-gel-like behavior typical of A–B–A TPEs at service temperatures approaching $T_{g,A}$ was analyzed in terms of a power-law distribution of relaxation times derived from the wedge distribution, shown to be equivalent to Chambon–Winter's critical gel model and to the mechanical behavior of a fractional element. A relation between the observed power-law exponent and molecular structure was established. The measured low-frequency response, originating from the incipient glass transition of the A

domains, was exploited and extrapolated to lower frequencies via a sequential application of the fractional Maxwell model and the fractional Zener model. With only a few, physically meaningful material parameters a realistic description of the A–B–A self-similar relaxation was obtained over a frequency range much broader than the experimental window and not accessible via time-temperature superposition.

The relationship between large-strain response and network structure of A–B–A triblocks was investigated, by examining (1) the effect of linear relaxation mechanisms on the tensile behavior, (2) the sources of elastic and viscoelastic nonlinearities, and (3) the strain rate dependence of the ultimate properties. Because of the numerous typos that appear in the original papers as well as in a recent *Macromolecules* review, a detailed analysis of the Edwards–Vilgis slip-link model was performed and the main steps leading to the determination of the chemical and topological contributions to the reduced stress were outlined. After establishing an operational definition of initial modulus for critical-gel-like materials subjected to start-up extensional tests, it was possible to determine the relationship between the dimensionless stress in tensile tests at constant strain rate and the step-strain extensional damping function. Based on the molecular picture of the strain-induced structural changes gained from exposing time and strain effects, the governing mechanism of rupture was identified with ductile/fragile rupture of A domains. To the best of our knowledge, this is the first experimental evidence linking the strain rate dependence of ultimate properties of triblock TPEs to the strain-induced glass-rubber transition of the domains. In addition, experimental results on the ultimate properties of A–B–A/B–A blends were consistent with this mechanism of rupture.

For the first time in the literature, the complex high-dimensional rheological signature of chewing gum was analyzed, especially in response to nonlinear and unsteady deformations in both shear and extension. A unique rheological fingerprint was obtained that is sufficient to provide a new robust definition of chewing gum that is independent of specific molecular composition.

Table of Contents

List of Tables

List of Figures

Chapter 1

Introduction

1.1 Thesis Outline

1.1.1 Melt Chain Dimensions and Macroscopic Properties

The unperturbed size of polymer coils is one of the most fundamental properties in polymer physics, affecting both the thermodynamics of macromolecules and their viscoelastic properties such as the shear plateau modulus (G_N^0) and the critical molar mass for entanglement effect in viscosity (M_C). Relating unperturbed chain dimensions to macroscopic properties requires that molecular characteristics be defined by two independent parameters (measures of chain flexibility and "bulkiness" of the backbone bond). In Chapter 2, literature results on poly(D,L-lactide) (PLA) unperturbed chain dimensions, G_N^0, and M_C are reviewed and discussed in the framework of the *coil packing model*. Molecular characteristics of amorphous polylactide are identified. They are compared, in the melt state ($T > T_g$), with those of seven linear flexible polymers covering a relatively wide range of Witten–Fetters packing lengths (1.7–5.6 Å). Self-consistency between experimental estimates of melt chain dimensions and viscoelastic properties is discussed. Furthermore, we examine the scaling behaviors predicted by the coil packing model and how the polymer structure affects macroscopic properties in a melt: namely, the entanglement molar mass, the maximum stretch ratio of an entanglement strand ($\lambda_{max,e}$), and M_C.

1.1.2 Block Copolymer Thermoplastic Elastomers

Thermoplastic elastomers (TPEs) combine the flexibility and resilience of vulcanized rubbers with the processing properties of thermoplastics. They derive their toughness from inhibition of catastrophic failure from slow crack growth, and undergo a rapid and reversible transition from a processable melt to a rubber-like product upon cooling. At service temperatures, most thermoplastic elastomers are biphasic systems (macrophase-separated or microphase-segregated) due to thermodynamic incompatibility of the two structural components: a soft, amorphous, polymer (B) with a low glass transition temperature (T_g), and a hard polymer (A) with high T_g (or crystal melting point, T_m) whose discrete domains behave as thermo-reversible physical crosslinks. When TPEs consist of two incompatible phases at service temperatures, their final properties are influenced by the resulting interface and stem from the characteristics of the individual polymers that constitute the phases. Since each phase retains its own glass or melting transition, a rubber-like plateau viscoelastic response is confined between a lower and upper bound of service temperatures (related to the elastomeric and thermoplastic phases, respectively).[a]

---

[a] Holden, G. Thermoplastic Elastomers. In *Kirk-Othmer Encyclopedia of Chemical Technology*; Wiley Online Library, 2000; pp 1–23. Holden, G.; Kricheldorf, H. R.; and Quirk, R. P. *Thermoplastic Elastomers,* 3rd ed.; Hanser Gardner; 2004. Costa, F. R.; Dutta, N. K.; Choudhury, N. R.; and Bhowmick, A. K. Thermoplastic Elastomers. In *Current Topics in Elastomers Research*; CRC Press, 2009; pp 101–164.

Blending is a viable method of combining a hard thermoplastic with a rubber-like polymer (*plastic-rubber blends*), and sometimes the elastomeric phase is crosslinked while the mixture is being highly sheared (*thermoplastic vulcanizates*). TPEs also include alloys of ethylene interpolymer and chlorinated polyolefins (*single-phase systems*), and *ionomers* (hydrocarbon backbones containing pendant acid groups neutralized to form salts). *Block copolymers*, however, represent the major class of TPEs.[a] In this class, linear triblock and multiblock copolymers of the A–B–A and $(A–B)_n$ type are the most common molecular architectures, and the two structural units are covalently bonded together with both ends of the elastomeric polymer B confined to the interface with hard domains of the thermoplastic polymer A.[b] Owing to the wide range of physical properties they can display, applications of TPEs are diverse and span from the automotive and footwear industry, to wire insulation, food contact, sports equipment, medical devices, adhesives, and asphalt modifiers.

At service temperatures ($T_{g,B} < T < T_{g,A}$), A–B–A thermoplastic elastomers behave similarly to filled (and often entangled) B-rich rubbers since B block ends are anchored on rigid A domains. Therefore, their viscoelastic behavior is largely dictated by *chain mobility of the B block* rather than by microstructural order. Relating the small- and large-strain response of undiluted A–B–A triblocks to molecular parameters is a prerequisite

---

[b] Recently, a new class of TPEs has emerged in which synthetic polypeptides are genetically engineered into *protein-based* thermoplastic elastomers, often of the A–B–A type (e.g. with silk-like and elastin-like blocks), and are designed to exhibit microphase-segregated morphologies and form gels under physiological relevant conditions.

for designing associated TPE-based systems that can meet the desired linear and nonlinear rheological criteria. This dissertation is aimed at connecting the chemical and topological structure of A–B–A TPEs with their viscoelastic properties, both in the linear and in the nonlinear regime. Since extensional deformations are relevant for the processing and often the end-use applications of thermoplastic elastomers, the behavior is investigated predominantly in *uniaxial extension*. The analysis herein is independent from the specific choice of the constituent A and B blocks.

The linear viscoelastic response of undiluted A–B–A TPEs, at temperatures where the A domains are glassy, is examined in detail in Chapter 3. Comprehensive analyses of the linear and nonlinear viscoelastic behavior at a temperature near $T_{g,A}$ are presented, respectively, in Chapter 4 and Chapter 5. These three chapters constitute the body of the dissertation, complemented by the rheological behavior of chewing gums[c] (Chapter 6) and experimental results on A–B–A/A–B blends (Appendix I). Ideas for future work and theory testing are discussed in Chapter 7. Supplemental material, special topics, and excerpts of the programs developed for this research are offered in Appendices.

---

[c] This work was published in "Martinetti et al. A Critical Gel Fluid with High Extensibility: The Rheology of Chewing Gum. *Journal of Rheology* **2014**, *58*, 821–838".

1.2 Note to the Reader

The theoretical discussions leading to the major conclusions of each chapter grew out of a combination of numerous and disparate sources, and were developed for and tailored to the subject at hand. A few examples can illustrate this point. The *coil packing model* discussed in Chapter 2 relies upon a coherent set of characteristic length scales and tube model parameters, whereas inconsistent definitions are often adopted in the literature. Another example is provided by the *thermo-rheological complexity* examined in Chapters 3 and 4. Despite being a well-known topic in the polymer literature, recent papers on block copolymers usually lack any reference to the results of Tschoegl and Fesko, which identify the conditions under which simple shifts should fail and an alternative analytical approach may be pursued. The *linear elastic modeling* developed in Chapter 3 combines tube models ideas and rubber elasticity theories in a new way. It is based, for instance, on the concept of *entanglement modulus vs. plateau modulus*, examined in a 2002 paper by McLeish but not widely discussed in the literature. The *fractional modeling*, which may appear as a sort of "extra" topic at first sight, is fundamental to interpreting the results of Chapter 5 and thereby discerning the governing mechanism of rupture for triblock TPEs. This required an analysis of the asymptotic expansions of the *fractional Zener model*, which made it possible to estimate the PLA glass-rubber transition in conditions of thermo-rheological complexity. The simpler *fractional Maxwell model*, which permitted the application of the fractional Zener model in the first place, turned out to be suitable

for describing the ordered-structure response in block copolymers above $T_{g,A}$ and across the order-disorder transition temperature.

The object of this dissertation is to provide a framework for the better understanding of the viscoelasticity of TPEs of the A–B–A type by identifying the universal attributes of their molecular and topological structure. As a result, the conceptual basis of the theories underlying each topical area is explained while the emphasis is kept on fundamental principles and the molecular viewpoint. Purely empirical models and equations have been disregarded, and efforts have been made to elucidate the physical meaning of all the models used. This has led, for instance, to the use in Chapter 3 of a *continuous relaxation spectrum* rather than a discrete moduli distribution whose parameters would have lacked any physical meaning. For the same reason, the nonlinear elastic modeling discussed in Chapter 5 is based on *molecular theories of rubber elasticity*, namely the Rubinstein–Panyukov non-affine slip-tube model and the Edwards–Vilgis slip-link model.

A certain amount of background information was deemed necessary, and it is offered in Appendices. A consistent set of definitions of functions and theorems used throughout the dissertation is presented in Appendices B and C. While some of these functions, such as the *complete* and *incomplete Beta functions*, have different definitions, others, like the *ordinary* and *generalized Mittag-Leffler functions*, are not widely known. Some topics, like integral transformation calculus and the *Stieltjes transform*, are used in various derivations and arguments in the main chapters. The linear viscoelastic functions reviewed in Appendix D were included for three reasons: (1) to explain the *reference*

state and resulting *memory function* adopted in this dissertation, which follow Tschoegl's approach rather than the most commonly adopted convention for fluid mechanics; (2) to establish nomenclature and a framework applicable to both *liquid-like* and *solid-like* materials; (3) to introduce linear viscoelastic functions, such as the *operational respondances* and the *constant-strain-rate modulus*, upon which many derivations or discussions in the main chapters are based.

Appendices E and F provide the physical background and meaning for the power-law-type models used in Chapters 3 to 5. This is especially important for *fractional calculus* and *fractional mechanical models*. While the former may appear to be just complex mathematics, it is deeply grounded in the diffusion and relaxation behavior of any complex system. In a sense, the classical series-parallel models (classical calculus) are to fractional models (fractional calculus) what Newtonian physics is to General Relativity: a great and useful approximation, which yet fails under more general conditions. Block copolymers are an example of such conditions, out of many. Also, there has been a lot of debate in the recent literature on whether *quasi-properties* should be assigned physical meaning, due to their non-integer dimensions of mass (M), length (L), and time (T). The brief presentation of the *fractional Fokker–Planck equation* (and related parameters) should hopefully mitigate any doubt of this sort in the reader's mind.

Finally, Appendix H contains brief excerpts of the Mathematica® and MATLAB® programs developed for this research, partially describing some of the key algorithms which made it possible to obtain most of the results presented in Chapters 3, 4, and 5.

Chapter 2

Melt Chain Dimensions and Macroscopic Properties: The Curious Case of Poly(D,L-lactide)

The unperturbed size of polymer coils is one of the most fundamental properties in polymer physics, affecting both the thermodynamics of macromolecules and their viscoelastic properties such as the shear plateau modulus (G_N^0) and the critical molar mass for entanglement effect in viscosity (M_C). Relating unperturbed chain dimensions to macroscopic properties requires that molecular characteristics be defined by two independent parameters (measures of chain flexibility and "bulkiness" of the backbone bond). In this chapter, literature results on poly(D,L-lactide) (PLA) unperturbed chain dimensions, G_N^0, and M_C are reviewed and discussed in the framework of the coil packing model. Measurements from dilute solutions are usually in mutual disagreement and overestimate the PLA coil size (hence, its chain stiffness), while approximate empirical correlations or PLA samples not stabilized against thermal degradation result in inaccurate (i.e. too low) estimates of the undiluted PLA shear plateau modulus. For apparently the same reasons, its critical molar mass for entanglement effect in viscosity can be significantly overestimated. Molecular characteristics of amorphous polylactide are identified. They are compared, in the melt state ($T > T_g$), with those of seven linear flexible polymers covering a relatively wide range of Witten–Fetters packing lengths (1.7–5.6 Å). Self-consistency between experimental estimates of melt chain dimensions and viscoelastic properties is discussed. We also examine the scaling behaviors predicted

by the coil packing model and how the polymer structure affects macroscopic properties in a melt: namely, the entanglement molar mass, the maximum stretch ratio of an entanglement strand ($\lambda_{max,e}$), and M_C. Contrary to the widespread belief that amorphous polylactide must be intrinsically stiff, the coil packing model and accurate experimental measurements undoubtedly support the flexible nature of PLA. Both above and below its glass transition temperature, PLA fails Wu's criterion for the onset of brittle behavior. The apparent brittleness of PLA in mechanical testing can be attributed to a potentially severe physical aging occurring at room temperature and to the limited extensibility of the PLA tube statistical segment.

2.1 Introduction

Polylactide is an aliphatic linear polyester that can be derived from biorenewable resources such as corn. Because of the chiral center on its backbone, polymerization of L-lactide (*S*,*S*) or D-lactide (*R*,*R*)[a] results in two different enantiomeric forms of the polymer: isotactic, semicrystalline ($T_g \approx 60$ °C, $T_m \approx 180$ °C) poly(L-lactide) (PLLA) and poly(D-lactide) (PDLA), respectively. Atactic, amorphous ($T_g \approx 55$ °C) poly(D,L-lactide) (PLA) is typically prepared by polymerization of the racemic mixture.[1-4] Although PLA is a thermoplastic with physical properties similar to common flexible polymers like atactic polypropylene, it has also been shown to degrade hydrolytically[3,5,b] and *in vivo*[6-9]. Owing

---

[a] Absolute configurations of the two chiral centers in a C-6 repeating unit, according to the Cahn–Ingold–Prelog naming system.

[b] The degradation time of polylactide in the environment is on the order of weeks (amorphous polylactide, PLA) or 6–24 months (semicrystalline polylactide, PDLA or PLLA), compared to 500–1000 years for conventional plastics such as polystyrene.[3,5]

to its biodegradability and biocompatibility, PLA has found numerous applications in the medical and pharmaceutical fields.[10,11]

Unfortunately, most of the literature on PLA chain flexibility and viscoelastic parameters is highly mystifying and controversial. Unperturbed chain dimensions are often inaccurate or interpreted under the wrong premise that PLA chains must be intrinsically stiff. Experimental estimates of viscoelastic parameters, such as the shear plateau modulus (G_N^0) and the critical molar mass for entanglement effect in viscosity (M_C), are sometimes erroneous and inconsistent with the measured unperturbed coil size. In this chapter, literature results on PLA chain flexibility, G_N^0, and M_C are examined and discussed in the framework of the coil packing model for linear flexible polymers[12-20].

2.2 Unperturbed Chain Dimensions

As Flory[21] stated in 1969, "comprehension of the conformational statistics of chain molecules is indispensable for a rational interpretation and understanding of their properties". The structure of polymer coils, and in particular their unperturbed[22,23,c] size, is one of the most fundamental properties in polymer physics affecting both the thermodynamic and viscoelastic behavior of macromolecules. For example, differences in chain dimensions play a role in the self-assembly of block copolymers[24,25] and, more generally, have long been known to significantly impact polymer-polymer miscibility[26].

---

[c] The unperturbed state is defined by the lack of long-range interactions caused by excluded volume.[22,23]

The size of macromolecular chains is also related to the degree of their mutual "uncrossability" in the melt[27], thus governing viscoelastic properties such as the plateau modulus[12-15] and, in turn, adhesive bond performance[28,d]. Furthermore, since unperturbed dimensions of an amorphous polymer persist even below its glass transition[29], they are a key factor controlling the mechanical properties of glassy polymers[30] and in particular their brittle-ductile fracture behavior[31-33].

In the unperturbed state, the dimensions of a long chain (i.e. more than ≈ 100 backbone bonds[34,e]) of molar mass M and monomer molar mass M_0 can be conveniently expressed in terms of Flory's characteristic ratio, C_∞, as:[21,22]

$$R^2/M = C_\infty \cdot jl^2/M_0 \tag{2.1}$$

where R denotes the chain unperturbed root-mean-square end-to-end distance[23,35], j is the average number of backbone bonds per repeating configurational unit (monomer)[35-37], and l represents the monomer root-mean-square backbone bond length[23,38].[f] The characteristic

---

[d] According to the Dahlquist criterion for tack, good wetting and contact between the adhesive and substrate requires a shear storage modulus G' lower than 0.3 MPa during a 1-s bonding process.[28]

[e] In practice, Eq. (2.1) remains valid also for shorter chains as long as $n \geq$ no. of backbone bonds in a Gaussian submolecule (i.e. the smallest section of the polymer chain that is long enough to assume a random coil conformation), albeit with the n-dependent value of the characteristic ratio, C_n. While usually $C_n < C_\infty$, the opposite behavior has also been observed.[34]

[f] Polymers are self-similar (fractal) objects over a wide range of length scales, i.e. all chain sections with characteristic size x, where l (monomer root-mean-square backbone bond length) $< x < R$ (chain unperturbed root-mean-square end-to-end distance), display on average the same statistical properties. In the unperturbed state, the size of a long polymer chain scales as $R \sim M^{1/2}$ and therefore the polymer fractal dimension is $d_f = 2$.[22]

ratio is a measure of chain flexibility associated with restricted bond angles and steric hindrance to bond rotation (i.e. a measure of the local correlations decay between neighbouring backbone bond vectors). As a result, the lowest values that it can assume correspond to ideal chains that are freely-jointed ($C_\infty = 1$) or with torsion angles equally likely and independent of each other ($C_\infty \simeq 2$, for backbones made up of carbon single bonds).[22,23,g] Real chains are never as flexible as their ideal counterparts, and linear flexible polymers typically display C_∞ lying in the range ≈ 4–9.[17,20] The ratio R^2/M is thus independent of chain length (for large M) and affected by temperature primarily[22,h] through C_∞. Table 2.1 shows the temperature dependence of the unperturbed chain dimension for PLA[39] and 8 other linear polymers: polyethylene (PE)[20], poly(ethylene oxide) (PEO)[20], atactic polypropylene (*a*-PP)[20], polyisoprene with a 7% 3,4 microstructure (7% 3,4-PI)[40], hydrogenated 75% 3,4-polyisoprene (75% 3,4-HPI)[40], atactic poly(methyl)methacrylate (*a*-PMMA)[40], atactic polystyrene (*a*-PS)[20], and its hydrogenated form atactic poly(cyclohexyl)ethylene (*a*-PCHE)[40]. For simple backbone structures, such as those of PE and PLA, an increase in temperature is easily related to a change in the relative populations of *trans* and *gauche* states of torsion angles and therefore determines a reduction in C_∞ (i.e. the population of states shifts towards *gauche*

---

[g] If β represents the average backbone angle, $C_\infty = 1$ for a freely-jointed chain ($\beta = 90°$), $C_{\infty,\min} \simeq 2.16$ for a freely-rotating chain ($\beta_{\max} = \pi - \cos^{-1}(e^{-1}) \simeq 111.58°$), and $C_{\infty,\min} = 2$ for a worm-like chain ($\beta_{\max} = 90°$).[22,23]

[h] The bond length l, if anything, increases with temperature but its fluctuations (typically ± 0.005 nm) are modest and do not affect chain conformations.[22]

as temperature rises and so these chains are more flexible and coil up more tightly).[41] In more complicated structures (e.g. with steric repulsion of side groups), the characteristic ratio can increase (e.g. 75% 3,4-HPI, 7% 3,4-PI) or remain constant (e.g. *a*-PS, *a*-PCHE) with increasing T.[41] From Eq. (2.1) it is clear that, once the repeating unit is defined and its backbone bond length l suitably calculated, measurements of unperturbed coil sizes (R) and chain lengths (M) can be cast in terms of C_∞ and directly associated with chain flexibility.

Table 2.1. Temperature dependence of the unperturbed chain dimension ($\kappa \equiv \partial \ln R^2 / \partial T$) for selected homopolymers.

Polymer	$\kappa \equiv \partial \ln R^2 / \partial T$ [10^{-3} deg^{-1}]	*Reference*
PE	– 1.20	Fetters et al.[20]
PEO	– 0.30	Fetters et al.[20]
PLA	– 1.41	Anderson and Hillmyer[39]
a-PP	– 0.10	Fetters et al.[20]
75% 3,4-HPI	+ 1.20	Krishnamoorti et al.[40]
7% 3,4-PI	+ 0.40	Krishnamoorti et al.[40]
a-PMMA	+ 0.10	Krishnamoorti et al.[40]
a-PS	≈ 0	Fetters et al.[20]
a-PCHE	≈ 0	Krishnamoorti et al.[40]

2.3 Physical Meaning of C_∞ and Experimental Measure of Unperturbed Chain Dimensions

At coarse-grained levels, a long (i.e. flexible) polymer chain of degree of polymerization $N = M/M_0$ may be viewed as comprised of Y freely-jointed statistical segments (with $Y \leq N$) of suitably chosen length x (with $x \geq b > l$). Being the companion statistical parameter of N, b is referred to as the monomer-based statistical segment length (SSL).[23,35] The characteristic length x is usually associated with a particular physical property of the statistical chain that it defines. These freely-jointed statistical chains, however, share all a common feature in that their mean-square end-to-end distance must be equal to that of the real chain:[23,35,42-45,i]

$$R^2 = C_\infty n l^2 = Y x^2 \tag{2.2}$$

where $n = jN$ is the average number of backbone bonds per chain. From Eq. (2.2), the statistical significance of C_∞ can be extracted. Since $Y/n = C_\infty \cdot (l/x)^2$ and $l < x$, C_∞ is the (ensemble-average) maximum number of freely-jointed links per backbone bond required to form an equivalent (i.e. same R^2) statistical chain. Thus, a statistical representation of 7% 3,4-PI at 25 °C requires no more than $4.8 \cdot n$ freely-jointed units, while a maximum of $7 \cdot n$ is needed for PLA at 140 °C (values of C_∞ are later given in Table 2.3).

---

[i] A random flight/walk of Y steps of length x has mean-square end-to-end distance $R^2 = Yx^2$ and contour length $L = Yx$. If the number of steps is changing with time, the mean-square end-to-end distance at any time t is given by $R(t)^2 = 6Dt$ (simple diffusive motion or Brownian motion), where D is the diffusion coefficient.[22,41,45]

The monomer-based SSL is calculated according to Eq. (2.2) as $b = \left(C_\infty \cdot j\right)^{1/2} l$.[23,35] In polymer physics, three types of statistical segments are traditionally defined at length scales larger than chemical monomers, most notably (and in order of increasing length scales) the Kuhn segment, the Gaussian submolecule, and the tube segment (i.e. entanglement strand). For the corresponding *Y*–*x* dyads[j], we use the symbols N_k–b_k, *S*–σ, and *Z*–*a* (respectively), following largely[k] the nomenclature adopted by Ferry[42], Larson et al.[35], and Dealy and Larson[36]. Each of the statistical segment lengths has a specific physical meaning. The Kuhn chain (N_k units of length b_k), is defined in such a way that it possesses the same fully extended (contour) length *L* of the polymer chain in a rod-like zig-zag conformation, that is $L = K_{geom} nl = N_k b_k$, where $K_{geom} \equiv \sin(\beta/2) = \cos(\theta/2)$ and $\beta = \pi - \theta$ represents the average backbone bond angle (e.g. $\beta \simeq 112°$ for polyethylene).[20,22,35,36] In Flory's convention[21], the effect of bond angles is neglected and thus $K_{geom} = 1$. The length of a Kuhn segment[35,36], $b_k = \left(C_\infty / j\right)^{1/2} b / K_{geom} = \left(C_\infty / K_{geom}\right) l$, measures twice the distance along the chain at which local correlations between backbone bonds decay (i.e. $b_k = 2l_p$, where l_p is the persistence length)[46]. In other words, b_k is the

---

[j] The polymer literature abounds with symbols that, over the years, have often been used interchangeably when referring to a particular statistical segment length (SSL). For example, the monomer-based SSL was termed *a* by Ferry[42] and l_N by Graessley[41]; the Kuhn SSL was termed *b* by Rubinstein and Colby[22] and Fetters et al.[20], and l_K by Graessley[41]; the tube SSL was termed *d* by Ferry[42] and d_t by Fetters et al.[17]. In this study, we follow the SSL nomenclature adopted by Larson et al.[35] and Dealy and Larson[36].

[k] With the exception of the symbol *N*, which is used by Ferry for *S* and here for the degree of polymerization based on the monomer molar mass.

length scale at which the chain will, on average, bend 180°.[23] The ratio $C_\infty/K_{geom} \approx C_\infty$ can thus be thought of as the number of backbone bonds needed for the chain to easily bend 180°.[23] Therefore, on length scales smaller than b_k (or b), the chain is essentially rigid and its behavior (influenced by polymer-specific chemical details) resembles that of a linear elastic solid.[22] The characteristic dimension of a Gaussian submolecule, σ, represents the minimum length scale at which the real chain assumes a random coil conformation[47] and thus the probability distribution of the end-to-end distance can be approximated by a Gaussian function.[42,45] Consequently, at length scales smaller than σ the Rouse theory of chain dynamics no longer holds and semi-flexible chain models can better explain the viscoelastic behavior.[22] In entangled melts, the tube SSL, a, defines the length scale for topological constraints to become relevant and limit the transverse fluctuations of the polymer chains (i.e. at length scales $\approx a$, chains begin to experience the constraints imposed by the confining tube).[42,43]

Unperturbed chain dimensions are most accurately assessed by small-angle neutron scattering (SANS) of melt systems[48-51], although traditionally they have often been estimated via measurements of intrinsic viscosity or light scattering from dilute solutions. In the latter case, however, the conformation adopted by the dissolved polymer molecules can be different than in the melt (even if the solution is in its theta state), and it can also slightly change between two different theta solvents.[23,40] Moreover, long polymer chains frequently require the use of a good solvent and thus the solution-based unperturbed

dimensions must rely on theoretical models to correct for the resultant coil expansion (excluded volume effect).[36]

2.4 Chain Flexibility of PLA

Fetters and co-workers[17,18,20,40] tabulated SANS-based unperturbed chain dimensions of several linear flexible polymers, including PE, PEO, *a*-PP, 7% 3,4-PI, *a*-PMMA, *a*-PS, and *a*-PCHE (hereafter, we will sometimes use these names without prefixes). Conversely, most of the literature on PLA is based on measurements from dilute solutions in good solvents[2,52-55], and only in 2004 was the first SANS-based study[39] published. Not surprisingly, values of unperturbed PLA chain dimensions deduced from dilute solution measurements are sometimes in disagreement with one another and usually overestimate the coil size (hence, stiffness) compared to the SANS-based results. Among the several factors that can explain these inconsistencies are the use of different expansion-factor models when correcting data obtained in good solvents or neglecting to make such correction completely (e.g. Ren et al.[54]). Furthermore, literature reports disagree both on the absolute values of C_∞ and its trend with optical composition. Whereas several experimental[2,39,53,55] and theoretical[56] investigations indicated a decrease of C_∞ with decreasing stereo-regularity, Dorgan et al.[4] found no experimental evidence of a substantial change of chain flexibility with stereoisomers content. As a result, although the flexible nature of polymers such as PI or PEO is undisputed, most of the literature on PLA chain dimensions and intrinsic flexibility is extremely confounding and

controversial. Values of C_∞ are either inaccurate or interpreted under the wrong premise that amorphous polylactide must be intrinsically stiff. In addition, the temperature dependence of chain dimensions is often neglected.

A scrutiny of the literature is enlightening. Based on intrinsic viscosity measurements performed at room temperature by Schindler and Harper[52] on a benzene/chloroform solution, Grijpma et al.[53] calculated C_∞ = 9.3 for an amorphous polylactide containing 50% of D stereoisomers. Similar results were later obtained by Joziasse et al.[2] via light scattering from an acetonitrile solution at 25 °C, as they reported C_∞ = 9.5 (50% D) and C_∞ = 9.4 (29% D). In both of these studies the authors considered the lactoyl repeating unit as consisting of three freely rotating bonds (i.e. M_0 = 72.1 g/mol and j = 3) with an average length l = 1.41 Å. When converted to the same repeating unit, the result of Ren et al.[54] from intrinsic viscosity experiments on a benzene solution at room temperature, C_∞ = 9.3 (25% D), is remarkably in agreement with those of Grijpma et al.[53] and Joziasse et al.[2], despite the data obtained in this good solvent were not corrected to theta conditions. A significantly lower value of C_∞ was instead reported by Kang et al.[55], who measured the light scattered from a dilute solution of PLA (20% D) in acetonitrile/dichloromethane at 25 °C and found C_∞ = 8.5. For comparison, the result of Joziasse et al.[2] at the same stereoisomer content (20% D) was C_∞ = 11.0. Common to this literature was the conclusion that amorphous polylactide is supposedly an inherently stiff polymer at room temperature. The estimated values of C_∞ (centered around 9 at 25 °C, for j = 3, l = 1.41 Å,

and ≈ 25–50% D) were considered consistent with the brittle behavior of PLA subjected to mechanical testing[53,57].

These arguments, however, suffer from some fundamental flaws. First, characteristic ratios in the range ≈ 4–9 are typical of linear *flexible* polymers, as previously discussed. Conversely, *stiff* polymers such as poly(*p*-phenylene) or double-stranded DNA, characterized by large backbone bond angles and significant steric hindrance to bond rotation, have much greater values of C_∞. An estimate can be obtained via the freely-rotating chain model, or the (Kratky–Porod) worm-like chain (WLC) model[58] when the average backbone bond angle β is very large (i.e. $\beta > \approx 170°$)[22]. For β = 150°–175°, these models predict $C_\infty \simeq$ 14–525. Indeed, such large values of C_∞ have been measured for nitrocellulose (22), poly(*n*-butyl isocyanate) (500), and xanthan polysaccharide (750).[59,60] Second, PLA characteristic ratios deduced from dilute solution measurements are generally higher than the more accurate SANS-result reported by Anderson and Hillmyer[39], who found C_∞ = 8.4 at 30 °C for a PLA containing 28% of *R* stereocenters (in good agreement with the result of Kang et al.[55]). Equally important, when the temperature dependence is taken into account, C_∞ of amorphous polylactide *above* its glass transition ($T_g \approx$ 55 °C) decreases even further. At 200 °C, Anderson and Hillmyer measured C_∞ = 6.7 (28% *R*).[39] Some authors[2,53] appear to have based their deductions on a criterion for ductile-brittle fracture behavior proposed earlier by Wu[32,33]. According to Wu, the effect of physical aging can be decoupled from chain parameters, namely the entanglement density $\nu_e \equiv G_N^0/RT$ and the characteristic ratio C_∞, and polymers having $\nu_e < \approx 0.15$

mmol/cm^3 and $C_\infty > \approx 7.5$ are classified as intrinsically brittle.[32,33] However, inferring from Wu's criterion the flexible/brittle nature of a polymer demands taking into account the temperature dependence of both ν_e and C_∞.

In this chapter, we compare PLA with 7 linear flexible polymers (PE, PEO, *a*-PP, 7% 3,4-PI, *a*-PMMA, *a*-PS, and *a*-PCHE) at a fixed temperature above their respective glass transitions, based on molecular characteristics and Wu's criterion for the onset of brittle behavior. Casting unperturbed chain dimensions in terms of C_∞ requires knowledge of the average number and length of backbone bonds per monomer (j and l, respectively), as well as the average backbone bond angle β. For polymer species with constitutional isomerism, such as PI, these basic parameters will of course depend on the distribution of the different configurational repeating units. Their calculation, however, is not as obvious as it may seem. In particular, a choice has to be made whether to use real or virtual skeletal bonds in representing the repeating unit (i.e. whether to use real or virtual chemical monomers). In spite of considerations of bond rotational states, coplanarity and tautomerism, sometimes the choice is not clear-cut. For instance, Flory and colleagues[61,62] treated the C-3 repeating unit of PLA as being composed of one virtual bond (l = 3.70 Å), on the assumption of a rigid ester group in a planar *trans* configuration due to the partial double-bond character of C–O. On the other hand, according to Wu[63] the PLA monomer is better portrayed by three freely rotating real bonds of average length l = 1.41 Å. Several authors[2,39,53,55] later followed Wu's approach. The value of l (both for real and virtual bonds) can be obtained from the backbone bond lengths and angles of the

chemical structure. If Flory's convention ($K_{geom} = 1$)[21] is not adopted, an effective (average) backbone bond angle needs to be calculated.

We have chosen to use real chemical monomers, and to rely on literature data of real bond lengths and angles[3,64-66] for the computation of l and K_{geom}. With this approach, j_{RU} (where the subscript "RU" stands for "repeating unit") equals the number of backbone carbon atoms in the monomer, while $l_{RU} \equiv \left(j_{RU}^{-1} \sum l_i^2 \right)^{1/2}$ is the corresponding root-mean-square skeletal bond length[23,38]. To determine their effective backbone bond angle (expressed as $K_{geom,RU}$), the repeating units are considered in a rod-like zig-zag conformation (i.e. all *trans* states of torsion angles) and their projected length L_{RU} along the contour is calculated. $K_{geom,RU}$ is then given by the ratio $L_{RU} / j_{RU} l_{RU}$. Based on an equal ratio of PI *cis* and *trans* isomers, molar fraction-weighted arithmetic averages gave {$j = 3.86$, $l = 1.479$ Å, $K_{geom} = 0.792$}. The corresponding values for PEO were {$j = 3$, $l = 1.458$ Å, $K_{geom} = 0.826$}, while for PLA we calculated {$j = 3$, $l = 1.436$ Å, $K_{geom} = 0.836$}. For the remaining polymers, we used {$j = 2$, $l = 1.530$ Å, $K_{geom} = 0.829$} (i.e. $\beta = 112°$). The average backbone bond lengths thus calculated are consistent with other estimates reported in the literature, for instance $l = 1.48$ Å for 1,4-PI[41], $l = 1.453$ Å for PEO[67], and $l = 1.41$ Å for PLA[63]. These results, and the accompanying monomer molar masses, are summarized in Table 2.2.

Table 2.2. Parameters defining the configurational repeating unit of the selected homopolymers.

Polymer	M_0 [g/mol]	j	l [Å]	K_{geom}
PE	28.1	2	1.530	0.829
PEO	44.1	3	1.458	0.826
PLA	72.1	3	1.436	0.836
a-PP	42.1	2	1.530	0.829
7% 3,4-PI	68.1	3.86	1.479	0.792
a-PMMA	100.1	2	1.530	0.829
a-PS	104.1	2	1.530	0.829
a-PCHE	110.2	2	1.530	0.829

When PLA is compared with other flexible polymers in their melt states ($T > T_g$) (Table 2.3), it fails Wu's criterion for the onset of brittle behavior (i.e. fracture by crazing), as its characteristic ratio (in-between PE and *a*-PP) lies below 7.5 and $\nu_e = 0.29$ mmol/cm^3 (in-between 7% 3,4-PI and *a*-PP). PLA does not satisfy Wu's criterion also in the glassy state ($T < T_g$). At 25 °C, for instance, $C_\infty = 8.2$ (using the R^2/M measured by Anderson and Hillmyer at 30 °C[39], and the values of κ and l shown in Tables 2.1 and 2.2). Its entanglement density, however, remains well above the threshold of ≈ 0.15 mmol/cm^3. Indeed, it has been observed[17,18,40,68] that the entanglement molar mass (M_e) of polymers with $\kappa < 0$ (e.g. PE) decreases with decreasing temperature. M_e becomes almost temperature-independent for positive but modest values of κ (e.g. 7% 3,4-PI, whose M_e at 25 and 140 °C is shown in Table 2.3), and the trend is reversed if $\kappa \gg 0$ (e.g. 75%

3,4-HPI) (the T-dependence of M_e can be explained in the framework of the coil packing model, as will be discussed in §2.8.1). Therefore, at 25 °C the hypothetical[1] value of M_e for PLA ($\kappa < 0$) should be lower than in the melt state. Since $\nu_e \sim \rho/M_e$ and polymer density increases with decreasing temperature, $\nu_e > 0.29$ mmol/cm^3 below the PLA glass transition. In the literature, the seemingly brittle behavior of PLA (e.g. low impact strength) has been occasionally[53] equated to that shown by *a*-PMMA and *a*-PS. Noteworthily, both *a*-PMMA ($C_\infty = 9.0$, $\nu_e = 0.09$ mmol/cm^3) and *a*-PS ($C_\infty = 9.7$, $\nu_e = 0.06$ mmol/cm^3) were classified as brittle by Wu[32,33] and satisfy his criterion also in their melt state (i.e. $T = 140$ °C). A similar state of play holds for *a*-PCHE ($C_\infty = 7.6$, $\nu_e = 0.02$ mmol/cm^3) at 160 °C. As correctly pointed out by Dorgan et al.[4], a possible cause of the apparent rigidity of amorphous polylactide in mechanical testing is the severe physical aging occurring at room temperature (i.e. ≈ 30 degrees below its T_g).

[1] It is hypothetical because it cannot be measured in the glassy state.

Table 2.3. Literature values of density (ρ), SANS-measured unperturbed chain dimension (R^2/M), and rheology-measured shear plateau modulus (G_N^0) for the selected homopolymer melts. Calculated relevant lengths and parameters are also presented. Approximate values of $T–T_g$ trace iso-free volume conditions.

Polymer	T [°C]	$T–T_g$ [deg]	ρ [g/cm^3]	R^2/M [Å^2·mol/g]	C_∞	λ	p [Å]	G_N^0 [MPa]	ν_e [mmol/cm^3]	M_e^G [g/mol]
PE	140	225	0.784 [a)]	1.250 [a)]	7.5	0.61	1.69	2.60 [a)]	0.75	830
PEO	140	210	1.034 [b)]	0.791 [c)]	5.5	0.64	2.03	1.80 [d)]	0.52	1580
PLA	140	85	1.153 [e)]	0.603 [f)]	7.0	0.52	2.39	1.00 [g)]	0.29	3170
a-PP	140	150	0.786 [b)]	0.670 [a)]	6.0	0.50	3.15	0.47 [a)]	0.14	4590
7% 3,4-PI	25	90	0.900 [h)]	0.596 [h)]	4.8	0.56	3.10	0.35 [h)]	0.14	5100
7% 3,4-PI	140	205	0.834 [b)]	0.624 [i)]	5.0	0.54	3.19	0.42 [a)]	0.12	5460
a-PMMA	140	30	1.128 [b)]	0.421 [j)]	9.0	0.39	3.50	0.31 [a)]	0.09	10000
a-PS	140	40	0.969 [a)]	0.434 [a)]	9.7	0.36	3.95	0.20 [a)]	0.06	13310
a-PCHE	160	15	0.920 [k)]	0.323 [k)]	7.6	0.34	5.59	0.081 [l)]	0.02	32720

a) Tabulated in Fetters et al.[17].

b) Calculated according to Orwoll[69].

c) Calculated from the R^2/M value given in Fetters et al.[18] at 80 °C, using the κ_{PEO} value shown in Table 2.1.

d) Measured by Wu[70] at 180 °C.

e) Calculated according to Witzke[71].

f) Calculated from the R^2/M value measured by Anderson and Hillmyer[39] at 200 °C, using the κ_{PLA} value shown in Table 2.1.

g) Measured by Dorgan et al.[4] at 180 °C.

h) Tabulated in Fetters et al.[20].

i) Calculated from the R^2/M value given in Fetters et al.[20] at 25 °C, using the κ_{PI} value shown in Table 2.1.

j) Measured by Krishnamoorti et al.[40].

k) Tabulated in Fetters et al.[18].

l) Measured by Zhao et al.[72] at 187 °C.

Furthermore, C_∞ alone is not sufficient to fully define the molecular characteristics of a polymer chain. As suggested by Graessley and Edwards[73] in 1981, such task involves at least two independent length scales or parameters. While C_∞ reflects the intrinsic chain flexibility governed by short-range backbone bond correlations, a more local measure of chain dimensions is also required when connecting unperturbed coil sizes to macroscopic properties (e.g. plateau modulus). In 2000, Heymans[67] showed that the additional parameter is related to the "bulkiness" of the backbone bond (alternatively, the "bulkiness" of the chemical monomer). For a polymer of molar mass M, monomer molar mass M_0, melt density ρ, and average number of backbone bonds per chain n (= jM/M_0), the volume occupied by the chain is $V_{occ} = M/\rho N_{av}$ (where N_{av} is Avogadro's number) so the average volume of polymer per backbone bond is $v_b = V_{occ}/n = M/n\rho N_{av} = M_0/j\rho N_{av}$. If v_b is represented by a cylinder of length l along the backbone and radius r_b, the "bulkiness" of the backbone bond can be conveniently expressed by its aspect ratio:

$$\lambda \equiv \frac{l}{r_b} = l^{3/2}\left(\frac{\pi j \rho N_{av}}{M_0}\right)^{1/2} \tag{2.3}$$

Therefore, the smaller r_b is with respect to l the "thinner" the backbone bond and the larger its aspect ratio λ. Values of λ are listed in Table 2.3. Compared at approximately iso-free volume conditions, PLA (140 °C) and 7% 3,4-PI (25 °C) show a substantial difference in C_∞ but similar backbone bond aspect ratios. When both C_∞ and λ are considered, amorphous polylactide at 140 °C ($C_\infty = 7.0$, $\lambda = 0.52$) is more similar to fairly flexible polymers like PE ($C_\infty = 7.5$, $\lambda = 0.61$) and *a*-PP ($C_\infty = 6.0$, $\lambda = 0.50$) rather than

the relatively stiffer *a*-PMMA ($C_\infty = 9.0$, $\lambda = 0.39$) and *a*-PS ($C_\infty = 9.7$, $\lambda = 0.36$), which possess lower aspect ratios (due to voluminous sidegroups) and concurrently the largest characteristic ratios in the data set of Table 2.3. Examining the C_∞–λ relationship over the subset at 140 and 160 °C, we found in fact a power law correlation, $C_\infty \sim \lambda^m$ with $m \simeq -0.67$ (Figure 2.1), in substantial agreement with the result obtained by Heymans[67] over the whole 1994 Fetters data set[17] ($C_\infty \sim \lambda^{-1.18}$). Although present, the correlation between C_∞ and λ is far from perfect, therefore both ratios (or an equivalent pair of independent parameters) are essential to define molecular characteristics. The need to use both ratios, suitably combined in dimensionless parameters, will become clear in §2.7 when we examine how the polymer structure governs the entanglement molar mass (M_e^G) and the maximum stretch ratio of an entanglement strand ($\lambda_{max,e}$).

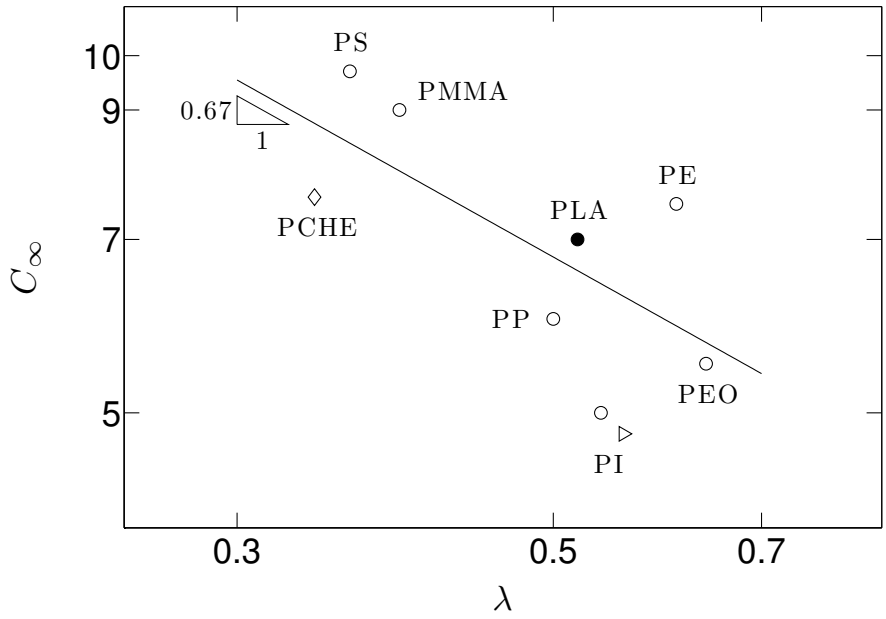

Figure 2.1. Characteristic ratio (C_∞) vs. backbone bond aspect ratio (λ): (▷) 25 °C, (○) and (●) 140 °C, (◇) 160 °C. Least-squares regression did not include data at 25 °C and gave $m = -0.6724$, where $C_\infty \sim \lambda^m$. Smaller values of C_∞ (i.e. more flexible chains) tend to correspond to larger values of λ (i.e. "thinner" monomers). In the C_∞–λ space, the behavior of PLA is close to that of PP and PE.

2.5 Coil Packing Model

Both the local correlations between consecutive backbone bond vectors (C_∞) and the backbone bond geometry (λ) dictate the macroscopic properties of macromolecular chains, and they seem to be combined in about the right proportions[m] in the packing

[m] Another parameter that incorporates both C_∞ and λ is the aspect ratio of the Kuhn statistical segment, $\lambda_k \equiv b_k/r_b = (C_\infty \cdot \lambda)/K_{geom}$. However, the inverse correlation between C_∞ and λ renders λ_k almost independent of molecular characteristics[67].

length p defined by Witten et al.[16] and Fetters et al.[17] as the ratio of the volume occupied by the chain (V_{occ}) to its square size (R^2):

$$p \equiv \frac{M}{\rho N_{av} R^2} = \frac{\pi l}{C_\infty \lambda^2} \tag{2.4}$$

Therefore, the more flexible the chain is (i.e. the smaller its the persistence length l_p, hence C_∞) the larger its packing length p would be providing C_∞ and λ were uncorrelated or λ were kept constant. Smaller values of C_∞, however, tend to correspond to larger values of λ (Figure 2.1), i.e. "thinner" monomers. The net effect, considering that C_∞ and λ are almost inversely proportional and $p \sim (C_\infty \lambda^2)^{-1}$, is that a *decrease* in packing length correlates with a *decrease* in monomer "bulkiness" and an *increase* in chain flexibility. Tables 2.2–2.6 list the polymers by ascending p at the same temperature. We will refer to p as the Witten–Fetters packing length, as opposed to the equally valid definition proposed earlier by Helfand and Sapse[74] that is based on the radius of gyration[23,n], R_g. In 1994, Fetters and co-workers[17] examined a vast data set of melt chain dimensions (R^2/M, measured by SANS) and shear plateau moduli (G_N^0, measured by rheology), and they were able to demonstrate that the following simple correlation holds for linear flexible polymers:

---

[n] For Gaussian coils, R_g (the unperturbed mean-square mass-weighted distance of the monomers from their center of mass) and R (the unperturbed mean-square end-to-end distance) are related by[23] $R_g = (1/6)^{1/2} R$. It follows that the Helfand–Sapse packing length $p' = 6p$. Note that, in either definition, the packing length is independent of any particular convention (e.g. definition of molar mass between entanglements) and can be obtained directly from the experimentally measured chain dimension (through Eq. (2.4)) or shear plateau modulus (through Eq. (2.5)).

$$G_N^0 = \frac{4}{5}\frac{kT}{P_e^2 p^3} \tag{2.5}$$

with

$$P_e \equiv \frac{a^3}{V_{occ,e}} = \frac{a}{p} \tag{2.6}$$

where k is Boltzmann's constant, T is the absolute temperature, P_e is the average number of entanglement strands in a cube with side equal to the tube statistical segment length a, and $V_{occ,e}$ is the volume occupied by an entanglement strand.[20,22] Eq. (2.5) thus permits the computation of p from the measured linear viscoelastic behavior. In fact, while originally thought of as a weakly temperature-dependent parameter, a follow-up investigation[19] concluded that P_e is essentially temperature-independent. A more recent review on linear flexible polymers[20] gives P_e in the range ≈ 16.9–19.9 and, on average, equal to 18.4. The latest average value provided by Fetters and colleagues[20], $\tilde{P}_e = 20.6 \pm 8\% = P_e \cdot (4/5)^{-1/2}$, is based on the Ferry definition[42] of molar mass between entanglements, M_e^F ("entanglement spacing" in Ferry's terminology), as opposed to the Graessley–Fetters definition[17,35,75], M_e^G, which is used here and was originally adopted in their 1994 paper[17]. They are obtained through the shear plateau modulus G_N^0 as:

$$M_e^G \equiv \frac{4}{5} M_e^F \equiv \frac{4}{5}\frac{\rho RT}{G_N^0} \tag{2.7}$$

where $R = k \cdot N_{av}$ stands for the universal gas constant[o]. Incorrect or inconsistent use of these two definitions of entanglement molar mass has produced numerous errors in the literature (as explained by Larson et al.[35]). The underlying reason for the 4/5 prefactor in the definition of M_e^G is ascribed to conformational equilibration of the tube via longitudinal Rouse-like motions of the monomers. While regular, 3-D Rouse-like modes are prohibited at length scales $\approx a$, 1-D Rouse-like motions re-equilibrate chain density and allow entangled chains (as opposed to chemically crosslinked systems, for which M_e^F was originally introduced) to relax 1/5 of the stress that would otherwise contribute to the plateau modulus G_N^0.[35,36,42,44,45] Accordingly, a is the root-mean-square end-to-end distance of a chain section of molar mass M_e^G (i.e. $a = \left(M_e^G / M_0\right)^{1/2} b$, from Eq. (2.2))[35,46], and $V_{occ,e} = M_e^G / \rho N_{av}$.

The development of Fetters and co-workers, motivated by the tube idea and originated by the proposals of Ronca[12], Lin[13], and Kavassalis and Noolandi[14,15], is usually referred to as "the packing theory of G_N^0" or "the coil packing model". P_e is in fact equivalent to the parameter n_t independently defined by Ronca[12] and Lin[13], and its seemingly constant value is now known as the "overlap criterion for entanglements" in polymer melts[20,22]. Assuming that an entanglement strand of molar mass M_e^G and radius of gyration $R_{g,e}$

---

[o] Although the universal gas constant and the polymer unperturbed end-to-end distance bear the same symbol, the temperature T always immediately follows the former, thus avoiding any confusion.

pervades a spherical volume $V_{\mathrm{per,e}} = (4\pi/3)R_{\mathrm{g,e}}^3$, P_e can be used to calculate the average number of pairwise contacts required to result in one entanglement, $n_\mathrm{e} - 1$, where n_e is the "critical packing ratio" defined as:

$$n_\mathrm{e} \equiv \frac{V_{\mathrm{per,e}}}{V_{\mathrm{occ,e}}} = \frac{4\pi}{3}\frac{1}{6^{3/2}}P_\mathrm{e} \tag{2.8}$$

in keeping with the central concept of the packing model that a strand becomes entangled when the ratio of its pervaded over occupied volume reaches a critical value.[17,45,67] Although the derivation given in Fetters et al.[17] was based on the hypothesis that $n_\mathrm{e} = 2$, it seems that entanglement coupling in flexible polymers corresponds to a slightly larger number of pairwise contacts. $P_\mathrm{e} = 18.4 \pm 8\%$ implies n_e in the range $\approx$ 4.8–5.7 and, on average, $n_\mathrm{e} = 5.3$. This value of n_e can thus be considered as an alternative, but equivalent overlap criterion for topological constraints. Since Eq. (2.5) successfully links melt chain dimensions to macroscopic behavior, it allows for the calculation of fundamental viscoelastic properties such as G_N^0, the entanglement molar mass and the tube SSL based on polymer structure. Therefore, the coil packing model is extremely useful for predicting viscoelastic properties of not yet synthesized polymers[17] as well as for judging the trustworthiness of experimental measurements[20]. In the latter case, if both the coil size (expressed as R^2/M or C_∞) and the shear plateau modulus (G_N^0) have been experimentally measured, P_e and n_e can be calculated through Eqs. (2.3)–(2.5) and (2.8): strong deviations ($\gg 8\%$) from the "universal values" 18.4 and 5.3 will signal a lack of accuracy in either measurement (or both). When the validity of an experiment is brought into

question or experimental data is unavailable, Eqs. (2.3)–(2.5) with $P_e = 18.4$ can be used to predict C_∞ (or R^2/M) from G_N^0, and vice versa, with reasonable accuracy. This will be discussed in the next section.

2.6 Shear Plateau Modulus of Undiluted PLA

As it turns out, disagreement in the literature on PLA is not limited to its unperturbed dimensions but encompasses also the experimentally measured (bulk) G_N^0. An accurate determination of the plateau modulus from the measured dynamic moduli is not trivial, and several methods have been proposed over the years (Chapter 4, §4.3.2.III-a).[36,42,45,76-79] Additionally, G_N^0 is weakly dependent on temperature[45], polymer molar mass (as a result of primitive path fluctuations and constraint release[35,44]) and, for PLA, it may in principle also depend on stereoisomers composition. Grijpma et al.[53] calculated the molar mass between entanglements for isotactic PLLA (0% D, $M_w > 300{\cdot}10^3$ g/mol) from the shear moduli at 200 °C, by means of an empirical correlation previously proposed by Wu[70]. Based on their result, G_N^0(200 °C) = 0.41 MPa. A similar value was later obtained by Ren et al.[54], who studied amorphous polylactide (25% D) of varying molar mass (M_w = 7–$120{\cdot}10^3$ g/mol) and by averaging the experimental values of the storage modulus at 100 °C inferred G_N^0(100 °C) = 0.51 MPa. In 2005, Dorgan et al.[4] investigated a sample set that included several stereoisomers compositions (0–20–50–100% D) and a wide range of chain lengths, M_w = 5–$1500{\cdot}10^3$ g/mol. In their work, samples were stabilized against

thermal degradation and the plateau modulus was obtained through integration of the relaxation spectrum and the loss modulus following the procedure described by Ferry[42]. In stark contrast to earlier studies, they reported G_N^0(180 °C) = 1.00 ± 0.2 MPa, independent of stereoisomeric composition (which explains the agreement between the results of Grijpma et al.[53], 0% D, and Ren et al.[54], 25% D). A twofold difference in G_N^0 (hence, in the entanglement molar mass) has a large effect on the predictions of the rheology of slowly relaxing systems such as branched polymers or microphase-segregated block copolymers. Therefore, it is imperative that the correct value of G_N^0 be used in the calculations of tube model parameters.

2.6.1 Self-Consistency between Melt Chain Dimensions and Viscoelastic Properties

Fortunately, using Eqs. (2.3)–(2.5) and (2.8) it is straightforward to show that the (bulk) shear plateau modulus measured by Dorgan et al.[4] is in nice agreement with the unperturbed chain dimension measured by Anderson and Hillmyer[39], and it is thus the correct value for PLA. Neglecting the weak temperature dependence of G_N^0 over the span of 40 degrees, we can safely assume G_N^0(140 °C) ≃ 1.00 MPa. From the results of Anderson and Hillmyer[39], we calculated C_∞(140 °C) = 7.0. The consequential values of P_e = 18.3 and n_e = 5.2 (Table 2.4) are typical of a linear flexible polymer and very close to the "universal values". Furthermore, we can use the packing theory to predict G_N^0 from

the SANS-measured C_∞ and, vice versa, to calculate C_∞ from the rheology-measured G_N^0. Application of Eqs. (2.3)–(2.5) (using the average value $P_e = 18.4$) gave $G_{N,SANS}^0$(140 °C) = 0.99 MPa and $C_{\infty,RHEO}$(140 °C) = 7.1, respectively to within 1% and 0.4% of the experimental results. We interpret these calculations as being indicative of the *flexible* nature of PLA and undoubtedly in favor of the experimental investigations conducted by Anderson and Hillmyer[39] and Dorgan et al.[4]. Similar self-consistency between melt chain dimensions and viscoelastic properties was found for all the other polymers considered here, as shown in Table 2.4.

In light of the highly mystifying and divisive literature on PLA, it is thus instructive to compute the consequences of accepting different experimental values of either C_∞ or G_N^0. If a slightly higher C_∞ were accepted, in line with the widespread belief of the stiffer character of PLA chains[2,53-55], for instance C'_∞(140 °C) = 8.0, then the packing theory would give P'_e = 22.4, n'_e = 6.4, and $G_N^{\emptyset}$(140 °C) = 1.48 MPa (48% higher than what was measured by Dorgan et al.[4] at 180 °C, and higher than any PLA plateau modulus ever reported). If a slightly lower G_N^0 were accepted, as the studies of Grijpma et al.[53] and Ren et al.[54] would suggest, for example $G_N^{\emptyset}$(140 °C) = 0.50 MPa, then the packing theory would give P'_e = 25.9, n'_e = 7.4, and C'_∞(140 °C) = 5.6 (20% lower than what the measurements of Anderson and Hillmyer[39] imply at 140 °C, and lower than any PLA characteristic ratio ever reported at this temperature). Therefore, not only would different experimental estimates of either C_∞ or G_N^0 be mutually inconsistent but, most

importantly, the associated values of P_e ($\gg$ 19.9) and n_e ($\gg$ 5.7) would classify PLA as "distinct from the hundreds of linear polymer chains to which the packing model has been applied" (quoted from Dorgan et al.[4]).

Table 2.4. Coil packing model critical parameters P_e and n_e, and self-consistency between the melt chain dimensions and shear plateau moduli shown in Table 2.3.

Polymer	T [°C]	P_e	n_e	$G^0_{N,SANS} - G^0_N$ [%]	$C_{\infty,RHEO} - C_\infty$ [%]
PE	140	19.0	5.4	+ 7	– 2
PEO	140	17.4	5.0	–11	+ 4
PLA	140	18.3	5.2	– 1	+ 0.4
a-PP	140	17.6	5.0	– 9	+ 3
7% 3,4-PI	25	17.8	5.1	– 6	+ 2
7% 3,4-PI	140	18.3	5.2	– 1	+ 0.4
a-PMMA	140	18.5	5.3	+ 2	– 0.5
a-PS	140	19.2	5.5	+ 9	– 3
a-PCHE	160	18.4	5.2	0	0
"Universal values"		18.4	5.3		

2.7 Scaling Behavior

So far, we have examined literature results on polylactide unperturbed chain dimensions and bulk G^0_N, in terms of Wu's criterion for the onset of brittle behavior and in the framework of the coil packing model. This has enabled us to identify the experimental measurements of R^2/M and G^0_N that are self-consistent, and a set of

parameters $\{C_\infty, \lambda\}$ that adequately defines molecular characteristics. We are now in a position to discuss how the polymer structure of PLA affects its macroscopic properties in the melt. To this end, we first need to consider the scaling behavior of the characteristic lengths and tube model parameters in terms of C_∞ and λ. The scaling behavior of the packing length was examined in §2.5, and followed directly from the definition of p. A similar scaling analysis for other basic characteristic lengths yields:

$$\begin{aligned} R &\sim b \sim C_\infty^{1/2} \\ b_k &\sim l_p \sim C_\infty \\ a &\sim p \sim \frac{1}{C_\infty \lambda^2} \end{aligned} \tag{2.9}$$

while molar masses scale as:

$$\begin{aligned} M &\sim M_0 \sim \frac{1}{\lambda^2} \\ M_{0,k} &\sim \frac{C_\infty}{\lambda^2} \\ M_e^G &\sim \frac{1}{C_\infty^3 \lambda^6} \end{aligned} \tag{2.10}$$

where $M_{0,k} = M \big/ N_k = \left(C_\infty \big/ jK_{geom}^2 \right) M_0$ is the molar mass of a Kuhn unit[35,36]. The C_∞- and λ- dependence of other characteristic lengths and parameters can be obtained through Eqs. (2.9) and (2.10). In particular, we are interested in how the polymer structure dictates the entanglement molar mass (M_e^G) and the maximum stretch ratio of an entanglement strand ($\lambda_{max,e}$).

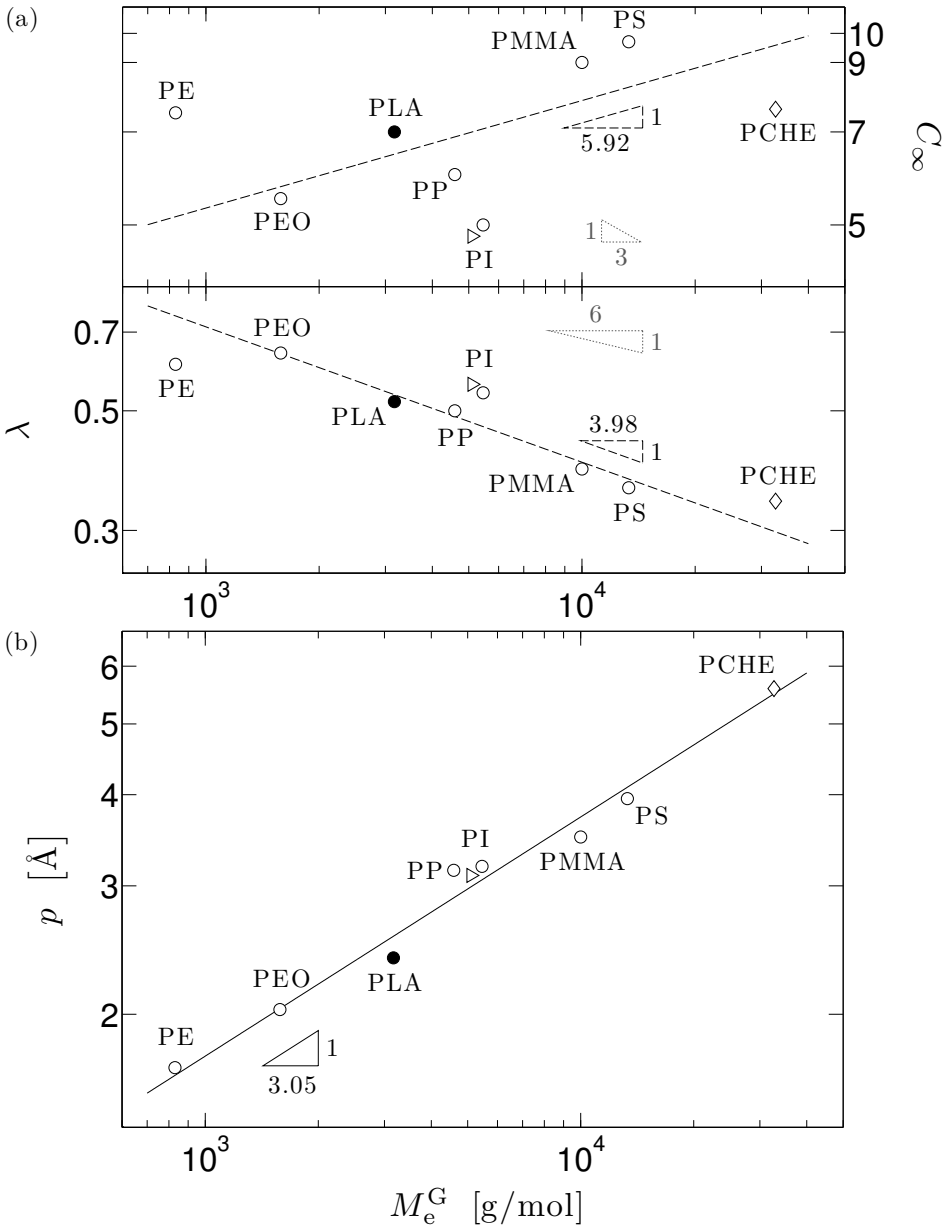

Figure 2.2. (a) Entanglement molar mass (M_e^G) vs. characteristic ratio (C_∞) and vs. backbone bond aspect ratio (λ). The slopes (5.92 and –3.98) were calculated based on the correlation $C_\infty \sim \lambda^m$ (Figure 2.1) and Eq. (2.10)c. In light gray is shown the scaling behavior that would be observed if C_∞ and λ were uncorrelated. (b) Entanglement molar mass (M_e^G) vs. packing length (p). Data refer to the following temperatures: (▷) 25 °C,

(○) and (●) 140 °C, (◇) 160 °C. Least-squares regression did not include data at 25 °C. The net effect is that a *decrease* in entanglement molar mass correlates with a *decrease* in packing length and an *increase* in chain flexibility. In the $p - M_e^G$ space, the behavior of PLA is close to that of PEO, PP, and PI.

2.7.1 Dependence of M_e^G on Molecular Characteristics

Entanglements are believed to stem from a collective topological restriction of neighbouring chains.[22] The packing model predicts $M_e^G \sim p^3 \sim C_\infty^{-3}\lambda^{-6}$ (Eqs. (2.9)c and (2.10)c), which indicates that a *decrease* in chain flexibility tends to *decrease* the entanglement molar mass. This effect can thus be intuitively explained by assuming that less flexible chains, which are less closely coiled ($R \sim C_\infty^{1/2}$, Eq. (2.9)a), interact more with one another: a shorter length is thereby necessary (all other factors being the same) for a topological restriction to arise. The entanglement molar mass, however, also depends on the backbone bond geometry through λ: a *decrease* in monomer "bulkiness" tends to *decrease* M_e^G. Both tendencies share the same origin, albeit their magnitudes differ. In the framework of the packing model, a chain section becomes entangled when the ratio of its pervaded over occupied volume reaches a critical value n_e (seemingly constant and equal to ≈ 5.3 – Table 2.4). Since the pervaded volume $V_{per} \sim (R^2/M)^{3/2}M^{3/2}$ (with the ratio R^2/M independent of M, for random coils), and the occupied volume $V_{occ} \sim M$, the packing ratio scales as:

$$\frac{V_{\text{per}}}{V_{\text{occ}}} \sim \left(C_\infty \lambda^2\right)^{3/2} M^{1/2} \tag{2.11}$$

where we have made use of Eqs. (2.9)a and (2.10)a. Therefore, if chain flexibility *decreases* (while keeping λ constant) or monomer "bulkiness" *decreases* (while keeping C_∞ constant) a shorter M is needed to reach the critical value $n_e \equiv V_{\text{per,e}}/V_{\text{occ,e}}$. Eq. (2.11) also explains the relative magnitudes of the C_∞- and λ- dependence of M_e^G.

The separate effects of C_∞ and λ on M_e^G are illustrated in Figure 2.2(a). In light gray is shown the scaling behavior ($M_e^G \sim C_\infty^{-3}$ and $M_e^G \sim \lambda^{-6}$) that would be observed if C_∞ and λ were uncorrelated. Indeed, if we limit our attention to the polymers having roughly the same λ – that is the dyads PE–PEO ($\lambda \approx 0.625$), PLA–PP ($\lambda \approx 0.51$), and PS–PCHE ($\lambda \approx 0.35$) – the predicted scaling $M_e^G \sim C_\infty^{-3}$ is approximately obeyed. On the other hand, if we only consider the polymers having roughly the same C_∞ – that is the triad PE–PLA–PCHE ($C_\infty \approx 7.4$), and the dyad PEO–PI ($C_\infty \approx 5.1$) – the entanglement molar mass scales almost as $M_e^G \sim \lambda^{-6}$. Owing to the C_∞–λ relationship shown in Figure 2.1, however, the theoretical trend is reversed for C_∞ ($M_e^G \sim C_\infty^{5.92}$) and attenuated for λ ($M_e^G \sim \lambda^{-3.98}$). As could have been anticipated from Eq. (2.10)c or (2.11), overall the effect of λ dominates and the largest entanglement molar masses (i.e. those of PCHE, PS, and PMMA) correspond to the smallest λ's (Figure 2.2(a)) and the largest p's (Figure 2.2(b)). The net effect is that a *decrease* in entanglement molar mass correlates with a *decrease* in packing length, a *decrease* in monomer "bulkiness", and an *increase* in chain flexibility.

This suggests that the small entanglement molar mass of PLA, M_e^G = 3170 g/mol, is dictated primarily by its relatively "thin" monomer (i.e. relatively large value of λ). In the $p - M_e^G$ space, the behavior of PLA is close to that of PEO, PP, and PI.

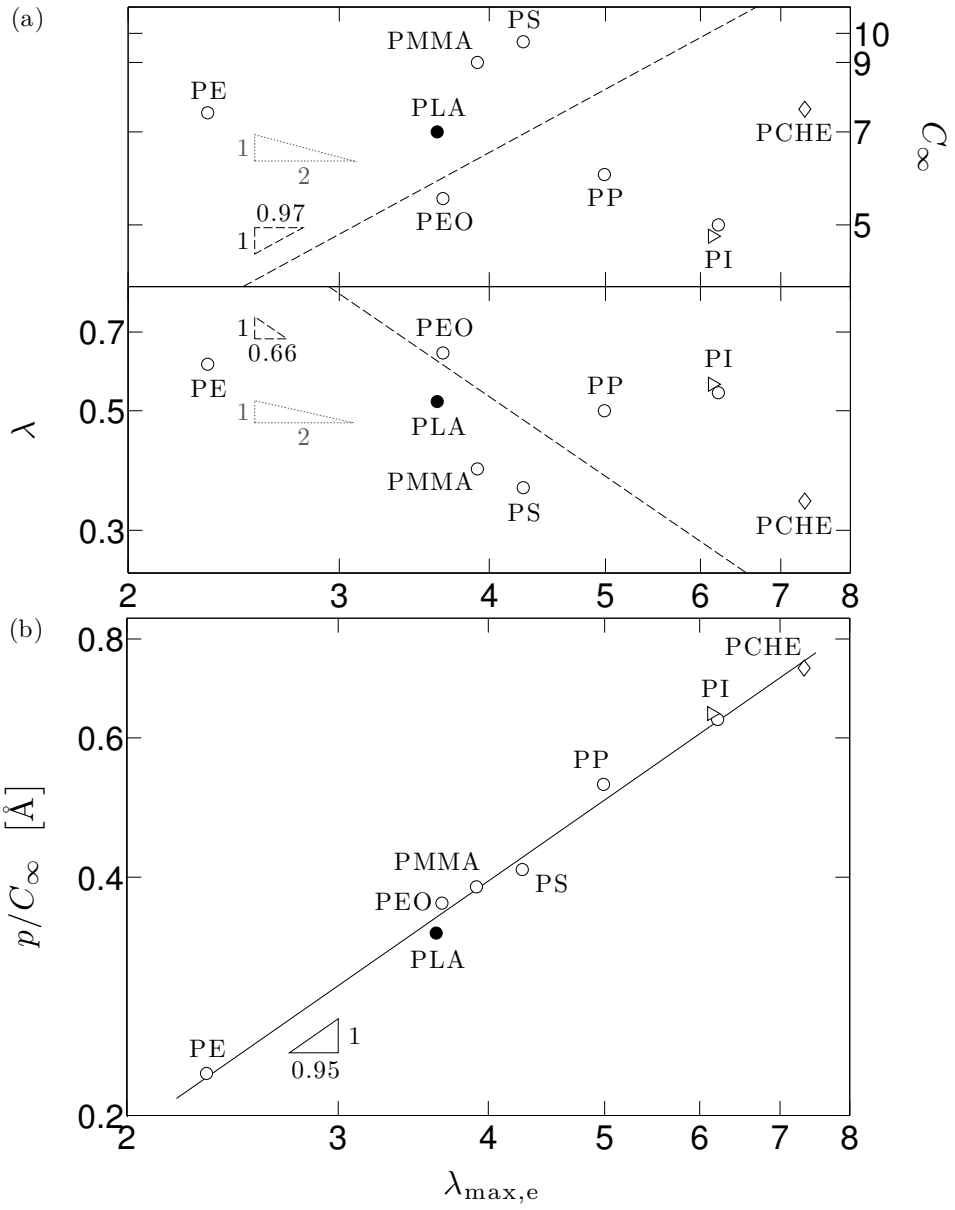

Figure 2.3. (a) Maximum stretch ratio of an entanglement strand ($\lambda_{max,e}$) vs. characteristic ratio (C_∞) and vs. backbone bond aspect ratio (λ). The slopes (0.97 and –0.66) were calculated based on the correlation $C_\infty \sim \lambda^m$ (Figure 2.1) and Eq. (2.12). In light gray is shown the scaling behavior that would be observed if C_∞ and λ were uncorrelated. (b) Maximum stretch ratio of an entanglement strand ($\lambda_{max,e}$) vs. packing length over characteristic ratio (p/C_∞). Data refer to the following temperatures: (▷) 25 °C, (○) and

(●) 140 °C, (◇) 160 °C. Least-squares regression did not include data at 25 °C. The net effect is that a *decrease* in the extensibility of an entanglement strand correlates with a *decrease* in p/C_∞ and, very roughly, with an *increase* in chain flexibility. In the p/C_∞–$\lambda_{max,e}$ space, the behavior of PLA is close to that of PEO, PMMA, and PS.

Table 2.5. Monomer-based SSL (b), Kuhn SSL (b_k), tube SSL (a), and maximum stretch ratio of an entanglement strand ($\lambda_{max,e}$) calculated using the values shown in Tables 2.2 and 2.3.

Polymer	*T* [°C]	*b* [nm]	b_k [nm]	*a* [nm]	$\lambda_{max,e}$
PE	140	0.593	1.385	3.22	2.33
PEO	140	0.591	0.966	3.54	3.66
PLA	140	0.659	1.207	4.37	3.62
a-PP	140	0.531	1.112	5.55	4.99
7% 3,4-PI	25	0.637	0.898	5.51	6.14
7% 3,4-PI	140	0.652	0.940	5.84	6.21
a-PMMA	140	0.649	1.661	6.49	3.91
a-PS	140	0.672	1.781	7.60	4.27
a-PCHE	160	0.597	1.403	10.28	7.33

2.7.2 Dependence of $\lambda_{max,e}$ on Molecular Characteristics

As discussed in §2.4, the brittle behavior of PLA in mechanical testing[53,57] was often attributed to his supposedly stiff character at room temperature[2,53-55]. In 2005, an alternative hypothesis was put forward by Dorgan et al.[4], who suggested that severe physical aging is the likely cause of the apparent rigidity of amorphous polylactide tested

a few tens of degrees below its glass transition. Since the unperturbed dimension of an amorphous, glassy polymer are known to control its brittle-ductile fracture behavior[31-33] and the effect of physical aging can be decoupled from chain parameters[32,33], the molecular characteristics of PLA (C_∞ and/or λ) may also be responsible for its brittleness. A tube model-related parameter that often determines the maximum extensibility of entangled polymer melts is the maximum stretch ratio of the tube statistical segment, $\lambda_{max,e}$. Indeed, the stress of rubber networks in various deformation modes seems to be accurately described[80-82] by the Edwards–Vilgis slip–link model[83,84] (Chapter 5, and Appendix H, §H.2.2), which attributes the maximum stretch of the network to that of the trapped entanglement strands therein. It is thus of interest to calculate the maximum stretch ratio of an entangled PLA strand, and to examine how $\lambda_{max,e}$ depends on polymer structure.

$\lambda_{max,e}$ is the ratio of the entanglement strand fully extended (contour) length (L_e) over its unperturbed root-mean-square end-to-end distance ($R_e = a$). Indicating with $N_e \equiv M_e^G / M_0$ and $N_{e,k} \equiv M_e^G / M_{0,k}$ the average number of chemical monomers and Kuhn segments (respectively) per entanglement strand, it follows from Eq. (2.2) that[35,46] $a = N_e^{1/2} b = N_{e,k}^{1/2} b_k$. From the definition of Kuhn chain, $L_e = N_{e,k} b_k$. Therefore:

$$\lambda_{max,e} = N_{e,k}^{1/2} = \frac{a}{b_k} \sim \frac{1}{C_\infty^2 \lambda^2} \sim \frac{p}{C_\infty} \tag{2.12}$$

where we have made use of Eqs. (2.9)b and (2.9)c. Table 2.5 summarizes the monomer-based SSL (b), the Kuhn SSL (b_k), the tube SSL (a), and the maximum stretch ratio of an

entanglement strand ($\lambda_{max,e}$) calculated using the values shown in Tables 2.2 and 2.3. For comparison, Anderson and Hillmyer[39] measured $b = (\sqrt{2}/2)\cdot 1.00 = 0.707$ nm for amorphous polylactide (28% *R*) at 30 °C (where the factor $\sqrt{2}/2$ converts the literature result, 1.00 nm, which is based on a C-6 repeating unit), in good agreement with our calculation. In fact, bearing in mind that PLA chains coil up more tightly with increasing temperature, our development implies $b = 0.710$ nm at 30 °C. The prediction of the packing model, $\lambda_{max,e} \sim C_\infty^{-2}\lambda^{-2}$, indicates that a *decrease* in chain flexibility or a *decrease* in monomer "bulkiness" tends to *decrease* $\lambda_{max,e}$. Both chain flexibility and monomer "bulkiness" play a role in determining the unperturbed size of an entangled strand ($a \sim 1/C_\infty\lambda^2$, Eq. (2.9)c): the less flexible the chain at constant λ or the "thinner" the monomer at constant C_∞, the smaller the molar mass required to reach the critical packing ratio (as described by Eq. (2.11)), hence the smaller a is. This is the same underlying mechanism that explains the C_∞- and λ- dependence of M_e^G. Chain flexibility, however, also affects $\lambda_{max,e}$ through the Kuhn length ($b_k \sim C_\infty$, Eq. (2.9)b). As a result, the strength of the C_∞- and λ- dependence of $\lambda_{max,e}$ is the same, as opposed to M_e^G for which λ is the dominant parameter.

The separate effects of C_∞ and λ on $\lambda_{max,e}$ are illustrated in Figure 2.3(a). In light gray is shown the scaling behavior ($\lambda_{max,e} \sim C_\infty^{-2}$ and $\lambda_{max,e} \sim \lambda^{-2}$) that would be observed if C_∞ and λ were uncorrelated. Limiting our attention to the polymers having roughly the same λ – that is the dyads PE–PEO ($\lambda \approx 0.625$), PLA–PP ($\lambda \approx 0.51$), and PS–PCHE ($\lambda \approx 0.35$)

the expected scaling $\lambda_{\max,e} \sim C_\infty^{-2}$ is approximately observed. Conversely, if we only consider the polymers having roughly the same C_∞ – that is the triad PE–PLA–PCHE ($C_\infty \approx 7.4$), and the dyad PEO–PI ($C_\infty \approx 5.1$) – the maximum stretch ratio of a tube segment scales almost as $\lambda_{\max,e} \sim \lambda^{-2}$. Yet, because $C_\infty \sim \lambda^m$ (Figure 2.1), the theoretical trend is again inverted for C_∞ ($\lambda_{\max,e} \sim C_\infty^{0.97}$) and weakened for λ ($\lambda_{\max,e} \sim \lambda^{-0.66}$). These $\lambda_{\max,e} - C_\infty$ and $\lambda_{\max,e} - \lambda$ overall correlations are poorer than the corresponding $M_e^G - C_\infty$ and $M_e^G - \lambda$ relationships previously examined (owing to the different C_∞- and λ- dependences of M_e^G and $\lambda_{\max,e}$, which heighten to different degrees the poor quality of the C_∞–λ correlation itself). As expected from Eq. (2.12), C_∞ and λ weigh equally upon $\lambda_{\max,e}$: the largest entanglement strand extensibilities correspond to either the most flexible chains with intermediate values of λ (PP and PI), or the "bulkiest" chain with a modest value of C_∞ (PCHE). The simultaneous influence of C_∞ and λ is captured by the combined dimensionless parameter p/C_∞, which is directly proportional to $\lambda_{\max,e}$ as shown in Figure 2.3(b). The net effect is that a *decrease* in the extensibility of an entanglement strand correlates with a *decrease* in p/C_∞ and, very roughly, with a *decrease* in monomer "bulkiness" and an *increase* in chain flexibility. The small extensibility of an entangled PLA strand, $\lambda_{\max,e} = 3.62$, is therefore dictated by its relatively "thin" monomer ($\lambda = 0.52$) coupled with its intermediate chain flexibility ($C_\infty = 7.0$). In the p/C_∞–$\lambda_{\max,e}$ space, the behavior of PLA is close to that of PEO, PMMA, and PS. This suggests that the

molecular characteristics of PLA (both C_∞ and λ) are responsible for its brittleness, in addition to a potential physical aging occurring at room temperature.

In §2.5, we discussed the cooperative nature of topological interactions and showed that, in entangled flexible polymers, each "locus of adherence" may be represented by an average of ≈ 5 neighbouring chains in pairwise contact. While this is undoubtedly an appealing visual interpretation of the entanglement coupling, it provides no information as to how long of a chain is required for the onset of such effect. Determination of the PLA critical molar mass for entanglement effect in viscosity (M_C) is thus the subject of the next section.

2.8 Critical Molar Mass for the Onset of Entanglement Coupling in Undiluted PLA

The Rouse–Bueche theory[47,85,86] correctly predicts the linear molar mass dependence of the steady-state zero-shear viscosity, i.e. $\eta_0 \sim M$, for "sufficiently" short chains. It is well known, however, that when M exceeds a critical (polymer-specific and T-dependent) value, M_C, the η_0–M relationship can be approximated by a power-law, $\eta_0 \sim M^\alpha$, with $\alpha > 1$.[42,85,87] The exponent α is not a universal constant, and although its value is often close to 3.4[88,89], linear flexible chains have been observed[36,45] to display α in the range 3.3–3.7.[p]

---

[p] When $M > M_C$, the M-dependence of η_0 can be explained by a combination of reptation (which predicts $\eta_0 \sim M^3$) and primitive path fluctuations (whose contribution to relaxation depends on the ratio M/M_e^G and becomes negligible for $M/M_e^G > \approx$ 100–1000).[45,88,89]

For a long time, this crossover molar mass was considered to be related to M_e^F by the approximate correlation $M_C \approx 2M_e^F$.[42,87,90] In 1999, however, Fetters and colleagues[18] demonstrated that the ratio M_C/M_e^F is not constant, but depends on the packing length of the polymer species. This represented a significant achievement of the packing theory. According to a later review on 16 linear flexible polymers[20], the dependence of M_C on the entanglement molar mass and Witten–Fetters packing length (expressed in Å) can be empirically described by:

$$\begin{aligned} M_C &= M_e^F (3.420)\, p^{-0.534} \\ &= M_e^G (4.275)\, p^{-0.534} \end{aligned} \tag{2.13}$$

Two fundamental considerations can be drawn from the above equation. First, because the ratio M_C/M_e decreases with increasing p (i.e. increasing monomer "bulkiness"), fewer topological interactions per chain are required to reach the crossover regime of entanglement-dominated dynamics. In other words, polymers with different p have a different degree of "entanglement efficiency".[18,q] Therefore, M_e alone (in either definition) is not sufficient to fully characterize the entanglement effects in polymer melts[18] (just like C_∞ is not sufficient to define their molecular characteristics). Perhaps more strikingly, this correlation predicts $M_C = M_e^F$ for $p \simeq 10$ Å (and $M_C = M_e^G$ for $p \simeq$

Therefore, the value of α depends on the range of molar masses over which the fit is made.

[q] This should not be confused with the seemingly constant values of P_e and n_e, which are a measure of the number of binary contacts corresponding to one entanglement and, for linear flexible polymers, do not depend on p.

15 Å), a behavior that has been partially verified experimentally in four polymers with large packing lengths (p = 9.8–11.5 Å)[20]. Since $M_C < M_e^G$ seems unlikely for any polymer, for p > 15 Å it is conceivable to assume that the relationship $M_C = M_e^G$ should hold.

M_C for undiluted PLA can thus be estimated through Eq. (2.13). Using the p value deduced (through Eq. (2.4)) from the SANS-measured coil size and shown in Table 2.3, as well as that obtained (through Eq. (2.5), with P_e = 18.4) from the rheology-measured G_N^0, we found M_C = 8510–8600 g/mol (at 140 °C). Analogous calculations were carried out for the other polymers, and are summarized in Table 2.6. Based on the Graessley–Fetters definition of entanglement molar mass, the onset of entanglement coupling in their respective melt states requires for instance ≈ 3.1 entanglements per chain for PE (smallest p), ≈ 2.7 for PLA, and ≈ 1.7 for *a*-PCHE (largest p). In terms of both M_e^G and M_C/M_e^G, the entanglement effects in PLA and PP melts are similar.

2.8.1 Comparison between Packing Model Predictions and Experimental Estimates of M_C

Comparison with experimental estimates of M_C is noteworthy. Table 2.6 contains literature values of M_C and the temperature T^* at which experiments were performed[18,20,54], generally different from the temperature T at which the packing model predictions have been calculated (with the only exception of PI at 25 °C). Hence, we first

need to address the T-dependence of M_C, which requires identifying the parameters and the scaling involved in the temperature behavior of M_e. We discussed earlier the experimental observations[17,18,40,68] that linked the change of M_e with temperature to the change in coil size. The observed behavior can be explained and accounted for in the framework of the packing model. From the definition of M_e^G, Eq. (2.7), the packing model correlation for G_N^0, Eq. (2.5), and the definition of packing length p, Eq. (2.4), the T-dependence of M_e^G is given by:

$$M_e^G \sim \frac{1}{\rho^\beta} \frac{1}{\left(R^2/M\right)^{\beta+1}} \tag{2.14}$$

where $\beta = 2$. Polymers with $\kappa < 0$ will decrease their unperturbed dimension with increasing temperature, thereby increasing their M_e. However, if $\kappa \gg 0$ (e.g. 75% 3,4-HPI, Table 2.1), the increase in coil size with increasing temperature can counteract the decrease in density and determine a reduction of the entanglement molar mass. None of the polymers considered here has a value of κ comparable to that of 75% 3,4-HPI, therefore their M_e is expected to increase with T. The entanglement molar mass of 7% 3,4-PI, for instance, experimentally increases – albeit slightly – from 5100 g/mol at 25 °C to 5460 g/mol at 140 °C (Table 2.3). The T-dependence of M_C can be obtained through Eqs. (2.13), (2.14), and (2.4), yielding:

$$M_C \sim \frac{1}{\rho^\gamma} \frac{1}{\left(R^2/M\right)^{\gamma+1}} \tag{2.15}$$

with $\gamma = 1.466$. The relative effect of chain dimension and density on M_C is similar to that described by Eq. (2.14), so the critical molar masses of PLA and the other 7 polymers are predicted to increase with increasing temperature. Table 2.6 includes the deviation between the packing model prediction $M_{C,THEORY}$ at T and the experimental measurement $M_{C,EXP}$ at T^*, $\Delta M_C \equiv (M_{C,THEORY} - M_{C,EXP})/M_{C,EXP}$, as well as $\Delta T \equiv T - T^*$. In light of the foregoing discussion, $\Delta M_C \cdot \Delta T < 0$ signals an inconsistency between the two estimates of M_C. Except for PEO and PLA, the theoretical predictions and the experimental values are consistent with each other – although to varying degrees. While for PI the two estimates at the same temperature almost coincide, the ΔM_C for PCHE seems a bit too high considering the magnitude of ΔT and that $\kappa \approx 0$ (Table 2.1). For PEO, a value lower than 4900 g/mol would be expected at 80 °C, as opposed to the experimental measurement[18] of 5870 g/mol. The deviation, however, is minor and it may be accounted for by a slight inaccuracy in the measured plateau modulus (as inferred from Table 2.4). Conversely, extreme caution must be exerted if one wishes to rely on the experimentally measured M_C for PLA. The critical molar mass of poly(D,L-lactide) at 100 °C is expected to be smaller than 8560 g/mol, as opposed to the experimental value of 16000 g/mol measured by Ren et al.[54]. This deviation – more than twofold, when compared at the same temperature – is significant. As discussed in §2.6, the same study[54] reported a value of G_N^0 two times smaller than both the theoretical prediction (based on SANS-measured unperturbed chain dimensions) and the experimental result obtained by Dorgan et al.[4] on PLA that had been properly stabilized against thermal degradation. The high self-consistency between the

PLA shear plateau modulus measured by Dorgan et al.[4] and the PLA unperturbed chain dimension measured by Anderson and Hillmyer[39] (Table 2.4) suggests that this large discrepancy is due to an inaccurate experimental determination of M_C. Bearing in mind the earlier analysis of the PLA literature, it is hardly surprising the extent to which experimental estimates of $M_{C,PLA}$ can be erroneous, potentially leading to severe misinterpretations of the behavior of the material under investigation.

Table 2.6. Critical molar mass for entanglement effect in viscosity: experimental value ($M_{C,EXP}$), packing model prediction ($M_{C,THEORY}$), and "entanglement efficiency" ($M_{C,THEORY}/M_e^G$).

Polymer	T^* [°C]	$M_{C,EXP}$ [g/mol]	T [°C]	$M_{C,THEORY}$ [g/mol]	ΔM_C [%]	ΔT [deg]	$M_{C,THEORY}/M_e^G$
PE	170	3480 [a]	140	2600	– 25	– 30	3.1
PEO	80	5870 [a]	140	4900	– 17	+ 60	3.1
PLA	100	*16000* [b]	140	8560	– 47	+ 40	2.7
a-PP			140	11130			2.4
7% 3,4-PI	25	13100 [c]	25	12330	– 6	0	2.4
7% 3,4-PI			140	12630			2.3
a-PMMA	217	29500 [a]	140	21730	– 26	– 77	2.2
a-PS	217	31200 [a]	140	26150	– 16	– 77	2.0
a-PCHE	180	80000 [d]	160	55820	– 30	– 20	1.7

a) Tabulated in Fetters et al.[18].

b) Measured by Ren et al.[54] – likely inaccurate.

c) Tabulated in Fetters et al.[20].

d) Tabulated in Fetters et al.[20] – based on unpublished results.

2.9 Conclusions

A scrutiny of the literature on poly(D,L-lactide) (PLA) unperturbed chain dimensions[2,39,52-56] and viscoelastic parameters[4,53,54], examined in the framework of the coil packing model for linear flexible polymers[12-20], revealed experimental estimates that are inaccurate and mutually inconsistent. Measurements from dilute solutions usually overestimated the PLA coil size (hence, its chain stiffness)[2,52-54], while approximate empirical correlations or PLA samples not stabilized against thermal degradation resulted in inaccurate (i.e. too low) estimates[53,54] of the undiluted PLA shear plateau modulus G_N^0. For apparently the same reasons, its critical molar mass for entanglement effect in viscosity was overestimated.[54] Self-consistency between melt chain dimensions and viscoelastic parameters is achieved through the SANS-based coil size measured by Anderson and Hillmyer[39] in 2004 and the shear plateau modulus determined by Dorgan et al.[4] in 2005. The consequential values of P_e = 18.3 (average no. of entanglement strands in a cube with side equal to the tube statistical segment length)[12,13] and n_e = 5.2 (average no. of chains in pairwise contact required to result in one entanglement)[17,45,67] are typical of a linear *flexible* polymer and very close to the "universal values" (18.4 and 5.3, respectively)[20].

In the melt state (140 °C), PLA fails Wu's criterion for the onset of brittle behavior (i.e. fracture by crazing)[32,33], having a characteristic ratio C_∞ = 7.0 and entanglement density G_N^0/RT = 0.29 mmol/cm^3. Considering the temperature dependence of the PLA

unperturbed size, the entanglement density remains higher then Wu's threshold (≈ 0.15 mmol/cm^3) also *below* its glass transition ($T_g \approx 55$ °C).

Following the analysis of Graessley and Edwards[73] and Heymans[67], we have considered the PLA backbone bond aspect ratio λ as the additional, more local measure of chain dimensions needed to define molecular characteristics. Based on the set of parameters $\{C_\infty, \lambda\}$ and the scaling behavior predicted by the coil packing model, we have compared amorphous polylactide at 140 °C with 7 linear flexible polymers. The comparison was conducted at the same temperature – i.e. with polyethylene (PE), poly(ethylene oxide) (PEO), atactic polypropylene (*a*-PP), polyisoprene with a 7% 3,4 microstructure (7% 3,4-PI), atactic poly(methyl)methacrylate (*a*-PMMA), and atactic polystyrene (*a*-PS) – at a temperature slightly higher (160 °C) – i.e. with atactic poly(cyclohexyl)ethylene (*a*-PCHE) – and at approximately iso-free volume conditions – i.e. with 7% 3,4-PI. In particular, we have examined how the polymer structure affects macroscopic properties in the melt: namely, the entanglement molar mass (M_e^G, according to the Graessley–Fetters definition[17,35,75]), the maximum stretch ratio of an entanglement strand ($\lambda_{max,e}$), and the critical molar mass for entanglement effect in viscosity (M_C).

As first noted by Heymans[67], smaller values of C_∞ tend to correspond to larger values of λ, i.e. "thinner" monomers. This causes a *decrease* in the Witten–Fetters packing length[16,17] p to correlate with a *decrease* in monomer "bulkiness" and an *increase* in chain flexibility. Evaluated at approximately iso-free volume conditions, PLA and 7% 3,4-PI show a substantial difference in C_∞ but similar values of λ. In the C_∞–λ space, the

behavior of PLA is close to that of *a*-PP and PE. Owing to the C_∞–λ correlation and the scaling of the coil packing model, λ is the dominant parameter for the entanglement molar mass. The small entanglement molar mass of PLA, M_e^G = 3170 g/mol, is therefore dictated primarily by its relatively "thin" monomer (λ = 0.52). In the $p - M_e^G$ space, the behavior of PLA is close to that of PEO, *a*-PP, and 7% 3,4-PI.

C_∞ and λ weigh equally upon $\lambda_{max,e}$, and their simultaneous influence can be captured by the combined dimensionless parameter p/C_∞. The small extensibility of an entangled PLA strand, $\lambda_{max,e}$ = 3.62, can thus be attributed to its relatively "thin" monomer coupled with its intermediate chain flexibility. In the p/C_∞–$\lambda_{max,e}$ space, the behavior of PLA is close to that of PEO, *a*-PMMA, and *a*-PS. This implies that the molecular characteristics of PLA (both C_∞ and λ) are responsible for its brittleness[53,57] during mechanical testing. The potentially severe physical aging occurring at room temperature, suggested by Dorgan et al.[4] in 2005, may also play a role.

The coil packing model, based on the unperturbed coil size measured by Anderson and Hillmyer[39] and the shear plateau modulus measured by Dorgan et al.[4], predicts[20] M_C = 8560 g/mol for PLA at 140 °C. In terms of both M_e^G and "entanglement efficiency"[18] M_C/M_e^G, the entanglement effects in PLA and PP melts are similar.

Overall, PLA is more similar to fairly flexible polymers such as PEO and *a*-PP, rather than the relatively stiffer *a*-PMMA and *a*-PS (which were classified as brittle by Wu[32,33] and satisfy his criterion also in the melt state). Contrary to the widespread belief that

amorphous polylactide must be intrinsically stiff[2,53-55], the coil packing model and accurate experimental measurements undoubtedly support the *flexible* nature of PLA.

Chapter 3

Linear Extensional Behavior of A–B–A Thermoplastic Elastomers well below $T_{g,A}$: Characteristic Length Scales, Rouse and Arm Retraction Dynamics

At service temperatures ($T_{g,B} < T < T_{g,A}$), A–B–A thermoplastic elastomers (TPEs) behave similarly to filled (and often entangled) B-rich rubbers since B block ends are anchored on rigid A domains. Therefore, their linear viscoelastic response is dominated by chain mobility of the B block rather than by microstructural order. This chapter deals with the linear behavior of an undiluted A–B–A TPE subjected to uniaxial extension. The analysis herein is independent from the specific choice of the constituent blocks and thus applies to any microphase-segregated thermoplastic elastomer of the A–B–A type. Characteristic length scales and tube model parameters governing the physical properties of the material are determined, and the role of the glassy A domains on the entangled rubbery B network is examined. Thermo-rheological complexity, observed near and below $T_{g,A}$, is attributed to augmented motional freedom of the B block ends at the corresponding A/B interfaces. This hypothesis is in harmony with the theoretical treatment of thermo-rheological complexity for two-phase materials developed by Fesko and Tschoegl, and with literature studies on poly(styrene–*b*–isoprene–*b*–styrene) systems. In a limited range of temperature and frequency, the shift behavior is dominated by the B-rich matrix and simple time-temperature superposition applies. Under these conditions, all contributions to the measured viscoelastic properties involve a single monomeric friction coefficient,

and the temperature dependence of the time-scale shift factor follows the WLF equation. When the magnitude of the steepness index is taken into account, the shift behavior of the triblock is analogous to the response measured for pure B melts. This result collides with the early findings of Fesko and Tschoegl, and suggests that perhaps significantly different steepness indices were involved in their comparison. Using the nonlinear regression with regularization technique developed by Honerkamp and Weese, we calculate the continuous relaxation spectrum from the time-temperature superposed dynamic moduli. Building upon the procedure proposed by Ferry and co-workers for entangled and unfilled polymer melts, we show how the Rouse–Bueche theory can be applied to a filled system to extract the matrix monomeric friction coefficient from the linear behavior in the rubber-glass transition region, and to estimate the size of Gaussian submolecules. The length scale defining the Gaussian submolecules is of particular importance in polymer physics, being relevant to both unentangled and entangled macromolecules. The characteristic Rouse dimensions of the B block are in good agreement with estimates based on the Kratky–Porod worm-like chain model. The macroscopic response is thus connected to the chemical and topological structure and the A–B–A dynamics fully resolved over a wide range of time and length scales. Stress relaxation beyond the path equilibration time is qualitatively and quantitatively compatible with dynamically undiluted arm retraction dynamics. Consistently with the microstructure inferred from thermal analysis (DSC and isochronal viscoelastic measurements), we attribute this low-frequency behavior to star-like motion of single-free-end-type midblocks, i.e. the entangled dangling structures of the material originating from the fraction of triblock chains having one end residing outside A domains. Alternatively, this could also be explained by the presence of diblock impurities. This finding represents, to the best of our knowledge, the first compelling evidence of star-like relaxation in pure A–B–A triblocks. By employing tube models and rubber elasticity theories, suitably modified to account for microphase-segregation, we model the linear elastic behavior across the rubbery plateau and up to the entanglement time. This allows us to estimate the filler effect and aspect

ratio of the glassy A domains, the distribution of midblock conformations, and the relative contribution of physical endlinks and entanglements to the pseudo-equilibrium modulus. In addition, we obtain a simple analytical expression relating the Langley trapping factor with the fraction of entangled and unentangled dangling structures of the material. The effect of microphase-segregation on topological constraints is also discussed in the framework of high-functionality chemically endlinked networks as modeled by the theory developed by Miller and Macosko. Relating the linear behavior of undiluted A–B–A triblocks to molecular parameters is a prerequisite for designing associated TPE-based systems that can exhibit the desired linear and nonlinear rheological properties. Matrix dilution and arm retraction dynamics emerge as powerful tools that can tune the ultimate properties of triblock- and multiblock-type networks, whereas the contribution of the microstructure (for cubic phases) is expected to be negligible compared to the endlink and entanglement contributions.

3.1 Introduction

3.1.1 Thermoplastic Elastomers

Thermoplastic elastomers (TPEs) combine the flexibility and resilience of vulcanized rubbers with the processing properties of thermoplastics. At service temperatures, most TPEs are biphasic systems (macrophase-separated or microphase-segregated) due to thermodynamic incompatibility of the two structural components: a soft, amorphous, polymer (B) with a low glass transition temperature (T_g), and a hard polymer (A) with high T_g (or crystal melting point, T_m) whose discrete domains behave as thermo-reversible physical crosslinks. Hence, their final properties are influenced by the resulting interface and stem from the characteristics of the individual polymers that constitute the phases.

Block copolymers represent the major class of TPEs. In this class, linear triblock and multiblock copolymers of the A–B–A and $(A–B)_n$ type (with $n \geq 2$) are the most common molecular architectures, and the two structural units are covalently bonded together with both ends of the elastomeric polymer B confined to the interface with hard domains of the thermoplastic polymer A.[91-93]

3.1.2 Block Copolymer TPEs

In block copolymer TPEs, covalent bonds restrict phase separation to mesoscopic length scales (5–100 nm) as thermodynamic incompatibility drives polymer chains to self-assemble into A-rich and B-rich domains capable of forming periodically ordered microstructures at length scales comparable to chain dimensions (short-range order).[94-96] Gibbs free energy optimization is the basic physical principal governing block copolymer phase behavior, underlying the selection of the equilibrium domain size (or, equivalently, the interfacial area per molecule) under the constraint of uniform density (caused by short-range hard-core repulsions). Interfacial energy (*contact enthalpy*) drives local segregation of A and B blocks, and the tendency to develop a uniform interfacial curvature. The consequential stretching energy (*loss in conformational entropy*) opposes segregation, and lies in favor of uniform domain thickness. In compositionally asymmetric block copolymers, the balance of stretching energies between A and B blocks determines the development of a spontaneous curvature towards the minority

domain.[25,97,a] Consequently, block copolymer phase behavior is predominantly determined by three experimentally accessible parameters: the overall *degree of polymerization N*, the magnitude of the Flory-Huggins segment-segment *interaction parameter* χ, and the composition expressed as volume fraction f_A of type-A repeating units. Since the enthalpic and entropic contributions to the Gibbs free energy density scale as χ and N^{-1}, respectively, it is the product χN ("*incompatibility degree*") that controls the state of segregation.[96] For $\chi N \ll 1$, a block copolymer melt is in a disordered, homogeneous state, and the individual chains are in their ideal coiled conformations. With increasing χN, chains become progressively extended from their unperturbed Gaussian dimensions.[94,98] In the limit $\chi N > \approx 100$ (strong segregation regime, SSR)[99], highly stretched chains (in a coarse-grained sense)[97] segregate into nearly pure A and B microdomains with well-defined narrow interfaces and whose characteristic dimensions scale as[94] $d \sim N^{2/3}$. The state of segregation (minimum free energy) is also sensitive to a difference in statistical segment lengths (SSL) (i.e. conformational asymmetry)[24,25], and composition fluctuations become relevant near the order-disorder transition (ODT)[94,95].

When quenched below the ODT in absence of any hydrodynamic or electromagnetic bias field (or prepared by solvent casting), a disordered block copolymer melt will nucleate and grow ordered microdomains randomly without a preferential direction.[95,98] In this process of quiescent self-assembly, microdomains propagate until impingement,

---

[a] A spontaneous curvature is also produced in compositionally symmetric, but conformationally asymmetric block copolymers.[25]

leading to *short-range order* within the individual grains (similar to that found in liquid crystals and surfactant systems) and a *grain structure* much like a polycrystalline material.[100,101] Since typical grain sizes fall in the range[102] 1–10 μm, a microphase-segregated block copolymer will usually exhibit isotropic properties at macroscopic length scales (> 1 mm). Accordingly, block copolymer TPEs can develop a structural hierarchy. As in homopolymer melts, the local chemical microstructure of the blocks is relevant at length scales comparable to the statistical segment lengths of the constituent polymers ($b \approx 1$ nm). In addition, microdomains have characteristic lengths (size and spacing) of order the radii of gyration of the A and B blocks ($R_g \approx 5$–50 nm). When present, supermolecular structures (such as grains, grain boundaries, and isolated line defects) provide another level of architectural order at even larger length scales (≥ 1 μm). A global minimum free energy state is reached when a multi-grain (polycrystalline) sample is macroscopically oriented (*long-range order*, i.e. anisotropy).[95] Therefore, block copolymer TPEs are characterized by fluid-like disorder on the molecular scale and the potential of higher degrees of order at larger length scales.[96]

Above the glass transition of the higher T_g block and below the ODT, the free energy penalty in deforming the periodic unit cell makes linear viscoelastic properties of block copolymer TPEs highly sensitive to the underlying state of order (shape and long-range order of microdomains).[98,101,103-109] At temperatures relevant for end-use applications (i.e. below the glass transition of the hard phase) block copolymer TPEs tend to display a similar and broad power-law viscoelastic response[110-113] regardless of block type and

length (hence, state of segregation χN), microphase geometry and crystalline order (cylinders vs. spheres), presence of diblock impurities[100,113], sample preparation method (solvent casting vs. pressure molding), and processing history (macroscopically oriented vs. non-oriented samples). Because of the nature of the physical endlinks (hard phase domains), such systems may be regarded to as filled elastomeric networks[92,110,114] and chain mobility of the rubbery block, rather than the degree and perfection of structural order (both short- and long-range), is the main factor in determining their viscoelastic response at service temperatures.

3.1.3 Goals of This Study

In this study, we aim to investigate the linear uniaxial extensional behavior of an undiluted A–B–A thermoplastic elastomer at service temperatures ($T_{g,B} < T < T_{g,A}$). The role of the thermo-reversible physical endlinks (i.e. A microdomains) on the entangled rubbery B network will be examined, and characteristic length scales associated with the A–B–A dynamics will be determined. We are concerned with collective microdomain dynamics responsible for a broad power-law viscoelastic behavior, 1-D and 3-D Rouse modes across and within entanglement strands (respectively), as well as semi-flexible chain dynamics at length scales smaller than Gaussian submolecules. Time-temperature superposition will be applied and discussed in the framework of thermo-rheological complexity for two-phase and single-phase materials. For the first time in literature, we will show how the Rouse–Bueche theory[47,85,86] for unentangled melts can be applied to a

filled system to estimate the size of Gaussian submolecules, and to determine the monomeric friction coefficient of the elastomeric phase from the continuous (extensional) relaxation spectrum derived from time-temperature superposed dynamic moduli. The slow relaxation of the network towards a (pseudo) mechanical equilibrium will be associated with entangled dangling structures and compared, qualitatively and quantitatively, with arm retraction dynamics. Tube models and rubber elasticity theories will then be used to interpret the linear elastic behavior in the plateau and pseudo-equilibrium regions, and to estimate the distribution of midblock conformations.

Extensional deformations are relevant for the processing and often the end-use applications of thermoplastic elastomers. This study focuses on connecting the chemical and topological structure of the material with its viscoelastic properties in the linear regime. The analysis herein is independent from the specific choice of the constituent A and B blocks, and relevant at large deformations as well. Furthermore, it provides the benchmark for understanding the rheological response of more complex TPE architectures, in either bulk or solution. In this Chapter, the focus is on the linear behavior of undiluted A–B–A thermoplastic elastomers at temperatures where the A domains are glassy. Although briefly mentioned in §3.3.4.III-a, the linear behavior at a temperature approaching the T_g of A is the main topic of Chapter 4. Nonlinear extensional behavior and ultimate properties have also been extensively investigated, and the results will be presented in Chapter 5. Relating the linear and nonlinear behavior of undiluted A–B–A

triblocks to molecular parameters is the key to guide the design of associated TPE-based systems that can exhibit the desired rheological properties.

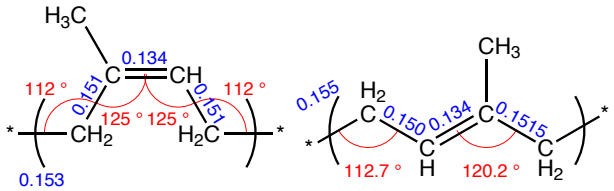

cis-1,4 polyisoprene *trans*-1,4 polyisoprene

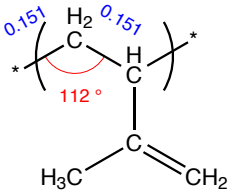

3,4 polyisoprene

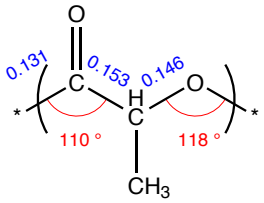

poly(D,L-lactide)

Figure 3.1. Configurational repeating units of the constituent blocks, complemented by relevant bond lengths (in nm) and angles.

3.2 Experimental Section

3.2.1 Material

The thermoplastic elastomer used in this study is an undiluted linear poly(D,L-lactide–*b*–isoprene–*b*–D,L-lactide) (L–I–L) triblock copolymer. Polylactide is an aliphatic linear polyester that can be derived from biorenewable resources such as corn. Owing to its biodegradability and biocompatibility[6-9], amorphous polylactide (PLA) has found numerous applications in the medical and pharmaceutical fields[10,11]. The unsaturated linkages on the polyisoprene (PI) backbone (Figure 3.1) render the midblock susceptible to thermal- and/or oxidative-induced chain cleavage, thus making L–I–L triblocks entirely degradable thermoplastic elastomers. As a result of the strong interactions (χ(25 °C) > 0.1) between lactide and isoprene segments[115,116,b] this TPE can microphase-segregate at relatively low molar masses (i.e. small values of N). Synthesis, molecular and morphological characterization, as well as differential scanning calorimetry (DSC) are discussed in Appendix A.

3.2.2 Experiments

Linear viscoelastic properties of the L–I–L triblock copolymer were measured using a TA Instruments RSA-G2 solids analyzer equipped with a film/fiber geometry clamp. The fixture was contained in an insulated oven, with a temperature control to within 0.1 °C,

---

[b] $\chi_{IL}(25\ °C) = 230/T - 0.38$, where T is in K.[116]

and nitrogen purge gas was used to prevent oxidative damage to the material. The rheological behavior was tested in small-amplitude oscillatory (uniaxial) extension. After loading, specimens were thermally equilibrated (5 min) and subjected to a small static axial force (well within the linear regime) to counteract sample buckling and ensure a state of tension throughout the gage length. The static axial force was always (about 30%) higher than the dynamic axial force, so that a state of tension was maintained for the whole duration of the measurements.

Critical strains for the onset of nonlinear viscoelastic behavior were determined by isochronal strain sweeps usually performed at three frequencies (1, 10, and 100 rad/s) for each temperature, which varied in the range from –100 to 70 °C. In these tests, the largest strain amplitude (3–6%)[c] was frequency-dependent and dictated by the maximum axial excursion of the drive motor (1.5 mm). During linear tests, the strain amplitude was varied (in the range 0.03–1%) based on temperature and frequency of oscillation, to adjust for sample stiffness (at low temperatures) and comply with the resolution of the normal force transducer (at low frequencies). Isochronal temperature ramps (discussed in Appendix A) were conducted at a frequency of 1 rad/s while heating and/or cooling at 0.2 °C/min from –100 to 80 °C, while isothermal frequency sweeps were run at different temperatures (–50, –40, –20, 0, and 37 °C) in the frequency range 0.001–500 rad/s.

---

[c] At the small elongations typical of the linear regime, true/Hencky (ε) and nominal/engineering (ε_N) strains are equivalent: $\varepsilon \equiv \ln(L/L_0) = \ln(\varepsilon_N + 1) \simeq \varepsilon_N$, for $\varepsilon_N \ll 1$, where L and L_0 stand for the deformed and undeformed length, respectively (cf. Appendix D, §D.1 and footnote [a]).

Extensional rheology was limited to 80 °C (about 25 degrees above the PLA glass transition) due to the incipient buckling of the polymer film. Numerous attempts were made to measure the linear viscoelastic behavior in shear, using a TA Instruments ARES-G2 rheometer equipped with 8-mm parallel plates (contained in an insulated oven thermally regulated by nitrogen purge gas), but lack of grip (with serrated plates) or a modified sample response (using cyanoacrylate "super glue" or double-sided scotch tape) prevented accurate measurements. As shown in Figure A.3 (Appendix A), even above the glass transition of the hard phase this material maintains a relatively high modulus (E'(80 °C, 1 rad/s) > 1 MPa), hence its solid-like character. Although not accurate in absolute terms, isochronal (1 rad/s) and isothermal (80 °C) shear measurements were used to check for relative variations in the storage ($G'(t)$) and loss ($G''(t)$) moduli upon application of a 0.5% strain amplitude for 2 hours. Similar measurements (1 rad/s, 0.5 % strain amplitude) were performed in extension at 37 °C (i.e. below the PLA glass transition) for 24 hours.

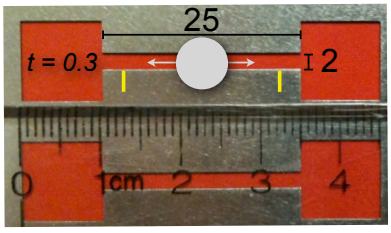

Figure 3.2. Sample specimen geometry (to scale).

3.2.3 Testing Specimens

Testing specimens were prepared by compression molding, to investigate rheological properties of the triblock copolymer under practical conditions. For technical applications, samples prepared by solution casting are not realistic and TPEs are usually manufactured via common processing routes like extrusion, and compression or injection molding.[92,93] For the triblock copolymer under study, the transition to a homogenous disordered state ($\chi N \ll 1$) was not experimentally accessible without inducing significant chain degradation (as will be discussed in §3.3.1, $T_{ODT} > 200$ °C). The material was thus microphase-segregated when processed, and potential domains orientation could have influenced the viscoelastic properties of the resulting specimens[109,111,117]. Furthermore, thermal stability of the polyisoprene block was of concern for prolonged air exposures at temperatures above 80 °C.[118] Therefore, a pressing temperature was chosen as a compromise between the need to effectively soften the compound above the PLA glass transition ($T_g \approx 55$ °C)[1,2,4] and the necessity to prevent appreciable polyisoprene degradation. The microphase-segregated structure and the limit imposed on the temperature resulted in the impossibility for this triblock to sufficiently flow and mix at the molecular level, so that each specimen had to be prepared from a single pellet of material. Using a stainless steel mold (0.3 mm thick) containing numerous dog-bone-like channels (Figure 3.2) allowed us to obtain a sufficient amount of testing specimens displaying a similar orientation of microdomains. The resulting hydrodynamic flow coarsely resembled that generated by channel die compression (shown to be equivalent to

planar extension by Khan and Larson[119]) in that the material was compressed in one direction (perpendicular to the mold), extended in the second direction (parallel to the channel length) and held at a constant width in the third direction (perpendicular to the channel length).

The pressing procedure was as follows. The rectangular mold (≈ 20 × 25 cm) was placed on a Teflon-coated sheet, and a polymer pellet (≈ 6.5 mm in diameter) was arranged at the center of each channel as schematically shown in Figure 3.2. The mass of each pellet (≈ 0.15 g) was roughly double the mass needed to completely fill up the dog-bone-like channel. An additional Teflon-coated sheet was positioned on top of the mold, which was then put in a hydraulic press with electrically heated plates previously brought to 100 °C. After allowing for thermal equilibrium to be attained (3 min), pressure (≈ 22 atm) was applied to squeeze the polymer for 3 min at 100 °C before cooling to 25 °C by passing water through the plates (≈ 7 min). The presence of the low modulus polyisoprene block imparted a slim tacky nature to the L–I–L triblock at room temperature. Release of the Teflon-coated sheets from the mold (without perturbing the specimens shape) was greatly facilitated by the use of 1,1-difluoroethane, a common refrigerant (listed as HFC-152a) contained as aerosol propellant in commercial dust remover spray cans. A mild use of this refrigerant, which has a boiling point of about –25 °C, provided the adequate cooling without inducing cracks that would have otherwise developed by approaching the glass transition of the polyisoprene phase ($T_g \approx -65$ °C)[120]. Specimens were then cut using a razor blade, and kept in a freezer until use. This allowed

us to produce similarly oriented, straight-sided strips with uniform cross-sectional area along the whole length.

An average thickness was assigned based on measurements near the ends and at the middle of the gage length, and the variation between films fell consistently in the range 0.38–0.48 mm. The yellow marks in Figure 3.2 delimit the material subjected to testing (20 mm long × 2 mm wide), while the two larger square shoulders (10 mm on a side) were used for grip and alignment. The testing cross-sectional area (≈ 0.8–1 mm^2) was designed to accommodate the wide range of sample stiffness ($E^*(\omega)$ ≈ 1–4000 MPa) over the explored frequency and temperature windows. By changing the mold geometry, and in particular the distance between the gage length and the shoulders, it was possible to determine that the tested specimens were not affected by local stress concentration and ends effects.

About 50 specimens were produced in one molding procedure, and at least 5 fresh samples were tested for each experimental condition. The resulting error bars (one standard deviation) in Figures A.3 (Appendix A), 3.3, and 3.4(a) are, for the dynamic moduli, smaller than or equal to the data point markers. The integrity of pressed and tested samples was confirmed by size exclusion chromatography (SEC).

Table 3.1. Molecular characteristics of the L–I–L triblock copolymer.

Sample	$M_{n,I}$ [a] [g/mol]	$M_{n,L}$ [a] [g/mol]	w_L [b]	f_L [c]	PDI [d]	*cis*-1,4 [e] [%]	*trans*-1,4 [e] [%]	3,4 [e] [%]
LIL50–12	49800	11650	0.32	0.25	1.05	46.5	46.5	7

a) Number-average molar masses of the individual PI and PLA blocks, determined by ^{1}H NMR spectroscopy.

b) Mass fraction of PLA.

c) Volume fraction of PLA at 25 °C, calculated using pure component densities.

d) Polydispersity index, determined by SEC.

e) Distribution of midblock configurational isomers, determined by infrared and ^{1}H NMR measurements.

3.3 Results and Discussion

3.3.1 Molecular Characterization and Microstructural Order

The molecular characterization showed that the L–I–L triblock copolymer, hereafter referred to as LIL50–12, is a model (i.e. PDI = M_w/M_n < 1.1) thermoplastic elastomer (Table 3.1), free of diblock or homopolymer contaminants. LIL50–12 has number-average molar mass M_n = 73100 g/mol and contains 32% by mass poly(D,L-lactide). Based on the corresponding homopolymer densities[20,69,71,d] at 25 °C, this compound

[d] For PI, ρ was calculated as $\rho(T) = 0.915 \cdot \exp(-6.6 \cdot 10^{-4} \cdot T)$ (where T is in °C), based on the density value tabulated in Fetters et al.[20] at 25 °C, and the thermal expansion coefficient given in Orwoll[69]. For PLA, ρ was calculated as $\rho(T) = 1.284 \cdot \exp(-7.7 \cdot 10^{-4} \cdot T)$ (where T is in °C), based on the measurements performed by Witzke[71].

contains 25% by volume PLA blocks[e]. The distribution of polyisoprene configurational isomers was determined to be 46.5% *cis*-1,4, 46.5% *trans*-1,4, and 7% 3,4 (Table 3.1), consistent with a predominant (≈ 93%) 1,4 head-to-tail addition characteristic of 1,3-dienes polymerizations in nonpolar solvents[37].

Small-angle X-ray scattering (SAXS) and transmission electron microscopy (TEM) analysis on specimens prepared by compression molding was compatible with a PI-rich matrix containing irregularly shaped PLA-rich microdomains lacking periodicity and long-range order (more details in Appendix A). Sample preparation and the inherent slow diffusivity of the long PI blocks hindered the attainment of an equilibrium morphological state, thus creating a kinetically trapped (metastable) microstructure.

As expected from the mixed-microstructures of the PI and PLA blocks, no evidence of crystallinity was found from the thermal (DSC) analysis. The material appeared to be completely amorphous, and exhibited two second-order-like transitions (fictive temperatures, T_f)[120] consistent with a biphasic system comprised of PI-rich ($T_{f,I}$ = –59.8 °C) and PLA-rich ($T_{f,L}$ = 50.7 °C) domains. Comparison of these block glass transitions with those that would be exhibited by the corresponding pure homopolymers suggests partial inclusion of PLA chains in the PI-rich microphase (i.e. despite the strong driving force towards segregation, a fraction of endblocks may still dwell outside PLA microdomains), and nearly pure PLA domains (more details in Appendix A).

---

[e] Assuming volumes additivity: $f_A = (w_A/\rho_A)/[(w_A/\rho_A) + (w_B/\rho_B)] = w_A \cdot (\rho/\rho_A) = 1 - f_B$, where the subscripts "A" and "B" refer to the constituent blocks of the copolymer.

In view of the large Flory-Huggins interaction parameter between lactide and isoprene segments[115,116,b] and the copolymer molar mass, we anticipated LIL50–12 to be strongly segregated ($\chi N > 100$). The "incompatibility degree" χN can be estimated by adopting a single statistical segment volume v_0 (which corresponds to using a single lattice size in the Flory-Huggins treatment), and calculating χ and N accordingly. To avoid confusion with the degree of polymerization N based on the monomers molar masses, the symbol $\hat{N}$ will be used here. More generally, when different definitions are possible, a hat will indicate quantities that are based on a common segment volume. Choosing v_0 = 110 Å^3 (geometric average of PI's and PLA's monomer volumes at 25 °C), and using the densities of the respective homopolymers, we calculate χ(25 °C) ≃ 0.39, $\hat{N}$(25 °C) = $M/(\rho N_{av} v_0)$ = 1114.5 (where M = 73100 g/mol and ρ(25 °C) = 0.990 g/cm^3 are the copolymer number-average molar mass and density, and N_{av} is Avogadro's number)[f], and $\chi\hat{N}$(25 °C) ≃ 436. For monodisperse, compositionally symmetric A–B–A triblock copolymers with degree of polymerization $\hat{N}$ and composition f_A = 0.25, self-consistent field theory (SCFT) predicts (Figure 3 of Matsen and Thompson[121]) an order-disorder transition at $\chi\hat{N}$ ≃ 31.6 (for conformationally symmetric segments, $\hat{b}_A/\hat{b}_B = 1$) and $\chi\hat{N}$ ≃ 32 (for conformationally asymmetric segments, $\hat{b}_A/\hat{b}_B = 1.3$). Assessing the degree of

---

[f] Assuming volumes additivity: $\rho = f_A\rho_A + f_B\rho_B = 1/[(w_A/\rho_A) + (w_B/\rho_B)]$. Calculating the overall degree of polymerization using a segment reference volume v_0 ($\hat{N}$(25 °C) = $M/(\rho N_{av} v_0)$ = 1114.5) or the monomers molar masses $M_{0,I}$ and $M_{0,L}$ ($N = M_I/M_{0,I} + 2M_L/M_{0,L}$ = 1054.4) gives slightly different, but comparable results.

conformational asymmetry of LIL50–12 requires knowledge of the ratio $\hat{b}_L/\hat{b}_I$ (where the subscripts "L" and "I" stand for the PLA and PI blocks, respectively). As will be shown in the next section, the monomer-based SSL of PLA and PI at 25 °C are b_L = 0.712 nm and b_I = 0.637 nm. The statistical segment length based on a common segment volume can then be obtained[g] as $\hat{b} = b(\rho_{homo}N_{av}v_0/M_0)^{1/2}$, where ρ_{homo} and M_0 are the homopolymer density and the monomer molar mass ($M_{0,L}$ = 72.1 g/mol, $M_{0,I}$ = 68.1 g/mol). At 25 °C, we thus find $\hat{b}_L$ = 0.766 nm and $\hat{b}_I$ = 0.596 nm. Therefore, LIL50–12 ($\hat{b}_L/\hat{b}_I$ = 1.3) is estimated to maintain a microphase-segregated structure below (approximately) $T_{ODT,SCFT} \simeq 290$ °C.

3.3.2 Characteristic Length Scales and Tube Model Parameters

As evidenced by the foregoing discussion about the conformational asymmetry of LIL50–12, differences in chain dimensions play a role in the self-assembly of block copolymers[24,25] and, more generally, have long been known to significantly impact polymer-polymer miscibility[26]. The size of macromolecular chains is also related to the degree of their mutual "uncrossability" in the melt[27], thus governing viscoelastic properties such as the critical molar mass for entanglement effect in viscosity[18] and the plateau modulus[12-15,17,19,20]. In this section, we discuss characteristic length scales and tube model parameters of LIL50–12, which are essential for the subsequent analysis of the

[g] Through Eq. (3.1), which implies $R_i^2 = N_i b_i^2 = \hat{N}_i \hat{b}_i^2$ with i = {A, B}.

associated dynamics (§3.3.4.IV-d). We consider, for simplicity, the ideal coiled states that PI and PLA would adopt in their respective melts. Therefore, the following discussion neglects the strong state of segregation of the system ($\chi\hat{N}(25\ ^\circ\mathrm{C}) \simeq 436$) that causes polymer coils to stretch and deviate from their unperturbed dimensions.

3.3.2.I Parameters defining the configurational repeating units

Calculations of melt chain dimensions and tube model parameters require knowledge of the average number and length of backbone bonds per monomer (j and l, respectively), as well as the average backbone bond angle β (expressed as $K_{geom} \equiv \sin(\beta/2) = \cos(\theta/2)$, where $\beta = \pi - \theta$)[20,22,23,35,36,38]. In Flory's convention[21], the effect of bond angles is neglected and thus $K_{geom} = 1$. For polymer species with constitutional isomerism, such as PI, these basic parameters will of course depend on the distribution of the different configurational repeating units. Their calculation, however, is not as obvious as it may seem. In particular, a choice has to be made whether to use real or virtual skeletal bonds in representing the repeating unit (i.e. whether to use real or virtual chemical monomers). In spite of considerations of bond rotational states, coplanarity and tautomerism, sometimes the choice is not clear-cut. For instance, Flory and co-workers[61,62] treated the C-3 repeating unit of PLA as being composed of one virtual bond (l = 3.70 Å), on the assumption of a rigid ester group in a planar *trans* configuration due to the partial double-bond character of C–O. On the other hand, according to Wu[63] the PLA monomer is better portrayed by three freely rotating real bonds of average length l = 1.41 Å. Several

authors[2,39,53,55] later followed Wu's approach. The value of l (both for real and virtual bonds) can be obtained from the backbone bond lengths and angles of the chemical structure. If Flory's convention ($K_{geom} = 1$)[21] is not adopted, an effective (average) backbone bond angle needs to be calculated. Both l and K_{geom} can be safely assumed to be temperature-independent.[22,h]

We have chosen to represent PI and PLA by their real chemical monomers, and to rely on literature data of real bond lengths and angles[3,64,65] for the computation of l and K_{geom}. The configurational repeating units are shown in Figure 3.1, complemented by the relevant bond lengths and angles. With this approach, j_{RU} (where the subscript "RU" stands for "repeating unit") equals the number of backbone carbon atoms in the monomer, while $l_{RU} = \left(j_{RU}^{-1} \sum l_i^2 \right)^{1/2}$ is the corresponding root-mean-square skeletal bond length[23,38]. To determine their effective backbone bond angle (expressed as $K_{geom,RU}$), the repeating units are considered in a rod-like zig-zag conformation (i.e. all *trans* states of torsion angles) and their projected length L_{RU} along the contour is calculated. $K_{geom,RU}$ is then given by the ratio $L_{RU}/j_{RU}l_{RU}$. While the variation of l_{RU} with PI constitutional isomers is modest and within the range ≈ 1.47 Å (*cis*-1,4) – 1.51 Å (3,4), $K_{geom,RU}$ changes from ≈ 0.731 (*cis*-1,4) to ≈ 0.848 (*trans*-1,4). Therefore, the PI length scales and tube model parameters depending on K_{geom} (i.e. number and length of Kuhn statistical segments, and the chain fully extended length) are significantly affected by the relative fractions of

---

[h] The bond length l, if anything, increases with temperature but its fluctuations (typically ± 0.005 nm) are modest and do not affect chain conformations.[22]

chemical microstructures. Based on the distribution of PI configurational isomers (Table 3.1), molar fraction-weighted arithmetic averages give $j_I = 3.86$, $l_I = 1.479$ Å, and $K_{geom,I} = 0.792$. The corresponding values for PLA are $j_L = 3$, $l_L = 1.436$ Å, and $K_{geom,L} = 0.836$. The average backbone bond lengths thus calculated are consistent with other estimates reported in the literature, for instance $l = 1.48$ Å for 1,4-PI[41] and $l = 1.41$ Å for PLA[63]. These results, and the accompanying monomer molar masses, are summarized in Table 3.2.

When discussing the phase behavior of LIL50–12, we considered the (temperature-dependent) overall degree of polymerization $\hat{N}$ based on a common segment volume. In tube models, it is customary to compute the (temperature-independent) average number of chemical monomers per chain as the ratio between the polymer (M) and the monomer (M_0) molar masses, $N = M/M_0$.[35] Using the number-average block molar masses from Table 3.1, $N_I = 731.3$ (PI) and $N_L = 161.6$ (PLA). Knowledge of the basic quantities j, l, and K_{geom} (Table 3.2), in conjunction with measurements of unperturbed coil sizes via small-angle neutron scattering (SANS)[20,39,40] and shear plateau moduli[4,17,20], permits the computation of several characteristic parameters. The calculation of these parameters[4,16-23,34-36,39-46,67-69,71,75,122], described in the next two sections, was performed at three temperatures (0, 25, and 140 °C), and the results are summarized in Tables 3.3 and 3.4. We remind the reader that Tables 3.3 and 3.4 refer to an unperturbed and undiluted state of the polymer coils. Tube model parameters, and associated characteristic length scales,

are shown when $T > T_g$. Approximate iso-free volume conditions (i.e. $T–T_g \approx 87$ deg) are obtained for PI at 25 °C and PLA at 140 °C.

Table 3.2. Parameters defining the configurational repeating unit of the constituent blocks.

Block	M_0 [a] [g/mol]	j [b]	l [c] [Å]	K_{geom} [d]
PI	68.1	3.86	1.479	0.792 [e]
PLA	72.1	3	1.436	0.836

a) Monomer molar mass.

b) Average no. of backbone bonds per repeating configurational unit (monomer).

c) Monomer root-mean-square backbone bond length (assumed to be T-independent).

d) $K_{geom} \equiv \sin(\beta/2) = \cos(\theta/2)$, where $\beta = \pi - \theta$ is the average backbone bond angle (assumed to be T-independent).

e) Strongly dependent on the relative fractions of PI configurational isomers.

Table 3.3. Densities and characteristic length scales for the unperturbed and undiluted PI and PLA blocks.

Block	*T* [°C]	ρ [a)] [g/cm^3]	R^2/M [b)] [Å^2·mol/g]	*b* [c)] [nm]	b_k [d)] [nm]	*a* [e)] [nm]	*R* [f)] [nm]	R_g [g)] [nm]	L_{tube} [h)] [nm]	*L* [i)] [nm]
PI	140	0.834	0.624	0.652	0.940 [j)]	5.84	17.6	7.20	53.2	330.6 [j)]
	25	0.900	0.596	0.637	0.898 [j)]	5.51	17.2	7.03	53.8	330.6 [j)]
	0	0.915	0.590	0.634	0.889 [j)]	5.49	17.1	7.00	53.6	330.6 [j)]
PLA	140	1.153	0.603	0.659	1.207	4.37	8.38	3.42	16.1	58.2
	25	1.260	0.704	0.712	1.409		9.06	3.70		58.2
	0	1.284	0.729	0.725	1.459		9.22	3.76		58.2

a) Density of undiluted PI and PLA homopolymers[d], calculated according to Witzke[71], Fetters et al.[20], and Orwoll[69].

b) Ratio of unperturbed chain dimension to molar mass. For PI, R^2/M was obtained from the value tabulated in Fetters et al.[20] at 25 °C, and[40] $\kappa_{PI} \equiv \partial \ln R_{PI}^2 / \partial T = +0.40 \cdot 10^{-3}$ deg^{-1}. For PLA, R^2/M was calculated based on the measurements performed by Anderson and Hillmyer at 30 and 200 °C, and $\kappa_{PLA} \equiv \partial \ln R_{PLA}^2 / \partial T = -1.41 \cdot 10^{-3}$ deg^{-1}.[39]

c) Monomer-based statistical segment length.

d) Kuhn statistical segment length.

e) Tube statistical segment length (i.e. unperturbed root-mean-square end-to-end distance of a chain M_e^G or N_e long), calculated when $T > T_g$.

f) Unperturbed root-mean-square end-to-end distance of the individual PI and PLA blocks.

g) Unperturbed root-mean-square mass-weighted distance of PI and PLA monomers from their respective centers of mass (i.e. radius of gyration).

h) Equilibrium contour length of the confining tube's centerline (i.e. equilibrium primitive path of the test chain), calculated when $T > T_g$.

i) Fully extended (contour) length of the test chain in a rod-like zig-zag conformation (i.e. all *trans* states of torsion angles). The temperature independence of L follows from its definition and from treating l and K_{geom} as T-independent parameters.

j) Strongly dependent on the relative fractions of PI configurational isomers.

Table 3.4. Tube model parameters for the unperturbed and undiluted PI and PLA blocks.

Block	T [°C]	G_N^{0} a) [MPa]	M_e^{G} b) [g/mol]	P_e c)	n_e d)	N e)	N_k f)	N_e g)	$N_{e,k}$ h)	Z i)
PI	140	0.42	5460	18.3	5.2	731.3	351.8 j)	80.2	38.6 j)	9.1
	25	0.35	5100	17.8	5.1	731.3	368.3 j)	74.9	37.7 j)	9.8
	0	0.35	5100	17.8	5.1	731.3	372.0 j)	74.9	38.1 j)	9.8
PLA	140	1.00	3170	18.3	5.2	161.6	48.2	44.0	13.1	3.7
	25					161.6	41.3			
	0					161.6	39.9			

a) Shear plateau modulus of undiluted PI and PLA homopolymers. For PI, G_N^0 was obtained from the values tabulated in Fetters et al.[17] at 140 °C, and Fetters et al.[20] at 25 °C. For PLA, G_N^0 is the value measured by Dorgan et al.[4] at 180 °C. Values of G_N^0 are given when $T > T_g$.

b) Molar mass between entanglements (Graessley–Fetters definition), calculated when $T > T_g$.

c) Average no. of entanglement strands in a cube with side equal to the tube statistical segment length a, calculated when $T > T_g$.

d) Average no. of chains in pairwise contact required to result in one entanglement, i.e. critical packing ratio, calculated when $T > T_g$.

e) Average no. of monomers per chain, i.e. degree of polymerization, based on the monomers molar masses.

f) Average no. of Kuhn units per chain.

g) Average no. of monomers per entanglement strand, i.e. degree of polymerization between entanglements, calculated when $T > T_g$.

h) Average no. of Kuhn units per entanglement strand, calculated when $T > T_g$.

i) Average no. of entanglement strands per chain, calculated when $T > T_g$.

j) Strongly dependent on the relative fractions of PI configurational isomers.

3.3.2.II Length scales

At coarse-grained levels (i.e. length scales larger than l), a flexible polymer chain of degree of polymerization $N = M/M_0$ may be viewed as comprised of Y freely-jointed statistical segments (with $Y \leq N$) of suitably chosen length x (with $x \geq b > l$). Being the companion statistical parameter of N, b is referred to as the *monomer-based* SSL.[23,35] The characteristic length x is usually associated with a particular physical property of the statistical chain that it defines. These freely-jointed statistical chains, however, share all a common feature in that their mean-square end-to-end distance must be equal to that of the real chain, R^2, according to:[23,35,42-45,i]

$$R^2 = C_\infty n l^2 = Y x^2 \tag{3.1}$$

where $C_\infty = (R^2/M)\cdot(M_0/jl^2)$ is Flory's characteristic ratio (measure of the local correlations decay between neighbouring backbone bond vectors)[21], and $n = j\cdot N > \approx 100$ is the average number of backbone bonds per chain[22,34,j].

The monomer-based SSL is calculated according to Eq. (3.1) as[23,35] $b = (C_\infty \cdot j)^{1/2}\cdot l$. At 25 °C, using the R^2/M values shown in Table 3.3, we find $b_I = 0.637$ nm and $b_L = 0.712$ nm.

---

[i] A random flight/walk of Y steps of length x has mean-square end-to-end distance $R^2 = Yx^2$ and contour length $L = Yx$. If the number of steps is changing with time, the mean-square end-to-end distance at any time t is given by $R(t)^2 = 6Dt$ (simple diffusive motion or Brownian motion), where D is the diffusion coefficient.[22,41,45]

[j] In practice, Eq. (3.1) remains valid also for shorter chains as long as $n \geq$ no. of backbone bonds in a Gaussian submolecule (i.e. the smallest section of the polymer chain that is long enough to assume a random coil conformation), albeit with the n-dependent value of the characteristic ratio, C_n. While usually $C_n < C_\infty$, the opposite behavior has also been observed.[34]

With the degree of polymerization N shown in Table 3.4, the unperturbed root-mean-square end-to-end distance R of the individual blocks at 25 °C is 17.2 nm (PI) and 9.06 nm (PLA). Since the blocks are treated as random coils, the unperturbed root-mean-square mass-weighted distance of the monomers from their respective centers of mass (i.e. radius of gyration) follows immediately as[23] $R_g = (1/6)^{1/2}R$, yielding 7.03 nm (PI) and 3.70 nm (PLA) (Table 3.3). In their ideal coil state, the PI block is about twice as large as the PLA block. Furthermore, by assuming[121] $R^2 = R_I^2 + 2R_L^2$, we can estimate the unperturbed overall size and statistic segment lengths (monomer-based and segment volume-based) of LIL50–12 at 25 °C: $R \simeq 21.5$ nm, $R_g \simeq 8.76$ nm, $b \simeq 0.661$ nm, and $\hat{b} \simeq 0.643$ nm.[k]

In polymer physics, three types of statistical segments are traditionally defined at length scales larger than chemical monomers, most notably (and in order of increasing length scales) the *Kuhn segment*, the *Gaussian submolecule*, and the *tube segment* (i.e. entanglement strand). All three will be considered in the analysis of the LIL50–12 dynamics. For the corresponding *Y–x* dyads[l], we use the symbols N_k–b_k, *S*–σ, and *Z*–*a*

---

[k] Assuming additivity of the unperturbed end-to-end distances: $b = \left(x_A b_A^2 + x_B b_B^2\right)^{1/2}$ and $\hat{b} = \left(f_A \hat{b}_A^2 + f_B \hat{b}_B^2\right)^{1/2}$, where x_A and x_B are the molar fractions of the A and B blocks.

[l] The polymer literature abounds with symbols that, over the years, have often been used interchangeably when referring to a particular statistical segment length (SSL). For example, the monomer-based SSL was termed a by Ferry[42] and l_N by Graessley[41]; the Kuhn SSL was termed b by Rubinstein and Colby[22] and Fetters et al.[20], and l_K by

(respectively), following largely[m] the nomenclature adopted by Ferry[42], Larson et al.[35], and Dealy and Larson[36]. Each of these statistical segment lengths, including b, has a specific physical meaning. The Kuhn chain (N_k units of length b_k), is defined in such a way that it possesses the same fully extended (contour) length L of the polymer chain in a rod-like zig-zag conformation, that is $L = K_{geom}nl = N_k b_k$.[20,22,35,36] The length of a Kuhn segment, b_k, measures twice the distance along the chain at which local correlations between backbone bonds decay (i.e. $b_k = 2l_p$, where l_p is the persistence length)[46]. In other words, b_k is the length scale at which the chain will, on average, bend 180°.[23] Therefore, on length scales smaller than b_k (or b), the chain is essentially rigid and its behavior (influenced by polymer-specific chemical details) resembles that of a linear elastic solid[22]. The characteristic dimension of a Gaussian submolecule, σ, represents the minimum length scale at which the real chain assumes a random coil conformation[47] and thus the probability distribution of the end-to-end distance can be approximated by a Gaussian function.[42,45] Consequently, at length scales smaller than σ the Rouse theory of chain dynamics no longer holds and semi-flexible chain models[22] can better explain the viscoelastic behavior. In entangled melts, the tube SSL, a, defines the length scale for topological constraints to become relevant and limit the transverse fluctuations of the polymer chains (i.e. at length scales $\approx a$, chains begin to experience the lateral constraints

---

Graessley[41]; the tube SSL was termed d by Ferry[42] and d_t by Fetters et al.[17]. In this study, we follow the SSL nomenclature adopted by Larson et al.[35] and Dealy and Larson[36].

[m] With the exception of the symbol N, which is used by Ferry for S and here for the degree of polymerization based on the monomer molar mass.

imposed by the confining tube).[42,43] Because of their physical significance, it is convenient to compare these characteristic length scales to the backbone bond length l. From Eq. (3.1), their ratio can be expressed as:

$$\frac{x}{l} = \left(C_\infty \cdot j \cdot m_y\right)^{1/2} = \left(C_\infty \cdot n_y\right)^{1/2} \tag{3.2}$$

where $m_y = N/Y$ and $n_y = j \cdot m_y$ are, respectively, the average number of chemical monomers and backbone bonds per statistical unit (for the real chain, $n = j \cdot N$). If the "type" of statistical segment (i.e. Kuhn, Gaussian, or tube SS) is identified by the subscripts "k", "s", and "z" (respectively), we then have $n_k = j \cdot m_k = j \cdot (N/N_k)$, $n_s = j \cdot m_s = j \cdot (N/S)$, and $n_z = j \cdot m_z = j \cdot (N/Z)$. While this would provide a consistent nomenclature, other symbols have been proposed in the past or are widely accepted and for those, namely q for m_s [42] and N_e for m_z [22,44] we will conform to the literature.

The first of these characteristic lengths, $b_k = (C_\infty/j)^{1/2} \cdot (b/K_{geom}) = (C_\infty/K_{geom}) \cdot l$ [35,36], follows directly from Eq. (3.1) or (3.2). For instance, at 0 °C $b_{k,I} = 0.889$ nm and $b_{k,L} = 1.459$ nm (Table 3.3). The average number of Kuhn units per block can be computed through Eq. (3.2) or, more directly, as[35,36] $N_k = M/M_{0,k} = (j/C_\infty) \cdot (K_{geom})^2 \cdot N$, where $M_{0,k}$ is the Kuhn unit molar mass. Hence, for the PI block at 0 °C there is roughly 1 Kuhn segment for every 8 backbone bonds ($n_k = 7.6$) or for every 2 monomers ($m_k = 2.0$), and each segment is about 6 times as long as the backbone bond ($b_k/l = 6.0$).

The length scale σ, which defines the Gaussian submolecule[47], is of particular importance in polymer physics being relevant to both unentangled and entangled macromolecules. Its determination, however, is not trivial. By analyzing the LIL50–12

dynamics at 0 °C, we will show in §3.3.4.IV-c how the Rouse–Bueche theory[47,85,86] for unentangled melts can be applied to an entangled and filled system to estimate σ (specifically, since $T_{g,I} < 0$ °C $< T_{g,L}$, we will determine σ for the PI block). In the meantime, two rules of thumb that have appeared in literature regarding the size of Gaussian submolecules are noteworthy (and will be used in §3.3.4.IV-c to check the reliability of our results). Ferry[42] estimated that typical polymers have Gaussian submolecules holding a number of backbone bonds on the order of ≈ 50, or more (i.e. $n_s >$ ≈ 50). Dealy and Larson[36], based on considerations relative to a polyethylene chain, argued that n_s can be roughly correlated to the number of backbone bonds present in a Kuhn unit, n_k, and that $n_s \approx n_k^2$ (i.e. $q \approx j \cdot m_k^2$). Yet another estimate can be inferred from the (Kratky–Porod) worm-like chain (WLC) model[58]. According to this model, a chain of contour length L and persistence length l_p begins to behave like a random coil when $L/l_p >$ ≈ 5 (Figure 6.7 on page 229 of Hiemenz and Lodge[23]). By identifying this minimum contour length ($L_{min} \approx 5l_p$) with σ, it follows that $\sigma \approx (5/2) \cdot b_k$ and (from Eq. (3.1)) $q \approx (25/4) \cdot m_k$. As a result, we can expect the PI Gaussian submolecule at 0 °C to contain approximately ≈ 12–15 monomers or ≈ 47–58 backbone bonds. This implies $S \approx$ 49–60, and $\sigma \approx$ 2.2–2.5 nm.

3.3.2.III Tube model parameters

The tube SSL and the tube diameter (i.e. the mean span of transverse fluctuations of the test chain) are analogous descriptions of the same physics (i.e. chains mutual

"uncrossability") and hence comparable in magnitude.[43] Very often, they are assumed to be equal to each other[36,42,46], although they need not be[43] and according to McLeish[44] "the notion of a tube radius is a rather inexact idea". Eq. (3.2) shows that the tube SSL depends on the average number of monomers per tube step (i.e. degree of polymerization between entanglements)[22,44], N_e. The tube model proposed by Doi and Edwards[46] permits the computation of N_e for flexible polymers, i.e. chains whose conformation can already be described by a random coil at length scales $\leq a$ (i.e. $\sigma \leq a$). Coherently with their theoretical approach, we calculated N_e as:

$$N_e = \frac{M_e^G}{M_0} \tag{3.3}$$

where M_e^G represents the Graessley–Fetters definition of molar mass between entanglements[17,35,75], obtained through the shear plateau modulus[n] G_N^0 as:

$$M_e^G \equiv \frac{4}{5} M_e^F \equiv \frac{4}{5} \frac{\rho RT}{G_N^0} \tag{3.4}$$

In the above equation, we follow the nomenclature proposed by Larson et al.[35] and thus use M_e^F for the Ferry definition of molar mass between entanglements ("entanglement spacing" in Ferry's terminology)[42], while in this case $R = k \cdot N_{av}$ stands for the universal

[n] The shear plateau modulus of an entanglement network is denoted by G_N^0 in uncrosslinked systems, and by G_N in crosslinked systems.[42]

gas constant[o] and k is Boltzmann's constant. Incorrect or inconsistent use of these two definitions of entanglement molar mass has produced numerous errors in the literature (as explained by Larson et al.[35]). An inaccurate value of the entanglement molar mass alters the tube model predictions, and the associated errors become quantitatively significant for slowly relaxing systems such as branched polymers or microphase-segregated block copolymers. The underlying reason for the 4/5 prefactor in the definition of M_e^G is ascribed to conformational equilibration of the tube via longitudinal Rouse-like motions of the monomers (§3.3.4.IV-d). While regular, 3-D Rouse-like modes are prohibited at length scales $\approx a$, 1-D Rouse-like motions re-equilibrate chain density and allow entangled chains (as opposed to chemically crosslinked systems, for which M_e^F was originally introduced) to relax one fifth of the stress that would otherwise contribute to the plateau modulus G_N^0.[35,36,42,44,45] The Graessley–Fetters entanglement molar masses, based on literature values[4,17,20,p] of the plateau moduli, are shown in Table 3.4. At 140 °C, M_e^G = 5460 g/mol and N_e = 80.2 for the PI block, M_e^G = 3170 g/mol and N_e = 44.0 for PLA. The PI entanglement molar mass is nearly temperature-independent[17,18,40,68] (as

---

[o] Although the universal gas constant and the polymer end-to-end distance bear the same symbol, the temperature T always immediately follows the former, thus avoiding any confusion.

[p] For PLA, experimental estimates of viscoelastic parameters, such as the shear plateau modulus (G_N^0) and the critical molar mass for entanglement effect in viscosity (M_C), are sometimes erroneous and inconsistent with the measured unperturbed coil size (see Chapter 2).

discussed in Chapter 2)[q], therefore we consider the values at 25 °C (M_e^G = 5100 g/mol, N_e = 74.9) to be also representative of the PI entanglement network at 0 °C. Because entanglements are believed to stem from a collective topological restriction of neighbouring chains[22], the entanglement molar mass alone is not sufficient to fully define the characteristics of the PI entanglement network. For linear flexible polymers, entanglements are controlled by a fixed number of binary intermolecular contacts. This can be expressed as the average number of entanglement strands in a cube with side equal to the tube SSL a:[20,22]

$$P_e \equiv \frac{a^3}{V_{occ,e}} = \frac{a}{p} \tag{3.5}$$

where $V_{occ,e} = M_e^G/\rho N_{av}$ is the volume occupied by an entanglement strand, and $p \equiv M/\rho N_{av}R^2$ is the Witten–Fetters packing length[16,17], defined as the ratio of the volume occupied by the chain to its square size. For flexible polymers, P_e is almost temperature-independent[19] and on average[20] equal to 18.4 ± 8%. Its seemingly constant value is known as the "overlap criterion for entanglements" in polymer melts.[20,22] Assuming that an entanglement strand of molar mass M_e^G and radius of gyration $R_{g,e}$ pervades a spherical volume $V_{per,e} = (4\pi/3)R_{g,e}^3$, P_e can be used to calculate the average number of pairwise

---

[q] It has been observed[17,18,40,68] that the entanglement molar mass (M_e) of polymers with $\kappa = \partial \ln R^2/\partial T < 0$ decreases with decreasing temperature. M_e becomes almost temperature-independent for positive but modest values of κ (e.g. 7% 3,4-PI), and the trend is reversed if $\kappa \gg 0$ (see Chapter 2).

contacts required to result in one entanglement, $n_e - 1$, where n_e is the "critical packing ratio" defined as:[17,45,67]

$$n_e \equiv \frac{V_{per,e}}{V_{occ,e}} = \frac{4\pi}{3}\frac{1}{6^{3/2}}P_e \tag{3.6}$$

The average value of $n_e = 5.3 \pm 8\%$ is an alternative, but equivalent overlap criterion for topological constraints in linear flexible polymers. Values of P_e and n_e for the PI and PLA blocks are shown in Table 3.4.

The average number of tube segments (entanglement strands) per chain, Z, is given by:[35,44,r]

$$Z \equiv \frac{M}{M_e^G} = \frac{N}{N_e} \tag{3.7}$$

yielding $Z_l(25\ °C) = 9.8$, and $Z_L(140\ °C) = 3.7$ (Table 3.4). Being the tube SSL the unperturbed root-mean-square end-to-end distance of a chain M_e^G or N_e long[22,35,46], it is calculated (consistently with Eq. (3.2)) as:

$$a = N_e^{1/2} b \tag{3.8}$$

Owing to its freely-jointed nature[22,41,45], the equilibrium contour length of the confining tube's centerline (i.e. equilibrium primitive path of the test chain) is $L_{tube} = Z \cdot a$.[43,44,122] Consequently, about 10 tube segments of length 5.49 nm, ≈ 49–60 Gaussian submolecules of length ≈ 2.2–2.5 nm, or 372 Kuhn units of length 0.889 nm, can

---

[r] The symbol E is used by Graessley[45] for the ratio M / M_e^F, sometimes referred to as the "number of entanglements" per molecule[35].

equivalently (i.e. same R^2) represent the PI block at 0 °C. Because $b_k \ll \sigma \ll a$, however, their fully extended lengths are quite different. While $L_{tube,I}$ = 53.6 nm, the Kuhn chain contour length (by construction, equal to that of the real chain) is much larger, L_I = 330.6 nm. Similar considerations hold for each PLA block (Tables 3.3 and 3.4). Indeed, this is a general feature of flexible polymers for which the characteristic length scales are usually widely separated, i.e. $l \ll b < b_k \ll \sigma \ll a \ll R \ll L_{tube} \ll L$. For this reason, the associated dynamics covers a wide range of time scales (as will be demonstrated for LIL50–12).

Since characteristic lengths and tube model parameters of PI play a fundamental role in the analysis of the LIL50–12 dynamics at service temperatures (§3.3.4.IV-d), it is important to determine whether the values we found are reasonable when compared to the literature. For 7% 3,4-PI at 25 °C, Fetters and co-workers[20] provide the Kuhn and tube SSL, as well as the average number of Kuhn units per entanglement strand[s], $N_{e,k}$, corresponding to 0.844 nm, $(4/5)^{1/2}\cdot(6.16)$ = 5.51 nm and $(4/5)\cdot(53.2)$ = 42.6 (respectively). The factors $(4/5)^{1/2}$ and (4/5) take into account that the tabulated values were calculated according to Ferry's definition of molar mass between entanglement, M_e^F, rather than M_e^G. Using the parameters shown in Tables 3.2–4, we obtain $N_{e,k} = M_e^G/M_{0,k} = (j/C_\infty)\cdot(K_{geom})^2\cdot(M_e^G/M_0)$ = 37.7 for PI at 25 °C. Therefore, our results (b_k = 0.898

[s] The symbols b, N_e, M_0, and M_e used in Fetters et al.[20] stand for our b_k, $N_{e,k}$, $M_{0,k}$, and M_e^F (respectively).

nm, a = 5.51 nm, $N_{e,k}$ = 37.7) appear to befittingly represent the PI block. The Kuhn chain-based values, in particular, are sufficiently consonant with the literature, in light of their relatively strong dependence from the specific distribution of PI configurational isomers (for which, in Fetters et al.[20], only the 3,4 vinyl content is indicated).

In this section, relevant length scales and parameters governing the viscoelastic behavior of entangled PI and PLA chains have been calculated. Assessing the characteristic dimensions of PI Gaussian submolecules requires an analysis of the continuous relaxation spectrum, and it is thus deferred to §3.3.4.IV-c. Albeit a cue about the potential entangled nature of the PLA blocks, the value of Z_L(140 °C) = 3.7 is small enough to warrant an additional, independent, confirmation. Determination of the PI and PLA critical molar masses for entanglement effect in viscosity (M_C) is thus the subject of the next section.

3.3.3 Critical Molar Masses for The Onset of Entanglement Coupling in Undiluted PI and PLA Melts

For a long time, the critical molar mass for entanglement effect in viscosity was considered to be related to M_e^F by the approximate correlation $M_C \approx 2M_e^F$.[42,87,90] In 1999, however, Fetters and colleagues[18] demonstrated that the ratio M_C/M_e^F is not constant, but depends on the packing length p of the polymer species. According to a later review on 16 linear flexible polymers[20], the dependence of M_C on the entanglement molar mass and packing length (expressed in Å) can be empirically described by:

$$\begin{aligned} M_C &= M_e^F (3.420) p^{-0.534} \\ &= M_e^G (4.275) p^{-0.534} \end{aligned} \tag{3.9}$$

Using p values deduced from the SANS-measured[20,39,40] coil size shown in Table 3.3 as well as those obtained[17,20,t] from the rheology-measured[4,17,20] shown in Table 3.4, we calculated $M_{C,PI}$ = 12630 g/mol and $M_{C,PLA}$ = 8560 g/mol at 140 °C. M_C for PI is nearly temperature-independent (as discussed in Chapter 2)[q], and $M_{C,PI}$ = 12330 g/mol at 25 °C. According to the number-average molar masses shown in Table 3.1, these results imply that both the PI and the PLA blocks are entangled ($M_n/M_C \approx 4$ and 1.4, respectively), although to a different degree ($Z \simeq 9.8$ and 3.7, respectively – Table 3.4). Comparison with experimental estimates of M_C is noteworthy. The value tabulated by Fetters and co-workers[20] for a 7% 3,4-PI melt at 25 °C is 13100 g/mol, in close agreement with the packing model prediction. Conversely, extreme caution must be exerted if one wishes to rely on experimentally measured M_C (and G_N^0 or M_e) for PLA[p], as we discussed in Chapter 2.

---

[t] $p = \left(4kT/5P_e^2 G_N^0\right)^{1/3}$, based on the correlation found by Fetters et al.[17] (see Chapter 2).

3.3.4 Rheology

3.3.4.I Time evolution

In light of the metastable character of the microstructure, we monitored the time evolution of the dynamic moduli in the linear regime. Both extensional (37 °C, 24 h) and shear (80 °C, 2 h) measurements showed time-invariant responses in specimens that had just undergone the pressing procedure. Subsequent analysis (whose results are presented in the following sections of this Chapter, as well as in Chapters 4, 5 and in Appendix A) was conducted on either freshly prepared samples or within two weeks from preparation for testing specimens that had been stored in a freezer. Therefore, any potential and spontaneous change of the microstructure towards a lower free energy state had only a minor impact (if any) on the measured viscoelastic properties of LIL50–12.

3.3.4.II Thermal behavior

The results of isochronal (ω = 1 rad/s) temperature ramps are shown in Figure A.3 and discussed in Appendix A. As expected[123], the microphase-segregation of LIL50–12 is manifested in the appearance of two separate glass transitions stemming from the PI-rich matrix and the embedded PLA domains. Temperature values were assigned based on the locus of the loss modulus peak, yielding $T_{g,I}$ = –61.1 °C and $T_{g,L}$ = 53.6 °C.

3.3.4.III Viscoelastic behavior for $T_{g,B} < T < T_{g,A}$: time-temperature superposition

Two-phase polymeric materials, such as polymer blends[124,125] and block copolymers[126-129], are inherently thermo-rheologically complex. Their response functions measured at different temperatures cannot, in general, be superposed by a simple horizontal shift along the logarithmic time or frequency axis. For these materials, the horizontal shift factors are functions of time/frequency in addition to temperature, i.e. $a_T(\omega, T)$.[127] Furthermore, $a_T(\omega, T)$ is different for the storage and the loss components of the harmonic response.[127] Applicability of time-temperature superposition (TTS) in its simple form or thermo-rheological simplicity[130] (i.e. $a_T(T)$) depends on several factors: the separation of the T_g's, the location of T_{ODT}, the shift behavior of the constituent phases, and the experimental frequency and temperature windows.[42,105,127,129,131-133] A simple translation may apply only in regions of time/frequency and temperature over which the shift behavior is (i) completely dominated by one or the other phase[127] (with no interfacial effects[128,129]), and (ii) not influenced by the underlying state of order[105]. Under these conditions, providing the dominant phase is itself thermo-rheologically simple[42,131-133], a_T is time/frequency independent and the same for all viscoelastic functions. This simpler shift behavior is the result of all relaxation times τ_p and spectral strengths E_p originating from related molecular mechanisms, thereby having the same temperature dependence.[133] Predictions of flexible chain theories, $\tau_p \sim \zeta_0 b^2/T$ (where ζ_0 represents the monomeric friction coefficient) and $E_p \sim \rho T$ (entropic elasticity)[42], can then be used as guides to a reduction scheme. To this end, it is customary to define the horizontal (time-scale) shift

factor as[42] $a_T \equiv \tau_p(T)/\tau_p(T_0) \simeq \zeta_0(T)/\zeta_0(T_0)$, and the vertical (modulus-scale) shift factor as[134,u] $b_T \equiv E_p(T)/E_p(T_0) = \rho T/\rho(T_0)T_0$. In the expression for a_T, the temperature dependence is largely due to the change in ζ_0 (if $T > T_0$, $a_T < 1$), and the terms T and $b(T)$ can be neglected.[42]

At temperatures above both T_g's and below (approximately) $T_{ODT,SCFT} \simeq 290$ °C, the underlying state of order is anticipated to play a key role and dictate, at *low enough* frequencies (i.e. large time and length scales), the viscoelastic response of LIL50–12.[98,101,103,105,107-109] At service temperatures ($T_{g,I} < T < T_{g,L}$), the I block ends are anchored on rigid L domains. Therefore, the microstructural order is no longer a dominant factor in controlling the viscoelastic response (at any frequency), and LIL50–12 behaves similarly to a filled and entangled PI-rich rubber (as shown in Appendix A). We measured the frequency-dependent linear viscoelastic behavior of LIL50–12 at five service temperatures (–50, –40, –20, 0, and 37 °C) in the frequency range 0.001–500 rad/s (i.e. ≃ 5.7 decades[v]). Inasmuch as the PLA microdomains acted as rigid space-filling physical endlinks for the PI chains (i.e. $T \leq 0$ °C $\ll T_{g,L}$) and the experimental window did not involve relaxations of PI subchains at length scales shorter than b_I (i.e. $T > T_{g,I}$ and ω *sufficiently* low), TTS was applicable in its simple form. Therefore, for this experimental

---

[u] When the reference temperature T_0 is of interest, shift factors are sometimes assigned the symbols $a_T^{T_0}$ and $b_T^{T_0}$.

[v] According to Plazek[132], a definitive test of simple TTS requires an experimental window spanning more than 3 decades of time/frequency.

range of temperature and frequency, the PI-rich matrix dominates the shift behavior of the triblock[127] and is thermo-rheologically simple[42,130-133]. Indicating with τ_0 the PI *segmental time*[23], i.e. the time scale at which a PI monomer would diffuse a distance of order b_I if it were not attached to the chain[22], the frequency requirement can be expressed as $\omega < 1/\tau_0$ (henceforth, we will often refer to characteristic parameters of the PI block, and for simplicity the corresponding symbols will lack the subscript "I"). Under these conditions ($T_{g,I} < T \ll T_{g,L}$ and $\omega < 1/\tau_0$), all contributions to the measured viscoelastic properties of LIL50–12 involved a single monomeric friction coefficient, ζ_0, which represents the average drag force per PI monomer per unit velocity encountered by a PI Gaussian submolecule moving through its free-draining surroundings[42,w]. By means of reduced variables, namely $\omega_R \equiv \omega \cdot a_T$, it was possible to investigate the LIL50–12 dynamics over a wide range of time scales ($\simeq$ 11 decades). The experimental data of the loss tangent, $\tan\delta(\omega, T)$, were horizontally shifted to determine a_T and construct the associated master curves ($E'(\omega_R)$, $E''(\omega_R)$, $\tan\delta(\omega_R)$ vs. ω_R) at four service temperatures (–50, –40, –20, and 0 °C)[x]. Owing to thermo-rheologically simplicity, a single set of horizontal shift factors could reduce the data in the range from –50 to 0 °C. Vertical shift factors were not applied (i.e. $b_T = 1$). Horizontal shift factors and master curves at the

---

[w] ζ_0 increases with molar mass but approaches a constant limiting value ζ_{00} at high molar mass. In this regime, it applies only to short relaxation times corresponding to motions between entanglement points.[42]

[x] The horizontal shift factors at different reference temperatures were determined such that $a_T^{T_0} = 1/a_{T_0}^{T}$.

reference temperature of 0 °C are shown in Figures 3.3(a) and 3.4(a) (respectively). Remarkably, an excellent superposition over the explored frequency-temperature range did not require the use of vertical shift factors, including the regions where the viscoelastic functions are relatively flat and hence the influence of b_T is often much more apparent[42].

3.3.4.III-a Thermo-rheological complexity near $T_{g,A}$

Any attempt to superpose the data measured at 37 °C failed, as the dynamic moduli at this temperature showed a different frequency dependence (i.e. increasing *T* from 0 to 37 °C changed the *shape* of the linear viscoelastic functions). The validity of the method of reduced variables (i.e. TTS) within a single zone of time/temperature scale is based on the fundamental assumption that the internal structure of the system does not change with changing *T*.[23,42] Therefore, thermo-rheological complexity (i.e. TTS failure over an extended region of *T*) reflects structural modifications that induce the development of a new class (i.e. different ω- and *T*-dependence) of relaxation mechanisms.[42,131,132] We attribute the development of a dissimilar relaxation mechanism at 37 °C to the softening of PLA microdomains as $T_{g,L}$ (53.6 °C) is approached, which would partially release the tethering constraint on the I block ends at the corresponding I/L interfaces. This hypothesis is in harmony with literature studies on poly(styrene–*b*–butadiene–*b*–styrene) (S–B–S) and poly(styrene–*b*–isoprene–*b*–styrene) (S–I–S) systems. For S–B–S triblocks with a cylindrical microstructure, and with an experimental frequency range of roughly

four decades, Tschoegl and co-workers[127-129] showed that neither phase completely dominated the shift behavior within about 20 degrees of the polystyrene glass transition. In other words, the dynamic moduli could not be brought to superpose, for $T \in [\approx T_{g,S} - 20 \text{ deg}, \approx T_{g,S} + 20 \text{ deg}]$, without point-by-point shifts that were functions of both ω and T (i.e. $a_T(\omega, T)$). For S–I–S triblocks either in bulk or solution, several authors reported thermo-rheological complexity near the glass transition of the S endblock (for lamellae-forming S–I–S in *n*-tetradecane (C14)[135], sphere-forming S–I–S in C14 or I[136], and sphere- and cylinder-forming bulk S–I–S[112]), or below (for bulk S–I–S[137]). These findings were independent of block copolymer microstructure (spheres, cylinders, or lamellae) and attributed to augmented motional freedom of the I block ends at the I/S interfaces (in the linear regime)[135,136] or pullout of the S blocks from the softened S domains (in the nonlinear regime)[112,135]. The behavior of LIL50–12 at 37 °C will be examined in Chapter 4.

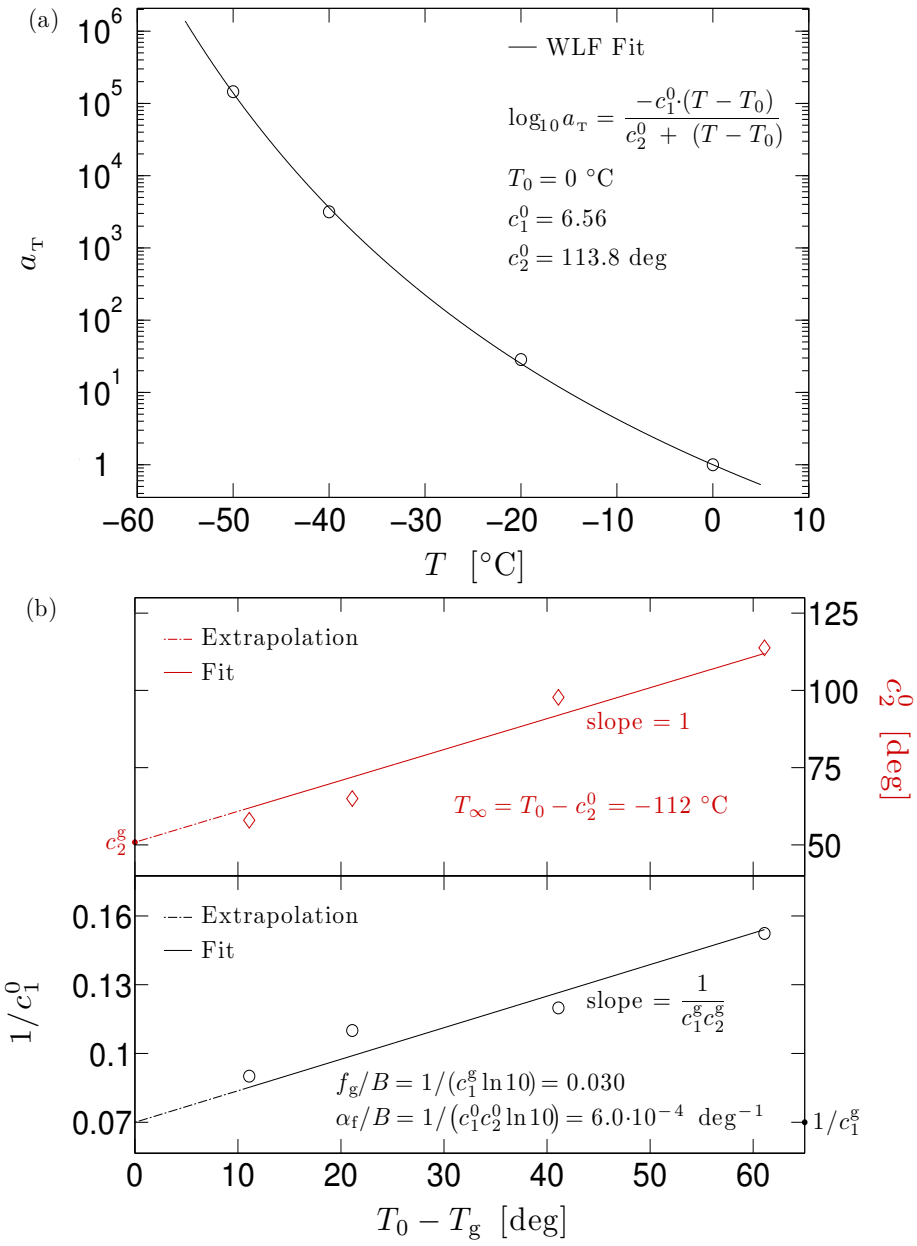

Figure 3.3. (a) Temperature dependence of the horizontal (time-scale) shift factor a_T used in Figure 3.4(a) (determined by horizontally shifting $\tan\delta(\omega, T)$ at the reference temperature of 0 °C), and the corresponding fit to the WLF equation. (b) Dependence of the WLF parameters c_1^0 and c_2^0 on the reference temperature T_0, and linear fits used to estimate c_1^g, c_2^g, and T_∞.

3.3.4.III-b Temperature dependence of a_T

Before dwelling into the various aspects of the LIL50–12 dynamics at 0 °C (Figure 3.4), we analyze the temperature dependence of the time-scale shift factor a_T and the information that it yields about chain mobility of the PI block (Figure 3.3 and Table 3.5). Although the validity of the TTS principle does not require a specific form for the *T*-dependence of a_T[42], the experimentally-determined $a_T(T)$ data are often found to obey the analytical expression (WLF equation) first introduced (on free volume grounds) by Williams, Landel, and Ferry[138] in 1955:

$$\log a_T = \frac{-c_1^0 \cdot (T - T_0)}{c_2^0 + (T - T_0)} \qquad \forall\ T:\ 0 < (T - T_g)/\mathrm{deg} < 100 \tag{3.10}$$

where c_1^0 and c_2^0 are empirical constants (dimensionless and [deg], respectively)[42,y] associated with the reference temperature T_0 (arbitrarily chosen within the interval [T_g, T_g + 100 deg]). The WLF equation is based on the premise that either the steady-state zero-shear viscosity, η_0, or the relaxation times, τ_p, depend exponentially on the fractional free

---

[y] The correct units of c_1^0 and c_2^0 are given on page 277 of Ferry's book[42]. The literature, however, abounds with incorrect dimensions for the WLF parameters. For example, K (Ngai and Plazek[133] p 457) and K^{-1} (Dorgan et al.[4]) for c_1^0; K (Dorgan et al.[4]; Ngai and Plazek[133] p 457; Klopffer et al.[139]) and °C (Hiemenz and Lodge[23] p 484; Graessley[45] p 145; Chapman et al.[140]) for c_2^0. While c_1^0 may appear to have dimension of deg^{-1}, the derivation of the WLF equation makes it clear that c_1^0 is a pure number. On the other hand, assigning the dimension °C or K to c_2^0 would imply that is possible to convert its numerical value from °C to K, and vice versa.

volume, f, according to the functional form proposed by Doolittle[141-143], i.e. η_0 or[z] $\tau_p \sim \exp[B(1/f - 1)]$. The fractional free volume is usually defined as $f \equiv \hat{v}_f / (\hat{v}_f + \hat{v}_{occ})$, where $\hat{v}_f$ and $\hat{v}_{occ}$ are (respectively) the free volume and the occupied volume per gram of material (i.e. specific volumes, $\hat{v} = 1/\rho$)[42,138], while the empirical constant B varies from 0.2 to 1.6 (depending on the assumptions) and it is often set arbitrarily[42,45] equal to 1. By assuming that f depends linearly on T above T_g, i.e. $f = f_0 + \alpha_f \cdot (T - T_0)$ for $T > T_0 \geq T_g$ (where α_f indicates the thermal expansion coefficient of the free volume[42,aa], and f_0 is the fractional free volume at T_0), the WLF equation can be derived, with $c_1^0 = B/(f_0 \ln 10)$ and $c_2^0 = f_0/\alpha_f$.[42] The temperature dependence of a_T could be successfully described by the WLF equation at all four reference temperatures (–50, –40, –20, and 0 °C), indicating that the key assumption $f \sim T$ is satisfied. The nonlinear least-square fit to Eq. (3.10), and the associated values of c_1^0 and c_2^0, are shown in Figure 3.3(a) for $T_0 = 0$ °C.

Because $a_T(T) \simeq \zeta_0(T)/\zeta_0(T_0)$, and ζ_0 applies only to short relaxation times corresponding to motions of PI monomers between entanglement points[42], the class of molecular mechanisms responsible for the measured shift factors should be oblivious of the presence of glassy PLA microdomains. In other words, statistical segments of the PI

---

[z] If $\eta_0 \sim \exp[B(1/f - 1)]$ is assumed, then derivation of the WLF equation requires the additional condition $b_T = 1$.

[aa] $\alpha_f \equiv \alpha_l - \alpha_{occ} \simeq \Delta\alpha \equiv \alpha_l - \alpha_g$, where α_l, α_{occ}, and α_g are the thermal expansion coefficients of (respectively) the polymer in the equilibrium liquid state (i.e. $T > T_g$), the occupied volume (not measurable experimentally), the polymer in the glassy state (i.e. $T < T_g$).[42]

blocks at length scales < a (PI tube SSL) should exhibit the same local friction $\zeta_0(T)$, hence the same $a_T(T)$, as they would in a pure PI melt. In the studies on S–B–S triblocks mentioned earlier, this naïve expectation was not always met. When the shift behavior was governed by the B matrix, and in a temperature range where secondary viscoelastic mechanisms (i.e. entanglement "slippage" and relaxation of the interface) were irrelevant, Fesko and Tschoegl[128] found horizontal shift factors different than those obtained for pure homopolymer B. This was tentatively attributed to the filler raising the apparent glass transition as seen in the mechanical properties by increasing the rubbery plateau.

It is thus of interest to compare the measured WLF parameters with values reported in literature for undiluted PI homopolymers. For this purpose, it is convenient the use of T_g as reference temperature. Knowledge of c_1^0 and c_2^0 at T_0 permits calculation of the WLF parameters c_1^1 and c_2^1 corresponding to a different reference temperature T_1. In fact, from the assumption $f \sim T$ and the identity $c_2^0 = f_0/\alpha_f$, it is possible to show[42,138] that $T_0 - c_2^0 = T_1 - c_2^1 \equiv T_\infty$, where T_∞ is the Vogel temperature[144] of the polymer. T_∞ represents the hypothetical[bb] temperature at which the horizontal shift factor a_T and all quantities proportional to it (i.e. any relaxation or retardation time τ, ζ_0, and η_0) become infinite, and it corresponds to the glass transition that would be measured at an infinitely slow rate of cooling[145], $T_g(\partial T/\partial t \to 0) = T_\infty$. From the above equation relating c_2^0 and c_2^1, and the

---

[bb] T_∞ is hypothetical because it is implicitly assumed that voluminal equilibrium persists below T_g.

identity $a_T^{T_0} = 1/a_{T_0}^T$, it follows that $c_1^0 c_2^0 = c_1^1 c_2^1$.[42,138] The WLF parameters calculated at 0 °C (Figure 3.3(a)) could then be used to estimate c_1^g, c_2^g, and T_∞. However, c_1^0 and in particular c_2^0 are quite sensitive to the fitting of Eq. (3.10) to $a_T(T)$ data which, in turn, already contain some degree of experimental uncertainty. For this reason, estimating c_1^g, c_2^g, and T_∞ directly from c_1^0 and c_2^0 gave slightly different results depending on the reference temperature T_0 (in the range 13.5–14.4, 43.9–56.7 deg, and from –118 to –105 °C respectively). More accurate estimates of c_1^g and c_2^g (hence, T_∞) could be obtained by a graphical least-square fitting procedure involving c_1^0 and c_2^0 at all four reference temperatures (–50, –40, –20, and 0 °C). Based on the foregoing relations converting the WLF parameters from T_0 to T_1, the following equations hold:

$$c_2^0 = c_2^g + \left(T_0 - T_g\right) \tag{3.11}$$

$$\frac{1}{c_1^0} = \frac{1}{c_1^g} + \frac{\left(T_0 - T_g\right)}{c_1^g c_2^g} \tag{3.12}$$

Extrapolation of the linear fits shown in Figure 3.3(b) gave $c_1^g = 14.3$, $c_2^g = 50.9$ deg, and T_∞ = –112 °C. Using these results, we estimated the fractional free volume at T_g, $f_g/B = 1/\left(c_1^g \ln 10\right) = 0.030$, and the free volume thermal expansion coefficient, $\alpha_f/B = 1/\left(c_1^0 c_2^0 \ln 10\right) = 6.0 \cdot 10^{-4}$ deg^{-1}, of the PI block. Moreover, differentiation of the WFL equation gives $\left[d \log a_T / dT\right]_{T_g} = -c_1^g / c_2^g$ and $dT_g / d \log a_T = c_1^g c_2^g / \left(c_1^g + \log a_T\right)^2 \simeq c_2^g / c_1^g$. The values of c_1^g and c_2^g thus imply[42,45] that,

near $T_{g,I}$, the PI segmental relaxation times decrease by about a factor of 10 for each 3.6 degrees increase in T or, alternatively, that the locus of the PI loss function peaks in Figure A.3 would shift by about 3.6 degrees with a change in time scale of a factor of 10. The former equation is sometimes presented in dimensionless form as "steepness index", $S_{T_g} \equiv -T_g \left[d \log a_T / dT \right]_{T_g} = T_g c_1^g / c_2^g$, which has been shown to correlate with the width of the relaxation spectrum near T_g, i.e. a high steepness index (> 100) is indicative of a broad viscoelastic response.[146]

3.3.4.III-c Comparison with the literature

Table 3.5 compares WLF parameters and steepness index of the PI block with literature values for undiluted PI homopolymers[134,139,147], Hevea Rubber[148] (*cis*-1,4 PI)[149], as well as average values obtained by fitting data on a large number (17) of polymers in the first application of the WLF equation[138]. It must be reminded, however, that horizontal shift factors may depend on the zones of viscoelastic behavior (terminal region, rubbery plateau region, or rubber-glass transition) associated with the experimental dynamic mechanical data, as Plazek unequivocally demonstrated 50 years ago[131,132]. In the terminal region of entangled systems, the relevant relaxations correspond to drag through entanglements or chain disengagement from the confining tube. Consequently, the longest relaxation times become proportional to the steady-state zero-shear viscosity, η_0, and the time-scale shift factors can be calculated as[42] $a_T = \eta_0(T)/\eta_0(T_0) b_T \simeq \eta_0(T)/\eta_0(T_0)$. Since mechanisms contributing to different loss peaks often have different temperature

dependences, measurements in the terminal region and near the rubber-glass transition may yield different values of c_1^0 and c_2^0 (i.e. two different sets of $a_T(T)$).[133] For a proper comparison of our results with the literature, it is therefore important to know from which regions the WLF parameters were determined and Table 3.5 contains such information as well.

The PI homopolymers listed in Table 3.5 differ from our PI block in terms of chain length and distribution of constitutional isomers. However, since all polymers have a relatively high molar mass (≈ 50–1800 kg/mol), the chain length dependence of T_g is avoided (more details in Appendix A). Differences in glass transitions thus stem from the type of experiment in which T_g was determined, the rate of cooling/heating, the isomers distribution (as discussed in Appendix A) and potential diluent impurities. Furthermore, as Gotro and Graessley[134] and later Klopffer et al.[139] have shown, c_1^0 and c_2^0 are independent from the PI microstructures when evaluated at constant distant from T_g. For polymer systems, f_g depends on the experimental time scale but it is often centered around 0.025.[42] α_f, on the other hand, usually shows a stronger variation although the value we measured is consistent with the thermal expansion coefficients of 1,4-PI and natural rubber in their equilibrium liquid state (i.e. $T > T_g$), respectively[45,69] 6.7 and 6.6 $\cdot 10^{-4}$ deg^{-1}. When our PI block is compared with undiluted PIs having a similar magnitude of the steepness index (i.e. analogous breadth of the viscoelastic spectrum near T_g), the WLF parameters are similar. This contrasts with the behavior of the S–B–S triblock studied by Fesko and Tschoegl[128], and suggests that perhaps significantly

different steepness indices were involved in their comparison. It is also worth noting that literature values for PI were mainly determined from experiments in the terminal region (Table 3.5). Yet, they agree with the WLF parameters we determined from the rubbery plateau and the rubber-glass transition regions. Thermo-rheological simplicity extending over the different regions of viscoelastic behavior is usually attributed to a weak temperature dependence of the entanglement molar mass[42]. Indeed, the entanglement molar mass of PI is weakly dependent on temperature[17,18,40,68,q] (Table 3.4), as discussed in §3.3.2.III (for more details, see Chapter 2). The analysis of Table 3.5 thus seems to validate our results and confirm the initial hypothesis that the glassy PLA microdomains did not alter the temperature (hence, time) dependence of the relaxation mechanisms involving portions of PI chains at length scales < a. With this in mind, we can expect the local friction of PI monomers in our system, $\zeta_0(T)$, to mirror that experienced in pure PI melts. Determination of the PI monomeric friction coefficient in LIL50–12, and the associated chain dynamics at 0 °C, will be discussed in the next section.

Table 3.5. Parameters characterizing the temperature dependence of the horizontal (time-scale) shift factor a_T, based on the WLF equation and determined from dynamic mechanical data (storage and loss moduli) measured in the indicated region of viscoelastic behavior.

Polymer	T_g [°C]	T_∞ [a)] [°C]	c_1^g	c_2^g [b)] [deg]	f_g/B [c)]	α_f/B [d)] [$deg^{-1}\cdot10^{-4}$]	S_{T_g} [e)]	*Region* [f)]	*Ref.* [g)]
LIL50–12 [h)]	– 61	– 112	14.3	50.9	0.030	6.0	59.6	2, 3	this study
PI [i)]	– 62	– 107	13.5	45	0.032	7.1	63.3	1, 2, 3	[1]
PI [j)]	– 61	– 115	12.2	53.7	0.036	6.6	48.1	1	[2]
PI [k)]	– 67	– 97	16.7	30	0.026	8.7	114.8	1	[3]
Hevea Rubber [l)]	– 73	– 127	16.8	53.6	0.026	4.8	62.7	3	[4]
"*Universal values*" [m)]			17.4	51.6	0.025	4.8		1	[5, 6]

a) Vogel temperature, calculated using c_2^g.

b) Literature values are reported (when available) or calculated as $c_1^g = c_1^0 c_2^0 / c_2^g$ and $c_2^g = c_2^0 + T_g – T_0$ when given at an arbitrary reference temperature T_0.

c) Fractional free volume at T_g.

d) Thermal expansion coefficient of the free volume.

e) Steepness index.

f) Zones of viscoelastic behavior from which the parameters c_1 and c_2 were mainly determined: 1 = terminal region, 2 = rubbery plateau region, 3 = rubber-glass transition.

g) *Ref.* [1] = Klopffer et al.[139]; [2] = Roovers and Toporowski[147]; [3] = Gotro and Graessley[134]; [4] = Payne[148]; [5] = Williams et al.[138]; [6] = Ferry[42].

h) 46.5/46.5/7 *cis*-1,4/*trans*-1,4/3,4 PI block, with number-average molar mass M_n = 49.8 kg/mol. $T_{g,I}$ determined from the maximum in the loss modulus $E''(\omega)$ obtained at an angular frequency ω = 1 rad/s and at a rate $\partial T/\partial t$ = 0.2 °C/min (upon cooling and heating).

i) 92/5/3 *cis*-1,4/*trans*-1,4/3,4 undiluted linear PI homopolymer, with mass-average molar mass M_w = 1820 kg/mol. T_g determined by DSC as the onset of the transition, upon heating at a rate $\partial T/\partial t$ = 5 °C/min.

j) 70/23/7 *cis*-1,4/*trans*-1,4/3,4 undiluted linear PI homopolymer, with mass-average molar mass M_w = 63.4 kg/mol. T_g determined by DSC as the midpoint of the heat capacity change, upon heating at a rate $\partial T/\partial t$ = 10 °C/min.

k) 74/18/8 *cis*-1,4/*trans*-1,4/3,4 undiluted linear PI homopolymer, with mass-average molar mass M_w = 164 kg/mol. T_g determined by DSC by extrapolation to zero heating rate.

l) Typical composition (by mass) of Hevea rubber latex: 33% *cis*-1,4 PI with $M_w \geq$ 1000 kg/mol, 60% water, 7% other substances like proteins, resins, ash, and sugars.[149] T_g determined by volume dilatometry.

m) Average values obtained by fitting data on a large number (17) of polymers in the first application of the WLF equation.[138]

3.3.4.IV Viscoelastic behavior for $T_{g,B} < T \ll T_{g,A}$: dynamics

For entangled[cc] polymer melts, a method for obtaining ζ_0 from the linear response behavior in the rubber-glass transition region was developed by Ferry and co-workers[42], based on a fitting procedure of the (shear) relaxation spectrum to the prediction of the Rouse–Bueche model[47,85,86]. Although in filled systems (such as LIL50–12 at service temperatures) their approach cannot be directly applied[42], in this section we show how the Rouse–Bueche theory[47,85,86] can still be used to extract ζ_0 from the (extensional) relaxation spectrum derived from the superposed $E'(\omega)$ and $E''(\omega)$ data at 0 °C. Knowledge of ζ_0 will then allow us to determine the characteristic time scales of LIL50–12 at 0 °C and connect the viscoelastic response to the structure of the material at different length scales.

3.3.4.IV-a Relaxation spectrum

Linear experimental responses of isotropic materials can be described by time-independent viscoelastic constants (associated with purely elastic or viscous behavior) coupled with integral transforms of spectral distribution functions (governing the viscoelastic behavior – Appendix D, §D.5).[150] Specifically, the time-varying part of linear harmonic responses can be conveniently expressed in terms of discrete or continuous distributions of relaxation times or moduli. In uniaxial extension, the relation between

---

[cc] Both uncrosslinked and lightly crosslinked, providing the crosslinking process does not change the chemical composition of the polymer.[42]

sinusoidal steady-state stress response ($\sigma_{ss}(\omega)$) and strain excitation ($\varepsilon(\omega)$) is given by (Appendix D, Eqs. (D.80)a, (D.89)a and Table D.1):[150]

$$E^*(\omega) \equiv \frac{\sigma_{ss}(\omega)}{\varepsilon(\omega)} = E_{eq} + \sum_{p=1}^{\infty} \frac{E_p \cdot i\omega\tau_p}{1 + i\omega\tau_p}$$
$$= E_{eq} + \int_0^{\infty} \hat{Y}(\tau) \frac{i\omega\tau}{1 + i\omega\tau} d\tau \qquad (3.13)$$
$$= E_{eq} + \int_{-\infty}^{\infty} H_E(\tau) \frac{i\omega\tau}{1 + i\omega\tau} d\ln\tau$$

where $E^*(\omega) = E'(\omega) + i \cdot E''(\omega)$ is the complex modulus[dd], E_{eq} is the equilibrium modulus (i.e. $E'(\omega \to 0) = E_{eq}$, for viscoelastic solids[ee]), E_p is the spectral strength associated with the discrete relaxation time τ_p, while $\hat{Y}(\tau)$ [Pa/s] and $H_E(\tau) = \tau \cdot \hat{Y}(\tau)$ [Pa] are (respectively) the continuous distributions of relaxation times and moduli (Appendix D, §D.5). Furthermore, describing the time-dependent response of real materials requires the spectral distributions (both discrete and continuous) to be bounded (Appendix D, Eqs. (D.85)a and (D.98)c), i.e. $\sum_{p=1}^{\infty} E_p = \int_{-\infty}^{\infty} H_E(\tau) d\ln\tau = E_g - E_{eq}$, where E_g denotes the glassy modulus (i.e. $E'(\omega \to \infty) = E_g$). The task of determining spectral distributions that reflect the molecular structure of the material under study is not trivial. A discrete relaxation spectrum can easily be obtained by fitting Eq. (3.13)a to the experimental data, using a

---

[dd] In Eq. (3.13), ω is the angular or radian frequency (rad/s) – see Appendix D.

[ee] For viscoelastic liquids, $E'(\omega \to 0) = 0$. In Tschoegl's terminology, viscoelastic solids and liquids are referred to as arrheodictic and rheodictic materials (respectively).[150]

finite set of parameters $\{E_p, \tau_p\}$ with $p = \{1, 2, 3, \ldots, Q\}$[ff]. The resulting constants, however, depend on the choice of Q and cannot be related to a molecular theory, hence have no physical significance.[36] In addition, information present in the original data will be lost and artifacts not associated with the structure of the polymer will be introduced.[36,151] Inferring the spectrum that is a material property thus requires the use of a continuous distribution of relaxation times or moduli. This calculation, involving the deconvolution of Fredholm integral equations of the first kind (i.e. Eqs. (3.13)b and (3.13)c), is an ill-posed problem[gg] and several methods have been proposed over the years[36,42,150]. A reliable procedure was developed in 1993 by Honerkamp and Weese[152], who implemented a nonlinear regression with regularization (NLREG) technique that converges to a physical meaningful spectrum (close to the one that uniquely characterizes the polymer). By taking into account noise in the data as well as the enormous variation of the dynamic moduli over the different regions of viscoelastic behavior, their method yields a smooth relaxation spectrum curve and it is now widely accepted[36].

Using the NLREG program and the time-temperature superposed dynamic moduli at 0 °C (Figure 3.4(a)), we obtained the relaxation spectrum (moduli distribution) $H_E(\tau)$ shown in Figure 3.4(b). The harmonic response functions ($E'(\omega)$, $E''(\omega)$, $\tan\delta(\omega)$) resulting from the calculated spectrum are overlaid in Figure 3.4(a) onto the experimental

---

[ff] The mode index p should not be confused with the Witten–Fetters packing length, although both bear the same symbol.

[gg] Because small perturbations in the experimental data can lead to arbitrarily large perturbations in the spectrum.

data. Dash-dot lines are used outside the measured frequency window (Figure 3.4(a)) and to indicate regions of relaxation times (shaded areas) where the accuracy of $H_E(\tau)$ is not guaranteed (Figure 3.4(b)). When relaxation spectra are inferred from harmonic responses, Davies and Anderssen[153] have in fact shown that the range of relaxation times over which they can be reliably determined is $e^{\pi/2}/\omega_{max} < \tau < e^{-\pi/2}/\omega_{min}$, i.e. 1.36 decades less than the range of frequencies $[\omega_{min}, \omega_{max}]$ over which experimental data are available. While this is undoubtedly a useful mathematical criterion, a qualitative inspection of the calculated $H_E(\tau)$ may provide additional information regarding the accuracy of the result.

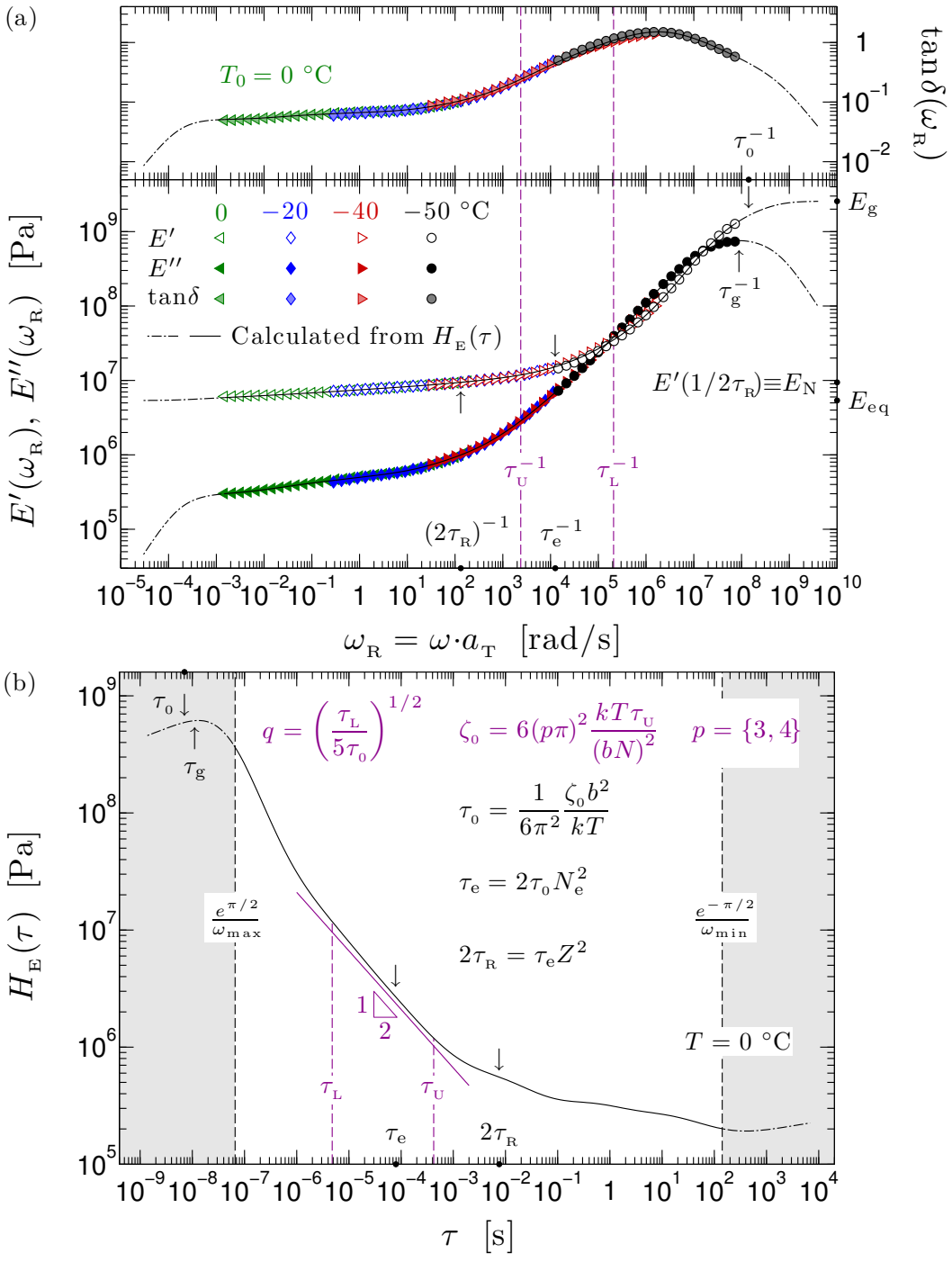

Figure 3.4. (a) Master curves of storage modulus, $E'(\omega_R)$, loss modulus, $E''(\omega_R)$, and loss tangent, tan$\delta(\omega_R)$, and (b) relaxation spectrum, $H_E(\tau)$, of LIL50–12 at 0 °C.

3.3.4.IV-b Qualitative analysis of the linear viscoelastic response

The shape of $H_E(\tau)$ for LIL50–12 at 0 °C (Figure 3.4(b)) resembles that measured for lightly crosslinked rubbers[42]. At the shortest times ($\tau \ll e^{\pi/2}/\omega_{max}$), the mechanical behavior does not approach perfect elasticity: $H_E(\tau)$ remains finite and at a rather high level, indicative of the persistence of dissipative processes even in the glassy regime. This behavior corresponds, in Figure 3.4(a), to a storage modulus $E'(\omega)$ that continues to increase slightly at the highest frequencies instead of approaching a real asymptotic value E_g, and $E''(\omega \to \infty) \neq 0$. With increasing τ, $H_E(\tau)$ goes through a maximum (at about 12 ns) and then drops steeply (PI glass-rubber transition), until it reaches a region where is relatively flat (rubbery plateau).

The qualitative behavior of $H_E(\tau)$ in the glassy zone seems to correctly represent the material response even if $\tau < e^{\pi/2}/\omega_{max}$. The locus of the peak in the spectrum ($\simeq$ 12 ns) is in agreement with the glass transition of the PI block determined by the isochronal measurements (ω = 1 rad/s) in Figure A.3. As discussed in Appendix A, the segmental relaxation processes of the PI backbones occur within 1 s (i.e. the reciprocal of the applied angular frequency) at $T_{g,I}$ = –61.1 °C. Using the WLF parameters c_1^g and c_2^g from Table 3.5, the time scale of these relaxations at 0 °C can be calculated (through Eq. (3.10)) as $a_{0\,^\circ C}^{T_{g,I}} = 10^{-c_1^g(61.1)/\left(c_2^g+61.1\right)} \simeq 16$ ns. Coherently with this estimate, the concentration of dissipative processes associated with $T_{g,I}$ gives rise to a maximum in $H_E(\tau)$ in the neighborhood of 16 ns (below $e^{\pi/2}/\omega_{max}$). Furthermore, since we identified $T_{g,I}$ through the

locus of the loss modulus peak, $a_{0\,^\circ\mathrm{C}}^{T_{g,I}}$ approximates the reciprocal frequency $\tau_g \simeq 11$ ns at which $E''(\omega)$ is maximum at 0 °C (Figure 3.4(a)). The relaxation spectrum and the loss modulus hence exhibit their peaks almost at corresponding time/frequency (12 ns vs. (11 ns)$^{-1}$, respectively). Their similarity is not limited to the glassy region.

A visual examination of Figures 3.4(a) and 3.4(b) reveals that the shape of $H_E(\tau)$ and $E''(1/\tau)$ are somewhat analogous, which is a general feature for polymers[42]. This can be rationalized by noticing that, according to Eq. (3.13), $E'(\omega)$ and $E''(\omega)$ are essentially Stieltjes transforms of the spectral distributions[150] (Appendix B, §B.5). An approximate inversion of the Stieltjes transform on the real time axis yields[150], to the zeroth-order, $H_{E,0}(\tau) = (2/\pi)\cdot E''(1/\tau)$ (Appendix D, Eq. (D.95)): the loss modulus is weighed more heavily in the calculation of $H_E(\tau)$ than the storage modulus, thereby explaining the similar shapes of $H_E(\tau)$ and $E''(1/\tau)$. We will return to this point in §3.3.4.IV-d, when we analyze the dynamics of LIL50–12 across the glass-rubber transition.

At very long times ($\tau \gg e^{-\pi/2}/\omega_{min}$), for viscoelastic solids (like crosslinked polymers and LIL50–12) $H_E(\tau)$ may be expected to approach zero (corresponding to the equilibrium state, $E'(\omega \to 0) = E_{eq}$ and $E''(\omega \to 0) = 0$). Most commonly, however, some degree of relaxation persists and thus $H_E(\tau)$ maintains a finite (slowly decreasing or seemingly constant) value.[42] For viscoelastic liquids (such as entangled amorphous polymers), $H_E(\tau)$ goes through a maximum in the neighborhood of the longest relaxation time, and then drops sharply approaching zero.[42] At this temperature (more than 50 degrees below $T_{g,L}$), relaxation occurs in the PLA domains at reduced frequencies which

are exceedingly low. In principle, master curves at 0 °C that include the PLA glass-rubber transition could be constructed with additional isothermal data near and above $T_{g,L}$. Time-temperature superposition with the data shown in Figure 3.4(a) could be carried out using the theoretical treatment of thermo-rheological complexity developed by Fesko and Tschoegl[127,128], by taking into account the shift behavior of PLA (above and below its T_g) coupled with the shift behavior of PI. The resulting inter-transition plateau would be enormously drawn out due to the PLA viscoelastic transition probably occurring at reduced frequencies of order 10^{-10} rad/s or so ($t \geq \approx 300$ years). On these time scales, the storage modulus would start a sharp descent and level off at about 1 MPa (i.e. the plateau modulus of 1,4-PI at 0 °C, Appendix A). Thus, for practical purposes, at 0 °C the material behaves as a viscoelastic solid with an "effective" or "pseudo" equilibrium modulus E_{eq}. Based on these qualitative considerations, we conclude that the slight increase of $H_E(\tau)$ for $\tau > \approx 500$ s may reflect a lack of accuracy as expected from the analysis of Davies and Anderssen[153] (for $\tau > e^{-\pi/2}/\omega_{min}$) or signal a concentration of dissipative processes on a time scale of order 10^4 s. The analysis of the dynamics, presented in §3.3.4.IV-d, will shed some light on the matter.

Significant features also emerge from the observation of the storage ($E'(\omega)$) and loss ($E''(\omega)$, $\tan\delta(\omega)$) functions (Figure 3.4(a)). In regions where the storage modulus is weakly frequency-dependent (i.e. outside the rubber-glass transition), the response is more elastic and thus the energy dissipated per cycle ($\sim E''(\omega)$) is considerably less than the energy stored ($\sim E'(\omega)$). At very low frequencies, linear viscoelasticity predicts

$E''(\omega) \sim \omega$ (Appendix D, Eqs. (D.104)b and (D.109)b). For viscoelastic solids, this regime usually lies below the experimentally accessible window[42], but the loss modulus calculated from $H_E(\tau)$ seems to confirm such behavior (the computation of $H_E(\tau)$ expanded the frequency window from about 11 to 15 decades). Overall, the frequency dependence of the dynamic moduli is reminiscent of the behavior of very lightly crosslinked rubbers (e.g. vulcanized styrene–butadiene random copolymer (SBR)) containing entangled dangling structures[42].

The loss tangent, however, is most revealing. In very lightly crosslinked rubbers, $\tan\delta(\omega)$ exhibits two maxima: a pronounced peak due to the glass-rubber transition, and a subsidiary maximum at lower frequencies.[42] This additional dispersion is usually associated with rearrangements of configurations by "slippage" of untrapped entanglements (i.e. disengagement of entanglements on dangling structures).[42] A similar behavior was also found in blends of diblock/triblock copolymers (S–B/S–B–S), when the B chain of the diblock was entangled.[154] A secondary peak in $\tan\delta(\omega)$ is not observed in Figure 3.4(a), and the monotonic decrease signals a slowly-approaching (pseudo) equilibrium state most commonly observed in lightly crosslinked systems with no untrapped entanglements[155,156]. This suggests either the absence of such relaxation mechanism in LIL50–12 or a very low concentration of entangled dangling structures. In some of the S–B–S triblocks studied by Tschoegl and co-workers[126-129] $\tan\delta(\omega)$ exhibited also a shallow broad peak preceding the glass-rubber transition of the hard phase, which was attributed to the relaxation of a diffuse B/S interlayer. This additional dispersion

emerged at temperatures within about 40 degrees from the polystyrene transition, and only when the midblock was predominantly 1,4-B (determining a very large separation of T_g's of about 175 degrees). In our material, relaxation of the I/L interface is completely masked (if present at all, in the low-frequency region of Figure 3.4(a)) by the relaxation of the matrix. This is not surprising considering the distance from the PLA glass transition (> 50 degrees), the separation of T_g's (≈ 115 degrees), and the strong driving force towards segregation ($\chi\hat{N}$ (25 °C) ≃ 436) that should result in narrow I/L interfaces.

We now briefly review the main features of the Rouse–Bueche theory[47,85,86] of flexible chain dynamics (some of which have already been mentioned in §3.3.2.II), and describe how it can be applied to a filled system for the determination of ζ_0.

3.3.4.IV-c Rouse–Bueche theory and the calculation of ζ_0 in a filled system

The Rouse model[42,47] views a polymer chain of mean-square size R^2 and N chemical monomers as comprised of S (massless) Gaussian subchains connected by $S + 1$ frictional particles ("beads"). Each subchain contains $q = N/S$ monomers and is long just enough[47] to assume a random coil conformation (with mean-square size $\sigma^2 = R^2/S$, as described by Eq. (3.1)). Each bead represents the mass of one subchain (for large S, $S \simeq S + 1$), and it is thus assigned the friction coefficient $\zeta_{bead} = N\cdot\zeta_0/(S + 1) \simeq q\cdot\zeta_0$.[42,45] The simultaneous, free-draining motions of all beads is described through an orthonormal transformation of

coordinates as a series of S cooperative normal modes[hh] (eigenmodes) identified by the mode index[ff,ii] $p = \{1, 2, 3, \ldots, S\}$.[45,47] The eigenmode p involves the coherent motion of p sections of the chain with N/p monomers, and each section relaxes independently on the time scale τ_p.[22,47] By calculating the eigenvalues of the connectivity matrix (expressing the coupling of connector forces between adjacent beads), the discrete relaxation times τ_p of the Rouse spectrum are conveniently approximated as:[42,47,jj]

$$\begin{aligned} \tau_p &= \frac{1}{6\pi^2}\frac{\zeta_0 b^2}{kT}\left(\frac{N}{p}\right)^2 \\ &= \quad \tau_0 \quad \left(\frac{N}{p}\right)^2 \qquad \text{for } \tau_p \geq 5\tau_S = 5\tau_0 q^2, \text{ i.e. } p \leq \mathrm{Int}\left(S/\sqrt{5}\right) \end{aligned} \tag{3.14}$$

where k is Boltzmann's constant, T is the absolute temperature, $\tau_0 = \zeta_0 b^2/6\pi^2 kT$ is the segmental time[kk] (i.e. time scale for motion of individual monomers at length scale b)[22,23],

---

[hh] The Rouse normal modes are to some degree analogous to the modes of motion in a vibrating string fastened at both ends.[36,42]

[ii] The $p = 0$ mode corresponds to uniform translation and does not contribute to viscoelasticity.[42,45]

[jj] The derivation of Eq. (3.14) includes the approximation of the eigenvalues of the connectivity matrix, $\lambda_p = 4\sin^2(\pi \cdot p/2(S+1))$, as $\lambda_p = (\pi \cdot p/S)^2$ for $p \ll S$.[45] The error in the approximation is less than 22% for $p < S/\sqrt{5}$, and less than 8% for $p < S/5$. The requirement $\tau_p > 5\tau_S$, given on page 189 of Ferry's book[42], implies (through Eq. (3.14)) $p < S/\sqrt{5}$. However, in both Ferry's book[42] and Dealy and Larson's book[36] the condition $p < S/5$ is reported as convergence requirement instead. The reason for this discrepancy is not clear. Since the mode index is an integer number, we use the notation Int($S/\sqrt{5}$) to indicate the integer part of $S/\sqrt{5}$.

[kk] τ_0 should not be confused with the $p = 0$ mode, which is independent of chain conformation (see footnote [ii]). As a result, the mode index varies from 1 (τ_1, longest Rouse relaxation time, involving the coherent motion of all N monomers) to S (τ_S,

and Int($S/\sqrt{5}$) denotes the integer part of $S/\sqrt{5}$. Except for the three smallest mode indices (i.e. three longest τ_p's), these relaxation times are closely enough spaced that at intermediate times (i.e. away from glassy and terminal modes) the discrete Rouse spectrum (in shear) can be described by a continuous (moduli) distribution function as:[42]

$$H^{\text{Rouse}}(\tau) = \frac{\rho N_{\text{av}}}{M_0}\frac{b}{2\pi}\left(\frac{\zeta_0 kT}{6}\right)^{1/2}\tau^{-1/2} \qquad \text{for } \tau \in \left[5\tau_0 q^2, \approx \tau_3\right] \tag{3.15}$$

Originally intended to describe dilute polymer solutions[47], when applied to unentangled melts[85,86] the Rouse model is referred to as the Rouse–Bueche theory[36,47,85,86]. In entangled undiluted polymers, flexible enough that the characteristic dimensions of the Gaussian subchain and the tube SSL are widely separated (i.e. $\sigma \ll a$), there exists a corresponding region of time/frequency scales (often about one decade or less) where the linear response follows the power-law Rouse–Bueche predictions described by Eq. (3.15) (i.e. $H(\tau) \sim \tau^{-1/2}$, $G'(\omega) = G''(\omega) \sim \omega^{1/2}$).[36,42] This behavior is usually called the Bueche–Ferry law[157] (cf. Appendix E, §E.1). For these systems, Ferry and co-workers[42] have shown that ζ_0 can be obtained by matching the experimental (shear) relaxation spectrum $H(\tau)$ in the rubber-glass transition zone with the prediction of Eq. (3.15). Since the slope of $H(\tau)$ in this region is often gradually increasing (with decreasing τ), their procedure consists in drawing a tangent with the theoretical slope of –1/2. From Eq. (3.15), with values of $H(\tau)$ and τ taken from any point in the Bueche–Ferry-law region, ζ_0 can be calculated.

---

shortest Rouse relaxation time, involving the coherent motion of S sections of the chain each with N/S monomers).

Ferry's procedure, however, cannot be directly applied to our system for two reasons. First, the Rouse–Bueche theory predicts the linear response in shear. The shear $H(\tau)$ and the uniaxial extensional $H_E(\tau)$ spectra are close but generally differ both in magnitude ($H_E(\tau) > H(\tau)$) and shape.[150] An expression for the extensional spectrum can be obtained as $H_E(\tau) = g(\tau) \cdot H(\tau)$, where $g(\tau) > 1$ is an unknown function of τ that depends on the relative magnitude of the relaxation bulk $K(t)$ and shear $G(t)$ moduli. As discussed in Appendix A, when the frequency/time-dependent Poisson's ratio can be approximated by a real constant μ (i.e. in the glassy and equilibrium states), linear harmonic responses in shear and uniaxial extension can be interconverted through[150] $E^*(\omega) = 2(1+\mu)G^*(\omega)$. According to Eq. (3.13) and its analogous for shear, this implies $g(\tau) = 2(1+\mu)$ (for a restricted τ domain). Assuming that in the Bueche–Ferry-law region the change in volume is negligible compared with the change in shape (i.e. $K_{eq} \gg G_{eq}$), $\mu \simeq 1/2$ and $H_E(\tau) \simeq 3H(\tau)$.

While this may be true, the analysis of the thermal behavior for $T_{g,I} < T < T_{g,L}$ (Figure A.3) showed that LIL50–12 does not behave simply like an entangled PI-rich matrix. At service temperatures, the glassy PLA domains act as physical endlinks for the PI chain ends (thus increasing the number of network junctions with respect to a pure and entangled PI melt) as well as pseudo-rigid occupiers of space (like filler particles). The augmented number of network junctions is analogous to what would result from increasing the entanglement density or inducing chemical crosslinking in the PI-rich matrix, and its contribution to the linear response is outweighed by the filler effect of the

PLA domains (these simultaneous contributions will be examined quantitatively in §3.3.4.IV-e). With respect to an entangled PI melt, this filler effect causes the dynamic moduli of LIL50–12 to increase by a frequency-dependent factor $\xi(\omega) > 1$ (e.g. ξ(1 rad/s, 0 °C) $\approx$ 9, – see Appendix A). Similarly, the filler effect amplifies the extensional relaxation spectrum[42], with respect to the Rouse prediction, by a time-dependent factor $\xi'(\tau) > 1$. While both $\xi(\omega)$ and $\xi'(\tau)$ express the effect of filler particles on the system, their definition is different: the former compares the dynamic moduli with the response of the entangled matrix (whether or not it obeys the Bueche–Ferry law), the latter measures the deviation of the spectrum from the Rouse theory (Eq. (3.15)). Outside the Bueche–Ferry-law region, their numerical value will be different.

The general relation between the extensional spectrum for a filled system and the Rouse spectrum can then be expressed as:

$$H_{\mathrm{E}}^{\mathrm{Filled}}(\tau) = \xi'(\tau) \cdot g(\tau) \cdot H^{\mathrm{Rouse}}(\tau) \tag{3.16}$$

Although $g(\tau)$ can easily be approximated by a numerical factor, a theoretical expression for $\xi'(\tau)$ (or $\xi(\omega)$) would require knowledge of the shape and distribution of the filler particles. Thus, under many practical conditions (e.g. non-spherical particles, multimodal distribution, or non-equilibrium morphology for block copolymer TPEs), Eqs. (3.15) and (3.16) cannot be directly applied to extract information about ζ_0 from the measured linear dynamic behavior. There exists, however, a direct and simple way to use the Rouse–Bueche theory for determining ζ_0 in filled systems such as LIL50–12.

Motivated by Ferry's procedure, we calculated the slope of the extensional spectrum, $c = d\log H_E(\tau)/d\log\tau$, and identified the Bueche–Ferry-law region by a ± 10% deviation from the theoretical value of –1/2. This allowed us to determine the lower and upper limits of relaxation times between which $H_E(\tau) \sim \tau^{-1/2}$, respectively $\tau_L \simeq 4.8{\cdot}10^{-6}$ s and $\tau_U \simeq 4.2{\cdot}10^{-4}$ s. A line with slope –1/2 is drawn in Figure 3.4(b) close to $H_E(\tau)$ in the glass-rubber transition region, complemented with the position of τ_L and τ_U.

Knowledge of τ_L and τ_U permits the calculation of ζ_0 and the characteristic Rouse dimensions of the PI block, as follows. The Rouse–Bueche theory, in the form of Eqs. (3.14) and (3.15), is only valid for relaxation times in the interval $[5\tau_0 q^2, \approx \tau_3]$. Whereas the measured relaxation spectrum (Figure 3.4(b)) is higher than the Rouse prediction (as described by Eq. (3.16)), the relaxation times of PI statistical segments at length scales < *a* are oblivious of the presence of glassy PLA domains (as shown by the analysis of $a_T(T)$ in §3.3.4.III-b-c) and should not be very different between shear and uniaxial extension (they will be, of course, at larger length scales). It seems then legitimate to identify τ_L with $5\tau_0 q^2$, and τ_U with $\approx \tau_3$. Given the vagueness in the upper theoretical limit[42], we can more safely assume $\tau_U = \tau_p$ with $p = \{3, 4\}$. Ascertaining which value of p is more appropriate for our system is momentarily deferred. From these relations and Eq. (3.14), the PI monomeric friction coefficient can be calculated as:

$$\zeta_0 = 6(p\pi)^2 \frac{kT\tau_U}{(bN)^2} \qquad \text{with } p = \{3,4\} \tag{3.17}$$

while the number of monomers in a PI Gaussian submolecule is given by:

$$q = \left(\frac{\tau_L}{5\tau_0} \right)^{1/2} \tag{3.18}$$

With the values of b_I(0 °C) and N_I from Tables 3.3 and 3.4, Eq. (3.17) yields $\zeta_0 = 3.94 \cdot 10^{-9}$ N·s·m^{-1} ($p = 3$) and $\zeta_0 = 7.0 \cdot 10^{-9}$ N·s·m^{-1} ($p = 4$) for the PI block at 0 °C. Accordingly, the PI segmental time is $\tau_0 \simeq 7.1$ ns ($p = 3$) and $\tau_0 \simeq 12.6$ ns ($p = 4$). From Eqs. (3.1) and (3.18), the parameters defining the PI Rouse chain (i.e. average number of monomers q and backbone bonds n_s per Gaussian submolecule, average number of submolecules S and their root-mean-square size σ) are $\{q, n_s, S, \sigma\} = \{11.6, 44.9, 62.9, 2.16 \text{ nm}\}$ for $p = 3$, and $\{q, n_s, S, \sigma\} = \{8.7, 33.7, 83.9, 1.87 \text{ nm}\}$ for $p = 4$. In either case, $\sigma \ll a = 5.49$ nm (Table 3.3), as expected from the intrinsic flexibility of the PI chain.

Since the segmental time τ_0 represents the time scale for motion of individual monomers, probed on time scales shorter than τ_0 polymers exhibit predominantly an elastic response[22]. Therefore, it is reasonable to expect that τ_0 be close to the time scale of the PI glass transition, represented either by the time at which $H_E(\tau)$ reaches its maximum ($\simeq$ 12 ns) or by the inverse frequency corresponding to the peak in the loss modulus $E''(\omega)$ ($\simeq$ 11 ns). Both estimates of τ_0 approximate the time scale of the PI glass transition. Based on this argument alone, $p = 4$ ($\tau_0 \simeq 12.6$ ns) would seem a proper choice for our system. However, when discussing the characteristic length scales of LIL50–12 (§3.3.2.II), we examined two rules of thumb that have been put forward directly (by Ferry[42]) and indirectly (by Dealy and Larson[36]) related to the number of monomers and backbone bonds per Gaussian subchain. In the same context, we also developed an

argument drawn from the (Kratky–Porod) worm-like chain model[58]. As a result, we anticipated that the parameters of the PI Rouse chain at 0 °C should fall roughly in the range $\{q, n_s, S, \sigma\} \approx \{12–15, 47–58, 49–60, 2.2–2.5 \text{ nm}\}$. Considering these estimates, $p = 3$ ($\zeta_0 = 3.94 \cdot 10^{-9}$ N·s·m^{-1}, $\tau_0 \simeq 7.1$ ns) is a more suitable choice for LIL50–12.

In §3.3.4.III-b-c, the analysis of $a_T(T)$ suggested that the local friction of PI monomers in our system should be similar to that experienced in pure PI melts. The viscoelastic monomeric friction coefficient of two undiluted PIs, measured by Klopffer et al.[139] and Dickie and Ferry[42,158] from dynamic mechanical data in the rubber-glass transition zone, is listed at different temperatures in Table 3.6 for comparison. The literature values at 0 °C, $6.7 \cdot 10^{-9}$ N·s·m^{-1} and $5.8 \cdot 10^{-9}$ N·s·m^{-1} (respectively), are slightly higher than what we measure by choosing $p = 3$. The molar masses of those polymers, however, are considerably larger ($M_w = 1820$ kg/mol and $M_v = 230–770$ kg/mol, respectively) compared with our PI block ($M_n = 49.8$ kg/mol). Therefore, the minor difference may originate from the chain length dependence of ζ_0[42]: while $6.7 \cdot 10^{-9}$ N·s·m^{-1} and $5.8 \cdot 10^{-9}$ N·s·m^{-1} are the asymptotic limiting values at high molar mass, $3.94 \cdot 10^{-9}$ N·s·m^{-1} for our PI block may reflect the additional free volume associated with molecular ends. Bearing this in mind, the agreement between our measurement and the corresponding values for PI melts is satisfactory. This represents additional evidence that the local segmental dynamics is unaffected by the presence of the glassy PLA domains, and seems to validate the foregoing procedure for calculating ζ_0 in filled systems.

We would also like to point out that although it is often not possible to determine the filler effect $\xi'(\tau)$ *a priori*, its value within the Bueche–Ferry-law region can be inferred directly from the measured spectrum. If the Rouse spectrum is expressed in discrete form (cf. Appendix E, Eq. (E.1)), $H^{\text{Rouse}}(\tau_p) = (p/2)\cdot(\rho N_{av}/M)\cdot kT$ for $5\tau_0 q^2 \leq \tau_p \leq \approx \tau_3$, Eq. (3.16) yields $\xi'(\tau_p) = (2H_E^{\text{Filled}}(\tau_p)M)/(g(\tau_p)p\rho N_{av}kT)$. For $p = 3$ and $g(\tau_3) = 3$ (i.e. "incompressibility"), $\xi'(\tau_3 \simeq 0.42 \text{ ms}, 0\ ^\circ\text{C}) \simeq 6.4$.

Table 3.6. Viscoelastic monomeric friction coefficient of PI, calculated from dynamic mechanical data (storage and loss moduli or relaxation spectrum) obtained in the rubber-glass transition zone.

Polymer	T_g [°C]	log $\zeta_{0,PI}$ [N·s·m^{-1}] at T_g	0 °C	25 °C	T_g + 100 deg	∞	*Ref.* [e]
LIL50–12 [a]	– 61	– 0.60	– 8.40 [d]	– 9.59	– 10.08	– 14.90	this study
PI [b]	– 62	– 0.35	– 8.17	– 9.25 [d]	– 9.66	– 13.85	[1]
Hevea Rubber [c]	– 73	1.45	– 8.24	– 9.41 [d]	– 9.49	– 15.35	[7]

a) 46.5/46.5/7 *cis*-1,4/*trans*-1,4/3,4 PI block, with number-average molar mass M_n = 49.8 kg/mol. $T_{g,I}$ determined from the maximum in the loss modulus $E''(\omega)$ obtained at an angular frequency ω = 1 rad/s and at a rate $\partial T/\partial t$ = 0.2 °C/min (upon cooling and heating).

b) 92/5/3 *cis*-1,4/*trans*-1,4/3,4 undiluted linear PI homopolymer, with mass-average molar mass M_w = 1820 kg/mol. T_g determined by DSC as the onset of the transition, upon heating at a rate $\partial T/\partial t$ = 5 °C/min. Note that there is a typo in [1], where $\log(\zeta_0(\infty)) = -13.4$ N·s·m^{-1} instead of –13.85 N·s·m^{-1}.

c) Natural rubber lightly vulcanized with dicumyl peroxide, with viscosity-average molar mass M_v = 230–770 kg/mol. T_g determined by volume dilatometry.

d) ζ_0 was obtained at this temperature and calculated at different temperatures neglecting the terms T and b in the definition of a_T (see §3.3.4.III), i.e. using the parameters c_1^g and c_2^g shown in Table 3.5 and the WLF equation with $a_T(T) = \zeta_0(T)/\zeta_0(T_g)$ or, equivalently, $\log(\zeta_0(T)) = \log(\zeta_0(\infty)) + c_1^g c_2^g / (c_2^g + T - T_g)$ where $\log(\zeta_0(\infty)) = \log(\zeta_0(T_g)) - c_1^g$.

e) *Ref.* [1] = Klopffer et al.[139]; [7] = Dickie and Ferry[42,158].

Table 3.7. Power-law exponents for the storage modulus, $E'(\omega)$, loss modulus, $E''(\omega)$, and relaxation spectrum, $H_E(\tau)$, of LIL50–12 at 0 °C.

Characteristic Frequencies [rad/s]	ω [rad/s]	$E'(\omega) \sim \omega^m$ m	$E''(\omega) \sim \omega^n$ n	τ	$H_E(\tau) \sim \tau^c$ c
$1/\tau_0 \simeq 1.4 \cdot 10^8$					
	$3 \cdot 10^6 - 1 \cdot 10^7$	0.75		0.15 – 0.5 μs	– 1
				1 μs	– 0.75
	$4 \cdot 10^5 - 7 \cdot 10^5$	0.5			
$1/\tau_L \simeq 2.1 \cdot 10^5$					
$\omega_c \simeq 1.5 \cdot 10^5$	ω_c	0.38	0.65	$\tau_L - \tau_U$	– 0.5
$1/\tau_e \simeq 1.3 \cdot 10^4$					
$1/\tau_U \simeq 2.4 \cdot 10^3$	$2 \cdot 10^3 - 8 \cdot 10^3$		0.5		
$1/2\tau_R \simeq 1.3 \cdot 10^2$				1.5 – 100 ms	– 0.17
				0.1 – 20 s	– 0.07
	$1 \cdot 10^{-3} - 1/2\tau_R$	0.04	0.09		
	$\leq 1 \cdot 10^{-4}$	$\simeq 0$	1		

Table 3.8. Characteristic time scales, length scales, and relevant dynamics of LIL50–12 at 0 °C.

Time scales		*Length scales* [nm]		PI *Monomers*		*Dynamics*	
						$t < \tau_0$	Linear Elastic Solid
τ_0	7 ns	b	0.6		1		
						$\tau_0 < t < \tau_L$	Semi-Flexible Chain
τ_L	5 μs	$5^{1/4}\cdot\sigma$	3.2	$5^{1/2}\cdot q$	26		
						$\tau_L \leq t < \tau_e$	3-D Rouse
τ_e	0.08 ms	a	5.5	N_e	75		
τ_U	0.42 ms						
						$\tau_e \leq t \leq 2\tau_R$	1-D Rouse
$2\tau_R$	7.6 ms	$(a\cdot R/2)^{1/2}$	6.9	N	731		
						$2\tau_R < t \leq \tau_{late}$	Arm Retraction
τ_{late}	$1.9\cdot10^4$ s	R	17.1				

3.3.4.IV-d Characteristic time scales and relevant dynamics

Knowledge of ζ_0 for the PI block allows us to determine the characteristic time scales of LIL50–12 at 0 °C, hence to connect the viscoelastic response shown in Figure 3.4 to the chemical and topological structure of the material at different length scales. The following analysis is summarized in Tables 3.7 and 3.8.

***t* < τ_0**

On time scales shorter than the PI segmental time $\tau_0 \simeq 7$ ns ($\omega > 1/\tau_0 \simeq 1.4\cdot10^8$ rad/s), strain excitations probe length scales smaller than $b \simeq 0.6$ nm (Table 3.3) thereby causing stress relaxations occurring within the PI chemical monomers. At the highest frequencies

($\omega > 10^9$ rad/s), the mechanical behavior is mostly elastic ($E'(\omega) \approx const. \gg E''(\omega)$) and approximates, at still higher frequencies, the perfect *linear* (*enthalpic*) *elasticity*[22,23,42] ($E'(\omega) = E_g \simeq 2.6$ GPa, $E''(\omega) \rightarrow 0$) of glassy PI homopolymer (Table 3.8 – for more details, see Appendix A)[ll].

$\tau_0 < t < \tau_L$

With increasing time scale, in the range $\tau_0 < t < \tau_L \simeq 5$ μs ($1/\tau_L \simeq 2.1 \cdot 10^5$ rad/s $< \omega < 1/\tau_0$), stress relaxation in a PI chain is limited to length scales $x < 5^{1/4} \cdot \sigma \simeq 3.2$ nm. Indeed, since we identified τ_L with $5\tau_S$ (corresponding to the mode index $p = \text{Int}(S/\sqrt{5}) = 28$)[jj], at $t = \tau_L$ the eigenmode $\text{Int}(S/\sqrt{5})$ involves the coherent Rouse-like motion of about 28 sections of the PI chain, each made up of $N/p = q\sqrt{5} \simeq 26$ monomers (i.e. roughly 2 PI Gaussian submolecules). Therefore, by neglecting the strong state of segregation of the system each PI subchain at τ_L can be viewed as a random coil with mean-square-size $R^2/p = 5^{1/2} \cdot \sigma^2$ (from Eq. (3.1)), and root-mean-square size $5^{1/4} \cdot \sigma$.

This regime (7 ns $< t <$ 5 μs, 0.6 nm $< x <$ 3.2 nm) corresponds to the PI glass-rubber transition. Still influenced by polymer-specific chemical details, the dynamics at these time and length scales is not universal. Nevertheless, the measured viscoelastic response partially obeys the scaling of *semi-flexible chain* models[22], $H_E(\tau) \sim \tau^{-3/4}$ and $E'(\omega) \sim \omega^{3/4}$,

---

[ll] The slight temperature dependence of the glassy storage modulus, E'(–100 °C, 1 rad/s) = 4 GPa > E'(0 °C, 10^{10} rad/s) = 2.6 GPa, is indicative of *enthalpic* elasticity (Ferry[42] pp 272–273, 304–305; Rubinstein and Colby[22]pp 254–255; Hiemenz and Lodge[23] pp 396–399) in agreement with the results of the isochronal temperature ramps shown in Figure A.3 (see Appendix A).

over a narrower range of times and frequencies (around 1 μs for $H_E(\tau)$, and in the interval $3{\cdot}10^6 - 1{\cdot}10^7$ rad/s for $E'(\omega)$) (Tables 3.7 and 3.8).

Towards the low-frequency end of the transition zone, the scaling of the storage modulus is qualitatively described by the power-law prediction of the Rouse–Bueche theory, with $E'(\omega) \sim \omega^{1/2}$ for $4{\cdot}10^5$ rad/s $\leq \omega \leq 7{\cdot}10^5$ rad/s (Table 3.7), consistently with the behavior occasionally observed in entangled homopolymers[22,42,159]. The end of the transition zone almost coincides with the crossover frequency $\omega_c \simeq 1.5{\cdot}10^5$ rad/s at which $E'(\omega_c) = E''(\omega_c) \simeq 31$ MPa. Noteworthily, neither modulus at the crossover obeys the Bueche–Ferry law, since $E'(\omega)\big|_{\omega=\omega_c} \sim \omega^{0.38}$ and $E''(\omega)\big|_{\omega=\omega_c} \sim \omega^{0.65}$ (Table 3.7).

$\tau_L \leq t < \tau_e$

For $t \geq \tau_L$, the cooperative motion of multiple PI monomers engages sections of the chain all long enough to assume a random coil conformation (albeit stretched by chain segregation). Even though the PI-rich matrix is well entangled (Z(0 °C) = 9.8, Table 3.4), transverse fluctuations of PI monomers remain unencumbered by the topological constraints therein on time scales shorter than the *equilibration time of a tube segment*:[35,36,44-46,mm]

[mm] The relaxation times τ_p of the Rouse model are half of the end-to-end vector correlation times of normal modes.[22] Therefore, the *longest Rouse relaxation time* (or *Rouse time*) of a chain with N monomers, $\tau_1 = \tau_0 N^2$, is half of the *Rouse reorientation time* (or *rotational relaxation time*) defined by Doi and Edwards[46]. The *equilibration time*, $\tau_e = 2\tau_0(N_e)^2$, is calculated as the *Rouse reorientation time* (i.e. twice the Rouse time) of an entanglement strand.[35,36] τ_e is sometimes called the *step equilibration time*[45] or the *entanglement time*[44].

$$\tau_e \equiv 2\tau_0 N_e^2 \tag{3.19}$$

With N_e from Table 3.4 and $\tau_0 \simeq 7$ ns, $\tau_e \simeq 0.08$ ms. τ_e, sometimes called the *entanglement time*[44] or the *step equilibration time*[45], represents the time scale for a PI entanglement strand to diffuse a distance of order its size ($a \simeq 5.5$ nm, Table 3.3) if it were not attached to the chain.

At $t = \tau_e$, the PI entanglement network comes into play. As a result, for 5 μs $\leq t <$ 0.08 ms (3.2 nm $\leq x <$ 5.5 nm) the dynamics is oblivious of chemical details of the polymer chains as well as of large-scale molecular architecture. In this regime, stress relaxation proceeds as though the matrix were unentangled, i.e. via 3-D *Rouse-like motions* of the 75 monomers within a PI tube segment (Table 3.8), with mean-square monomer displacement $x^2(t)$ given by the subdiffusive motion of the Rouse model[22], $x^2(t) \sim (t/\tau_0)^{1/2} b^2 \sim (t/\tau_e)^{1/2} a^2$ (from Eqs. (3.1), (3.8), and (3.14)).

The estimate of τ_e, delimiting the crossover between Rouse-like and entanglement-dominated dynamics, falls well within the Bueche–Ferry-law region of the relaxation spectrum: the Rouse scaling $H_E(\tau) \sim \tau^{-1/2}$ persists beyond the entanglement time τ_e and up to τ_U (Figure 3.4(b) and Table 3.7), in spite of a storage modulus $E'(\omega)$ that signals (in the corresponding region of frequencies [$1/\tau_U \simeq 2.4 \cdot 10^3$ rad/s, $1/\tau_e \simeq 1.3 \cdot 10^4$ rad/s]) the presence of a network structure beginning to hamper further relaxation (Figure 3.4(a)). The resolution of this apparent paradox lies in the definition of $H_E(\tau)$ through Eq. (3.13)c. As discussed in §3.3.4.IV-b, $E''(\omega)$ is weighed more heavily in the calculation of $H_E(\tau)$ than $E'(\omega)$ (to the zeroth-order, $H_{E,0}(\tau) = (2/\pi) \cdot E''(1/\tau)$)[150]. Both moduli obey the Bueche–

Ferry-law outside the frequency window $[1/\tau_e, 1/\tau_L]$: $E''(\omega) \sim \omega^{1/2}$ for $\omega < 1/\tau_e$ and $E'(\omega) \sim \omega^{1/2}$ for $\omega > 1/\tau_L$ (Table 3.7). The 1/2 power-law behavior of $H_E(\tau)$ stems from the corresponding scaling of the dynamic moduli, but it is more strongly affected by the frequency-dependence of $E''(\omega)$.[nn]

$$\boldsymbol{\tau_e \leq t \leq 2\tau_R}$$

On time scales shorter than τ_e, stress relaxation in LIL50–12 is unaltered by the network structure of the material and follows the same dynamics characteristic of an unentangled PI melt. For $t \geq \tau_e$, the dynamics is ruled by large-scale molecular architecture. On these time scales, the accessible relaxation mechanisms are dictated by the network structure of LIL50–12 (schematically illustrated in Figure 3.5).

Since the block copolymer is microphase-segregated and $T < T_{g,L}$, network junctions derive both from PI entanglements and from PLA microdomains acting as physical endlinks for (a fraction of) the PI chains. Indeed, the specific molecular architecture depends on the different midblock chain conformations typical of microphase-segregated block copolymers of the A–B–A type.[105,109] Only a fraction x_b of PI chains interconnects two different PLA domains (*bridge* conformation). On the other hand, a fraction x_l of PI chains assumes a *loop* conformation, in which both ends of the midblock are anchored to the interface of the same PLA domain. Within this class, some PI chains (x_k) are

---

[nn] Since the harmonic responses $E'(\omega)$ and $E''(\omega)$ are functionals, they would simultaneously follow the Bueche–Ferry-law if the relaxation spectrum scaled as $H_E(\tau) \sim \tau^{-1/2}$ over its entire τ domain (Tschoegl[150] pp 163, 350 – Appendix D, §D.5).

connected to the network through entanglements (*knotted-loop* conformation) while the remaining ($x_d = x_l - x_k$) act as dangling ends and can be viewed as a network defect (*dangling-loop* conformation). In compositionally symmetric A–B–A block copolymers, the equilibrium bridging fraction of B chains ($x_b = 1 - x_l$) has been estimated both theoretically[121,160,161] and experimentally[136,162-164] for different morphologies. The metastable state of LIL50–12 prevents us from making use of these results, but given the high entanglement density of the PI-rich matrix we can assume that the vast majority of loops be in a knotted conformation (i.e. $x_d \simeq 0$, $x_l \simeq x_k$)[165]. Lastly, we need to take into account those triblock chains ($x_f = 1 - x_b - x_l$) having one ($x_{f,1}$) or both ends ($x_{f,2} = x_f - x_{f,1}$) residing outside PLA domains (*single-* or *double-free-end* conformation). As mentioned in §3.3.1, the presence of unsegregated endblocks embedded in the PI-rich matrix (i.e. partial segregation for lack of thermodynamic equilibrium) is suggested by the DSC results and the thermal behavior shown in Figure A.3 (for more details, see Appendix A).

The rubbery (E_N) and pseudo-equilibrium (E_{eq}) stress-strain behaviors of LIL50–12 depend on the concentration of elastically active network strands, therefore are affected by x_b, x_k, and x_f (this will be examined quantitatively in §3.3.4.IV-e). In contrast, the viscoelastic behavior of the network is also influenced by the unentangled dangling structures (x_d). In both dielectric and viscoelastic measurements, bridge and knotted-loop conformations are essentially indistinguishable.[163] For simplicity, the schematic drawing in Figure 3.5 only shows PI chains either in bridge (x_b) or single-free-end ($x_{f,1}$) conformations.

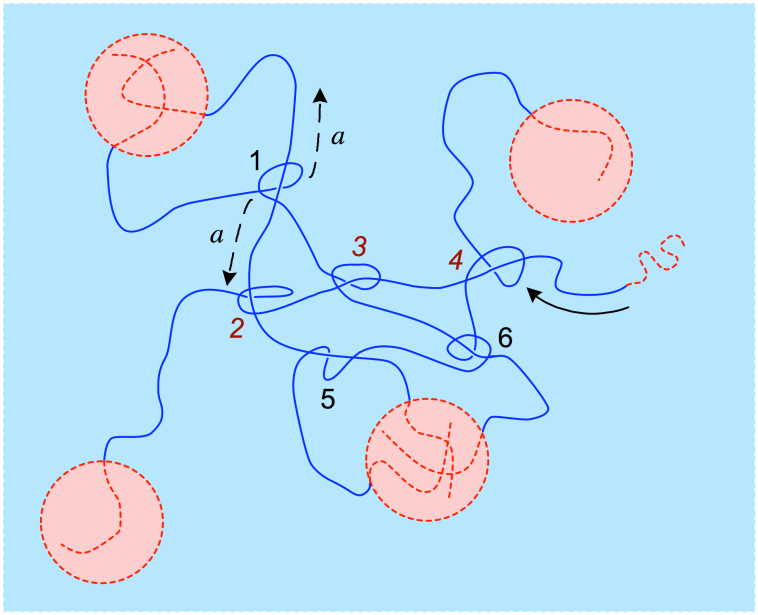

Figure 3.5. Schematic illustration of the LIL50–12 microphase-segregated morphology. Shaded regions are block-segregated microdomains colored according to monomer type, with blue for type I and red for type L monomers. Entanglements (indicated by numbers) are given the crude visual representation of local kinks between two neighbouring chains[oo], and are separated by an average distance *a* (i.e. the PI tube SSL). Both the shape of the PLA microdomains and the entanglement density are chosen for simplicity and do not reflect the actual morphology of the system. The presence of unsegregated endblocks embedded in the PI-rich matrix (suggested by the DSC results and the thermal behavior shown in Figure A.3), or diblock impurities, gives rise to untrapped entanglements (indicated by red italic numbers) and a slow relaxation mechanism (solid black arrow) similar to the arm retraction of star polymers.

[oo] In entangled flexible polymers, topological interactions are highly cooperative and each "locus of adherence" may be represented by an average of ≈ 5 neighbouring chains in pairwise contact (cf. Table 3.4 and Chapter 2).

At time scales $t \geq \tau_e$ (length scales $x \geq a$), regular 3-D Rouse-like motions are unattainable due to the intervening lateral confinement of entanglements. Monomer displacement along the primitive path, however, remains unconstrained and follows the Rouse model (Eq. (3.14)): as time progresses, an increasing number of PI monomers ($\sim (t/\tau_0)^{1/2}$) coherently participate in longitudinal Rouse-like motions along the tube's centerline[22]. Their curvilinear mean-square displacement $s^2(t)$ thus scales as $s^2(t) \sim (t/\tau_0)^{1/2}b^2 \sim (t/\tau_e)^{1/2}a^2$ (from Eqs. (3.8), (3.14), and (3.19)). In three-dimensional space, the scaling of the mean-square monomer displacement becomes $x^2(t) \sim a \cdot s(t) \sim (t/\tau_e)^{1/4}a^2$.[22,44] The numerical prefactor was calculated by Doi and Edwards[46,89] from a detailed 1-D Rouse model, giving $s^2(t) = (4/3\pi^{3/2})\cdot(t/\tau_e)^{1/2}a^2 \simeq (1/4)\cdot(t/\tau_e)^{1/2}a^2$ and $x^2(t) = (4/3\pi^{3/2})^{1/2}\cdot(t/\tau_e)^{1/4}a^2 \simeq (1/2)\cdot(t/\tau_e)^{1/4}a^2$.

These curvilinear Rouse-like motions contribute to stress relaxation by re-equilibrating the distribution of PI monomers between tube segments ("*chain unit sharing*"[45]), until chain density along the primitive path returns to its equilibrium value N/L_{tube}.[36,44,45] Consistently with the definition of τ_e, the time scale for this relaxation mechanism (sometimes termed *full chain* or *path equilibration time*[45]) is twice the Rouse time of the PI chain:[35,36,44-46,pp]

$$2\tau_R = 2\tau_0 N^2 = \tau_e Z^2 \tag{3.20}$$

[pp] In tube models, the *path equilibration time* $2\tau_R$ is approximately equal to the *retraction time* (or *stretch relaxation time*) τ_s associated, in the nonlinear regime, with stretching of the primitive path from its equilibrium value (Dealy and Larson[36] pp 330–331, 341–342, 416–417).

and we find $2\tau_R \simeq 7.6$ ms.

At $t = 2\tau_R$, all PI monomers partake in the coherent and curvilinear Rouse-like motion of the midblock chain, each traveling a contour distance $s(2\tau_R) \simeq (1/2)\cdot(2\tau_R/\tau_e)^{1/4}a \simeq Z^{1/2}a/2 \simeq R/2 \simeq 8.6$ nm (from Eqs. (3.1) and (3.20)). In three-dimensional space, $x(2\tau_R) = [a\cdot s(2\tau_R)]^{1/2} \simeq (a\cdot R/2)^{1/2} \simeq 6.9$ nm. Therefore, for 0.08 ms $\leq t \leq$ 7.6 ms (5.5 nm $\leq x \leq$ 6.9 nm) stress relaxation in LIL50–12 proceeds via 1-D *Rouse-like motions* ("*local reptation*"[166]) of the 731 PI monomers along the chain primitive path (Table 3.8).

As will be discussed in §3.3.4.IV-e, the storage modulus at $\omega = 1/2\tau_R$ represents the *plateau modulus* of the material[43-45], $E_N \equiv E'(1/2\tau_R)$ (Figure 3.4(a)). Not surprisingly, $\tau = 2\tau_R$ falls in a region where the relaxation spectrum is relatively flat ($H_E(\tau) \sim \tau^{-0.17}$, Figure 3.4(b) and Table 3.7). This is consistent with the behavior usually observed in very lightly crosslinked amorphous polymers (such as vulcanized SBR)[42], and with the qualitative analysis of the shape of $H_E(\tau)$ presented in §3.3.4.IV-b.

For LIL50–12 chains with the midblock either in bridge (x_b) or knotted-loop (x_k) conformation, 1-D Rouse-like motion shuttling monomers across tube segments is the only mode of relaxation available beyond the entanglement time τ_e.

Richer dynamics is possible for LIL50–12 chains (x_f) in free-end conformations (Figure 3.5). For these chains, "chain unit sharing" is not the only relaxation mechanism available for $t \geq \tau_e$. Given the strong interactions between lactide and isoprene segments ($\chi(25\ °C) \simeq 0.39$)[b], PLA blocks embedded in the PI-rich matrix will assume a collapsed conformation ($R_{g,L} < 3.76$ nm, Table 3.4), thereby refrain from participating in

topological constraints with the surrounding chains (Chapter 2). Consequently, 1-D Rouse-like motions of PI monomers near the "free" chain end will cause the PI tube length $L_{tube}(t)$ to fluctuate around its equilibrium value L_{tube} = 53.6 nm (Table 3.4). The nature of this kind of motions, usually referred to as "*primitive path fluctuations*" (PPF) or "*contour length fluctuations*" (CLF)[36,44,88,89], is the same as for the "chain unit sharing": both follow the dynamics of Rouse modes confined to a tube ("local reptation"[166]), and both occur on time scales[44,167] between τ_e and $2\tau_R$. As opposed to "chain unit sharing", PPF contribute to stress relaxation by vacating, hence relaxing the outermost portions of the tube.

In absence of the collapsed PLA blocks, at $t = 2\tau_R$ these unactivated, thermal fluctuations ("*early-time chain end fluctuations*"[167,168]) would alter the PI tube length by a factor $s(2\tau_R) \simeq R/2 \simeq 8.6$ nm, involving a fraction of outer tube segments $s(2\tau_R)/L_{tube} \simeq (1/2)\cdot Z^{-1/2} \simeq 0.16$ (from Eq. (3.1) and $L_{tube} = Z\cdot a$), that is one PI entanglement strand. The associated root-mean-square monomer displacement in three-dimensional space, $x(2\tau_R) \simeq (a\cdot R/2)^{1/2} \simeq 6.9$ nm, is not much larger than the size of the unsegregated PLA block, $R_{g,L} <$ 3.76 nm. Therefore, the additional drag of the PLA block on the PI chain cannot be neglected: Rouse motion of the "free" chain end should be delayed and, at $t = 2\tau_R$, perhaps none of the PI tube segments will have been vacated by PPF. This additional relaxation mechanism only applies to a small fraction (x_f) of chains, thus "chain unit sharing" governs the triblock stress relaxation for $\tau_e \le t \le 2\tau_R$. In §3.3.4.IV-e, we will estimate x_f and verify that, indeed, $x_b+x_k \gg x_f$.

$2\tau_R < t \leq \tau_{late}$

As shown in Figure 3.4(a), stress relaxation in LIL50–12 persists beyond the path equilibration time $2\tau_R$ and up to a time scale of order 10^4 s. At these temperature and range of reduced frequency, relaxation in PLA domains is completely negligible (as discussed in §3.3.4.IV-b). This behavior cannot be caused by triblock chains in bridge (x_b) or knotted-loop (x_k) conformation, for which neither PPF nor reptation are possible. Unentangled dangling structures (x_d), if present, would relax the stress on a time scale τ_R. Therefore, we attribute the low-frequency viscoelastic response to the motion of free-end-type midblocks (x_f), i.e. the entangled dangling structures of LIL50–12.

As we explained earlier, small curvilinear displacements of the "free" PI chain end (for $t \leq 2\tau_R$, $s \leq R/2$) correspond to a free energy change of order kT and follow Rouse dynamics. Deeper fluctuations along the PI primitive path are entropically unfavorable and need to counteract a "thermal tension" of order kT per tube segment.[46] This type of motion is similar to the *arm retraction* for star polymers, first described by De Gennes[169] in 1975. If the collapsed PLA block were not present, the motion of the "free" chain end would be nearly identical (for $s < \approx L_{tube}/2$) to the arm retraction in a melt of PI stars with arm molar mass equal to the molar mass of the midblock chain. The "branch point", however, is represented by the PLA domain to which the other end of the PI chain is connected. Repulsive interactions will then become significant when deep fluctuations bring the "free" PI chain end in proximity to the PLA domain (for $t \gg 2\tau_R$, $s \rightarrow L_{tube}$). On the other hand, the additional drag caused by the collapsed PLA block should delay the

arm retraction of the "free" PI chain end irrespective of its curvilinear displacement, affecting both shallow fluctuations (for $\tau_e \le t \le 2\tau_R$) and deep fluctuations (for $t > 2\tau_R$). Given the relative size of the blocks ($R_{g,I}/R_{g,L} \simeq 2$), we may expect both of these features to influence the arm retraction dynamics in LIL50–12.

The time scale for a full arm retraction can be estimated with the theory developed by Milner and McLeish[35,168] in 1997:

$$\begin{aligned} \tau_{pre} &= \left(\frac{\pi^5}{6}\right)^{1/2} \tau_e Z_a^{3/2} \left(\frac{3\cdot Z_a}{1+\alpha}\right)^{\frac{\alpha}{1+\alpha}} \Gamma\left(\frac{1}{1+\alpha}\right) \\ \tau_{late} &= \tau_{pre} \exp\left[\frac{3}{(1+\alpha)(2+\alpha)}\cdot Z_a\right] \end{aligned} \tag{3.21}$$

where τ_{pre} is an "attempt frequency", Z_a is the average number of tube segments in the retracting arm, α is the dilution exponent, $\Gamma(m)$ is the complete gamma function (Appendix C, §C.1), and τ_{late} is the relaxation time of a deep fluctuation ("*late-time chain end fluctuation*") corresponding to a full arm retraction. Eq. (3.21) applies to both star and linear polymers: deep fluctuations are exponentially unlikely, thus depend strongly on the number of tube segments (each yielding an activation barrier of order kT). The exponential dependence on Z_a explains why an incorrect calculation of the number of tube segments (i.e. inconsistent definitions of M_e and Z, §3.3.2.III) is quantitatively significant for the predictions of arm retraction dynamics. For stars, the curvilinear coordinate along the primitive path s runs from 0 (at the end of the chain) to L_{tube} (at the branch point); therefore, Z_a is the total number of tube segments as defined by Eq. (3.7). Linear polymers can be thought of as two-arm stars, and the retraction is modeled as if

the center of the chain were fixed.[167] Therefore, s goes from 0 to $L_{tube}/2$ (the "joint" of the two-arm star), and $Z_a = Z/2$ with Z given by Eq. (3.7).[36]

α is the exponent that dictates how shear plateau modulus and entanglement molar mass change with polymer volume fraction ϕ:[36,41,45]

$$\begin{aligned} G_N^0(\phi) &= G_N^0 \cdot \phi^{1+\alpha} \\ M_e(\phi) &= M_e \cdot \phi^{-\alpha} \end{aligned} \tag{3.22}$$

where G_N^0 and M_e indicate the corresponding values in bulk ($\phi = 1$). Experimentally, α varies approximately[41,45] from 1.1 to 1.3, in agreement with the theoretical predictions for good solvents ($\alpha = 5/4$)[170] and theta conditions ($\alpha = 4/3$)[171]. The dilution exponent α takes into account that primitive path fluctuations are described by a very broad spectrum of relaxation times, much broader than for reptation. In an entangled melt of star or linear polymers, the outer portions of the chain relax by arm retraction on time scales much smaller than the inner "cores" (e.g. $\tau_{early}(s = R/2) = 2\tau_R \ll \tau_{late}$). Thus, when deep fluctuations reach the inner "cores", entanglements that were imposed by the branch tips will have disappeared. At long times, branch tips act as nothing more than solvent. By decreasing the number of effective topological constraints, their fast relaxation (compared to the inner "cores") "enlarges" or "dilates" the confining tube, $a(\phi) = a \cdot \phi^{-\alpha/2}$ (from Eqs. (3.3), (3.8), and (3.22)), as if the polymer were being diluted. This mechanism of constraint release, called "*dynamic dilution*" or "*tube enlargement*", was first proposed by Marrucci[172] in the context of linear polymers and later applied by Ball and McLeish[173] to star polymer melts.

With $\tau_e \simeq 0.08$ ms and $Z_a = Z = 9.8$, Eq. (3.21) yields $\tau_{late} \simeq 4{\cdot}10^4$ s (without dynamic dilution, $\alpha = 0$) and $\tau_{late} \simeq 15.5$ s (with dynamic dilution and $\alpha = 1$). With the effect of PLA taken into account, these theoretical predictions represent the lower bounds for arm retraction in the triblock matrix.

For a TPE of the A–B–A type, dynamic dilution should be relevant when $x_f/(x_b+x_k) \gg 1$. In this case, the vast majority of entanglements would arise from dangling structures (x_f) and constraint release would act as in a melt of stars with molar mass equal to the molar mass of the midblock. For $x_f/(x_b+x_k) \ll 1$ and a uniform distribution of free-end-type midblocks throughout the matrix, dynamic dilution should not take place. This limiting case is equivalent to assuming that each untrapped entanglement is associated with no more than one midblock chain in free-end conformation (as depicted in Figure 3.5). In fact, if two free-end-type midblocks participate in the same entanglement this will disappear as soon as the first chain end reaches its locus by arm retraction.

The slowly-approaching pseudo-equilibrium state observed in Figure 3.4(a) ($E'(\omega) \rightarrow E_{eq}$ and $E''(\omega) \sim \omega$, for $\omega < 10^{-4}$ rad/s) is qualitatively in agreement with the prediction of the Milner–McLeish theory for $\alpha = 0$ ($\tau_{late} \simeq 4{\cdot}10^4$ s). This indicates that the low-frequency behavior of the triblock may be consistent with a dynamically undiluted, star-like relaxation of the single-free-end-type midblocks.

For a quantitative comparison with the Milner–McLeish theory, we subtracted the effective equilibrium modulus calculated from $H_E(\tau)$ (see Eq. (3.13)), $E_{eq} \simeq 5.4$ MPa, from the storage modulus $E'(\omega)$ shown in Figure 3.4(a). Factoring out the elastic

contribution of the permanent network strands exposes the relaxation of the entangled dangling structures of LIL50–12. (As explained in §3.3.4.IV-b, network strands arising from the anchoring effect of glassy PLA domains can be considered "permanent", at 0 °C, on time scales $t \leq \approx 300$ years.) The reduced storage modulus, $E'(\omega) - E_{eq}$, and the loss modulus, $E''(\omega)$, are plotted in Figure 3.6 over the frequency range relevant for arm retraction dynamics ($\omega < 1/2\tau_R$). Dash-dot lines are used in the frequency region where the accuracy of the data is dubious. This region was calculated by taking into account the accuracy of $H_E(\tau)$ in Figure 3.4(b) (as discussed in §3.3.4.IV-a), and a potential 10% error in E_{eq}.

The shape of the curves is similar to the experimental results for entangled melts of PI stars obtained (in shear) at 60 °C by Pearson and Helfand[174] and Fetters et al.[175]. At the lowest frequencies, the dynamic moduli exhibit liquid-like terminal behavior ($E'(\omega) - E_{eq} \sim \omega^2$, $E''(\omega) \sim \omega$). The frequency at which $E'(\omega) - E_{eq}$ crosses $E''(\omega)$, $\omega = 1/\tau_c$, approximates the reciprocal of the longest relaxation time.[22] At frequencies higher than $1/\tau_c$, the value of $E''(\omega)$ continues to increase. This behavior is the signature of deep primitive path fluctuations[168], thus providing further support to the hypothesis of arm retraction dynamics in LIL50–12. In contrast, reptation and fast-relaxing contour length fluctuations would result (for a narrow distribution of chain lengths) in a decreasing loss modulus after the crossover.[36,167]

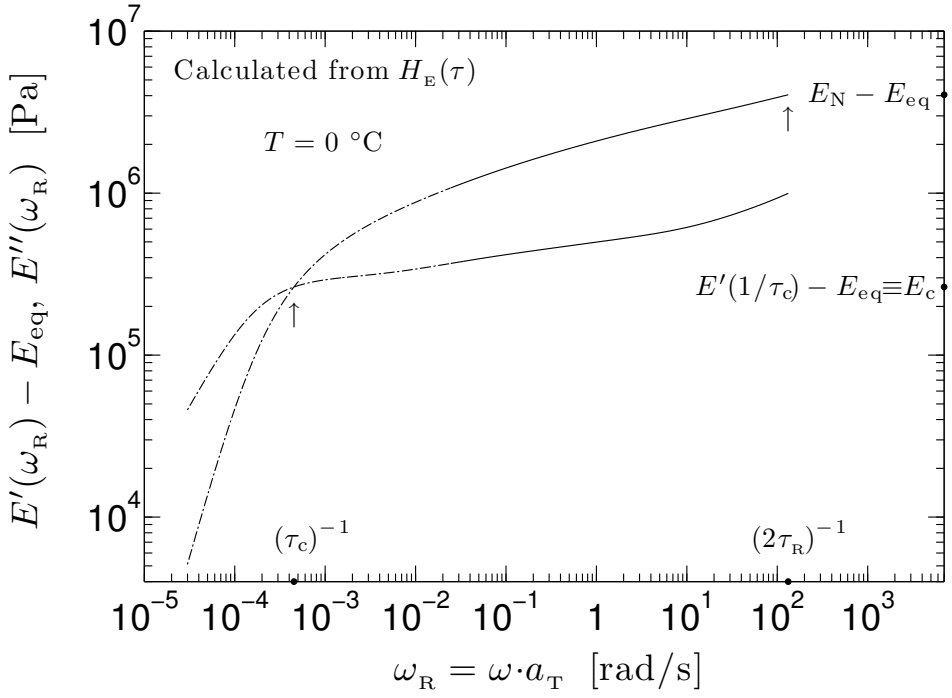

Figure 3.6. Reduced storage modulus, $E'(\omega) - E_{eq}$, and loss modulus, $E''(\omega)$, from Figure 3.4(a), plotted over the frequency range relevant for arm retraction dynamics ($\omega < 1/2\tau_R$). Dash-dot lines are used in the frequency region where the accuracy of the data is questionable.

The approximate longest relaxation time deduced from Figure 3.6, $\tau_c \simeq 2200$ s, is about 1 order of magnitude smaller than the time scale for full, dynamically undiluted arm retraction estimated with the Milner–McLeish theory. This is at variance with our expectation that arm retraction dynamics in LIL50–12 should be delayed compared with the theoretical prediction (as previously discussed). This expectation is also supported by the results obtained by Watanabe and co-workers[176-182] on diblock copolymer micellar

systems. For micelles randomly dispersed in polymeric solvents chemically identical to the corona, the star-like relaxation of the corona blocks was delayed by 2–3 orders of magnitude when corona and core were comparable in size.[176-182]

The hypothesis that dynamic dilution does not intervene ($\alpha = 0$) is grounded in the molecular picture sketched in Figure 3.5 (valid for $x_f/(x_b+x_k) \ll 1$ and a uniform distribution of free-end-type midblocks throughout the matrix), as well as in the experimental evidence of arm retraction in a fixed network environment. For example, stress relaxation experiments performed by Kan et al.[183] showed suppression of constraint release in the arm retraction of star polybutadiene (star-B) dispersed in the matrix of a microphase-segregated S–B–S triblock (chosen to approximate the fixed network idealization). While the condition $x_f/(x_b+x_k) \ll 1$ is verified (as will be shown in §3.3.4.IV-e), uniform distribution of free-end-type midblocks in the matrix remains an arbitrary, if plausible, assumption. A concentration gradient for these midblocks is certainly possible. If so, there could be regions of space where the concentration is high enough such that more than one midblock in free-end conformation emanates from an untrapped entanglement. These chains would experience a reduced number of topological constraints and retract in a dilated tube. On the other hand, regions of the matrix where the concentration of free-end-type midblocks is depleted would still relax the stress without dynamic dilution. This would result in a bimodal distribution of the (longest) relaxation times, for which there is no evidence in the data (Figure 3.6). Obviously, it is possible to imagine a limiting case in which the concentration gradient effectively

becomes a step function, thereby having $x_f/(x_b+x_k) \gg 1$ in some regions of the matrix and $x_f = 0$ in others. In this extreme scenario, agreement with $\tau_c \simeq 2200$ s is straightforward: arm retraction with dynamic dilution ($\tau_{late} \simeq 15.5$ s) is delayed by the PLA block and PLA domain by about 2 orders of magnitude, consistent with the results of Watanabe and co-workers[176-182]. Although possible, this scenario seems improbable. More likely, the apparent "fast" arm retraction in LIL50–12 originates from the uncertainty in $E'(\omega) - E_{eq}$ and $E''(\omega)$ in the low-frequency region (Figure 3.6). These curves were obtained from $H_E(\tau)$ outside of the domain where the calculated spectrum is reliable (see discussion in §3.3.4.IV-a and Figure 3.4). A shift of the $E''(\omega) \sim \omega$ scaling towards lower frequencies coupled with a small error in the estimate of E_{eq}, of the order of 10% or so, would make the reciprocal crossover frequency τ_c close to or even higher than the theoretical prediction for $\alpha = 0$ ($\tau_{late} \simeq 4 \cdot 10^4$ s).

With these considerations in mind, we take τ_{late} with $\alpha = 0$ as representative of the arm retraction dynamics in LIL50–12. In §3.3.4.IV-e, the calculation of x_f (i.e. the average fraction of free-end-type midblocks in the matrix) will allow us to refine the estimate of τ_{late}, which becomes about $1.9 \cdot 10^4$ s (for $\alpha = 0$).

When arm retraction is complete (whether it be at $t = \tau_c$ or $t = \tau_{late}$), the "free" PI chain end will have traveled a distance $s = L_{tube} = 53.6$ nm along the primitive path, and $x \simeq (a \cdot L_{tube})^{1/2} \simeq R \simeq 17.1$ nm (from Eq. (3.1) and $L_{tube} = Z \cdot a$) in three-dimensional space. Thus, the linear viscoelastic response of LIL50–12 is governed by collective microdomain dynamics for 7.6 ms $< t \leq \approx 1.9 \cdot 10^4$ s and 6.9 nm $< x \leq 17.1$ nm (Table 3.8).

Furthermore, a characteristic relaxation time of about $1.9 \cdot 10^4$ s provides an explanation for the concentration of dissipative processes only hinted at by the behavior of $H_E(\tau)$ for $\tau > \approx 500$ s (see Figure 3.4(b) and related discussion in §3.3.4.IV-b).

The quantitative analysis so far has been based on free-end conformations involving only one PLA block embedded in the PI-rich matrix, $x_{f,1}$ (as shown in Figure 3.5). Of course, some triblock chains, $x_{f,2}$, may have both PLA blocks unsegregated (not depicted in Figure 3.5). These chains can be thought of as two-arm stars.[167] As such, for $t > 2\tau_R$ they will relax the stress by deep contour length fluctuations of their "free" ends (each connected to a collapsed PLA block). Application of Eq. (3.21), with $Z_a = Z/2$, gives the time scale for full arm retraction ($s = L_{tube}/2$): $\tau_{late} \simeq 9.3$ s (for $\alpha = 0$) and $\tau_{late} \simeq 0.3$ s (for $\alpha = 1$). However, before these chain ends have the chance to visit the innermost PI tube segments, arm retraction will be cut off by the faster relaxation mechanism of reptation.[36,167] Therefore, the *tube disengagement time*[35,46,184] $\tau_d = 3\tau_e Z^3 \simeq 0.2$ s, rather than τ_{late}, is the longest relaxation time for this type of chains. Stress relaxation on time scale $\tau_d \simeq 0.2$ s cannot account for the measured low-frequency behavior of LIL50–12. This implies that the conformation shown in Figure 3.5 certainly applies to some (if not the majority) of the free-end-type midblocks. Interestingly, τ_d approximates the locus on the τ scale at which the slope of the relaxation spectrum increases from about –0.17 to –0.07 (Figure 3.4(b) and Table 3.7). For a corresponding PI melt (with molar mass equal to the midblock molar mass), $H_E(\tau)$ would exhibit a peak in the neighborhood of τ_d (§3.3.4.IV-b).

Closing remarks

Overall, the evidence for arm retraction dynamics in LIL50–12 is strong. This finding is in line with the behavior of polymer networks with entangled dangling structures.[185,186,qq] When examining the characteristic length scales of the triblock (§3.3.2.II and III), we briefly stated that the associated dynamics would cover a wide range of time scales. Based on the analysis presented in this section, Rouse-like dynamics extends for about 3.2 decades in time (about 0.3 decades on a spatial scale). Arm retraction dynamics, with a similar spread of length scales (about 0.4 decades), covers about 6.6 decades in time.

One additional comment is worth making. Unlike some polymer species, most notably polyethylene (PE)[187,188] and poly(ethylene–*alt*–propylene) (PEP, i.e. hydrogenated 7% 3,4-PI)[189], arm retraction dynamics in 7% 3,4-PI is not associated with thermo-rheological complexity[175,189,190]. This explains why the experimental data measured at 0 °C (almost all of which governed by arm retraction dynamics, see Figure 3.4(a)) could be time-temperature superposed by a simple shift. Thermo-rheological complexity associated with arm retraction dynamics is believed to originate from a large negative temperature coefficient of chain dimensions[45,191,192], i.e. $\kappa \equiv \partial \ln R^2/\partial T < -1$. This condition is satisfied for PE ($\kappa = -1.20 \cdot 10^{-3}$ deg^{-1})[20] and PEP ($\kappa = -1.10 \cdot 10^{-3}$ deg^{-1})[20], but not for 7% 3,4-PI

[qq] Indeed, by applying De Gennes' idea of relaxation by arm retraction[169] to strands dangling from a network, Curro and co-workers[185,186] were able to provide a molecular interpretation to the empirical Chasset–Thirion equation[155] for stress relaxation in lightly crosslinked polymers (Appendix E, Eq. (E.48)).

(κ = +0.40·10^{-3} deg^{-1})[40]. When $\kappa < 0$, the transition *gauche* states during arm retraction have higher energy than *trans* conformations. Therefore, chains must overcome not only an unfavorable entropic barrier but an energetic barrier as well. This produces an excess temperature dependence of the Arrhenius form, thereby leading to thermo-rheological complexity.[45,189,191,192] As a stronger test of our conclusions, it would be interesting to examine the linear, rubbery behavior of an A–B–A with either PE or PEP as midblock. With a significant fraction of unsegregated A chains embedded in the matrix (e.g. as a result of A chains pullout at large deformations coupled with slow ordering kinetics), thermo-rheological complexity in the appropriate range of frequency and temperature (i.e. when interfacial relaxation does not intervene) would represent a more compelling evidence of star-like relaxation.

3.3.4.IV-e Characteristic moduli and fraction of partially segregated chains

In the preceding section, we associated the viscoelastic response shown in Figure 3.4 with characteristic time and length scales, and we identified the relevant dynamics at play. This explained, qualitatively, how stress in LIL50–12 is relaxed as a function of the reduced frequency. In this section, we examine the relaxing stress from a quantitative standpoint, based on the molecular picture illustrated in Figure 3.5 and the behavior predicted at different length scales by the associated dynamics. This will allow us to determine key parameters such as the filler contribution $\xi(\omega)$ in the rubbery plateau and

pseudo-equilibrium regions, and the average fraction x_f (= $x_{f,1}$+$x_{f,2}$) of free-end-type midblocks in the matrix.

$\tau_0 \leq t \leq \tau_L$

The storage modulus at the onset of the glass-rubber viscoelastic transition, $E'(1/\tau_0) \simeq$ 1.6 GPa, is still similar to the extensional glassy modulus of PI homopolymer[22], $E_g \simeq 4$ GPa (Appendix A). Assuming a Poisson's ratio $\mu^*(\omega) \simeq \mu_g \simeq 1/3$ (hence, $E'(\omega) \simeq 2(1+\mu_g)G'(\omega) \simeq (8/3)G'(\omega)$ – §3.3.4.IV-c and Appendix A), a shear modulus of order kT per PI monomer[22], $(8/3)\cdot(kT/b^3)$, underestimates $E'(1/\tau_0)$ by a factor of about 42. This large mismatch is due to neglecting the enthalpic energy component of the force in the stretched polymer network[22,42,rr] (by treating the N PI monomers as independent entropic springs), as well as to the filler effect of PLA microdomains. Across the glass-rubber transition (covering a time span of about 2.8 decades), the storage modulus drops by about 1.7 decades and $E'(1/\tau_L) \simeq 35$ MPa.

At $t = \tau_L$, stress is relaxed via coherent Rouse-like motion of about 28 sections of the PI chain, each containing $N/p = q\sqrt{5} \simeq 26$ monomers. Assuming a Poisson's ratio $\mu^*(\omega) \simeq \mu_{eq} \simeq 1/2$ (hence, $E'(\omega) \simeq 3G'(\omega)$ – §3.3.4.IV-c and Appendix A), a shear modulus of order kT per PI section with $q\sqrt{5}$ monomers, $3\cdot(kT/b^3q\sqrt{5})$, is about 21 times smaller than

---

[rr] While in the rubbery state the conformational entropy component typically accounts for more than 90% of the total force in a stretched polymer network (Rubinstein and Colby[22] pp 254–255), the *enthalpic* energy contribution (i.e. conformational energy and intermolecular interactions) becomes non negligible near or below the rubber-glass viscoelastic transition (Ferry[42] pp 272–273, 304–305).

$E'(1/\tau_L)$. At this frequency, the difference can be attributed almost entirely to the filler effect of glassy PLA, i.e. $\xi(1/\tau_L) \approx 21$.

***$\tau_e \leq t \leq \tau_{late}$* – Modeling the linear elastic behavior of LIL50–12**

For $t \geq \tau_e$, the response is dictated by the underlying network structure, arising from PI entanglements and PLA microdomains acting as physical endlinks (Figure 3.5), as discussed in §3.3.4.IV-d. Therefore, the value of the storage modulus $E'(\omega)$ for $1/\tau_{late} \leq \omega \leq 1/\tau_e$ can be estimated from the linear elasticity of an equivalent PI network, suitably modified to account for the microphase-segregated structure. This type of approach was first proposed by Bard and Chung[110] in 1987 to describe (under the assumption $x_b = 1$) the linear pseudo-equilibrium stress-strain behavior of S–B–S triblocks. We extend their approach by modeling the linear elastic response across the rubbery plateau and up to the entanglement time τ_e, and by considering a distribution of midblock conformations (i.e. $x_b < 1$).

Assumptions

In our calculations, several simplifying hypotheses will be made. First, we treat the domains of the glassy PLA microphase as non-deformable. This assumption, plausible at the testing temperature (0 °C) and for the considered range of reduced frequency (Figure 3.4(a)), is equivalent to replacing LIL50–12 with an equivalent network of PI chains in which there are no PLA domains, but in which the effect of these domains is accounted for through the filler effect $\xi(\omega)$. This also implies that the number densities of elastically

effective strands are calculated based on the matrix volume rather than on the total volume.

Furthermore, we consider the unstrained PI chains as unperturbed Gaussian coils (i.e. R_I prior to deformation is given by Eq. (3.1)). This hypothesis is tantamount to using a Tobolsky front factor[193,194] of unity, by (i) neglecting excluded volume effects between PI and PLA (which may yield non-Gaussian and stretched conformations), and (ii) assuming no swelling or supercoiling of the strands subsequent to network formation. For A–B–A triblocks with well-defined equilibrium morphologies, the condition (i) may be relaxed: stretching of Gaussian coils of the B matrix due to segregation can be accounted for with the expansion parameter calculated by Meier[195,196]; non-Gaussian chain distribution functions resulting from non-deformable A domains on a simple cubic lattice have been developed by Gaylord and Lohse[197,198]. Neglecting swelling or supercoiling effects on the network rests on the premise that the network was formed and tested at the same volume and temperature.[41] We further assume that the molecular architecture of the network was established almost in the undiluted state ($\phi_{ref} \simeq \phi = 1$). To a first approximation, these conditions should be satisfied considering the process of network formation in LIL50–12 (i.e. during freeze-drying from a benzene solution, Appendix A), the preparation and testing of the specimens (§3.2.3 and §3.3.4.I), and the small temperature coefficient of chain dimensions for 7% 3,4-PI (§3.3.2.II, Table 3.3, and §3.3.4.IV-d).

Two additional hypotheses need to be made, concerning the motion of junction points (both PLA microdomains and PI entanglements) and the combined effect of endlinks and

entanglements on the elastic modulus. For present purposes, affine motion of junction points[199] is assumed. Stated differently, we consider topological constraints in the matrix as effective as the physical endlinks (i.e. as opposed to treating them as "slip-links")[83,84,ss] and for both we neglect thermal fluctuations around their mean positions. For typical TPEs of the A–B–A type, the A domains can be viewed as endlinks with functionality f of order 100 or so.[200,201] Their thermal fluctuations, if present, would reduce their contribution to the linear elastic modulus by a negligible factor of $(f - 2)/f$.[202,203] Even if their functionality were lower, entanglements in the B matrix would likely suppress their fluctuations just as they would in the corresponding endlinked B homopolymer[204-207]. Following this line of reasoning, we feel justified in neglecting thermal fluctuations of PI entanglements as well: they can be viewed as tetrafunctional crosslinks, but they are closely enough spaced along the PI chains ($a/R = Z^{-1/2} \simeq 0.32$) to mutually impede thermal fluctuations.

Finally, we consider the contributions of endlinks and entanglements as simply additive[ss], following the approach developed by Langley and Ferry[156,208,209] for vulcanized rubbers. The simple additivity of the two contributions has been verified experimentally[156,206,207,209-211] as well as by computer simulations[212-216], and it is now a customary assumption for vulcanized elastomeric networks[22,23,41].

[ss] In the Edwards–Vilgis slip-link model[83,84], entanglements (as deduced from the plateau modulus in the system before crosslinking) and permanent crosslinks may not necessarily contribute in an additive fashion to equilibrium mechanical properties, even in the region of small deformations (Chapter 5, and Appendix H, §H.2.2).

Equations

With these assumptions, the measured storage modulus $E'(\omega)$ is interpreted as the amplified ($\xi(\omega) > 1$) linear response of the undiluted ($\phi_{ref} \simeq \phi = 1$) network of PI Gaussian strands whose junctions (i.e. PI entanglements, and PLA microdomains acting as physical endlinks) move affinely with the macroscopic deformation. Owing to simple additivity, the total number density of elastically active strands (based on the matrix volume) is:

$$\nu(\omega) = \nu_{cross} + \nu_{ent}(\omega) \tag{3.23}$$

where ν_{cross} is the number density of PI strands terminated by endlinks regardless of whether entanglements intervene (typically referred to as the "crosslink"[42] or "chemical"[207] contribution, in vulcanized rubbers), and $\nu_{ent}(\omega)$ is the number density of PI strands terminated by entanglements regardless of whether endlinks intervene. The reason for the frequency dependence of ν_{ent} is twofold and will be discussed shortly. Since $\mu^*(\omega) \simeq \mu_{eq} \simeq 1/2$ for $\omega \leq 1/\tau_e$, and each elastically active strand contributes energy of order kT to the shear storage modulus $G'(\omega)$, the extensional storage modulus of LIL50–12 can be calculated as:

$$\begin{aligned} E'(\omega) &= 3 \cdot G'(\omega) \\ &= 3 \cdot \xi(\omega) \cdot \left[\nu_{cross} + \nu_{ent}(\omega)\right] \cdot kT \\ &= E'_{cross}(\omega) + E'_{ent}(\omega) \end{aligned} \tag{3.24}$$

Predictive capability for $\xi(\omega)$ demands knowledge of the shape and distribution of the PLA domains, as well as the Poisson ratios $\mu^*(\omega)$ of PI and PLA in the corresponding frequency range (§3.3.4.IV-c). As such, it is beyond the scope of this study. Moreover,

theoretical expressions of this sort have usually been developed only for the simpler case of monodisperse spherical filler particles[217-219]. We therefore treat $\xi(\omega)$ as an unknown parameter to be determined from the comparison of Eq. (3.24) with the experimental data.

For crosslinked rubbers, the criteria for junctions and strands to be elastically active were proposed by Scanlan[220] and Case[221] in 1960: a junction is elastically active if at least three paths leading away from it are independently attached to the network; a strand is elastically active if it connects two elastically active junctions. Accordingly, all PLA microdomains and all PI entanglements (present at $t \leq 2\tau_R$) are elastically active junctions, and the elastically active strands originating from endlinks are the midblocks in either bridge or knotted-loop conformation ($x_b+x_k = 1-x_d-x_f$, §3.3.4.IV-d). Their number density is:

$$\begin{aligned} \nu_{cross} &= \left(x_b + x_k\right)\cdot \nu_I^{matrix} \\ &= \left(x_b + x_k\right)\cdot \phi_I^{matrix} \cdot \nu_I^{hI} \\ &= \left(1 - x_d - x_f\right)\cdot \phi_I^{matrix} \cdot \frac{\rho_I N_{av}}{M_I} \end{aligned} \tag{3.25}$$

where ν_I^{matrix} is the number density of PI blocks in the matrix, $\nu_I^{hI} = \rho_I N_{av}/M_I$ is the number density of PI blocks in homopolymer PI, ϕ_I^{matrix} is the volume fraction of PI in the matrix (< 1 for the presence of unsegregated PLA blocks), and ρ_I and M_I are the PI block density and molar mass given in Tables 3.3 and 3.1 (respectively). From Eqs. (3.24) and (3.25), the contribution of the endlink network at any given frequency ω is then:

$$E'_{\text{cross}}(\omega) = 3 \cdot \xi(\omega) \cdot \left[\left(1 - x_{\text{d}} - x_{\text{f}}\right) \cdot \phi_{\text{I}}^{\text{matrix}} \cdot \frac{1}{M_{\text{I}}} \right] \cdot \rho_{\text{I}} RT \tag{3.26}$$

where $R = k \cdot N_{\text{av}}$ stands for the universal gas constant[o].

Elastically active strands originating from entanglements can be formed by all midblocks but those in dangling-loop conformation (§3.3.4.IV-d). Their number, however, is frequency-dependent. At $t = \tau_{\text{e}}$, the PI entanglement network just comes into play: bridge-, knotted-loop-, and free-end-type midblocks are entangled (Figure 3.5), and "chain unit sharing" has not yet had time to occur (§3.3.4.IV-d). For an undiluted PI homopolymer with the same molar mass as the midblock, this time scale would correspond to a shear modulus – called the "*entanglement modulus*"[44] – $G_{\text{e}} \equiv G'(1/\tau_{\text{e}}) = (\rho_{\text{I}} N_{\text{av}} / M_{\text{e,hI}}^{\text{G}}) \cdot kT$, because $\nu_{\text{ent,hI}}(1/\tau_{\text{e}}) = \nu_{\text{I}}^{\text{hI}} \cdot Z_{\text{I}}^{\text{hI}} = \rho_{\text{I}} N_{\text{av}} / M_{\text{e,hI}}^{\text{G}}$ entanglement strands per unit volume (with $Z_{\text{I}}^{\text{hI}} = M_{\text{I}} / M_{\text{e,hI}}^{\text{G}} = 9.8$ and $M_{\text{e,hI}}^{\text{G}} = 5100$ g/mol, Table 3.4) would each contribute energy of order kT to the modulus. For LIL50–12, the contribution of the entanglement network at $t = \tau_{\text{e}}$ is thus $E'_{\text{ent}}(1/\tau_{\text{e}}) = 3 \cdot \xi(1/\tau_{\text{e}}) \cdot \nu_{\text{ent}}(1/\tau_{\text{e}}) \cdot kT$ (from Eq. (3.24)), with

$$\begin{aligned} \nu_{\text{ent}}\left(1/\tau_{\text{e}}\right) &= \left(1 - x_{\text{d}}\right) \cdot \nu_{\text{I}}^{\text{matrix}} \cdot Z_{\text{I}}\left(1/\tau_{\text{e}}\right) \\ &= \left(1 - x_{\text{d}}\right) \cdot \phi_{\text{I}}^{\text{matrix}} \cdot \nu_{\text{I}}^{\text{hI}} \cdot Z_{\text{I}}\left(1/\tau_{\text{e}}\right) \\ &= \left(1 - x_{\text{d}}\right) \cdot \phi_{\text{I}}^{\text{matrix}} \cdot \frac{\rho_{\text{I}} N_{\text{av}}}{M_{\text{I}}} \cdot Z_{\text{I}}\left(1/\tau_{\text{e}}\right) \end{aligned} \tag{3.27}$$

where $\phi = (1 - x_{\text{d}}) \cdot \phi_{\text{I}}^{\text{matrix}}$ represents the volume fraction occupied by the entangled midblocks: the LIL50–12 matrix contains a fraction $\phi_{\text{I}}^{\text{matrix}}$ of PI chains, of which only a fraction $(1 - x_{\text{d}})$ at $t = \tau_{\text{e}}$ is entangled. Consequently, the value of $Z_{\text{I}}(1/\tau_{\text{e}})$ in Eq. (3.27) is

different than the corresponding value for a PI homopolymer $Z_{\mathrm{I}}^{\mathrm{hI}}$: when the network is formed the unsegregated PLA blocks, as well as the dangling-loops[163] (if present), act as "diluent" for the entangled PI chains. Combining Eqs. (3.7) and (3.22)b, the average number of tube segments per entangled PI chain is given by:

$$\begin{aligned} Z_{\mathrm{I}}\left(1/\tau_{\mathrm{e}}\right) &= \frac{M_{\mathrm{I}}}{M_{\mathrm{e,I}}^{\mathrm{G}}\left(\phi\right)} \\ &= Z_{\mathrm{I}}^{\mathrm{hI}} \cdot \left(1-x_{\mathrm{d}}\right)^{\alpha} \cdot \left(\phi_{\mathrm{I}}^{\mathrm{matrix}}\right)^{\alpha} \end{aligned} \tag{3.28}$$

corresponding, based on Eq. (3.1), to a "dilated" confining tube with statistical segment length:

$$\begin{aligned} a_{\mathrm{I}}\left(1/\tau_{\mathrm{e}}\right) &= R_{\mathrm{I}} \cdot \left[Z_{\mathrm{I}}\left(1/\tau_{\mathrm{e}}\right)\right]^{-1/2} \\ &= R_{\mathrm{I}} \cdot \left(Z_{\mathrm{I}}^{\mathrm{hI}}\right)^{-1/2} \cdot \left(1-x_{\mathrm{d}}\right)^{-\alpha/2} \cdot \left(\phi_{\mathrm{I}}^{\mathrm{matrix}}\right)^{-\alpha/2} \end{aligned} \tag{3.29}$$

Accordingly, Eq. (3.27) becomes:

$$\nu_{\mathrm{ent}}\left(1/\tau_{\mathrm{e}}\right) = \left(1-x_{\mathrm{d}}\right)^{1+\alpha} \cdot \left(\phi_{\mathrm{I}}^{\mathrm{matrix}}\right)^{1+\alpha} \cdot \frac{\rho_{\mathrm{I}} N_{\mathrm{av}}}{M_{\mathrm{e,hI}}^{\mathrm{G}}} \tag{3.30}$$

From Eqs. (3.24) and (3.30), the contribution of the entanglement network at $t = \tau_{\mathrm{e}}$ is calculated as:

$$E'_{\mathrm{ent}}\left(1/\tau_{\mathrm{e}}\right) = 3 \cdot \xi_{\mathrm{e}} \cdot \left[\left(1-x_{\mathrm{d}}\right)^{1+\alpha} \cdot \left(\phi_{\mathrm{I}}^{\mathrm{matrix}}\right)^{1+\alpha} \cdot \frac{1}{M_{\mathrm{e,hI}}^{\mathrm{G}}}\right] \cdot \rho_{\mathrm{I}} RT \tag{3.31}$$

where $\xi_{\mathrm{e}} \equiv \xi(1/\tau_{\mathrm{e}})$. The *entanglement modulus* of LIL50–12, $E_{\mathrm{e}} \simeq 15.3$ MPa (Figure 3.4(a)), is obtained by combining Eq. (3.26) with $\xi_{\mathrm{e}} \equiv \xi(1/\tau_{\mathrm{e}})$ and Eq. (3.31):

$$E_e \equiv E'\left(1/\tau_e\right) = 3\cdot\xi_e\cdot\left[\left(1-x_d-x_f\right)\cdot\phi_I^{matrix}\cdot\frac{1}{M_I}+\left(1-x_d\right)^{1+\alpha}\cdot\left(\phi_I^{matrix}\right)^{1+\alpha}\cdot\frac{1}{M_{e,hI}^G}\right]\cdot\rho_I RT \quad (3.32)$$

For $\tau_e \le t \le 2\tau_R$, "chain unit sharing" re-equilibrates chain density along the primitive path of the entangled PI chains, while the effect of "early-time chain end fluctuations" on free-end-type midblocks can be assumed to be negligible (§3.3.4.IV-d). For an undiluted PI homopolymer with the same molar mass as the midblock, the time scale for path equilibration $2\tau_R$ would correspond to the shear plateau modulus[43-45] $G'(1/2\tau_R) = (4/5)\cdot(\rho_I N_{av}/M_{e,hI}^G)\cdot kT$, which would be assigned the symbol G_N^0 or G_N depending on whether or not the system were crosslinked[42,n,tt]. The effect of "chain unit sharing" in entangled homopolymers is thus to reduce the storage modulus measured at τ_e by 20%, which explains the Graessley–Fetters definition of entanglement molar mass given by Eq. (3.4) (see related discussion in §3.3.2.III). Stress relaxation due to "chain unit sharing" can be expressed in two (equivalent) ways: (i) as a 20% reduction in the "effective" number density of entanglement strands, i.e. $\nu_{ent,eff}(1/2\tau_R) = (4/5)\cdot\nu_{ent}(1/\tau_e)$ with each strand at $t \ge 2\tau_R$ still contributing kT to the shear modulus; (ii) as a 20% decrease in the contribution of each strand to the shear modulus, i.e. $(4/5)kT$, with $\nu_{ent}(1/2\tau_R) = \nu_{ent}(1/\tau_e)$. In either case, entanglement strands at $t = 2\tau_R$ still originate from *all* entanglements in

---

[tt] With "early-time chain end fluctuations", this modulus would be multiplied by $(1 - X\cdot Z_I^{-1/2})$[44], where X is a constant of order unity[88,89].

LIL50–12 (whether they are trapped or not). Therefore, $Z_I(1/2\tau_R) = Z_I(1/\tau_e)$ and the tube SSL is unchanged:

$$\begin{aligned} a_{I,early} &\equiv a_I\left(1/2\tau_R\right) \\ &= R_I \cdot \left[Z_I\left(1/2\tau_R\right)\right]^{-1/2} \\ &= a_I\left(1/\tau_e\right) \\ &= R_I \cdot \left(Z_I^{hI}\right)^{-1/2} \cdot \left(1-x_d\right)^{-\alpha/2} \cdot \left(\phi_I^{matrix}\right)^{-\alpha/2} \end{aligned} \tag{3.33}$$

while the average number of "effective" entanglement strands per entangled PI chain is:

$$Z_{I,eff}\left(1/2\tau_R\right) = \frac{4}{5} \cdot Z_I\left(1/\tau_e\right) \tag{3.34}$$

and their number density in the matrix becomes (using Eq. (3.27)):

$$\begin{aligned} \nu_{ent,eff}\left(1/2\tau_R\right) &= \frac{4}{5} \cdot \nu_{ent}\left(1/\tau_e\right) \\ &= \frac{4}{5} \cdot \left(1-x_d\right)^{1+\alpha} \cdot \left(\phi_I^{matrix}\right)^{1+\alpha} \cdot \frac{\rho_I N_{av}}{M_{e,hI}^G} \end{aligned} \tag{3.35}$$

with $\nu_{ent}(1/2\tau_R) = (5/4)\cdot\nu_{ent,eff}(1/2\tau_R)$. The contribution of the entanglement network at $t = 2\tau_R$ follows from Eqs. (3.24) and (3.35) as:

$$E'_{ent}\left(1/2\tau_R\right) = 3 \cdot \xi_N \cdot \left[\left(1-x_d\right)^{1+\alpha} \cdot \left(\phi_I^{matrix}\right)^{1+\alpha} \cdot \frac{4}{5}\frac{1}{M_{e,hI}^G}\right] \cdot \rho_I RT \tag{3.36}$$

where $\xi_N \equiv \xi(1/2\tau_R)$. The *plateau modulus* of LIL50–12, $E_N \simeq 9.4$ MPa (Figure 3.4(a)), is obtained by combining Eq. (3.26) with $\xi_N \equiv \xi(1/2\tau_R)$ and Eq. (3.36):

$$\begin{aligned} E_N &\equiv E'\left(1/2\tau_R\right) \\ &= 3 \cdot \xi_N \cdot \left[\left(1-x_d-x_f\right) \cdot \phi_I^{matrix} \cdot \frac{1}{M_I} + \left(1-x_d\right)^{1+\alpha} \cdot \left(\phi_I^{matrix}\right)^{1+\alpha} \cdot \frac{4}{5}\frac{1}{M_{e,hI}^G}\right] \cdot \rho_I RT \end{aligned} \tag{3.37}$$

On time scales larger than $2\tau_R$, arm retraction (in single-free-end-type midblocks, $x_{f,1}$, Figure 3.5) and reptation (in those with two "free" ends, $x_{f,2}$) take place (§3.3.4.IV-d). Eventually, at $t = \tau_{late}$ all untrapped entanglements will have disappeared. Therefore, the number densities of elastically active entanglement strands at $t = \tau_{late}$ and $t = 2\tau_R$ are related by:

$$T_e = \frac{\nu_{ent}(1/\tau_{late})}{\nu_{ent}(1/2\tau_R)} = \frac{\nu_{ent,eff}(1/\tau_{late})}{\nu_{ent,eff}(1/2\tau_R)} \tag{3.38}$$

where T_e represents the fraction of trapped (i.e. permanent) entanglements in the system, called[41] the "*Langley trapping factor*". Since entanglements can be thought of as crosslinks of functionality $f = 4$ (in a loose sense, because topological interactions are not as local as chemical crosslinks), the number density of entanglement strands ν_{ent} is proportional to the number density of entanglements μ_{ent} ($\nu_{ent} = f{\cdot}\mu_{ent}/2 = 2{\cdot}\mu_{ent}$), and $T_e = \mu_{ent,trapped}/\mu_{ent,tot} = \nu_{ent,trapped}/\nu_{ent,tot}$. In our system, $\nu_{ent,trapped} = \nu_{ent}(1/\tau_{late})$ and $\nu_{ent,tot} = \nu_{ent}(1/2\tau_R)$ (when the contribution of each entanglement strand to the modulus is counted as $(4/5)kT$).

For crosslinked rubbers, Langley[208] defined T_e as the probability that all four paths leading away from an entanglement site between two chains lead independently to the network. In other words, T_e characterizes the degree of network perfection: $T_e = 1$ if the crosslinked rubber is without *entangled dangling structures* (i.e. load-bearing structures partially attached to the network that, given time, can completely relax their conformations). Defining the degree of network perfection through the Langley trapping

factor obviously neglects the *unentangled dangling structures* (i.e. the dangling-loops, for LIL50–12), which can be present and constitute a different type of network defect: being unentangled (hence, disengaged from the load-bearing network), such structures relax within a time scale τ_R and do not affect neither the plateau nor the equilibrium modulus of the system (§3.3.4.IV-d). While for a perfectly crosslinked rubber plateau and equilibrium moduli coincide ($E_{eq} = E_N$, when $T_e = 1$), in a real system entangled dangling structures will eventually relax a portion of the network stress ($E_{eq} < E_N$, when $T_e < 1$)[42]; providing the concentration of these network defects is high enough, their slow relaxation mechanism is manifested in the appearance of a secondary dispersion in the loss tangent[42,156,uu]. This behavior is consistent with the analyses of the viscoelastic response of LIL50–12 presented in §3.3.4.IV-b and -d.

From Eqs. (3.35) and (3.38), the number density of "effective" entanglement strands at $t = \tau_{late}$ becomes:

$$\begin{aligned} \nu_{ent,eff}\left(1/\tau_{late}\right) &= T_e \cdot \nu_{ent,eff}\left(1/2\tau_R\right) \\ &= T_e \cdot \frac{4}{5} \cdot \left(1 - x_d\right)^{1+\alpha} \cdot \left(\phi_I^{matrix}\right)^{1+\alpha} \cdot \frac{\rho_I N_{av}}{M_{e,hI}^G} \end{aligned} \tag{3.39}$$

with $\nu_{ent}(1/\tau_{late}) = (5/4)\cdot\nu_{ent,eff}(1/\tau_{late})$. At $t = \tau_{late}$, only bridges and knotted-loops are entangled, and the number density of entangled chains in the matrix is reduced to $(x_b+x_k)\cdot$

[uu] From Eq. (3.24) with $\xi(\omega) = 1$ (for a vulcanized rubber), the relationship between the ratio E_{eq}/E_N and the magnitude of T_e is given by $E_{eq}/E_N = [\nu_{cross} + \nu_{ent,trapped}]/[\nu_{cross} + \nu_{ent,tot}]$. This equation was experimentally verified by Langley and Ferry[156] in 1968.

$\nu_{\mathrm{I}}^{\mathrm{matrix}}$. Hence, the average numbers of entanglement strands per entangled PI chain are now given by:

$$Z_{\mathrm{I,eff}}\left(1/\tau_{\mathrm{late}}\right) = T_{\mathrm{e}} \cdot \left(1 + \frac{x_{\mathrm{f}}}{x_{\mathrm{b}} + x_{\mathrm{k}}}\right) \cdot \frac{4}{5} \cdot Z_{\mathrm{I}}\left(1/2\tau_{\mathrm{R}}\right) \tag{3.40}$$

and

$$Z_{\mathrm{I}}\left(1/\tau_{\mathrm{late}}\right) = T_{\mathrm{e}} \cdot \left(1 + \frac{x_{\mathrm{f}}}{x_{\mathrm{b}} + x_{\mathrm{k}}}\right) \cdot Z_{\mathrm{I}}\left(1/2\tau_{\mathrm{R}}\right) \tag{3.41}$$

obtained (respectively) by the ratios of $\nu_{\mathrm{ent,eff}}(1/\tau_{\mathrm{late}})$ and $\nu_{\mathrm{ent}}(1/\tau_{\mathrm{late}})$ to $(x_{\mathrm{b}}+x_{\mathrm{k}})\cdot\nu_{\mathrm{I}}^{\mathrm{matrix}}$. Since $Z_{\mathrm{I}}(1/\tau_{\mathrm{late}}) \neq Z_{\mathrm{I}}(1/2\tau_{\mathrm{R}})$, the tube SSL changes (according to Eqs. (3.1), (3.33), and (3.41)) to:

$$\begin{aligned} a_{\mathrm{I,late}} &\equiv a_{\mathrm{I}}\left(1/\tau_{\mathrm{late}}\right) \\ &= R_{\mathrm{I}} \cdot \left[Z_{\mathrm{I}}\left(1/\tau_{\mathrm{late}}\right)\right]^{-1/2} \\ &= a_{\mathrm{I,early}} \cdot \left(T_{\mathrm{e}}\right)^{-1/2} \cdot \left(1 + \frac{x_{\mathrm{f}}}{x_{\mathrm{b}} + x_{\mathrm{k}}}\right)^{-1/2} \\ &= R_{\mathrm{I}} \cdot \left(Z_{\mathrm{I}}^{\mathrm{hI}}\right)^{-1/2} \cdot \left(1 - x_{\mathrm{d}}\right)^{-\alpha/2} \cdot \left(\phi_{\mathrm{I}}^{\mathrm{matrix}}\right)^{-\alpha/2} \cdot \left(T_{\mathrm{e}}\right)^{-1/2} \cdot \left(1 + \frac{x_{\mathrm{f}}}{x_{\mathrm{b}} + x_{\mathrm{k}}}\right)^{-1/2} \end{aligned} \tag{3.42}$$

From Eqs. (3.24) and (3.39), the contribution of the entanglement network at $t = \tau_{\mathrm{late}}$ is:

$$E'_{\mathrm{ent}}\left(1/\tau_{\mathrm{late}}\right) = 3 \cdot \xi_{\mathrm{eq}} \cdot \left[T_{\mathrm{e}} \cdot \left(1 - x_{\mathrm{d}}\right)^{1+\alpha} \cdot \left(\phi_{\mathrm{I}}^{\mathrm{matrix}}\right)^{1+\alpha} \cdot \frac{4}{5} \frac{1}{M_{\mathrm{e,hI}}^{\mathrm{G}}}\right] \cdot \rho_{\mathrm{I}} RT \tag{3.43}$$

where $\xi_{\mathrm{eq}} \equiv \xi(1/\tau_{\mathrm{late}})$. The *pseudo-equilibrium modulus* of LIL50–12, $E_{\mathrm{eq}} \simeq 5.4$ MPa (Figure 3.4(a)), is obtained by combining Eq. (3.26) with $\xi_{\mathrm{eq}} \equiv \xi(1/\tau_{\mathrm{late}})$ and Eq. (3.43):

$$\begin{aligned} E_{\mathrm{eq}} &\equiv E'\left(1/\tau_{\mathrm{late}}\right) \\ &= 3\cdot\xi_{\mathrm{eq}}\cdot\left[\left(1-x_{\mathrm{d}}-x_{\mathrm{f}}\right)\cdot\phi_{\mathrm{I}}^{\mathrm{matrix}}\cdot\frac{1}{M_{\mathrm{I}}}+T_{\mathrm{e}}\cdot\left(1-x_{\mathrm{d}}\right)^{1+\alpha}\cdot\left(\phi_{\mathrm{I}}^{\mathrm{matrix}}\right)^{1+\alpha}\cdot\frac{4}{5}\frac{1}{M_{\mathrm{e,hI}}^{\mathrm{G}}}\right]\cdot\rho_{\mathrm{I}}RT \\ &= E_{\mathrm{eq,cross}}+E_{\mathrm{eq,ent}} \end{aligned} \quad (3.44)$$

At (pseudo) mechanical equilibrium, not only is the storage modulus given by the simple superposition of endlink ($E_{\mathrm{eq,cross}}$) and entanglement ($E_{\mathrm{eq,ent}}$) contributions, but also both of them originate from the same midblock conformations (bridges and knotted-loops). It is therefore convenient to consider $E_{\mathrm{eq,cross}}$ and $E_{\mathrm{eq,ent}}$ in dimensionless form, as:

$$\begin{aligned} \tilde{E}_{\mathrm{cross}} &\equiv \frac{E_{\mathrm{eq,cross}}}{\nu_{\mathrm{b,k}}\cdot kT} \\ &= 3\cdot\xi_{\mathrm{eq}}\cdot\frac{\phi_{\mathrm{I}}^{\mathrm{matrix}}}{f_{\mathrm{I}}} \end{aligned} \quad (3.45)$$

and

$$\begin{aligned} \tilde{E}_{\mathrm{ent}} &\equiv \frac{E_{\mathrm{eq,ent}}}{\nu_{\mathrm{b,k}}\cdot kT} \\ &= 3\cdot\xi_{\mathrm{eq}}\cdot Z_{\mathrm{I,eff}}\left(1/\tau_{\mathrm{late}}\right)\cdot\frac{\phi_{\mathrm{I}}^{\mathrm{matrix}}}{f_{\mathrm{I}}} \\ &= \tilde{E}_{\mathrm{cross}}\cdot Z_{\mathrm{I,eff}}\left(1/\tau_{\mathrm{late}}\right) \end{aligned} \quad (3.46)$$

where $\nu_{\mathrm{b,k}} \equiv (x_{\mathrm{b}}+x_{\mathrm{k}})\cdot\nu_{\mathrm{I}}$ is the number density of bridges and knotted-loops, $\nu_{\mathrm{I}} = f_{\mathrm{I}}\cdot\nu_{\mathrm{I}}^{\mathrm{hI}}$ is the number density of midblocks, and f_{I} is the volume fraction of PI in the triblock (given in Table 3.1). $\tilde{E}_{\mathrm{cross}}$ and $\tilde{E}_{\mathrm{ent}}$ represent the contributions to the pseudo-equilibrium modulus, of endlinks and entanglements (respectively), per chain and in units of kT. If the PLA microdomains were chemical endlinks ($\xi(\omega) = \xi_{\mathrm{eq}} = 1$, $f_{\mathrm{I}} = 1$), and the network did not contain dangling structures ($x_{\mathrm{d}} = x_{\mathrm{f}} = 0$, $T_{\mathrm{e}} = 1$) nor sol fraction ($\phi_{\mathrm{I}}^{\mathrm{matrix}} = 1$), then

$\tilde{E}_{\text{cross}} = 3$ and $\tilde{E}_{\text{ent}} = 3\cdot(4/5)\cdot Z_{\text{I}}^{\text{hI}}$ (from Eqs. (3.28) and (3.40)). In §3.3.4.IV-c, we briefly stated that the main contribution of glassy PLA to the modulus comes from the filler effect, rather than from the augmented number of network junctions. This is most easily seen by considering the ratio $\tilde{E}_{\text{ent}} / \tilde{E}_{\text{cross}} = Z_{\text{I,eff}}(1/\tau_{\text{late}})$: at equilibrium, there are $Z_{\text{I,eff}}(1/\tau_{\text{late}})$ "effective" entanglement strands (each contributing kT to the modulus) for each endlink, and if the midblock chain is well entangled $Z_{\text{I,eff}}(1/\tau_{\text{late}}) \gg 1$.

For TPEs of the A–B–A and $(\text{A–B})_n$ type, the ideal condition $T_{\text{e}} = 1$ is achieved when all the A blocks are confined within glassy A domains (i.e. when the local A-block volume fraction is described by a step function, except at the interface). On the other hand, $T_{\text{e}} \to 0$ when $T \to T_{\text{ODT}}$ or $T \to T_{\text{g,A}}$. Thus, it should be possible, at least in principle, to express T_{e} as a function of the fraction of midblocks in free-end-type conformation x_{f}. We seek to obtain such an analytical expression, applicable to the network structure of LIL50–12. The schematic drawing in Figure 3.5, which is consistent with the dynamics of the system (§3.3.4.IV-d), is of help. Although not depicted in Figure 3.5, we will consider the more general case in which the structure contains also knotted-loops (x_{k}) and unentangled dangling chains (x_{d}). Based on Eqs. (3.28), (3.35), and the identity $\nu_{\text{I}}^{\text{matrix}} = \phi_{\text{I}}^{\text{matrix}} \cdot \nu_{\text{I}}^{\text{hI}}$, we can write the total number density of entanglement strands as $\nu_{\text{ent,tot}} = (1–x_{\text{d}})\cdot \nu_{\text{I}}^{\text{matrix}} \cdot Z_{\text{I}}(1/\tau_{\text{e}})$ (dropping the 4/5 prefactor as explained earlier). Similarly, Eq. (3.39) can be rewritten as $\nu_{\text{ent,trapped}} = T_{\text{e}}\cdot(1–x_{\text{d}})\cdot \nu_{\text{I}}^{\text{matrix}} \cdot Z_{\text{I}}(1/\tau_{\text{e}})$. For the network drawn in Figure 3.5, $x_{\text{b}} = 3/4$, $x_{\text{k}} = x_{\text{d}} = 0$, $x_{\text{f}} = 1/4$, $\phi_{\text{I}}^{\text{matrix}} \simeq 1$, $\nu_{\text{I}}^{\text{hI}} = 4$, $Z_{\text{I}}(1/\tau_{\text{e}}) = 3$,

and $T_e = 1/2$; hence, there are a total of $\nu_{ent,tot} = 2\cdot\mu_{ent,tot} \simeq 12$ entanglement strands, of which $\nu_{ent,trapped} = 2\cdot\mu_{ent,trapped} \simeq 6$ persist at mechanical equilibrium (the three untrapped entanglements are indicated by red italic numbers). The number density of untrapped entanglement strands $\nu_{ent,untrapped}$ is of course given by the difference, $\nu_{ent,untrapped} = \nu_{ent,tot} - \nu_{ent,trapped} = (1-T_e)\cdot(1-x_d)\cdot\nu_I^{matrix}\cdot Z_I(1/\tau_e)$. However, if the network structure is such that each untrapped entanglement is associated with no more than one midblock in free-end conformation (i.e. if $x_f/(x_b+x_k) \ll 1$ and the distribution of free-end-type midblocks is uniform throughout the matrix, §3.3.4.IV-d), the number density of untrapped entanglement strands $\nu_{ent,untrapped}$ is also given by $\nu_{ent,untrapped} = 2\cdot x_f\cdot\nu_I^{matrix}\cdot Z_I(1/\tau_e)$. By comparing the two expressions, we obtain:

$$T_e = 1 - \frac{2x_f}{(1-x_d)} \qquad \text{for } x_f/(x_b+x_k) \ll 1 \tag{3.47}$$

which gives a reasonable dependence of T_e on network architecture: T_e is unity when $x_f = 0$, and it decreases with increasing population of free-end-type midblocks x_f with respect to the total ensemble of entangled chains $(1-x_d)$. Of course, the behavior for $T_e \to 0$ cannot be correctly described by Eq. (3.47), since it would correspond to $x_f/(x_b+x_k) \to 1$. Eq. (3.47) allows us to rewrite Eq. (3.42) as:

$$\begin{aligned} a_{I,late} &= a_{I,early}\cdot C^{-1/2} \\ &= R_I\cdot\left(Z_I^{hI}\right)^{-1/2}\cdot\phi^{-\alpha/2}\cdot C^{-1/2} \end{aligned} \tag{3.48}$$

where $\phi = (1-x_d)\cdot\phi_I^{matrix}$ and $C = 1-x_f/(x_b+x_k)$. Compared to an entangled and undiluted PI homopolymer, $a_{I,late}$ increases by a factor $\phi^{-\alpha/2}$ due to the "dilation" effect of dangling-

loops and unsegregated PLA chains, and by a factor $C^{-1/2}$ that only depends on the distribution of midblock conformations. Combining Eqs. (3.44) and (3.47), we obtain:

$$\begin{aligned} E_{\mathrm{eq}} &\equiv E'\left(1/\tau_{\mathrm{late}}\right) \\ &= 3\cdot\xi_{\mathrm{eq}}\cdot\left\{\left(1-x_{\mathrm{d}}-x_{\mathrm{f}}\right)\cdot\phi_{\mathrm{I}}^{\mathrm{matrix}}\cdot\frac{1}{M_{\mathrm{I}}}+\left[1-\frac{2x_{\mathrm{f}}}{\left(1-x_{\mathrm{d}}\right)}\right]\cdot\left(1-x_{\mathrm{d}}\right)^{1+\alpha}\cdot\left(\phi_{\mathrm{I}}^{\mathrm{matrix}}\right)^{1+\alpha}\cdot\frac{4}{5}\frac{1}{M_{\mathrm{e,hI}}^{\mathrm{G}}}\right\}\cdot\rho_{\mathrm{I}}RT \\ &\quad \text{for } x_{\mathrm{f}}/\left(x_{\mathrm{b}}+x_{\mathrm{k}}\right)\ll 1 \end{aligned} \tag{3.49}$$

To use Eqs. (3.32), (3.37), and (3.49), we need to relate the volume fraction of PI in the matrix $\phi_{\mathrm{I}}^{\mathrm{matrix}}$ to x_{f}. Mass balance gives:

$$w_{\mathrm{L,un}}=\frac{w_{\mathrm{L}}^{\mathrm{matrix}}}{\left(1-w_{\mathrm{L}}^{\mathrm{matrix}}\right)}\cdot\left(1-w_{\mathrm{L}}\right) \tag{3.50}$$

where $w_{\mathrm{L,un}}$ is the mass fraction of unsegregated PLA blocks, $w_{\mathrm{L}}^{\mathrm{matrix}}$ is the mass fraction of (unsegregated) PLA blocks in the matrix, and w_{L} is the mass fraction of PLA given in Table 3.1. The number density of unsegregated PLA blocks is $\nu_{\mathrm{L,un}} = w_{\mathrm{L,un}}\cdot\rho_{\mathrm{LIL}}\cdot N_{\mathrm{av}}/M_{\mathrm{L}}$, where ρ_{LIL} is the density of the block copolymer[d,f], and M_{I} is the PLA number-average molar mass given in Table 3.1. Since the number density of PLA blocks is $\nu_{\mathrm{L}} = 2\cdot\rho_{\mathrm{LIL}}\cdot N_{\mathrm{av}}/M_{\mathrm{LIL}}$, the fraction of unsegregated PLA blocks $x_{\mathrm{L,un}}$ is given by:

$$\begin{aligned} x_{\mathrm{L,un}} &\equiv \frac{\nu_{\mathrm{L,un}}}{\nu_{\mathrm{L}}}=\frac{w_{\mathrm{L,un}}}{w_{\mathrm{L}}} \\ &= \frac{w_{\mathrm{L}}^{\mathrm{matrix}}}{\left(1-w_{\mathrm{L}}^{\mathrm{matrix}}\right)}\cdot\frac{\left(1-w_{\mathrm{L}}\right)}{w_{\mathrm{L}}} \end{aligned} \tag{3.51}$$

If all midblocks in free-end conformation had only one “free” end (as shown in Figure 3.5), then x_{f} (= $x_{\mathrm{f,1}}$) would be twice as large as $x_{\mathrm{L,un}}$; if both ends resided outside the I/L

interfaces, then x_f (= $x_{f,2}$) would be equal to $x_{L,un}$. Note, however, that the latter scenario would be inconsistent with the measured low-frequency behavior of LIL50–12, as discussed in §3.3.4.IV-d. Taking the geometric average and using Eq. (3.51), x_f is related to the composition of the matrix w_L^{matrix} as:

$$\begin{aligned} x_f &= \sqrt{2} \cdot x_{L,un} \\ &= \sqrt{2} \cdot \frac{w_L^{matrix}}{\left(1 - w_L^{matrix}\right)} \cdot \frac{\left(1 - w_L\right)}{w_L} \end{aligned} \tag{3.52}$$

Lastly, by assuming volume additivity:

$$\phi_I^{matrix} = \frac{\left(1 - w_L^{matrix}\right) / \rho_I}{\left(1 - w_L^{matrix}\right) / \rho_I + w_L^{matrix} / \rho_L} \tag{3.53}$$

where ρ_I and ρ_L are the densities of the PI and PLA blocks[d] shown in Table 3.3. The $\phi_I^{matrix} - x_f$ relationship is thus given by Eqs. (3.52) and (3.53).

As written, Eqs. (3.32), (3.37), and (3.49) contain 5 unknowns: ξ_e, ξ_N, ξ_{eq}, x_d, and x_f. However, considering the length of the PI block, we can reasonably assume[165] $x_d \simeq 0$ (§3.3.4.IV-d). In addition, the weak frequency dependence of $E'(\omega)$ in the range $[1/\tau_{late}, 1/2\tau_R]$ implies that $\xi_{eq} \simeq \xi_N$. We can then rewrite Eqs. (3.32), (3.37), and (3.49) as a system with 3 unknowns:

$$\begin{cases} E_e = 3 \cdot \xi_e \cdot \left[\left(1 - x_f\right) \cdot \phi_I^{matrix} \cdot \dfrac{1}{M_I} + \left(\phi_I^{matrix}\right)^{1+\alpha} \cdot \dfrac{1}{M_{e,hI}^G} \right] \cdot \rho_I RT \\ E_N = 3 \cdot \xi_{eq} \cdot \left[\left(1 - x_f\right) \cdot \phi_I^{matrix} \cdot \dfrac{1}{M_I} + \left(\phi_I^{matrix}\right)^{1+\alpha} \cdot \dfrac{4}{5} \dfrac{1}{M_{e,hI}^G} \right] \cdot \rho_I RT \\ E_{eq} = 3 \cdot \xi_{eq} \cdot \left[\left(1 - x_f\right) \cdot \phi_I^{matrix} \cdot \dfrac{1}{M_I} + \left(1 - 2x_f\right) \cdot \left(\phi_I^{matrix}\right)^{1+\alpha} \cdot \dfrac{4}{5} \dfrac{1}{M_{e,hI}^G} \right] \cdot \rho_I RT \end{cases} \tag{3.54}$$

which can be solved iteratively (the implemented MATLAB® algorithm is provided in Appendix H, §H.3.3). The PI matrix is first considered to be compositionally pure ($\phi_I^{matrix} = 1$), and Eq. (3.54) is solved for ξ_e, ξ_{eq}, and x_f; the new matrix composition ϕ_I^{matrix} is calculated according to Eqs. (3.52) and (3.53), and the procedure is repeated to convergence. For the dilution exponent α we considered both the classical value[42] $\alpha = 1$ and the Colby–Rubinstein[171] prediction for theta conditions $\alpha = 4/3$. The classical value gives a slightly smaller M_e (Eq. (3.22)b). For this reason, Watanabe and co-workers[164,222] argued that $\alpha = 1$ is more appropriate for block copolymer systems: the tethering to microdomain interfaces would make the chain more easily entangled than the corresponding homopolymer of equal molar mass. Under the assumption of unperturbed strand dimensions, the development proposed by Bard and Chung[110] in 1987 is analogous to using Eq. (3.54)c with $x_f = 0$ and $\phi_I^{matrix} = 1$.

Although a reliable prediction of $\xi(\omega)$ is not available, the value ξ_{eq} obtained from Eqs. (3.54) approximates the filler effect at equilibrium and should only depend on the volume fraction (f_L) and aspect ratio (δ) of the PLA domains (Brownian motion and inertia should be negligible, i.e. Pe $\rightarrow \infty$ and Re $\rightarrow 0$). Applied to our system, the model proposed by Guth[223] for rod-like filler particles embedded in a continuous matrix gives:

$$\xi_{eq}(\delta, f_L) = 1 + 0.67 \cdot (\delta \cdot f_L) + 1.62 \cdot (\delta \cdot f_L)^2 \qquad (3.55)$$

under the assumptions of large aspect ratio ($\delta \gg 1$) and semi-dilute suspension ($f_L \leq 0.1$). While the first condition is approximately satisfied (from TEM, $\delta \approx 5$ – Figure A.1(b) in

Appendix A), f_L = 0.25 (Table 3.1). Therefore, by using Eq. (3.55) we do not expect to infer more than a rough approximation for δ.

Table 3.9. Parameters obtained by modeling the linear elastic behavior of LIL50–12 at 0 °C.

ξ_{eq}	ξ_e	x_f	$x_b + x_k$	$x_{L,un}$	w_L^{matrix}	ϕ_I^{matrix}	T_e	δ
9.8	12.9	0.237	0.763	0.168	0.073	0.947	0.53	8.5

$M_{e,I}^G$ [g/mol]	$a_{I,early}$ [nm]	$a_{I,late}$ [nm]	$Z_I(1/2\tau_R)$	$Z_I(1/\tau_{late})$	$Z_{I,eff}(1/\tau_{late})$	$\tilde{E}_{ent}$	$\tilde{E}_{cross}$	$E_{eq,ent}/E_{eq}$ [%]
5385	5.64	6.79	9.25	6.4	5.1	188.4	36.9	83.6

Results

With $E_e \simeq$ 15.3 MPa, $E_N \simeq$ 9.4 MPa, $E_{eq} \simeq$ 5.4 MPa (Figure 3.4(a)), M_I = 49800 g/mol (Table 3.1), ρ_I = 0.915 g/cm^3 (Table 3.3), $M_{e,hI}^G$ = 5100 g/mol (Table 3.4), and α = 1 we obtained the results summarized in Table 3.9. The choice of α did not affect significantly the result of the calculations, leaving unchanged distribution of midblock conformations and matrix composition, while giving slightly different values of the entanglement molar mass and the average number of tube segments per chain ($M_{e,I}^G$ = 5385 g/mol and $Z_I(1/2\tau_R)$ = 9.25, for α = 1; $M_{e,I}^G$ = 5484 g/mol and $Z_I(1/2\tau_R)$ = 9.08, for α = 4/3). We also compared the results against a possible 10% error in the estimate of the pseudo-equilibrium modulus (see related discussion in §3.3.4.IV-d). Decreasing E_{eq} by 10%

yields a slightly higher fraction of free-end-type midblocks, $x_f = 0.268$, and accordingly a lower value of Langley trapping factor, $T_e = 0.46$, as well as a lower value of "effective" entanglement strands per entangled chain at equilibrium, $Z_{I,eff}(1/\tau_{late}) = 4.7$.

Since the behavior is predominantly elastic for $\omega \leq 1/\tau_e$, the filler effect $\xi(\omega)$ is weakly dependent on frequency ($\xi_{eq} = 9.8$, $\xi_e = 12.9$ vs. $\xi(1/\tau_L) \approx 21$), which supports the validity of the assumption $\xi_{eq} \simeq \xi_N$. Remarkably, ξ_{eq} is rather close to the estimate obtained from the analysis of the isochronal measurements (§3.3.4.IV-c and Appendix A). Application of Eq. (3.55) gives $\delta \approx 8.5$, roughly in agreement with the aspect ratio deduced from TEM ($\delta \approx 5$). The discrepancy is likely due to the different hydrodynamic flow employed for specimens used for TEM (*radial* – Figure A.1(b) and §A.2.1) and for specimens used for rheology (*planar extension*-like – Figure 3.2 and §3.2.3).

The arm retraction dynamics discussed in §3.3.4.IV-d is the result of a small fraction of partially segregated chains ($x_{f,1} \leq x_f \simeq 24\%$): the PI-rich matrix contains approximately 7% by mass PLA and the majority of midblocks is either in bridge or knotted-loop conformation ($x_b+x_k \simeq 76\%$). The condition $x_f/(x_b+x_k) \ll 1$ is therefore verified, which justifies the use of Eqs. (3.47) and (3.49); furthermore, it implies that the legitimacy of the network structure sketched in Figure 3.5 rests solely on the premise that the free-end-type midblocks be (more or less) uniformly distributed in the matrix (§3.3.4.IV-d). The distribution of midblock conformations is not surprising, in view of the microstructure that would form at thermodynamic equilibrium. In the strong segregation regime, self-assembly of monodisperse and compositionally symmetric A–B–A triblock copolymers

with composition $f_A = 0.25$ is expected[121] to generate cylindrical A domains embedded in the B matrix. For these systems, the predicted[121] equilibrium distribution of midblock conformations is $x_b = 1–x_l = 60–65\%$ (with $x_l = x_d+x_k$, and $x_f = 0$). Long B chains would hardly form unentangled loops[165], thereby causing $x_b+x_k \rightarrow 100\%$. Given the strong driving force towards segregation ($\chi\hat{N}(25\ °C) \simeq 436$), if our system were in thermodynamic equilibrium x_f would be vanishingly small; $x_f \simeq 24\%$ is thus a direct scalar measure of the metastable degree of the microstructure. A rough estimate of x_f can also be obtained by thermal analysis, through the Fox equation[224]. For a compositionally pure PI matrix, the estimated glass transition is about –64 °C (Appendix A). The increase from –64 °C to about –60 °C (measured by DSC, §3.3.1), can then be associated with a mass fraction of (unsegregated) PLA blocks in the matrix $w_L^{matrix} \approx 6\%$. Using Eqs. (3.51) and (3.52), this corresponds to $x_f \approx 19\%$. A more accurate estimate of w_L^{matrix} based on the glass transitions would require the use of a different formulation, of the type proposed by Couchman[225-228], and glass transition temperatures determined (for each microphase and corresponding homopolymers) by isochronal dynamic measurements rather than DSC (Appendix A). Nevertheless, the above estimate of x_f based on the simpler Fox equation gives the correct order of magnitude, and shows consistency between thermal analysis and linear elastic behavior as modeled by Eqs. (3.52), (3.53), and (3.54). Since partial segregation stems from either lack of thermodynamic equilibrium or equilibrium self-assembly in the intermediate segregation regime[98] ($\chi N < \approx 100$), it is not uncommon in commercial TPEs of the A–B–A type. This can lead to much higher values of x_f than

what we estimated for our material. For instance, for a commercially produced S–I–S triblock with $w_S = 17\%$, Hotta et al.[112] inferred by thermal analysis (via the Fox equation) $w_S^{matrix} \approx 8\%$. Using Eqs. (3.51) and (3.52), this implies $x_f \approx 60\%$. In their report[112], the authors argued that dangling structures were responsible for the slow stress relaxation of the S–I–S network, although a qualitative or quantitative comparison with arm retraction dynamics was not attempted.

In our system, about half of the PI entanglements was made permanent by microphase-segregation ($T_e = 0.53$, from Eq. (3.47)), similarly to the situation depicted in Figure 3.5. Since the PLA microdomains act as endlinks for (the majority of) the PI chains, it is instructive to consider this value of T_e in the context of high-functionality chemically endlinked networks. For these systems, a recursive method for deriving post-gel properties was developed by Miller and Macosko[229,230] in 1976, assuming that (i) all functional groups of the same type are equally reactive, (ii) all groups react independently of one another, and (iii) there are no intramolecular reactions. The network formed in TPEs of the A–B–A type can be considered as if it originated by endlinking long monodisperse bifunctional B_2 chains with small *f*-functional A_f molecules (i.e. $A_f + B_2 \rightarrow$ network). A single triblock chain is then viewed as A_2–B_2–A_2, whereas A_f represents the *f*-functional A microdomain. If we indicate with $A_{f,0}$ the initial moles of A_f, and with $B_{2,0}$ the initial moles of B_2, then $A_{f,0} = (4/f)\cdot B_{2,0}$ (because $A_{f,0} = (2/f)\cdot A_{2,0}$, and $A_{2,0} = 2\cdot B_{2,0}$ for A–B–A triblocks). This implies that the stoichiometric ratio of reactant groups is $r =$

$(f/2)\cdot A_{f,0}/B_{2,0} = 2$, and their fractional conversions are related by $p_B = r\cdot p_A = 2\cdot p_A$.[229] The Langley trapping factor is connected to the network architecture as:[230]

$$T_e = (1-z)^4 \tag{3.56}$$

where z represents the probability that a randomly chosen B_2 chain will lead to a dangling structure. Based on the analytical expressions derived by Miller and Macosko[230], we find that z must satisfy the following equation:

$$\left[\frac{1}{p_B}\cdot(z-1+p_B)\right]^{\frac{1}{f-1}} - \frac{p_B}{2}(z-1) - 1 = 0 \tag{3.57}$$

For a given functionality f and Langley trapping factor T_e, z can be calculated from Eq. (3.56) and p_B is obtained from Eq. (3.57). As we discussed earlier, microdomain functionality is typically of order 100 or so[200,201]. For present purposes, however, the precise value of f is not important: if $T_e = 0.53$, Eq. (3.57) admits a physically acceptable solution (i.e. $0 \le p_B \le 1$) for $f \ge 5$, which becomes essentially independent of f for $f \ge 19$. More generally, when $f \gg 10$ Eqs. (3.56) and (3.57) simplify to $T_e \simeq (p_B)^4$ and $p_B \simeq 1–z$, showing how sensitive T_e is to slight incompleteness in the endlinking. $T_e = 0.53$ thus corresponds to $p_B = 0.853$ (i.e. about 85% fractional conversion of the B groups), for an equivalent chemically endlinked network. Indeed, a very similar Langley trapping factor, $T_e = 0.52$, was obtained by Meyers et al.[231] for a model endlinked poly(dimethylsiloxane) (PDMS) network with $f = 44$, $r = 1.8$, and $p_B = 0.848$. It is interesting to note that the study of Meyers et al.[231], published in 1980, was the first investigation utilizing model endlinked networks with high functionality. Block copolymers (in particular, pure

triblocks or triblock/diblock blends) naturally lend themselves as models for quantitative studies of the elasticity of multifunctional elastomeric networks.

Since the entangled PI chains prior to deformation occupy a volume fraction $(1–x_d)\cdot\phi_I^{matrix} \simeq 95\%$, the entanglement molar mass increases, $M_{e,I}^{G} = 5385$ g/mol (Eq. (3.22)b), the tube SSL increases, $a_{I,early} = 5.64$ nm (Eq. (3.33)), and the average number of tube segments per chain decreases, $Z_I(1/\tau_e) = Z_I(1/2\tau_R) = 9.25$ (Eq. (3.28)), with respect to homopolymer PI of equal molar mass (cf. Table 3.4). Using $Z_I(1/2\tau_R)$ we can refine our estimate of τ_{late} (§3.3.4.IV-d), obtaining $\tau_{late} \simeq 1.9\cdot10^4$ s for dynamically undiluted arm retraction (Eq. (3.21) with $\alpha = 0$, Table 3.8). Owing to the exponential dependence in Eq. (3.21)b, the slight decrease in Z_I (from 9.8 to 9.25) determines a twofold change in τ_{late} (from $4\cdot10^4$ s to $1.9\cdot10^4$ s). This signifies that a quantitative study of arm retraction dynamics in A–B–A triblocks cannot prescind from a determination of x_f (either via thermal analysis or modeling of the linear elastic behavior) and an estimate of x_d. Although $Z_I(1/\tau_e)$ is also involved in the definitions of the entanglement time τ_e (Eq. (3.19)) and the disengagement time τ_d (§3.3.4-IV-d), their values remain nearly unaffected (e.g. $\tau_e \simeq 0.09$ ms, instead of 0.08 ms). The more accurate value of the average number of tube segments per chain allows us to test a specific prediction of arm retraction dynamics. Whether dynamically diluted or not, both experiments[174,175,232] and theory[45,174] have shown that, in the low-frequency region, the magnitude of $G'(\omega)$ when $G'(\omega) = G''(\omega)$ decreases approximately with the reciprocal of the arm molar mass, that is:

$$G_c \approx \frac{1}{Z_a} \cdot G_N^0 \tag{3.58}$$

where $G_c \equiv G'(1/\tau_c) = G''(1/\tau_c)$ is the crossover modulus, $1/\tau_c$ is the crossover frequency, and Z_a is the average number of tube segments in the retracting arm (Eq. (3.21), §3.3.4.IV-d). Applied to our system, Eq. (3.58) translates into:

$$E_c \approx \frac{1}{Z_I(1/2\tau_R)} \cdot \left(E_N - E_{eq}\right) \tag{3.59}$$

where $E_c \equiv E'(1/\tau_c) - E_{eq} = E''(1/\tau_c)$ is the crossover modulus (Figure 3.6), and $\tau_c \simeq 2200$ s approximates the longest relaxation time of the retracting single-free-end-type midblocks (§3.3.4.IV-d and Figure 3.6). With $Z_I(1/2\tau_R) = 9.25$ and $E_N - E_{eq} \simeq 4.1$ MPa, Eq. (3.59) predicts a crossover modulus E_c of order 0.4 MPa, in close agreement with $E_c \simeq 0.3$ MPa deduced from Figure 3.6. This represents additional evidence that the slow relaxation of the LIL50–12 network is quantitatively accounted for by arm retraction dynamics, thereby supporting the conclusions drawn in §3.3.4.IV-d.

At (pseudo) mechanical equilibrium, entanglements formed between bridges (or knotted-loops) and free-end-type midblocks have disappeared (cf. Figure 3.5). Accordingly, the tube SSL increases to $a_{I,late} = 6.79$ nm (Eq. (3.42) or (3.48)), and each entangled chain is left, on average, with $Z_{I,eff}(1/\tau_{late}) \simeq 5$ "effective" entanglement strands (Eqs. (3.28) and (3.40)). In spite of untrapped entanglements, entanglement junctions outnumber PLA endlinks by 5 to 1, and the pseudo-equilibrium modulus E_{eq} is largely dictated by the entanglement network ($E_{eq,ent}/E_{eq} \simeq 84\%$, Eq. (3.44)), as anticipated in §3.3.4.IV-c. Each bridge and knotted-loop contributes to E_{eq} about 189 kT because chains

are entangled (Eq. (3.46)), and only about 37 kT because chain ends are tightly anchored to I/L interfaces (Eq. (3.45)).

Closing remarks

Relating the linear behavior of undiluted A–B–A triblocks to molecular parameters is a prerequisite for designing associated TPE-based systems that can exhibit the desired linear and nonlinear rheological properties. By identifying the leading dynamics at play, we have connected the linear viscoelastic response of LIL50–12 to molecular parameters from which characteristic time scales and moduli can be calculated.

The analyses presented in the last two sections are independent from the specific choice of the constituent blocks, and relevant at large deformations as well. This can be readily appreciated by considering, for instance, how the structure of an A–B–A network may affect its maximum extensibility at different time scales. According to the studies of Urayama and co-workers[80-82], the pseudo-equilibrium stress-strain behavior of elastomeric networks in various deformation modes is well described by the Edwards–Vilgis (E–V) slip–link model[83,84] (Chapter 5, and Appendix H, §H.2.2). This model assumes that the maximum stretch of the network λ_{max} is that of the trapped entanglement strands therein $\lambda_{max,e}$, i.e. the ratio of the entanglement strand fully extended (contour) length (L_e) over its unperturbed root-mean-square end-to-end distance ($R_e = a$). Since $L_e = N_{e,k} b_k$ (from the definition of Kuhn chain, §3.3.2.II), and $a = (N_e)^{1/2} b = (N_{e,k})^{1/2} b_k$ (from Eqs. (3.1) and (3.8)), it follows that:

$$\begin{aligned}\lambda_{\max,e} &\equiv \frac{L_e}{a} \\ &= N_{e,k}^{1/2} = \frac{a}{b_k}\end{aligned} \tag{3.60}$$

For an entangled and undiluted 7% 3,4-PI homopolymer, the E–V slip–link model predicts $\lambda_{max} \simeq 6.2$ (using the values of a and b_k for PI at 0 °C, Table 3.3). This stretch ratio corresponds to a nominal/engineering strain $\varepsilon_{N,max} = \lambda_{max} - 1 \simeq 520\%$, and true/Hencky strain $\varepsilon_{max} = \ln(\lambda_{max}) \simeq 1.8$.[c] Since entanglements persist for $t < \tau_d$, this E–V prediction would hold true for any deformation rate $\dot{\varepsilon} > 1/\tau_d$.[vv] If the PI chain were the constituent block of a triblock, i.e. a TPE of the A–I–A type, the same E–V prediction would apply (for any deformation rate within the rubbery plateau) as long as $x_d = x_f = 0$ and $\phi_I^{matrix} = 1$; otherwise, both λ_{max} and its rate-dependence would be different. The effect of network architecture on λ_{max} can be illustrated by applying the E–V slip–link model to the hypothetical nonlinear extensional behavior of LIL50–12 at 0 °C. On time scales $t \leq 2\tau_R$ ($\dot{\varepsilon} \geq 1/2\tau_R$), the tube SSL, hence λ_{max} (Eq. (3.60)), is increased compared to homopolymer PI by a factor $\phi^{-\alpha/2} \simeq 1.028$ (Eq. (3.33)), and the E–V slip–link model predicts $\lambda_{max} \simeq 6.4$ ($\varepsilon_{N,max} \simeq 540\%$, $\varepsilon_{max} \simeq 1.8$). On time scales $t > \tau_{late}$ ($\dot{\varepsilon} < 1/\tau_{late}$), the tube SSL, hence λ_{max}, is increased by a factor $\phi^{-\alpha/2} \cdot C^{-1/2} \simeq 1.238$ (Eq. (3.48)), and the prediction of the E–V slip–link model becomes $\lambda_{max} \simeq 7.6$ ($\varepsilon_{N,max} \simeq 660\%$, $\varepsilon_{max} \simeq 2.0$).

[vv] Tube models predict loss of entanglements due to *convective constraint release* in steady state flow, for deformation rates $\dot{\varepsilon} > 1/\tau_d$.[36] This additional (nonlinear) relaxation mechanism is being neglected in the present discussion.

Despite the low PLA content in the LIL50–12 matrix ($w_L^{matrix} \simeq 7\%$), neglecting the distribution of midblock conformations (determined from the analysis of the linear response at 0 °C) may result in underestimating the maximum extensibility of our material (λ_{max}) by as much as 24%. It is useful to note that almost the same deviation from pure matrix behavior (i.e. $\phi^{-\alpha/2} \cdot C^{-1/2}$) may also apply at different temperatures. In conditions of slow ordering kinetics (cf. §3.3.1 and §3.3.4.I), small deformations, and $T < T_{g,A}$, the distribution of midblock conformations may remain approximately constant (for the experimental time scale) and equal to the distribution established when the network was formed. In this scenario, the temperature dependence of the "dilution" factor $\phi^{-\alpha/2} \cdot C^{-1/2}$ would only originate from $\phi_I^{matrix}(T)$ (Eq. (3.53)). The nonlinear extensional behavior of LIL50–12 at 37 °C will be examined in Chapter 5.

From our analysis, matrix dilution and partial segregation (either inherent or induced by chain pullout) emerge as powerful tools that can tune the ultimate properties of triblock- or multiblock-type networks. Matrix dilution ($\phi = (1-x_d) \cdot \phi_I^{matrix}$) and midblock length ($2\tau_R \sim N$, Eq. (3.20)) govern the magnitude and time scale of the "early-time" extensional behavior ($\lambda_{max} = a_{I,early}/b_k$, for $t \leq 2\tau_R$), whereas distribution of midblock conformations ($C = \tilde{C}(x_f, x_b + x_k)$) and number of tube segments per retracting arm ($\tau_{late} \sim \exp(Z_a)$, Eq. (3.21)) dictate the extensional behavior at "late" times ($\lambda_{max} = a_{I,late}/b_k$, for $t > \tau_{late}$). By exploiting matrix dilution and arm retraction dynamics, block polymer systems can be designed that meet the desired linear and nonlinear extensional properties. For example, a precise control over the network architecture could be achieved by

blending an A–B–C triblock terpolymer with an A–B diblock copolymer. Strong, unfavorable segment-segment interactions (e.g. $\chi_{AB}, \chi_{AC} > 0.1$) coupled with equilibrium self-assembly in the strong segregation regime would result in $x_b = 1$ ($x_l = x_f = 0$) for the triblock[233,234], whereas the entangled B tails of the diblock would provide the elastomeric network with retracting arms of known concentration. Varying the length and concentration of the B tails would then control the star-like relaxation as discussed in §3.3.4.IV-d.

The analysis of the linear elastic behavior outlined by Eqs. (3.32), (3.37), and (3.44) has been developed for an undiluted TPE of the A–B–A type, but the approach itself is more flexible in principle and potential uses extend well beyond what is covered here. Suitably modified, a similar set of equations can model the linear elastic behavior (for $T < T_{g,A}, T_{ODT}$) of multiblocks, as well as block polymer solutions and blends[ww]. In the more general case, Eq. (3.44) should contain the potential contribution of the microstructure, $E_{eq,cubic}$. Indeed, morphologies with three-dimensional translational order (e.g. spheres on a body centered cubic lattice, or gyroid) can exhibit, being isotropic, a low-frequency plateau in the storage modulus.[101,109,136,163,164,179,235-242] This additional, elastic plateau has been experimentally measured in $(A–B)_n$ systems (with $n \geq 1$) both in bulk[101,109] and in concentrated solutions in selective solvents (good to B but nonsolvent to A)[136,163,164,179,235-

[ww] Preliminary results show that Eq. (3.44), modified to account for binary mixture and microstructure contribution (Eq. (3.61)), qualitatively describes the linear elastic behavior of L–I–L/I–L blends prepared and tested in our laboratory[116].

[242]. Its origin is entropic and described by the same thermodynamics governing the selection of microdomain shape and size (§3.1.2).[xx] The value of $E_{\text{eq,cubic}}$ can be expressed in dimensionless form as:

$$\begin{aligned}\tilde{E}_{\text{cubic}} &\equiv \frac{E_{\text{eq,cubic}}}{\nu \cdot kT} \\ &= 3 \cdot \Im\end{aligned} \tag{3.61}$$

where ν is the number density of block copolymer molecules, and $\Im$ is the contribution to the shear modulus per molecule and in units of kT. For a variety of A–B melts tested above the glass transition of the higher T_g block and below the ODT, Kossuth et al.[101] related $\Im$ to molecular parameters (such as the characteristic domain spacing d, §3.1.2) and found that:

$$\Im \simeq 0.1\left(\tilde{V}_{\text{AB}}\right)^{-0.2} \tag{3.62}$$

where $\tilde{V}_{\text{AB}}$ is the diblock molar volume in m^3/mol. Based on the weak power-law correlation of Eq. (3.62), $\Im$ is equal to just a few tenths of a kT per molecule. In both

---

[xx] As discussed in the Introduction (§3.1.2), microphase-segregation is driven by the need to minimize energetically unfavorable A/B interactions (i.e. contact enthalpy). When A and B blocks segregate, the overlapping B chains (in bulk or concentrated solutions) are also required to maintain a uniform density distribution in the matrix so as to decrease their osmotic free energy ("osmotic constraint"[237]). Being tethered on A/B interfaces, the B chains satisfy this requirement by assuming mutually correlated, distorted conformations. The consequential stretching energy (i.e. loss in conformational entropy) is minimized when microdomains are regularly arranged in space to form a lattice (short-range order). Any small, but finite strain tends to alter the local density distribution of B chains in the matrix. Therefore, further reduction of the conformational entropy of the B chains stabilizes the lattice against small deformations, and the material exhibits a low-frequency plateau in the storage modulus.[136,179,235-237]

entangled and unentangled A–B systems that spanned a wide range of molar volumes, Kossuth et al.[101] found $\mathfrak{I}$ to be relatively insensitive to the presence of a small density of crystal defects and to lie within a range 0.1–0.3. The results of Watanabe and co-workers on concentrated A–B solutions in selective solvents agree with Eq. (3.62) at temperatures above both T_g's[240], and indicate an increase in $\mathfrak{I}$ (up to three times, compared to the value predicted by Eq. (3.62)) when one of the blocks is glassy[136,163,164,239]. Eq. (3.62) also applies to compositionally symmetric A–B–A systems, which can be viewed as the coupling product of A–B/2 diblocks of half the molar mass. Whereas A–B–A and A–B/2 share the same microdomain shape and nearly identical d[243-245], their cubic plateau moduli are approximately related by[109] $E^{ABA}_{eq,cubic} \simeq 0.5E^{AB}_{eq,cubic}$. Since $\nu_{ABA} = 0.5\nu_{AB}$, Eq. (3.61) implies $\mathfrak{I}_{ABA} \simeq \mathfrak{I}_{AB}$. When present, the contribution of the microstructure (Eq. (3.61)) is nevertheless negligible compared to the endlink (Eq. (3.45)) and entanglement (Eq. (3.46)) contributions.

Alternative reason for slow dynamics: The arm retraction dynamics discussed in §3.3.4.IV-d could in principle stem from diblock impurities originating from incomplete coupling reaction.[yy] Although their presence was not revealed by SEC (§3.3.1 and Appendix A), diblock chains would relax in a star-like fashion. This alternative hypothesis would explain the measured low-frequency behavior while also being consistent with the strong segregation strength of the system.

[yy] Or from single-free-end-type midblocks with short PLA blocks due to polydispersity (as predicted, for instance, by the Schulz–Zimm distribution).

3.4 Conclusions

Block copolymers represent the major class of thermoplastic elastomers (TPEs). In this class, linear triblock and multiblock copolymers of the A–B–A and $(A–B)_n$ type (with $n \geq 2$) are the most common molecular architectures[91-93] (§3.1.1). At temperatures relevant for end-use applications ($T_{g,B} < T < T_{g,A}$), the B block ends are tightly anchored on rigid A domains and these materials behave similarly to filled (and often entangled) B-rich rubbers[92,110,114]. Therefore, their linear viscoelastic response is dominated by chain mobility of the B block rather than by the degree and perfection of microstructural order (both short- and long-range) (§3.1.2).

As a first step towards understanding the rheological response of more complex TPE-based systems (in either bulk or solution), we set out to investigate the linear behavior of an undiluted A–B–A thermoplastic elastomer at service temperatures ($T_{g,B} < T < T_{g,A}$). The material in this study was a monodisperse, entirely degradable, compositionally symmetric ($f_A = 0.25$, at 25 °C), conformationally asymmetric ($\hat{b}_A / \hat{b}_B = 1.3$, at 25 °C), microphase-segregated ($T_{ODT,SCFT} \simeq 290$ °C) triblock copolymer (§3.3.1). Despite the strong driving force towards segregation ($\chi\hat{N} \simeq 436$, at 25 °C), sample preparation and the inherent slow diffusivity of the long B blocks hindered the attainment of an equilibrium morphological state, thereby creating a kinetically trapped (metastable) microstructure with irregularly shaped A microdomains lacking periodicity and long-range order (§3.3.1, Appendix A). Our goal was to connect the chemical and topological structure of the material with its viscoelastic properties in the linear regime. The analysis

herein is independent from the specific choice of the constituent A and B blocks, and relevant at large deformations as well (§3.1.3 and §3.3.4.IV-e).

The linear response was measured in small-amplitude oscillatory (uniaxial) extension (§3.2.2). Testing specimens displaying a similar orientation of microdomains were prepared by compression molding, to investigate rheological properties of the triblock copolymer under practical conditions[92,93]. The integrity of pressed and tested samples was confirmed by size exclusion chromatography (§3.2.3). DSC results and isochronal measurements (§3.3.1, §3.3.4.II, and Appendix A) suggested the presence of unsegregated endblocks embedded in the B-rich matrix, and nearly pure A microdomains.

Characteristic length scales and tube model parameters were calculated for the unperturbed and undiluted A and B blocks (§3.3.2), based on freely-jointed chain models[21-23,34-36,38,41-46,122] (§3.3.2.II), literature data of real bond lengths and angles[3,64,65] (§3.3.2.I), measurements of unperturbed coil sizes via small-angle neutron scattering[20,39,40] (§3.3.2.II) and shear plateau moduli[4,17,20] (§3.3.2.III), and the packing model for linear flexible polymers[12-20,67] (§3.3.2.III, §3.3.3). In this context, we considered two rules of thumb that have been put forward directly (by Ferry[42]) and indirectly (by Dealy and Larson[36]) related to the number of monomers and backbone bonds per Gaussian subchain[47] (§3.3.2.II). We also estimated the parameters of the Gaussian B submolecules based on the statistics of the (Kratky–Porod) worm-like chain model[58] (§3.3.2.II).

Considered in their respective melts[4,17,20,39,40] (§3.3.2.III), both the A and the B blocks were entangled[18,20] ($M_n/M_C \approx 1.4$ and 4), although to a different degree ($Z \approx 3.7$ and 9.8).

Any potential and spontaneous change of the microstructure towards a lower free energy state had only a minor impact (if any) on the measured viscoelastic properties of our triblock (§3.3.4.I). In isochronal measurements, microphase-segregation was manifested in the appearance of two separate glass transitions stemming from the B-rich matrix and the embedded A domains. Temperature values were assigned based on the locus of the loss modulus peak, yielding $T_{g,B} = -61.1$ °C and $T_{g,A} = 53.6$ °C (§3.3.4.II, Appendix A).

The role of the thermo-reversible physical endlinks (i.e. A microdomains) on the entangled rubbery B network was examined. The material exhibited thermo-rheological complexity near and below $T_{g,A}$ (§3.3.4.III-a). We attributed this behavior to the softening of A microdomains, which would partially release the tethering constraint on the B block ends at the corresponding A/B interfaces. This hypothesis is in harmony with the theoretical treatment of thermo-rheological complexity for two-phase materials developed by Tschoegl and co-workers[127-129], and with literature studies on poly(styrene–*b*–isoprene–*b*–styrene) (S–I–S) systems[112,135-137] (§3.3.4.III-a). In a limited range of temperature ($T_{g,B} < T \ll T_{g,A}$) and frequency ($\omega < 1/\tau_0$), the B-rich matrix dominated the shift behavior of the triblock[127] and exhibited thermo-rheological simplicity[42,131-133] (§3.3.4.III). Under these conditions, all contributions to the measured viscoelastic properties involved a single monomeric friction coefficient, ζ_0, which represented the

average drag force per B monomer per unit velocity encountered by a B Gaussian submolecule moving through its free-draining surroundings[42] (§3.3.4.III). The temperature dependence of the horizontal (time-scale) shift factor a_T could be successfully described by the WLF equation[138] (§3.3.4.III-b) at all four reference temperatures (–50, –40, –20, and 0 °C). From the measured shift behavior, WLF parameters referenced to $T_{g,B}$ were calculated (including the Vogel temperature[144] T_∞, the fractional free volume[42,138] f_g/B, and the free volume thermal expansion coefficient[42,138] α_f/B), and compared with literature values[134,139,147] for undiluted B homopolymers (§3.3.4.III-c). When the magnitude of the steepness index[146] was taken into account (i.e. analogous breadth of the viscoelastic spectrum near T_g), the shift behavior of our triblock was analogous to the behavior measured for pure B melts. This result collides with the early findings of Fesko and Tschoegl[128] (on a different triblock copolymer), and suggests that perhaps significantly different steepness indices were involved in their comparison (§3.3.4.III-c). Our analysis showed that the glassy A microdomains did not alter the temperature (hence, time) dependence of the relaxation mechanisms involving portions of B chains at length scales < a (i.e. the B tube SSL).

Using the nonlinear regression with regularization (NLREG) technique developed by Honerkamp and Weese[152] in 1993, we calculated the continuous relaxation spectrum (moduli distribution)[150] $H_E(\tau)$ from the time-temperature superposed dynamic moduli at 0 °C (§3.3.4.IV-a). The computation of $H_E(\tau)$ allowed us to investigate the A–B–A dynamics over a wide range of time scales (15 decades). Qualitatively, the frequency

dependence of the dynamic moduli was reminiscent of the behavior of very lightly crosslinked rubbers (e.g. vulcanized styrene–butadiene random copolymer (SBR)) containing entangled dangling structures[42] (§3.3.4.IV-b). The shape of $H_E(\tau)$ (somewhat analogous to that of $E''(1/\tau)$) was compatible with a concentration of dissipative processes on a time scale of order 10^4 s. However, a secondary peak in $\tan\delta(\omega)$ was not observed, and the monotonic decrease of $\tan\delta(\omega)$ was indicative of a slowly-approaching (pseudo) equilibrium state most commonly observed in lightly crosslinked systems without untrapped entanglements[155,156] (§3.3.4.IV-b). Furthermore, relaxation of the A/B interface[126-129] was completely masked (if present at all, in the low-frequency region) by the relaxation of the matrix (§3.3.4.IV-b).

We developed a procedure to extract the matrix monomeric friction coefficient ζ_0 from the linear response behavior in the rubber-glass transition region, based on calculated extensional relaxation spectrum and the Rouse–Bueche theory[47,85,86] for unentangled melts (§3.3.4.IV-c). Our method, applicable to filled systems such as TPEs of the A–B–A type, builds upon the procedure proposed by Ferry and co-workers[42] for entangled and unfilled polymer melts, and it is linked to the characteristic parameters of the Gaussian submolecules (§3.3.4.IV-c). The length scale σ, which defines the Gaussian submolecule[47], is of particular importance in polymer physics being relevant to both unentangled and entangled macromolecules. The calculated parameters of the Gaussian submolecules were in good agreement with estimates based on the (Kratky–Porod) worm-like chain model[58] (§3.3.4.IV-c). The value of ζ_0 was consistent with the

viscoelastic monomeric friction coefficient of two undiluted B homopolymers[42,139,158] measured from dynamic mechanical data in the rubber-glass transition zone. This represented additional evidence that the local segmental dynamics was unaffected by the presence of the glassy A domains, and seems to validate the proposed method for calculating ζ_0 in filled systems (§3.3.4.IV-c).

Knowledge of ζ_0 allowed us to determine characteristic time and length scales, and to identify the relevant dynamics at play, thereby connecting the measured viscoelastic response to the chemical and topological structure of the network (§3.3.4.IV-d). It was possible to discriminate the peculiar features of five leading dynamics: linear enthalpic elasticity[22,23,42] (for $t \ll \tau_0 \simeq 7$ ns, $x \ll b \simeq 0.6$ nm), semi-flexible chain dynamics[22] (within the range $\tau_0 < t < \tau_L \simeq 5$ μs, $b < x < 5^{1/4} \cdot \sigma \simeq 3.2$ nm), 3-D Rouse-like motions[47,85,86] (for $\tau_L \leq t < \tau_e \simeq 0.08$ ms, $5^{1/4} \cdot \sigma \leq x < a \simeq 5.5$ nm), 1-D Rouse-like motions[36,44-46,88,89,167] or local reptation[166] (for $\tau_e \leq t \leq 2\tau_R \simeq 7.6$ ms, $a \leq x \leq (a \cdot R/2)^{1/2} \simeq 6.9$ nm), and arm retraction dynamics[46,168,169] (for $2\tau_R < t \leq \tau_{late} \simeq 1.9 \cdot 10^4$ s, $(a \cdot R/2)^{1/2} < x \leq R \simeq 17.1$ nm). On time scales shorter than the entanglement time τ_e, stress relaxation was unaltered by the network structure of the material and followed the same dynamics characteristic of an unentangled B melt. For $t \geq \tau_e$, the dynamics was ruled by large-scale molecular architecture (§3.3.4.IV-d). 1-D Rouse-like motions shuttling monomers across tube segments ("chain unit sharing"[45]) governed the triblock stress relaxation for $\tau_e \leq t \leq 2\tau_R$. Stress relaxation beyond the path equilibration time $2\tau_R$ was attributed to star-like motion of entangled dangling structures ($x_{f,1}$), formed either by single-free-end-type

midblocks or diblock impurities. The measured low-frequency behavior was qualitatively[168,174,175] (§3.3.4.IV-d) and quantitatively[35,45,168,174,175,203] (§3.3.4.IV-d-e) compatible with dynamically undiluted[172,173] arm retraction dynamics (possibly delayed by the microstructure[176-182]). This finding is in line with the behavior of polymer networks with entangled dangling structures[185,186] and, to the best of our knowledge, represents the first compelling evidence of star-like relaxation in pure A–B–A triblocks. The analysis of the dynamics explained, qualitatively, how stress was relaxed as a function of the reduced frequency.

We also examined the relaxing stress from a quantitative standpoint, based on the molecular picture illustrated in Figure 3.5 and the behavior predicted at different length scales by the associated dynamics (§3.3.4.IV-e). In particular, tube models[35,36,41-46,168,169,171-173] and rubber elasticity theories[22,41,42,156,193,194,199,202-209,220,221,223] were used to interpret the linear elastic behavior in the pseudo-equilibrium and plateau regions. The pseudo-equilibrium modulus $E_{eq} \equiv E'(1/\tau_{late})$, the plateau modulus[43-45] $E_N \equiv E'(1/2\tau_R)$, and the entanglement modulus[44] $E_e \equiv E'(1/\tau_e)$ were calculated from the linear elasticity of an equivalent B network, suitably modified to account for the microphase-segregated structure. This allowed us to determine key parameters such as the filler effect $\xi(\omega)$ and aspect ratio δ of the glassy A domains, the Langley trapping factor[41,208] T_e, and the distribution of midblock conformations (§3.3.4.IV-e). In addition, we obtained a simple analytical expression relating T_e with the fraction of entangled (x_f) and unentangled (x_d) dangling structures of the material. The results showed that in our system about half of

the midblock entanglements was made permanent by microphase-segregation ($T_e = 0.53$). The same Langley trapping factor would be obtained for an equivalent chemically endlinked network of high functionality with about 85% fractional conversion of the B groups[229,230] (§3.3.4.IV-e). The majority of midblocks was determined to be either in bridge or knotted-loop conformation ($x_b+x_k \simeq 76\%$), while the remaining represented partially segregated chains ($x_f \simeq 24\%$) corresponding to about a 7% mass fraction of A chains in the B-rich matrix. Estimating the fraction of free-end-type midblocks from thermal analysis[224] yielded a similar result (§3.3.4.IV-e). At (pseudo) mechanical equilibrium, entanglements formed between bridges (or knotted-loops) and free-end-type midblocks disappeared (cf. Figure 3.5). Accordingly, the tube SSL increased by 24% with respect to an undiluted B melt, and each entangled B chain was left, on average, with $Z_{I,eff}(1/\tau_{late}) \simeq 5$ "effective" entanglement strands. In spite of untrapped entanglements, entanglement junctions outnumbered physical endlinks by 5 to 1, and the pseudo-equilibrium modulus E_{eq} was largely dictated by the entanglement network ($E_{eq,ent}/E_{eq} \simeq 84\%$). Each bridge and knotted-loop contributed to E_{eq} about 189 kT because B chains were entangled, and only about 37 kT because B chain ends were tightly anchored to A/B interfaces (§3.3.4.IV-e).

Based on our analysis, matrix dilution and arm retraction dynamics emerge as powerful tools that can tune the ultimate properties[80-84] of triblock- or multiblock-type networks, whereas the contribution of the microstructure (for cubic phases)[101,109,136,163,164,179,235-242] is expected to be negligible compared to the endlink and entanglement contributions.

Chapter 4

Linear Extensional Behavior of A–B–A Thermoplastic Elastomers near $T_{g,A}$: Critical-Gel-Like Response and Fractional Dynamics

At service temperatures ($T_{g,B} < T < T_{g,A}$), A–B–A thermoplastic elastomers (TPEs) behave similarly to filled (and often entangled) B-rich rubbers since B block ends are anchored on rigid A domains. Therefore, their linear viscoelastic response is dominated by chain mobility of the B block rather than by microstructural order. We report on the linear behavior of an undiluted A–B–A TPE subjected to uniaxial extension, at a service temperature approaching the T_g of the endblock where the hard A domains begin to behave as thermo-reversible physical endlinks. The analysis herein is independent from the specific choice of the constituent blocks and thus applies to any microphase-segregated thermoplastic elastomer of the A–B–A type. The material exhibits a critical-gel-like response that we associate with star-like motion of entangled dangling structures formed either by triblock chains having one end residing outside A domains or by diblock impurities, coupled with augmented motional freedom of the B block ends at the B/A interfaces. This critical-gel-like behavior is first analyzed in terms of a power-law distribution of relaxation times (PL) (derived from the wedge distribution), which is equivalent to Chambon–Winter's critical gel model (CGM). A relation between the observed power-law exponent and molecular structure is established. Understanding the measured material parameters inherently leads to fractional calculus and to the concept of

quasi-properties, which are intimately related to the stochastic behavior on a microscopic level. We show that PL, CGM, and the mechanical behavior of a fractional element (FE) are analogous representations of the underlying fractional dynamics. By means of fractional calculus, we model the A–B–A self-similar relaxation over a broad range (12 decades) of timescales. The measured low-frequency behavior, originating from the incipient glass transition of the A domains, is exploited via a sequential application of the fractional Maxwell model (FMM) and the fractional Zener model (FZM). This allows us to estimate the dynamics of the A block glass-rubber transition – outside of the experimental window and in spite of thermo-rheological complexity. The analytical expressions of the FMM and FZM relaxation spectra are derived. In addition, fractional models and fractal networks are discussed in relation to the ordered-structure response in block copolymers, and a convenient (finite) measure of the spread of the FMM terminal dispersion is proposed.

4.1 Introduction

4.1.1 Block Copolymer TPEs *Above* the Glass Transition of the Higher T_g Block

At temperatures above the glass transition of the higher T_g block and below the order-disorder transition (ODT), the free energy penalty in deforming the periodic unit cell makes linear viscoelastic properties of block copolymer thermoplastic elastomers (TPEs) highly sensitive to the underlying state of order (shape and long-range order of microdomains). The hierarchical structure leads to a collective relaxation process that is manifested at length and time scales beyond single-chain dynamics and/or entanglements.[98,105] In macroscopically non-oriented samples, such multimodal and cooperative dynamics results in the absence of a liquid-like terminal regime yielding

extremely slow power-law relaxations in the time ($G(t)$ or $E(t) \sim t^{-\alpha}$) and frequency ($G^*(\omega)$ or $E^*(\omega) \sim (i\omega)^{\alpha}$) domains, with the power-law exponent α dictated by the dimensionality of crystalline order of the microphase ($0 \leq \alpha < 1$). Globally isotropic lamellar phases ($\alpha \approx 1/2$) have been the subject of early experimental[103,105,246] and theoretical investigations[104,106]. Later experimental studies associated $\alpha \approx 1/3$ and $\alpha \approx 0$ with macroscopically isotropic hexagonal phases[108,109] and defect-free cubic phases[101,107], respectively.

4.1.2 Block Copolymer TPEs *Below* the Glass Transition of the Higher T_g Block

A much broader power-law viscoelastic response (larger correlation length) is displayed by commercial block copolymer TPEs at temperatures relevant for end-use applications (i.e. below the glass transition of the hard phase), albeit apparently less dependent on the equilibrium morphological state of the microphase. Attaining short- and long-range order relies on ordering kinetics[247] and it is influenced by sample preparation (e.g. extrusion vs. solvent casting), thermal and mechanical history, as well as by blocks length, polydispersity[93,248-250] and topological constraints (entanglements)[101]. Not surprisingly, the morphology is not very well defined in industrially produced A–B–A TPEs, which are far from equilibrium[93] and may contain non-negligible amounts of diblock contaminant (often on the order of ≈ 20 wt% and half the length of the corresponding triblock).

Perhaps the most familiar examples of commercial TPEs are the linear triblock copolymers of the form poly(styrene–*b*–elastomer–*b*–styrene) (S–elastomer–S), in which the styrenic content is usually in the range[100,113] 15–30 wt% and consequently the hexagonal-packed cylinder phase is the most prevalent morphology. These commercially available styrene-diene-based TPE materials frequently exhibit power-law behavior when their viscoelastic response is measured at temperatures where the hard phase is in a glassy state. Examples include the work of Bard and Chung[110] on poly(styrene–*b*–butadiene–*b*–styrene) (S–B–S) (Kraton® D1101, 25–30 wt% S), with samples prepared by solvent casting and tested at 29 °C in extensional stress relaxation ($E(t) \sim t^{-\alpha}$); the study of Daniel and Hamley[111] on sphere- and cylinder-forming poly(styrene–*b*–ethylene–*co*–butylene–*b*–styrene) (S–EB–S) (Kraton® G1657 13 v% S, and G1650 29 v% S), with samples (oriented and non-oriented) prepared by pressure molding followed by channel die compression and tested at 22 °C in small-amplitude oscillatory extension ($E'(\omega) \sim \omega^{\alpha}$); and the results of Hotta et al.[112] on cylinder-forming poly(styrene–*b*–isoprene–*b*–styrene) (S–I–S) (Aldrich Chemical Corp., 17 wt% S), with samples prepared by pressure molding and tested at $T \leq 30$ °C in nonlinear extensional stress relaxation ($E(t,\varepsilon) \sim t^{-\alpha}$). A power-law behavior was also observed by Roos and Creton[113], for a sphere-forming S–I–S triblock (Vector® 4100 D, 15 wt% S) with samples prepared by solvent casting and tested at 22 °C in small-amplitude oscillatory shear ($G'(\omega) \sim \omega^{\alpha}$). Interestingly, of the above authors only Daniel and Hamley[111] and Hotta et al.[112] explicitly acknowledged the

appearance of a power-law response. None of these studies, however, attempted to explain the value of the power-law exponent α based on molecular structure.

The fact that different commercial A–B–A systems display a similar behavior below the T_g of A, regardless of block type and length (hence, state of segregation χN), microphase geometry and crystalline order (cylinders vs. spheres), presence of diblock impurities ($\approx$ 15 wt% in Kraton® D1101, $\approx$ 30 wt% in Kraton® G1657), sample preparation method (solvent casting vs. pressure molding) and processing history (macroscopically oriented vs. non-oriented samples), seems to indicate that the degree and perfection of structural order (both short- and long-range) are not the main factors in determining the viscoelastic response of block copolymer TPEs at service temperatures ($T_{g,B} < T < T_{g,A}$). Because of the nature of the physical endlinks (hard phase domains) and likelihood of partial segregation (stemming from either lack of thermodynamic equilibrium or equilibrium self-assembly in the intermediate segregation regime[98], i.e. $\chi N < \approx 100$), such systems may be regarded to as filled elastomeric networks[92,110,114] (cf. Chapter 3, §3.3.4.IV-e, and Appendix A, §A.2.3.I-b) with entangled dangling structures (cf. Chapter 3, §3.3.4.IV-b-d-e and Figure 3.5), and their power-law viscoelastic response can be assigned a more universal character.

4.1.3 The Ubiquity of Self-Similar Dynamics

Slow relaxation processes evolving in an algebraic fashion ($\sim t^{-\alpha}$ or $\sim \omega^{\alpha}$, where α plays the role of a fractal dimension in the time or frequency domain) are often the signature of

multimodal and cooperative dynamics, marked by multiple trapping events and lack of a characteristic relaxation time[a], i.e. broad distributions (Appendix F, §F.3.5).[251,252] Power-law relaxation patterns are an expression of *mechanical self-similarity*, i.e. the relaxation is the same at all scales of observations. In analogy with geometrical self-similarity[253-258], self-similar dynamics is often called "*scale invariant*", "*scale free*", "*fractal*", or "*fractional*" (Appendix F, §F.3).[251,252,259-261] Indeed, the mathematical description of self-similar dynamics naturally leads to the so-called *fractional calculus* (Appendix F, §F.2–3).

Self-similar dynamics, characterized by power-law relaxations coupled with subdiffusive behavior[252,260-263] (Appendix F, §F.3), is the hallmark of complex systems composed of a large diversity of elementary units interacting on a wide range of length and time scales[264,265], and materials that are far from thermodynamic equilibrium[266].

Within the realm of polymer science, Rouse dynamics[47] and local reptation (i.e. Rouse motion of a chain confined to a tube)[46,89,166] are well-known examples of power-law relaxation and subdiffusive behavior (Chapter 3, §3.3.4.IV-d). Furthermore, self-similar dynamics has been observed in numerous systems, including homopolymers undergoing the glass-rubber transition[267,268], linear entangled homopolymers (both polydisperse[269] and monodisperse[270,271]), branched polymers with star-, H-, or comb-like topologies[44,272-279],

---

[a] While average relaxation times (in the classical sense) diverge, finite characteristic timescales can be identified in the framework of fractional mechanical models (§4.3.2.III).

ring polymers[280], polymer blends[276,281-284], crosslinked[155] and uncrosslinked[285,286] rubbers, polymer fractals[287,288], and chemical gels at the gel point[289-294] (Appendix E, §E.3.1). In the class of physical gels, microphase-segregated block copolymers represent one of many examples of macromolecules exhibiting self-similar dynamics. Other systems include filled polymers[295,296], associating polymers[275,297,298], crystallizing polymers[299], foams[300], liquid crystalline polymers[301], microgel dispersions[302,303], soft glassy materials[304,305], suspensions[306,307], and chewing gum[308] (Chapter 6).

Being the result of long-range spatial or temporal correlations, self-similar dynamics is not even a prerogative of polymeric materials. Rocks, metals, inorganic glasses[309-311], and proteins[310,312] have been found to exhibit power-law relaxations. In fact, self-similar dynamics has been predicted and observed in various disciplines including physics, chemistry, engineering, geology, biology, economy, meteorology, astrophysics and others.[252,263]

4.1.4 Goals of This Study

We investigate the linear uniaxial extensional behavior of an undiluted A–B–A thermoplastic elastomer at a service temperature ($T_{g,B} < T < T_{g,A}$) approaching the T_g of the endblock, where the hard A domains begin to behave as thermo-reversible physical endlinks (§4.3.1 and §4.3.2.I). By contrast, the linear behavior of A–B–A with glassy A domains was examined in Chapter 3. Similarly to the analysis presented in Chapter 3, the

analysis herein is independent from the specific choice of the constituent blocks and thus applies to any microphase-segregated thermoplastic elastomer of the A–B–A type.

The collective microdomain dynamics responsible for a broad power-law viscoelastic behavior, originating from the star-like motion of single-free-end-type midblocks or diblock impurities coupled with augmented motional freedom of the B block ends at the B/A interfaces, will be first analyzed in terms of a power-law distribution of relaxation times (PL) derived from the wedge distribution (§4.3.2.II). This is tantamount to using Chambon–Winter's critical gel model (CGM). In an effort to advance the current understanding of block copolymer self-similar dynamics, a relation between the observed power-law exponent and molecular structure will be established (§4.3.2.II-c). Interpreting the measured material parameters will naturally lead to fractional calculus and to the concept of quasi-properties, which are intimately connected to the stochastic behavior on a microscopic level (§4.3.2.II-d). We will show that PL, CGM, and the mechanical behavior of a fractional element (FE) are analogous representations of the underlying fractional dynamics (§4.3.2.II-d).

Fractional calculus will then be applied to model the A–B–A dynamics over a wide range of time scales (§4.3.2.III). In particular, the measured low-frequency behavior will be exploited via a sequential application of the fractional Maxwell model (FMM) and the fractional Zener model (FZM). This will allow us to estimate the dynamics of the A block glass-rubber transition (§4.3.2.III-b), which lies outside of the experimental window and cannot be accessed via time-temperature superposition (§4.3.2.I). The analytical

expressions of the FMM and FZM stress response functions and relaxation spectra will be derived (§4.3.2.III-a-b). In addition, fractional models and fractal networks will be discussed in relation to the ordered-structure response in block copolymers, and a convenient (finite) measure of the spread of the FMM terminal dispersion will be proposed (§4.3.2.III-a).

4.2 Experimental Section

4.2.1 Material

The thermoplastic elastomer used in this study is an undiluted linear poly(D,L-lactide–*b*–isoprene–*b*–D,L-lactide) (L–I–L) triblock copolymer with number-average molar mass M_n = 73100 g/mol and containing 32% by mass poly(D,L-lactide) (PLA). Configurational repeating units and molecular characteristics of the material, hereafter referred to as LIL50–12, are displayed in Figure 3.1 and Table 3.1 of Chapter 3. Here, we briefly review the main features of the triblock that are pertinent to this study and refer the reader to Chapter 3 (§3.3.1, §3.3.2.III, §3.3.4.I-II, and §3.3.4.IV-d-e) for the related discussion. Synthesis, molecular and morphological characterization, as well as differential scanning calorimetry (DSC) and isochronal viscoelastic measurements are presented and discussed in Appendix A.

LIL50–12 is a monodisperse, entirely degradable, compositionally symmetric (f_L = 0.25, at 25 °C), conformationally asymmetric ($\hat{b}_L / \hat{b}_I = 1.3$, at 25 °C), microphase-segregated ($T_{ODT,SCFT} \simeq 290$ °C) triblock copolymer. Considered in their respective melts,

both the PLA and the PI blocks are entangled ($M_n/M_C \approx 1.4$ and 4), although to a different degree ($Z \approx 3.7$ and 9.8). Despite the strong driving force towards segregation ($\chi\hat{N} \simeq 436$, at 25 °C), sample preparation and the inherent slow diffusivity of the long PI blocks hindered the attainment of an equilibrium morphological state, thereby creating a kinetically trapped (metastable) microstructure with irregularly shaped PLA microdomains lacking periodicity and long-range order. Any potential and spontaneous change of the microstructure towards a lower free energy state had only a minor impact (if any) on the measured viscoelastic properties of our triblock.

Upon thermal analysis (i.e. DSC and isochronal viscoelastic measurements), microphase-segregation was manifested in the appearance of two separate glass transitions stemming from the PI-rich matrix and the embedded PLA domains. Temperature values were assigned based on the locus of the loss modulus peak, yielding $T_{g,I}$ = –61.1 °C and $T_{g,L}$ = 53.6 °C. Closer inspection of DSC results and isochronal measurements suggested the presence of unsegregated endblocks embedded in the PI-rich matrix, and nearly pure PLA microdomains. This would necessarily give rise to untrapped entanglements and a slow relaxation mechanism similar to the arm retraction of star polymers. We therefore tested this hypothesis by analyzing the low-frequency behavior of LIL50–12 at temperatures well below the glass transition of the PLA domains. Stress relaxation beyond the path equilibration time, $2\tau_R$, was found to be qualitatively and quantitatively compatible with star-like motion of single-free-end-type midblocks, i.e. the entangled dangling structures originating from the fraction $x_{f,l}$ of

triblock chains having one end residing outside PLA domains. By employing tube models and rubber elasticity theories, suitably modified to account for the microphase-segregated structure, we modeled the linear elastic behavior in the pseudo-equilibrium and plateau regions. In so doing, the majority of midblocks was determined to be either in bridge (x_b) or knotted-loop (x_k) conformation, $x_b+x_k \simeq 76\%$, while the remaining represented partially segregated chains, $x_f \simeq 24\%$, corresponding to a mass fraction of PLA chains residing in the PI-rich matrix $w_L^{matrix} \simeq 7\%$.

In conditions of slow ordering kinetics, small deformations, and $T < T_{g,L}$, the distribution of midblock conformations may remain approximately constant (for the experimental time scale) and equal to the distribution established when the network was formed. The results of Chapter 3, obtained from measurements at 0 °C, are therefore relevant to this study as well.

4.2.2 Experiments and Testing Specimens

Linear viscoelastic properties of LIL50–12 were measured using a TA Instruments RSA-G2 solids analyzer equipped with a film/fiber geometry clamp. The rheological behavior was tested at 37 °C in small-amplitude oscillatory (uniaxial) extension, and the results presented in the next sections are representative of data acquired on at least 5 fresh samples at the same experimental condition. The resulting error bars in Figures 4.1 (for $\varepsilon_0 \geq 3 \cdot 10^{-3}$), 4.2(a), 4.5(a), and 4.7(a) are, for the dynamic moduli, smaller than or equal to the data point markers. The integrity of pressed and tested samples was confirmed by size

exclusion chromatography (SEC). Experimental details and sample preparation method are discussed in Chapter 3, §3.2.2 and §3.2.3.

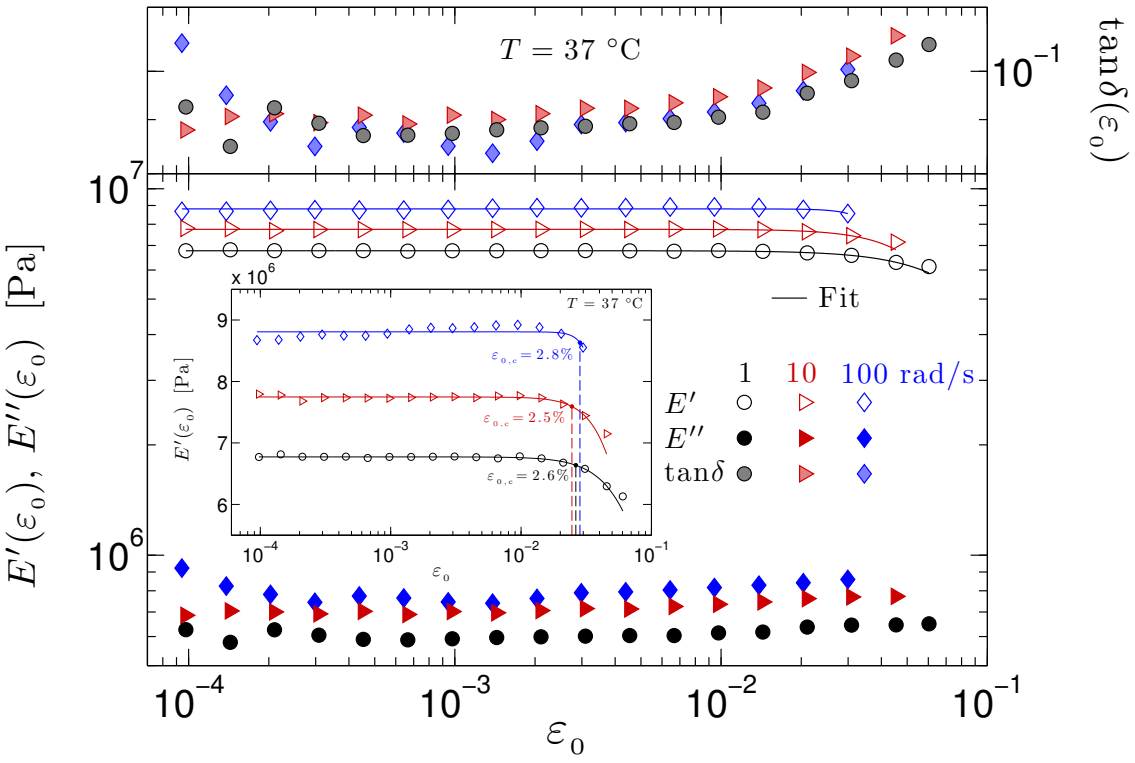

Figure 4.1. Representative data of isochronal strain sweep experiments performed on LIL50–12 at 37 °C and three angular frequencies: (○) 1 rad/s, (▷) 10 rad/s, and (◇) 100 rad/s. The solid lines depict least-squares regressions to the Cole–Cole[313] matching function, Eq. (4.1). The inset shows $E'(\varepsilon_0)$ vs. ε_0 on a semi-log plot, and critical strains determined by a 2.5% offset from the plateau values (cf. Figure 5.6).

4.3 Results and Discussion

4.3.1 Limit of Linear Response

Representative isochronal strain sweeps conducted (on freshly prepared samples) at a temperature T = 37 °C are shown in Figure 4.1. The experimental data of the storage modulus ($E'(\varepsilon_0)$) were used to perform nonlinear least-squares fits to the Cole–Cole[313] matching function[b]

$$y(x) = y_0 \frac{1}{1+\left(x/x_0\right)^c} \qquad \text{with } c > 0 \tag{4.1}$$

and critical strains were determined by a 2.5% offset from the plateau values. The monotone non-increasing fitting model (Eq. (4.1)) can be derived from the kernel function of the canonical representation of the storage compliance[150] (Appendix D, Eq. (D.94)b), and was chosen due to its extensive use in the literature on linear viscoelastic[314] and dielectric[313] behavior. Asymptotically ($x \to \infty$), the Cole–Cole model approaches the inverse power-law equation introduced in 1921 by Nutting[315,316] (Appendix F, Eq. (F.30)) to describe the non-exponential shear creep response observed in many "pitchlike" substances.

---

[b] The parameter x_0 locates the curve along the logarithmic x-axis, while the exponent c broadens its spread. The upper and lower halves of the curve can be superposed by an isometry, thus making the Cole-Cole function geometrically self-congruent.

At this service temperature, LIL50–12 is predominantly elastic with $E'(\varepsilon_0) \simeq 11 \cdot E''(\varepsilon_0)$, and yields at a strain amplitude $\varepsilon_{0,c} \approx 3\%$[c] that is weakly dependent on frequency. If we were to choose a larger deviation from the plateau response, the critical strain would shift to about 4–5% and fall outside the experimental window at high frequencies. The decrease in the storage modulus indicates that the reduced effectiveness of network junctions (possibly associated with slippage of PI entanglements and/or PLA chains pullout from the PLA domains – cf. Chapter 5, §5.3.3.II-d) dominates any potential elastic stiffening (which would result from the finite extensibility of the stretched PI chains – cf. Chapter 5, §5.3.4). The seemingly frequency independence of the critical strain implies that the rate of softening/disruption of network junctions remains constant over the explored frequency window. We return to these observations later by examining the dynamics of the PLA glass-rubber transition at 37 °C (§4.3.2.III-b).

As explained in §3.2.2 of Chapter 3, the maximum strain amplitude in these tests (3–6%) was limited by the finite axial excursion of the drive motor (1.5 mm), so that large amplitude oscillatory extensions could not be explored. Nonetheless, closer inspection of the larger strains regime ($\varepsilon_0 > 1\%$) revealed the same general trend for all the specimens tested, i.e. a monotonic decrease of elasticity ($E'(\varepsilon_0)$) and a (weaker) increase of dissipation ($E''(\varepsilon_0)$, $\tan\delta(\varepsilon_0)$) of the network structure by perturbations entering the

---

[c] At the small elongations typical of the linear regime, true/Hencky (ε) and nominal/engineering (ε_N) strains are equivalent: $\varepsilon \equiv \ln(L/L_0) = \ln(\varepsilon_N + 1) \simeq \varepsilon_N$, for $\varepsilon_N \ll 1$, where L and L_0 stand for the deformed and undeformed length, respectively (cf. footnote [f]).

nonlinear regime. This strain-dependent response appears to be reminiscent of the behavior of many yielding materials (including diblock melts forming cubic phases) in large amplitude oscillatory shear (LAOS), where a monotonically decreasing storage modulus $G'(\gamma_0)$ is accompanied by an initially-increasing loss modulus $G''(\gamma_0)$ that later displays a local maximum.[101,317]

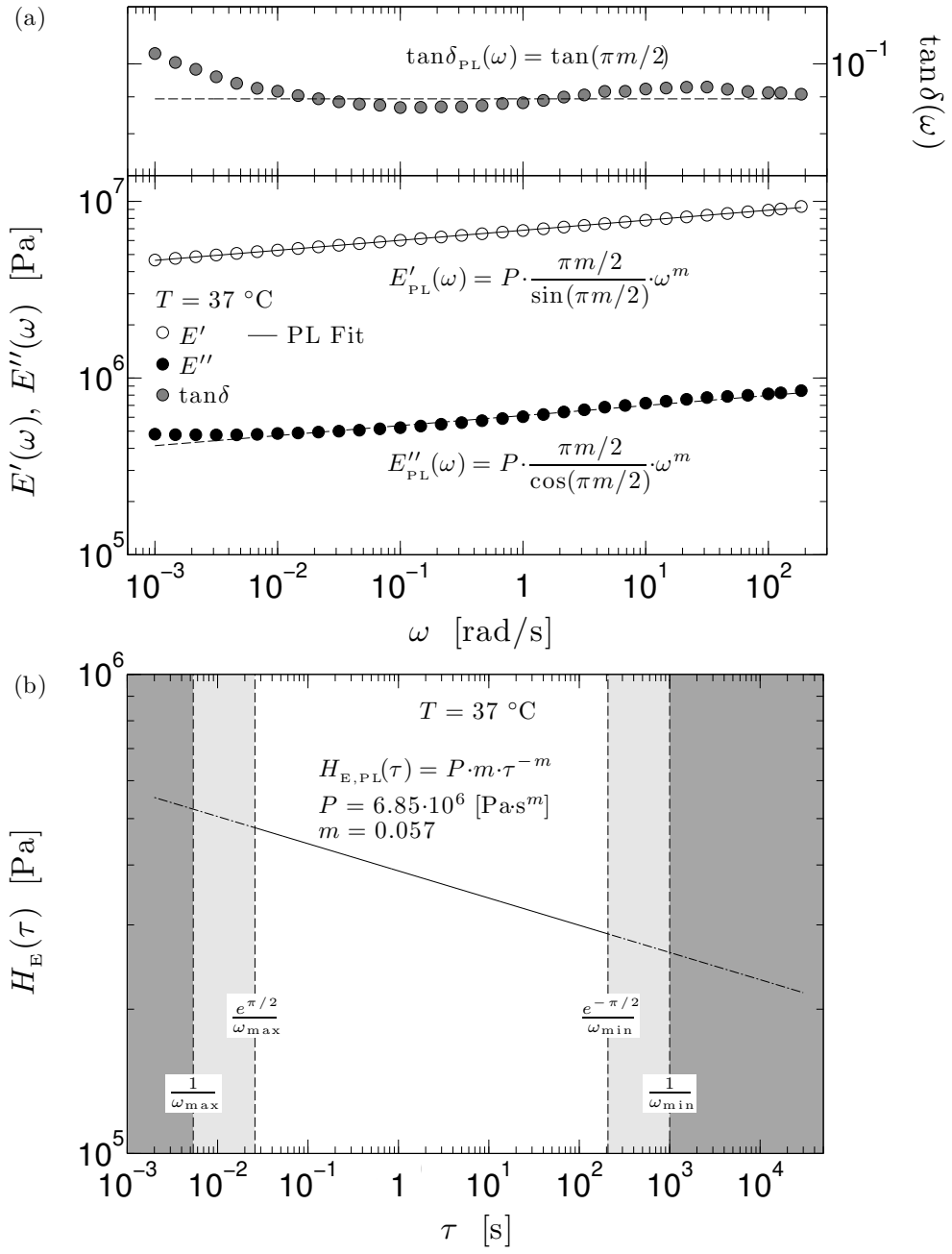

Figure 4.2. (a) Storage modulus, $E'(\omega)$, loss modulus, $E''(\omega)$, and loss tangent, $\tan\delta(\omega)$, of LIL50–12 at 37 °C. The solid line depicts the PL fit (Eq. (4.4)a). The dashed lines show the PL prediction of the loss functions (Eqs. (4.4)b and (4.5)). (b) PL relaxation spectrum (Eq. (4.2)).

4.3.2 Viscoelastic Behavior near $T_{g,A}$

We measured the frequency-dependent linear viscoelastic behavior of LIL50–12 at 37 °C in the frequency range 0.001–200 rad/s. Representative data of storage modulus, $E'(\omega)$, loss modulus, $E''(\omega)$, and loss tangent, $\tan\delta(\omega)$, are shown in Figure 4.2(a). Notice that the storage modulus measured at 1 rad/s, about 6.8 MPa (Figure 4.2(a)), coincides with the plateau value deduced from isochronal strain sweeps at the same frequency (Figure 4.1), and it is almost identical to the storage modulus measured in isochronal temperature ramps (E'(37 °C, 1 rad/s) ≃ 6.7 MPa, Figure A.3 of Appendix A). Therefore, the agreement among different tests is satisfactory.

4.3.2.I Thermo-rheological complexity

As discussed in §3.3.4.III-a of Chapter 3, the data shown in Figure 4.2(a) could not be superposed by a simple time-temperature shift to data measured at lower temperatures (Figure 3.4(a)). Applicability of time-temperature superposition (TTS) in its simple form is precluded by the proximity of the testing temperature to the glass transition of the PLA domains, $T_{g,L}$ = 53.6 °C. Thermo-rheological complexity arises from the softening of PLA microdomains, which partially releases the tethering constraint on the I block ends at the corresponding I/L interfaces, thereby inducing the development of a new class (i.e. different ω- and T-dependence) of relaxation mechanisms. This argument is in harmony with the theoretical treatment of thermo-rheological complexity for two-phase materials

developed by Tschoegl and co-workers[127-129], and with literature studies on poly(styrene–*b*–isoprene–*b*–styrene) (S–I–S) systems[112,135-137] (Chapter 3, §3.3.4.III-a).

At 37 °C, and for most of the experimental frequency window (cf. §4.3.2.II-b), neither phase completely dominates the shift behavior of the triblock and therefore the horizontal shift factors are functions of time/frequency in addition to temperature, i.e. $a_T(\omega, T)$.[127] Furthermore, $a_T(\omega, T)$ is different for the storage and the loss components of the harmonic response.[127] As a result, not only are data measured at 37 °C not superimposable – via simple horizontal $a_T(T)$ and vertical $b_T(T)$ shifts – with data obtained at lower temperatures, but simple time-temperature superposition of data at and above 37 °C covering the PLA glass transition fails as well.

In principle, a master curve at 37 °C that extends to frequencies across the PLA glass transition could be constructed according to the theoretical approach of Fesko and Tschoegl[127,128], by taking into account the shift behavior of PLA (above and below its T_g) coupled with the shift behavior of PI. In practice, however, this scheme is hampered by experimental and theoretical restraints. From an experimental standpoint, we are not aware of studies investigating the time-temperature shift behavior of glassy PLA. On the theoretical side, the Fesko–Tschoegl method for generating the time-temperature shift factors $a_T(\omega, T)$ yields equations that cannot be integrated, whose solution must then rely on a model of mechanical coupling of the two phases.[127] For the materials of the Kraton type studied by Fesko and Tschoegl, the experimental additivity of the compliances enabled a series coupling of the two phases to be postulated.[127] In addition, the

contributions of various mechanisms to the mechanical properties could be isolated by decomposition.[128] This included the primary viscoelastic dispersions (due to the glass-rubber transition of the individual phases) and the additional dispersions associated with rearrangements of configurations by "slippage" of untrapped entanglements (i.e. disengagement of entanglements on dangling structures)[42] and with relaxation of the interface (cf. Chapter 3, §3.3.4.IV-b).

For our system, lack of experimental data on the shift behavior of glassy PLA is arguably the main limitation preventing the applicability of Fesko–Tschoegl's theory. In §4.3.2.III, we will show how this problem may be circumvented through a sequential application of simple fractional mechanical models, which will allow us to estimate the PLA glass-rubber dynamics at 37 °C.

4.3.2.II Critical-gel-like response

Throughout the frequency range tested (Figure 4.2(a)), the material exhibits an elastic response ($E'(\omega) \simeq 11 \cdot E''(\omega)$) whose frequency dependence resembles that of a *critical gel* ($E'(\omega)$, $E''(\omega) \sim \omega^m$ – vide infra). As a first step towards understanding the measured viscoelastic behavior, it is thus germane to assume a *power-law relaxation spectrum* (PL) of the form (cf. Appendix E, Tables E.2–3)

$$H_{\mathrm{E,PL}}(\tau) = \begin{cases} E_{\mathrm{PL},0} \cdot m\left(\tau_{\min}\right)^m \tau^{-m} = P \cdot m \cdot \tau^{-m} & \text{for } \tau \in \left[\tau_{\min}, \infty\right) \\ 0 & \text{for } \tau < \tau_{\min} \end{cases} \tag{4.2}$$

where τ_{min} represents the lower time limit of self-similar dynamics, $E_{PL,0}$ is a characteristic modulus associated with τ_{min}, $P = E_{PL,0}\cdot(\tau_{min})^m$ (with dimensions of Pa·s^m) is a *quasi-property*[318] (Appendix F, §F.3.4–5) related to the fractional dynamics of the system (§4.3.2.II-d), and the power-law exponent m is restricted to the open interval (0, 1) (cf. Appendix E, Eq. (E.11), and Appendix F, §F.2.1). We chose the letter P to denote the quasi-property that stems from the power-law relaxation spectrum $H_{E,PL}(\tau)$, to distinguish it from closely-related quasi-properties associated with a single power-law relaxation pattern (vide infra). Notice that the (extensional) *relaxation spectrum* $H_E(\tau)$ represents a continuous distribution of moduli (with dimensions of Pa), while $\hat{Y}(\tau) = H_E(\tau)/\tau$ is the corresponding *distribution of relaxation times* (with dimensions of Pa/s – cf. Appendix D, §D.5, and Table D.1). In Eq. (4.2), it is assumed that τ_{min} is very small compared with the high-frequency region accessed experimentally, i.e. $\omega\tau_{min} \ll 1$, and that the material does not possess an equilibrium modulus, i.e. $E_{eq} = 0$. The *complex modulus* associated with such power-law relaxation spectrum is given by (cf. Appendix D, Eq. (D.34), and Appendix E, Eq. (E.45))

$$E^*_{PL}(\omega) = P\cdot\frac{\pi m}{\sin(\pi m)}\cdot(i\omega)^m \qquad \text{with } 0<m<1 \tag{4.3}$$

Separation of the real and imaginary parts yields (cf. Appendix E, Eq. (E.46))

$$\begin{aligned} E'_{PL}(\omega) &= P\cdot\frac{\pi m/2}{\sin(\pi m/2)}\cdot\omega^m \\ E''_{PL}(\omega) &= P\cdot\frac{\pi m/2}{\cos(\pi m/2)}\cdot\omega^m \end{aligned} \tag{4.4}$$

with (cf. Appendix E, Eq. (E.47))

$$\tan\delta_{\mathrm{PL}}(\omega)=\tan\left(\pi m/2\right) \tag{4.5}$$

Eqs. (4.2)–(4.5) thus introduced originate from the *wedge distribution* (W) *of relaxation times*, $\hat{Y}_{\mathrm{W}}(\tau)=H_{\mathrm{E,W}}(\tau)/\tau$, defined by the relaxation spectrum[150,267] (Appendix E, §E.2)

$$H_{\mathrm{E,W}}(\tau)=\begin{cases}H_{\mathrm{W},0}\cdot\left(\tau/\tau_{\min}\right)^{-m} & \text{for } \tau\in\left[\tau_{\min},\tau_{\max}\right]\\ 0 & \text{elsewhere}\end{cases} \tag{4.6}$$

under the assumptions $\omega\tau_{\min}\ll 1$, $\tau_{\max}\to\infty$, and $E_{\mathrm{eq}}=0$ (Appendix E, §E.3). The wedge relaxation spectrum, Eq. (4.6), was first proposed in 1952 by Tobolsky[267,268] to model the glass-rubber viscoelastic transition of polyisobutylene. One of the main features of the self-similar behavior expressed by Eqs. (4.2) and (4.6) is the lack of a characteristic time scale or, equivalently, the coexistence in a self-similar manner of a great number of internal time scales (cf. footnote [a]).

It is straightforward to show that Eqs. (4.2)–(4.5) are equivalent to *Chambon–Winter's critical gel model* (CGM)[266,289-292,319] describing the linear viscoelastic response of polymers at the gel point. For polymeric materials, the *gel point* marks the transition from liquid-like (i.e. $E_{\mathrm{eq}}=0$ and $\eta_{\mathrm{E},0}<\infty$) to solid-like (i.e. $E_{\mathrm{eq}}>0$ and $\eta_{\mathrm{E},0}\to\infty$) behavior, i.e. it represents a *liquid-solid viscoelastic transition* (LST). As a result, a polymer at the gel point does not yet possess an equilibrium modulus ($E_{\mathrm{eq}}=0$) but already exhibits a divergent longest relaxation time ($\tau_1\to\infty$), hence (cf. Appendix D, Eqs. (D.108), (D.109)a, (D.110), and (D.118)) a divergent steady-state viscosity ($\eta_{\mathrm{E},0}\to\infty$).[320,321] This LST is caused by a growth of *connectivity*, which correlates molecular motion over larger

and larger distances. The spatial extent of this connectivity, i.e. the z-average cluster size R_z, is the *correlation length*.[320,321] At the gel point, the correlation length diverges and so does τ_{max}, i.e. the mechanical behavior is self-similar on all timescales larger than τ_{min}. To some extent, the gel point is thus analogous to the Curie point for appearance of spontaneous magnetization, or to the vapor-liquid critical point in thermodynamics (Appendix F, §F.3.5).[320,321] The definition of gel point in terms of the equilibrium mechanical properties E_{eq} and $\eta_{E,0}$ dates back to the classical mean-field theory of Flory[322-325] and Stockmayer[326,327], developed for chemically crosslinked polymers (*chemical gels*). The term *physical gels* is used when the LST occurs via physical linking. Since a polymer at the gel point is in a *critical state*[320,328,329], the name *critical gel* was proposed by Winter and Vilgis[330,331] to distinguish it from the various materials that are commonly called gels.

In a series of papers[289-292] published between 1985 and 1987, Chambon and Winter investigated the (terminal) linear viscoelastic behavior of chemical gels at the gel point. Rather than assuming a power-law spectrum and deriving the corresponding material response functions accordingly, they hypothesized a power-law complex modulus, $G^*(\omega) \sim (i\omega)^m$, as a means to interpret their experimental data and then applied the Kramers–Kronig relations[332,333] to check for internal consistency. The phenomenological approach adopted by Chambon and Winter gave the relaxation modulus as (cf. Appendix E, Eq. (E.49))

$$E_{CGM}(t) = S \cdot t^{-m} \qquad \text{with } 0 < m < 1 \tag{4.7}$$

where S, with dimensions of Pa·s^m, was called the *gel strength*.[d] Later investigations[293,294,334,335] concluded that $S = E_{eq}(\tau_{min})^m$, where E_{eq} is the equilibrium modulus of the fully crosslinked material[334,335] and $E_{eq}\tau_{min}$ is the steady-state viscosity of the precursor molecule (building block of the chemical gel)[293,294]. Accordingly, a large value of S (i.e. strong gel) is always associated with a small value of m.[266,319] The power-law response functions, Eqs. (4.2)–(4.5), are equivalent to Chambon–Winter's critical gel model with (cf. Appendix E, §E.3.1)

$$P \cdot \Gamma(1+m) = S \tag{4.8}$$

where $\Gamma(m)$ is the complete gamma function defined in Appendix C (§C.1).

By fitting Eq. (4.4)a to the experimental $E'(\omega)$ data, we obtained P = 6.85 MPa·s^m, m = 0.057, and the solid line shown in Figure 4.2(a). Notice that it is not possible, without additional information, to resolve P into the individual components $E_{PL,0}$ and τ_{min}. Furthermore, the fundamental material property that characterizes the observed power-law behavior is the unique quasi-property P, which measures the material response in terms of a single material parameter (cf. §4.3.2.II-d).[336] As a result of Eq. (4.2), all the material response functions of the power-law distribution depend on the quasi-property P and a numerical coefficient containing m and/or its gamma-function-related values (Appendix E, §E.3, Tables E.2–3).

---

[d] Interestingly, a power-law decay for the relaxation modulus had already been proposed in 1965 by Chasset and Thirion[155] to model the long-time relaxation behavior of rubber networks with entangled dangling structures (i.e. lightly crosslinked polymers). Indeed, Eq. (4.7) follows from the Chasset–Thirion[155] equation (Appendix E, Eq. (E.48)) on the assumption that $E_{eq} = 0$.

We then used Eqs. (4.4)b and (4.5) to predict the loss modulus and the loss tangent (respectively) based on the quasi-property P and power-law exponent m found from the fit to the storage modulus. The results are shown by dashed lines in Figure 4.2(a). The relaxation spectrum of the model, $H_{E,PL}(\tau)$, is shown in Figure 4.2(b). $H_{E,PL}(\tau)$ was obtained directly from Eq. (4.2), rather than by deconvolution of Fredholm integral equations involving $E'(\omega)$ and $E''(\omega)$ (Appendix D, Eqs. (D.89)b-c, and Chapter 3, §3.3.4.IV-a) or processes of differentiation of the experimental data (Appendix D, Eq. (D.96)). For completeness, however, dash-dot lines are used in Figure 4.2(b) to indicate regions of relaxation times (shaded areas) where the accuracy of a spectrum inferred from $E'(\omega)$ and $E''(\omega)$ would not be guaranteed. According to the analysis of Davies and Anderssen[153] (presented in Chapter 3, §3.3.4.IV-a), this corresponds to relaxation times outside of the open interval $(e^{\pi/2}/\omega_{max}, e^{-\pi/2}/\omega_{min})$, where $[\omega_{min}, \omega_{max}]$ is the range of frequencies over which experimental data are available (Figure 4.2(b)).

4.3.2.II-a Low-frequency region

Clearly, the power-law distribution of relaxation times is capable of describing most of the viscoelastic response shown in Figure 4.2(a). Slight deviations from the data only occur in the predicted loss functions at the low-frequency end of the experimental window, i.e. for $\omega \leq 10^{-2}$ rad/s. Given the relative magnitude of the moduli ($E'(\omega)/E''(\omega) \simeq 11$), one might be tempted to explain such deviations by an increasing experimental error in the measurement of $E''(\omega)$ with decreasing frequency.[337] To ascertain whether or

not the observed low-frequency behavior was a true material response of LIL50–12, we performed measurements at different strain amplitudes (within the linear regime) on a minimum of 5 fresh samples for each experimental condition. The results invariably showed lack of substantial noise in the raw displacement and axial force signals. The error bars of $E''(\omega)$ in Figure 4.2(a), corresponding to 95% confidence intervals, are enclosed within the data point markers. We therefore attribute the increase in $E''(\omega)$ and $\tan\delta(\omega)$ at low frequencies to the onset of dissipative processes associated with the glass transition of the PLA domains. In this region, the augmented motion at the I/L interfaces couples significantly with arm retraction dynamics of single-free-end-type midblocks. Hence, the description of self-similar behavior through a single power-law relaxation pattern becomes inadequate and a more complex model is required. This will be discussed in §4.3.2.III.

4.3.2.II-b High-frequency region

In §4.3.2.I, we stated that for most of the experimental frequency window in Figure 4.2(a) neither phase completely dominates the shift behavior of the triblock, and therefore the material is thermo-rheologically complex. Nevertheless, the underlying principle of corresponding states still holds that higher-frequency behavior corresponds to lower-temperature properties. Hence, at high enough frequencies, largely outside of the range accessible from experiments, we expect deformation within PLA domains and PLA/PI interfaces to become completely negligible and the shift behavior to be then controlled by

PI alone. In this limit, all relaxation times τ_p and spectral strengths E_p should have the same temperature dependence and the simple TTS should apply (cf. Chapter 3, §3.3.4.III).

To verify this hypothesis we need to prove that, for instance, the storage modulus measured at frequency ω and temperature T = 37 °C can be obtained from a measurement at a lower temperature T_0 through the relation[42]

$$E'(\omega,T) = b_T^{T_0} \cdot E'\left(\omega a_T^{T_0}, T_0\right) \tag{4.9}$$

where $b_T^{T_0} \equiv E_p(T)/E_p(T_0) = \rho T/\rho_0 T_0$ is the vertical (modulus-scale) shift factor[42,134,e], ρ and ρ_0 are the copolymer densities at T and T_0 (respectively), and $a_T^{T_0} \equiv \tau_p(T)/\tau_p(T_0)$ is the horizontal (time-scale) shift factor[42] obeying the Williams–Landel–Ferry (WLF) equation[138] with the parameters determined in Chapter 3 (cf. Figure 3.3, §3.3.4.III-b, and Table 3.5). Let us consider T_0 = 0 °C. Based on the homopolymer densities and triblock composition (cf. Chapter 3, Tables 3.1 and 3.3, footnotes [d] and [f]), $\rho \simeq 0.982$ g/cm^3 and $\rho_0 \simeq 1.008$ g/cm^3, therefore $b_T^{T_0} \simeq 1.106$ (from 0 to 37 °C, the modulus-scale shift factor increases due merely to thermal expansion). Using the WLF parameters c_1^g and c_2^g (from Table 3.5) and Eq. (3.10), we obtain $a_T^{T_0} = a_T^{T_g} \big/ a_{T_0}^{T_g} \simeq 2.43 \cdot 10^{-2}$ (from 0 to 37 °C, the molecular mobility of PI monomers increases by two orders of magnitude).

---

[e] When the reference temperature T_0 is of interest, shift factors are sometimes assigned the symbols $a_T^{T_0}$ and $b_T^{T_0}$.

In choosing the frequency ω to test the validity of Eq. (4.9), let us consider some characteristic time scales associated with the dynamics of LIL50–12. Namely, the *equilibration time*[35,36,44-46] of a PI tube segment (also called the *entanglement time*[44]), τ_e (Eq. (3.19)), and the *path equilibration time*[35,36,44-46] of the PI chain, $2\tau_R$ (Eq. (3.20)). At $t = \tau_e$, the PI entanglement network just comes into play: bridge-, knotted-loop-, and free-end-type midblocks are entangled (Figure 3.5), and "chain unit sharing"[45] has not yet had time to occur (§3.3.4.IV-d). For $\tau_e \leq t \leq 2\tau_R$, stress relaxation in LIL50–12 proceeds via 1-D *Rouse-like motions* ("*local reptation*"[166]) of the PI monomers along the chain primitive path (Table 3.8): "chain unit sharing" re-equilibrates chain density along the primitive path of the entangled PI chains, while the effect of "early-time chain end fluctuations"[167,168] on free-end-type midblocks can be assumed to be negligible (§3.3.4.IV-d). At 0 °C, $\tau_e \simeq 0.08$ ms and $2\tau_R \simeq 7.6$ ms (Table 3.8). It follows from the horizontal shift factor $a_T^{T_0}$ that $\tau_e \simeq 2$ μs and $2\tau_R \simeq 0.18$ ms at 37 °C. The characteristic frequencies $1/\tau_e \simeq 5.2 \cdot 10^5$ rad/s and $1/2\tau_R \simeq 5.4 \cdot 10^3$ rad/s are both higher than the highest frequency accessible from measurements at 37 °C (Figure 4.2(a)). Having to rely on Eq. (4.4)a, with $P = 6.85$ MPa·s^m and $m = 0.057$, to extrapolate the storage modulus beyond ω_{max}, we therefore choose $\omega = 1/2\tau_R$. This gives $E'_{PL}(\omega,T) \simeq 10.9$ MPa, which is in agreement with the prediction of Eq. (4.9), $b_T^{T_0} \cdot E'\left(\omega a_T^{T_0}, T_0\right) \simeq 10.4$ MPa (cf. Figure 3.4(a)). Thus, at 37 °C and frequencies comparable to and higher than $1/2\tau_R$, the domains of the PLA microphase behave as non-deformable inert filler particles (cf. §3.3.4.IV-e). This observation allows us to take advantage of the model developed in Chapter 3 to

describe the linear elastic behavior of LIL50–12 with *glassy* PLA domains (§3.3.4.IV-e), and therefore to relate the power-law exponent m to molecular parameters. This is the subject of the next section.

4.3.2.II-c Dependence of the power-law exponent *m* on molecular structure

In 1985, Cates[287] and Muthukumar[288] showed that polymeric fractals naturally exhibit self-similar dynamics. Vice versa, it may be concluded that polymers at the gel point possess a fractal structure.[331] This implies that a power-law scaling exists between the size R of a molecular cluster and its molar mass M, i.e. $R \sim M^{1/d_f}$, where d_f represents the single-cluster fractal dimension[321] (cf. Chapter 2, Eq. (2.1) and footnote [f]). For chemical gels, several different relationships between the power-law exponent m and the fractal dimension d_f have been proposed.[287,288,320,321,331,338,339] The power-law exponent m, however, does not have a universal value[319], as one might expect for a property at a critical point[320,321,328,329]. Furthermore, a general theory that connects the value of m with molecular architecture has yet to be proposed.[266] It is the goal of this section to seek a relationship between the power-law exponent m deduced from the viscoelastic behavior shown in Figure 4.2(a) and the molecular structure of LIL50–12. This can be accomplished by exploiting some of the key results presented at the end of Chapter 3.

In §3.3.4.IV-e it was shown that, under certain conditions, the measured storage modulus $E'(\omega)$ of an A–B–A with *glassy* A domains and arbitrary distribution of midblock conformations can be interpreted as the amplified ($\xi(\omega) > 1$) linear response of

the undiluted ($\phi_{ref} \simeq \phi = 1$) network of B Gaussian strands whose junctions (i.e. B entanglements, and A microdomains acting as physical endlinks) move affinely with the macroscopic deformation. Owing to simple additivity of "crosslink" ("endlink") and entanglement contributions, $E'(\omega)$ across the rubbery plateau and up to the entanglement time τ_e is given by (Eq. (3.24))

$$\begin{aligned} E'(\omega) &= 3 \cdot G'(\omega) \\ &= 3 \cdot \xi(\omega) \cdot \left[\nu_{cross} + \nu_{ent}(\omega) \right] \cdot kT \\ &= E'_{cross}(\omega) + E'_{ent}(\omega) \qquad \text{for } \omega \le 1/\tau_e \end{aligned} \tag{4.10}$$

where $\xi(\omega)$ is the filler effect of the glassy A domains, ν_{cross} is the number density of B strands terminated by endlinks regardless of whether entanglements intervene, $\nu_{ent}(\omega)$ is the number density of B strands terminated by entanglements regardless of whether endlinks intervene, k is Boltzmann's constant, and T is the absolute temperature. Based on Eq. (4.10), characteristic moduli can be calculated. Specifically, the *entanglement modulus*[44] $E_e \equiv E'(1/\tau_e)$ (Eq. (3.32)), the *plateau modulus*[43-45] $E_N \equiv E'(1/2\tau_R)$ (Eq. (3.37)), and the *pseudo-equilibrium modulus* $E_{eq} \equiv E'(\omega \to 0)$ (Eq. (3.44)).

Let us now consider the relative magnitude of endlink and entanglement contributions to $E'(\omega)$, and how it is affected by a change in time scale. In Chapter 3, we applied Eq. (4.10) to model the linear elastic behavior of LIL50–12 at 0 °C and showed that at (pseudo) mechanical equilibrium (cf. Eqs. (3.45)–(3.46) and Table 3.9)

$$\frac{E'_{ent}(\omega \to 0)}{E'_{cross}(\omega \to 0)} \simeq 5.1 \tag{4.11}$$

In the low-frequency limit, all untrapped entanglements (formed between bridges or knotted-loops and free-end-type midblocks) have disappeared (cf. Figure 3.5). Nevertheless, entanglement junctions outnumber PLA endlinks by 5 to 1, and the pseudo-equilibrium modulus is largely dictated by the entanglement network. At the path equilibration time, $2\tau_R$, arm retraction dynamics has not yet had time to occur; therefore, both trapped and untrapped entanglements contribute to $E'_{ent}(\omega)$, and the ratio becomes (cf. Eqs. (3.36) and (3.43))

$$\frac{E'_{ent}\left(1/2\tau_R\right)}{E'_{cross}\left(1/2\tau_R\right)} = \frac{1}{T_e}\cdot\frac{E'_{ent}\left(\omega\to 0\right)}{E'_{cross}\left(\omega\to 0\right)} \simeq 9.6 \tag{4.12}$$

where T_e = 0.53 represents the fraction of trapped (i.e. permanent) entanglements in the system (cf. Eq. (3.38) and Table 3.9). At the entanglement time, τ_e, "chain unit sharing" has yet to take place, and the entanglement contribution increases by an additional factor of 5/4 (cf. Eqs. (3.31), (3.32), and (3.36))

$$\begin{aligned}\frac{E'_{ent}\left(1/\tau_e\right)}{E'_{cross}\left(1/\tau_e\right)} &= \frac{5}{4}\cdot\frac{1}{T_e}\cdot\frac{E'_{ent}\left(\omega\to 0\right)}{E'_{cross}\left(\omega\to 0\right)} \\ &= \frac{\left(1-x_d\right)^{1+\alpha}\left(\phi_I^{matrix}\right)^{\alpha}}{\left(1-x_d-x_f\right)}\cdot\frac{M_I}{M_{e,hI}^{G}} \simeq 12\end{aligned} \tag{4.13}$$

where $x_d \simeq 0$ is the fraction of PI chains in dangling-loop conformation (§3.3.4.IV-d), $x_f \simeq 24\%$ is the fraction of PI chains having at least one end residing outside PLA domains (§3.3.4.IV-d, Figure 3.5, and Table 3.9), $\alpha = 1$ is the dilution exponent that dictates how shear plateau modulus and entanglement molar mass change with polymer volume fraction[41,42,45,170,171] (Eq. (3.22) and §3.3.4.IV-e), $\phi_I^{matrix}(0\ °C) \simeq 95\%$ is the volume

fraction of PI in the matrix (Table 3.9), M_I = 49800 g/mol is the PI block molar mass (Table 3.1), and $M_{e,hI}^{G}(0\ °C)$ = 5100 g/mol is the Graessley–Fetters[17,35,75] entanglement molar mass of homopolymer PI (Eq. (3.4) and Table 3.4).

We now turn our attention to Figure 4.2(a), at frequencies equal to or higher than $1/2\tau_R$ where the PLA domains are glassy (§4.3.2.II-b). In this region (about a decade beyond the maximum frequency ω_{max} accessed experimentally), Eqs. (4.10), $(4.12)_2$, and (4.13)b apply. The numerical values (9.6 and 12) remain almost unchanged from 0 to 37 °C. Indeed, the distribution of midblock conformations may be treated as temperature-independent (Experimental Section); T_e only depends on x_d and x_f (Eq. (3.47)); ϕ_I^{matrix} depends very slightly on temperature through the densities of the constituent blocks (Eq. (3.53)); and the PI entanglement molar mass is nearly temperature-independent[17,18,40,68] (cf. Chapter 2, §2.4 and Table 2.3, and Chapter 3, Table 3.4). It follows from Eqs. (4.12) and (4.13) that, on time scales between the path equilibration time and the entanglement time, the entanglement contribution to $E'(\omega)$ – both at 0 and 37 °C – is one order of magnitude larger than the endlink contribution. To a good approximation, we may thus rewrite Eq. (4.10) as

$$E'(\omega) \simeq E'_{ent}(\omega) \qquad \text{for } 1/2\tau_R \le \omega \le 1/\tau_e \tag{4.14}$$

with (cf. Eqs. (3.31) and (3.36))

$$E'_{ent}\left(1/2\tau_R\right) = \frac{4}{5} \cdot E'_{ent}\left(1/\tau_e\right) \tag{4.15}$$

By combining Eqs. (4.4)a, (4.14), and (4.15), we obtain

$$\left(\tau_{\mathrm{e}}\right)^{m} = \frac{4}{5}\cdot\left(2\tau_{\mathrm{R}}\right)^{m} \qquad \text{for } 1/2\tau_{\mathrm{R}} \le \omega \le 1/\tau_{\mathrm{e}} \tag{4.16}$$

Now, τ_{e} and $2\tau_{\mathrm{R}}$ are related by[35,36,44-46] (cf. Eq. (3.20))

$$2\tau_{\mathrm{R}} = \tau_{\mathrm{e}}\left(Z_{\mathrm{I}}\right)^{2} \tag{4.17}$$

where Z_{I} represents the average number of tube segments per entangled PI chain, determined as (cf. Eq. (3.28))

$$Z_{\mathrm{I}} = Z_{\mathrm{I}}^{\mathrm{hI}}\cdot\left(1-x_{\mathrm{d}}\right)^{\alpha}\cdot\left(\phi_{\mathrm{I}}^{\mathrm{matrix}}\right)^{\alpha} \tag{4.18}$$

where $Z_{\mathrm{I}}^{\mathrm{hI}}(0\ ^{\circ}\mathrm{C}) \simeq Z_{\mathrm{I}}^{\mathrm{hI}}(37\ ^{\circ}\mathrm{C}) \simeq 9.8$ is the average number of tube segments in the corresponding PI homopolymer (Table 3.4). By assuming volume additivity, $\phi_{\mathrm{I}}^{\mathrm{matrix}}$ at 37 °C can be calculated as (cf. Eq. (3.53))

$$\phi_{\mathrm{I}}^{\mathrm{matrix}} = \frac{\left(1-w_{\mathrm{L}}^{\mathrm{matrix}}\right)/\rho_{\mathrm{I}}}{\left(1-w_{\mathrm{L}}^{\mathrm{matrix}}\right)/\rho_{\mathrm{I}} + w_{\mathrm{L}}^{\mathrm{matrix}}/\rho_{\mathrm{L}}} \simeq 0.947 \tag{4.19}$$

where $w_{\mathrm{L}}^{\mathrm{matrix}} \simeq 7\%$ is the mass fraction of PLA blocks in the matrix (Table 3.9), and $\rho_{\mathrm{I}} \simeq 0.893$ g/cm^3 and $\rho_{\mathrm{L}} \simeq 1.248$ g/cm^3 are the densities of the PI and PLA blocks at 37 °C (respectively – cf. Chapter 3, footnote [d]). It follows from Eq. (4.18) that $Z_{\mathrm{I}} \simeq 9.25$. As expected, the temperature dependence of $\phi_{\mathrm{I}}^{\mathrm{matrix}}$ and Z_{I} in the range [0 °C, 37 °C] is negligible (cf. Table 3.9). Substituting Eq. (4.17) into Eq. (4.16) gives the sought-after relation between the power-law exponent *m* and molecular structure

$$\left(Z_{\mathrm{I}}\right)^{2m} = \frac{5}{4} \qquad \text{for } 1/2\tau_{\mathrm{R}} \le \omega \le 1/\tau_{\mathrm{e}} \tag{4.20}$$

or, equivalently,

$$\begin{aligned} m &= \frac{1}{2}\log\frac{5}{4}\cdot\left(\log Z_I\right)^{-1} \\ &\simeq 0.0485\cdot\left(\log Z_I\right)^{-1} \qquad \text{for } 1/2\tau_R \le \omega \le 1/\tau_e \end{aligned} \tag{4.21}$$

With $Z_I \simeq 9.25$, Eq. (4.21) gives $m \simeq 0.05$. The consistency with the value found from the PL fit, $m = 0.057$, is remarkable. Even more so considering that the experimental result was obtained in a frequency range (below $1/2\tau_R$) where the LIL50–12 dynamics should be governed by star-like motion of single-free-end-type midblocks and incipient softening of PLA domains. Nevertheless, the prediction of m based merely on 1-D Rouse dynamics is rather close to the observed self-similar behavior at 37 °C which, in turn, is itself intermediate between the power-law exponents measured for $E'(\omega)$, $m \simeq 0.04$, and $E''(\omega)$, $n \simeq 0.09$, at 0 °C (Table 3.7). This result deserves further investigation, but it is beyond the scope of this report. It would be interesting to test the accuracy of Eq. (4.21) for other well-entangled A–B–A systems at temperatures close to the T_g of A, especially those with a large fraction of unsegregated chains.

It is worth mentioning that the dependence on molecular structure in Eq. (4.21) is compatible with the requirement of the power-law spectrum that m lie between 0 ($Z \to \infty$) and 1 ($Z \simeq 1.12$). In practice, m is predicted to be between ≈ 0.016 ($Z \approx 1000$) and ≈ 0.16 ($Z \approx 2$). Although Eq. (4.21) gives $m \to \infty$ in the limit $Z \to 1$, the actual minimum value that Z can approach in a melt, $Z(\phi = 1)\big|_{min} = Z_{min}$, is species-dependent. This stems from the fact that a polymer strand becomes entangled when the ratio of its pervaded over occupied volume reaches a critical value[17,45,67] (Chapter 2, Eq. (2.8)), thereby the minimum length for the onset of entanglement coupling is set by molecular

characteristics[18] (Chapter 2, Eq. (2.13)). For a linear flexible polymer of molar mass M, unperturbed root-mean-square end-to-end distance R, and melt density ρ, Z_{min} can be estimated as[16,17,20] (cf. Chapter 2, Eqs. (2.4) and (2.13))

$$\begin{aligned} Z_{min} = \frac{M_C}{M_e^G} &= 4.275 \cdot p^{-0.534} \\ &= 4.275 \cdot \left(\frac{\rho N_{av} R^2}{M} \right)^{0.534} \end{aligned} \tag{4.22}$$

where M_C is the critical molar mass for entanglement effect in viscosity, M_e^G is the entanglement molar mass (according to the Graessley–Fetters definition[17,35,75], Eq. (2.7)), p is the Witten–Fetters packing length[16,17] (expressed in Å, Eq. (2.4)), and N_{av} is Avogadro's number. While this empirical correlation predicts $Z_{min} = 1$ for $p \simeq 15$ Å (cf. Chapter 2, §2.8), polymers with such large packing length have yet to be synthesized and p is typically between about 1.5 and 6.5 Å (cf. Chapter 2, Figure 2.2(b)).[20] It follows that, for example, $Z_{min} = 1.7$ for atactic poly(cyclohexyl)ethylene (*a*-PCHE) at 160 °C[18], $Z_{min} = 2.4$ for polyisoprene with a 7% 3,4 microstructure (7% 3,4-PI) at 25 °C[20], and $Z_{min} = 3.1$ for polyethylene (PE) at 140 °C[17] (cf. Chapter 2, Tables 2.3 and 2.6). For these melts, the largest power-law exponent m_{max} according to Eq. (4.21) is $m_{max} \simeq 0.21$ (*a*-PCHE), $m_{max} \simeq 0.13$ (7% 3,4-PI), and $m_{max} \simeq 0.10$ (PE). Eq. (4.21) can therefore offer some guidance in the design of complex materials that can mimic a specific self-similar behavior (e.g. the linear viscoelastic response of chewing gums, Chapter 6).

4.3.2.II-d Physical meaning of the quasi-property *P*

For a polymer undergoing a chemically-induced liquid-solid transition, the value of the power-law exponent $m(t)$ at any given time t is inherently related to the extent of reaction.[334,335] As such, the m-dependent gel strength S represents a material quasi-property that is, both numerically and dimensionally, intermediate between the steady-state viscosity of the precursor molecule[293,294] and the equilibrium modulus of the fully crosslinked material[334,335] (§4.3.2.II). S reduces to the former when $m = 1$, and to the latter when $m = 0$. This transitional nature of quasi-properties, viewed as quantities lying at a certain distance between prototypes, was termed the "*principle of intermediacy*" by Scott Blair and co-workers[318] in 1947. A similar state of play holds for LIL50–12. In this case, the power-law exponent m is time-independent (§4.3.2.II-c), but the quasi-property P is again dimensionally intermediate between a viscosity (with units of Pa·s) and a modulus (with units of Pa). Thus, a physical interpretation of the dyad (P, m) is most easily found in terms of an idealized *mechanical element*.

Mechanical models furnish a convenient way of modeling linear viscoelastic behavior. In these models, the underlying physical system is replaced by idealized counterparts of its actual constitutive elements. Let us consider the time-dependent scalar stress $\sigma(t)$ and strain $\varepsilon(t)$ associated with a linear viscoelastic response. Without loss of generality, we can assume these functions to be defined on $[0, \infty)$ and with *zero initial conditions* (cf. Appendix B, §B.2.3, and Appendix D, §D.1, §D.2). The functions $\sigma(t)$ and $\varepsilon(t)$ represent the infinitesimal shear stress and strain (respectively) in simple shear, and the

infinitesimal tensile stress and strain (respectively) in uniaxial extension.[f] In classical mechanical models, it is customary to use the symbol of a *spring* to represent storage of potential energy, and the symbol of a *dashpot* to represent dissipation of mechanical energy (Figure 4.3). It is further assumed that the spring behaves as a *Hookean* (i.e. *linear*) *solid with negligible mass* and modulus E, thereby obeying the constitutive equation

$$\sigma(t) = E\varepsilon(t) \qquad \text{spring} \tag{4.23}$$

The spring is therefore the idealized mechanical element exhibiting *purely elastic linear behavior*, and it is fully defined by the single parameter E (Figure 4.3). Conversely, the dashpot is assumed to behave as a *Newtonian* (i.e. *linear*) *liquid with negligible mass* and viscosity $\eta_E = E\tau$ (τ being a characteristic retardation time), thereby obeying the constitutive equation

$$\begin{aligned} \sigma(t) &= E\tau \frac{d\varepsilon(t)}{dt} \\ &= \eta_E \frac{d\varepsilon(t)}{dt} \qquad \text{dashpot} \end{aligned} \tag{4.24}$$

---

[f] Based on the definition of the *infinitesimal strain tensor* adopted by Tschoegl[150], the scalar strain component in *simple shear* equals half of the (traditionally defined) shear strain γ. In *uniaxial extension*, the scalar strain component equals ε_N, where ε_N denotes the nominal/engineering strain. Since the true/Hencky strain is defined as $\varepsilon \equiv \ln(L/L_0) = \ln(\lambda) = \ln(\varepsilon_N + 1)$ – where L and L_0 stand for the deformed and undeformed length (respectively), and λ is the elongation ratio – in the limit of infinitesimal uniaxial deformation the scalar strain component and the Hencky strain coincide. Note that the infinitesimal strain tensor is often defined (e.g. Ferry[42], Bird et al.[340], and Graessley[45]) as twice the tensor used by Tschoegl; in this case, the scalar strain component in simple shear equals the shear strain γ, while in uniaxial extension is $2\varepsilon_N \simeq 2\varepsilon$.

The dashpot is thus the idealized mechanical element exhibiting *purely viscous linear behavior*, and it is fully defined by the single parameter η_E (Figure 4.3). Springs and dashpots are the basic units of classical mechanical models.

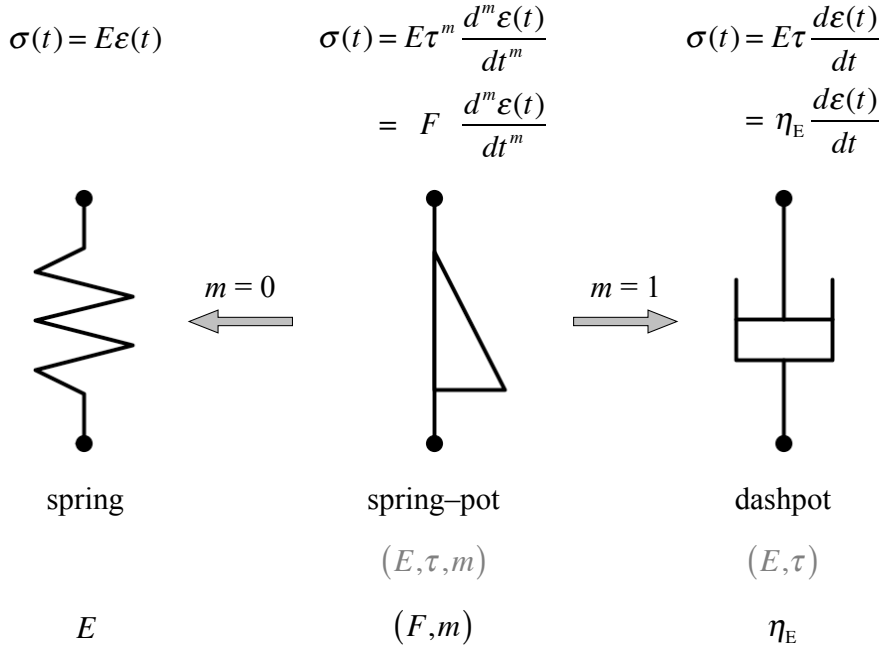

Figure 4.3. Model representation and constitutive equation of the spring-pot as a fractional element (FE) that interpolates between a spring ($m = 0$) and a dashpot ($m = 1$) (cf. Appendix D, Figure D.1). The spring-pot is fully characterized by two parameters: the quasi-property $F = E\tau^m$ (with dimensions of Pa·s^m), and m (with $0 \le m \le 1$).

It follows from Eqs. (4.23) and (4.24) that an intermediate modal response is described by the constitutive equation

$$\begin{aligned} \sigma(t) &= E\tau^m \frac{d^m\varepsilon(t)}{dt^m} && \text{with } 0 \le m \le 1 \\ &= F \frac{d^m\varepsilon(t)}{dt^m} && \text{spring-pot} \end{aligned} \tag{4.25}$$

where d^m/dt^m is a shorthand notation for the *fractional operator* ${}_0D_t^m$ representing the derivative to non-integer order m.

In the *Riemann–Liouville formalism*, the *fractional* (*differintegral*) *operator* ${}_{t_0}D_t^\alpha$ is defined for any real number α as[341] (Appendix F, §F.2)

$$ {}_{t_0}D_t^\alpha f(t) = \begin{cases} \dfrac{1}{\Gamma(-\alpha)} \displaystyle\int_{t_0}^{t} (t-u)^{-\alpha-1} f(u)\,du & \text{for } \alpha \in \mathbb{R},\ \alpha < 0 \\ f(t) & \text{for } \alpha = 0 \\ \dfrac{d^n}{dt^n}\left[{}_{t_0}D_t^{\alpha-n} f(t) \right] = \dfrac{1}{\Gamma(n-\alpha)} \dfrac{d^n}{dt^n} \displaystyle\int_{t_0}^{t} (t-u)^{n-\alpha-1} f(u)\,du & \text{for } \alpha \in \mathbb{R},\ \alpha > 0 \end{cases} \tag{4.26} $$

with n being the smallest positive integer larger than or equal to α, i.e.

$$ n \geq \alpha > n-1, \quad \text{and } n \in \mathbb{Z}^+ \tag{4.27} $$

and d^n/dt^n denoting the ordinary n-fold derivative. When α is negative, Eq. (4.26)a defines the operation of *fractional integration* to non-integer order α; for positive values of α, Eqs. (4.26)c and (4.27) define the operation of *fractional differentiation* to non-integer order α. For integer values of α, the fractional operator ${}_{t_0}D_t^\alpha$ reduces to the ordinary integration and ordinary differentiation. If $\alpha = -n$, it follows from Eq. (4.26)a that

$$ {}_{t_0}D_t^{-n} f(t) = \frac{1}{\Gamma(n)} \int_{t_0}^{t} (t-u)^{n-1} f(u)\,du \qquad \text{for } n \in \mathbb{Z}^+ \tag{4.28} $$

which corresponds to the ordinary n-fold integral, i.e. Cauchy's multiple integral. If $\alpha = n$, Eqs. (4.26)b-c and (4.27) give

$$ {}_{t_0}D_t^n f(t) = \frac{d^n}{dt^n}\left[{}_{t_0}D_t^0 f(t)\right] = \frac{d^n}{dt^n} f(t) \qquad \text{for } n \in \mathbb{Z}^+ \tag{4.29} $$

which corresponds to the ordinary *n*-fold derivative. Since we are considering the infinitesimal stress $\sigma(t)$ and strain $\varepsilon(t)$ to be defined on $[0, \infty)$ and with zero initial conditions, we can restrict our attention to the domain $t > 0$. As a result, we can choose the lower limit of integration $t_0 = 0$, i.e. the fractional operator becomes ${}_0D_t^\alpha$, and use the shorthand notation (cf. Eq. (4.25))

$$ {}_0D_t^\alpha f(t) \equiv \frac{d^\alpha}{dt^\alpha} f(t) \qquad \alpha \in \mathbb{R} \tag{4.30} $$

The idealized mechanical element obeying Eq. (4.25), termed "*spring-pot*" by Koeller[342] in 1984, interpolates between a spring ($m = 0$) and a dashpot ($m = 1$). The spring-pot, schematically shown in Figure 4.3, is thus fully characterized by two parameters: the quasi-property $F = E\tau^m$ (with dimensions of Pa·s^m), and the power-law exponent m (with $0 \le m \le 1$). It is evident that in the limiting cases, $m = 0$ and $m = 1$, the quasi-property F reduces to a modulus and a viscosity, respectively. Here, the letter F is a reminder that this quasi-property is the material parameter associated with the fractional mechanical element (FE). Between 1993 and 1994, Schiessel and Blumen[343] and Heymans and Bauwens[344] were able to prove that this fractional element is equivalent to hierarchical and fractal arrays (infinite "trees" or "ladders") of springs and dashpots. Since then, it has become customary to depict the spring-pot by an upright triangle symbolizing a "ladder".[345] By means of *fractional calculus* (Appendix F), hence quasi-properties, a large number of hierarchical relaxation processes can thus be captured into a

single mechanical element. This enables the quantitative description of self-similar dynamics over a broad range of timescales with only a few, physically meaningful material parameters (cf. §4.3.2.III). Although it is always possible to model any power-law relaxation patter through a finite (albeit large) array of exponential relaxation modes (i.e. combinations of springs and dashpots), the values of the fitted parameters would depend on the experimental timescale over which the fit is performed and the chosen number of relaxation modes, and hence lack physical meaning.[36,151,346] Indeed, this would be tantamount to using discrete relaxation spectra, equivalent to generalized Maxwell or Voigt models (Appendix D, §D.4.5), as opposed to continuous spectral distributions (cf. Chapter 3, §3.3.4.IV-a).

The constitutive equation of a spring-pot, Eq. (4.25), was introduced through formal replacement of a first-order derivative (d/dt) by the fractional derivative (d^m/dt^m) of non-integer order m (with $0 \leq m \leq 1$). It is important to realize, however, that fractional calculus arises naturally when dealing with materials that exhibit a power-law spectrum. In particular, Eq. (4.25) (with $0 < m < 1$) follows directly from the Boltzmann superposition integral (Appendix D, Eq. (D.15)d) and a power-law decay of the relaxation modulus, $E(t) \sim t^{-m}$ (the proof is given in Appendix F, §F.2.1).

As could be inferred from Eq. (4.25), a single fractional element with parameters F and m exhibits a single power-law relaxation pattern of the type shown in Figure 4.2, with $0 < m < 1$. In other words, the power-law spectrum $H_{E,PL}(\tau)$ (Eq. (4.2)), the critical-gel-like relaxation modulus $E_{CGM}(t)$ (Eq. (4.7)), and the spring-pot (Eq. (4.25), with $0 < m <$

1) are analogous representations of the same underlying fractional dynamics. We seek to prove this intuitive statement, and thereby find the relation connecting the quasi-properties P, S, and F (notice that the relation between P and S, Eq. (4.8), follows immediately from a comparison of Eq. (4.3) with the power-law expression of the complex modulus given in the original papers[289-292] of Chambon and Winter). This can be achieved, for instance, by determining – through *integral transformation calculus* (Appendix B) – the relaxation spectrum $H_{\mathrm{E,FE}}(\tau)$ associated with the mechanical behavior of the spring-pot, and comparing it with the power-law spectrum $H_{\mathrm{E,PL}}(\tau)$ given by Eq. (4.2).

It is well known that the *Laplace transform* of the ordinary n^{th} order derivative or the ordinary n^{th} order integral is, for zero initial conditions, (Appendix B, Eq. (B.9))

$$\mathcal{L}\left\{\frac{d^n}{dt^n}f(t)\right\} = s^n \overline{f}(s) \qquad n \in \mathbb{Z} \tag{4.31}$$

It is easy to show (Appendix F, §F.2) that Eq. (4.31) generalizes to include non-integer α by the simple extension[341]

$$\mathcal{L}\left\{{}_0D_t^{\alpha} f(t)\right\} = s^{\alpha} \overline{f}(s) \qquad \alpha \in \mathbb{R} \tag{4.32}$$

The Laplace transformation of the fractional operator, Eq. (4.32), is particularly useful as it transforms linear differential or integral equations to non-integer order (the so-called *extraordinary differential equations*)[341] into polynomials in the transform variable s. Solutions to extraordinary differential equations are thus accomplished through the use of Eq. (4.32) (cf. §4.3.2.III). Upon Laplace transformation, the constitutive equation of the spring-pot, Eq. (4.25), becomes

$$\bar{\sigma}(s) = Fs^m \bar{\varepsilon}(s) \qquad \text{spring-pot} \tag{4.33}$$

where $\bar{\sigma}(s)$ and $\bar{\varepsilon}(s)$ denote, respectively, the *stress* and *strain transforms*. Constitutive equations in the complex domain, such as Eq. (4.33), are equivalent to the Boltzmann superposition integrals in the time domain (cf. Appendix D, §D.2).[150] By definition, the ratio

$$\bar{Y}_{\mathrm{FE}}(s) \equiv \frac{\bar{\sigma}(s)}{\bar{\varepsilon}(s)} = Fs^m \qquad \text{spring-pot} \tag{4.34}$$

is the *operational* (extensional) *relaxance* of the spring-pot. In the time domain, $Y_{\mathrm{FE}}(t)$ represents the stress response of the fractional element to a unit impulse of strain (i.e. it is the *material* or *memory function* of the model – cf. Appendix D, §D.2, §D.3.1, and Table D.1).[150]

Now, the operational relaxance $\bar{Y}(s)$ and the relaxation spectrum $H_{\mathrm{E}}(\tau)$ are related by (cf. Appendix D, Eq. (D.86) and Table D.1)[150]

$$\bar{Y}(s) = E_{\mathrm{eq}} + \int_0^\infty H_{\mathrm{E}}(\tau) \frac{s}{1+\tau s} d\tau \tag{4.35}$$

For viscoelastic liquids and critical gels the equilibrium modulus E_{eq} vanishes, and Eq. (4.35) can be rewritten as

$$\bar{Y}(s) = \tilde{H}_{\mathrm{E}}\left(1/s\right) \tag{4.36}$$

or, equivalently, as

$$\tilde{H}_{\mathrm{E}}(s) = \bar{Y}\left(1/s\right) \tag{4.37}$$

where $\tilde{H}_{\mathrm{E}}(s) = \mathcal{S}\left[H_{\mathrm{E}}(\tau);\ s\right]$ represents the *Stieltjes transform* of $H_{\mathrm{E}}(\tau)$ (cf. Appendix B, Eq. (B.22)). If $\tilde{H}_{\mathrm{E}}(s)$ is known, the *inverse Stieltjes transform* $\mathcal{S}^{-1}\left[\tilde{H}_{\mathrm{E}}(s);\ \tau\right]$ with

$$\begin{aligned} s &= -x \pm iy \qquad x, y \in \mathbb{R}^+ \\ &= |s| \exp(\pm i\theta) \end{aligned} \tag{4.38}$$

and

$$\begin{aligned} |s| &= \left(x^2 + y^2\right)^{1/2} = z^{-1} \\ \theta &= \pi - \arctan(y/x) \end{aligned} \tag{4.39}$$

permits the calculation of the relaxation spectrum $H_{\mathrm{E}}(\tau)$ as (cf. Appendix B, Eqs. (B.29) and (B.30))

$$H_{\mathrm{E}}(\tau) = \mp \frac{1}{\pi} \lim_{y \to 0} \left[\mathrm{Im}\ \tilde{H}_{\mathrm{E}}(-\tau \pm iy) \right] \qquad \tau \in \mathbb{R}^+ \tag{4.40}$$

with

$$\lim_{y \to 0} (-\tau \pm iy) = \tau \exp(\pm i\pi) \tag{4.41}$$

Combining Eqs. (4.37)–(4.41) leads to

$$H_{\mathrm{E}}(\tau) = \mp \frac{1}{\pi} \lim_{y \to 0} \left[\mathrm{Im}\ \bar{Y}\left(z \exp(\mp i\theta)\right) \right] \qquad \tau \in \mathbb{R}^+ \tag{4.42}$$

with

$$\lim_{y \to 0} z \exp(\mp i\theta) = \frac{1}{\tau} \exp(\mp i\pi) \tag{4.43}$$

Thus, Eqs. (4.42) and (4.43) make it possible to calculate the relaxation spectrum $H_{\mathrm{E}}(\tau)$ from the operational relaxance $\bar{Y}(s)$ for models that do not possess an equilibrium modulus E_{eq}.

Let us now turn our attention to the specific model of linear viscoelastic behavior portrayed by the spring-pot, and restrict our treatment to power-law exponents m in the open interval (0, 1) (this ensures the possibility of defining a relaxation spectrum and satisfies the condition $E_{eq} = 0$). Substituting Eq. (4.34) into Eq. (4.42) yields

$$\begin{aligned} H_{\mathrm{E,FE}}(\tau) &= +\frac{1}{\pi}\lim_{y\to 0}\left[\mathrm{Im}\ \bar{Y}_{\mathrm{FE}}\left(z\exp\left(+i\theta\right)\right)\right] \\ &= +\frac{1}{\pi}\lim_{y\to 0}\left[\mathrm{Im}\ F\cdot z^{m}\exp\left(+i\theta m\right)\right] \\ &= +\frac{1}{\pi}\lim_{y\to 0}\left[F\cdot z^{m}\sin\left(\theta m\right)\right] \\ &= F\cdot\frac{\sin\left(\pi m\right)}{\pi}\cdot\tau^{-m} \qquad \text{spring-pot, for } 0<m<1 \end{aligned} \tag{4.44}$$

As anticipated, the constitutive equation of the spring-pot, Eq. (4.25), generates a power-law relaxation spectrum (with $0 < m < 1$). It follows from Eqs. (4.2)a, (4.8), and (4.44) that

$$\frac{F}{\Gamma(1-m)} = P\cdot\Gamma(1+m) = S \tag{4.45}$$

where we have made use of the identity $\Gamma(1-m)\Gamma(1+m) = \pi m/\sin(\pi m)$ (Appendix C, Eqs. (C.2) and (C.4)a).

Any of the basic models discussed so far – i.e. the simplified version of the wedge distribution of relaxation times (Eq. (4.2)), the empirical approach developed by Chambon and Winter for critical gels (Eq. (4.8)), and the mechanical behavior of a single spring-pot (Eq. (4.34)) – are therefore equally able to describe a single power-law regime, such as that exhibited by LIL50–12 over most of the experimental frequency window in Figure 4.2(a). Since the observed power-law exponent for LIL50–12 is small compared to

unity, $m = 0.057$, the quasi-properties F, P, and S are numerically similar: $F = 6.89$ MPa·s^m, $P = 6.85$ MPa·s^m, and $S = 6.65$ MPa·s^m. Some of the most familiar response functions are given in Table 4.1 for each of these three models (cf. Appendix E, Tables E.2–3); their numerical coefficients, involving the quasi-properties and the power-law exponent, are interrelated through Eq. (4.45) together with recurrence and reflection properties of the gamma function (Appendix C, §C.1.2).

Table 4.1. Linear viscoelastic functions for the *spring-pot* (FE), the *power-law relaxation spectrum derived from the wedge distribution* (PL), and *Chambon–Winter's critical gel model* (CGM). They are equivalent descriptions (cf. Eq. (4.45)) of fractional dynamics characterized by a single power-law relaxation pattern. In all of these models, it is assumed $E_{eq} = 0$ and $0 < m < 1$. Shaded areas indicate the premises upon which each model is built (cf. Eqs. (4.2), (4.8), and (4.34)).

	fractional element (FE)	*power-law spectrum derived from the wedge distribution* (PL)	*Chambon–Winter's critical gel model* (CGM)
$H_E(\tau)$	$F \cdot \frac{1}{\Gamma(1-m)\Gamma(m)} \cdot \tau^{-m}$	$P \cdot m \cdot \tau^{-m}$	$S \cdot \frac{1}{\Gamma(m)} \cdot \tau^{-m}$
$\bar{Y}(s)$	$F \cdot s^m$	$P \cdot \Gamma(1-m)\Gamma(1+m) \cdot s^m$	$S \cdot \Gamma(1-m) \cdot s^m$
$E(t)$	$F \cdot \frac{1}{\Gamma(1-m)} \cdot t^{-m}$	$P \cdot \Gamma(1+m) \cdot t^{-m}$	$S \cdot t^{-m}$
$\eta_E(t)$	$F \cdot \frac{1}{(1-m)\Gamma(1-m)} \cdot t^{1-m}$	$P \cdot \frac{\Gamma(1+m)}{1-m} \cdot t^{1-m}$	$S \cdot \frac{1}{1-m} \cdot t^{1-m}$
$E'(\omega)$	$F \cdot \cos(\pi m/2) \cdot \omega^m$	$P \cdot \frac{\pi m/2}{\sin(\pi m/2)} \cdot \omega^m$	$S \cdot \Gamma(1-m)\cos(\pi m/2) \cdot \omega^m$
$E''(\omega)$	$F \cdot \sin(\pi m/2) \cdot \omega^m$	$P \cdot \frac{\pi m/2}{\cos(\pi m/2)} \cdot \omega^m$	$S \cdot \Gamma(1-m)\sin(\pi m/2) \cdot \omega^m$
$\tan\delta(\omega)$	$\tan(\pi m/2)$	$\tan(\pi m/2)$	$\tan(\pi m/2)$

It may be argued that quasi-properties are not true material properties because they contain non-integer powers of the fundamental dimensions of mass M, length L, and time T. However, as first suggested by Scott Blair et al.[318] in 1947, quasi-properties are numerical measures of a *dynamic process* rather than of an equilibrium state. Building on the ideas introduced by Scott Blair and co-workers[318], in 2001 Podlubny[347] proposed a physical and geometrical interpretation of fractional operators as converting between an *external/laboratory Newtonian time scale* (with regularly spaced intervals) and an *internal/material time scale* (with irregularly spaced intervals). It is the different character of these time scales that gives quasi-properties non-integer dimensions in M, L, and T.[318]

Fractional calculus and quasi-properties are a direct consequence of fractional (i.e. self-similar) dynamics in complex systems. In 1983, Bagley and Torvik[285] demonstrated that the Rouse[47] theory modeling the behavior of monodisperse linear polymer chains in dilute solutions is equivalent to a fractional differential equation of order 1/2. More generally, transport dynamics in systems governed by subdiffusion and non-exponential relaxations can be described by the *fractional generalization of the Fokker–Planck equation* (Appendix F, Eq. (F.38)) introduced by Metzler and co-workers[252,261] in 1999. Their theoretical approach, which accounts for the observed anomalous diffusion and relaxation in complex systems through a fractional kinetic equation of order $1–\alpha$, inherently leads to the *generalized friction coefficient* ζ_α (with dimensions of $MT^{\alpha-2}$), the *generalized diffusion coefficient* D_α (with dimensions of $L^2T^{-\alpha}$), and the *generalized Einstein–Stokes–*

Smoluchowski relation[251,252,261] $D_\alpha = kT/\zeta_\alpha$. Interestingly, Metzler and colleagues[252] were able to derive the fractional Fokker–Planck equation from a continuous time random walk scheme, and connect it to a *multiple trapping process* with broad waiting time distribution (Appendix F, §F.3.5). It may then be concluded that fractional dynamics originates from molecular processes with a certain statistics, and quasi-properties such as P or D_α are related to the stochastic behavior on a microscopic level.

Hence, fractional stress-strain relationships are not merely a convenient mathematical notation. Just like the shapes of objects in nature are in general better described in the language of fractal geometry[253-258] rather than by Euclidian geometry, fractional calculus is a mathematical construct that captures the main features of the dynamics in complex systems.

Although the FE, PL, and CGM are equivalent to each other (Eq. (4.45) and Table 4.1), they are not equally versatile in their ability to describe non-exponential relaxations in complex systems. Their common limitation is that the storage and loss moduli must remain parallel to each other at all frequencies, thereby requiring that the loss tangent $\tan\delta(\omega) = \tan(\pi m/2)$ be frequency-independent. While this behavior can accurately match the experimental response over some frequency range (cf. Figure 4.2(a)), most materials exhibit two or more power-law regions and often an ultimate crossover to a liquid-like terminal response. Orderly arrangements of (a few) fractional elements naturally lend themselves to the description of such general relaxation patterns. This is the subject of the next section.

4.3.2.III Fractional mechanical models

In the limit of infinitesimal (tensile) deformation, viscoelastic behavior of an isotropic material can be described by a linear *ordinary* differential equation with constant coefficients, i.e. an ordinary constitutive equation (CE) of the form[150]

$$\sum_{n=0} l_n \frac{d^n \sigma(t)}{dt^n} = \sum_{m=0} y_m \frac{d^m \varepsilon(t)}{dt^m} \qquad \text{with } n,m \in \{0\} \bigcup \mathbb{Z}^+ \tag{4.46}$$

where l_n and y_m are the constant coefficients, and d^n/dt^n and d^m/dt^m denote the *ordinary* n- and m-fold derivatives. Laplace transformation of Eq. (4.46) gives, for zero initial conditions (cf. Appendix B, §B.2.3),

$$\overline{l}(s)\overline{\sigma}(s) = \overline{y}(s)\overline{\varepsilon}(s) \tag{4.47}$$

where $\overline{\sigma}(s)$ and $\overline{\varepsilon}(s)$ are the stress and strain transforms, respectively, and (cf. Eq. (4.31))

$$\begin{aligned} \overline{l}(s) &= \sum_{n=0} l_n s^n \\ \overline{y}(s) &= \sum_{m=0} y_m s^m \end{aligned} \tag{4.48}$$

are polynomials in the transform variable s. The Laplace-transformed constitutive equation, Eq. (4.47), leads to *Hooke's laws in the complex plane*[150] (cf. Appendix D, Eq. (D.4) and Table D.1)

$$\begin{aligned} \overline{\sigma}(s) &= \overline{Y}(s)\overline{\varepsilon}(s) \\ \overline{\varepsilon}(s) &= \overline{L}(s)\overline{\sigma}(s) \end{aligned} \tag{4.49}$$

with (cf. Appendix D, Eq. (D.5))

$$\overline{Y}(s)\overline{L}(s) = 1 \tag{4.50}$$

where the rational algebraic functions $\overline{Y}(s)=\overline{y}(s)/\overline{l}(s)$ and $\overline{L}(s)=\overline{l}(s)/\overline{y}(s)$ are the *operational* (extensional) *relaxance* and *retardance*, respectively[150] (cf. Eqs. (4.33) and (4.34)). In the time domain, $Y(t)$ and $L(t)$ represent the material response to unit impulses of strain and stress, respectively (i.e. they are the *material* or *memory functions* – Appendix D, §D.2, §D.3.1, and Table D.1).

In principle, *fractional* constitutive equations (FCEs) could be obtained from Eq. (4.46) simply by substituting fractional (differintegral) Riemann–Liouville operators for the ordinary derivatives, i.e.

$$\sum_n l_{\alpha_n 0} D_t^{\alpha_n} \sigma(t) = \sum_m y_{\beta_m 0} D_t^{\beta_m} \varepsilon(t) \qquad \text{with } \alpha_n, \beta_m \in \mathbb{R} \tag{4.51}$$

Such a formal replacement, however, cannot assure a priori that the resulting fractional (integral or differential) models be consistent with the laws of thermodynamics (namely, that they exhibit non-negative internal work and non-negative rate of energy dissipation).[345]

The problem of *thermodynamic admissibility* of fractional generalizations of Eq. (4.46) was addressed by several authors.[286,343,345,348-352] Based on rational mechanics arguments it was concluded that, as a sufficient condition for thermodynamic admissibility of fractional differential equations,

$$\sum_n l_{\alpha_n 0} D_t^{\alpha_n} \sigma(t) = \sum_m y_{\beta_m 0} D_t^{\beta_m} \varepsilon(t) \qquad \text{with } \alpha_n, \beta_m \in \{0\} \cup \mathbb{R}^+ \tag{4.52}$$

the order of the fractional operator on the stress must be smaller than or equal to the order of the fractional operator on the strain.[286,343,345,349-351] Owing to the composition rule of the

Riemann–Liouville fractional operator[341] (Appendix F, Eqs. (F.6) and (F.7)), differential and integral FCEs are not, in general, equivalent. As pointed out by Friedrich[351], differential FCEs are thermodynamically admissible for a wider range of parameters and provide a more accurate description of viscoelastic behavior than the integral versions. Rather than introducing fractional derivatives in Eq. (4.46) and then checking for thermodynamic admissibility, a simpler and more powerful approach to developing FCEs exists. By investigating the admissibility criteria for linear viscoelastic kernels, Beris and Edwards[353] have shown that mechanical models containing springs and dashpots with positive parameters always lead to thermodynamically valid CEs. Since a suitable arrangement of springs and dashpots gives rise to spring-pot behavior[343,344] (§4.3.2.II-d), deriving a differential FCE, Eq. (4.52), from a mechanical model (i.e. a combination of springs, dashpots, and spring-pots) automatically fulfills the required thermodynamic constraints[345,354,355].

Schiessel et al.[345] and Friedrich et al.[356] provided good overviews of fractional (differential) versions of classical *series-parallel models* (Appendix D, Figures D.2 and D.3): the *Maxwell model*[357], the *Voigt model*[358], and the two models of the standard linear solid[150] (the *3-parameter Maxwell model*[150] or *Zener model*[359], and the *3-parameter Voigt model*[150] or *Poynting–Thomson model*[359]). For series-parallel models, obtaining the corresponding Hooke's laws in the complex plane (Eq. (4.49)) is straightforward. In a series combination, the strains are additive and the same stress acts through all of the elements. In a parallel combination, all elements see the same strain and the stresses in

the elements are additive. Hence, series-parallel models obey the *combination rules* (known as *equations of congruence*, in structural mechanics[360]) that *retardances* $\bar{L}(s)$ *add in series* and *relaxances* $\bar{Y}(s)$ *add in parallel*.[150] Inverse Laplace transformation of Eq. (4.49) via Eq. (4.32) then yields the fractional constitutive equation of the model in the time domain, Eq. (4.52).

Solving extraordinary differential equations, however, is mathematically challenging[341] and the analytical determination of the response functions of fractional models is sometimes subjected to parameter constraints[345]. Furthermore, fractional differential (Riemann–Liouville) equations of order α require n initial conditions expressed in terms of fractional derivatives, where n is the smallest positive integer larger than or equal to α ($n \geq \alpha > n-1$, and $n \in \mathbb{Z}^+$).[341] A physical interpretation of such initial conditions was provided by Heymans and Podlubny[361] in 2006. For the mechanical models listed above, the corresponding differential FCEs may admit closed-form, analytical solutions in terms of power-laws and/or the *generalized Mittag-Leffler function* (vide infra).[345,356]

We have previously pointed out that the low-frequency behavior of LIL50–12 shown in Figure 4.2(a) reflects a true material response originating from the incipient glass transition of the PLA domains (§4.3.2.II-a). With the help of fractional calculus this response can, in fact, be exploited to extract useful information about the dynamics of the PLA glass transition at 37 °C, which lies outside of the experimental window and cannot be accessed via time-temperature superposition (§4.3.2.I). The interrelation between a fractional relaxation equation and simple TTS was analyzed in the framework of

statistical mechanics by Glöckle and Nonnenmacher[352]. In 2003, Heymans[362] considered the thermo-rheologically complex behavior of a hot-melt S–I–S adhesive across the polystyrene glass transition, and was able to fit the experimental data to a finite Gross–Marvin ladder model[363-365] in which dashpots had been replaced by spring-pots (yielding nested fractional subunits of the Zener-type). Here, our approach is different. Rather than using (nested) fractional mechanical models to fit experimental data across the glass transition of the PLA microphase, we seek to show how (single) fractional models can extrapolate the behavior of LIL50–12 at 37 °C to lower frequencies to *predict* the softening of the PLA domains. This is a two-step procedure, involving the sequential application of the fractional Maxwell model (§4.3.2.III-a) and the fractional Zener model (§4.3.2.III-b).

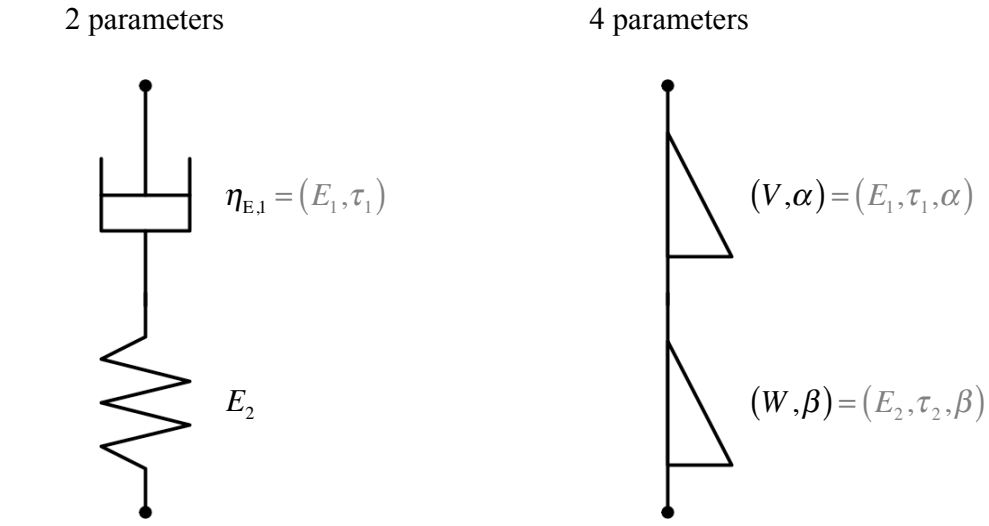

Figure 4.4. (a) The ordinary 2-parameter Maxwell model (MM) (cf. Appendix D, Figure D.2(a)). (b) The fractional Maxwell model (FMM), with $0 \leq \beta < \alpha \leq 1$.

4.3.2.III-a The fractional Maxwell model

The series combination of a dashpot and a spring, schematically shown in Figure 4.4(a), is commonly referred to as the *Maxwell model*[357] (MM). Replacing the classical mechanical elements by spring-pots (Figure 4.4(b)), respectively with parameters (V, α) and (W, β), yields the *fractional Maxwell model* (FMM).[345] Without loss of generality, we can take $\beta < \alpha$.[345] It is evident that for $\beta = \alpha$ the FCE of the single spring-pot (Eq. (4.25)) is recovered, whereas the FMM reduces to the ordinary Maxwell model for $\{0 = \beta, \alpha = 1\}$.

In this section, we concern ourselves with finding the stress response of the FMM to four unit standard strain excitations (impulse, step, slope, and harmonic – Appendix D, §D.3). Thus, we will calculate the following material functions (respectively): the operational relaxance $\overline{Y}_{\mathrm{FMM}}(s)$, the relaxation modulus $E_{\mathrm{FMM}}(t)$, the transient viscosity $\eta_{\mathrm{E,FMM}}(t)$, and the complex modulus $E^{*}_{\mathrm{FMM}}(\omega)$. In addition, we will derive the analytical expression of the FMM relaxation spectrum $H_{\mathrm{E,FMM}}(\tau)$. The exposition that follows differs in two main aspects from that given by Schiessel et al.[345] and Friedrich et al.[356]. Stress response functions will be obtained through integral transformation calculus, and a detailed analysis of their asymptotic behaviors (and associated characteristic timescales) will be provided. In our development, the quasi-properties *V* and *W* are considered as the fundamental material parameters rather than the equivalent, composed quantities $E_1\tau_1^{\alpha}$ and $E_2\tau_2^{\beta}$ (cf. Eq. (4.25), Figure 4.3, and Figure 4.4). We will then apply the complex modulus $E^{*}_{\mathrm{FMM}}(\omega)$ to model the behavior of LIL50–12 shown in Figure 4.2(a), discuss the FMM in relation to the ordered-structure response in block copolymers, and propose a convenient (finite) measure of the spread of the FMM terminal dispersion.

Stress response functions and relaxation spectrum of the FMM

If $\overline{L}_{\mathrm{FE},\alpha}(s)$ and $\overline{L}_{\mathrm{FE},\beta}(s)$ denote the operational retardances of the spring-pots, it follows from the combination rule, Eq. (4.34), and Eq. (4.50) that

$$\overline{L}_{\mathrm{FMM}}(s) = \overline{L}_{\mathrm{FE},\alpha}(s) + \overline{L}_{\mathrm{FE},\beta}(s) \tag{4.53}$$

and (cf. Eq. (D.56)b of Appendix D)

$$\begin{aligned}\bar{Y}_{\mathrm{FMM}}(s) &= \frac{Vs^{\alpha}}{1+\dfrac{V}{W}s^{\alpha-\beta}} \\ &= \frac{E_{\mathrm{FMM},0}\left(\tau_{\mathrm{FMM}}\cdot s\right)^{\alpha}}{1+\left(\tau_{\mathrm{FMM}}\cdot s\right)^{\alpha-\beta}}\end{aligned} \tag{4.54}$$

where

$$\tau_{\mathrm{FMM}} = \left(\frac{V}{W}\right)^{\frac{1}{\alpha-\beta}} \tag{4.55}$$

is the *relaxation time* of the model, and

$$\begin{aligned}E_{\mathrm{FMM},0} &= V\left(\tau_{\mathrm{FMM}}\right)^{-\alpha} = W\left(\tau_{\mathrm{FMM}}\right)^{-\beta} \\ &= V\left(\frac{W}{V}\right)^{\frac{\alpha}{\alpha-\beta}}\end{aligned} \tag{4.56}$$

represents a *characteristic modulus*. Substitution of Eq. (4.54) into Eq. (4.49)a and inverse Laplace transformation via Eq. (4.32) lead to the constitutive equation of the FMM in the time domain (cf. Eqs. (4.25) and (4.52))

$$\sigma(t)+\frac{V}{W}\,{}_0D_t^{\alpha-\beta}\sigma(t) = V\,{}_0D_t^{\alpha}\varepsilon(t) \qquad \text{FMM} \tag{4.57}$$

or, equivalently (cf. Eq. (D.57) of Appendix D),

$$\sigma(t)+\left(\tau_{\mathrm{FMM}}\right)^{\alpha-\beta}\,{}_0D_t^{\alpha-\beta}\sigma(t) = E_{\mathrm{FMM},0}\left(\tau_{\mathrm{FMM}}\right)^{\alpha}\,{}_0D_t^{\alpha}\varepsilon(t) \qquad \text{FMM} \tag{4.58}$$

In the rheological literature, the constitutive equation of the FMM is often written in the form of Eq. (4.58).[345,349,350,356] While it may be considered simply a matter of notational convenience, Jaishankar and McKinley[336] correctly pointed out that this formulation (Eq. (4.58)) may draw attention away from the fact that quasi-properties (V and W, for this model) are the fundamental material parameters that characterize self-similar dynamics.

Before we embark in the calculation of the relaxation spectrum and other response functions of the model, it is useful to consider the implications of Eq. (4.54). Based on the canonical representation of the stress response functions[150] (Appendix D, §D.5 and Table D.1), the definition of the viscoelastic constants[150] (Appendix D, §D.5.1), and the *limit value theorems* of the Laplace transform[150] (Appendix B, Eqs. (B.13) and (B.14)), the instantaneous response of the FMM is given by (cf. Appendix D, Eq. (D.98))

$$\begin{aligned} E_{\mathrm{g,FMM}} &= \lim_{t\to 0} E_{\mathrm{FMM}}(t) = \lim_{\omega\to\infty} E'_{\mathrm{FMM}}(\omega) \\ &= \lim_{s\to\infty} \overline{Y}_{\mathrm{FMM}}(s) \\ &= \lim_{s\to\infty} W \cdot s^{\beta} \\ &= \begin{cases} W = E_{\mathrm{FMM},0} & \text{for } \beta = 0 \\ \infty & \text{for } \beta \neq 0 \end{cases} \end{aligned} \tag{4.59}$$

while the equilibrium response is (cf. Appendix D, Eq. (D.99))

$$\begin{aligned} E_{\mathrm{eq,FMM}} &= \lim_{t\to\infty} E_{\mathrm{FMM}}(t) = \lim_{\omega\to 0} E'_{\mathrm{FMM}}(\omega) \\ &= \lim_{s\to 0} \overline{Y}_{\mathrm{FMM}}(s) \\ &= \lim_{s\to 0} V \cdot s^{\alpha} \\ &= 0 \end{aligned} \tag{4.60}$$

If a spring-pot is replaced by a spring ($\beta = 0$), then the characteristic modulus $E_{\mathrm{FMM},0}$ represents the instantaneous (i.e. glassy) modulus of the model, $E_{\mathrm{g,FMM}} = W = E_{\mathrm{FMM},0}$. For $\beta \neq 0$, the FMM exhibits *non-standard* behavior[150], i.e. a divergent instantaneous modulus (Appendix D, §D.4.2). In all cases, the FMM does not possess an equilibrium modulus $E_{\mathrm{eq,FMM}}$. The short- and long-time behavior of the FMM with $0 < \beta < \alpha \leq 1$ is thus analogous to the behavior of the PL and the CGM (cf. Eqs. (4.4) and (4.7)).

Since $E_{\text{eq,FMM}} = 0$, the analytical expression for the (extensional) relaxation spectrum $H_{\text{E,FMM}}(\tau)$ can be determined from the operational relaxance $\bar{Y}_{\text{FMM}}(s)$ via Eqs. (4.42) and (4.43). We find,

$$\begin{aligned} H_{\text{E,FMM}}(\tau) &= +\frac{1}{\pi}\lim_{y\to 0}\left[\text{Im}\ \bar{Y}_{\text{FMM}}\left(z\exp\left(+i\theta\right)\right)\right] \\ &= \frac{V}{\pi}\cdot\tau^{-\alpha}\cdot\frac{\sin\left(\pi\alpha\right)+\dfrac{V}{W}\tau^{\beta-\alpha}\sin\left(\pi\beta\right)}{1+2\dfrac{V}{W}\tau^{\beta-\alpha}\cos\left(\pi\left(\beta-\alpha\right)\right)+\left(\dfrac{V}{W}\tau^{\beta-\alpha}\right)^{2}} \end{aligned} \tag{4.61}$$

which can be written in a more compact form in terms of the dimensionless variable $z = \tau/\tau_{\text{FMM}}$ (i.e. *dimensionless time scale*),

$$\begin{aligned} H_{\text{E,FMM}}(z) &= \frac{E_{\text{FMM},0}}{\pi}\cdot z^{-\alpha}\cdot\frac{\sin\left(\pi\alpha\right)+z^{\beta-\alpha}\sin\left(\pi\beta\right)}{1+2z^{\beta-\alpha}\cos\left(\pi\left(\beta-\alpha\right)\right)+z^{2(\beta-\alpha)}} \\ &\text{with } z=\tau/\tau_{\text{FMM}} \end{aligned} \tag{4.62}$$

Not surprisingly, the series combination of two spring-pots (i.e. $0 < \beta < \alpha < 1$) gives rise to a *double power-law behavior*,

$$0<\beta<\alpha<1 \qquad H_{\text{E,FMM}}(z)\sim\begin{cases} E_{\text{FMM},0}\cdot\dfrac{\sin\left(\pi\beta\right)}{\pi}\cdot z^{-\beta} & \text{for } z\to 0 \\ E_{\text{FMM},0}\cdot\dfrac{\sin\left(\pi\alpha\right)}{\pi}\cdot z^{-\alpha} & \text{for } z\to\infty \end{cases} \tag{4.63}$$

i.e. in the short- and long-time limits, the behavior of a single spring-pot is recovered (cf. Eqs. (4.44) and (4.56)a), consistently with the results of Eqs. (4.59)c and (4.60)c. Eq. (4.62) was derived, in a slightly different form, by Friedrich and Braun[366] as a special case of the fractional Zener model subjected to simple shear.

The operational relaxance $\bar{Y}_{\mathrm{FMM}}(s)$ enables also the calculation of the (extensional) *relaxation modulus* in the complex domain[150] $\bar{E}_{\mathrm{FMM}}(s) = \bar{Y}_{\mathrm{FMM}}(s)/s$ (cf. Appendix D, Eq. (D.14)a and Table D.1), yielding

$$\frac{\bar{Y}_{\mathrm{FMM}}(s)}{s} = \bar{E}_{\mathrm{FMM}}(s) = \frac{V s^{\alpha-1}}{1+\frac{V}{W}s^{\alpha-\beta}} = \frac{W}{s^{1-\beta}\left(1+\frac{W}{V}s^{\beta-\alpha}\right)} \tag{4.64}$$

Inverse Laplace transformation using LTP (13) (Appendix B, Table B.1) gives

$$E_{\mathrm{FMM}}(t) = W \cdot t^{-\beta} \cdot E_{\alpha-\beta,1-\beta}\left(-\frac{W}{V}t^{\alpha-\beta}\right) \tag{4.65}$$

and[345]

$$E_{\mathrm{FMM}}(z) = E_{\mathrm{FMM},0} \cdot z^{-\beta} \cdot E_{\alpha-\beta,1-\beta}\left(-z^{\alpha-\beta}\right) \quad \text{with } z = t/\tau_{\mathrm{FMM}} \tag{4.66}$$

where $E_{a,b}(x)$ is the *generalized* (or two-parameter) *Mittag-Leffler function*[367-371] defined in Appendix C (§C.6), and $z = t/\tau_{\mathrm{FMM}}$ is the dimensionless time scale. With the help of Eqs. (C.19), (C.20), and (C.24–26), the asymptotic behavior of the relaxation modulus $E_{\mathrm{FMM}}(z)$ at short and long times can be established. In the parameter range $0 < \beta < \alpha < 1$, $E_{\mathrm{FMM}}(z)$ obeys

$$0 < \beta < \alpha < 1 \qquad E_{\mathrm{FMM}}(z) \sim \begin{cases} E_{\mathrm{FMM},0} \cdot \dfrac{1}{\Gamma(1-\beta)} \cdot z^{-\beta} & \text{for } z \to 0 \\ E_{\mathrm{FMM},0} \cdot \dfrac{1}{\Gamma(1-\alpha)} \cdot z^{-\alpha} & \text{for } z \to \infty \end{cases} \tag{4.67}$$

The asymptotic expansions are again equivalent to the behavior of individual fractional elements (cf. Table 4.1 and Eq. (4.56)a), and they are in agreement with Eq. (4.63). Let us now consider the special cases $0 = \beta < \alpha \leq 1$ and $0 < \beta < \alpha = 1$.

For $0 = \beta < \alpha \leq 1$, the generalized Mittag-Leffler function in Eq. (4.66) reduces to the *ordinary* (or one-parameter) *Mittag-Leffler function*[369-373,391] $E_a(x)$ defined in Appendix C (§C.5). This parameter set corresponds to a spring ($\beta = 0$) in series with either a spring-pot ($0 < \alpha < 1$) or a dashpot ($\alpha = 1$), and the limiting behavior becomes

$$0 = \beta < \alpha \leq 1 \qquad E_{\mathrm{FMM}}(z) \sim \begin{cases} E_{\mathrm{FMM},0} \cdot \exp\left(-\dfrac{z^{\alpha}}{\Gamma(1+\alpha)} \right) & \text{for } z \to 0 \\ E_{\mathrm{FMM},0} \cdot \dfrac{1}{\Gamma(1-\alpha)} \cdot z^{-\alpha} & \text{for } z \to \infty \end{cases} \tag{4.68}$$

i.e. $E_{\mathrm{FMM}}(z)$ interpolates between an initial *stretched exponential*[374,375] pattern – often referred to as the Kohlrausch–Williams–Watts (KWW) law[376-378] or the Weibull distribution[379] – and a terminal *inverse power-law decay* – often referred to as the Nutting law[315,316,318,380-382] (cf. §4.3.1) –, both of index α. As expected, setting $\beta = 0$ affects the mechanical response at short times (cf. Eqs. (4.67) and (4.68)), rendering the FMM able to deform instantaneously when subjected to a step strain, $E_{\mathrm{FMM}}(z \to 0) = E_{\mathrm{FMM},0}$. If $\alpha = 1$, the ordinary Mittag-Leffler function $E_a(x)$ reduces to the exponential function e^x,

$$0 = \beta < \alpha = 1 \qquad E_{\mathrm{FMM}}(z) = E_{\mathrm{FMM},0} \cdot \exp(-z) \tag{4.69}$$

and the relaxation behavior of the standard Maxwell model is recovered. The FMM with $0 = \beta < \alpha \leq 1$ was first studied by Koeller[342] in 1984.

Lastly, for $0 < \beta < \alpha = 1$ the FMM is equivalent to a spring-pot ($0 < \beta < 1$) in series with a dashpot ($\alpha = 1$), and the limiting behavior of $E_{\text{FMM}}(z)$ is given by

$$0 < \beta < \alpha = 1 \qquad E_{\text{FMM}}(z) \sim \begin{cases} E_{\text{FMM},0} \cdot \dfrac{1}{\Gamma(1-\beta)} \cdot z^{-\beta} & \text{for } z \to 0 \\ E_{\text{FMM},0} \cdot \dfrac{1-\beta}{\Gamma(\beta)} \cdot z^{\beta-2} & \text{for } z \to \infty \end{cases} \tag{4.70}$$

Predictably, setting $\alpha = 1$ influences the long-time asymptotic response (cf. Eqs. (4.67) and (4.70)). Indeed, this is the only parameter range of the FMM that produces steady-state flow[349,350], i.e. a finite value for the steady-state viscosity $\eta_{\text{E},0}^{\text{FMM}}$ (vide infra). Fractional calculus was first applied in the field of rheology in 1936 by Gemant[383,384]; the equation he used corresponds to the FMM with $\beta = 1/2$ and $\alpha = 1$. Expressions analogous to Eqs. (4.67) and (4.70) were derived in 1991 by Friedrich[349,350] and in 1995 by Schiessel et al.[345].

The *transient* (extensional) *viscosity* of the FMM, $\eta_{\text{E,FMM}}(t)$, can be computed directly in the time domain by integrating Eq. (4.65) (cf. Appendix D, Eq. (D.23)b and Table D.1). It is easier, however, to proceed via integral transformation calculus. The transient viscosity in the complex domain, $\overline{\eta}_{\text{E,FMM}}(s)$, follows immediately from the operational relaxance[150] (cf. Appendix D, Eq. (D.23)a and Table D.1)

$$\begin{aligned} \frac{\overline{Y}_{\text{FMM}}(s)}{s^2} = \overline{\eta}_{\text{E,FMM}}(s) &= \frac{Vs^{\alpha-2}}{1 + \dfrac{V}{W} s^{\alpha-\beta}} \\ &= \frac{W}{s^{2-\beta}\left(1 + \dfrac{W}{V} s^{\beta-\alpha}\right)} \end{aligned} \tag{4.71}$$

Inverse Laplace transformation using LTP (13) (Appendix B, Table B.1) gives

$$\eta_{\mathrm{E,FMM}}(t) = W \cdot t^{1-\beta} \cdot E_{\alpha-\beta,2-\beta}\left(-\frac{W}{V}t^{\alpha-\beta}\right) \tag{4.72}$$

and[366]

$$\begin{aligned}\eta_{\mathrm{E,FMM}}(z) &= E_{\mathrm{FMM},0}\tau_{\mathrm{FMM}} \cdot z^{1-\beta} \cdot E_{\alpha-\beta,2-\beta}\left(-z^{\alpha-\beta}\right) \\ &\text{with } z = t/\tau_{\mathrm{FMM}}\end{aligned} \tag{4.73}$$

Based on the asymptotic expansion of the generalized Mittag-Leffler function (Appendix C, Eq. (C.26)b), the long time behavior of $\eta_{\mathrm{E,FMM}}(z)$ is given by

$$\lim_{z\to\infty}\eta_{\mathrm{E,FMM}}(z) = \begin{cases} E_{\mathrm{FMM},0}\tau_{\mathrm{FMM}} = \eta_{\mathrm{E},0}^{\mathrm{FMM}} & \text{for } \alpha = 1 \\ \infty & \text{for } \alpha \neq 1 \end{cases} \tag{4.74}$$

i.e. the FMM exhibits steady-state flow only when one mechanical element is a dashpot ($\alpha = 1$).[349,350]

The *complex* (extensional) *modulus* of the FMM, $E^*_{\mathrm{FMM}}(\omega)$, is obtained from the relaxance as[150] $E^*_{\mathrm{FMM}}(\omega) = \bar{Y}_{\mathrm{FMM}}(s)\big|_{s=i\omega}$ (cf. Appendix D, Eq. (D.34)a and Table D.1),

$$\begin{aligned}\bar{Y}_{\mathrm{FMM}}(s)\big|_{s=i\omega} = E^*_{\mathrm{FMM}}(\omega) &= \frac{V(i\omega)^{\alpha}}{1+\frac{V}{W}(i\omega)^{\alpha-\beta}} \\ &= \frac{E_{\mathrm{FMM},0}\left(i\omega\tau_{\mathrm{FMM}}\right)^{\alpha}}{1+\left(i\omega\tau_{\mathrm{FMM}}\right)^{\alpha-\beta}}\end{aligned} \tag{4.75}$$

Separation of the real and imaginary parts yields

$$
\begin{aligned}
E'_{\mathrm{FMM}}(\omega) &= \frac{\left(W\omega^{\beta}\right)^{2} V\omega^{\alpha}\cos\left(\pi\alpha/2\right)+\left(V\omega^{\alpha}\right)^{2} W\omega^{\beta}\cos\left(\pi\beta/2\right)}{\left(W\omega^{\beta}\right)^{2}+\left(V\omega^{\alpha}\right)^{2}+2V\omega^{\alpha}W\omega^{\beta}\cos\left(\pi\left(\alpha-\beta\right)/2\right)} \\
&= E_{\mathrm{FMM},0}\cdot\left(\omega\tau_{\mathrm{FMM}}\right)^{\alpha}\cdot\frac{\cos\left(\pi\alpha/2\right)+\left(\omega\tau_{\mathrm{FMM}}\right)^{\alpha-\beta}\cos\left(\pi\beta/2\right)}{1+2\left(\omega\tau_{\mathrm{FMM}}\right)^{\alpha-\beta}\cos\left(\pi\left(\alpha-\beta\right)/2\right)+\left(\omega\tau_{\mathrm{FMM}}\right)^{2(\alpha-\beta)}}
\end{aligned}
\tag{4.76}
$$

$$
\begin{aligned}
E''_{\mathrm{FMM}}(\omega) &= \frac{\left(W\omega^{\beta}\right)^{2} V\omega^{\alpha}\sin\left(\pi\alpha/2\right)+\left(V\omega^{\alpha}\right)^{2} W\omega^{\beta}\sin\left(\pi\beta/2\right)}{\left(W\omega^{\beta}\right)^{2}+\left(V\omega^{\alpha}\right)^{2}+2V\omega^{\alpha}W\omega^{\beta}\cos\left(\pi\left(\alpha-\beta\right)/2\right)} \\
&= E_{\mathrm{FMM},0}\cdot\left(\omega\tau_{\mathrm{FMM}}\right)^{\alpha}\cdot\frac{\sin\left(\pi\alpha/2\right)+\left(\omega\tau_{\mathrm{FMM}}\right)^{\alpha-\beta}\sin\left(\pi\beta/2\right)}{1+2\left(\omega\tau_{\mathrm{FMM}}\right)^{\alpha-\beta}\cos\left(\pi\left(\alpha-\beta\right)/2\right)+\left(\omega\tau_{\mathrm{FMM}}\right)^{2(\alpha-\beta)}}
\end{aligned}
\tag{4.77}
$$

with

$$
\begin{aligned}
\tan\delta_{\mathrm{FMM}}(\omega) &= \frac{\left(W\omega^{\beta}\right)^{2} V\omega^{\alpha}\sin\left(\pi\alpha/2\right)+\left(V\omega^{\alpha}\right)^{2} W\omega^{\beta}\sin\left(\pi\beta/2\right)}{\left(W\omega^{\beta}\right)^{2} V\omega^{\alpha}\cos\left(\pi\alpha/2\right)+\left(V\omega^{\alpha}\right)^{2} W\omega^{\beta}\cos\left(\pi\beta/2\right)} \\
&= \frac{\sin\left(\pi\alpha/2\right)+\left(\omega\tau_{\mathrm{FMM}}\right)^{\alpha-\beta}\sin\left(\pi\beta/2\right)}{\cos\left(\pi\alpha/2\right)+\left(\omega\tau_{\mathrm{FMM}}\right)^{\alpha-\beta}\cos\left(\pi\beta/2\right)}
\end{aligned}
\tag{4.78}
$$

Notice that Eqs. (4.76) and (4.77) differ only in the numerator in terms of the trigonometric functions, cosine for the storage modulus and sine for the loss modulus. It is useful to examine the asymptotic behavior of the harmonic response functions. In the short-time limit, $\omega \to \infty$, we obtain

$$
\begin{aligned}
E'_{\mathrm{FMM}}(\omega\to\infty) &\sim W\cdot\cos\left(\pi\beta/2\right)\cdot\omega^{\beta} \\
E''_{\mathrm{FMM}}(\omega\to\infty) &\sim \begin{cases} W\cdot\sin\left(\pi\beta/2\right)\cdot\omega^{\beta} & \beta\neq 0 \\ \dfrac{W^{2}}{V}\cdot\sin\left(\pi\alpha/2\right)\cdot\dfrac{1}{\omega^{\alpha}} & \beta=0 \end{cases} \\
\tan\delta_{\mathrm{FMM}}(\omega\to\infty) &\sim \begin{cases} \tan\left(\pi\beta/2\right) & \beta\neq 0 \\ \dfrac{W}{V}\cdot\sin\left(\pi\alpha/2\right)\cdot\dfrac{1}{\omega^{\alpha}} & \beta=0 \end{cases}
\end{aligned}
\tag{4.79}
$$

whereas in the long-time limit, $\omega \to 0$,

$$
\begin{aligned}
E'_{\mathrm{FMM}}(\omega \to 0) \quad &\sim \begin{cases} V \cdot \cos\left(\pi\alpha/2\right) \cdot \omega^{\alpha} & \alpha \neq 1 \\ \dfrac{V^2}{W} \cdot \cos\left(\pi\beta/2\right) \cdot \omega^{2-\beta} & \alpha = 1 \end{cases} \\
E''_{\mathrm{FMM}}(\omega \to 0) \quad &\sim \quad V \cdot \sin\left(\pi\alpha/2\right) \cdot \omega^{\alpha} \\
\tan\delta_{\mathrm{FMM}}(\omega \to 0) &\sim \begin{cases} \tan\left(\pi\alpha/2\right) & \alpha \neq 1 \\ \dfrac{W}{V} \cdot \dfrac{1}{\cos\left(\pi\beta/2\right)} \cdot \dfrac{1}{\omega^{1-\beta}} & \alpha = 1 \end{cases}
\end{aligned}
\tag{4.80}
$$

Eqs. (4.79) and (4.80) are of course consistent with the limiting behavior of $\overline{Y}_{\mathrm{FMM}}(s)$, Eqs. (4.59)–(4.60), $H_{\mathrm{E,FMM}}(z)$, Eq. (4.63), $E_{\mathrm{FMM}}(z)$, Eqs. (4.67)–(4.70), and $\eta_{\mathrm{E,FMM}}(z)$, Eq. (4.74). Indeed, the steady-state viscosity calculated from the low-frequency response (cf. Appendix D, Eq. (D.102))

$$
\begin{aligned}
\lim_{\omega\to 0} \frac{E''_{\mathrm{FMM}}(\omega)}{\omega} &= V \sin\left(\pi\alpha/2\right) \lim_{\omega\to 0} \frac{\omega^{\alpha}}{\omega} \\
&= \begin{cases} E_{\mathrm{FMM},0}\tau_{\mathrm{FMM}} = \eta_{\mathrm{E},0}^{\mathrm{FMM}} & \text{for } \alpha = 1 \\ \infty & \text{for } \alpha \neq 1 \end{cases}
\end{aligned}
\tag{4.81}
$$

is equivalent to Eq. (4.74), and for $\{0 = \beta, \alpha = 1\}$

$$
0 = \beta < \alpha = 1 \qquad \begin{cases} E'_{\mathrm{FMM}}(\omega \to \infty) \sim W = E_{\mathrm{FMM},0} \\ E''_{\mathrm{FMM}}(\omega \to \infty) \sim \dfrac{W^2}{V} \cdot \dfrac{1}{\omega} \\ \\ E'_{\mathrm{FMM}}(\omega \to 0) \sim \dfrac{V^2}{W} \cdot \omega^2 \\ E''_{\mathrm{FMM}}(\omega \to 0) \sim V \cdot \omega \end{cases}
\tag{4.82}
$$

the single exponential relaxation is recovered (i.e. high-frequency plateau followed by liquid-like terminal behavior – cf. Appendix D, Eq. (D.109)).

We find it convenient to evaluate the harmonic responses of the FMM, $E'_{\mathrm{FMM}}(\omega)$ and $E''_{\mathrm{FMM}}(\omega)$, on the dimensionless time scale defined as $z = 1/\omega\tau_{\mathrm{FMM}}$. This provides a more compact notation and enables a direct comparison between the viscoelastic functions in the time and frequency domains. It follows from Eqs. (4.76)b–(4.78)b that

$$E'_{\mathrm{FMM}}(z) = E_{\mathrm{FMM},0} \cdot z^{-\alpha} \cdot \frac{\cos(\pi\alpha/2) + z^{\beta-\alpha}\cos(\pi\beta/2)}{1 + 2z^{\beta-\alpha}\cos(\pi(\beta-\alpha)/2) + z^{2(\beta-\alpha)}} \tag{4.83}$$

$$E''_{\mathrm{FMM}}(z) = E_{\mathrm{FMM},0} \cdot z^{-\alpha} \cdot \frac{\sin(\pi\alpha/2) + z^{\beta-\alpha}\sin(\pi\beta/2)}{1 + 2z^{\beta-\alpha}\cos(\pi(\beta-\alpha)/2) + z^{2(\beta-\alpha)}} \tag{4.84}$$

$$\tan\delta_{\mathrm{FMM}}(z) = \frac{\sin(\pi\alpha/2) + z^{\beta-\alpha}\sin(\pi\beta/2)}{\cos(\pi\alpha/2) + z^{\beta-\alpha}\cos(\pi\beta/2)} \quad \text{with } z = 1/\omega\tau_{\mathrm{FMM}} \tag{4.85}$$

In this form, the resemblance with the functional dependence of the relaxation spectrum $H_{\mathrm{E,FMM}}(z)$, Eq. (4.62), is apparent. In particular, the loss modulus $E''_{\mathrm{FMM}}(z)$ differs from $H_{\mathrm{E,FMM}}(z)$ only by the numerical prefactor π and the factor of 2 in the argument of the sine and cosine functions. This is not surprising considering that the zeroth order approximation of $H_{\mathrm{E}}(\tau)$, based on an inversion of the Stieltjes transform on the real time axis, is[150] (cf. Appendix D, Eq. (D.95))

$$H_{\mathrm{E},0}(\tau) = \frac{2}{\pi}E''(1/\tau) \tag{4.86}$$

i.e. the loss modulus is weighed more heavily in the calculation of $H_{\mathrm{E}}(\tau)$ than the storage modulus, thereby conferring a similar shape to $H_{\mathrm{E}}(\tau)$ and $E''(1/\tau)$ (cf. Figure 3.4 of Chapter 3, as well as Figures 4.2, 4.5, and 4.7).

From Eqs. (4.63), (4.67), (4.79), and (4.80), the relaxation behavior of the FMM in the parameter range $0 < \beta < \alpha < 1$ becomes clear: the viscoelastic functions ($H_{E,FMM}(z)$, $E_{FMM}(z)$, and $E'_{FMM}(z)$) first decrease with slope $-\beta$ within pseudo-plateau regions of order $E_{FMM,0}/\Gamma(\beta)$ and $E_{FMM,0}$ (vide infra), and then transition into a steeper terminal descent of slope $-\alpha$. The intersection of these limiting power-laws occurs at characteristic times and frequency (respectively, τ^*, t^*, and ω^*) that are relatively close to the relaxation time of the model, τ_{FMM}. In fact, the asymptotic behaviors for $0 < \beta < \alpha < 1$ give

$$0<\beta<\alpha<1 \qquad \begin{cases} \dfrac{\tau_{FMM}}{\tau^*} = \left(\dfrac{\sin(\pi\beta)}{\sin(\pi\alpha)}\right)^{\frac{1}{\alpha-\beta}} \\ \dfrac{\tau_{FMM}}{t^*} = \left(\dfrac{\Gamma(1-\alpha)}{\Gamma(1-\beta)}\right)^{\frac{1}{\alpha-\beta}} \\ \omega^*\cdot\tau_{FMM} = \left(\dfrac{\cos(\pi\beta/2)}{\cos(\pi\alpha/2)}\right)^{\frac{1}{\alpha-\beta}} \end{cases} \tag{4.87}$$

and these three ratios remain of order ten or less except for $\alpha \to 1$.

It is also worth mentioning that the FMM does not always possess a crossover frequency[336], i.e. the characteristic frequency ω_c at which $E'_{FMM}(\omega_c) = E''_{FMM}(\omega_c)$. By setting $\tan\delta_{FMM}(z) = 1$ in Eq. (4.85) and solving for ω_c, we obtain

$$0 \le \beta < \frac{1}{2} < \alpha \le 1 \qquad \omega_c\cdot\tau_{FMM} = \left(\frac{\cos(\pi\alpha/2)-\sin(\pi\alpha/2)}{\sin(\pi\beta/2)-\cos(\pi\beta/2)}\right)^{\frac{1}{\alpha-\beta}} \tag{4.88}$$

where the parameter range guarantees a finite, non-zero, and positive value for ω_c. Obviously, the right-hand side of Eq. (4.88) diverges if $\beta = 1/2$, becomes zero if $\alpha = 1/2$, and negative if $\beta > 1/2$ or $\alpha < 1/2$ (i.e. when the response of the model is predominantly viscous or elastic, respectively, at all frequencies). However, contrary to the idea expressed by Jaishankar and McKinley[336], lack of a crossover frequency does not imply lack of a characteristic time scale for the FMM. The relaxation time τ_{FMM} exists for any parameter range (cf. Eq. (4.55)) and identifies, through Eq. (4.87), the characteristic times and frequency at which the asymptotic behaviors of $H_{E,FMM}(z)$, $E_{FMM}(z)$, and $E'_{FMM}(z)$ intersect.

The stress response behavior of the FMM is summarized in Table 4.2.

Table 4.2. Linear viscoelastic functions for the *fractional Maxwell model* (FMM) with parameters $\{V, \alpha, W, \beta\}$ and $0 \le \beta < \alpha \le 1$. The FMM describes fractional dynamics characterized by a double power-law relaxation pattern. The shaded area indicates the premise upon which the model is built (cf. Eqs. (4.53) and (4.54)).

	Eq.
$\tau_{\mathrm{FMM}} = \left(V/W\right)^{1/(\alpha-\beta)}$	(4.55)
$E_{\mathrm{FMM},0} = V\left(\tau_{\mathrm{FMM}}\right)^{-\alpha} = W\left(\tau_{\mathrm{FMM}}\right)^{-\beta}$	(4.56)
$H_{\mathrm{E,FMM}}\left(z=\tau/\tau_{\mathrm{FMM}}\right) = \dfrac{E_{\mathrm{FMM},0}}{\pi}\cdot z^{-\alpha}\cdot\dfrac{\sin\left(\pi\alpha\right)+z^{\beta-\alpha}\sin\left(\pi\beta\right)}{1+2z^{\beta-\alpha}\cos\left(\pi\left(\beta-\alpha\right)\right)+z^{2(\beta-\alpha)}}$	(4.62)
$\bar{Y}_{\mathrm{FMM}}(s) = \dfrac{E_{\mathrm{FMM},0}\left(\tau_{\mathrm{FMM}}\cdot s\right)^{\alpha}}{1+\left(\tau_{\mathrm{FMM}}\cdot s\right)^{\alpha-\beta}}$ from $\bar{L}_{\mathrm{FMM}}(s) = \bar{L}_{\mathrm{FE},\alpha}(s) + \bar{L}_{\mathrm{FE},\beta}(s)$	(4.54)
$E_{\mathrm{FMM}}\left(z=t/\tau_{\mathrm{FMM}}\right) = E_{\mathrm{FMM},0}\cdot z^{-\beta}\cdot E_{\alpha-\beta,1-\beta}\left(-z^{\alpha-\beta}\right)$	(4.66)
$E_{\mathrm{FMM}}\left(z\to 0\right) = E_{\mathrm{g,FMM}} = \begin{cases}\infty & \beta\neq 0\\ W = E_{\mathrm{FMM},0} & \beta = 0\end{cases}$	(4.59)
$E_{\mathrm{FMM}}\left(z\to\infty\right) = E_{\mathrm{eq,FMM}} = 0$	(4.60)
$\eta_{\mathrm{E,FMM}}\left(z=t/\tau_{\mathrm{FMM}}\right) = E_{\mathrm{FMM},0}\tau_{\mathrm{FMM}}\cdot z^{1-\beta}\cdot E_{\alpha-\beta,2-\beta}\left(-z^{\alpha-\beta}\right)$	(4.73)
$\eta_{\mathrm{E,FMM}}\left(z\to\infty\right) = \eta_{\mathrm{E},0}^{\mathrm{FMM}} = \begin{cases}\infty & \alpha\neq 1\\ E_{\mathrm{FMM},0}\tau_{\mathrm{FMM}} & \alpha = 1\end{cases}$	(4.74)
$E'_{\mathrm{FMM}}\left(z=1/\omega\tau_{\mathrm{FMM}}\right) = E_{\mathrm{FMM},0}\cdot z^{-\alpha}\cdot\dfrac{\cos\left(\pi\alpha/2\right)+z^{\beta-\alpha}\cos\left(\pi\beta/2\right)}{1+2z^{\beta-\alpha}\cos\left(\pi\left(\beta-\alpha\right)/2\right)+z^{2(\beta-\alpha)}}$	(4.83)
$E''_{\mathrm{FMM}}\left(z=1/\omega\tau_{\mathrm{FMM}}\right) = E_{\mathrm{FMM},0}\cdot z^{-\alpha}\cdot\dfrac{\sin\left(\pi\alpha/2\right)+z^{\beta-\alpha}\sin\left(\pi\beta/2\right)}{1+2z^{\beta-\alpha}\cos\left(\pi\left(\beta-\alpha\right)/2\right)+z^{2(\beta-\alpha)}}$	(4.84)
$\tau_{\mathrm{FMM}} = \tau^{*}\left(\dfrac{\sin\left(\pi\beta\right)}{\sin\left(\pi\alpha\right)}\right)^{\frac{1}{\alpha-\beta}} = t^{*}\left(\dfrac{\Gamma\left(1-\alpha\right)}{\Gamma\left(1-\beta\right)}\right)^{\frac{1}{\alpha-\beta}} = \dfrac{1}{\omega^{*}}\left(\dfrac{\cos\left(\pi\beta/2\right)}{\cos\left(\pi\alpha/2\right)}\right)^{\frac{1}{\alpha-\beta}}, \beta\neq 0, \alpha\neq 1$	(4.87)
$\omega_{\mathrm{c}}\cdot\tau_{\mathrm{FMM}} = \left(\dfrac{\cos\left(\pi\alpha/2\right)-\sin\left(\pi\alpha/2\right)}{\sin\left(\pi\beta/2\right)-\cos\left(\pi\beta/2\right)}\right)^{\frac{1}{\alpha-\beta}}$ $0\le\beta<\dfrac{1}{2}<\alpha\le 1$	(4.88)

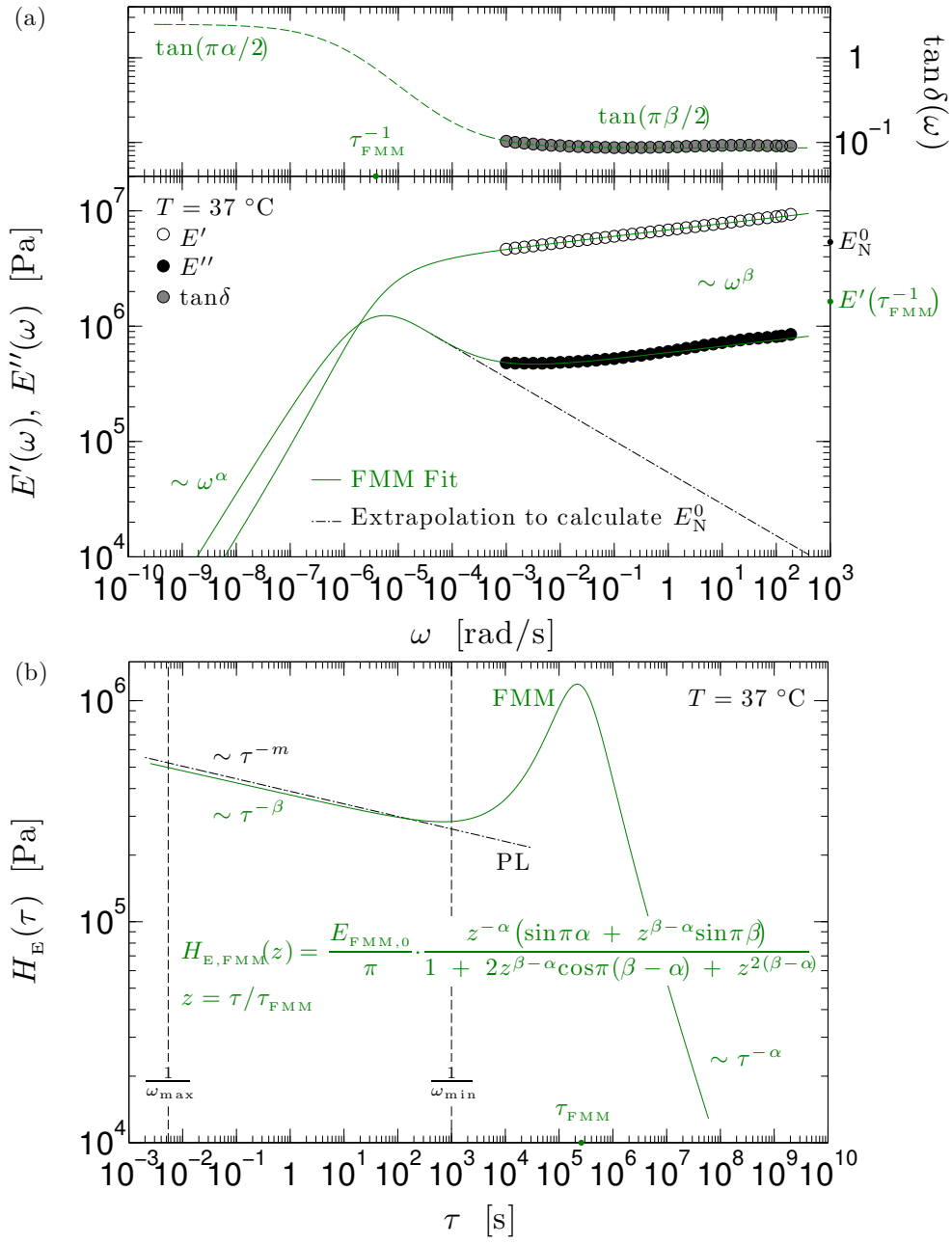

Figure 4.5. (a) Experimental data of Figure 4.2. The solid lines depict the FMM fit (Eqs. (4.76)a and (4.77)a). The dash-dot line is the power-law extrapolation (Eq. (4.102)) used to resolve the terminal loss peak. (b) FMM relaxation spectrum (solid line, Eq. (4.61)b) vs. PL relaxation spectrum (dash-dot line).

Modeling the self-similar dynamics of LIL50–12 with the FMM

As a first step towards the modeling of the low-frequency dispersion of LIL50–12 at 37 °C (Figure 4.2(a)), we fitted Eqs. (4.76)a and (4.77)a to the measured $E'(\omega)$ and $E''(\omega)$ values over the reduced frequency range 10^{-3}–1 rad/s (the implemented MATLAB® algorithm is provided in Appendix H, §H.3.4). The results are shown by solid lines in Figure 4.5(a). From these fits, the FMM parameters were determined to be $\alpha = 0.756$, $V = 43.18$ GPa·s$^{\alpha}$, $\beta = 0.055$, and $W = 6.86$ MPa·s$^{\beta}$. We then used Eq. (4.61)b to calculate the corresponding relaxation spectrum, $H_{E,FMM}(\tau)$ (Figure 4.5(b)).

Obviously, the power-law exponent β and the associated quasi-property W are very similar to the parameters of the single fractional element ($m = 0.057$, $F = 6.89$ MPa·s^{m}) responsible for the short-time self-similar dynamics. On the other hand, the series addition of a second spring-pot (with parameters α and V) provides a satisfactory description of the experimental low-frequency behavior in the range 10^{-3}–10^{-2} rad/s. At these time scales, the inceptive deviation from single power-law dynamics is clearly seen in Figure 4.5(b), where the PL relaxation spectrum is shown for comparison by the dash-dot line. Consistently with the analysis of Davies and Anderssen[153], such deviation occurs in a region of relaxation times (for $\tau > \simeq 200$ s) where the accuracy of $H_{E,PL}(\tau)$ was not guaranteed (cf. Figure 4.2(b)). Thus, the storage modulus $E'_{FMM}(\omega)$ and the relaxation spectrum $H_{E,FMM}(\tau)$ decrease with slope $-\beta$ within pseudo-plateau regions of order $E_{FMM,0} \simeq 3.47$ MPa and $E_{FMM,0}/\Gamma(\beta) \simeq 0.2$ MPa (respectively), and then transition into a steeper terminal descent of slope $-\alpha$ at time scales larger than $\tau_{FMM} \simeq 2.6 \cdot 10^5$ s. As expected, the

characteristic frequency ω^* and time τ^* at which these asymptotic power-laws intersect are within a factor of ten (on either side) of the FMM relaxation time, $1/\omega^* \simeq 0.25\tau_{\text{FMM}}$ and $\tau^* \simeq 7.3\tau_{\text{FMM}}$ (Eqs. (4.87)c,a). Furthermore, the high- and low-frequency limiting behaviors correspond (respectively) to a predominantly elastic and viscous response, i.e. the model exhibits a crossover frequency ω_c at a time scale $1/\omega_c \simeq 2\tau_{\text{FMM}}$ (Eq. (4.88)). Not surprisingly, the local maxima in the loss modulus and relaxation spectrum share similar magnitudes, $\left[E''_{\text{FMM}}(\omega)\right]^{\max} \simeq 1.24$ MPa and $\left[H_{\text{E,FMM}}(\tau)\right]^{\max} \simeq 1.19$ MPa, and time scales, $1/\omega_{E''\to\max} \simeq 0.68\tau_{\text{FMM}}$ and $\tau_{H_E\to\max} \simeq 0.85\tau_{\text{FMM}}$ (cf. Eqs. (4.62), (4.84), and (4.86)). Notice that the characteristic times $1/\omega_c$, $1/\omega_{E''\to\max}$, and $\tau_{H_E\to\max}$ are all closely approximated by the relaxation time of the model τ_{FMM}.

If the FMM relaxation pattern shown in Figure 4.5(a) were representative of the viscoelastic response of LIL50–12 at all frequencies, it would be legitimate to identify the time scale for the PLA glass-rubber transition by the locus of the loss modulus peak ($\simeq 1.8{\cdot}10^5$ s $\simeq$ 2 days). While we do expect our material to exhibit a peak in $E''(\omega)$ at low frequencies, the response of the FMM below $\omega_{E''\to\max}$ is not compatible with the behavior of LIL50–12. Following the softening of the PLA microphase, PI and PLA chains are still entangled (Appendix A, §A.2.3.I-c) and therefore a secondary pseudo-plateau region persists prior to full (terminal) stress relaxation (Appendix A, Figure A.3). Nevertheless, by capturing the response of LIL50–12 in the range 10^{-3}–10^{-2} rad/s, this simple fractional model provides an initial estimate of the PLA glass-rubber dynamics at 37 °C, and it

enables (as will be shown in §4.3.2.III-b) the application of a more complex model by which a realistic description of the low-frequency dynamics can be obtained.

FMM and ordered-structure response in block copolymers

Although inadequate to represent the behavior of entangled A–B–A TPEs across $T_{g,A}$, the FMM can accurately portray the double power-law relaxation of lamellae-[103,105,246] and cylinder-forming[108,109] isotropic A–B and A–B–A block copolymers at temperatures above the glass transition of the higher T_g block and below the order-disorder transition (ODT). In this temperature range, the transition between entanglement-dominated dynamics ($G^*(\omega) \sim (i\omega)^{\beta}$) and non-liquid-like terminal regime characteristic of the ordered state ($G^*(\omega) \sim (i\omega)^{\alpha}$) can be captured by the series arrangement of two spring-pots. This conclusion rests on a comparison between the qualitative behavior of the FMM shown in Figure 4.5(a) and, for instance, the experimental results obtained in 1990 by Rosedale and Bates[103] from a set of lamellae-forming, macroscopically non-oriented poly(ethylenepropylene)–poly(ethylethylene) (PEP–PEE) diblock copolymers. At a temperature above the T_g's of the blocks and below the ODT, the harmonic response of these systems (Figure 6 of Rosedale and Bates[103]) can be precisely mapped onto a FMM model with $\alpha = 1/2$. Similarly, isotropic samples of LIL50–12 in thermodynamic equilibrium would exhibit, for 54 °C < T < 290 °C (Experimental Section), a FMM-type response with $\alpha \approx 1/3$ (cf. Appendix A, Figure A.2).[108,109] It can also be inferred, from the asymptotic behavior of $E'_{FMM}(\omega)$ and $E''_{FMM}(\omega)$ in the terminal regime (Eqs. (4.80) and (4.82)), that the FMM is amenable to a quantitative description of the low-frequency

response across the ODT, including the effect of composition fluctuations (cf. Figure 7 of Rosedale and Bates[103]).

Commenting their results, Rosedale and Bates remarked "this ordered-structure response bears a striking resemblance to that obtained from critical gels. However, we are unable at this point to suggest a microscopic model, consistent with both a gel structure and a microphase-separated block copolymer, which recovers $G' \sim G'' \sim \omega^{0.5}$". A microscopic interpretation was put forth by Rubinstein and Obukhov[106] in 1993. Based on an exponential distribution in the number of entanglements per chain in the interpenetration zone coupled with arm retraction dynamics, they were able to successfully predict $G^*(\omega) \sim (i\omega)^{1/2}$ for randomly oriented lamellae in the strong segregation regime ($\chi N > \approx 100$)[99]. Given the mechanical equivalence between a spring-pot and hierarchical (fractal) arrays of springs and dashpots[343,344], a mesoscopic interpretation of the ordered-structure response for lamellar and cylindrical morphologies can be found in terms of the sequential relaxation of mechanical networks. As Schiessel and Blumen[385] have shown in 1995, fractal networks of springs and dashpots lead to a terminal power-law behavior $G^*(\omega) \sim (i\omega)^{\alpha}$, where $\alpha = 1–d_s/2$ and d_s is the spectral dimension of the network. For an infinite ladder structure, $d_s = 1$ and $\alpha = 1/2$; for the classical Sierpinski gasket embedded in a 2-dimensional Euclidean space, $d_s = 2\ln(3)/\ln(5)$ and $\alpha \approx 1/3$.[385] Overall, the relevance of the FMM in the context of A–B–A self-similar dynamics is evident. It is thus instructive to analyze the FMM terminal

behavior in more detail, particularly with respect to the *plateau modulus* and *spectral width*.

Plateau modulus of the FMM

As can be seen in Figure 4.5(a), the characteristic modulus $E_{\mathrm{FMM},0} \simeq 3.47$ MPa falls within the pseudo-plateau region preceding the PLA viscoelastic transition. An accurate determination of this (high-frequency) plateau modulus E_{N}^{0} is, however, no easy matter. Various methods have been published over the years to extract the value of E_{N}^{0} from the measured step or harmonic linear response. An excellent critical review of the different techniques was provided in 2006 by Liu et al.[386], and further discussion can be found in the books by Ferry[42], Dealy and Larson[36], and Graessley[45]. Here, we are interested in methods validated for linear chains with narrow molar mass distribution that are suitable for the FMM pattern shown in Figure 4.5(a). Experimentally, it is well known that the flattening of the storage modulus prior to terminal relaxation is often accompanied by a plateau or local minimum in the loss modulus and/or relaxation spectrum.[42] Hence, the simplest approach is that the plateau modulus E_{N}^{0} be determined from the value of $E'(\omega)$ at the frequency $\omega_{E''\to\min}$ where $E''(\omega)$ reaches a local minimum[35,109,386]

$$E_{\mathrm{N}}^{0} = E'\left(\omega_{E''\to\min}\right) \tag{4.89}$$

or from the value of $E'(1/\tau)$ at the relaxation time $\tau_{H_{\mathrm{E}}\to\min}$ where $H_{\mathrm{E}}(\tau)$ reaches a local minimum[36]

$$E_{\mathrm{N}}^{0} = E'\left(1/\tau_{H_{\mathrm{E}}\to\min}\right) \tag{4.90}$$

Other methods involve numerical integration over the terminal relaxation peak of either $E''(\omega)$ or $H_E(\tau)$. Based on the properties of the Fourier transform[150] (Appendix B, §B.3–4) and the canonical representation of the stress response functions[150] (Appendix D, §D.5 and Table D.1), it can be shown that (cf. Eqs. (D.50)a and (D.98)c)

$$E_g - E_{eq} = \frac{2}{\pi}\int_0^\infty \frac{E''(\omega)}{\omega}d\omega = \int_0^\infty \frac{H_E(\tau)}{\tau}d\tau \tag{4.91}$$

where E_g and E_{eq} denote, respectively, the glassy and equilibrium modulus. Eq. (4.91) can be used to integrate over a relatively isolated maximum in $E''(\omega)$ or $H_E(\tau)$, to obtain the contribution to E_g from the particular class of relaxation mechanisms it represents.[42] Applied to the terminal spectrum of viscoelastic liquids or critical gels (E_{eq} = 0), Eq. (4.91) yields the plateau modulus E_N^0 provided that the terminal peak of either $E''(\omega)$ or $H_E(\tau)$ is somehow resolved from significant overlap with high-frequency 3-D Rouse modes (cf. Chapter 3, Table 3.8 and §3.3.4.IV-d). This spectral resolution problem is sometimes addressed in an empirical manner by restricting the integration domain of Eq. (4.91) using a characteristic frequency a or relaxation time a' so that high-frequency relaxation mechanisms are not included,[42]

$$E_N^0 = \frac{2}{\pi}\int_0^a \frac{E''(\omega)}{\omega}d\omega = \int_{a'}^\infty \frac{H_E(\tau)}{\tau}d\tau \tag{4.92}$$

In line with this approach, Chompff and Prins[78] proposed letting a' be the relaxation time $\tau_{H_E\to\min}$ at which $H_E(\tau)$ reaches a local minimum in the transition zone, i.e.

$$E_{\mathrm{N}}^{0} = \int_{\tau_{H_{\mathrm{E}}\to\min}}^{\infty} \frac{H_{\mathrm{E}}(\tau)}{\tau} d\tau \tag{4.93}$$

Alternatively, the plateau modulus E_{N}^{0} can be obtained from Eq. (4.91) as[36]

$$E_{\mathrm{N}}^{0} = \frac{2}{\pi}\int_{0}^{\infty} \frac{\left[E''(\omega)\right]_{\mathrm{FP}}}{\omega} d\omega = \int_{0}^{\infty} \frac{\left[H_{\mathrm{E}}(\tau)\right]_{\mathrm{FP}}}{\tau} d\tau \tag{4.94}$$

where the subscript "FP" signifies that only contributions from the flow and plateau regions should be taken into account. Some guesswork is therefore necessary to decompose the high-frequency end of $E''(\omega)$ (short-time end of $H_{\mathrm{E}}(\tau)$) as measured experimentally and separate the portion attributed to the entanglement network contributions. This is often accomplished via a straight- or curved-line extrapolation to zero (on a logarithmic frequency/time scale) for purposes of integration. Using this technique on several monodisperse and well-entangled linear polymer species, Raju et al.[79] established a relationship between the plateau modulus E_{N}^{0} and the terminal loss modulus maximum $\left[E''(\omega)\right]^{\max}$,

$$E_{\mathrm{N}}^{0} = 3.56\left[E''(\omega)\right]^{\max} \tag{4.95}$$

where the "universal" proportionality constant 3.56 reflects the experimental observation suggesting a "universal" terminal spectrum for this class of polymers (i.e. the loss peaks seem to converge toward the same limiting shape).

We now turn our attention to the terminal dispersion exhibited by the FMM in Figure 4.5. The FMM spectrum $H_{\mathrm{E,FMM}}(\tau)$ reaches a local minimum at the relaxation time $\tau_{H_{\mathrm{E}}\to\min} \simeq 700$ s, thereby giving $E_{\mathrm{N}}^{0} \simeq 4.7$ MPa according to Eq. (4.90). On the other

hand, the simple relationship established by Raju et al.[79], Eq. (4.95), yields $E_N^0 \simeq 4.4$ MPa. We can also estimate the plateau modulus E_N^0 via differentiation and integration of the FMM viscoelastic functions (the corresponding Mathematica® routine is provided in Appendix H, §H.2.1). With the analytical expression of $H_{E,FMM}(\tau)$, Eq. (4.61), numerical integration of Eq. (4.93) gives $E_N^0 \simeq 4.7$ MPa. Notice that these values of E_N^0 are in agreement with each other and slightly larger than the characteristic modulus $E_{FMM,0}$. For a more accurate estimate of the plateau modulus, the transition contributions on the high-frequency side of the loss peak maximum must be resolved away. Consistently with the approach first illustrated by Ferry and co-workers[387,388] in 1968, we obtain an approximate "fully resolved" terminal loss peak by extrapolating to zero the linear portion of the $E''_{FMM}(\omega)$ curve that lies to the right of $\omega_{E''\to max}$. To this end, we first determine the position of the maximum ($\omega_{E''\to max}$) and inflection point ($\omega_{E''\to inflection}$) in the log $E''_{FMM}(\omega)$ vs. log ω curve. The location of the maximum follows from

$$\frac{d\log_{10} f(x)}{d\log_{10} x} = \frac{d\ln f(x)}{d\ln x} = \frac{x}{f(x)} f'(x) \tag{4.96}$$

where the prime denotes ordinary differentiation with respect to the argument. Therefore, the condition for an extremum is the same in logarithmic and linear coordinates, i.e.

$$f'(x) = 0 \tag{4.97}$$

Since

$$\frac{d^2\log_{10} f(x)}{d\log_{10} x^2} = x\cdot\ln 10\cdot\frac{\left[f(x)-xf'(x)\right]f'(x)+xf(x)f''(x)}{\left[f(x)\right]^2} \tag{4.98}$$

the condition for an inflection point in logarithmic coordinates is

$$\left[f(x)-xf'(x)\right]f'(x)+xf(x)f''(x)=0 \tag{4.99}$$

From Eq. (4.99), we find the frequency value $\omega_{E''\to\text{inflection}}$ at which the inflection on the log $E''_{\text{FMM}}(\omega)$ vs. log ω plot occurs for the FMM,

$$\frac{d^2\log_{10}E''_{\text{FMM}}(\omega)}{d\log_{10}\omega^2}=0 \qquad \text{at } \omega=\omega_{E''\to\text{inflection}}\simeq 4.1\cdot10^{-5}\,\text{rad/s} \tag{4.100}$$

and calculate the slope n at the inflection point from Eq. (4.96),

$$\left.\frac{d\log_{10}E''_{\text{FMM}}(\omega)}{d\log_{10}\omega}\right|_{\omega=\omega_{E''\to\text{inflection}}}=n\simeq -0.275 \tag{4.101}$$

This allows us to obtain the power-law extrapolation

$$\begin{aligned} E''_{\text{extrapolation}}(\omega)&=c\cdot\omega^n \qquad && \text{for } \omega\geq\omega_{E''\to\text{inflection}} \\ & && \text{with } c\simeq 53.9\ \text{kPa}\cdot\left(\text{s/rad}\right)^n \end{aligned} \tag{4.102}$$

shown by the dash-dot line in Figure 4.5(a). The "fully resolved" terminal loss peak is thus defined by

$$\left[E''(\omega)\right]_{\text{FP}}=\begin{cases} E''_{\text{FMM}}(\omega) & \text{for } \omega\leq\omega_{E''\to\text{inflection}} \\ E''_{\text{extrapolation}}(\omega) & \text{for } \omega\geq\omega_{E''\to\text{inflection}} \end{cases} \tag{4.103}$$

and numerical integration of Eq. $(4.94)_1$ leads to

$$E_{\text{N}}^0=\frac{2}{\pi}\left[\int_0^{\omega_{E''\to\text{inflection}}}\frac{E''_{\text{FMM}}(\omega)}{\omega}d\omega+\int_{\omega_{E''\to\text{inflection}}}^{\infty}\frac{E''_{\text{extrapolation}}(\omega)}{\omega}d\omega\right]\simeq 5.4\ \text{MPa} \tag{4.104}$$

This value of the plateau modulus is remarkably close to the pseudo-equilibrium modulus $E_{\text{eq}}\simeq 5.4$ MPa deduced from measurements at 0 °C (Chapter 3, Figure 3.4(a) and §3.3.4.IV-b-d-e), suggesting that the dissipative processes related to the softening of the

PLA domains at 37 °C are effectively captured by the FMM and the adopted power-law extrapolation. Accordingly, the value $E_N^0 \simeq 5.4$ MPa specifies the elastic contribution of the permanent network strands of LIL50–12 (originating from PI entanglements and glassy PLA "endlinks").

Average relaxation times and spread of the FMM terminal regime

Having determined a reliable estimate for E_N^0, we can now examine the spread, or breadth, of the FMM terminal dispersion. In analogy with the moments of the distribution of molar masses in a polymer chain, for the *terminal spectrum* of viscoelastic *liquids* (i.e. $E_{eq} = 0$ and $\eta_{E,0} < \infty$) it is always possible to define[27,45] a *number-average relaxation time* τ_n,

$$\tau_n = \frac{\eta_{E,0}}{E_N^0} \tag{4.105}$$

a *weight-average relaxation time* τ_w,

$$\tau_w = \eta_{E,0} D_{eq}^0 \tag{4.106}$$

and a *polydispersity index of relaxation times* τ_w/τ_n,

$$\frac{\tau_w}{\tau_n} = \mathrm{PDI}_{\text{terminal spectrum}} = D_{eq}^0 E_N^0 \tag{4.107}$$

where D_{eq}^0 represents the *steady-state* (extensional) *compliance* (cf. Appendix D, Eqs. (D.83), (D.97)b, (D.101), (D.123), and Table D.1). Analogous expressions hold in simple shear, where the symbols $\eta_{E,0}$, E_N^0, and D_{eq}^0 are replaced by η_0, G_N^0, and J_{eq}^0 (respectively). In terms of classical mechanical models, the steady-state compliance is a

measure of the energy stored in all the springs during steady-state flow (cf. Appendix D, Eq. (D.71) and Figure D.4(b)). The average relaxation times τ_n and τ_w thus introduced are ratios of successive moments of the relaxation spectrum (cf. Appendix D, Eqs. (D.119) and (D.120)), and it is customary to consider τ_w as a *characteristic relaxation time* for viscoelastic liquids[232,272,389]. The ratio τ_w/τ_n is a dimensionless measure of the spread of the distribution (cf. Appendix D, Eqs. (D.116) and (D.117)).[27,45] If the terminal dispersion were described by a single Maxwell model, then $\tau_w/\tau_n = 1$. Hence, the value of τ_w/τ_n measures the *deviation from a single exponential relaxation*. As opposed to the plateau modulus, the steady-state compliance is very sensitive to large-scale structural features such as molar mass distribution and long-chain branching.[45] As a result, τ_w/τ_n increases as the molar mass distribution becomes broader.[27] Shear experiments on melts and solutions of nearly monodisperse and well-entangled linear chains have shown that the product $J_{eq}^0 G_N^0$ is insensitive to both concentration and chain molar mass M, and[27,45,79]

$$J_{eq}^0 G_N^0 \approx 2.5 \qquad \text{for } Z = \frac{M}{M_e^G} >\approx 7 \qquad \text{linear polymers (exp)} \tag{4.108}$$

Eq. (4.108) is another manifestation of the "universal" character of the terminal relaxation spectrum for this class of polymeric liquids (cf. Eq. (4.95)). By contrast, the tube model proposed by Doi and Edwards[46] for an entangled, monodisperse linear polymer predicts

$$J_{eq}^0 G_N^0 = \frac{6}{5} \qquad \text{linear polymers (theory)} \tag{4.109}$$

which reflects the nearly-exponential relaxation pattern predicted by this model.

The series combination of two spring-pots always exhibits a divergent steady-state compliance,

$$\begin{aligned} D^0_{\text{eq,FMM}} &= \lim_{\omega\to 0} D'_{\text{FMM}}(\omega) \\ &= \lim_{\omega\to 0} \frac{E'_{\text{FMM}}(\omega)}{\left[E'_{\text{FMM}}(\omega)\right]^2 + \left[E''_{\text{FMM}}(\omega)\right]^2} \\ &= \begin{cases} \dfrac{1}{W} = \dfrac{1}{E_{\text{FMM},0}} & \text{for } \beta = 0,\ \alpha = 1 \text{ (MM)} \\ \infty & \text{otherwise} \end{cases} \end{aligned} \tag{4.110}$$

where $D'_{\text{FMM}}(\omega)$ denotes the storage (extensional) compliance of the FMM, and we have made use of Eq. (D.43)a, Eq. (D.101)b, and the long-time limiting behavior of the FMM storage and loss moduli, Eqs. (4.80)a-b-c (cf. Appendix D, Eq. (D.105)). Therefore, applying to the FMM the ordinary expressions for the average relaxation times and spectral width (Eqs. (4.105)–(4.107)) leads to

$$\begin{aligned} \tau_{\text{n}} &= \frac{\eta^{\text{FMM}}_{\text{E},0}}{E^0_{\text{N}}} = \begin{cases} \dfrac{E_{\text{FMM},0}}{E^0_{\text{N}}}\tau_{\text{FMM}} \approx \tau_{\text{FMM}} & \alpha = 1 \\ \infty & \alpha \neq 1 \end{cases} \\ \tau_{\text{w}} &= \eta^{\text{FMM}}_{\text{E},0} D^0_{\text{eq,FMM}} = \infty \\ \frac{\tau_{\text{w}}}{\tau_{\text{n}}} &= D^0_{\text{eq,FMM}} E^0_{\text{N}} = \infty \end{aligned} \tag{4.111}$$

i.e. only the first moment about the origin (the mean of the distribution), τ_{n}, may remain finite, in the special case of a spring-pot ($0 < \beta < 1$) in series with a dashpot ($\alpha = 1$); the second moment about the origin, $\tau_{\text{n}}\tau_{\text{w}}$, as well as the breadth of the distribution always diverge. This is, of course, the natural consequence of self-similar dynamics. We seek to devise a convenient (finite) measure of the spread of the FMM terminal dispersion.

Liquid-like linear viscoelastic behavior is easily modeled through a finite array of exponential relaxation modes, i.e. combinations of springs and dashpots equivalent to generalized Maxwell or Voigt models (Appendix D, §D.4.5). Let τ_1 be the *longest relaxation time* of the generalized Maxwell model describing the stress response of a viscoelastic liquid, i.e. $\tau_1 = \max\{\tau_n\}_{n=1}^{N}$. It is straightforward to show that[22]

$$\begin{aligned} \eta_0 &\approx G(\tau_1)\cdot\tau_1 \\ J_{eq}^0 &\approx \frac{1}{G(\tau_1)} \end{aligned} \tag{4.112}$$

therefore[22,340]

$$\tau_w \approx \tau_1 \tag{4.113}$$

If we adopt the right-hand side of the expressions in Eq. (4.112) as finite measures of the corresponding viscoelastic constants for the FMM, i.e.

$$\begin{aligned} \eta_{E,0}^{FMM} &\Rightarrow E_{FMM}(\tau_{FMM})\cdot\tau_{FMM} \\ D_{eq,FMM}^0 &\Rightarrow \frac{1}{E_{FMM}(\tau_{FMM})} \end{aligned} \tag{4.114}$$

then the FMM average relaxation times and spectral width become

$$\begin{aligned} \tau_n^{FMM} &= \frac{E_{FMM}(\tau_{FMM})}{E_N^0}\tau_{FMM} \\ \tau_w^{FMM} &= \tau_{FMM} \\ PDI^{FMM} &= \frac{E_N^0}{E_{FMM}(\tau_{FMM})} \end{aligned} \tag{4.115}$$

Eq. (4.115) can be viewed as a fractional generalization of Eqs. (4.105)–(4.107) for systems, such as microphase-segregated A–B and A–B–A block copolymers, exhibiting a double power-law relaxation behavior. Alternatively, the more easily accessible quantity

$E'_{\mathrm{FMM}}\left(1/\tau_{\mathrm{FMM}}\right)$ could be used in Eqs. (4.114)–(4.115) instead of $E_{\mathrm{FMM}}(\tau_{\mathrm{FMM}})$.[g] Notice, however, that $E'(1/t) > E(t)$ at all times[42,390] (cf. Appendix D, Eq. (D.51)).

For LIL50–12, the relaxation modulus at the relaxation time follows from Eq. (4.65), $E_{\mathrm{FMM}}(\tau_{\mathrm{FMM}}) \simeq 1.28$ MPa, and we obtain

$$\begin{aligned} \tau_{\mathrm{n}}^{\mathrm{FMM}} &\simeq 0.24\,\tau_{\mathrm{FMM}} \\ \tau_{\mathrm{w}}^{\mathrm{FMM}} &= \tau_{\mathrm{FMM}} \\ \mathrm{PDI}^{\mathrm{FMM}} &\simeq 4.2 \end{aligned} \tag{4.116}$$

Interestingly, the number-average relaxation time $\tau_{\mathrm{n}}^{\mathrm{FMM}}$ is almost identical to the characteristic time $1/\omega^*$ at which the limiting power-law behaviors of $E'_{\mathrm{FMM}}(\omega)$ intersect. As long as the frequency-dependent Poisson's ratio $\mu^*(\omega)$ can be approximated by a real constant μ over the entire time scale associated with J_{eq}^0 (D_{eq}^0) and G_{N}^0 (E_{N}^0), then[h] $J_{\mathrm{eq}}^0 G_{\mathrm{N}}^0 \simeq D_{\mathrm{eq}}^0 E_{\mathrm{N}}^0$ and the "universal" terminal spectrum expressed by Eq. (4.108) translates nearly unchanged to uniaxial extension. It is then legitimate to compare the FMM

---

[g] Numerical calculation of $E_{\mathrm{FMM}}(t)$, Eq. (4.65), is not trivial. It can be performed using either an analytical approximation, such as the Padé approximation suggested by Friedrich and Braun[366], or computational software programs, such as MATLAB® and Mathematica® (Appendix C, §C.5–6). The latest version of Mathematica is equipped with a built-in algorithm that calculates the generalized Mittag-Leffler function (Appendix H, §H.2.1).

[h] For isotropic viscoelastic materials, linear harmonic responses in shear and uniaxial extension can be interconverted through[150] $E^*(\omega) = 2[1+\mu^*(\omega)]G^*(\omega)$, which generally requires knowledge of the frequency-dependent Poisson's ratio, $\mu^*(\omega)$. However, in the glassy and equilibrium states the imaginary component of $\mu^*(\omega)$ vanishes and Poisson's ratio can be approximated by a real constant, μ (Appendix A, §A.2.3.I-a-b).[42,150] Since $J_{\mathrm{eq}}^0 \approx 1/G\left(\tau_1\right)$, $\mu^*(\omega) \simeq \mu$ implies $J_{\mathrm{eq}}^0 G_{\mathrm{N}}^0 \simeq D_{\mathrm{eq}}^0 E_{\mathrm{N}}^0$.

spectral width, $PDI^{FMM} \simeq 4.2$, with the value of about 2.5 expected for a nearly monodisperse linear polymer with $Z > \approx 7$ (recall that $Z_I \simeq 9.25$, §4.3.2.II-b, Eq. (4.18)). For nearly monodisperse linear PI homopolymers, similar to our PI block in 3,4 content and with $Z \in [20, 44]$, Gotro and Graessley[134] measured $J_{eq}^0 G_N^0 \in [2.2, 2.6]$ at 25 °C. The foregoing results are summarized in Table 4.3.

So far, we have considered the linear response of a single fractional element (FE), and of a series combination of two spring-pots (FMM). While the former yields a single power-law relaxation pattern, the latter gives rise to a double-power law behavior, i.e. viscoelastic functions undergoing a transition between an initial gradual relaxation (pseudo-plateau region) and a steeper power-law descent to full relaxation. The dual counterpart of the FMM, i.e. the parallel arrangement of two spring-pots called the *fractional Voigt model* (FVM)[345], describes relaxation to a pseudo-plateau region from a sheer power-law decay[356]. Modeling the so-called Z- or S-shaped transitions between two pseudo-plateaus requires a minimum of three fractional elements.[356] In analogy with the classical series-parallel models of springs and dashpots, fractional models of increasing complexity are usually constructed by adding to a FMM in parallel (*fractional Maxwell models*) and to a FVM in series (*fractional Voigt models*). In the next section, it will be shown how a parallel combination of the FMM with a FE can correctly extrapolate the behavior of LIL50–12 at 37 °C to lower frequencies, to predict the softening of the PLA domains and exhibit a secondary pseudo-plateau region consistent with the entanglement network of the system.

Table 4.3. FMM parameters, characteristic times and moduli obtained by modeling the self-similar dynamics of LIL50–12 at 37 °C.

Power-Law Exponents and Quasi-Properties	
$\alpha = 0.756$	$V = 43.18$ GPa·s$^{\alpha}$
$\beta = 0.055$	$W = 6.86$ MPa·s$^{\beta}$
Relaxation Time	*Characteristic Moduli* [MPa]
$\tau_{\mathrm{FMM}} \simeq 2.6 \cdot 10^5$ s	$E_{\mathrm{FMM},0} \simeq 3.47$
	$E'_{\mathrm{FMM}}\left(1/\tau_{\mathrm{FMM}}\right) \simeq 1.63$
	$E_{\mathrm{FMM}}\left(\tau_{\mathrm{FMM}}\right) \simeq 1.28$
Characteristic Times	
$1/\omega^* \simeq 0.25\tau_{\mathrm{FMM}}$	$E'_{\mathrm{FMM}}\left(\omega^*\right) \simeq 2.87$
$t^* \simeq 0.16\tau_{\mathrm{FMM}}$	$E_{\mathrm{FMM}}\left(t^*\right) \simeq 2.73$
$\tau^* \simeq 7.3\tau_{\mathrm{FMM}}$	$H_{\mathrm{E,FMM}}\left(\tau^*\right) \simeq 0.23$
$\tau_{H_{\mathrm{E}}\to\max} \simeq 0.85\tau_{\mathrm{FMM}}$	$\left[H_{\mathrm{E,FMM}}(\tau)\right]^{\max} \simeq 1.19$
$1/\omega_{E''\to\max} \simeq 0.68\tau_{\mathrm{FMM}}$	$\left[E''_{\mathrm{FMM}}(\omega)\right]^{\max} \simeq 1.24$
$1/\omega_{\mathrm{c}} \simeq 2\tau_{\mathrm{FMM}}$	$E'_{\mathrm{FMM}}\left(\omega_{\mathrm{c}}\right) = E''_{\mathrm{FMM}}\left(\omega_{\mathrm{c}}\right) \simeq 1.04$
	Plateau Modulus [MPa]
	$E_{\mathrm{N}}^0 \simeq 5.4$
Average Relaxation Times and Spectral Width	
$\tau_{\mathrm{n}}^{\mathrm{FMM}} \simeq 0.24\tau_{\mathrm{FMM}}$	
$\tau_{\mathrm{w}}^{\mathrm{FMM}} = \tau_{\mathrm{FMM}}$	
$\mathrm{PDI}^{\mathrm{FMM}} \simeq 4.2$	

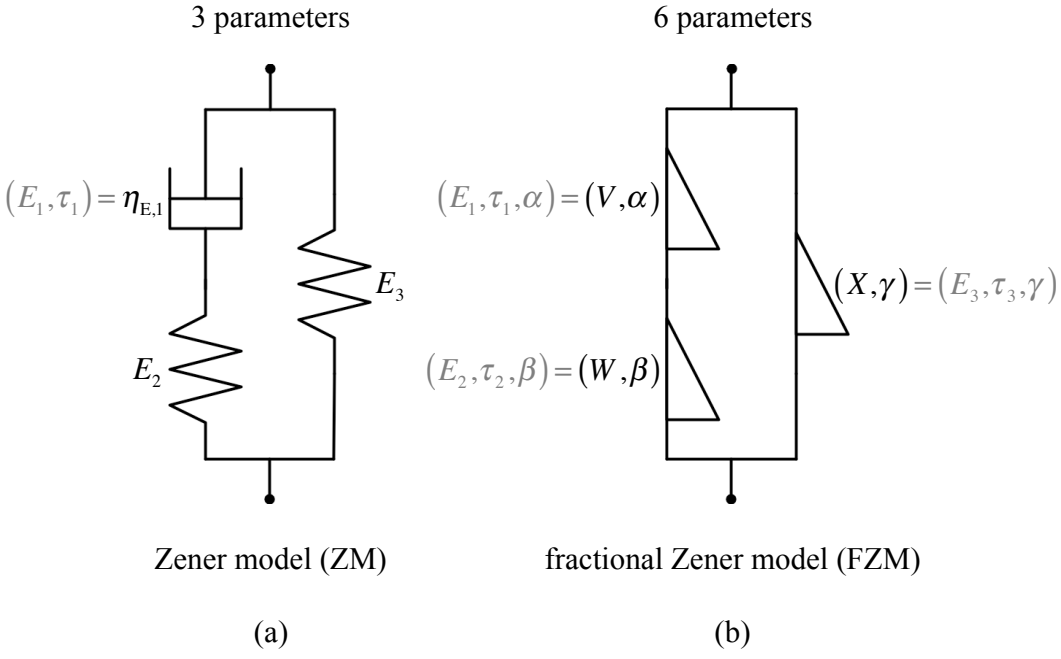

Figure 4.6. (a) The ordinary 3-parameter Maxwell model or Zener model (ZM) (cf. Appendix D, Figure D.3(a)). (b) The fractional Zener model (FZM), with $0 \le \gamma \le \beta < \alpha \le 1$.

4.3.2.III-b The fractional Zener model

The parallel combination of a Maxwell model (MM) and a spring, schematically shown in Figure 4.6(a), is commonly referred to as the *3-parameter Maxwell model*[150] or *Zener model*[359] (ZM). It represents one of the two conjugate models of the standard linear solid[150] (Appendix D, §D.4.3). Substituting two spring-pots with parameters (V, α) and (W, β) for the dashpot and spring of the MM subunit, and a spring-pot with parameters (X, γ) for the spring on the right branch of the ZM (Figure 4.6(b)), yields the *fractional*

Zener model (FZM).[345] For the FMM subunit shown in Figure 4.6(b), we take once again $\beta < \alpha$ (§4.3.2.III-a). In addition, we restrict the value of the power-law exponent γ to the closed interval $[0, \beta]$ (cf. footnote [i]). It is evident that the FZM reduces to the ordinary Zener model for $\{0 = \gamma = \beta, \alpha = 1\}$.

Mirroring the approach of the previous section, here we first concern ourselves with finding the stress response of the FZM to four unit standard strain excitations (impulse, step, slope, and harmonic – Appendix D, §D.3). Hence, we will calculate the following material functions (respectively): the operational relaxance $\overline{Y}_{\mathrm{FZM}}(s)$, the relaxation modulus $E_{\mathrm{FZM}}(t)$, the transient viscosity $\eta_{\mathrm{E,FZM}}(t)$, and the complex modulus $E^{*}_{\mathrm{FZM}}(\omega)$. The analytical expression of the FZM relaxation spectrum $H_{\mathrm{E,FZM}}(\tau)$ will also be derived. As before, stress response functions will be obtained through integral transformation calculus, and a detailed analysis of the asymptotic behavior of $E'_{\mathrm{FZM}}(\omega)$ (and associated characteristic timescales) will be provided. In our development, the quasi-properties V, W, and X are considered as the fundamental material parameters rather than the equivalent, composed quantities $E_1\tau_1^{\alpha}$, $E_2\tau_2^{\beta}$, and $E_3\tau_3^{\gamma}$ (cf. Eq. (4.25), Figure 4.3, and Figure 4.6). We will then apply the complex modulus $E^{*}_{\mathrm{FZM}}(\omega)$ to model (and extrapolate) the behavior of LIL50–12 shown in Figure 4.2(a).

Stress response functions and relaxation spectrum of the FZM

If $\overline{Y}_{\text{FMM}}(s)$ and $\overline{Y}_{\text{FE}}(s)$ denote the operational relaxances of the FMM subunit and the isolated spring-pot, it follows from the combination rule, Eq. (4.54), and Eq. (4.34) that (cf. Eq. (D.60) of Appendix D)

$$\begin{aligned}\overline{Y}_{\text{FZM}}(s) &= \overline{Y}_{\text{FMM}}(s) + \overline{Y}_{\text{FE}}(s) \\ &= \frac{Vs^{\alpha}}{1+\frac{V}{W}s^{\alpha-\beta}} + Xs^{\gamma} \\ &= \frac{E_{\text{FMM},0}\left(\tau_{\text{FMM}}\cdot s\right)^{\alpha}}{1+\left(\tau_{\text{FMM}}\cdot s\right)^{\alpha-\beta}} + E_0\left(\tau_{\text{FMM}}\cdot s\right)^{\gamma}\end{aligned} \tag{4.117}$$

where

$$\tau_{\text{FMM}} = \left(\frac{V}{W}\right)^{\frac{1}{\alpha-\beta}} \tag{4.118}$$

is the *relaxation time* of the model, while

$$\begin{aligned}E_{\text{FMM},0} &= V\left(\tau_{\text{FMM}}\right)^{-\alpha} = W\left(\tau_{\text{FMM}}\right)^{-\beta} \\ &= V\left(\frac{W}{V}\right)^{\frac{\alpha}{\alpha-\beta}}\end{aligned} \tag{4.119}$$

and

$$\begin{aligned}E_0 &= X\left(\tau_{\text{FMM}}\right)^{-\gamma} \\ &= X\left(\frac{W}{V}\right)^{\frac{\gamma}{\alpha-\beta}}\end{aligned} \tag{4.120}$$

represent *characteristic moduli*. Notice that we have assigned the subscript "FMM" to quantities, τ_{FMM} and $E_{\text{FMM},0}$, that only depend on the parameters of the FMM subunit. Such convention will be kept for the remainder of this section. Substitution of Eq. (4.117) into

Eq. (4.49)a and inverse Laplace transformation via Eq. (4.32) lead to the constitutive equation of the FZM in the time domain (cf. Eqs. (4.52) and (4.57))

$$\sigma(t)+\frac{V}{W}\,{}_0D_t^{\alpha-\beta}\sigma(t)=V\,{}_0D_t^{\alpha}\varepsilon(t)+ X\,{}_0D_t^{\gamma}\varepsilon(t)+\frac{V}{W}X\,{}_0D_t^{\alpha-\beta+\gamma}\varepsilon(t) \qquad \text{FZM} \tag{4.121}$$

or, equivalently (cf. Eq. (D.65) of Appendix D),

$$\sigma(t)+\left(\tau_{\text{FMM}}\right)^{\alpha-\beta}\,{}_0D_t^{\alpha-\beta}\sigma(t)=E_{\text{FMM},0}\left(\tau_{\text{FMM}}\right)^{\alpha}\,{}_0D_t^{\alpha}\varepsilon(t)+ E_0\left(\tau_{\text{FMM}}\right)^{\gamma}\,{}_0D_t^{\gamma}\varepsilon(t)+E_0\left(\tau_{\text{FMM}}\right)^{\alpha-\beta+\gamma}\,{}_0D_t^{\alpha-\beta+\gamma}\varepsilon(t) \qquad \text{FZM} \tag{4.122}$$

The simpler version of this FCE with $\beta = \gamma = 0$, adopted in the early investigations of Caputo and Mainardi[309] and Bagley and Torvik[286], was obtained by Tschoegl[150] in 1989 by modeling the operational relaxance with the Cole–Cole[313] matching function, Eq. (4.1) , discussed in §4.3.1. It was then derived for $\gamma = 0$ by Friedrich and Braun[366] in 1992, and extended to arbitrary parameters by Schiessel et al.[345] in 1995.

From the operational relaxance $\overline{Y}_{\text{FZM}}(s)$, Eq. (4.117), the instantaneous and equilibrium responses of the FZM can be determined (cf. §4.3.2.III-a). We obtain,

$$\begin{aligned} E_{\text{g,FZM}} &= \lim_{t\to 0} E_{\text{FZM}}(t) = \lim_{\omega\to\infty} E'_{\text{FZM}}(\omega) \\ &= \lim_{s\to\infty} \overline{Y}_{\text{FZM}}(s) \\ &= \lim_{s\to\infty}\left(W\cdot s^{\beta}+X\cdot s^{\gamma}\right) \\ &= \begin{cases} W+X=E_{\text{FMM},0}+E_0 & \text{for } \beta=\gamma=0 \\ \infty & \text{otherwise} \end{cases} \end{aligned} \tag{4.123}$$

and

$$\begin{aligned} E_{\text{eq,FZM}} &= \lim_{t\to\infty} E_{\text{FZM}}(t) = \lim_{\omega\to 0} E'_{\text{FZM}}(\omega) \\ &= \lim_{s\to 0} \overline{Y}_{\text{FZM}}(s) \\ &= \lim_{s\to 0} \left(V \cdot s^{\alpha} + X \cdot s^{\gamma} \right) \\ &= \begin{cases} X = E_0 & \text{for } \gamma = 0 \\ 0 & \text{otherwise} \end{cases} \end{aligned} \tag{4.124}$$

If two spring-pots are replaced by springs ($\beta = \gamma = 0$), then the sum of the characteristic moduli $E_{\text{FMM},0}$ and E_0 represents the instantaneous (i.e. glassy) modulus of the model, $E_{\text{g,FZM}} = W + X = E_{\text{FMM},0} + E_0$. Otherwise, the FZM exhibits non-standard behavior[150], i.e. a divergent instantaneous modulus (Appendix D, §D.4.2). On the other hand, the FZM possesses an equilibrium modulus, $E_{\text{eq,FZM}} = X = E_0$, only for the special case $\gamma = 0$. The short- and long-time behavior of the FZM with $0 < \gamma \le \beta < \alpha \le 1$ is thus analogous to the behavior of the PL, the CGM, and the FMM (cf. Eqs. (4.4), (4.7), (4.59), and (4.60)).

For $\gamma > 0$ ($E_{\text{eq,FZM}} = 0$), the analytical expression for the (extensional) relaxation spectrum $H_{\text{E,FZM}}(\tau)$ follows from the operational relaxance $\overline{Y}_{\text{FZM}}(s)$ via Eqs. (4.42) and (4.43). We find,

$$\begin{aligned} H_{\text{E,FZM}}(\tau) &= +\frac{1}{\pi} \lim_{y\to 0} \left[\text{Im } \overline{Y}_{\text{FZM}}\left(z\exp\left(+i\theta\right)\right)\right] \\ &= +\frac{1}{\pi} \lim_{y\to 0} \left[\text{Im } \overline{Y}_{\text{FMM}}\left(z\exp\left(+i\theta\right)\right)\right] + \frac{1}{\pi} \lim_{y\to 0} \left[\text{Im } \overline{Y}_{\text{FE}}\left(z\exp\left(+i\theta\right)\right)\right] \\ &= H_{\text{E,FMM}}(\tau) + X \cdot \frac{\sin(\pi\gamma)}{\pi} \cdot \tau^{-\gamma} \qquad \text{for } \gamma > 0 \end{aligned} \tag{4.125}$$

where the relaxation spectrum originating from the FMM subunit, $H_{\text{E,FMM}}(\tau)$, is given by Eq. (4.61), and the second term in Eq. (4.125)c is the contribution of the γ-spring-pot

according to Eq. (4.44). By adopting the dimensionless variable $z = \tau/\tau_{\mathrm{FMM}}$, Eq. (4.125)c becomes

$$H_{\mathrm{E,FZM}}(z) = H_{\mathrm{E,FMM}}(z) + E_0 \cdot \frac{\sin(\pi\gamma)}{\pi} \cdot z^{-\gamma} \qquad \text{for } \gamma > 0 \quad \text{with } z = \tau/\tau_{\mathrm{FMM}} \tag{4.126}$$

The simple additivity of the relaxances, Eq. (4.117)a, carries over into every stress response function of the FZM. Hence, from the equations shown in Table 4.1 and those derived in the previous section, we obtain

$$E_{\mathrm{FZM}}(t) = E_{\mathrm{FMM}}(t) + X \cdot \frac{1}{\Gamma(1-\gamma)} \cdot t^{-\gamma} \tag{4.127}$$

$$\eta_{\mathrm{E,FZM}}(t) = \eta_{\mathrm{E,FMM}}(t) + X \cdot \frac{1}{(1-\gamma)\Gamma(1-\gamma)} \cdot t^{1-\gamma} \tag{4.128}$$

$$\begin{aligned} E'_{\mathrm{FZM}}(\omega) &= E'_{\mathrm{FMM}}(\omega) + X \cdot \cos(\pi\gamma/2) \cdot \omega^{\gamma} \\ E''_{\mathrm{FZM}}(\omega) &= E''_{\mathrm{FMM}}(\omega) + X \cdot \sin(\pi\gamma/2) \cdot \omega^{\gamma} \end{aligned} \tag{4.129}$$

in the time and frequency domains, and

$$E_{\mathrm{FZM}}(z) = E_{\mathrm{FMM}}(z) + E_0 \cdot \frac{1}{\Gamma(1-\gamma)} \cdot z^{-\gamma} \quad \text{with } z = t/\tau_{\mathrm{FMM}} \tag{4.130}$$

$$\eta_{\mathrm{E,FZM}}(z) = \eta_{\mathrm{E,FMM}}(z) + E_0\tau_{\mathrm{FMM}} \cdot \frac{1}{(1-\gamma)\Gamma(1-\gamma)} \cdot z^{1-\gamma} \quad \text{with } z = t/\tau_{\mathrm{FMM}} \tag{4.131}$$

$$\begin{aligned} E'_{\mathrm{FZM}}(z) &= E'_{\mathrm{FMM}}(z) + E_0 \cdot \cos(\pi\gamma/2) \cdot z^{-\gamma} \\ E''_{\mathrm{FZM}}(z) &= E''_{\mathrm{FMM}}(z) + E_0 \cdot \sin(\pi\gamma/2) \cdot z^{-\gamma} \end{aligned} \quad \text{with } z = 1/\omega\tau_{\mathrm{FMM}} \tag{4.132}$$

on a dimensionless time scale z. Obviously, the isolated spring-pot dictates the long-time response and precludes the FZM from exhibiting a finite steady-state viscosity (cf. Eq. (D.62) of Appendix D),

$$\lim_{t\to\infty}\eta_{\mathrm{E,FZM}}(t)=\eta_{\mathrm{E},0}^{\mathrm{FZM}}\to\infty \tag{4.133}$$

Depending on the values of the parameters, the FZM may display up to three[i] time regimes of self-similar dynamics. Let us consider, for instance, the limiting behaviors of the storage modulus, $E'_{\mathrm{FZM}}(\omega)$, for power-law exponents in the range $0<\gamma\le\beta<\alpha<1$ (the special cases $0=\gamma=\beta$ and $\alpha=1$ are not relevant to the viscoelastic behavior of LIL50–12, and will be henceforward disregarded). The intersection of the asymptotic expansions of the FMM contribution to $E'_{\mathrm{FZM}}(\omega)$ defines the characteristic frequency (cf. Eq. (4.87)c)

$$\omega_{\alpha\beta}^{*}=\left(\frac{\cos(\pi\beta/2)}{\cos(\pi\alpha/2)}\right)^{\frac{1}{\alpha-\beta}}\cdot\frac{1}{\tau_{\mathrm{FMM}}} \tag{4.134}$$

For $\omega\gg\omega_{\alpha\beta}^{*}$, the behavior of the FMM subunit is dominated by the β-spring-pot, hence $E'_{\mathrm{FMM}}(\omega)\sim W\cdot\cos(\pi\beta/2)\cdot\omega^{\beta}$ (Eq. (4.79)a); for $\omega\ll\omega_{\alpha\beta}^{*}$, the α-spring-pot governs the relaxation and $E'_{\mathrm{FMM}}(\omega)\sim V\cdot\cos(\pi\alpha/2)\cdot\omega^{\alpha}$ (Eq. (4.80)a – cf. Figure 4.5). Consequently, the asymptotic expansions of $E'_{\mathrm{FZM}}(\omega)$ are

$$\omega_{\alpha\beta}^{*}\ll\omega\qquad E'_{\mathrm{FZM}}(\omega)\sim W\cdot\cos(\pi\beta/2)\cdot\omega^{\beta}+X\cdot\cos(\pi\gamma/2)\cdot\omega^{\gamma} \tag{4.135}$$

---

[i] The number of possible time regimes increases to four if $\beta<\gamma<\alpha$, a parameter range not considered here.[345]

and

$$\omega \ll \omega^*_{\alpha\beta} \qquad E'_{\mathrm{FZM}}(\omega) \sim V \cdot \cos\left(\pi\alpha/2\right) \cdot \omega^{\alpha} + X \cdot \cos\left(\pi\gamma/2\right) \cdot \omega^{\gamma} \tag{4.136}$$

which, in turn, lead to the definition of two additional characteristic frequencies,

$$\gamma \neq \beta \qquad \omega^*_{\beta\gamma} = \left(\frac{E_0}{E_{\mathrm{FMM},0}} \frac{\cos\left(\pi\gamma/2\right)}{\cos\left(\pi\beta/2\right)} \right)^{\frac{1}{\beta-\gamma}} \cdot \frac{1}{\tau_{\mathrm{FMM}}} \tag{4.137}$$

and

$$\omega^*_{\alpha\gamma} = \left(\frac{E_0}{E_{\mathrm{FMM},0}} \frac{\cos\left(\pi\gamma/2\right)}{\cos\left(\pi\alpha/2\right)} \right)^{\frac{1}{\alpha-\gamma}} \cdot \frac{1}{\tau_{\mathrm{FMM}}} \tag{4.138}$$

from the intersection of the power-laws in Eq. (4.135) and Eq. (4.136), respectively. This, of course, requires $\gamma \neq \beta$ (whereas the condition $\gamma \neq \alpha$ is assumed a priori – cf. Figure 4.6). The number of power-law regimes exhibited by the FZM depends on the extent of separation of these three timescales, i.e. it is controlled by the ratios

$$\frac{\omega^*_{\beta\gamma}}{\omega^*_{\alpha\beta}} = \left(\frac{E_0}{E_{\mathrm{FMM},0}} \right)^{\frac{1}{\beta-\gamma}} \left(\frac{\cos\left(\pi\gamma/2\right)}{\cos\left(\pi\beta/2\right)} \right)^{\frac{1}{\beta-\gamma}} \left(\frac{\cos\left(\pi\alpha/2\right)}{\cos\left(\pi\beta/2\right)} \right)^{\frac{1}{\alpha-\beta}} \tag{4.139}$$

and

$$\frac{\omega^*_{\alpha\gamma}}{\omega^*_{\alpha\beta}} = \left(\frac{E_0}{E_{\mathrm{FMM},0}} \right)^{\frac{1}{\alpha-\gamma}} \left(\frac{\cos\left(\pi\gamma/2\right)}{\cos\left(\pi\alpha/2\right)} \right)^{\frac{1}{\alpha-\gamma}} \left(\frac{\cos\left(\pi\alpha/2\right)}{\cos\left(\pi\beta/2\right)} \right)^{\frac{1}{\alpha-\beta}} \tag{4.140}$$

whose magnitudes are largely dictated by the ratio $E_0/E_{\mathrm{FMM},0}$ and, therefore, cannot vary independently from one another. In particular, for the parameter range $0 < \gamma < \beta < \alpha < 1$, we obtain

$$0 < \gamma < \beta < \alpha < 1$$

$$\begin{aligned}
&\frac{E_0}{E_{\mathrm{FMM},0}} \ll 1 \qquad E'_{\mathrm{FZM}}(\omega) \sim \begin{cases} W \cdot \cos(\pi\beta/2) \cdot \omega^{\beta} & \omega^*_{\alpha\beta} \ll \omega \\ V \cdot \cos(\pi\alpha/2) \cdot \omega^{\alpha} & \omega^*_{\alpha\gamma} \ll \omega \ll \omega^*_{\alpha\beta} \\ X \cdot \cos(\pi\gamma/2) \cdot \omega^{\gamma} & \omega \ll \omega^*_{\alpha\gamma} \end{cases} \\
&\frac{E_0}{E_{\mathrm{FMM},0}} \approx 1 \qquad E'_{\mathrm{FZM}}(\omega) \sim \begin{cases} W \cdot \cos(\pi\beta/2) \cdot \omega^{\beta} & \omega^*_{\alpha\beta} \ll \omega \\ X \cdot \cos(\pi\gamma/2) \cdot \omega^{\gamma} & \omega \ll \omega^*_{\alpha\beta} \end{cases} \\
&\frac{E_0}{E_{\mathrm{FMM},0}} \gg 1 \qquad E'_{\mathrm{FZM}}(\omega) \sim \begin{cases} W \cdot \cos(\pi\beta/2) \cdot \omega^{\beta} & \omega^*_{\beta\gamma} \ll \omega \\ X \cdot \cos(\pi\gamma/2) \cdot \omega^{\gamma} & \omega \ll \omega^*_{\beta\gamma} \end{cases}
\end{aligned} \tag{4.141}$$

and for $0 < \gamma = \beta < \alpha < 1$,

$$0 < \gamma = \beta < \alpha < 1$$

$$\begin{aligned}
&\frac{E_0}{E_{\mathrm{FMM},0}} \ll 1 \qquad E'_{\mathrm{FZM}}(\omega) \sim \begin{cases} (W+X) \cdot \cos(\pi\beta/2) \cdot \omega^{\beta} & \omega^*_{\alpha\beta} \ll \omega \\ V \cdot \cos(\pi\alpha/2) \cdot \omega^{\alpha} & \omega^*_{\alpha\gamma} \ll \omega \ll \omega^*_{\alpha\beta} \\ X \cdot \cos(\pi\beta/2) \cdot \omega^{\beta} & \omega \ll \omega^*_{\alpha\gamma} \end{cases} \\
&\text{otherwise} \qquad E'_{\mathrm{FZM}}(\omega) \sim \begin{cases} (W+X) \cdot \cos(\pi\beta/2) \cdot \omega^{\beta} & \omega^*_{\alpha\beta} \ll \omega \\ X \cdot \cos(\pi\beta/2) \cdot \omega^{\beta} & \omega \ll \omega^*_{\alpha\beta} \end{cases}
\end{aligned} \tag{4.142}$$

i.e. the FZM exhibits three distinct (fully developed) time regimes of power-law behavior only if $E_0/E_{\mathrm{FMM},0} \ll 1$. In this case, the characteristic frequencies $\omega^*_{\alpha\gamma}$ and $\omega^*_{\alpha\beta}$ are widely separated and an intermediate power-law regime $E'_{\mathrm{FZM}}(\omega) \sim \omega^{\alpha}$ emerges between the two pseudo-plateau regions. Analogous analyses can be carried out for the relaxation spectrum $H_{\mathrm{E,FZM}}(\tau)$ and relaxation modulus $E_{\mathrm{FZM}}(t)$, yielding similar results.

The stress response behavior of the FZM is summarized in Table 4.4.

Table 4.4. Linear viscoelastic functions for the *fractional Zener model* (FZM) with parameters $\{V, \alpha, W, \beta, X, \gamma\}$ and $0 \le \gamma \le \beta < \alpha \le 1$. The FZM describes the so-called Z- or S-shaped transitions between two pseudo-plateaus, and exhibits three distinct (fully developed) power-law regimes if $E_0/E_{\mathrm{FMM},0} \ll 1$. The shaded area indicates the premise upon which the model is built (cf. Eq. (4.117)).

$$\tau_{\mathrm{FMM}} = \left(V/W\right)^{1/(\alpha-\beta)}$$

$$E_{\mathrm{FMM},0} = V\left(\tau_{\mathrm{FMM}}\right)^{-\alpha} = W\left(\tau_{\mathrm{FMM}}\right)^{-\beta} \qquad E_0 = X\left(\tau_{\mathrm{FMM}}\right)^{-\gamma}$$

$$H_{\mathrm{E,FZM}}\left(z=\tau/\tau_{\mathrm{FMM}}\right) = \frac{E_{\mathrm{FMM},0}}{\pi}\cdot z^{-\alpha}\cdot\frac{\sin\left(\pi\alpha\right)+z^{\beta-\alpha}\sin\left(\pi\beta\right)}{1+2z^{\beta-\alpha}\cos\left(\pi\left(\beta-\alpha\right)\right)+z^{2(\beta-\alpha)}} + E_0\cdot\frac{\sin\left(\pi\gamma\right)}{\pi}\cdot z^{-\gamma}$$

$$\overline{Y}_{\mathrm{FZM}}(s) = \overline{Y}_{\mathrm{FMM}}(s) + \overline{Y}_{\mathrm{FE}}(s) = \frac{E_{\mathrm{FMM},0}\left(\tau_{\mathrm{FMM}}\cdot s\right)^{\alpha}}{1+\left(\tau_{\mathrm{FMM}}\cdot s\right)^{\alpha-\beta}} + E_0\left(\tau_{\mathrm{FMM}}\cdot s\right)^{\gamma}$$

$$E_{\mathrm{FZM}}\left(z=t/\tau_{\mathrm{FMM}}\right) = E_{\mathrm{FMM},0}\cdot z^{-\beta}\cdot E_{\alpha-\beta,1-\beta}\left(-z^{\alpha-\beta}\right) + E_0\cdot\frac{1}{\Gamma\left(1-\gamma\right)}\cdot z^{-\gamma}$$

$$E_{\mathrm{FZM}}\left(z\to 0\right) = E_{\mathrm{g,FZM}} = \begin{cases} W+X = E_{\mathrm{FMM},0}+E_0 & \text{for } \beta=\gamma=0 \\ \infty & \text{otherwise} \end{cases}$$

$$E_{\mathrm{FZM}}\left(z\to \infty\right) = E_{\mathrm{eq,FZM}} = \begin{cases} X = E_0 & \text{for } \gamma = 0 \\ 0 & \text{otherwise} \end{cases}$$

$$\eta_{\mathrm{E,FZM}}\left(z=t/\tau_{\mathrm{FMM}}\right) = E_{\mathrm{FMM},0}\tau_{\mathrm{FMM}}\cdot z^{1-\beta}\cdot E_{\alpha-\beta,2-\beta}\left(-z^{\alpha-\beta}\right) + E_0\tau_{\mathrm{FMM}}\cdot\frac{1}{\left(1-\gamma\right)\Gamma\left(1-\gamma\right)}\cdot z^{1-\gamma}$$

$$\eta_{\mathrm{E,FZM}}\left(z\to\infty\right) = \eta_{\mathrm{E},0}^{\mathrm{FZM}} \to \infty$$

$$E'_{\mathrm{FZM}}\left(z=1/\omega\tau_{\mathrm{FMM}}\right) = E_{\mathrm{FMM},0}\cdot z^{-\alpha}\cdot\frac{\cos\left(\pi\alpha/2\right)+z^{\beta-\alpha}\cos\left(\pi\beta/2\right)}{1+2z^{\beta-\alpha}\cos\left(\pi\left(\beta-\alpha\right)/2\right)+z^{2(\beta-\alpha)}} + E_0\cdot\cos\left(\pi\gamma/2\right)\cdot z^{-\gamma}$$

$$E''_{\mathrm{FZM}}\left(z=1/\omega\tau_{\mathrm{FMM}}\right) = E_{\mathrm{FMM},0}\cdot z^{-\alpha}\cdot\frac{\sin\left(\pi\alpha/2\right)+z^{\beta-\alpha}\sin\left(\pi\beta/2\right)}{1+2z^{\beta-\alpha}\cos\left(\pi\left(\beta-\alpha\right)/2\right)+z^{2(\beta-\alpha)}} + E_0\cdot\sin\left(\pi\gamma/2\right)\cdot z^{-\gamma}$$

$$\omega^*_{\alpha\beta} = \left(\frac{\cos\left(\pi\beta/2\right)}{\cos\left(\pi\alpha/2\right)}\right)^{\frac{1}{\alpha-\beta}}\cdot\frac{1}{\tau_{\mathrm{FMM}}} \qquad \omega^*_{\alpha\gamma} = \left(\frac{E_0}{E_{\mathrm{FMM},0}}\frac{\cos\left(\pi\gamma/2\right)}{\cos\left(\pi\alpha/2\right)}\right)^{\frac{1}{\alpha-\gamma}}\cdot\frac{1}{\tau_{\mathrm{FMM}}}$$

$$\omega^*_{\beta\gamma} = \left(\frac{E_0}{E_{\mathrm{FMM},0}}\frac{\cos\left(\pi\gamma/2\right)}{\cos\left(\pi\beta/2\right)}\right)^{\frac{1}{\beta-\gamma}}\cdot\frac{1}{\tau_{\mathrm{FMM}}} \qquad \gamma\neq\beta$$

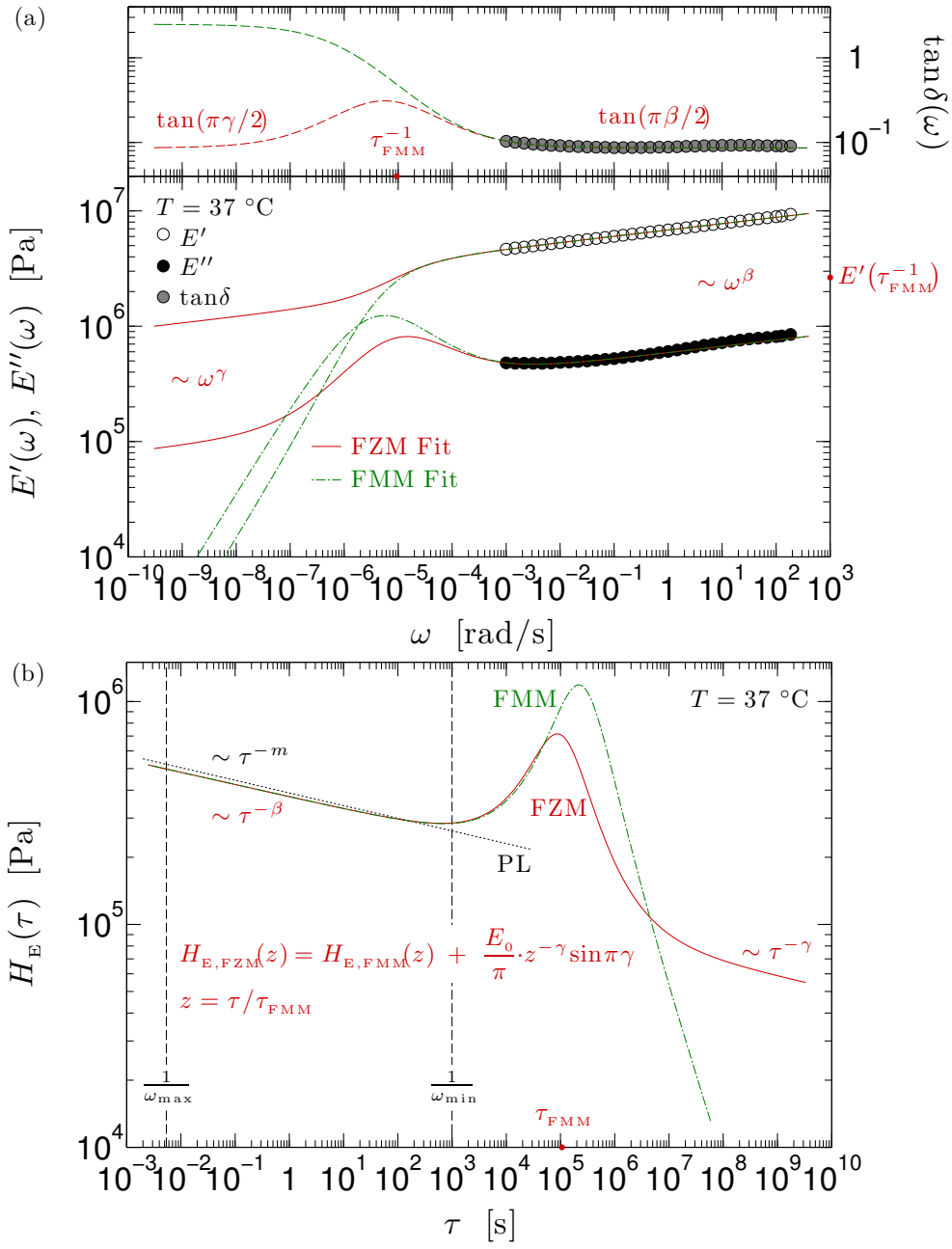

Figure 4.7. (a) Experimental data of Figure 4.2. The solid lines depict the constrained FZM fit (Eqs. (4.129), (4.144), and (4.145) – cf. Figure 5.6). The FMM fit of Figure 4.5 is shown for comparison by the dash-dot lines. (b) FZM relaxation spectrum (solid line, Eq. (4.125)c) vs. FMM relaxation spectrum (dash-dot line) and PL relaxation spectrum (dotted line).

Modeling the self-similar dynamics of LIL50–12 with the FZM

From the analysis of the asymptotic behavior of $E'_{\mathrm{FZM}}(\omega)$, Eqs. (4.141)–(4.142), it is clear that the experimental data shown in Figure 4.2(a) contain no information about the power-law exponent γ. They cover the high-frequency pseudo-plateau region dominated by the β-spring-pot, and partially embrace the low-frequency response concealing clues about the PLA glass-rubber transition (related to the intermediate power-law regime governed by the α-spring-pot). It is reasonable, however, to assume that the high- and low-frequency pseudo-plateaus be rather similar in slope. For present purposes, we therefore take $\gamma = \beta$. This approximation is also corroborated by the results of isochronal temperature ramp experiments shown in Figure A.3 of Appendix A.

A somewhat similar state of play holds for the quasi-property X of the γ-spring-pot. For the parameter range $0 < \gamma = \beta < \alpha < 1$, it follows from Eq. (4.142) that the high- and low-frequency pseudo-plateau regions are modeled, respectively, by

$$\begin{aligned} E'_{\mathrm{FZM}}(\omega) &\sim (W+X)\cdot\cos(\pi\beta/2)\cdot\omega^{\beta} && \omega^{*}_{\alpha\beta} \ll \omega \\ E'_{\mathrm{FZM}}(\omega) &\sim \quad X \ \cdot\cos(\pi\beta/2)\cdot\omega^{\beta} && \omega \ll \min\left\{\omega^{*}_{\alpha\gamma}, \omega^{*}_{\alpha\beta}\right\} \end{aligned} \tag{4.143}$$

Although the experimental data of the storage modulus are oblivious to the secondary pseudo-plateau following the softening of the PLA microphase (Eq. (4.143)b), information about the latter can be inferred from the topological structure of the system. After the PLA domains have lost their glass-like consistency (hence, their ability to act as space-filling physical endlinks for the PI chains), topological constraints persist in both microphases. Nonetheless, since the PLA chains are only slightly entangled ($M_{\mathrm{n}}/M_{\mathrm{C}} \approx 1.4$

and $Z \approx 3.7$) and amount to about 25% of the system volume (Experimental Section), the elastic response of the network is largely dictated by the entangled PI-rich matrix. To a good approximation, the secondary pseudo-plateau modulus of LIL50–12 thus originates from the extensional plateau modulus of undiluted 1,4-PI at 37 °C, $E^0_{\mathrm{N,PI}} \simeq 1$ MPa (Appendix A, Figure A.3 and §A.2.3.I-c). We may then calculate the quasi-property X as

$$X = \frac{E^0_{\mathrm{N,PI}} - V \cdot \cos\left(\pi\alpha/2\right) \cdot \omega_{\mathrm{L}}^{\alpha}}{\cos\left(\pi\beta/2\right) \cdot \omega_{\mathrm{L}}^{\beta}} \qquad \text{with } \omega_{\mathrm{L}} \ll \min\left\{\omega^*_{\alpha\gamma}, \omega^*_{\alpha\beta}\right\} \tag{4.144}$$

i.e. by including in Eq. (4.143)b the α-term of the asymptotic expansion from Eq. (4.136), and setting $E'_{\mathrm{FZM}}(\omega) = E^0_{\mathrm{N,PI}}$ for a sufficiently low frequency $\omega = \omega_{\mathrm{L}}$. The value of ω_{L} is not arbitrary. In fact, the quasi-property X obtained from Eq. (4.144) must also satisfy the requirement imposed by Eq. (4.143)a which, combined with the results of the FMM fit (Table 4.3), translates into

$$W + X = 6.86 \text{ MPa} \cdot \text{s}^{\beta} \tag{4.145}$$

By examining the asymptotic behavior of the FZM, taking into account the structure of the entanglement network, and leaning on the previous FMM modeling, we are therefore able to connect the parameters of the γ-spring-pot to the viscoelastic response of our system. Furthermore, consistency with the results of the previous section requires $\beta = 0.055$ and $\alpha \approx 0.7$, i.e. the FMM and FZM responses must coincide over the experimental frequency range and for frequencies leading up to the PLA glass-rubber transition.

With these considerations in mind, we modeled and extrapolated to lower frequencies the self-similar dynamics of LIL50–12 at 37 °C (Figure 4.2(a)) with a FZM containing

five parameters, $\{V, \alpha, W, \beta, X\}$. We fitted Eqs. (4.129)a and (4.129)b to the measured $E'(\omega)$ and $E''(\omega)$ values over the reduced frequency range 10^{-3}–1 rad/s and applied, at each iteration, the restraints of Eqs. (4.144) and (4.145). The results are shown by solid lines in Figure 4.7(a). From these fits, we obtained $\omega_L \simeq 3{\cdot}10^{-10}$ rad/s and the FZM parameters were determined to be $\alpha = 0.746$, $V = 10.50$ GPa·s$^{\alpha}$, $\beta = \gamma = 0.055$, $W = 3.53$ MPa·s$^{\beta}$, and $X = 3.33$ MPa·s$^{\gamma}$ (cf. Chapter 5, Figure 5.6). We then used Eq. (4.125)c to calculate the corresponding relaxation spectrum, $H_{E,FZM}(\tau)$ (Figure 4.7(b)).

The fractional modeling is satisfactory. While the storage modulus $E'_{FZM}(\omega)$ and the relaxation spectrum $H_{E,FZM}(\tau)$ decrease with slope $-\beta$ within high-frequency pseudo-plateau regions of order $(E_{FMM,0} + E_0) \simeq 3.64$ MPa and $(E_{FMM,0} + E_0)/\Gamma(\beta) \simeq 0.2$ MPa (respectively), the α-spring-pot is able to capture the experimental low-frequency behavior in the range 10^{-3}–10^{-2} rad/s. At time scales larger than $\tau_{FMM} \simeq 1.1{\cdot}10^5$ s, the parallel addition of the γ-spring-pot allows the FZM to exhibit a long-time rubbery response compatible with the entanglement network of LIL50–12, and the behavior remains predominantly elastic at all frequencies (cf. Figure A.3 of Appendix A). As expected, the characteristic frequencies $\omega^*_{\alpha\beta}$ and $\omega^*_{\alpha\gamma}$ are within a factor of ten of the relaxation time, $1/\omega^*_{\alpha\beta} \simeq 0.26\tau_{FMM}$ and $1/\omega^*_{\alpha\gamma} \simeq 0.28\tau_{FMM}$ (Eqs. (4.134) and (4.138)). They are, however, almost identical, $\omega^*_{\alpha\gamma}/\omega^*_{\alpha\beta} \simeq 0.92$ – owing to the relative magnitude of the characteristic moduli, $E_0/E_{FMM,0} \simeq 0.95$ (Eq. (4.140)) –, and a clear power-law regime $E'_{FZM}(\omega) \sim \omega^{\alpha}$ between the two pseudo-plateaus is absent (cf. Eq. (4.142)). Once

again, the local maxima in the loss modulus and relaxation spectrum share similar magnitudes, $\left[E''_{\mathrm{FZM}}(\omega)\right]^{\max} \simeq 0.81$ MPa and $\left[H_{\mathrm{E,FZM}}(\tau)\right]^{\max} \simeq 0.72$ MPa, and time scales, $1/\omega_{E''\to\max} \simeq 0.63\tau_{\mathrm{FMM}}$ and $\tau_{H_{\mathrm{E}}\to\max} \simeq 0.82\tau_{\mathrm{FMM}}$ (cf. Eq. (4.86) and Table 4.4). These results are summarized in Table 4.5.

Since the FZM relaxation pattern shown in Figure 4.7(a) is representative of the viscoelastic response of LIL50–12 at all frequencies, we can legitimately identify the time scale for the PLA glass-rubber transition by the locus of the loss modulus peak ($\simeq 6.7{\cdot}10^4$ s $\simeq$ 19 h). If PLA chains pullout from PLA domains is the dominant mechanism responsible for the decrease in the storage modulus at large strains, we can thus explain the seemingly frequency independence of the critical strain shown in Figure 4.1, and expect an increased rate of disruption of network junctions only at frequencies in the neighborhood of $1.5{\cdot}10^{-5}$ rad/s. On the other hand, if the strain-induced softening of network junctions is caused by slippage of PI entanglements, a frequency-dependent critical strain would be observed only at frequencies well above those accessible experimentally (cf. §5.3.3.II-d). Notice that the above estimate of the PLA segmental relaxation time is not too far off from the FMM result. Application of the FZM, however, allows us to obtain a realistic description of the LIL50–12 self-similar dynamics at 37 °C over a frequency range ($\simeq$ 12 decades) much broader than the experimental window ($\simeq$ 5 decades) and not accessible via time-temperature superposition (§4.3.2.I).

It would be interesting to study the shift behavior of glassy PLA and, with the theoretical framework developed by Fesko and Tschoegl[127-129] for thermo-rheological

complex materials, obtain an experimental master curve of LIL50–12 at 37 °C to be compared with the FZM extrapolation in Figure 4.7(a).

Table 4.5. FZM parameters, characteristic times and moduli obtained by modeling the self-similar dynamics of LIL50–12 at 37 °C.

Power-Law Exponents and Quasi-Properties	
$\alpha = 0.746$	$V = 10.50$ GPa·s$^{\alpha}$
$\beta = 0.055$	$W = 3.53$ MPa·s$^{\beta}$
$\gamma = \beta$	$X = 3.33$ MPa·s$^{\gamma}$
Relaxation Time	*Characteristic Moduli* [MPa]
$\tau_{\mathrm{FMM}} \simeq 1.1 \cdot 10^5$ s	$E_{\mathrm{FMM},0} \simeq 1.87$
	$E_0 \simeq 1.77$
	$E'_{\mathrm{FZM}}\left(1/\tau_{\mathrm{FMM}}\right) \simeq 2.65$
	$E_{\mathrm{FZM}}\left(\tau_{\mathrm{FMM}}\right) \simeq 2.40$
Characteristic Times	
$1/\omega^*_{\alpha\beta} \simeq 0.26\tau_{\mathrm{FMM}}$	$E'_{\mathrm{FZM}}\left(\omega^*_{\alpha\beta}\right) \simeq 3.43$
$1/\omega^*_{\alpha\gamma} \simeq 0.28\tau_{\mathrm{FMM}}$	$E'_{\mathrm{FZM}}\left(\omega^*_{\alpha\gamma}\right) \simeq 3.38$
$\omega^*_{\alpha\gamma}/\omega^*_{\alpha\beta} \simeq 0.92$	
$\tau_{H_{\mathrm{E}}\to\max} \simeq 0.82\tau_{\mathrm{FMM}}$	$\left[H_{\mathrm{E,FZM}}(\tau)\right]^{\max} \simeq 0.72$
$1/\omega_{E''\to\max} \simeq 0.63\tau_{\mathrm{FMM}}$	$\left[E''_{\mathrm{FZM}}(\omega)\right]^{\max} \simeq 0.81$

4.4 Conclusions

At temperatures relevant for end-use applications (i.e. below the glass transition of the hard phase), A–B–A thermoplastic elastomers (TPEs) frequently exhibit a broad power-law linear viscoelastic response (large correlation length) regardless of the degree and perfection of microstructural order (both short- and long-range).[110-113] Because of the nature of the physical endlinks (hard phase domains) and likelihood of partial segregation (stemming from either lack of thermodynamic equilibrium or equilibrium self-assembly in the intermediate segregation regime), such systems may be regarded to as filled elastomeric networks[92,110,114] with entangled dangling structures. Literature studies[110-113], however, lack any attempt to relate the observed power-law exponents to molecular structure and chain mobility of the B block.

In an effort to advance the current understanding of block copolymer self-similar dynamics, we investigated the linear behavior of a monodisperse, compositionally symmetric (f_A = 0.25, at 25 °C), microphase-segregated ($T_{ODT,SCFT} \simeq$ 290 °C) triblock copolymer (Chapter 3, §3.3.1). Considered in their respective melts, both the A and the B blocks were entangled ($M_n/M_C \approx$ 1.4 and 4), although to a different degree ($Z \approx$ 3.7 and 9.8 – Chapter 3, §3.3.2.III). Despite the strong driving force towards segregation ($\chi\hat{N} \simeq 436$, at 25 °C – Chapter 3, §3.3.1), sample preparation and the inherent slow diffusivity of the long B blocks hindered the attainment of an equilibrium morphological state, thereby creating a kinetically trapped (metastable) microstructure with irregularly shaped A microdomains lacking periodicity and long-range order (Appendix A, §A.2.1).

Any potential and spontaneous change of the microstructure towards a lower free energy state had only a minor impact (if any) on the measured viscoelastic properties of our triblock (Chapter 3, §3.3.4.I).

The linear response was measured in small-amplitude oscillatory (uniaxial) extension (§4.2.2), at a service temperature ($T_{g,B} < T < T_{g,A}$) approaching the T_g of the endblock, where the hard A domains began to behave (at low frequencies) as thermo-reversible physical endlinks (§4.3.1 and §4.3.2.I). Testing specimens with similar orientation of microdomains were prepared by compression molding (Chapter 3, §3.2.3), to investigate rheological properties of the thermoplastic elastomer under practical conditions[92,93]. The analysis herein is independent from the specific choice of the constituent blocks, and relevant at large deformations as well (cf. Chapter 5).

The material exhibited a critical-gel-like response that we associated with star-like motion of entangled dangling structures originating either from single-free-end-type midblocks or from diblock impurities, coupled with augmented motional freedom of the B block ends at the B/A interfaces. Such collective microdomain dynamics was first modeled via a power-law distribution of relaxation times[150] (PL), as derived from the wedge distribution proposed in 1952 by Tobolsky[267,268] to describe the glass-rubber viscoelastic transition of polyisobutylene (§4.3.2.II and Appendix E). The power-law relaxation spectrum matched the observed viscoelastic behavior over most of the experimental frequency window.

At timescales comparable to the path equilibration time[35,36,44-46] of the midblock, the domains of the A microphase behaved as non-deformable inert filler particles (§4.3.2.II-b). This allowed us to take advantage of the model developed in Chapter 3 to describe the linear elastic behavior of A–B–A TPEs with glassy PLA domains (§3.3.4.IV-e), and therefore to relate the measured power-law exponent m to molecular parameters (§4.3.2.II-c). In particular, a simple relation was established between m and the average number of tube segments per entangled B chain, $Z_B^{2m} = 5/4$, which satisfies the requirement of the power-law spectrum that m lie between 0 and 1. The agreement between the theoretical prediction (based merely on 1-D Rouse dynamics) and the value found from the PL fit was remarkable (§4.3.2.II-c). This result deserved further investigation, but it was beyond the scope of this report. It would be interesting to test the accuracy of our equation for other well-entangled A–B–A systems at temperatures close to the T_g of A, especially those with a large fraction of unsegregated chains. Nevertheless, this first attempt at explaining the observed power-law exponent based on molecular structure can offer some guidance in the design of complex TPE-based materials that can mimic a specific self-similar behavior (§4.3.2.II-c).

Understanding the measured material parameters inherently led to fractional calculus[341] and to the concept of quasi-properties[318], which are intimately related to the stochastic behavior on a microscopic level[251,252,261,285] (§4.3.2.II-d and Appendix F). Through integral transformation calculus[150] (Appendix B), we showed that the simplified version of the wedge distribution of relaxation times[150] (PL), Chambon–Winter's critical gel model[289-292]

(CGM), and the mechanical behavior of a fractional element[342] (FE) are analogous representations of fractional dynamics characterized by a single power-law regime. Indeed, if P denotes the quasi-property that originates from the power-law relaxation spectrum, S is Chambon–Winter's gel strength, and F is the quasi-property associated with a spring-pot[342], they are related by $F/\Gamma(1-m) = P \cdot \Gamma(1+m) = S$ (Eq. (4.45)). Therefore, all the material response functions for these basic models depend on the corresponding quasi-property and a numerical coefficient containing m and/or its gamma-function-related values (Table 4.1).

Owing to the onset of dissipative processes associated with the glass transition of the A domains, the description of the A–B–A self-similar behavior through a single power-law relaxation pattern became inadequate at low frequencies (§4.3.2.II-a). We thus turned to fractional differential versions of classical series-parallel models: the fractional Maxwell model[345] (FMM – §4.3.2.III-a), and the fractional Zener model[345] (FZM – §4.3.2.III-b). Stress response functions and relaxation spectra were obtained through integral transformation calculus, and a detailed analysis of their asymptotic behaviors (and associated characteristic timescales) was performed (Tables 4.2 and 4.4).

Although inadequate to represent the behavior of entangled A–B–A TPEs across $T_{g,A}$, the FMM can accurately portray the double power-law relaxation of lamellae-[103,105,246] and cylinder-forming[108,109] isotropic A–B and A–B–A block copolymers at temperatures above the glass transition of the higher T_g block and below the order-disorder transition (ODT). Furthermore, the FMM is amenable to a quantitative description of the low-

frequency response across the ODT, including the effect of composition fluctuations. A mesoscopic interpretation of the ordered-structure response for lamellar and cylindrical morphologies was discussed in terms of the sequential relaxation of mechanical networks[385] (an infinite ladder structure, and the classical Sierpinski gasket – §4.3.2.III-a). We also devised a convenient (finite) measure of the spread of the FMM terminal dispersion for systems, such as microphase-segregated A–B and A–B–A block copolymers, exhibiting a double power-law relaxation behavior (§4.3.2.III-a).

The measured low-frequency response, originating from the incipient glass transition of the A domains, was exploited and extrapolated to lower frequencies via a sequential application of the FMM and the FZM. The combination of dynamic measurements performed at exceedingly small frequencies and fractional calculus thus allowed us to estimate the dynamics of the A block glass-rubber transition, and a secondary pseudo-plateau region consistent with the entanglement network of the system (§4.3.2.III-b). With only a few, physically meaningful material parameters, we obtained a realistic description of the A–B–A self-similar relaxation over a frequency range ($\simeq$ 12 decades) much broader than the experimental window ($\simeq$ 5 decades) and not accessible via time-temperature superposition (§4.3.2.I).

Chapter 5

Nonlinear Extensional Behavior of A–B–A Thermoplastic Elastomers near $T_{g,A}$: Elastic and Viscoelastic Nonlinearities, Elastic Modeling, and Governing Mechanism of Rupture

For selecting or designing triblock TPEs that can meet the desired nonlinear rheological criteria in uniaxial extension, it is first necessary to determine how their large-strain behavior and ultimate properties are controlled by network structure and experimental conditions. In this Chapter, we investigate the behavior of a microphase-segregated A–B–A triblock at a service temperature approaching the glass transition of the hard domains. The response is measured in start-up of steady uniaxial extension, at Hencky strain rates covering six orders of magnitude. Care is taken to ensure that the initial stress response accurately represents the material linear behavior, and the error associated with a random, small degree of anisotropy of the test specimens is minimized. By highlighting the viscous character of the response, use of the secant modulus allows us to identify the effect of linear relaxation on tensile behavior. Strain hardening, whose onset can be predicted from the nonlinear elasticity of an entanglement strand, is preceded by strain softening possibly originating from entanglement slippage. Analyzing the experimental data at constant values of strain reveals a strain-induced relaxation associated with the glass-rubber transition of the microphase. Since the effects of time and strain are

inherently intertwined, the nonlinear behavior cannot be modeled by the classical constitutive equations for viscoelastic materials. We thus turn to rubber elasticity theories that can account for the observed elastic nonlinearities (entanglement slippage and chain stretching), namely the Rubinstein–Panyukov (R–P) non-affine slip-tube model and the Edwards–Vilgis (E–V) slip-link model. Because of the numerous typos that appear in the original papers as well as in a recent *Macromolecules* review, a detailed analysis of the E–V slip-link model is performed and the main steps leading to the determination of the chemical and topological contributions to the reduced stress are outlined. After establishing an operational definition of initial modulus for critical-gel-like materials subjected to start-up extensional tests, it is possible to determine the relationship between the dimensionless stress in tensile tests at constant strain rate and the step-strain extensional damping function. The R–P non-affine slip-tube model is unable to capture the observed strain dependence of the stress, while the E–V slip-link model provides a reasonable description of the data even at the higher rates of strain. Based on the molecular picture of the strain-induced structural changes gained from exposing time and strain effects, the governing mechanism of rupture is identified with ductile/fragile rupture of A domains. To the best of our knowledge, this is the first experimental evidence linking the strain rate dependence of ultimate properties of triblock TPEs to the strain-induced glass-rubber transition of the domains. In addition, application of the Bailey criterion allows us to quantitatively account for the deformation rate dependence of the ultimate properties in the regime of rubbery response.

5.1 Introduction

Extensional deformations are relevant for the processing and often the end-use applications of A–B–A thermoplastic elastomers. At service temperatures ($T_{g,B} < T < T_{g,A}$), their nonlinear viscoelasticity is largely controlled by chain mobility of the B block

and by deformation and rupture of A domains, regardless of the initial state of microstructural order.[391] For selecting or designing triblock TPEs that can meet the desired nonlinear rheological criteria in uniaxial extension, it is first necessary to determine how their large-strain behavior and ultimate properties are controlled by network structure and experimental conditions. Therefore, an adequate characterization of large deformation phenomena leading to macroscopic rupture requires that linear relaxation mechanisms, as well as elastic and viscoelastic nonlinearities, be identified and connected to molecular parameters. In the recent literature, however, both linear and nonlinear relaxations have often been neglected and the tensile behavior analyzed only in a framework appropriate for perfect elastic solids.[92,113,164,201,222,392,393,394] This oversimplified approach precludes the possibility of understanding the governing mechanism of rupture and predicting how ultimate properties will change under different experimental conditions.

In an effort to advance the current understanding of the tensile properties of triblock TPEs, we investigate the behavior of a microphase-segregated A–B–A triblock at a service temperature approaching the T_g of the hard domains. Our goals are to (1) study the effect of linear relaxation mechanisms on the tensile behavior, (2) characterize the elastic and viscoelastic nonlinearities, (3) analyze the ultimate properties, and (4) infer the governing mechanism of rupture.

5.2 Experimental Section

5.2.1 Material

The thermoplastic elastomer used in this study is an undiluted linear poly(D,L-lactide–*b*–isoprene–*b*–D,L-lactide) (L–I–L) triblock copolymer with number-average molar mass M_n = 73100 g/mol and containing 32% by mass poly(D,L-lactide) (PLA). Configurational repeating units and molecular characteristics of the material, hereafter referred to as LIL50–12, are displayed in Figure 3.1 and Table 3.1 of Chapter 3. The main features of the triblock that are pertinent to this study are discussed in Chapter 3 (§3.3.1, §3.3.2.III, §3.3.4.I-II, and §3.3.4.IV-d-e), and briefly reviewed in §4.2.1 of Chapter 4. Synthesis, molecular and morphological characterization, as well as differential scanning calorimetry (DSC) and isochronal viscoelastic measurements are presented and discussed in Appendix A.

5.2.2 Experiments

Linear and nonlinear viscoelastic behavior of LIL50–12 was probed in uniaxial extension, using a TA Instruments ARES-G2 rheometer equipped with the extensional viscosity fixture (EVF). The fixture was contained in an insulated oven, with a temperature control to within 0.1 °C, and nitrogen purge gas was used to prevent oxidative damage to the material. Specimens were tested in *start-up of steady uniaxial extension*. A sample initially in its rest state was subjected to a constant extensional *strain rate* $\dot{\varepsilon}$ at time t = 0 (i.e. $\varepsilon(t) = \dot{\varepsilon} \cdot t$), and the resulting (transient) *net tensile stress*

$\sigma_{\mathrm{E}}^{+}(t,\dot{\varepsilon})$ was measured until rupture occurred. The strain used in this discussion, $\varepsilon(t)$, is the *Hencky measure*[395] (or *true strain*), defined as

$$\varepsilon(t) = \ln\big(\lambda(t)\big) = \ln\big(\varepsilon_{\mathrm{N}}(t)+1\big) \tag{5.1}$$

where $\lambda(t) = L(t)/L_0$ is the principal elongation ratio in the stretch direction, $L(t)$ and L_0 stand for the deformed and undeformed length (respectively), and $\varepsilon_{\mathrm{N}}(t)$ is the nominal/engineering strain. Accordingly, the *true stress* $\sigma_{\mathrm{E}}^{+}(t,\dot{\varepsilon})$ equals the retractive force $F(t)$ divided by the cross-sectional area $A(t)$ of the deformed specimen. Under the assumption of incompressibility, an extension ratio λ is accompanied by shrinkage of both width and thickness by a factor of $\lambda^{-1/2}$, therefore

$$\begin{aligned} A(t) &= A_0 e^{-\dot{\varepsilon}\cdot t} \\ \sigma_{\mathrm{E}}^{+}(t,\dot{\varepsilon}) &= \sigma_{\mathrm{E,N}}^{+}(t,\dot{\varepsilon})\cdot\lambda(t) \end{aligned} \tag{5.2}$$

where A_0 represents the cross-sectional area of the undeformed specimen, and $\sigma_{\mathrm{E,N}}^{+}(t,\dot{\varepsilon})$ is the nominal/engineering net tensile stress defined as $F(t)/A_0$.

The EVF consists of two vertical drums of equal diameter (D = 10.3 mm) that stretch/wind up a rectangular specimen within a confined space, as shown in Figure 5.1. One drum (on the left) is driven directly by the rheometer motor, while the other (on the right) is stationary and attached to the torque transducer. The moving cylinder rotates at constant velocity on a circular orbit around the fixed cylinder, while also spinning around its own axis. As a result, the specimen is wound up equally on the two drums and evenly stretched on both sides. Since the torque measurement is decoupled form all the moving parts (Figure 5.1), gear friction and inertia contributions do not affect the material

response. Uniaxial extension is achieved when the wound-up portion of the specimen can freely change its width. As the moving drum spins at constant angular velocity Ω, the specimen is subjected to a constant (true) strain rate $\dot{\varepsilon} = (\Omega \cdot D) / L_0$, where L_0 = 12.7 mm is the distance between the drums axes (Figure 5.1) and corresponds to the length of the sample being stretched at every moment. The resulting force $F(t)$ is calculated from the ratio of the torque output $M(t)$ to the cylinder radius, $F(t) = 2 \cdot M(t)/D$, and the cross-sectional area $A(t)$ computed according to Eq. (5.2)a. With this apparatus, the maximum extension rate is $\dot{\varepsilon}_{max} = 10\ s^{-1}$. At this rate, the manufacturer claims that a reliable torque signal is measured after 100 ms (this becomes a key in our later discussion of the measured transient stress and ultimate properties at $\dot{\varepsilon} = 10\ s^{-1}$). A practical limitation is also imposed on the maximum attainable strain, ε_{max}. One full revolution of the moving cylinder ($\Omega \cdot t = 2\pi$) corresponds to $\varepsilon \simeq 5.1$ ($\lambda \simeq 164$). However, as the specimen wraps around both the rotating and the fixed cylinders, it will eventually wind up on top of itself thereby affecting the torque signal. This occurs at a strain ε_{max} that depends on the specimen thickness. For specimens 0.7 mm thick, the contact is reached at $\varepsilon_{max} \simeq 4.3$ ($\lambda_{max} \simeq 74$).

Uniaxial extensional measurements were conducted at 37 °C and at six strain rates, $\dot{\varepsilon} / s^{-1} = 10^{-4}$, 10^{-3}, 10^{-2}, 10^{-1}, 1, and 10. Test specimens were loaded horizontally and clamped over the drums with scotch tape (Figure 5.1). Short incisions of the tape were made alongside the material (past the ends of the gauge length) to allow the specimen width to change freely and uniformly during elongation. Great care was taken to ensure

that the initial stress response accurately represented the material linear behavior. To this end, the *dwell time*, when temperature homogeneity was established and residual stresses (introduced upon loading) were relaxed, varied from 12 h (at the lowest strain rate) to 5 min (at the highest strain rate). The sample shape during the elongation was monitored with a camera attached directly to the EVF. At the end of each test, the ends of the specimen were inspected for signs of slip. All specimens deformed uniformly up to rupture (i.e. without necking), and no slip was detected. Rupture always occurred towards the middle section of the gauge length (i.e. end effects were not observed), and before the specimen could wind up on top of itself (therefore, the maximum attainable strain, ε_{max}, did not represent an experimental limitation).

Since the mechanical failure depends on quantities that are prone to statistical fluctuations, the values of stress (σ_b), strain (ε_b), and time (t_b) at the moment of rupture are notoriously far less reproducible than the relation between stress and strain up to the breaking point. To determine precision and obtain meaningful ultimate properties, each test was repeated between six and ten times (cf. Figure 5.2). The error bars in Figures 5.21–25 represent one standard deviation from the average values.

5.2.3 Testing Specimens

Testing specimens were prepared by compression molding, following the procedure described in §3.2.3 of Chapter 3. The specimen geometry is illustrated in Figure 3.2, while the material subjected to uniaxial extension (13 mm long × 2 mm wide × 0.4 mm

thick) is shown in Figure 5.1. The two larger square shoulders (10 mm on a side) were used for grip and alignment. The initial cross-sectional area (≈ 0.8–1 mm^2) was designed to accommodate the material stiffness and to comply with the resolution of the torque transducer over the explored strain rate window. The integrity of pressed and tested samples was confirmed by size exclusion chromatography (SEC).

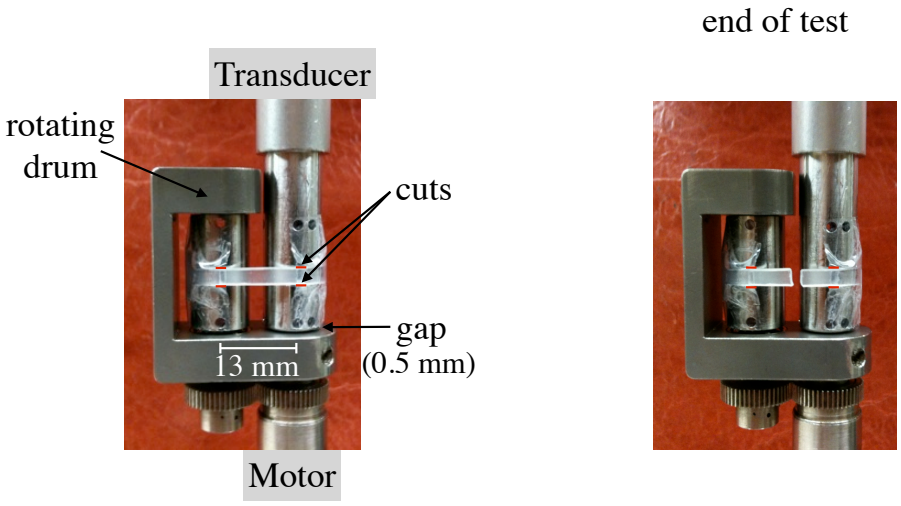

Figure 5.1. Photos of a test specimen loaded onto the extensional viscosity fixture (EVF), before and after the test. Test specimens were clamped over the drums with scotch tape, positioned mainly onto the large square shoulders (cf. Figure 3.2). Short incisions of the tape were made alongside the material (past the ends of the gauge length) to allow the specimen width to change freely and uniformly during elongation. The sample shown was subjected to the maximum strain rate attainable, $\dot{\varepsilon} = 10\ s^{-1}$, and ruptured after 0.2 s (corresponding to about 14° of drum rotation). Sample geometry and the use of scotch tape enabled a uniform elongation (i.e. deformation without necking) and prevented slip for all specimens tested. Rupture always occurred towards the middle section of the gauge length (i.e. end effects were not observed), and before the specimen could wind up on top of itself (i.e. the maximum strain attainable, ε_{max}, did not limit the measurements).

5.3 Results and Discussion

5.3.1 Theoretical Preliminaries and Terminology

In the following discussion, we assume *isotropy* and *incompressibility* throughout. The hypothesis of incompressibility is justified for liquids and soft solids, i.e. materials (such as elastomeric networks) possessing a bulk modulus K much greater than the shear modulus G. Under this condition, the change in volume becomes negligible compared to the change in shape, and Poisson's ratio approaches the "ideal value" of 1/2 (cf. Appendix A, §A.2.3.I).[42,150] Furthermore, we assume the material to have been completely at rest for $t < 0$, and thereby we choose the state at $t = 0$ as the *reference state*. This choice of reference state, also adopted by Tschoegl[150], bears upon the definitions of historic time u and memory function $Q(t)$ (cf. Appendix D, §D.1–2 and footnote [b]).

5.3.1.I Response of elastic solids

5.3.1.I-a Models

The Rivlin equation

The most general constitutive equation for isotropic, incompressible, elastic solids is the *Rivlin equation*[396-398]

$$\boldsymbol{\sigma}_{\mathrm{NLE}} = 2\frac{\partial W}{\partial I_1}\cdot\boldsymbol{B} - 2\frac{\partial W}{\partial I_2}\cdot\boldsymbol{B}^{-1} \qquad \text{elastic solids} \tag{5.3}$$

where $\boldsymbol{\sigma}_{\mathrm{NLE}}$ is the large-strain *extra stress tensor* (i.e. that part of the stress tensor that depends on the material itself and how it has been deformed)[45], W is the *elastic energy*

density due to the deformation[a] ($W = \Delta A/V$, where A is the Helmholtz free energy and V is the volume)[41], I_1 and I_2 are the *first* and *second scalar invariants* of $\boldsymbol{B}$, with $\boldsymbol{B}$ and $\boldsymbol{B}^{-1}$ representing measures of finite strain called[45,340] the *Finger/Green tensor* and the *Cauchy/Piola tensor* (respectively)[b]. From a physical standpoint, these finite strain tensors account for the strain-induced *large-scale orientation* of the material structural elements. Thus, the Rivlin equation describes the stress-strain relationship in terms of a single material function, i.e. the elastic energy density W. Since Eq. (5.3) is the most general stress-strain relationship for isotropic, incompressible elastic solids, we chose to denote the extra stress tensor by the symbol $\boldsymbol{\sigma}_{\text{NLE}}$, where the subscript "NLE" stands for *nonlinear* (i.e. large-strain) *elastic behavior*. In contrast, the large-strain extra tensors predicted under specific assumptions (vide infra) will be identified by the author(s) of the model using superscripts.

For *simple shear-free flows*[340], the components of $\boldsymbol{B}$ and $\boldsymbol{B}^{-1}$ are

$$\boldsymbol{B} = \begin{pmatrix} \lambda_1^2 & 0 & 0 \\ 0 & \lambda_2^2 & 0 \\ 0 & 0 & \lambda_3^2 \end{pmatrix} = \begin{pmatrix} e^{2\varepsilon} & 0 & 0 \\ 0 & e^{-(1+b)\varepsilon} & 0 \\ 0 & 0 & e^{-(1-b)\varepsilon} \end{pmatrix} \tag{5.4}$$

and

---

[a] Sometimes called the *stored-energy function*.[396]

[b] The Finger tensor (often denoted by $\boldsymbol{C}^{-1}$) differs from the Green tensor only in the choice of the reference state. A similar state of play holds for the Cauchy tensor (often denoted by $\boldsymbol{C}$) and the Piola tensor.[45]

$$\boldsymbol{B}^{-1} = \begin{pmatrix} \lambda_1^{-2} & 0 & 0 \\ 0 & \lambda_2^{-2} & 0 \\ 0 & 0 & \lambda_3^{-2} \end{pmatrix} = \begin{pmatrix} e^{-2\varepsilon} & 0 & 0 \\ 0 & e^{(1+b)\varepsilon} & 0 \\ 0 & 0 & e^{(1-b)\varepsilon} \end{pmatrix} \tag{5.5}$$

where the parameter b defines the type of shear-free flow ($b = 0$ in uniaxial and biaxial extension, $b = 1$ in planar elongation)[340], λ_i are the *principal elongation ratios*, their corresponding axes are the principal axes of $\boldsymbol{B}$ and $\boldsymbol{B}^{-1}$, and ε is the *true/Hencky strain*[395]. Therefore, the scalar invariants of $\boldsymbol{B}$ are given by[340]

$$\begin{aligned} I_1 &= \mathrm{tr}\,\boldsymbol{B} = \sum_i \lambda_i^2 \\ I_2 &= \mathrm{tr}\,\boldsymbol{B}^{-1} = \sum_i \lambda_i^{-2} \\ I_3 &= \det \boldsymbol{B} = 1 \end{aligned} \tag{5.6}$$

Since $\det \boldsymbol{B} = \det \boldsymbol{B}^{-1} = 1$ for any volume-conserving deformation, these tensorial strain measures have only two strain-dependent scalar invariants, I_1 and I_2. For *uniaxial extension* with axis-1 as the extension direction, i.e.

$$\begin{aligned} \lambda_1 &= \lambda \\ \lambda_2 &= \lambda_3 = \lambda^{-1/2} \end{aligned} \tag{5.7}$$

I_1 and I_2 are

$$\begin{aligned} I_1 &= \lambda^2 + \frac{2}{\lambda} \quad = e^{2\varepsilon} + 2e^{-\varepsilon} \\ I_2 &= \frac{1}{\lambda^2} + 2\lambda = \varepsilon^{-2\varepsilon} + 2e^{\varepsilon} \end{aligned} \tag{5.8}$$

while the *net tensile stress* is defined as the applied axial stress minus that acting on the free surface,[340]

$$\sigma_{\mathrm{E}} \equiv \sigma_{11} - \sigma_{22} = \sigma_{11} - \sigma_{33} \tag{5.9}$$

The Mooney–Rivlin equation

By assuming that the free energy derivatives be independent of strain, Eq. (5.3) yields the *Mooney–Rivlin* (M–R) *equation*

$$\boldsymbol{\sigma}^{\text{M–R}} = 2C_1 \cdot \boldsymbol{B} - 2C_2 \cdot \boldsymbol{B}^{-1} \tag{5.10}$$

where the coefficients C_1 and C_2 represent material constants. For uniaxial extension, combining Eq. (5.10) with Eqs. (5.4)–(5.5), (5.7), and (5.9) leads to

$$\frac{\sigma_{\text{E}}^{\text{M–R}}(\lambda)}{\left(\lambda^2 - \lambda^{-1}\right)} = 2C_1 + \frac{2C_2}{\lambda} \tag{5.11}$$

This equation was proposed in 1940 by Mooney[399], and later derived in the framework of continuum mechanics (Eqs. (5.3) and (5.10)) by Rivlin[396,397].

The neo-Hookean model

By setting $C_2 = 0$ in Eq. (5.10), one obtains the equation for the *neo-Hookean* (n-H) *model*

$$\boldsymbol{\sigma}^{\text{n-H}} = G_0 \cdot \boldsymbol{B} \tag{5.12}$$

where the constant G_0 represents the small-strain, i.e. linear elastic (LE), shear modulus.[45,400] Notice that the use of the Finger tensor in Eq. (5.12) implies that the deformation is *affine*. In turn, this requires *large-scale orientation* of network strands and, for many deformations such as uniaxial extension, *chain stretching*.[36] This is the simplest, yet physically plausible large-strain solid model, and it can be directly obtained by generalizing Hooke's law (Eq. (5.17)b) to finite deformations. In uniaxial extension, the neo-Hookean model yields the relationship

$$\frac{\sigma_{\mathrm{E}}^{\text{n-H}}(\lambda)}{\left(\lambda^2-\lambda^{-1}\right)}=G_0 \tag{5.13}$$

Eq. (5.13) is also the constitutive equation that arises from the classical theories of rubber elasticity, i.e. the *affine network model* suggested by Kuhn[199] and later developed by Wall[401,402] and Treloar[403], and the *phantom network model* introduced by James and Guth[404] and Flory and Rehner[405]. Both models consider a network of Gaussian strands and predict, on statistical mechanics ground,

$$W=\frac{G_0}{2}\left(I_1-3\right) \tag{5.14}$$

while the expression for the net tensile stress, Eq. (5.13), is derived using[41]

$$\sigma_{\mathrm{E}}(\lambda)=\lambda\frac{\partial W}{\partial\lambda} \tag{5.15}$$

It is important to realize, however, that the assumption of Gaussian network strands does not necessarily lead to neo-Hookean behavior.[41] An example of a Gaussian network deviating (and severely so) from neo-Hookean behavior is provided by the Ball et al.[83] slip-link model, to be discussed in §5.3.4.II-b.

Linear elastic behavior (i.e. Hooke's law)

In the limit of small strains,[45,340]

$$\left.\begin{array}{r}\boldsymbol{B}\to\boldsymbol{I}+\boldsymbol{S}\\ \boldsymbol{B}^{-1}\to\boldsymbol{I}-\boldsymbol{S}\\ \varepsilon\to\varepsilon_{\mathrm{N}}\end{array}\right\}\quad\text{for } I_1, I_2\to 3 \tag{5.16}$$

where ε_{N} is the *nominal/engineering strain*, $\boldsymbol{I}$ is the identity matrix, and $\boldsymbol{S}$ is the *infinitesimal deformation tensor* (as defined, for instance, by Graessley[45] – cf. Appendix

D, footnote [a]). Thus, the extra stress tensor and the deviatoric (i.e. trace-free) stress tensor[150] coincide, and the neo-Hookean model reduces to LE behavior, i.e. *Hooke's law* (H),[41]

$$\begin{aligned} \boldsymbol{\sigma}_{\mathrm{LE}} &= G_0 \cdot \boldsymbol{S} \qquad \text{for } I_1, I_2 \to 3 \\ \boldsymbol{\sigma}^{\mathrm{H}} &= G_0 \cdot \boldsymbol{S} \qquad \text{Hooke's law} \end{aligned} \tag{5.17}$$

For uniaxial extension,

$$\begin{aligned} \sigma_{\mathrm{E,LE}}(\varepsilon) &= 3G_0 \cdot \varepsilon \ = E_0 \cdot \varepsilon \qquad \text{for } I_1, I_2 \to 3 \\ \sigma_{\mathrm{E}}^{\mathrm{H}}(\varepsilon_{\mathrm{N}}) &= 3G_0 \cdot \varepsilon_{\mathrm{N}} = E_0 \cdot \varepsilon_{\mathrm{N}} \qquad \text{Hooke's law} \end{aligned} \tag{5.18}$$

where $3G_0 = E_0$ is Young's modulus (i.e. the LE tensile modulus).

5.3.1.I-b The initial modulus for elastic solids

It follows from Eqs. (5.16) and (5.18) that the *initial* (i.e. small-strain) *modulus* for elastic solids subjected to tensile tests can be defined as the stress-strain ratio in the small-strain limit,[41]

$$3G_0 = E_0 = \lim_{\lambda \to 1} \frac{\sigma_{\mathrm{E,NLE}}(\lambda)}{\lambda - 1} = \lim_{\varepsilon \to 0} \frac{\sigma_{\mathrm{E,NLE}}(\varepsilon)}{\varepsilon} \tag{5.19}$$

Since

$$\lim_{\lambda \to 1} \frac{\lambda^2 - \lambda^{-1}}{\lambda - 1} = 3 \tag{5.20}$$

Eq. (5.19) can also be written as[41]

$$G_0 = \frac{E_0}{3} = \lim_{\lambda \to 1} \frac{\sigma_{\mathrm{E,NLE}}(\lambda)}{\lambda^2 - \lambda^{-1}} \tag{5.21}$$

Thus, $G_0 = 2C_1 + 2C_2$ for a Mooney-Rivlin solid.

5.3.1.I-c Strain measure, reduced stress, and dimensionless stress

In the context of uniaxial deformation of rubbers, the quantity $(\lambda^2-\lambda^{-1})$ is referred to as the "*strain measure*", i.e. it is a scalar measure of finite strain only applicable to uniaxial extension kinematics, as opposed to the general, tensorial measures $\boldsymbol{B}$ and $\boldsymbol{B}^{-1}$.

The ratio

$$\sigma_{\mathrm{E,red}}(\lambda) \equiv \frac{\sigma_{\mathrm{E,NLE}}(\lambda)}{\left(\lambda^2-\lambda^{-1}\right)} \tag{5.22}$$

is called[41] the "*reduced stress*"[c]. Use of the reduced stress implies that the neo-Hookean model, $\sigma_{\mathrm{E,red}}^{\text{n-H}} = G_0$ (cf. Eq. (5.13)), is chosen as a basis of comparison. Strain dependence of the reduced stress signals a deviation from neo-Hookean behavior.

Since elastic models yield different predictions for G_0, it is convenient to use the reduced stress normalized by initial modulus,

$$S(\lambda) \equiv \frac{\sigma_{\mathrm{E,red}}(\lambda)}{G_0} = \frac{\sigma_{\mathrm{E,NLE}}(\lambda)}{G_0\left(\lambda^2-\lambda^{-1}\right)} \tag{5.23}$$

$S(\lambda)$ is called[41] the "*dimensionless stress*". When plotted in this manner, the resulting stress-strain curves are forced to pass through unity at $\lambda = 1$ (Eq. (5.21)), and distinctions are based solely on the functional form of the constitutive equation.

---

[c] Sometimes also called the "*Mooney stress*"[406], or the "*reduced force*"[41,42].

5.3.1.II Response of viscoelastic materials

Numerous constitutive equations for viscoelastic materials (liquids or solids) have been proposed over the years.[45] Here, we limit our discussion to a group of stress-strain relationships that have roots in molecular ideas (albeit not in a detailed, statistical-mechanics sense), and have not been ruled out by the Lodge consistency test[407]. All these models begin as elastic solids to which relaxation is added, and yield single-integral constitutive equations[340].

5.3.1.II-a Models

The Rivlin–Sawyers equation

As long as the effects on the stress at time t of the deformations at different historic times u are independent of each other[340], the most general constitutive equation for isotropic, incompressible, viscoelastic materials is the *Rivlin–Sawyers equation*[408]

$$\boldsymbol{\sigma}_{\mathrm{NLVE}}(t)=\int_0^t\left[Q_1\left(t-u,I_1,I_2\right)\cdot\boldsymbol{B}(u)-Q_2\left(t-u,I_1,I_2\right)\cdot\boldsymbol{B}^{-1}(u)\right]du \tag{5.24}$$

where Q_1 and Q_2 are the time- and strain-dependent memory functions, i.e. the *nonlinear memory functions* in simple shear. As opposed to the Rivlin equation for elastic solids (Eq. (5.3)), the Rivlin–Sawyers model does not possess a strain energy function W. As a result, Eq. (5.24) is comprehensive and flexible, but it may also lead to thermodynamic violations[409]. Since the Rivlin–Sawyers equation is the most general stress-strain relationship for isotropic, incompressible viscoelastic materials, we chose to denote the extra stress tensor by the symbol $\boldsymbol{\sigma}_{\mathrm{NLVE}}$, where the subscript "NLVE" stands for *nonlinear*

(i.e. large-strain) *viscoelastic behavior*. In contrast, the large-strain extra tensors predicted under specific assumptions (vide infra) will be identified by the author(s) of the model using superscripts.

The Kaye–Bernstein–Kearsley–Zapas (K–BKZ) equation

By imposing that Q_1 and Q_2 be the components of an elastic energy gradient, i.e. $Q_1 = \partial W/\partial I_1$ and $Q_2 = \partial W/\partial I_2$, one obtains the *K–BKZ equation*

$$\boldsymbol{\sigma}^{\text{K–BKZ}}(t) = \int_0^t \left[\frac{\partial W}{\partial I_1}(t-u, I_1, I_2) \cdot \boldsymbol{B}(u) - \frac{\partial W}{\partial I_2}(t-u, I_1, I_2) \cdot \boldsymbol{B}^{-1}(u) \right] du \tag{5.25}$$

which was proposed independently by Kaye[410] and by Bernstein, Kearsley, and Zapas[411]. In this model, the material is viewed as a Rivlin network whose structural elements have finite lifetimes (cf. Eq. (5.3)).

The factorized Rivlin–Sawyers and K–BKZ equations

Very little work on describing material functions has been done with the Rivlin–Sawyers and the K–BKZ equations in their general forms shown above.[340] Instead, it has been customary to assume that the scalar functions $Q_i(t–u,I_1,I_2)$ and $W(t–u,I_1,I_2)$ may be represented, over some range of times and strains[412-417], as a product of time-dependent and strain-dependent factors as[340]

$$Q_i(t-u, I_1, I_2) = Q(t-u) \cdot \phi_i(I_1, I_2) \tag{5.26}$$

$$W(t-u, I_1, I_2) = Q(t-u) \cdot W(I_1, I_2) \tag{5.27}$$

with

$$Q(t) = \frac{dG(t)}{dt} + G(0)\delta(t) \tag{5.28}$$

where $Q(t)$ is the *linear memory function* in simple shear[d] (cf. Appendix D, §D.1–2, footnote [b], Table D.1, and Chapter 4, Eq. (4.49)), $G(t)$ is the linear shear relaxation modulus, $G(0) = G_g$ is the instantaneous or glassy shear modulus, and $\delta(t)$ is the delta function (Appendix D, §D.2 and Eq. (D.14)b). For a correct reduction to the linear viscoelastic (LVE) response limit (Eq. (5.35)), it is further required that (cf. Eq. (5.16))[340]

$$\phi_1(3,3) + \phi_2(3,3) = 1 \tag{5.29}$$

$$\frac{\partial W}{\partial I_1}(3,3) + \frac{\partial W}{\partial I_2}(3,3) = 1 \tag{5.30}$$

Experimental evidence for *time-strain factorization* (TSF) dates back to the early studies on elastomers conducted by Tobolsky and Andrews[418,419], and by Guth and co-workers[420] with experiments of extensional stress relaxation, and by Smith[421,422] with tensile tests at constant rate of (nominal) strain. Its applicability to polymer melts and solutions was later suggested by White and Tokita[423], Zapas and Phillips[424], and Einaga et al.[412]. Furthermore, several molecular theories for polymeric systems predict time-strain factorization and a K–BKZ-type equation. Among these are the Rouse theory[47] for monodisperse dilute polymer solutions, and the original Doi–Edwards[46] (D–E) theory for monodisperse entangled melts (when it invokes the "independent alignment approximation").

---

[d] It represents the linear response to a unit impulse of strain (cf. Appendix D, §D.3.1 and Table D.1).

With this additional (non trivial) assumption, Eq. (5.24) becomes the *factorized Rivlin–Sawyers equation*

$$\boldsymbol{\sigma}_{\mathrm{NLVE}}(t)=\int_0^t\left\{Q(t-u)\cdot\left[\phi_1(I_1,I_2)\cdot\boldsymbol{B}(u)-\phi_2(I_1,I_2)\cdot\boldsymbol{B}^{-1}(u)\right]\right\}du \qquad \text{(TSF)} \qquad (5.31)$$

and Eq. (5.25) yields the *factorized K–BKZ equation*

$$\boldsymbol{\sigma}^{\mathrm{K-BKZ}}(t)=\int_0^t\left\{Q(t-u)\cdot\left[\frac{\partial W}{\partial I_1}(I_1,I_2)\cdot\boldsymbol{B}(u)-\frac{\partial W}{\partial I_2}(I_1,I_2)\cdot\boldsymbol{B}^{-1}(u)\right]\right\}du \qquad \text{(TSF)} \qquad (5.32)$$

The Wagner equation

By setting $\phi_1(I_1,I_2) = h(I_1,I_2)$ and $\phi_2(I_1,I_2) = 0$ (with the consequence that the second normal stress difference in simple shear is neglected), Eq. (5.31) yields the *Wagner* (W) *equation*[425]

$$\boldsymbol{\sigma}^{\mathrm{W}}(t)=\int_0^t\left[Q(t-u)\cdot h(I_1,I_2)\cdot\boldsymbol{B}(u)\right]du \qquad \text{(TSF)} \qquad (5.33)$$

Wagner called[425] $h(I_1,I_2)$ the *damping function*, and viewed it as an empirical function to be determined by fitting experimental data (cf. §5.3.1.II-b).

The Lodge rubber-like liquid

If we set $h(I_1,I_2) = 1$, the Wagner equation transforms into the constitutive equation of the *Lodge* (L) *rubber-like liquid*

$$\boldsymbol{\sigma}^{\mathrm{L}}(t)=\int_0^t\left[Q(t-u)\cdot\boldsymbol{B}(u)\right]du \qquad (5.34)$$

Proposed by Lodge[426] in 1964, the model exemplifies the material as a neo-Hookean network of Gaussian strands that have *finite lifetimes* and deform affinely with the

macroscopic deformation (cf. Eq. (5.12)). Being a generalization of the Boltzmann superposition integral (Eq. (5.35)) to finite deformations, time and strain effects are obviously "factorized". The Lodge rubber-like liquid thus represents the simplest large-strain viscoelastic model.

Although the shear memory function $Q(t)$ is left unspecified in Eq. (5.34), and it can therefore be chosen so as to describe the linear response of either solids ($G(t \to \infty) = G_{eq} > 0$) or liquids ($G_{eq} = 0$), common choices for $Q(t)$ assume $G_{eq} = 0$. For instance, the so-called[340,400] *upper-convected generalized Maxwell model* (UCGM) or *Lodge network model* (LN) is obtained from Eq. (5.34) when using the memory function of a generalized (standard) Maxwell model with $G_{eq} = 0$ (Appendix D, Eq. (D.74)).

Linear viscoelastic behavior (i.e. Boltzmann's superposition integral)

In the limit of small strains (i.e. $\varepsilon(t) \to \varepsilon_N(t)$ and $\boldsymbol{B}(t) \to \boldsymbol{I} + \boldsymbol{S}(t)$), the Lodge rubber-like liquid reduces to LVE behavior, i.e. *Boltzmann's superposition integral*[150] (cf. Appendix D, Eq. (D.6)a),

$$\boldsymbol{\sigma}_{LVE}(t) = \int_0^t \left[Q(t-u) \cdot \boldsymbol{S}(u) \right] du \qquad \text{for } I_1, I_2 \to 3 \tag{5.35}$$

However, reduction to LVE behavior in the limit of small strains is a general feature that does not depend on the particular nonlinear model. This is most easily illustrated by comparing the response of the factorized Rivlin–Sawyers equation to that predicted by Eq. (5.35). In uniaxial extension, for any strain history $\varepsilon(t)$ and arbitrary choice of the

scalar functions $\phi_i(I_1,I_2)$, the extra stress tensors $\boldsymbol{\sigma}_{NLVE}(t)$ and $\boldsymbol{\sigma}_{LVE}(t)$ will yield the same net tensile stress $\sigma_E(t,\varepsilon)$ if

$$\phi_1(I_1,I_2)\cdot\frac{e^{2\varepsilon(u)}-e^{-\varepsilon(u)}}{3\varepsilon_N(u)}+\phi_2(I_1,I_2)\cdot\frac{e^{\varepsilon(u)}-e^{-2\varepsilon(u)}}{3\varepsilon_N(u)}=1 \qquad (5.36)$$

which is clearly satisfied when $\varepsilon(u)$ is small enough such that $\varepsilon(u) \to \varepsilon_N(u)$, $I_1 \to 3$, and $I_2 \to 3$ (cf. Eq. (5.29)). In start-up of steady uniaxial extension, i.e. $\varepsilon(t)=\dot{\varepsilon}\cdot t$, Eq. (5.36) implies that the material will exhibit a LVE response either at very low rates of strain or at very short times. Since LVE material functions are interrelated[42,150] (Appendix D), the LVE response in start-up of steady uniaxial extension can be obtained from *any* LVE material function, e.g. from the storage and loss moduli $E'(\omega)$ and $E''(\omega)$. Therefore, this provides a powerful criterion for assessing the reliability of nonlinear measurements (cf. §5.3.2 and §5.3.3). Obviously, analogous considerations hold for any other mode of deformation (e.g. simple shear) and different strain histories.

5.3.1.II-b The damping function

General definition

Even though the original damping function concept was based on time-strain factorization (Eq. (5.33)), the damping function can be defined in the most general terms[427] as a measure of the deviation of the observed nonlinear viscoelastic behavior from the prediction of the Lodge rubber-like liquid model (Eq. (5.34)),

$$h(t,I_1,I_2)\equiv\frac{\sigma_{NLVE}(t,I_1,I_2)}{\sigma^L(t,I_1,I_2)} \qquad \text{general definition} \qquad (5.37)$$

where $\sigma_{\mathrm{NLVE}}(t,I_1,I_2)$ indicates the measured stress, and $\sigma^{\mathrm{L}}(t,I_1,I_2)$ is the corresponding prediction of the Lodge model, both in response to the same arbitrary mode of deformation and strain history. In uniaxial extension, this leads to a time- and strain-dependent damping function defined as

$$h(t,\varepsilon) \equiv \frac{\sigma_{\mathrm{E,NLVE}}(t,\varepsilon)}{\sigma_{\mathrm{E}}^{\mathrm{L}}(t,\varepsilon)} \qquad \text{general definition, in uniaxial extension} \qquad (5.38)$$

for any strain history $\varepsilon(t)$. Thus, the extensional damping function, $h(t,\varepsilon)$, is the *generalization* to viscoelastic materials *of the dimensionless stress*, $S(\lambda)$, previously defined for perfectly elastic solids (Eq. (5.23)), in that both measure a deviation from neo-Hookean behavior (§5.3.1.II-c).

Physical meaning

Furthermore, interpreting the physical meaning of $h(t,I_1,I_2)$ is straightforward. Since Lodge's model makes use of the linear memory function $Q(t)$, the only nonlinear effects it accounts for are those induced by *large-scale orientation* and *stretching* of chain segments (through the Finger tensor $\boldsymbol{B}$). Nonlinear effects associated with *finite chain extensibility* and new (i.e. *nonlinear*) *relaxation mechanisms* are neglected. Therefore, a damping function $h(t,I_1,I_2)$ different from unity signals that nonlinear effects other than large-scale orientation and chain stretching are affecting the material response.

Damping function in polymer melts and solutions

Having been originally introduced in the context of polymer melts and under the assumptions of TSF, Wagner interpreted $h(I_1,I_2)$ in terms of structural changes (i.e. *disentanglement*) of the temporary polymer network due to deformation.[425,427]

Specifically, he and Meissner viewed it as a survival probability that depends on deformation.[428] As such, $h(I_1,I_2)$ for melts and solutions should always decrease monotonically with strain from its small-strain limit $h(3,3) = 1$ (Eq. (5.29)), approaching zero at large deformations.

In the framework of tube models, strain-induced disentanglement is explained by invoking a nonlinear relaxation mechanism called *chain retraction*.[36,45] The imposition of a large strain stretches the tube contour length, $L_{tube}(t = t_0)$, beyond its equilibrium value, $L_{tube}(t = 0) = L_{tube,eq} = Z{\cdot}a$ (where Z is the average number of entanglement strands per chain, and a is the tube statistical segment length at rest – Chapter 3, §3.3.2.III). This induces a large tension, which chains relieve by retracting quickly, and in a Rouse-like fashion, within their still distorted tubes, until $L_{tube}(t = \tau_s) = L_{tube,eq}$. The longest relaxation time governing this retraction process, which is called the *retraction time* or *stretch relaxation time*[36] τ_s, is taken to be equal to the *path equilibration time*[45] $2\tau_R$ (Eq. (3.20)).[36,45,46] Since the surplus fraction of the stretched tube $L_{tube}(t = t_0) - L_{tube,eq}$ has been abandoned and this process occurs for all chains, retraction leads inevitably to constraint release (CR), i.e. mutual loss of entanglements.[36,427,429] At steady-state, this type of CR proceeds at a rate dictated by the rate of flow, giving rise to an additional nonlinear relaxation mechanism called *convective constraint release* (CCR).[430-432]

In step-strain tests, stress relaxation following chain retraction proceeds in the same way as for small deformations (e.g. by reptation), and the time-dependency of this final relaxation is therefore the same as in linear viscoelasticity. In this way, the tube model

explains time-strain factorability.[e] Moreover, according to this mechanism, $h(I_1,I_2)$ can be thought of as the fraction of the initial stress that is not relaxed by retraction.[36]

In the original Doi–Edwards[46] model, it is assumed that the chain retraction process is complete[f] and instantaneous, so that in effect chains are never stretched at all and thus do not undergo affine deformation at large strains. Later versions of tube models have progressively refined the D–E theory so as to account for *chain stretching*, as in the Doi–Edwards–Marrucci–Grizzuti[433-435] (D–E–M–G) model, and CCR, as in the Mead–Larson–Doi[432] (M–L–D) model. The *finite extensibility* of polymer chains has also been included.[36] These refinements lead to a reduced degree of damping (i.e. $h(t,I_1,I_2)$ closer to unity) as compared to the D–E prediction.[36,436] However, since chains in polymer melts and solutions can ultimately slide past each other, $h(t,I_1,I_2)$ remains always lower than unity and monotonically decreasing with increasing strain (hence, the name "damping" function).

Damping function in cross/endlinked systems

In cross/endlinked systems, on the other hand, the finite extensibility of polymer chains may cause $h(t,I_1,I_2)$ to rise above unity and become unbounded at a sufficiently large deformation (cf. §5.3.4.II-b and Figure 5.14). Furthermore, the nonlinear mechanism of

---

[e] Even though experimental evidence often indicates that the *time required to attain time-strain factorization* after a step-strain experiment, τ_k, can be an order of magnitude larger than τ_s.[415-417]

[f] "Complete" chain retraction in the D–E theory means that L_{tube} remains constant in any flow.

chain retraction may be suppressed in entangled systems that are chemically or physically cross/endlinked. If both ends of an entangled chain are terminated by cross/endlinks, as would be the case for highly vulcanized rubbers or for A–B–A thermoplastic elastomers at temperatures below $T_{g,A}$, the large tension induced by a finite deformation cannot be relieved by chain retraction (cf. §5.3.3.II-d). In this situation, other nonlinear relaxation mechanisms may develop (e.g. *slippage of entanglements*). As will be discussed in §5.3.4.II-b, nonlinear effects in entangled, cross/endlinked systems are taken into account in the Edwards–Vilgis[84] (E–V) slip-link model.

5.3.1.II-c Stress relaxation in uniaxial extension

In uniaxial extension, and with a strain excitation of the form $\varepsilon(t) = \varepsilon \cdot H(t)$ with $H(t)$ being the Heaviside unit step function (i.e. a step of strain of height ε at $t = 0$), the response predicted by the Wagner and the Lodge models is (respectively),

$$\sigma_{E}^{W}(t,\varepsilon) = E(t) \cdot h(\varepsilon) \cdot \frac{e^{2\varepsilon} - e^{-\varepsilon}}{3} \qquad \text{(TSF)} \tag{5.39}$$

$$\sigma_{E}^{L}(t,\varepsilon) = E(t) \cdot \frac{e^{2\varepsilon} - e^{-\varepsilon}}{3} \tag{5.40}$$

where $E(t) = 3G(t)$ is the linear tensile relaxation modulus. While the LVE response is

$$\sigma_{E,LVE}(t,\varepsilon) = E(t) \cdot \varepsilon \qquad \text{for } I_1, I_2 \to 3 \tag{5.41}$$

The most general NLVE response, given by the Rivlin–Sawyers equation (Eq. (5.24)), can also be expressed in terms of a *nonlinear relaxation modulus*, $E(t,\varepsilon)$, defined such that[437]

$$\sigma_{\mathrm{E,NLVE}}(t,\varepsilon) = E(t,\varepsilon)\cdot\varepsilon \tag{5.42}$$

Since $E(t,\varepsilon) \rightarrow E(t)$ at small strains (Eq. (5.36)), it is convenient to introduce a function, $\Lambda_{\mathrm{E}}(t,\varepsilon)$, defined as[g]

$$\Lambda_{\mathrm{E}}(t,\varepsilon) \equiv \frac{E(t,\varepsilon)}{E(t)} = \frac{\sigma_{\mathrm{E,NLVE}}(t,\varepsilon)}{\sigma_{\mathrm{E,LVE}}(t,\varepsilon)} \tag{5.43}$$

$\Lambda_{\mathrm{E}}(t,\varepsilon)$ is a measure of the deviation of the nonlinear viscoelastic behavior from the linear response limit, and therefore it contains information about *all* the nonlinear effects that influence the measured response at large strains (§5.3.1.II-b). As such, it is, in general, a function of both time and strain. If the time dependencies of $E(t,\varepsilon)$ and $E(t)$ coincide, $\Lambda_{\mathrm{E}}(t,\varepsilon)$ becomes time-independent and TSF applies.

With the definition of damping function given in the previous section, the effect on the observed nonlinear response of strain-induced large-scale orientation and chain stretching can be decoupled from all the other nonlinear effects emerging at large strains. We may expand Eq. (5.43) as a product of two ratios,

$$\Lambda_{\mathrm{E}}(t,\varepsilon) = \frac{\sigma_{\mathrm{E,NLVE}}(t,\varepsilon)}{\sigma_{\mathrm{E}}^{\mathrm{L}}(t,\varepsilon)} \cdot \frac{\sigma_{\mathrm{E}}^{\mathrm{L}}(t,\varepsilon)}{\sigma_{\mathrm{E,LVE}}(t,\varepsilon)} \tag{5.44}$$

where we have multiplied and divided by the net tensile stress predicted by the Lodge model (Eq. (5.40)). The first ratios in Eq. (5.44), $\sigma_{\mathrm{E,NLVE}}(t,\varepsilon)/\sigma_{\mathrm{E}}^{\mathrm{L}}(t,\varepsilon)$, is the general definition of damping function, $h(t,\varepsilon)$ (Eq. (5.38)). The second ratio, $\sigma_{\mathrm{E}}^{\mathrm{L}}(t,\varepsilon)/\sigma_{\mathrm{E,LVE}}(t,\varepsilon)$

---

[g] A related function was proposed in 1965 by Halpin[438], and (for tensile tests at constant rate of nominal strain) by Smith and co-workers[439,440].

, takes into account only the effect of large-scale orientation and stretching of chain segments. Thus, it follows from Eqs. (5.38), (5.40), and (5.41) that

$$\Lambda_{\mathrm{E}}(t,\varepsilon) = h(t,\varepsilon)\cdot\frac{e^{2\varepsilon}-e^{-\varepsilon}}{3\varepsilon} \tag{5.45}$$

As ε is progressively reduced from a large value, $\Lambda_{\mathrm{E}}(t,\varepsilon)$ may become time-independent. In this case,

$$\Lambda_{\mathrm{E}}(\varepsilon) = h(\varepsilon)\cdot\frac{e^{2\varepsilon}-e^{-\varepsilon}}{3\varepsilon} \qquad \text{(TSF)} \tag{5.46}$$

where $h(\varepsilon)$ is the time-independent damping function introduced by Wagner (Eq. (5.39)). Regardless of whether time and strain effects are separable, in the limit of small strains,

$$\left.\begin{array}{l} h(t,\varepsilon) \quad \text{or} \quad h(\varepsilon) \to 1 \\ \dfrac{e^{2\varepsilon}-e^{-\varepsilon}}{3\varepsilon} \quad \to 1 \end{array}\right\} \Lambda_{\mathrm{E}}(t,\varepsilon)\to 1 \qquad \text{for } \varepsilon\to 0 \tag{5.47}$$

In terms of stretch ratio λ, the step-strain, extensional damping function is given by

$$\begin{aligned} h(t,\lambda) &= \frac{\sigma_{\mathrm{E,NLVE}}(t,\lambda)}{\sigma_{\mathrm{E}}^{\mathrm{L}}(t,\lambda)} \\ &= \frac{\sigma_{\mathrm{E,NLVE}}(t,\lambda)}{G(t)\left(\lambda^2-\lambda^{-1}\right)} \end{aligned} \tag{5.48}$$

where the right-hand side of Eq. (5.48) remains unchanged regardless of whether TSF applies. Since in a step-strain test t and λ are independent variables, applying the definition of initial modulus, Eq. (5.21)), gives

$$\begin{aligned} \lim_{\lambda\to 1}\frac{\sigma_{\mathrm{E,NLVE}}(t,\lambda)}{\lambda^2-\lambda^{-1}} &= G(t)\cdot\lim_{\lambda\to 1}h(t,\lambda) \\ &= G(t) \end{aligned} \tag{5.49}$$

Thus, $h(t,\lambda)$ can be thought of as the *generalization* to viscoelastic materials *of the dimensionless stress*, $S(\lambda)$, defined for perfectly elastic solids (Eq. (5.23)). We may then write

$$h(t,\lambda) = S_{\mathrm{E}}(t,\lambda) \tag{5.50}$$

At very short times, i.e. $G(t\to 0) = G_{\mathrm{g}}$, or at very long times for solid-like materials, i.e. $G(t\to\infty) = G_{\mathrm{eq}} > 0$ (equilibrium conditions), $S_{\mathrm{E}}(t,\lambda)$ becomes time-independent and numerically equal to $S(\lambda)$,

$$\left.\begin{aligned} S_{\mathrm{E}}(t\to 0,\lambda) &= \frac{\sigma_{\mathrm{E,NLVE}}(t\to 0,\lambda)}{G_{\mathrm{g}}\left(\lambda^2-\lambda^{-1}\right)} \\ S_{\mathrm{E}}(t\to\infty,\lambda) &= \frac{\sigma_{\mathrm{E,NLVE}}(t\to\infty,\lambda)}{G_{\mathrm{eq}}\left(\lambda^2-\lambda^{-1}\right)}, \quad \text{if } G_{\mathrm{eq}}>0 \end{aligned}\right\} = S(\lambda) \tag{5.51}$$

Notice that the subscript "E" in the functions Λ_{E} and S_{E} refers to the nonlinear relaxation modulus $E(t,\varepsilon)$, i.e. to tensile deformations in which the strain history is $\varepsilon(t) = \varepsilon\cdot H(t)$ (cf. §5.3.3.II-a).

5.3.2 Data Processing, Error Analysis, and Reproducibility

Accurate measurements in uniaxial extension are more difficult to obtain than in simple shear. The basic criterion for evaluating the reliability of extensional data is to compare the measured small-strain behavior with the linear response predicted by the Boltzmann superposition principle using the relaxation spectrum (cf. Eq. (5.36) and related discussion, and §5.3.3.I-a). Describing the type of nonlinearities exhibited by the material also relies upon a comparison with the LVE response limit (§5.3.3.II-a). Such comparisons, however, are meaningful as long as the sources of biased error have been identified (if any), and the unbiased error minimized.

The experimental data were processed in the MATLAB® environment. A program was developed to accomplish various tasks, which included the analysis of the instrument response at short times, the statistical treatment of the values of stress, strain, and time at the peak stress (σ_{max}, $\varepsilon|_{\sigma_{max}}$, and $t|_{\sigma_{max}}$) and at rupture (σ_b, ε_b, and t_b), and the data averaging from repetitive tests.

In transient measurements, repetitive tests generally yield data of unequal sample sizes and not collected at the same values of time. In start-up of steady uniaxial extension, small differences in time may correspond to significantly different values of strain when the extension rate is large (since $\varepsilon(t) = \dot{\varepsilon} \cdot t$). This was taken into account when implementing the averaging algorithm (a key script of this program is provided in Appendix H, §H.3.2). A separate issue stems from measuring the mechanical properties up to the breaking point. In our experiments, the peak stress was usually followed by a

more or less abrupt and irregular descent to the breaking stress. Since the time elapsed before rupture varied from specimen to specimen (under the same experimental conditions), the description of the final portion of the stress-strain curve in terms of average properties was achieved through extrapolation (for each curve shown in Figures 5.4–5 and 5.18–20, the last data point was obtained with this procedure, and it represents the average peak stress). During measurements, high-speed data acquisition was used to accurately identify the ultimate properties. After processing, experimental data were selected that were evenly spaced along the time/strain axes and sufficiently sparse to allow visualization through data point markers (the relevant algorithm is offered in §H.3.2).

Examples of this data processing are shown in Figure 5.2, for tests conducted at extension rates of 10^{-4} s^{-1} and 10^{-1} s^{-1}. The relative error on the measured stress (i.e. ratio of standard deviation to average value) is shown, as a function of strain at each strain rate, in Figure 5.3. Before reaching steady-state, the imposed rate of strain was either inaccurate (Figure 5.2(a)) or exhibited an overshoot due to the rotational inertia of the rheometer motor (Figure 5.2(b)). The *scatter* in the initial $\dot{\varepsilon}(t)$ data, observed for tests performed at the lower rates of strain ($\dot{\varepsilon} \leq 10^{-2}$ s^{-1}), had only a minor effect on the measured material response. The strain rate converged to the commanded value, on average, after 1.5 s at $\dot{\varepsilon} = 10^{-4}$ s^{-1} (Figure 5.2(a)) and 50 ms at $\dot{\varepsilon} = 10^{-2}$ s^{-1}, when the deformation of the specimen was still well within the linear regime ($\varepsilon < 10^{-3}$, Figure 5.3). This source of random error was largely mitigated by the averaging process. On the other

hand, the effect of the *strain rate overshoot* (instrument "*transient*" of about 30 ms), characteristic of measurements conducted at $\dot{\varepsilon} \geq 10^{-1}$ s^{-1}, is clearly visible in the short-time stress response (Figure 5.2(b)) as well as in the increased measurement error at small strains (Figure 5.3). This unavoidable experimental limitation (producing a systematic error) was rather severe at the maximum elongation rate of 10 s^{-1}, where deformation in the linear regime and up to Hencky strains of about 0.2 ($\lambda \simeq 1.2$) occurred entirely under non-ideal conditions (Figure 5.3).

Reproducibility was poorer at low and moderate extensions ($\lambda < 1.5$), especially for measurements at $\dot{\varepsilon} = 10^{-1}$ s^{-1} (Figures 5.2(b) and 5.3). The relative error, centered around 18%, decreased with increasing deformation. The reproducibility for mild extensions, and its strain dependence, may be explained by invoking a random, small degree of *anisotropy* of the test specimens.

It is well known that microdomains in polycrystalline (i.e. multi-grain) triblock copolymers can be highly oriented[100,441,442] as well as disrupted[100,391,443-445] under large deformations. Macroscopic alignment of the microdomains obviously leads to anisotropic mechanical properties. Anisotropy is exhibited either below[111,117,446] or above[109] the glass transition of the higher T_g block, depending on whether pre-oriented triblocks are tested in uniaxial extension or simple shear (respectively). The dramatic effect of microdomains alignment on mechanical properties was first revealed by the pioneering investigations of Keller and co-workers[441,446]. By extruding a poly(styrene–*b*–butadiene–*b*–styrene) triblock copolymer (S–B–S, Kraton® 102 25 wt% S), they obtained single crystal-type

samples with hexagonally-packed glassy S cylinders embedded in the softer B matrix. The elastic anisotropy was characterized at room temperature, and the ratio of the Young's moduli parallel ($E_{0,\parallel}$) and perpendicular ($E_{0,\perp}$) to the cylinder axis was determined to be about 100. More recently, Daniel and Hamley[111] studied the behavior of sphere- and cylinder-forming poly(styrene–*b*–ethylene–*co*–butylene–*b*–styrene) triblocks (S–EB–S, Kraton® G1657 13 v% S, and G1650 29 v% S), with macroscopically oriented samples prepared by pressure molding followed by lubricated channel die compression. At room temperature, the ratio of the linear storage moduli parallel ($E'_{\parallel}$) and perpendicular ($E'_{\perp}$) to the flow direction was about 2.5 (for Kraton® G1657, due to the alignment of the most densely packed [111] direction) and 10 (for Kraton® G1650, whose specimens possessed a mosaicity rather than being "single crystals"). Furthermore, $E'_{\parallel}$ increased with the compression ratio (for moderate compression ratios that did not break the bcc unit cell and the cylinders).

The microstructure in our material consisted in irregularly shaped PLA microdomains – prolate spheroids with aspect ratio $\delta \approx 8.5$ (Chapter 3, §3.3.4.IV-e and Table 3.9) – embedded in the PI matrix with no short-range order (§3.3.1 and Appendix A). Testing specimens were prepared at a temperature where the triblock was still microphase-segregated (§3.2.3), and the resulting hydrodynamic flow coarsely resembled that generated by channel die compression (Figure 3.2). For the measurement error at low elongations shown in Figure 5.3 to originate from different degrees of microdomains orientation, its magnitude should be consistent with the mechanical anisotropy

determined by Daniel and Hamley. In terms of relative error on the measured linear stress, their results can be loosely translated into an upper limit of about 45% for the bcc triblock, and about 85% for the hexagonally-packed cylinder structure. Considering that the PLA domains are prolate spheroids rather than cylinders[h], are not arranged in an ordered lattice, and the testing temperature is rather close to their T_g, we could anticipate that the relative error at small strains should lie below approximately 45%, as is observed in Figure 5.3. Most likely, different degrees of orientation were the result of different compression ratios (cf. §3.2.3).

That the measurement error at low elongations stemmed from random, small degrees of orientation of the PLA domains during our pressing procedure is also supported by the strain dependence of the relative error. When microphase-segregated triblock copolymers consisting of a minority glassy component embedded in a rubbery matrix are deformed, a competition ensues between chain orientation and domain orientation along the stretching direction.[100,391] As the deformation increases, bridge- and knotted-loop-type midblocks drive the re-orientation of glassy cylinders, which tend to rotate their long axis toward the stretching direction. The large-strain SAXS study conducted by Pakula et al.[391] showed that the same final morphological state (a zig-zag chevron structure of broken cylinders) is reached at high deformation regardless of the initial long-range order (i.e. of whether the cylinders are randomly dispersed or macroscopically oriented in any direction with

---

[h] The cylindrical domains in block copolymers have very large aspect ratios, of order 1000 for a poly-grain structure and essentially infinite for single crystal-type samples.[100]

respect to the stretch axis). We therefore interpret the strain dependence shown in Figure 5.3 as indicative of the PLA domains re-orientation process, probably occuring without fragmentation[391] in view of their rather small aspect ratio and length (cf. Appendix A, Figure A.1(b)).

We are now in a position to evaluate the accuracy of the short-time/small-strain response (§5.3.3.I), assess the type of (elastic and viscoelastic) nonlinearities exhibited by our triblock (§5.3.3.II), compare the large-strain behavior with rubber elasticity models (§5.3.4.IV), analyze the ultimate properties (§5.3.5), and infer the governing mechanism of rupture (§5.3.5.III).

The experimental data shown in Figures 5.3–5 and 5.18–25, obtained through the foregoing averaging process and statistical analysis, were color- and symbol-coded according to the applied rate of strain: black circles for 10^{-4} s^{-1} (○), red right-pointing triangles for 10^{-3} s^{-1} (▷), blue diamonds for 10^{-2} s^{-1} (◇), green left-pointing triangles for 10^{-1} s^{-1} (◁), orange squares for 1 s^{-1} (□), and violet down-pointing triangles for 10 s^{-1} (▽). Grayed out symbols refer to data collected during the intrument "*transient*". When appropriate, these data (and those collected at $\dot{\varepsilon} = 10$ s^{-1}) were excluded from further analysis (cf. Table 5.1 and Figure 5.6).

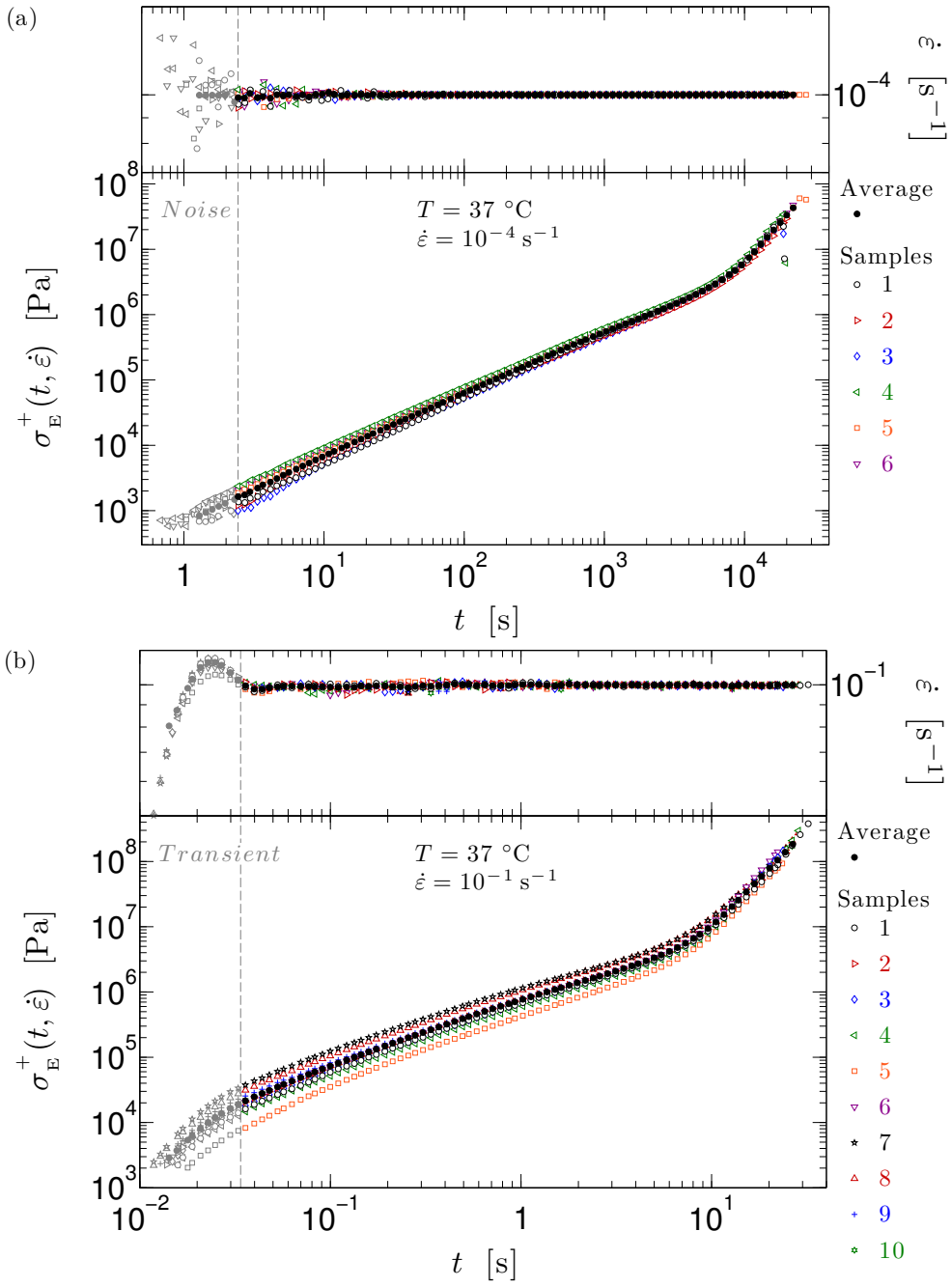

Figure 5.2. Examples of data processing and analysis, for elongational stress measured at $\dot{\varepsilon} = 10^{-4}$ s^{-1} (a), and at $\dot{\varepsilon} = 10^{-1}$ s^{-1} (b). In each plot, the upper panel shows the actual strain rate output during the test, $\dot{\varepsilon}(t)$. Before reaching steady-state, $\dot{\varepsilon}(t)$ was either (a)

inaccurate (labeled as "*noise*" on the plot, representative of tests conducted at $\dot{\varepsilon} \leq 10^{-2}$ s^{-1}), or (b) exhibited an overshoot due to the rotational inertia of the rheometer motor (instrument "*transient*" of about 30 ms, representative of tests conducted at $\dot{\varepsilon} \geq 10^{-1}$ s^{-1}). Reproducibility was poorer at low and moderate extensions ($\lambda < 1.5$), especially for measurements at $\dot{\varepsilon} = 10^{-1}$ s^{-1} (cf. Figure 5.3). Raw data were processed and averaged as described in the text. For each average stress-time curve (depicted here by filled circles), the last data point corresponds to the average peak stress, rather than the average stress-to-break.

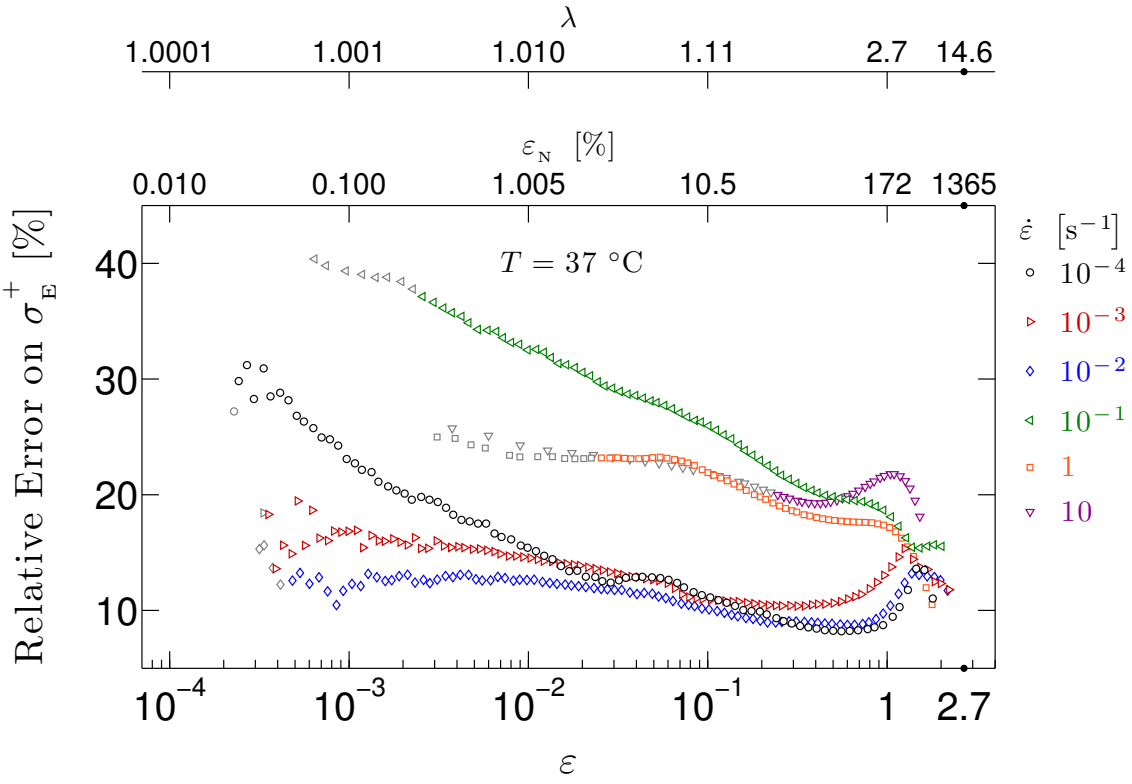

Figure 5.3. Relative error on the measured stress (i.e. ratio of standard deviation to average value), as a function of the applied strain. For $\dot{\varepsilon} \geq 10^{-1}$ s^{-1}, grayed out symbols refer to data collected during the instrument "*transient*". On the strain axes, the maximum strain at rupture is shown (exhibited for $\dot{\varepsilon} = 10^{-2}$ s^{-1}).

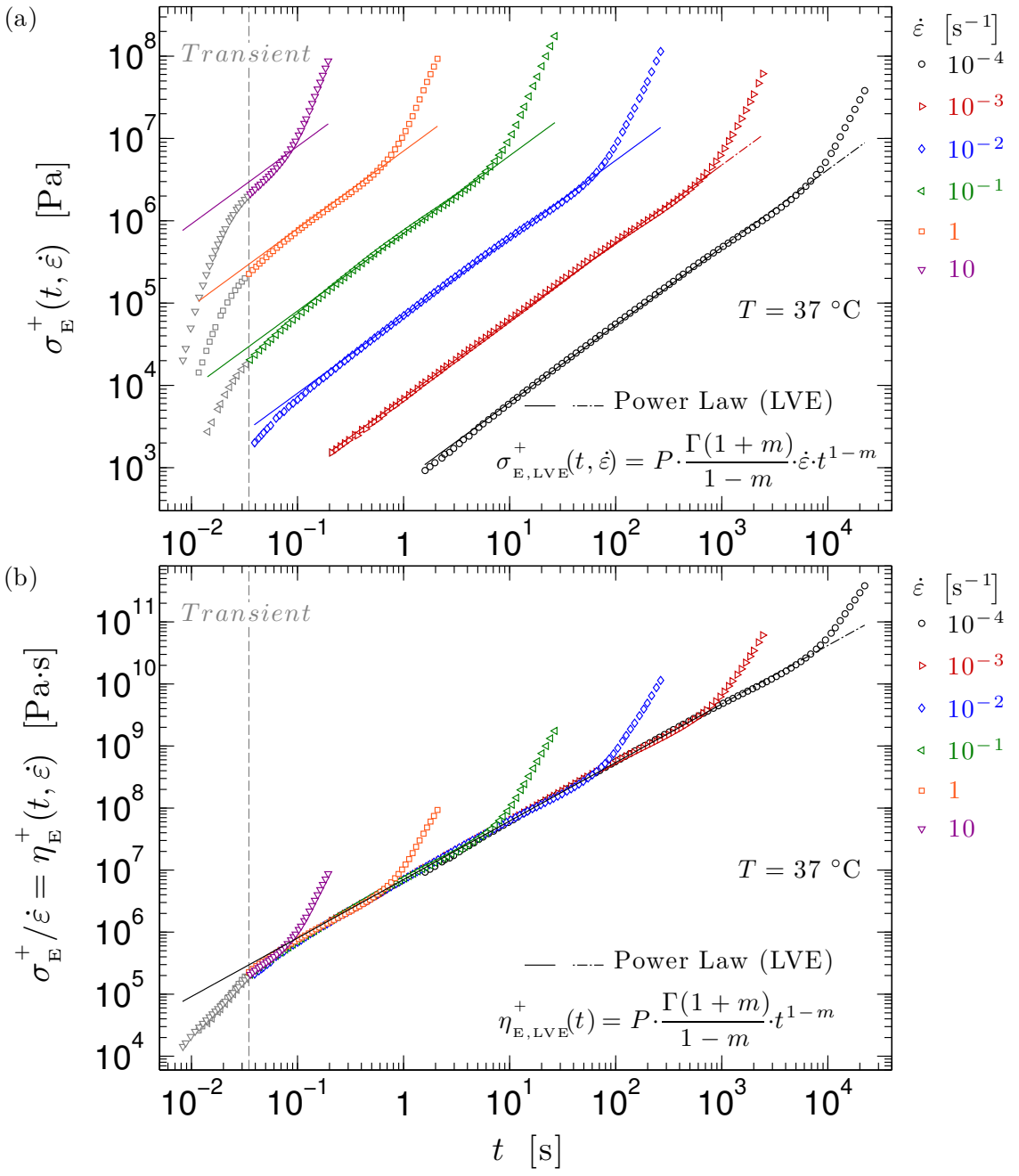

Figure 5.4. Elongational stress (a) and viscosity (b) vs. time. Lines depict the LVE predictions from the linear harmonic response modeled with a power-law relaxation spectrum (dot-dashed lines are used for $t > 1/\omega_{min}$ – Figure 4.2). The instrument "*transient*" ($\dot{\varepsilon} \neq$ const. for $t < 30$ ms) is shown.

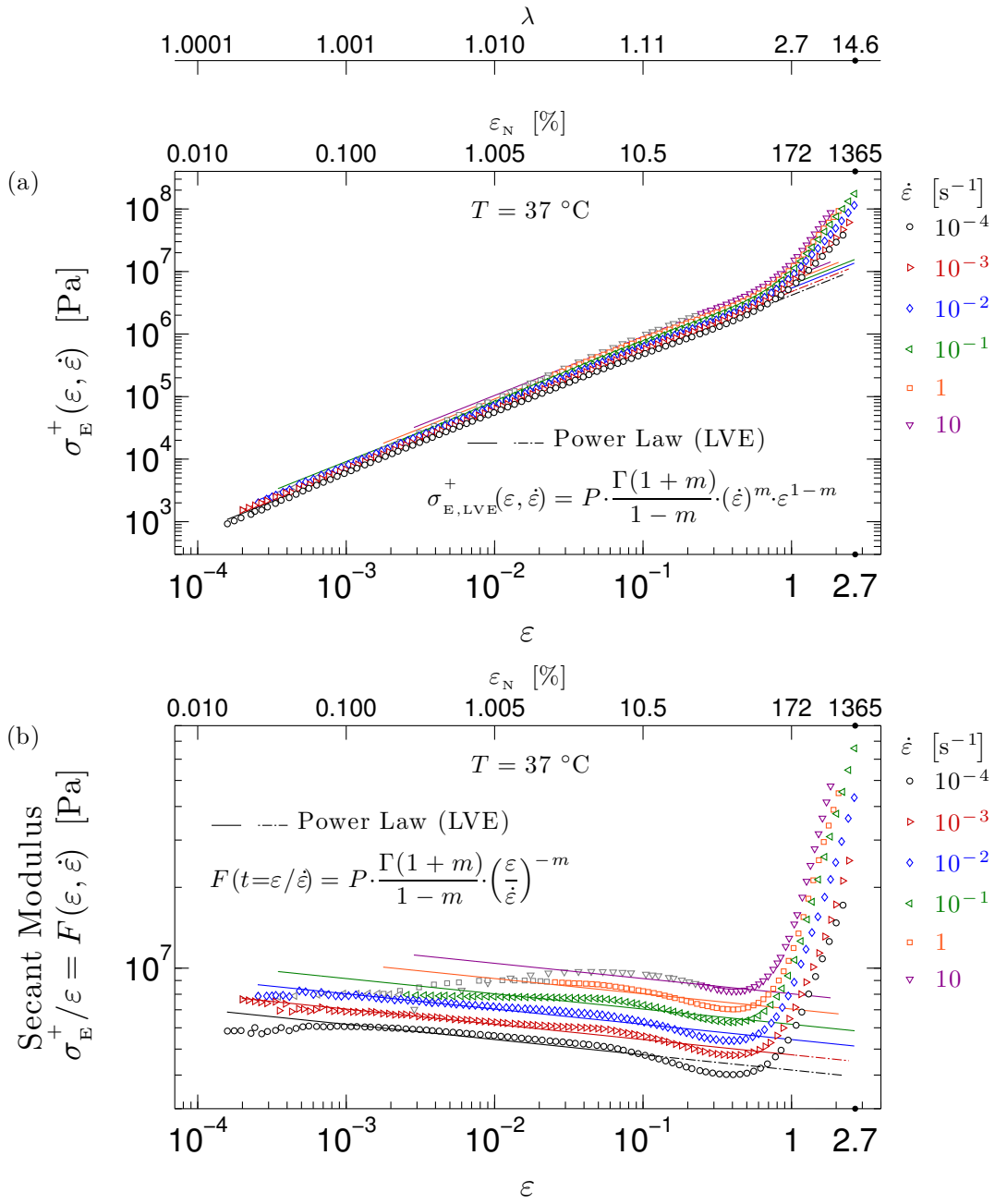

Figure 5.5. Elongational stress (a) and secant modulus (b) vs. strain. Lines depict the LVE predictions from the linear harmonic response modeled with a power-law relaxation spectrum (dot-dashed lines are used for $t > 1/\omega_{min}$ – Figure 4.2). On the strain axes, the maximum strain at rupture is shown (exhibited for $\dot{\varepsilon} = 10^{-2}$ s^{-1}).

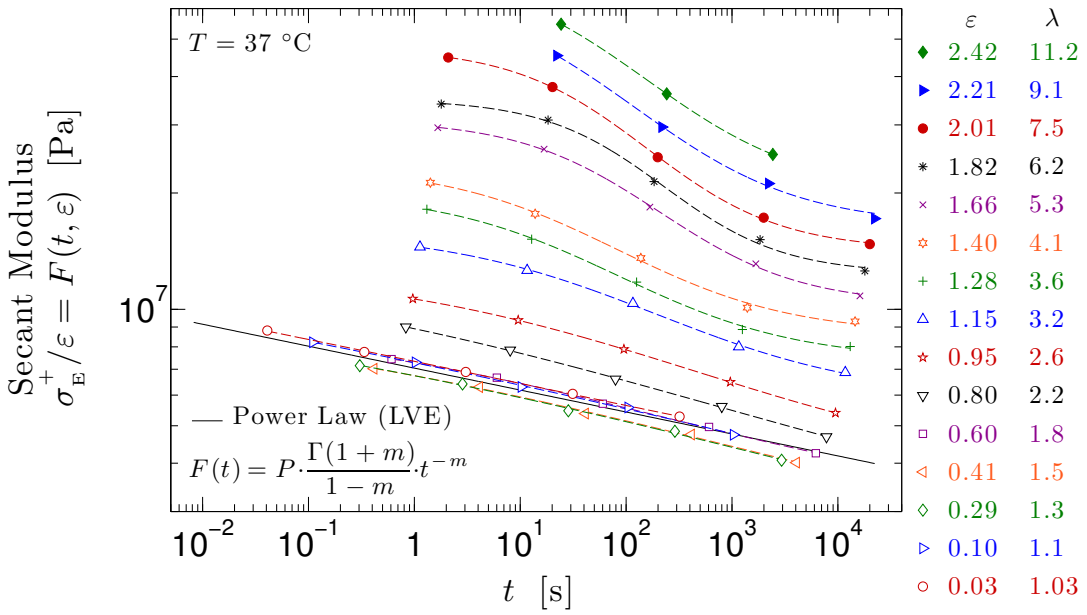

Figure 5.6. Secant modulus vs. time. *Iso-strain* data obtained from analysis of curves shown in Figure 5.5(b), after discarding data collected during the instrument "*transient*" and data measured at $\dot{\varepsilon} = 10\ s^{-1}$ (§5.3.2). The solid line represents the LVE prediction from the linear harmonic response modeled with a power-law relaxation spectrum (Figure 4.2). Linear viscoelastic behavior is observed for $\varepsilon = 0.03$ (○) (cf. Figure 4.1). Notice that these small-strain data fall to within 4.3% of the predicted LVE curve. Considering that they were extracted from tensile data subject to inevitable random and systematic errors (due to instrument limitations at short times, Figure 5.2), the agreement is excellent. At higher strains, three features emerge. The time dependence is progressively accelerated, and the modulus undergoes a Z-shaped transition mirroring the behavior of the linear storage modulus $E'(\omega)$ across the glass-rubber viscoelastic transition of the hard domains (cf. Figure 4.7(a)). The increased relaxation rate is already noticeable in the long-time behavior of data at $\varepsilon = 0.10$ (▷). Once fully developed ($\varepsilon \geq 1.66$), this transition appears centered around $t \approx 200$ s and with the same power-law decay, $F(t,\varepsilon) \sim t^{-m}$, at shorter and longer times (cf. Figure 4.7(a) and Table 4.5). In addition to this *strain-induced relaxation*, the modulus "*strain softens*" at $\varepsilon = 0.29$ (◇) and 0.41 (◁), and "*strain hardens*" for $\varepsilon > 0.60$, consistently with the behavior shown in Figure 5.5(b) (cf. Figures 5.21 and 5.22).

5.3.3 Linear and Nonlinear Viscoelastic Behavior

In start-up of steady uniaxial extension, strain, strain rate, and time are related by

$$\varepsilon(t) = \dot{\varepsilon} \cdot t, \quad \text{with } \dot{\varepsilon} = \text{const.} \tag{5.52}$$

Therefore, only two of them can be varied independently. In presenting our results, we will use all three combinations (for reasons that will become clear shortly). When strain is selected as independent variable, the notation ε will be adopted.

5.3.3.I Linear response

5.3.3.I-a LVE theoretical predictions

In the small-strain response limit, the stress-strain relationship can be represented by (cf. Eq. (5.41))

$$\begin{aligned} \sigma^{+}_{\text{E,LVE}}(t,\dot{\varepsilon}) &= F(t) \cdot \varepsilon(t) \\ &= F(t) \cdot \dot{\varepsilon} \cdot t \end{aligned} \tag{5.53}$$

where $\sigma^{+}_{\text{E,LVE}}$ stands for the transient LVE net tensile stress[i], and $F(t)$ is the (*linear*) *constant-strain-rate modulus* first introduced by Smith[421] in 1962 (cf. Appendix D, Eq. (D.26)a and Table D.1). $F(t)$ is also referred to as the *secant modulus*, because on a stress-strain plot it is the secant of the angle between the abscissa, $\varepsilon(t)$, and a straight line

[i] Also called the *tensile stress growth function*.[437]

drawn from the origin to $\sigma^{+}_{\mathrm{E,LVE}}(t,\dot{\varepsilon})$. It follows from Eq. (5.53) that the transient LVE extensional viscosity[j] is (cf. Appendix D, Eq. (D.26)b and Table D.1)

$$\begin{aligned}\eta^{+}_{\mathrm{E,LVE}}(t) &\equiv \frac{\sigma^{+}_{\mathrm{E,LVE}}(t,\dot{\varepsilon})}{\dot{\varepsilon}} \\ &= F(t)\cdot t\end{aligned} \tag{5.54}$$

Since the linear secant modulus is strain-independent, the transient extensional viscosity in the linear regime is a function of time alone. As a result, on a plot η^{+}_{E} vs. t curves obtained at different rates of strain $\dot{\varepsilon}$ must superpose when $\varepsilon(t)$ is small, thereby defining the so-called *LVE envelope*.[36] The stress, on the other hand, depends not only on the time to reach $\varepsilon(t)$ but also on the strain magnitude $\varepsilon(t)$.

The constant-strain-rate modulus $F(t)$ is related to the stress relaxation modulus $E(t)$ by the equation[421] (cf. Appendix D, Eq. (D.27) and Table D.1)

$$\left[1+\frac{d\log F(t)}{d\log t}\right]F(t)=E(t) \tag{5.55}$$

which, for material exhibiting *critical-gel-like behavior* (i.e. a single power-law relaxation pattern over some range of times/frequencies), translates into (cf. Appendix E, Tables E.2 and E.3)

$$(1-m)F(t)=E(t) \tag{5.56}$$

where m is the power-law exponent; $F(t)$ and $E(t)$ are thus similar in magnitude and share the same time dependence, i.e. they both decay as $\sim t^{-m}$.

---

[j] Also called the *tensile stress growth coefficient*.[437]

In small-amplitude oscillatory uniaxial extension, LIL50–12 exhibited a frequency dependence resembling that of a *critical-gel*[320,321,330,331] (Chapter 4, Figure 4.2(a)), which we modeled with a *power-law relaxation spectrum* (Figure 4.2(b) and §4.3.2.II). Accordingly, we can calculate $F(t)$ from the linear harmonic response as (Appendix E, Eq. (E.42) and Table E.3)

$$F(t) = P \cdot \frac{\Gamma(1+m)}{1-m} \cdot t^{-m} \tag{5.57}$$

where $P = 6.85$ MPa·s^m is a *quasi-property*[318], i.e. a fundamental material property related to the fractional dynamics of the system (Appendix F, §F.3.4–5), $m = 0.057$, and $\Gamma(\cdot)$ is the complete gamma function defined in Appendix C (§C.1). A relationship between m and the molecular structure of LIL50–12 was derived in §4.3.2.II-c of Chapter 4 (Eq. (4.21)). The physical interpretation of P in terms of the mechanical behavior of a *fractional element*[342] as well as of *Chambon–Winter's gel strength*[266,289-292,319] was discussed in §4.3.2.II-d.

With Eq. (5.57), the transient linear stress and viscosity can be predicted,

$$\sigma^{+}_{\mathrm{E,LVE}}(t,\dot{\varepsilon}) = P \cdot \frac{\Gamma(1+m)}{1-m} \cdot \dot{\varepsilon} \cdot t^{1-m} \tag{5.58}$$

$$\eta^{+}_{\mathrm{E,LVE}}(t) = P \cdot \frac{\Gamma(1+m)}{1-m} \cdot t^{1-m} \tag{5.59}$$

These predictions are, of course, within limits. In particular, the single power-law relaxation pattern will eventually break down at timescales close to the PLA glass-rubber viscoelastic transition (Figure 4.7). As a conservative estimate of this upper limit we can take the inverse of the characteristic frequency $\omega^{*}_{\alpha\beta}$, which defined the intersection of the

first two power-law regimes of the *fractional Zener model*[345] (Figure 4.6(b), Eq. (4.134), and Table 4.5). Thus, we can expect Eqs. (5.58) and (5.59) to apply as long as

$$\begin{aligned} t &\ll t_{\max} = \frac{1}{\omega^*_{\alpha\beta}} \approx 3\cdot 10^4 \text{ s} \\ \dot{\varepsilon} &\gg \dot{\varepsilon}_{\min} = \frac{\varepsilon_c}{t_{\max}} \approx 10^{-6} \text{ s}^{-1} \end{aligned} \tag{5.60}$$

where $\varepsilon_c \approx 3\%$ is the critical strain determined by isochronal strain sweep experiments (Figure 4.1 and §4.3.1 – cf. Figure 5.6). Eq. (5.60)b is clearly satisfied for the rates of strain employed in this study.

5.3.3.I-b Observed behavior

The observed stress-time response is shown in Figure 5.4(a). The choice of strain rates allowed us to cover wide experimental windows of stress and time. The lower bounds were set by the sensitivity of the instrument transducer coupled with the specimen geometry (≈ 1 kPa), and by the rotational inertia of the motor (≈ 30 ms, §5.3.2 and Figure 5.2). The upper bounds were imposed by the maximum stress at rupture (≈ 200 MPa, for $\dot{\varepsilon} = 10^{-1}$ s^{-1}), and by the longest time at rupture (≈ 6 h, for $\dot{\varepsilon} = 10^{-4}$ s^{-1}). Including the dwell time needed to relax stresses induced upon loading, a single test at 10^{-4} s^{-1} required about 18 h (§5.2.2). Performing tests at even lower rates of strain was deemed unpractical, since the time-to-break alone at a strain rate of 10^{-5} s^{-1} would have been approximately 60 h (cf. Figure 5.21(b)).

The agreement between the measured stress at small strains and the LVE prediction is solid. Even more so considering that the elongation rate used in Eq. (5.58) was the ideal, step-rate $\dot{\varepsilon}(t) = \dot{\varepsilon} \cdot H(t)$ rather than the actual instrument output (shown in Figure 5.2). For each rate of strain, the deviation at the shortest times is due to instrument limitations (namely, noise in the initial $\dot{\varepsilon}(t)$ signal for tests performed at $\dot{\varepsilon} \leq 10^{-2}$ s^{-1}, and the finite time response of the rheometer for tests conducted at $\dot{\varepsilon} \geq 10^{-1}$ s^{-1} – §5.3.2 and Figure 5.2). A special case is represented by the data at $\dot{\varepsilon} = 10$ s^{-1}. At this elongation rate, deformation in the linear regime and up to strains of about 0.2 ($\lambda \simeq 1.2$) occurred entirely under non-ideal conditions (i.e. $\dot{\varepsilon} \neq$ const. – cf. Figure 5.2(b) and 5.3). The stress that built up during this instrument "transient" was considerably lower than what would have been generated at $\dot{\varepsilon} = 10$ s^{-1}, and therefore the measured linear response lies wholly below the LVE prediction.

The stress normalized by extension rate, i.e. the transient tensile viscosity, is shown in Figure 5.4(b). For $t > 30$ ms, all the data superpose at small strains and fit nicely on the predicted linear viscoelastic curve. Data superposition implies that sources of random error were effectively mitigated by the averaging process discussed in §5.3.2. Agreement with the LVE prediction based on the linear harmonic response demonstrates that both data sets are accurate.[k] Notice that Eq. (5.59) yields, on a log-log plot, a straight line with

---

[k] Furthermore, since the linear response of the material to start-up of steady extension can be *predicted* using the same power-law exponent m and quasi-property P found from fits to the storage modulus $E'(\omega)$ (Figure 4.2), the quasi-property P truly characterizes the

slope equal to 1–m. Considering the dynamics of the PLA glass-rubber transition (§4.3.2.III-b), we may expect the LVE envelope to deviate from this simple behavior at times approaching $3{\cdot}10^4$ s (Eq. (5.60)a).

5.3.3.I-c The effect of linear relaxation on tensile behavior of critical-gel-like materials

It is also evident from Eqs. (5.58)–(5.59) that, for small values of m, the power-law relaxation spectrum tends to produce a linear time dependence of the transient viscosity, $\eta^{+}_{\mathrm{E,LVE}}(t) \sim t$, and linear time and strain dependencies of the transient stress, $\sigma^{+}_{\mathrm{E,LVE}}(t,\dot{\varepsilon}) \sim t$ and $\sigma^{+}_{\mathrm{E,LVE}}(\varepsilon,\dot{\varepsilon}) \sim \varepsilon$. The same data are shown in Figure 5.5(a), but now as tensile stress $\sigma^{+}_{\mathrm{E}}(\varepsilon,\dot{\varepsilon})$ vs. tensile strain ε. This view emphasizes the solid-like aspects of behavior and demonstrates more explicitly that the slow, power-law relaxation of LIL50–12 ($m = 0.057$) yields a small-strain response, $\sigma^{+}_{\mathrm{E,LVE}}(\varepsilon,\dot{\varepsilon}) \sim \varepsilon^{1-m}$ (shown by lines), close to the ideal linear elastic behavior, $\sigma_{\mathrm{E,LE}}(\varepsilon) \sim \varepsilon$, which in turn reduces to Hooke's law, $\sigma^{\mathrm{H}}_{\mathrm{E}}(\varepsilon_{\mathrm{N}}) \sim \varepsilon_{\mathrm{N}}$, for $\varepsilon < 0.1$ (Eq. (5.18)).

At service temperatures ($T_{\mathrm{g,B}} < T < T_{\mathrm{g,A}}$), microphase-segregated triblocks often exhibit critical-gel-like behavior with small values of the power-law exponent m. While a power-law relaxation is inherent to the ubiquitous Rouse dynamics[47] and local reptation[46,89,166]

---

linear viscoelasticity of LIL50–12 even though it contains a non-integer power of the fundamental dimension of time (Chapter 4, §4.3.2.II-d; Appendix F, §F.3.4–5).

(Chapter 3, §3.3.4.IV-d; Appendix F, §F.3.2), in block copolymers it may also stem from the slow star-like dynamics[35,168,169] of entangled dangling structures (§3.3.4.IV-b-d-e, Figure 3.5, and Eq. (3.21)). In uniaxial extension, examples of critical-gel-like behavior can be found in the work of Smith[447] on poly(styrene–*b*–butadiene–*b*–styrene) (S–B–S, Kraton® 101 30 wt% S, m = 0.033); the investigation of Bard and Chung[110] on S–B–S (Kraton® D1101 29 wt% S, m = 0.022); the study of Daniel and Hamley[111] on poly(styrene–*b*–ethylene–*co*–butylene–*b*–styrene) (S–EB–S, Kraton® G1657 13 v% S, m = 0.045, and G1650 29 v% S, m = 0.025); and the report of Hotta et al.[112] on poly(styrene–*b*–isoprene–*b*–styrene) (S–I–S, Aldrich Chemical Corp. 14 and 17 wt% S, respectively with m = 0.041 and 0.057).

However, when triblocks (or multiblocks) are subjected to tensile tests their linear viscoelastic relaxation is often neglected and data are presented only as stress vs. strain.[92,113,164,201,222,392,393,394] Furthermore, use of a single rate of strain is rather common.[92,201,392-394] Even when the tensile behavior is measured under different elongation rates, these usually cover no more than one[164,222] or two[113] orders of magnitude. Use of stress-strain plots coupled with a narrow range of applied strain rates may lead to underestimating the underlying relaxation (and its effect on tensile properties), hence treating the material as if it was a perfect elastic solid. Examples of this oversimplification include the study of Roos and Creton[113] on an undiluted S–I–S triblock (m = 0.026), and the more recent (and otherwise excellent) work of Watanabe and co-

workers[164,222] on 40 and 30 wt% solutions of $(S–I–S)_p$–type multiblocks in *n*-tetradecane ($m = 0.067$ and 0.076, respectively).

This type of approach, which unfortunately seems quite established in the literature of the last 30 years or so, is somewhat surprising. After all, the effect of linear and nonlinear relaxations on tensile behavior and ultimate properties of viscoelastic materials was clearly illustrated by the pioneering work of Smith on vulcanized rubbers[421,422,439,440,448-452] and triblock TPEs[447,451-453] between 1958 and 1978. An exception to the more recent literature is represented by the report of Hotta et al.[112]. By subjecting S–I–S triblocks to tensile tests at four strain rates (spanning about three orders of magnitude), these authors recognized the importance of taking into account the intrinsic power-law behavior of the material, with the inevitable consequence of acknowledging the lack of an experimental equilibrium stress-strain curve regardless of the test conditions (as long as $T < T_{g,S}$).[112] Their observation is in line with the earlier work of Smith, who showed that for real elastomers at service temperatures the equilibrium stress-strain curve (if any) can only be obtained through extrapolation.[439,440,451,452]

Thus, by masking almost completely the linear viscoelastic relaxation of LIL50–12, tensile data as shown in Figure 5.5(a) may be misleading. In particular, curves whose elongation rates differ only by an order of magnitude would appear essentially indistinguishable if slightly larger data point markers were used. If one insists on plotting tensile data as a function of strain, a better (more revealing) representation is achieved by considering the secant modulus $F(\varepsilon,\dot{\varepsilon})$, as shown in Figure 5.5(b). Here, the agreement

with the LVE predictions, i.e. the constant-strain-rate modulus $F(t)$ evaluated at $t = \varepsilon / \dot{\varepsilon}$, is clear. For the data obtained at $\dot{\varepsilon} \leq 10^{-2}$ s^{-1} slight deviations from the LVE curves can be observed at short times, due to the noise in the actual $\dot{\varepsilon}(t)$ signal, while the agreement is poorer for data at $\dot{\varepsilon} \geq 10^{-1}$ s^{-1} because of the instrument "transient" ($\dot{\varepsilon} \neq$ const. for $t <$ 30 ms). Overall, the small-strain data decay in a power-law fashion, $F(t = \varepsilon / \dot{\varepsilon}) \sim \varepsilon^{-m}$, as dictated by the linear viscoelastic relaxation of LIL50–12. As opposed to stress-strain plots, use of the secant modulus highlights the viscous character of the response. For a perfect elastic solid, the LVE curves would collapse onto a single curve with zero slope and intercept $P = E_0$ (cf. Eq. (5.57)).

5.3.3.II Nonlinear response

5.3.3.II-a Theoretical framework

In the large-strain regime, we can express the stress-strain relationship as follows (cf. Eq. (5.53))

$$\begin{aligned} \sigma^{+}_{\mathrm{E,NLVE}}(t,\dot{\varepsilon}) &= F(t,\dot{\varepsilon}) \cdot \varepsilon(t) \\ &= F(t,\dot{\varepsilon}) \cdot \dot{\varepsilon} \cdot t \\ &= F(t) \cdot \Lambda_{\mathrm{F}}(t,\dot{\varepsilon}) \cdot \dot{\varepsilon} \cdot t \end{aligned} \tag{5.61}$$

where $\sigma^{+}_{\mathrm{E,NLVE}}$ stands for the transient NLVE net tensile stress, $F(t,\dot{\varepsilon})$ is the *nonlinear constant-strain-rate modulus* (cf. Eq. (5.42)), and $\Lambda_{\mathrm{F}}(t,\dot{\varepsilon})$ is a measure of the deviation of the nonlinear viscoelastic behavior from the linear response limit (cf. Eq. (5.43)).

Thus, we have introduced a nonlinear material function[l], $F(t,\dot{\varepsilon})$, by analogy with the nonlinear relaxation modulus $E(t,\varepsilon)$. Factoring out the time dependence associated with the linear response, $F(t)$, leads to the definition of $\Lambda_F(t,\dot{\varepsilon})$.[m] It follows that $\Lambda_F(t,\dot{\varepsilon})$ contains information about *all* the nonlinear effects that influence the measured response at large strains (cf. §5.3.1.II-b-c). Hence, it is, in general, a function of both time and strain (or strain rate). The time dependence of $\Lambda_F(t,\dot{\varepsilon})$ stems from nonlinear relaxation mechanisms (e.g. chain retraction within the tube, for homopolymer melts – §5.3.1.II-b) and/or from a perturbation of mechanisms that occur at small strains.[440] If the time dependencies of $F(t,\dot{\varepsilon})$ and $F(t)$ coincide, $\Lambda_F(t,\dot{\varepsilon})$ becomes time-independent and TSF applies (cf. Eqs. (5.45)–(5.46)).

The transient NLVE extensional viscosity follows from Eq. (5.61),

$$\begin{aligned}\eta^{+}_{E,NLVE}(t,\dot{\varepsilon}) &\equiv \frac{\sigma^{+}_{E,NLVE}(t,\dot{\varepsilon})}{\dot{\varepsilon}} \\ &= F(t,\dot{\varepsilon})\cdot t \\ &= F(t)\cdot\Lambda_F(t,\dot{\varepsilon})\cdot t\end{aligned} \tag{5.62}$$

As opposed to $\eta^{+}_{E,LVE}(t)$, the transient tensile viscosity in the nonlinear regime depends on both time and strain (or strain rate).

---

[l] Although not explicitly introduced, the function $F(t,\dot{\varepsilon})$ was clearly alluded to by Smith[440] in 1969.

[m] The analogous function used by Smith[440] is $\Gamma(t,\lambda)=\Lambda_F(t,\lambda)\cdot\ln\lambda$. Obviously, the symbol Γ in Smith's notation bears no connection with the complete gamma function.

Since

$$\Lambda_{\mathrm{F}}(t,\dot{\varepsilon}) \equiv \frac{F(t,\dot{\varepsilon})}{F(t)} = \frac{\sigma^{+}_{\mathrm{E,NLVE}}(t,\dot{\varepsilon})}{\sigma^{+}_{\mathrm{E,LVE}}(t,\dot{\varepsilon})} = \frac{\eta^{+}_{\mathrm{E,NLVE}}(t,\dot{\varepsilon})}{\eta^{+}_{\mathrm{E,LVE}}(t)} \tag{5.63}$$

$\Lambda_{\mathrm{F}}(t,\dot{\varepsilon})$ gives a complete representation of the nonlinear viscoelastic behavior in tensile tests at constant rate of strain. In the literature, it has become customary to classify the transient extensional flow behavior from the way in which the nonlinear response departs from the linear one.[36] If the nonlinear data rise significantly above the linear curve at some point, the material is said to be *strain hardening*, and if they fall below, it is said to be *strain softening*.[36,340] In terms of $\Lambda_{\mathrm{F}}(t,\dot{\varepsilon})$, this classification scheme translates into

$$\Lambda_{\mathrm{F}}(t,\dot{\varepsilon}) \begin{cases} > 1 & \text{strain hardening} \\ = 1 & \text{LVE} \\ < 1 & \text{strain softening} \end{cases} \tag{5.64}$$

Because the transient LVE extensional viscosity is independent of strain (or strain rate), strain hardening/softening behavior is most easily visualized by an upward/downward deviation from the LVE envelope (Eq. (5.54)) on a plot η^{+}_{E} vs. t.

Although widely used[36], the above criterion for classifying the transient nonlinear response has been disputed[454,455], the observation being that a basis of comparison to define strain hardening/softening should involve the use of a finite strain tensor (rather than the infinitesimal strain tensor from which the LVE response originates, Eq. (5.35)). No universal consensus, however, has been found on what such a basis of comparison should be. While Dealy[454] proposed the Lodge rubber-like liquid (Eq. (5.34)), Wagner et al.[455] argued in favor of the original Doi–Edwards model. Dealy's proposal would make

the definition of strain hardening/softening coincide with the general definition of extensional damping function given by Eq. (5.38). As such, all uncrosslinked materials would exhibit strain softening behavior (§5.3.1.II-b). Conversely, according to the definition put forward by Wagner et al.[455], virtually no materials would be strain softening, since the original D–E theory gives the maximum degree of damping that can be predicted by any tube model[436] (§5.3.1.II-b).[n]

5.3.3.II-b Observed behavior

We are now in a position to analyze the nonlinear response exhibited by our triblock. Two features can be observed in Figure 5.4: the abrupt upturn from the LVE curves ($\Lambda_F(t,\dot{\varepsilon}) > 1$, *strain hardening*), and the *unattainability of a steady-state* even at the lowest applied strain rate. As the elongation rate increases, the data rise substantially above the linear response at progressively shorter times. In addition, stress and viscosity continue to increase steadily up to their peak values, which correspond to the onset of rupture (§5.3.2), never reaching a plateau. The onset of strain hardening occurs at a roughly

---

[n] The term "strain hardening" is also used for *metals* subjected to uniaxial extension. In this context, however, it refers to the shape of the stress-strain curve in the region of *plastic* (i.e. non-recoverable) deformation.[456] Past the yield point, the stress-strain relationship for many metals can be approximated by a power-law, $\sigma_E = K \cdot \varepsilon^n$, where K is called the strength coefficient and n is the "strain-hardening exponent". In this way, the ideal plastic and elastic behaviors correspond to $n = 0$ and $n = 1$ (respectively). At room temperature, metals usually exhibit values of n ranging from 0.1 to 0.5.[456] Therefore, they are said to be "strain hardening" because the stress required to produce continued plastic deformation increases with increasing plastic strain.[456]

constant value of strain, as can be inferred from a visual inspection of Figure 5.5(a). Here, Eq. (5.63) becomes

$$\Lambda_{\mathrm{F}}(\varepsilon,\dot{\varepsilon}) \equiv \frac{F(\varepsilon,\dot{\varepsilon})}{F(t=\varepsilon/\dot{\varepsilon})} = \frac{\sigma^{+}_{\mathrm{E,NLVE}}(\varepsilon,\dot{\varepsilon})}{\sigma^{+}_{\mathrm{E,LVE}}(\varepsilon,\dot{\varepsilon})} \tag{5.65}$$

Except for data at $\dot{\varepsilon} = 10\ \mathrm{s}^{-1}$, the stress response in the region $\varepsilon > 1$ could be modeled by a simple power-law expression,

$$\text{for } \varepsilon > 1 \quad \begin{cases} \sigma^{+}_{\mathrm{E,NLVE}}(t,\dot{\varepsilon}) = A\cdot\left(\dot{\varepsilon}\right)^{c(\dot{\varepsilon})}\cdot t^{\,b(\dot{\varepsilon})} \\ \sigma^{+}_{\mathrm{E,NLVE}}(\varepsilon,\dot{\varepsilon}) = A\cdot\left(\dot{\varepsilon}\right)^{c(\dot{\varepsilon})-b(\dot{\varepsilon})}\cdot \varepsilon^{\,b(\dot{\varepsilon})} \end{cases} \tag{5.66}$$

where A is a constant (a quasi-property with dimensions of $\mathrm{Pa}\cdot\mathrm{s}^{c-b}$), while $b(\dot{\varepsilon})$ and $c(\dot{\varepsilon})$ depend slightly on the rate of strain, varying from about 2.4 to 3.0. For data at $\dot{\varepsilon} = 10\ \mathrm{s}^{-1}$, time and strain dependencies in the region $\varepsilon > 1$ were found to obey a different power-law exponent, $b = 3.392$ and $b = 3.165$ (respectively). Since time and strain are related by Eq. (5.52), the exponent should be the same. This discrepancy signals a mismatch between the time and strain values calculated by the instrument, and therefore data at $\dot{\varepsilon} = 10\ \mathrm{s}^{-1}$ were excluded from this analysis. The interception between Eq. (5.66)b and the LVE predictions, i.e. Eq. (5.58) evaluated at $t = \varepsilon/\dot{\varepsilon}$, occurs approximately at a constant value of strain, $\varepsilon^{**} \simeq 0.82$ ($\lambda^{**} \simeq 2.27$), which can be taken as a rough estimate for the onset of strain hardening. These results are summarized in Table 5.1.

Table 5.1. Parameters characterizing the large-strain behavior ($\varepsilon > 1$) shown in Figures 5.4(a) and 5.5(a), according to Eqs. (5.66). The strain values, ε^{**} and λ^{**}, represent the interceptions between the LVE prediction, Eq. (5.58) evaluated at $t = \varepsilon / \dot{\varepsilon}$, and Eq. (5.66)b. Thus, they approximately identify the onset of strain hardening.

A [MPa·s^{c-b}]	$\dot{\varepsilon}$ [s^{-1}]	b	c	$c-b$	ε^{**}	λ^{**}
11.01	10^{-4}	2.433	2.496	0.063	0.77	2.16
	10^{-3}	2.663	2.759	0.096	0.90	2.46
	10^{-2}	2.825	2.894	0.069	0.81	2.25
	10^{-1}	3.001	3.058	0.057	0.81	2.25
	1	2.919	2.979	0.060	0.80	2.23
	Average	2.768	2.837	0.069	0.82	2.27

Once again, plotting the secant modulus $F(\varepsilon,\dot{\varepsilon})$ as a function of strain is most revealing. The strain hardening behavior in Figure 5.5(b) is apparent. By visual inspection, the data rise significantly above the LVE curves at a strain $\varepsilon \approx 0.7$ ($\lambda \approx 2$) that is weakly dependent on deformation rate, consistently with the results shown in Table 5.1. However, an additional feature emerges, for the modulus can also be observed to fall below the LVE curves ($\Lambda_F(\varepsilon,\dot{\varepsilon}) < 1$, *strain softening*) at relatively low strains. The onset of strain softening can be located within the range $0.10 < \varepsilon^* < 0.20$ ($1.1 < \lambda^* < 1.2$). Choosing as a basis of comparison the actual small-strain power-law responses rather than the predicted LVE curves shifts the beginning of strain softening to even smaller strains, roughly about 0.07–0.08. Notice that these strains are small enough that in this

regime the Hencky measure and the engineering/nominal strain almost coincide (so that $\varepsilon = 0.07$ is practically equivalent to $\varepsilon_N = 7\%$ – cf. Figure 5.5).

We are not aware of studies in which triblock TPEs were observed to exhibit strain softening followed by strain hardening behavior. Had the secant modulus been considered more often in the analysis of experimental data, other authors would have certainly noticed this behavior in the past.

5.3.3.II-c Expected behavior for undiluted, monodisperse PI homopolymer

The first natural step in understanding the nonlinear extensional behavior of LIL50–12 is to consider how the PI block would behave, under the same experimental conditions, if the PLA endblocks were not present. In other words, it is instructive to examine the expected start-up tensile response of an undiluted, monodisperse PI melt with the same molar mass as the midblock ($M_{n,I}$ = 49800 g/mol, Table 3.1). The experimental requirement to achieve steady-state elongational flow will be discussed first, followed by the theoretical explanation (and necessary conditions) for strain softening/hardening given by tube models.

Regimes of behavior in start-up of steady uniaxial extension of homopolymer melts and vulcanized rubbers

For melts, most extensional-flow experiments are interrupted by sample rupture before attainment of steady-state.[36,45] The current understanding of rupture of polymer liquids in extension largely stems from the work published by Vinogradov and collaborators[457-459] in

1975. In their investigations, numerous isothermal tensile tests at constant rate of (true/Hencky) strain were performed on long, linear polyisoprenes and polybutadienes of various lengths ($7 \le M_v/10^3$ g/mol ≤ 830) and with very narrow molar mass distribution ($M_w/M_n \le 1.1$). The experimental conditions were such that both elasticity and viscosity were expected to contribute to the measured response. Thus, a key aspect of their experimental approach was the decomposition of the ultimate deformation into an *elastic* (recoverable) part[o], $\varepsilon_b^{elastic}$, and a *viscous* (dissipative) part, $\varepsilon_b^{viscous}$, i.e. the non-recoverable deformation or flow. Their investigations were later extended to include many other linear, monodisperse homopolymer melts.[460,461]

Based on the experimental data obtained by Vinogradov and co-workers[457-461], there exist *four* universal *regimes of behavior* of polymer liquids in start-up of steady extension, as far as rupture is concerned.[462] These regimes are illustrated schematically in Figure 5.7. At low enough rates of strain ($\dot{\varepsilon} < \dot{\varepsilon}_{flow}$), steady elongational flow is possible and rupture can only happen because of surface tension (as for any other liquid).[462] In this regime (I), the elastic strain approaches some "equilibrium" level, while the total deformation is largely irreversible and essentially unlimited except by the size of the specimen. When a critical rate of deformation $\dot{\varepsilon}_{flow}$ is exceeded, rupture appears and prevents the attainment of a steady-state. This transition zone (II) is characterized by a superposition of viscous and elastic contributions of comparable magnitudes. The viscous

---

[o] By elastic strain it is meant the *equilibrium value of the elastic recoil* (which would in principle be observed after an infinite time).

deformation decreases rapidly with increasing strain rate, while the recoverable strain continues to increase. Consequently, the total strain-at-break exhibits a steep descent and may even pass through a minimum. As the elongation rate is increased further ($\dot{\varepsilon} > \dot{\varepsilon}_{\text{elastic}}$), the non-recoverable component of deformation becomes negligibly small (solid and dashed lines practically coincide in this zone). In this regime (III), there is virtually no flow and the behavior, essentially elastic, resembles that of vulcanized rubbers[422,440,448,450-452]. In the classification of Onogi and co-workers[463,464], this is the region where failure (defined as the onset of non-uniform extension or necking) and rupture occur simultaneously. Extremely high rates of strain ($\dot{\varepsilon} > \dot{\varepsilon}_{\text{glass}}$) result inevitably in the transition of the polymer into the glassy state, and the strain-at-break begins to diminish (zone IV).

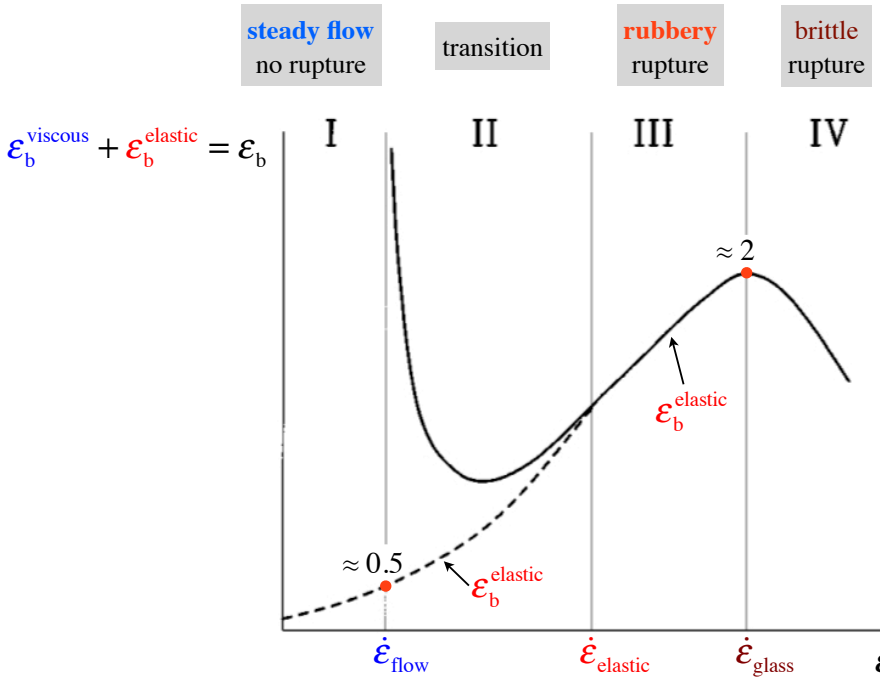

Figure 5.7. Schematic diagram relating the strain-at-break, ε_b, to the rate of deformation in uniaxial extension of *monodisperse homopolymer melts* (adapted from Malkin and Petrie[462], and Vinogradov et al.[457]). The dashed line shows the limiting elastic (recoverable) strain, $\varepsilon_b^{elastic}$. Zones III and IV also apply to *vulcanized rubbers* (cf. Figure 5.21(b)).

Experimental criterion for steady elongational flow of entangled melts

It has been shown experimentally[457,458] that the critical strain rate $\dot{\varepsilon}_{flow}$, corresponding to the transition from zone I to zone II, can be related to a relaxation time. For flows in

which the deformation rate and all the stresses are constant with time[p] it is possible to define a dimensionless quantity, called the *Weissenberg number We* (sometimes denoted by *Wi* or *Ws*), as the product of a characteristic relaxation time $\langle\tau\rangle$ governing the onset of *nonlinearity* and the rate of strain of the experiment.[36] Being a scalar measure of nonlinearity, *We* tends to zero for deformations in which linear viscoelastic behavior is approached.[36] In start-up of uniaxial extension at *steady-state*,[36,45]

$$We = \langle\tau\rangle\dot{\varepsilon} \qquad \text{steady elongational flow} \tag{5.67}$$

For any real polymers, the choice of an appropriate single characteristic relaxation time is necessary, and in extensional flows an average should be weighted towards longer relaxation times (more than it would be for shear)[465]. Thus, the *weight-average relaxation time* of the terminal region[27,45] τ_w (Appendix D, Eqs. (D.121) and (D.123)) is commonly used,[45]

$$We \simeq \tau_w\dot{\varepsilon} \qquad \text{steady elongational flow} \tag{5.68}$$

For materials whose viscoelastic behavior can be described by a generalized Maxwell model (§D.4.5), it is easy to show that[22,340] $\tau_w \approx \tau_1$ (Eq. (D.113)), where τ_1 is the *longest relaxation time* of the model.

The original Doi–Edwards[46] tube model for monodisperse, entangled melts is equivalent to a generalized Maxwell model with unequally-weighted relaxation times.

---

[p] Notice that these are flows in which the *Deborah number De* is zero, because *De* is a measure of the degree to which *elastic* behavior is expected in a flow that is *unsteady* from the point of view of a material element.[36]

Indeed, the D–E distributions of shear relaxation strengths G_n and relaxation times τ_n are, respectively, $G_n = G_N^0 \cdot 8/(n\pi)^2$ and $\tau_n = \tau_d/n^2$ (for odd values of the integer n), where G_N^0 is the shear plateau modulus[42] (cf. Eq. (3.4) and footnote [n] of Chapter 3), and τ_d is the *tube disengagement time*[35,46,184] or *reptation time*[36]. Furthermore, the D–E prediction of the linear *steady-state shear viscosity* (Eq. (D.24)) is $\eta_0 = \left(\pi^2/12\right)G_N^0\tau_d \simeq 0.822 G_N^0\tau_d$. Based on the definitions of average relaxation times in the terminal region[27,45] (Eqs. (D.123)) and the "universal" terminal spectrum for monodisperse and well-entangled linear polymers[27,45,79] (Eqs. (4.95), (4.108), and (D.124)), we obtain

$$\tau_w \simeq 2\tau_d \tag{5.69}$$

Therefore, the Weissenberg number for entangled melts subjected to steady uniaxial extension can be written as

$$We \simeq 2\tau_d\dot{\varepsilon} \qquad \text{steady elongational flow (entangled melts)} \tag{5.70}$$

From the results of Vinogradov et al.[457,458], it is possible to relate[462] the critical strain rate for the onset of rupture, $\dot{\varepsilon}_{flow}$, to a critical Weissenberg number,

$$\begin{aligned} &We_{critical} \simeq 2\tau_d\dot{\varepsilon}_{flow} \simeq \frac{1}{2} && \text{onset of rupture (entangled melts)} \\ &We \geq We_{critical} && \text{steady flow is impossible} \end{aligned} \tag{5.71}$$

Thus, the criterion for the attainability of a steady-state is[q]

---

[q] As pointed out by Graessley[45], the "effective" longest relaxation time for polymer melts in uniaxial extension must surely exceed any average such as τ_w. Thus, the estimate of $\dot{\varepsilon}_{flow}$ obtained from Eq. (5.72) should be considered as a rough upper bound.

$$\dot{\varepsilon} < \dot{\varepsilon}_{\text{flow}} \approx \frac{1}{4\tau_{\text{d}}} \qquad \text{exp criterion for steady elongational flow (entangled melts)} \quad (5.72)$$

Malkin and Petrie[462] were able to associate the experimental criterion for steady elongational flow, i.e. Eq. (5.71) written as $We_{\text{critical}} = \langle \tau \rangle \dot{\varepsilon} = 1/2$, to properties of various theoretical models of extensional deformation of viscoelastic liquids. As we discussed in §5.3.1.II-a, the simplest large-strain viscoelastic model is the Lodge rubber-like liquid[426], Eq. (5.34), which is commonly used in the form of the upper-convected generalized Maxwell model[400] (UCGM) also called the Lodge network model[340] (LN). In this case, the condition expressed by Eq. (5.72) arises naturally because at a strain rate $\dot{\varepsilon} = 1/2\tau_1$ the steady-state tensile stress predicted by the UCGM model diverges[45,340,400] (recall that $\tau_1 \approx \tau_{\text{w}} \simeq 2\tau_{\text{d}}$).

Using somewhat heuristic arguments, Malkin and Petrie[462] modified Eqs. (5.71) into

$$\begin{aligned} &\varepsilon_{\text{critical}}^{\text{elastic}} \simeq \frac{1}{2} && \text{onset of rupture (entangled melts)} \\ &\varepsilon_{\text{b}}^{\text{elastic}} \geq \varepsilon_{\text{critical}}^{\text{elastic}} && \text{steady flow is impossible} \end{aligned} \qquad (5.73)$$

This critical value of recoverable deformation agrees with the measurements of elastic recoil performed by Vinogradov and co-workers[457,458]. Notice that Eqs. (5.73) do not imply that rupture occurs at $\varepsilon_{\text{b}}^{\text{elastic}} = 1/2$, because rupture is a time-dependent phenomenon and $\varepsilon_{\text{b}}^{\text{elastic}}$ can certainly exceed 1/2 (cf. Figure 5.7). Eqs. (5.73) mean that uniaxial stretching of a polymer melt will yield steady flow only if the limiting elastic strain $\varepsilon_{\text{b}}^{\text{elastic}}$ does not exceed 1/2; otherwise, the testing specimen will break before a steady-state is reached.

In terms of tensile stress, the onset of rupture for monodisperse[457,458,460,461] and commercial (polydisperse)[466] polymer melts appears to be given by the conditions

$$\sigma_{\text{E,critical}} \simeq \begin{cases} 0.2 \text{ MPa} & \text{onset of rupture (\textit{monodisperse} entangled melts)} \\ 1.0 \text{ MPa} & \text{onset of rupture (\textit{polydisperse} entangled melts)} \end{cases} \tag{5.74}$$

For several polymer melts, the "critical" points ($\sigma_E \simeq 0.2$ MPa, $\varepsilon^{\text{elastic}} \simeq 0.5$) and ($\sigma_E \simeq 1.0$ MPa, $\varepsilon^{\text{elastic}} \simeq 0.5$) are "universal" and define the net tensile stress and elastic strain below which rupture does not occur.[462]

Relation between maximum elastic strain and molecular characteristics

Experimental evidence indicates that the maximum in the limiting (elastic) strain, which is exhibited across the transition from zone III to zone IV, can be as high as 2 (Figure 5.7). According to the results of Vinogradov and collaborators[457-461], the study of Cogswell on commercial polymer melts[466], and the work of Smith[451,452] on non-crystallizable elastomers, $\varepsilon_{\text{b,max}}^{\text{elastic}} \simeq 2$ appears to be the upper bound of elastic strain for many polymers.

By taking advantage of the discussion presented in Chapter 2, we can relate $\varepsilon_{\text{b,max}}^{\text{elastic}}$ to molecular characteristics of flexible polymer chains, namely to the *maximum stretch ratio of a tube statistical segment*, $\lambda_{\text{max,e}}$. This characteristic extension of macromolecules, i.e. the ratio of the entanglement strand fully extended (contour) length (L_e) over its unperturbed root-mean-square end-to-end distance ($R_e = a$), can be calculated as (Eqs. (2.12) and (3.60))

$$\lambda_{\max,e} \equiv \frac{L_e}{R_e} = \frac{a}{b_k} \tag{5.75}$$

where a is the tube statistical segment length[42,43] (SSL) (§2.3, §2.5, §3.3.2.II-III and Eq. (3.8)), and b_k is the Kuhn SSL[35,36] (§2.3 and §3.3.2.II). The dependence of $\lambda_{\max,e}$ on molecular characteristics is examined in detail in §2.7.2 of Chapter 2, and the results for several linear flexible polymers (including PI and PLA) are shown in Figure 2.3 and Table 2.5. Since the Witten–Fetters packing length[16,17] (Eq. (2.4)) of flexible polymers rarely exceeds[17,18,20] 6.5 Å (cf. Table 2.3 and Figure 2.2(b)), the maximum extensibility of an entanglement strand is usually limited to about $\lambda_{\max,e} \simeq 7.3$ (Figure 2.3 and Table 2.5), which corresponds to $\varepsilon_{\max,e} \simeq 2.0$. In the rubber-like regime the initial constraints imposed by the confining tube are permanent ($\dot{\varepsilon} > \dot{\varepsilon}_{\text{elastic}} \gg 1/\tau_d$), and therefore the microscopic deformation of a tube segment can be recovered. In this way, the maximum recoverable strain for melts and non-crystallizable rubbers can be explained.

Tube model predictions for the onset of strain softening/hardening

Within the tube model, nonlinear viscoelastic properties are thought to originate from orientation and stretching of tube segments, which, in turn, are controlled by the reptation time τ_d and the retraction time τ_s (assumed to be equal to the path equilibration time $2\tau_R$, §5.3.1.II-b and footnote [e]).

For linear, monodisperse, homopolymer melts, the so-called "standard molecular theory" developed in 2004 by Marrucci and Ianniruberto[467] gives the standard tube-model predictions of the behavior in the nonlinear regime. In start-up of steady uniaxial

extension, three regimes of behavior are predicted. At strain rates much lower than the reciprocal of the reptation time, $\dot{\varepsilon} \ll 1/\tau_d$, molecules have time to maintain their equilibrium conformations, and therefore the behavior is *linear* ($We \rightarrow 0$). At higher elongation rates, such that $1/\tau_d < \dot{\varepsilon} < 1/\tau_s$, the flow is fast enough to orient the primitive path of a molecule, but not to stretch it. In this intermediate regime, orientation of tube segments leads to *strain softening*. For fast rates of strain, $\dot{\varepsilon} \gg 1/\tau_s$, the extensional flow is able to stretch the polymer molecules, and thereby *strain hardening* is expected.

Tube model predictions also include the behavior at steady-state, in terms of *extension thinning* ($\eta_{E,NLVE}(\dot{\varepsilon}) \equiv \eta^+_{E,NLVE}(t \rightarrow \infty, \dot{\varepsilon})$ decreasing with $\dot{\varepsilon}$)[36] and *extension thickening* ($\eta_{E,NLVE}(\dot{\varepsilon})$ increasing with $\dot{\varepsilon}$)[36]. However, since rupture in entangled melts becomes possible for $\dot{\varepsilon} > 1/4\tau_d$ (Eq. (5.72)), the tube model predictions for steady flow have so far been observed only for solutions of linear polymers[36].

The tube concept has also been applied to describe the nonlinear viscoelastic properties of branched polymers. In 1998, McLeish and Larson[468] developed a theory for an idealized, monodisperse, branched polymer called the *pom-pom*. This molecular structure is a generalization of the H topology: the "backbone" segment of the molecule is "pinned down" on both ends by branch points that are permitted to have an arbitrary number of branches, q. Since the backbone segment has great difficulty relaxing, pronounced nonlinear effects are produced in extensional flow, especially strain hardening. By

predicting that the level of strain hardening is controlled by the number q of branches per branch point, the pom-pom model is able to describe qualitatively experimental data[r].[36]

To date, no tube model has yet been proposed to account for the nonlinear viscoelastic properties of microphase-segregated block copolymers. Given the similarities between the constraints imposed by the branch points on the backbone of the pom-pom molecule and those exerted by the endblocks in a microphase-segregated triblock, tube models for block copolymers may become possible in the near future.

Expected behavior for an undiluted PI melt with the same molecular characteristics as the midblock of LIL50–12

The foregoing discussion allows us to examine how the PI midblock would behave in bulk, at 37 °C, in tensile tests with elongation rates ranging from 10^{-4} to 10 s^{-1}. To this end, the relevant time scales are the path equilibration time $2\tau_R \simeq 0.2$ ms, i.e. the equilibration time of the whole PI chain via 1-D Rouse-like motions ("local reptation"[166]) along the chain primitive path[35,36,44-46], and the reptation time $\tau_d \simeq 5.4$ ms, i.e. the time scale at which the PI chain will curvilinearly diffuse a distance of order[22] $L_{tube} = Z \cdot a$ (where Z is the average number of entanglement strands per chain[35,44], Eq. (3.7)). These characteristic relaxation times, shown in Table 5.2, were calculated according to the analyses presented in Chapter 3 (Figure 3.4(b), Table 3.8, and §3.3.4.IV-d), and Chapter 4 (§4.3.2.II-b).

---

[r] Under conditions in which the flow is slow enough that the arms of the pom-pom molecule are undeformed.[36]

All the elongation rates employed in this study are much lower than the critical strain rate for the onset of rupture, $\dot{\varepsilon}_{\text{flow}} \approx 1/4\tau_{\text{d}} \simeq 47.5\ \text{s}^{-1}$ (Eq. (5.72)), therefore steady flow would be achieved before eventual rupture (due to the finite size of the specimens). Furthermore, since the condition $\dot{\varepsilon} \ll 1/\tau_{\text{d}} \simeq 190\ \text{s}^{-1}$ is clearly met, the extensional behavior would be *linear* ($We \rightarrow 0$). Thus, regardless of the applied strain rate ($10^{-4} \leq \dot{\varepsilon}/\text{s}^{-1} \leq 10$), the transient tensile viscosity data would follow the LVE envelope, $\eta^{+}_{\text{E,LVE}}(t)$, never deviating neither downward nor upward from it, before eventually reaching the linear plateau value[s], $\eta_{\text{E},0} \simeq 3\eta_0 \approx 3G^0_{\text{N}}\tau_{\text{d}} \approx 5700$ Pa·s (cf. Figure 5.4(b)).

The difference between this type of response and the behavior shown in Figure 5.4 originates from the microphase-segregation of the triblock and the additional constraints thus imposed on the PI chains. While the hard PLA domains are responsible for an overall increase in tensile stress (as the filler effect enhances the modulus – Eqs. (3.16) and (3.24)) and play a key role in the ultimate properties of the triblock (§5.3.3.II-e and §5.3.5), strain softening and hardening stem from the impeded molecular motions of the midblocks. Notice that, according to the tube model, observing strain hardening behavior for the PI block in bulk would be practically impossible at 37 °C, as it would require strain rates higher than $1/2\tau_{\text{R}} \simeq 5400\ \text{s}^{-1}$. The structural origins of strain softening and strain hardening behavior in LIL50–12 are the subject of the next section.

---

[s] Here, we are assuming incompressibility and using the shear plateau modulus of undiluted PI at 25 °C, $G^0_{\text{N}} = 0.35$ MPa (Chapter 3, Table 3.4).

Table 5.2. Viscoelastic monomeric friction coefficient[42,45] and characteristic time scales of the PI block at 37 °C, calculated from the corresponding values at 0 °C (Chapter 3, Tables 3.6 and 3.8, §3.3.4.IV-d) using the horizontal shift factor[42] $a_{37}^{0} \simeq 2.43 \cdot 10^{-2}$ (Chapter 4, §4.3.2.II-b).

$\log \zeta_0$ [a]	τ_0 [b]	τ_e [c]	$2\tau_R$ [d]	τ_d [e]	τ_{late} [f]	$1/\tau_{late}$	$1/\tau_d$	$1/2\tau_R$
$[N \cdot s \cdot m^{-1}]$	[ns]	[μs]	[ms]	[ms]	[s]	$[s^{-1}]$	$[s^{-1}]$	$[s^{-1}]$
– 9.97	0.2	1.9	0.2	5.4	460	$2.2 \cdot 10^{-3}$	190	$5.4 \cdot 10^{3}$

a) Monomeric friction coefficient, i.e. the average drag force per PI monomer per unit velocity encountered by a PI Gaussian submolecule moving through its free-draining surroundings[42] (§3.3.4.III and §3.3.4.IV-c). Calculated from Eq. (3.14) with $p = N$, using $\tau_0(37\ °C) = 0.172$ ns and $b(37\ °C) = 0.639$ nm (from Table 3.3 and[40] $\kappa_{PI} \equiv \partial \ln R_{PI}^2 / \partial T = +0.40 \cdot 10^{-3}\ deg^{-1}$).

b) *Segmental time*[23] (Eq. (3.14) with $p = N$), i.e. the time scale at which a PI monomer would diffuse a distance of order b if it were not attached to the chain[22] (§3.3.4.III, Figure 3.4(b), §3.3.4.IV-c, Table 3.8, and §3.3.4.IV-d).

c) *Entanglement time*[44] (Eq. (3.19)), i.e. the equilibration time of a PI tube segment via 3-D Rouse-like motions[35,36,44-46] (Figure 3.4(b), Table 3.8, §3.3.4.IV-d, and Figure 3.5).

d) *Path equilibration time*[45] (Eq. (3.20)), i.e. the equilibration time of the whole PI chain via 1-D Rouse-like motions ("local reptation"[166]) along the chain primitive path[35,36,44-46] (Figure 3.4(b), Table 3.8, §3.3.4.IV-d, and Figure 3.5).

e) *Tube disengagement time*[35,46,184] or *reptation time*[36] ($\tau_d = 3\tau_e Z^3$), i.e. the time scale at which the PI chain would curvilinearly diffuse a distance of order $L_{tube} = Z \cdot a$ if it were not attached to the PLA endblocks[22] (§3.3.4.IV-d and Figure 3.5).

f) Relaxation time of a deep primitive path fluctuation ("late-time chain end fluctuation")[35,167,168] (Eq. (3.21) with $\alpha = 0$ and $Z = 9.25$), i.e. the time scale for full, dynamically undiluted ($\alpha = 0$) star-like relaxation of entangled dangling structures (§3.3.4.IV-d, Figures 3.5 and 3.6, §3.3.4.IV-e, and Table 3.9).

Table 5.3. Characteristic length scales and stretch ratios of the PI block at 37 °C, calculated from Tables 3.2, 3.3, and 3.9 of Chapter 3 (cf. Table 2.5). Stretch ratios expressed as true/Hencky strains are shown in parenthesis.

b [a] [nm]	b_k [b] [nm]	a [c] [nm]	a_{early} [d] [nm]	a_{late} [e] [nm]	R [f] [nm]	L [g] [nm]
0.639	0.902	5.53	5.68	6.85	17.27	330.6

$\lambda_{max,e}$ ($\varepsilon_{max,e}$)			$\lambda_{max,full}$ ($\varepsilon_{max,full}$)
a/b_k	a_{early}/b_k	a_{late}/b_k	$L/R = R/b_k$
6.13 (1.81)	6.30 (1.84)	7.59 (2.03)	19.1 (2.95)

$\lambda^{**}_{theory} = 1/3\ \lambda_{max,e}$ ($\varepsilon^{**}_{theory}$)		
$1/3\ a/b_k$	$1/3\ a_{early}/b_k$	$1/3\ a_{late}/b_k$
2.04 (0.71)	2.10 (0.74)	2.53 (0.93)

a) Monomer-based statistical segment length[23,25] (§3.3.2.II).

b) Kuhn statistical segment length[35,36] (§3.3.2.II).

c) Tube statistical segment length[42,43] of PI in bulk, i.e. unperturbed root-mean-square end-to-end distance of a chain M_e^G or N_e long[22,35,46] (§3.3.2.II-III and Eq. (3.8)).

d) Tube statistical segment length at $t = \tau_e$ (Eq. (3.29)) and at $t = 2\tau_R$ (Eq. (3.33)), determined by PI chains in *bridge*, *knotted-loop*, and *free-end* conformations (§3.3.4.IV-d and Figure 3.5). With respect to undiluted PI homopolymer, the confining tube is "dilated" by the presence of unsegregated PLA blocks and dangling-loops (Table 3.9).

e) Tube statistical segment length at $t = \tau_{late}$ (Eqs. (3.42) and (3.48)), determined only by PI chains in *bridge* and *knotted-loop* conformations (§3.3.4.IV-d and Figure 3.5). With respect to a_{early}, a_{late} is increased by a factor that only depends on the distribution of midblock conformations (§3.3.4.IV-e and Table 3.9).

f) Unperturbed root-mean-square end-to-end distance[23,35,42-45] (§3.3.2.II and Eq. (3.1)).

g) Fully extended (contour) length of a PI chain in a rod-like zig-zag conformation (i.e. all *trans* states of torsion angles)[20,22,35,36] (Tables 3.2–4 and §3.3.2.II).

5.3.3.II-d Structural origins of strain softening and hardening in LIL50–12

To identify the possible nonlinear mechanisms responsible for the observed strain softening/hardening behavior we first need to consider the network structure and linear dynamics of LIL50–12.

A fundamental time scale is represented by the *entanglement time*[44] $\tau_e \simeq 1.9\ \mu$s (Eq. (3.19) and Table 5.2), i.e. the equilibration time of a PI tube segment via 3-D Rouse-like motions[35,36,44-46]. This characteristic time, controlled by the entanglement density of the matrix, corresponds to the time scale at which a PI entanglement strand would diffuse a distance of order its size, a, if it were not attached to the chain. On time scales shorter than τ_e (length scales smaller than a), the dynamics is oblivious of chemical details of the polymer chains as well as of large-scale molecular architecture (Figure 3.5 and §3.3.4.IV-d). In this regime, the stress in the matrix is relaxed as though the midblocks were unentangled and the PLA domains were not present. Even after the imposition of a large strain, stress relaxation for $t < \tau_e$ proceeds in the same way as for small deformations (i.e. by Brownian motion of the monomers within a PI tube segment progressing in Rouse-like fashion).[45]

Network structure at small and moderate strains ($\varepsilon < 1$)

For $t \geq \tau_e$, the dynamics is ruled by large-scale molecular architecture. On these time scales, the accessible relaxation mechanisms (both *linear* and *nonlinear*) are dictated by the network structure of LIL50–12. The specific molecular architecture depends on the different midblock chain conformations typical of microphase-segregated block copolymers of the A–B–A type.[105,109] Usually, only a fraction x_b of B chains interconnects

two different A domains (*bridge* conformation). On the other hand, a fraction x_l of B chains can assume a *loop* conformation, in which both ends of the midblock are anchored to the interface of the same A domain. Within this class, there can be B chains (x_k) connected to the network through entanglements (*knotted-loop* conformation) while the remaining ($x_d = x_l - x_k$) will act as dangling ends and can be viewed as a type of network defect (*dangling-loop* conformation). In both dielectric and viscoelastic measurements, bridge and knotted-loop conformations are essentially indistinguishable.[163] Being unentangled (hence, disengaged from the load-bearing network), dangling loops constitute the unentangled dangling structures of A–B–A triblocks. In conditions of partial segregation (stemming from either lack of thermodynamic equilibrium or equilibrium self-assembly in the intermediate segregation regime), one also needs to consider those triblock chains ($x_f = 1 - x_b - x_l$) having one ($x_{f,1}$) or both ends ($x_{f,2} = x_f - x_{f,1}$) residing outside A domains (*single-* or *double-free-end* conformation). Free-end-type midblocks (x_f) give rise to entangled dangling structures, i.e. load-bearing structures partially attached to the network that, given time, can completely relax their conformations.

By combining tube model ideas with rubber elasticity theories, suitable modified to account for the microphase-segregated structure, in Chapter 3 (§3.3.4.IV-e) we modeled the linear (harmonic) elastic response of LIL50–12 at 0 °C in the pseudo-equilibrium and plateau regions. In so doing, we determined the distribution of midblock conformations to be as follows (§3.3.4.IV-d and Table 3.9): $x_d \simeq 0$, $x_b + x_k \simeq 76\%$, and $x_f \simeq 24\%$

(corresponding to a small fraction of PLA chains residing in the PI-rich matrix, $x_{L,un} \simeq 17\%$ – Eqs. (3.51) and (3.52)). Although the fraction of partially segregated chains was not resolved into the individual components $x_{f,1}$ and $x_{f,2}$, stress relaxation beyond the path equilibration time, $2\tau_R$, was found qualitatively and quantitatively consistent with dynamically undiluted star-like motion of single-free-end-type midblocks (Figure 3.6 and §3.3.4.IV-e).

In conditions of slow ordering kinetics, moderate deformations, and $T < T_{g,L}$, the distribution of midblock conformations may remain approximately constant (for the experimental time scale) and equal to the distribution established when the network was formed. The results of Chapter 3, obtained from measurements at 0 °C, are therefore relevant to this study as well. The essential features of the network, at small and moderate elongations, are then captured by the simplified drawing shown in Figure 3.5, whose legitimacy rests solely on the premise that the free-end-type midblocks be (more or less) uniformly distributed throughout the matrix (§3.3.4.IV-d).

The LIL50–12 matrix thus contains a fraction $\phi_I^{matrix} \simeq 95\%$ (Eq. (4.19)) of PI chains, of which only a fraction $(1–x_d)$ is initially entangled. In other words, upon network formation unsegregated PLA blocks and dangling-loops (when present) act as "diluent" for the entangled PI chains (§3.3.4.IV-e). Consequently, when the entanglement network comes into play at $t = \tau_e$, the confining tube is "dilated" with respect to homopolymer PI and the tube SSL is $a_{early} \equiv a(t = \tau_e) = 5.68$ nm (Eq. (3.29) and Table 5.3). At this stage,

entanglements originate from midblocks in bridge, knotted-loop, and free-end conformations (Figure 3.5).

Linear relaxation mechanisms for $t \geq \tau_e$

For $\tau_e \leq t \leq 2\tau_R$, linear stress relaxation in LIL50–12 proceeds via 1-D Rouse-like motions ("local reptation"[166]) of the PI monomers along the chain primitive path: "*chain unit sharing*"[45] re-equilibrates chain density along the primitive path of the entangled PI chains, while the effect of "*early-time chain end fluctuations*"[167,168] on free-end-type midblocks can be assumed to be negligible (§3.3.4.IV-d). As shown in Chapter 4 (§4.3.2.II-b), on these time scales relaxation within PLA domains and PLA/PI interfaces is completely negligible in the linear regime (i.e. the domains of the PLA microphase behave as non-deformable inert filler particles). At the path equilibration time, $2\tau_R$, all entanglements in LIL50–12 (whether they are trapped or not) are still intact and the tube SSL is unchanged, $a(t = 2\tau_R) = a_{early}$ (Eq. (3.33) and Table 5.3).[t]

On time scales larger than $2\tau_R$, *star-like dynamics* for single-free-end-type midblocks ($x_{f,1}$), and *reptation* for those with two "free" ends ($x_{f,2}$), can take place, albeit both are possibly delayed by the microstructure (§3.3.4.IV-d). When the slower process of deep chain end fluctuations is completed, all untrapped entanglements (i.e. those formed by midblocks in free-end conformations) will have disappeared. The time scale for full, dynamically undiluted, star-like relaxation of single-free-end-type midblocks is $\tau_{late} \simeq$

---

[t] Note that, when present, dangling-loops would relax their conformation within a time scale τ_R (being unentangled).

460 s ("*late-time chain end fluctuations*"[167,168], Eq. (3.21) with $\alpha = 0$ and $Z = 9.25$, Table 5.2). At $t = \tau_{late}$, topological constraints are determined solely by PI chains in bridge and knotted-loop conformations, and the tube SSL is $a_{late} \equiv a(t = \tau_{late}) = 6.85$ nm (Eq. (3.42) and Table 5.3). With respect to a_{early}, a_{late} is increased by a factor that only depends on the distribution of midblock conformations (Eq. (3.48)). Star-like dynamics and incipient softening of PLA microdomains (which partially releases the tethering constraint on the PI block ends at the corresponding PLA/PI interfaces) give rise to the single power-law relaxation pattern shown in Figure 4.2(a) (cf. §4.3.2.I, §4.3.2.II-a, Eq. (5.57), and §5.3.3.I-c).

The two linear relaxation times, $2\tau_R \simeq 0.2$ ms and $\tau_{late} \simeq 460$ s, should be compared with the characteristic time scales of the experiments, $0.1 \text{ s} \leq 1/\dot{\varepsilon} \leq 10^4$ s. At small and moderate strains, we may thus expect the tube SSL to be a_{late} for tests performed at $\dot{\varepsilon} = 10^{-3}$ and 10^{-4} s^{-1}, and smaller (i.e. closer to a_{early}) at higher elongation rates.

Nonlinear relaxation mechanisms

Let us now consider the possible ways in which stress in LIL50–12 can be relaxed in the nonlinear regime. At large deformations, mechanical energy can be dissipated by mechanisms originating in the PI-rich matrix, in the dispersed phase (PLA), or cooperatively in both.

A mechanism that has often been invoked for vulcanized rubbers[469] and triblock TPEs[92,114] is *slippage of entanglements*. The idea that entanglements, being mechanically more compliant than chemical cross/endlinks, can partially "slide" along the chain

primitive path is incorporated in the Edwards–Vilgis[83,84] (E–V) slip-link model to be discussed in §5.3.4.II-b. Given the length scales involved (of order of the tube SSL), one may expect this mechanism to occur quickly (i.e. on a time scale τ^* of order τ_e or so) and at relatively small strains entering the nonlinear regime. It follows that all the entangled PI chains can partially relieve the stress by this mechanism, irrespective of the midblock conformation (whether it be bridge, knotted-loop, or free-end).

As explained in §5.3.1.II-b, the nonlinear mechanism of *chain retraction* is suppressed for entangled chains terminated by cross/endlinks. For LIL50–12, this mechanism can therefore only involve midblocks in free-end conformation, which represent the minority ($\simeq$ 24%) of the PI chains in the matrix. Since the "effective" time scale for chain retraction should lie approximately between $2\tau_R$ and $20\tau_R$ (§5.3.1.II-b and footnote [e]), the flow in our experiments is not fast enough to stretch the free-end-type midblocks (§5.3.3.II-c).

The increasing tension on bridges and knotted-loops induced by finite deformations cannot be relieved by chain retraction, so these PI chains can be progressively stretched as the macroscopic elongation increases. This situation is somewhat analogous to the stretching that occurs in systems with long-chain branching, i.e. structures (such as H-shaped molecules and the pom-pom molecule discussed in the previous section) having inner chain segments ("backbones") with branch points at both ends. As in those systems, stress relaxation can only proceed sequentially and in a highly cooperative fashion: the stretched bridges and knotted-loops ("backbones") cannot relax their conformations

unless the endblocks ("branch points") move. At temperatures/time scales at which the PLA domains are glassy, a large tension will build up resulting in either brittle fracture in the PLA domains or elastic failure in the matrix.[92] At temperatures/time scales at which the PLA domains are relatively soft, large strains inevitably lead to *stress-induced pullout* of PLA chains from PLA domains and *deformation-assisted chain transfer* of the PLA blocks (vide infra). As recently pointed out by Watanabe and co-workers[222], the time τ^{**} required for stress-induced pullout and deformation-assisted chain transfer, not the path equilibration time $2\tau_R$ of the midblock or the copolymer chain as a whole, governs chain stretching (hence, strain hardening behavior) in triblock and multiblock copolymers (cf. §5.3.3.II-c). Since our material exhibited strain hardening behavior even at the lowest applied rate of strain, this suggests $\tau^{**} > 10^4$ s.

Lastly, we need to consider that mechanical energy can also be dissipated through *viscoelastic deformation of the dispersed microphase*. This arises from the fact that the experimental temperature, 37 °C, is not significantly lower than the PLA glass transition, 53.6 °C (Chapter 3, §3.3.4.II, and Appendix A). Although the majority of the macroscopically applied strain is conceivably taken up by the rubbery matrix, tension developed along bridges and knotted-loops will eventually cause the PLA domains to deform. Obviously, the extent to which the deformed PLA domains can respond viscoelastically depends on the elongation rate. Given the proximity to the PLA glass transition and the mode of deformation (uniaxial extension), the time scale governing this nonlinear relaxation mechanism is inherently dependent on the microscopic deformation

of the domains. This subtle phenomenon, which will be shown to control the ultimate properties of LIL50–12 (§5.3.5), is analyzed and discussed in §5.3.3.II-e.

Proposed mechanisms for the onset of strain softening/hardening

Based on the above discussion, we attribute the onset of strain softening – roughly located within the range $0.07 < \varepsilon^* < 0.20$ ($1.07 < \lambda^* < 1.2$) – to *slippage of entanglements*, which would reduce the modulus (Figure 5.5(b)) by partially decreasing the tensile force supported by bridge-, knotted-loop-, and free-end-type midblocks. This hypothesis is consistent with the nonlinear behavior of the harmonic response functions shown in Figure 4.2, i.e. a monotonic decrease of elasticity ($E'(\varepsilon_0)$) and a weaker increase of dissipation ($E''(\varepsilon_0)$, $\tan\delta(\varepsilon_0)$) by perturbations entering the nonlinear regime ($\varepsilon_0 > 0.01$). The seemingly frequency independence of the critical strain (Figure 4.2) is also in harmony with this argument, since the time scale τ^* for entanglement slippage (controlling the rate of softening of network junctions) should lie well above the explored frequency window (if $\tau^* \approx \tau_e$, then $\omega^* = 1/\tau^* \approx 5 \cdot 10^5$ rad/s).

Ideally, strain-induced entanglement slippage could even lead to disengagement of entanglements on dangling structures, i.e. the free-end-type midblocks. In practice, however, the occurrence of slippage should be strongly dependent on the relative orientations of the tube segments with respect to the stretching direction. While some entanglements may "slide" or "slip" along the chain primitive path by an arc length of order a (the maximum amount of "slip", given by the tube SSL), others will experience little to no slippage at all, and the portion of the PI chain between two such

entanglements will become increasingly stretched with increasing deformation. If this is correct, then we should be able to relate the onset of strain hardening to the nonlinear elastic behavior of an entanglement strand. Let us consider the elongational behavior of the PI chain segment within an entanglement strand. At rest and in the small-strain regime, its conformation is Gaussian and therefore the tensile force increases linearly with elongation (i.e. it follows Hooke's law for an ideal chain).[22] As the elongation increases, the response will deviate from that of a linear entropic spring and the tensile force acting on the (freely-jointed) chain segment will be described by the inverse Langevin function.[22] The limit of the linear regime, for a single entanglement strand under tension, corresponds to a stretch ratio of the order of $(1/3)\cdot\lambda_{max,e}$.[22] With the values of a_{early} and a_{late} previously discussed, this critical stretch ratio is, respectively, $\lambda^{**}_{theory} \simeq 2.10$ ($\varepsilon^{**}_{theory} \simeq 0.74$) and $\lambda^{**}_{theory} \simeq 2.53$ ($\varepsilon^{**}_{theory} \simeq 0.93$) (Table 5.3). Taking into account the characteristic time scales of the experiments ($1/\dot{\varepsilon}$), this simple argument predicts that the onset of strain hardening should occur approximately at $\varepsilon^{**}_{theory} \simeq 0.93$ for tests performed at $\dot{\varepsilon} = 10^{-3}$ and 10^{-4} s^{-1}, and at slightly smaller strains at higher elongation rates ($\varepsilon^{**}_{theory} \simeq 0.74$ being relevant at rates ≥ 5400 s^{-1}). Except for tests at $\dot{\varepsilon} = 10^{-4}$ s^{-1}, the values of ε^{**} estimated from the experimental data (Table 5.1) are consistent with these predictions: for instance, $\varepsilon^{**} \simeq 0.90$ for $\dot{\varepsilon} = 10^{-3}$ s^{-1}, and $\varepsilon^{**} \simeq 0.80$ for $\dot{\varepsilon} = 1$ s^{-1}. In light of the uncertainty in the experimental estimates and the roughness of the theoretical predictions, the overall agreement is satisfactory.

Stress-induced pullout and deformation-assisted chain transfer

At large strains ($\varepsilon > 1, \lambda > 2.7$), the distribution of midblock conformations is modified, as PLA chains can be pulled out from their domains if the stress acting upon bridges and knotted-loops is high enough. This mechanism of *stress-induced pullout* was invoked by Watanabe and co-workers[135,136,164,222,238,241,242] to explain the observed large-strain ("elastoplastic") response of various $(A–B–A)_p$ systems (solutions of S–I–S[135,136], $(S–I–S)_p$[164,222], S–B–S[238], B–S–B[241], and $(B–S–B)_p$[242] in selective solvents) at temperatures $T \geq T_{g,A}$ (in simple shear)[135,136,238,241,242] and $T \geq T_{g,A}$–20 °C (in uniaxial extension)[164,222]. The different temperature range between shear and extension can be easily explained by the different kinematics involved. Shear flows are weak, in that the drag forces produce mainly coil rotation with relatively minor effects on conformation; extensional flow are strong, since drag forces not only stretch the polymer coils but also grow with increasing coil extension.[45,340] Therefore, a macroscopic extensional deformation readily stretches bridges and knotted-loops, and may enable the pullout of A blocks from the A domains even at temperatures below $T_{g,A}$.

The required tension for chain pullout is dictated by thermodynamics, because the mechanical energy needs to overcome the *unfavorable enthalpy of mixing* of the A and B blocks in the matrix phase.[238,470] At temperatures close to or above $T_{g,A}$, thermodynamic incompatibility and the deformation itself drive the so-called *deformation-assisted chain transfer*[222], a process in which the pulled-out A blocks can eventually be unmixed from the B matrix and go to other A domains or back to the same A domain[135,136,238]. In this

case, chain pullout does not correspond to macroscopic rupture[135,136,222]. As a result, stress-induced pullout and deformation-assisted chain transfer are often described in terms of the ability of microphase-segregated block copolymers to undergo "plastic" deformation (or to "flow") beyond a critical "yield" stress.[135,136,238] However, this does not necessarily imply the occurrence of non-recoverable (i.e. irreversible) deformations. Provided the ordering kinetics is not unduly slow, in deformed specimens at rest thermodynamics alone can drive the reformation of the original network structure[222,241,242], and the "plastic" deformation can be entirely recovered[222].

5.3.3.II-e Separating elastic and viscoelastic nonlinearities

Both entanglement slippage and chain stretching can be viewed as *elastic nonlinearities*, i.e. elastic contributions to the nonlinear secant modulus $F(t,\dot{\varepsilon})$. They occurred at all the applied elongation rates, each developed approximately at a constant strain ($\varepsilon \approx 0.1$ and $\varepsilon \approx 0.8$, respectively), and their magnitudes should only depend on elongation. Indeed, our theoretical predictions for the onset of strain hardening were based on a constant stretch ratio of the PI entanglement strand, and the minor time (strain rate) dependence originated from linear relaxation mechanisms (star-like dynamics and reptation of free-end-type midblocks, §5.3.3.II-d).

Apart from the effect on the PI tube SSL, we have also shown how linear relaxation influences the small-strain behavior of the secant modulus $F(t,\dot{\varepsilon})$ (Figure 5.5(b)). No information, however, has yet been revealed on the time dependence of relaxation at

large strains. Relaxation processes, especially those associated with nonlinear mechanisms (*viscoelastic nonlinearities*), play a key role in understanding the tensile behavior and ultimate properties of triblock TPEs. Thus, it is critical that they be identified and possibly separated from the large-strain elastic effects. To this end, we need to analyze the experimental data at constant values of strain[421] so that the time dependence of the nonlinear secant modulus $F(t,\varepsilon)$, and therefore of the ratio

$$\Lambda_F(t,\varepsilon) = \frac{F(t,\varepsilon)}{F(t)} \tag{5.76}$$

can be determined (cf. §5.3.1.II-c). It is reasonable to assume that the function $\Lambda_F(t,\varepsilon)$ and the analogous function obtained from measurements in step-strain uniaxial extension, $\Lambda_E(t,\varepsilon)$ (Eq. (5.43)), should be similar if not identical.[u] In the context of vulcanized rubbers, a comparable argument was put forth by Smith[422] in the special case where time-strain factorization applies. Providing $\Lambda_F(t,\varepsilon) \simeq \Lambda_E(t,\varepsilon)$, a relationship with the step-strain extensional damping function can be established,

$$\begin{aligned} \Lambda_F(t,\varepsilon) &\simeq \Lambda_E(t,\varepsilon) \\ &= h(t,\varepsilon)\cdot\frac{e^{2\varepsilon}-e^{-\varepsilon}}{3\varepsilon} \end{aligned} \tag{5.77}$$

and thereby the elastic effects of large-scale orientation and stretching of chain segments (as predicted by the neo-Hookean model, Eq. (5.13), and by the Lodge rubber-like liquid,

---

[u] Preliminary results obtained in our laboratory seem to confirm this hypothesis. Extensional stress relaxation experiments conducted in the nonlinear regime yielded results similar to those shown in Figure 5.6.

Eq. (5.40)) can be decoupled from all the other (elastic and viscoelastic) nonlinear effects emerging at large strains (cf. §5.3.1.II-b-c).

Iso-strain data were obtained from analysis of curves shown in Figure 5.5(b), after discarding data collected during the instrument "transient" and data measured at $\dot{\varepsilon} = 10$ s^{-1} (§5.3.2). A large number of strains were first arbitrarily selected that were evenly spaced on the logarithmic axis. From these, a subset was obtained that matched the strain values of the experimental curves at each strain rate. Values of secant modulus $F(t,\varepsilon)$ and time t, at each of these strains, were thus extracted. The entire procedure was carried out by implementing an appropriate MATLAB® algorithm. The resulting data, for a limited number of strains ε in the range 0.03–2.42 ($1.03 \leq \lambda \leq 11.2$), are plotted in Figure 5.6 as $F(t,\varepsilon)$ vs. t. Discarding data collected during the instrument "transient" and data measured at $\dot{\varepsilon} = 10$ s^{-1} set the availability of iso-strain data at short times, while modulus values at high strains were limited by sample rupture (cf. Figure 5.5(b)). The LVE prediction of the secant modulus, $F(t)$ (Eq. (5.57)), is shown by the solid line. Dashed lines depict least-squares regressions to the Cole–Cole[313] matching function (Eq. (4.1) of Chapter 4).

In accordance with the critical strain deduced from isochronal strain sweep experiments (Figure 4.1), linear viscoelastic behavior is observed for $\varepsilon = 0.03$ (○). Notice that these small-strain data fall to within 4.3% of the predicted LVE curve, and their power-law decay is given exactly by $m = 0.057$. Considering that they were extracted from tensile data subject to inevitable random and systematic errors (due to instrument limitations at short times, Figure 5.2), the agreement is excellent.

At higher strains, three features emerge associated with elastic and viscoelastic mechanisms. The time dependence is progressively accelerated, and the modulus undergoes a Z-shaped transition mirroring the behavior of the linear storage modulus $E'(\omega)$ across the glass-rubber viscoelastic transition of the PLA domains (cf. Figure 4.7(a)). The increased relaxation rate is already noticeable in the long-time behavior of data at $\varepsilon = 0.10$ (▷). Once fully developed ($\varepsilon \geq 1.66$), this transition appears centered around $t \approx 200$ s and with the same power-law decay, $F(t,\varepsilon) \sim t^{-m}$, at shorter and longer times. In addition to this *strain-induced relaxation*, the modulus "*strain softens*" at $\varepsilon = 0.29$ (◊) and 0.41 (◁), and "*strain hardens*" for $\varepsilon > 0.60$, consistently with the behavior shown in Figure 5.5(b) and with the onset of strain softening/hardening discussed in the previous section.

By exposing time and strain effects, not only do the data in Figure 5.6 identify the elastic nonlinearities stemming from the PI matrix (entanglement slippage and chain stretching), they also reveal how relaxation in LIL50–12 is affected by the increasing, macroscopic elongation. Since the time dependence of the nonlinear secant modulus, $F(t,\varepsilon)$, differs from that in the linear regime, $F(t)$, time-strain factorization does not apply (cf. §5.3.1.II) and therefore $h(t,\varepsilon)$ deviates from the Wagner damping function introduced in Eq.(5.33) (clearly, the curves in Figure 5.6 cannot be superposed by vertical shifts).

Strain-induced relaxation and viscoelastic deformation of PLA domains

The source of the observed viscoelastic nonlinearity, i.e. the strain-induced relaxation, deserves an explanation. Intuitively, it can be attributed to deformation of PLA domains,

since this is the only nonlinear mechanism that we have so far neglected (cf. §5.3.3.II-d). But why should such deformation induce a Z-shaped transition resembling so closely the PLA glass-rubber viscoelastic transition (Figure 4.7(a))? Furthermore, why does the effect of strain saturate to give a transition centered around $t \approx 200$ s rather than increasingly shifted towards shorter and shorter times?

To address these questions, we need to relax the assumption of incompressibility of the dispersed microphase. Extensional deformations, as opposed to simple shear, affect both the shape and the volume of a material. Over a wide range of time and temperature scales, polymers can be treated as if they were "incompressible", which is tantamount to approximating the viscoelastic Poisson's ratio as[42,150] $\mu^*(\omega) \simeq \mu_{eq} \simeq 1/2$ (Chapter 3, §3.3.4.IV-c; Appendix A, §A.2.3.I-b). However, when a polymer approaches glass-like consistency its Poisson's ratio decreases ($\mu^*(\omega) < 1/2$) and lateral contractions (or expansions, in compression) cause a non-negligible change in volume. This behavior is of course exacerbated at or below the glass transition when Poisson's ratio assumes its minimum value ($\mu^*(\omega) \simeq \mu_g \simeq 1/3$)[42,150]. When a glass-like polymer, such as PLA at 37 °C, is subjected to uniaxial extension, a portion of its volume increase determines an expansion of free volume, which in turn produces an acceleration of all relaxation times. This is indeed the underlying cause of the intrinsic strong nonlinearity of polymers *bulk viscoelasticity*, as illustrated by the classical studies of Kovacs[471-474] and Struik[475-477]. According to this argument, the Z-shaped transition can be assigned to the glass-rubber

viscoelastic transition of PLA. With increasing elongation, the PLA segmental time is progressively accelerated and brought within the range of the experimental time window.

This qualitative explanation can be supported by a simple calculation. For a perfect elastic material, the relative change in volume resulting from a uniaxial extension is[478]

$$\frac{\Delta V}{V_0} = \lambda_1\lambda_2^2 - 1 = \left(1+\varepsilon_{N,1}\right)\left(1+\varepsilon_{N,2}\right)^2 - 1 \qquad \left(\lambda_2 = \lambda_3\right) \tag{5.78}$$

With the definition of elastic Poisson's ratio[478], $\mu \equiv -\varepsilon_{N,2}/\varepsilon_{N,1} = -\varepsilon_{N,3}/\varepsilon_{N,1}$, Eq. (5.78) becomes

$$\frac{\Delta V}{V_0} = (1-2\mu)\varepsilon_{N,1} - \mu(2-\mu)\left(\varepsilon_{N,1}\right)^2 + \mu\left(\varepsilon_{N,1}\right)^3 \tag{5.79}$$

By neglecting all higher strain terms (i.e. by requiring that the uniaxial extension be small) and simplifying the notation ($\varepsilon_{N,1} = \varepsilon_N$), one obtains

$$\frac{\Delta V}{V_0} \simeq (1-2\mu)\varepsilon_N \tag{5.80}$$

or, in differential form,

$$\frac{\partial V}{\partial \varepsilon_N} \simeq V(1-2\mu) \tag{5.81}$$

Eqs. (5.80) and (5.81) yield the traditional incompressibility relation for Poisson's ratio, $\mu = 1/2$ when $\Delta V = \partial V/\partial\varepsilon_N = 0$. Since volume increase is caused by the dilatational component of the applied stress, the increase in fractional free volume is given approximately by[479]

$$\frac{\partial f}{\partial \varepsilon_{\mathrm{N}}} \simeq \frac{\beta_{\mathrm{f}}}{\beta}\frac{1}{V}\frac{\partial V}{\partial \varepsilon_{\mathrm{N}}} \simeq \frac{\beta_{\mathrm{f}}}{\beta}(1-2\mu) \tag{5.82}$$

where f is the fractional free volume (Chapter 3, §3.3.4.III-b), β_{f} is the compressibility of the free volume, and β is the total compressibility. For small tensile strains, Eq. (5.82) can be written as

$$\frac{f_2 - f_1}{\Delta \varepsilon_{\mathrm{N}}} \simeq \frac{\beta_{\mathrm{f}}}{\beta}(1-2\mu) \tag{5.83}$$

Now, the equation proposed by Doolittle[141-143] or, equivalently, the WLF equation[138] (Chapter 3, Eq. (3.10)), can be generalized to give the ratio a_{12} of a particular relaxation time τ_{p} in state 2 to that in state 1, in terms of the free volumes f_1 and f_2 in these states,[42]

$$\log a_{12} = \frac{B}{2.303}\left(\frac{1}{f_2} - \frac{1}{f_1}\right) \tag{5.84}$$

where B is a constant of order unity (§3.3.4.III-b). Combining Eqs. (5.83) and (5.84) leads to[42,479]

$$\log a_{\varepsilon} = -\frac{B}{2.303}\cdot\frac{\varepsilon_{\mathrm{N}}/f_1}{\varepsilon_{\mathrm{N}} + \dfrac{f_1}{(\beta_{\mathrm{f}}/\beta)(1-2\mu)}} \tag{5.85}$$

where a_{ε} (= a_{12}) is the *strain-induced shift factor*, and f_1 is the fractional free volume at zero strain. Near T_{g}, reasonable values of the parameters are[42,479] $B \simeq 1, f_1 \simeq 0.025, \beta_{\mathrm{f}}/\beta \simeq 0.4$, and $\mu \simeq 1/3$.

By exploiting the modeling of the linear harmonic response presented in Chapter 4, we can estimate the PLA segmental time at 37 °C and zero strain. The relaxation time of the

fractional Zener model, $\tau_{FMM} \simeq 1.1 \cdot 10^5$ s (Eq. (4.118) and Table 4.5), determined by the procedure described in §4.3.2.III-b, serves this purpose. According to Eq. (5.85), the strains required to shift the PLA segmental time to shorter times, say $3 \cdot 10^4$, 10^4, 10^3, and 200 s (where the Z-shaped transition is approximately centered, at high strains) are, respectively, $\varepsilon_N \approx 0.6$, 1.1, 2.4, and 3.4%. Notice that these estimates refer to the *microscopic* strain transmitted to the PLA domains, which is undoubtedly a tiny fraction of the macroscopic elongation. Given the average domain size (of the order of 16 nm – Appendix A, §A.2.1), the volume fraction ($f_L = 0.25$ – Table 3.1), and the glass-like consistency of PLA, the vast majority of the applied strain should be taken up by the rubbery matrix. This calculation shows that the observed strain-induced relaxation can be quantitatively accounted for by the accelerated glass-rubber dynamics of the dispersed microphase. It also offers an explanation as to why the Z-shaped transition is not shifted towards shorter and shorter times in the large-strain regime. Such behavior would simply reflect the upper limit of the microscopic elongation to which the PLA domains are subjected. We are not aware of studies on tensile behavior of triblock TPEs where a strain-induced glass-rubber transition of the microphase has been revealed.

It is worth mentioning that the experimental result shown in Figure 5.6 seems to corroborate the approach taken in Chapter 4 when we modeled the self-similar dynamics of LIL50–12 with the fractional Zener model. In that context, we assumed that the high- and low-frequency pseudo-plateaus, respectively preceding and following the PLA glass-rubber transition, should have a similar slope and we used $\beta = \gamma = 0.055$ (§4.3.2.III-b,

Figure 4.7(a), and Table 4.5). Despite the inevitable scatter in the data, the short- and long-time behavior of the strain-induced transition can indeed be described by the same power-law decay, $F(t,\varepsilon) \sim t^{-m}$, with $m = 0.055$.

Since the effects of time and strain are inherently intertwined, the nonlinear behavior of our triblock cannot be modeled by the classical constitutive equations for viscoelastic materials presented in §5.3.1.II-a. For present purposes, we thus turn to rubber elasticity theories that can account for the observed elastic nonlinearities (entanglement slippage and chain stretching), and defer to future work the development of a time-dependent nonlinear model for triblock TPEs.

5.3.4 Rubber Elasticity Models

5.3.4.I Modulus magnitude

The elasticity of the entangled LIL50–12 network with *glassy* PLA domains, expressed in terms of the linear storage modulus $E'(\omega)$, was examined in §3.3.4.IV-e of Chapter 3. In that context, the extensional storage modulus was modeled as the amplified ($\xi(\omega) > 1$) linear response of the *undiluted* ($\phi_{ref} \simeq \phi = 1$) network of *Gaussian* PI strands whose junctions (i.e. PI entanglements, and PLA microdomains acting as physical endlinks) moved *affinely* with the macroscopic deformation. Treating the unstrained PI chains as unperturbed Gaussian coils is tantamount to using a Tobolsky front factor[193,194] of unity (§3.3.4.IV-e). Assuming affine motion of junction points (as in the affine network model of Kuhn[199], Wall[401,402], and Treloar[403], §5.3.1.I-a) implies neglecting thermal fluctuations

around their mean positions (accounted for in the phantom network model of James and Guth[404] and Flory and Rehner[405], §5.3.1.I-a), and considering topological constraints in the matrix as effective as the physical endlinks (by neglecting their ability to partially "slide" along the chain primitive path, cf. §5.3.4.II-b). In addition, we considered the contributions of endlinks ($E'_c(\omega)$) and entanglements ($E'_e(\omega)$) as simply *additive*, following the approach developed by Langley and Ferry[156,208,209] for vulcanized rubbers[v] (§3.3.4.IV-e). Owing to this simple additivity and the assumption of "*incompressibility*" ($\mu^*(\omega) \simeq \mu_{eq} \simeq 1/2$), $E'(\omega)$ across the rubbery plateau and up to the entanglement time τ_e was calculated as (cf. Figure 3.4(a) and Eq. (3.24))

$$\text{at } 0\ ^\circ\text{C} \quad \begin{cases} E'(\omega) = 3 \cdot G'(\omega) \\ \qquad = 3 \cdot \xi(\omega) \cdot \left[\nu_c + \nu_{e,eff}(\omega) \right] \cdot kT \\ \qquad = E'_c(\omega) + E'_e(\omega) \qquad \text{for } 1/\tau_{late} \le \omega \le 1/\tau_e \end{cases} \tag{5.86}$$

where $\xi(\omega)$ is the filler effect of the glassy PLA domains, ν_c is the number density of PI strands terminated by endlinks regardless of whether entanglements intervene, $\nu_{e,eff}(\omega)$ is the "effective" number density of PI strands terminated by entanglements regardless of whether endlinks intervene, k is Boltzmann's constant, and T is the absolute temperature (§3.3.4.IV-e).

---

[v] For vulcanized rubbers, $E'_c(\omega)$ is referred to as the "crosslink"[42] or "chemical"[207] contribution, hence the subscript "c".

In §4.3.2.II-b of Chapter 4, we showed that at 37 °C the domains of the PLA microphase behave as non-deformable inert filler particles on time scales $t \leq 2\tau_R$. Therefore, rigorous application of Eq. (5.86) is confined to a reduced frequency range,

$$\text{at } 37\ ^\circ\text{C} \quad \begin{cases} E'(\omega) = 3\cdot G'(\omega) \\ \qquad = 3\cdot\xi(\omega)\cdot\left[\nu_c + \nu_{e,\text{eff}}(\omega)\right]\cdot kT \\ \qquad = E'_c(\omega) + E'_e(\omega) \qquad \text{for } 1/2\tau_R \leq \omega \leq 1/\tau_e \end{cases} \tag{5.87}$$

Endlink and entanglement contributions to the linear shear modulus

For later comparison with the fitting results presented in §5.3.4.IV, it is useful to calculate the endlink and entanglement contributions to the linear shear modulus $G'(\omega)$. Based on Eq. (3.25), $\nu_c \simeq 7.80\cdot10^{24}$ #strands/m^3. At $\omega = 1/2\tau_R$, the "effective" number density of entanglement strands is given by Eqs. (3.27) and (3.35), and we find $\nu_{e,\text{eff}}(1/2\tau_R) \simeq 7.57\cdot10^{25}$ #strands/m^3 (the values of the parameters involved in the calculation of both ν_c and $\nu_{e,\text{eff}}(1/2\tau_R)$ are given in §4.3.2.II-c). Since the *plateau modulus*[43-45] is $E_N \equiv E'(1/2\tau_R) \simeq 10.9$ MPa (§4.3.2.II-b), and $kT = 4.282\cdot10^{-21}$ N·m, the filler effect at $\omega = 1/2\tau_R$ is $\xi_N \equiv \xi(1/2\tau_R) \simeq 10.2$ (slightly higher than $\xi_N(0\ ^\circ\text{C}) \simeq 9.8$, Table 3.9). It follows that the endlink (G'_c) and entanglement (G'_e) contributions to the linear shear modulus at $\omega = 1/2\tau_R$ are, in units of kT,

$$\left.\begin{aligned} \frac{G'_c(1/2\tau_R)}{kT} &= \xi_N\cdot\nu_c \qquad\qquad \simeq 7.96\cdot10^{-1} \quad 10^{26}/\text{m}^3 \\ \frac{G'_e(1/2\tau_R)}{kT} &= \xi_N\cdot\nu_{e,\text{eff}}(1/2\tau_R) \simeq 7.72 \qquad 10^{26}/\text{m}^3 \end{aligned}\right\} \quad \text{at } \omega = 1/2\tau_R \tag{5.88}$$

The fraction of the linear shear modulus contributed by entanglements, $\psi = G'_e/G'$, and the relative magnitude of entanglement and endlink contributions, $\Omega = G'_e/G'_c = \psi/(1-\psi)$, are therefore (cf. Eq. (4.12))

$$\left.\begin{array}{l} \psi\left(1/2\tau_R\right) \simeq 0.91 \\ \Omega\left(1/2\tau_R\right) \simeq 9.6 \end{array}\right\} \quad \text{at } \omega = 1/2\tau_R \tag{5.89}$$

Notice that $\psi(1/2\tau_R)$ and $\Omega(1/2\tau_R)$ are rather close to the corresponding values at $\omega = 1/\tau_e$, $\psi_{max} = \psi(1/\tau_e) \simeq 0.92$ and $\Omega_{max} = \Omega(1/\tau_e) \simeq 12$ (cf. Eq. (4.13)). Since at the entanglement time τ_e "chain unit sharing" has yet to take place, the entanglement contribution reaches its maximum value (§3.3.4.IV-e and §4.3.2.II-c).

Given the time scales of the tensile tests, it is also useful to carry out analogous calculations for $\omega = 1/\tau_{late}$. At this frequency, the "effective" number density of entanglement strands is $\nu_{e,eff}(1/\tau_{late}) = T_e \cdot \nu_{e,eff}(1/2\tau_R) \simeq 4.01 \cdot 10^{25}$ #strands/m^3, where $T_e = 0.53$ represents the fraction of trapped (i.e. permanent) entanglements in the system (cf. Eqs. (3.35) and (3.38), and Table 3.9). Based on the weak power-law decay of $E'(\omega)$ (Figure 4.2(a)) and the results of §3.3.4.IV-e, we can approximate the filler effect at $\omega = 1/\tau_{late}$ as $\xi(1/\tau_{late}) \approx \xi_N$. Thus, we obtain

$$\left.\begin{array}{ll} \dfrac{G'_c\left(1/\tau_{late}\right)}{kT} \approx \xi_N \cdot \nu_c & \approx 7.96 \cdot 10^{-1} \quad 10^{26}/\mathrm{m}^3 \\ \dfrac{G'_e\left(1/\tau_{late}\right)}{kT} \approx \xi_N \cdot \nu_{e,eff}\left(1/\tau_{late}\right) & \approx 4.09 \qquad 10^{26}/\mathrm{m}^3 \end{array}\right\} \quad \text{at } \omega = 1/\tau_{late} \tag{5.90}$$

and (cf. Eq. (4.11))

$$\left.\begin{aligned}\psi_{\min} &= \psi\left(1/\tau_{\text{late}}\right) \approx 0.84 \\ \Omega_{\min} &= \Omega\left(1/\tau_{\text{late}}\right) \approx 5.1\end{aligned}\right\} \quad \text{at } \omega = 1/\tau_{\text{late}} \tag{5.91}$$

Topological constraints originating from free-end-type midblocks have disappeared, and the entanglement contribution reaches its minimum value (§3.3.4.IV-e and §4.3.2.II-c). On time scales larger than $2\tau_R$, however, relaxation within PLA domains and PLA/PI interfaces begins to influence the linear response of LIL50–12 and application of Eq. (5.87) is not strictly valid. The values thus calculated should be viewed only as approximations.

5.3.4.II Stress-strain relationship

Models of rubber elasticity yield different predictions of both the magnitude of the initial shear modulus G_0 (§5.3.1.I-b) and the shape of the stress-strain relationship. A broad distinction can be made between those developed from *continuum mechanics* arguments, and those based on *molecular theories*. While the approximations of Gaussian strands and affine motion are not always retained, they all assume *additivity* of chemical and topological contributions to the initial shear modulus[w],

$$G_0 = G_c + G_e \tag{5.92}$$

and "*incompressible*" and *unfilled* networks.[41] Large deformation phenomena (such as strain-induced crystallization, finite extensibility effects, and rupture) are obviously

---

[w] Notice that in the Edwards–Vilgis slip-link model[83,84] chemical and topological contributions are additive, but the latter may differ from the value deduced from the plateau modulus in the system before crosslinking (§5.3.4.II-b).

associated with non-Gaussian conformation of network strands. Theories of entangled network elasticity have been recently reviewed by Schlögl et al.[480].

Continuum models of finite elasticity were introduced in §5.3.1.I-a, namely the neo-Hookean model[45,400] (Eq. (5.12)) and the Mooney–Rivlin equation[396,397,399] (Eq. (5.10)). In uniaxial extension, and in terms of the *reduced stress* (Eq. (5.22)), they yield, respectively,

$$\sigma_{\mathrm{E,red}}^{\mathrm{n\text{-}H}} = G_0 \tag{5.93}$$

and

$$\sigma_{\mathrm{E,red}}^{\mathrm{M\text{–}R}}(\lambda) = 2C_1 + \frac{2C_2}{\lambda}, \quad \text{with } G_0 = 2C_1 + 2C_2 \tag{5.94}$$

Negative departures from neo-Hookean behavior are the norm, and appear notably in elastomeric networks with significant entanglement contribution.[481-483] (Recall that, for vulcanized rubbers, this is equivalent to the "damping" effect, $h(t,\varepsilon) < 1$, at small and moderate strains discussed in §5.3.1.II-b) As a result, they have been attributed to the ability of entanglements to respond to deformation in a softer way than do chemical cross/endlinks (i.e. by partially "sliding" along the chain primitive paths, §5.3.3.II-d)[469]. On the other hand, the Mooney–Rivlin equation is able to describe the behavior of polymer networks only over a modest range of uniaxial extension, $1 \le \lambda < 2$. In addition, it is inconsistent with behavior in other types of deformation, especially uniaxial compression.[41,400] Initially it was believed that C_1, which quantifies the neo-Hookean contribution to the reduced stress, was associated with cross/endlinks, and that C_2, which quantifies the departures, was associated with entanglements. Experimental evidence,

however, openly indicated otherwise. By analyzing data for several vulcanized networks, Ferry and Kan[484] were able to express C_1 and C_2 as

$$\begin{aligned} 2C_1 &= (1+k)\cdot G_c + k\cdot G_e \\ 2C_2 &= \quad -k\cdot G_c \; + (1-k)\cdot G_e \\ &\text{with } k = 0.275 \;\; \left(C_2/C_1 \simeq 2.6 \;\; \text{for} \;\; G_e/G_0 \gg 1\right) \end{aligned} \tag{5.95}$$

Slightly different expressions for the Mooney–Rivlin coefficients were later found by Dossin, Pearson, and Graessley[206,207]

$$\begin{aligned} 2C_1 &= G_c + k\cdot G_e \\ 2C_2 &= \quad (1-k)\cdot G_e \\ &\text{with } k = 0.5 \;\; \left(C_2/C_1 \simeq 1 \;\; \text{for} \;\; G_e/G_0 \gg 1\right) \end{aligned} \tag{5.96}$$

Common to both investigations is the conclusion that C_1 depends on both cross/endlinks and entanglements.

From molecular theory, only a purely topological contribution is often calculated. In this case, a convenient framework for theory testing is obtained by expressing the reduced stress as

$$\sigma_{E,red}(\lambda) = G_c + G_e \cdot Y_e(\lambda) \tag{5.97}$$

where $Y_e(\lambda)$ is the *normalized entanglement contribution* (dictating the fraction of the stress supported by chain entanglement), with $Y_e(\lambda) = 1$ at $\lambda = 1$ (cf. Eq. (5.21)). In terms of *dimensionless stress* (Eq. (5.23)),

$$S(\lambda) = (1-\psi) + \psi \cdot Y_e(\lambda) \tag{5.98}$$

where $\psi = G_e/G_0$ is the fraction of the initial shear modulus contributed by entanglements. This form of expressing the stress was introduced in 1988 by Heinrich and Straube[485].

Clearly, neo-Hookean behavior implies

$$Y_e^{\text{n-H}} = 1 \quad \text{and} \quad S^{\text{n-H}} = 1 \tag{5.99}$$

while the Mooney–Rivlin formulation translates into

$$Y_e^{\text{M–R}}(\lambda) = k + (1-k)\cdot\frac{1}{\lambda} \tag{5.100}$$

with k ranging from 0.275 to 0.5, according to the experimental results of Ferry and Kan[484], and Dossin, Pearson, and Graessley[206,207]. Contrary to the claim of Schlögl et al.[480], the normalized entanglement contribution of the Mooney–Rivlin equation is not equal to $1/\lambda$.

As a basis of comparison with both continuum and molecular theories, it is instructive to consider the functional form of Y_e associated with Hooke's law, Eq. (5.18)b, under the assumption $\psi = 1$. From the definition of dimensionless stress and Eq. (5.1), we find

$$Y_e^{\text{H}}(\lambda) = 3\frac{\lambda^2 - \lambda}{\lambda^3 - 1} \tag{5.101}$$

Since slow power-law decays in the linear regime result in small-strain tensile behaviors approximated by $\sigma_{\text{E,LE}}(\varepsilon) \sim \varepsilon$ (§5.3.3.I-c), the *modified Hooke's law*, $\sigma_{\text{E}}^{\text{modH}}(\varepsilon) = 3G_0 \cdot \varepsilon = E_0 \cdot \varepsilon$, is of interest as well. In this case,

$$Y_e^{\text{modH}}(\lambda) = 3\frac{\ln\lambda}{\left(\lambda^2 - \lambda^{-1}\right)} \tag{5.102}$$

and we notice that $Y_{\mathrm{e}}^{\mathrm{mod\,H}}(\lambda)$ is identical to the normalized entanglement contribution of the empirical *Heinrich–Straube model*[485,486], for a special case of the model parameter ($\beta = 0$) that yields the best agreement with experimental data of vulcanized rubbers[41]. Surprisingly, this equivalence seems to have escaped recognition by the recent literature, as no mention of it is made neither in Graessley's book[41] nor in the 2014 *Macromolecules* review of Schlögl et al.[480].

5.3.4.II-a The Rubinstein–Panyukov non-affine slip-tube model

Several tube models have been proposed to describe the elasticity of entangled networks[41,81], notable examples being the *constant mesh-size tube model*[487] and the *affine tube model*[488] developed in 1979 and 1981 by Marrucci.

In 1997, Rubinstein and Panyukov[489] introduced a *non-affine tube model*. By combining the main ideas of the constrained junction model[204,205,490-492] and the Doi–Edwards tube model[46], they argued that the tube SSL should vary with elongation in what seems a counterintuitive manner: $a_i = a_0 \lambda_i^{1/2}$, where $i = x, y, z$, and a_0 is the rest state SSL. Thus, in the Rubinstein–Panyukov tube monomer fluctuations increase along the stretching direction, and decrease along the compression direction.

In 2002, Rubinstein and Panyukov[493] presented an extended version of their model, the so-called *non-affine slip-tube model*, which accounts for path equilibration along the tube (§5.3.3.II-d). The resulting dependence of stress on deformation does not have a simple

analytical form, but in the experimentally relevant range of $0.1 \le \lambda \le 10$ it is adequately approximated by

$$Y_e^{R-P}(\lambda) \simeq \frac{1}{0.74\lambda + 0.61\lambda^{-1/2} - 0.35} \qquad 0.1 \le \lambda \le 10 \tag{5.103}$$

Unlike other entanglement models, this one contains no adjustable parameters (except G_c and G_e), and provides an excellent description of the data for vulcanized rubbers in both uniaxial extension ($1 \le \lambda \le 10$) and compression ($0.1 \le \lambda \le 1$).[22,41]

The models discussed so far are compared in Figure 5.8, in terms of the functional dependences of Y_e and its first derivative $dY_e/d\lambda$.

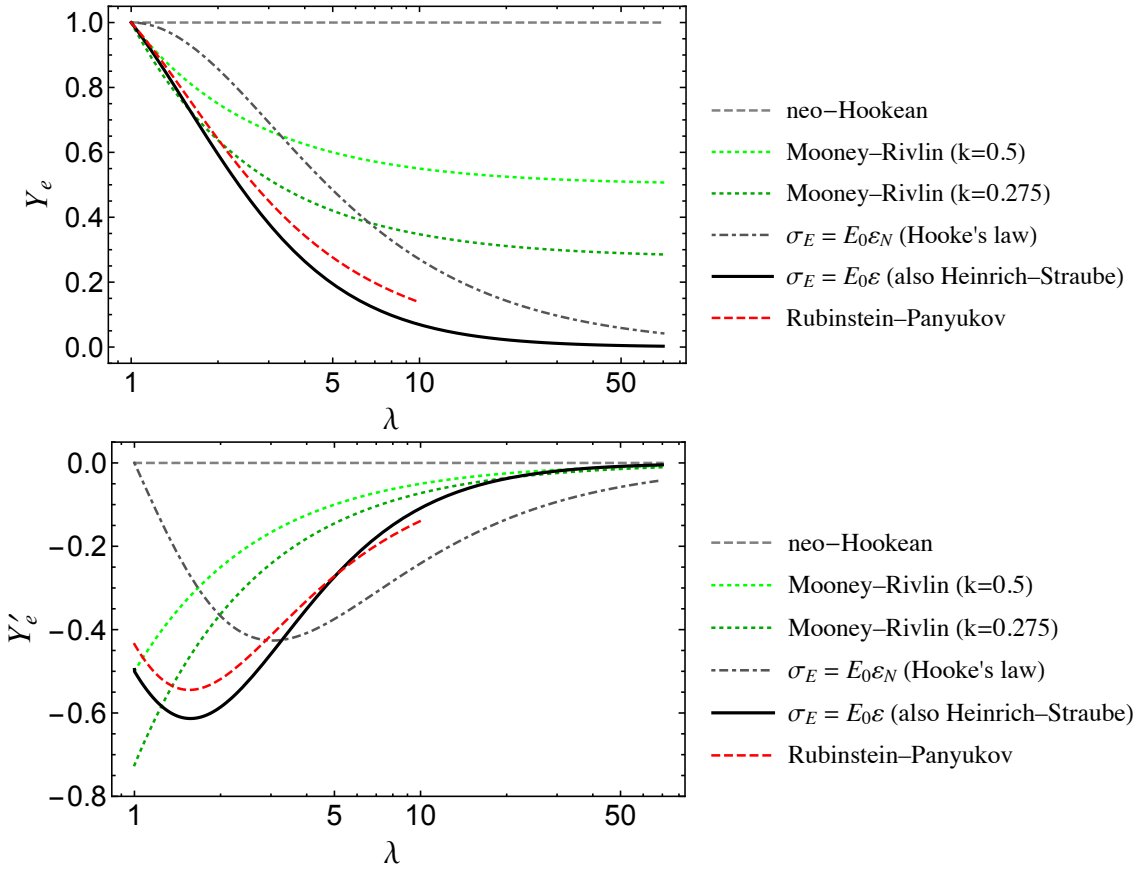

Figure 5.8. Normalized entanglement contribution Y_e (top) and $dY_e/d\lambda$ (bottom) vs. extension ratio λ, for selected rubber elasticity models (developed from either continuum mechanics arguments or molecular theories). For the Mooney–Rivlin (M–R) equation[396,397,399], the parameter k is based on the experimental investigations of Dossin, Pearson, and Graessley[206,207] (k = 0.5), and Ferry and Kan[484] (k = 0.275). Hooke's law, $\sigma_E^H(\varepsilon_N) = E_0 \cdot \varepsilon_N$ (where E_0 is Young's modulus, and ε_N is the nominal strain), reduces to neo-Hookean behavior at small strains. The modified Hooke's law, $\sigma_E^{modH}(\varepsilon) = E_0 \cdot \varepsilon$ (where ε is the Hencky strain), coincides with a special case of the Heinrich–Straube model[485,486]. Notice the striking similarity between the response of the Rubinstein–Panyukov (R–P) non-affine slip-tube model[489,493] and the modified Hooke's law.

As expected, Hooke's law reduces to neo-Hookean behavior at small strains ($\lambda \ll 2$). In contrast, an unforeseen result is the striking similarity between the response of the R–P non-affine slip-tube model and the modified Hooke's law. Especially considering the rather involved derivation of the former and the empirical, simple nature of the latter. This result seems to suggest that the R–P model's descriptive abilities may stem from the ubiquity of self-similar dynamics in polymeric systems (§4.1.3 and Appendix F), rather than from the specific details of the model itself. It is therefore not surprising that the empirical Heinrich–Straube model, whose parameter β is of unclear molecular origins, describes both compression ($0.1 \leq \lambda \leq 1$) and tensile behavior ($1 \leq \lambda \leq 10$) rather well only[41] when $\beta = 0$.

Except for Hooke's law, all the other models exhibit a similar, negative departure from neo-Hookean behavior at small strains, with $dY_e/d\lambda$ at $\lambda = 1$ restricted between –0.725 and –0.435 (Figure 5.8(b)). Notice that this behavior is sharply different from what is expected for materials, like triblock TPEs, following a power-law relaxation pattern in the linear regime. When $\sigma^{+}_{\mathrm{E,LVE}}(\varepsilon) \sim \varepsilon^{1-m} \sim (\ln\lambda)^{1-m}$ (§5.3.3.I-a and c),

$$\left.\begin{aligned} \left.\frac{d\sigma_{\mathrm{E}}(\lambda)}{d\lambda}\right|_{\lambda=1} &\to +\infty \\ \left.\frac{d\sigma_{\mathrm{E,red}}(\lambda)}{d\lambda}\right|_{\lambda=1} = \left.\frac{dS(\lambda)}{d\lambda}\right|_{\lambda=1} &\to -\infty \end{aligned}\right\} \text{ for critical-gel-like behavior} \qquad (5.104)$$

thus, the slope of Y_e at $\lambda = 1$ diverges as well (cf. Figures 5.18–20).

As pointed out by Urayama and co-workers[81] in 2001, a stricter experimental test to discern unambiguously which molecular theories correctly account for the effect of

entanglements on rubber elasticity is *general biaxial extension* (i.e. Eqs. (5.4) and (5.5) with $b = 0$ and two independent rates of strain, $\dot{\varepsilon}_1$ and $\dot{\varepsilon}_2$). Based on their extensive analysis[81,82], the pseudo-equilibrium stress-strain behavior of elastomeric networks in various deformation modes is best described by the Edwards–Vilgis slip-link model[83,84] (cf. §2.7.2 and §3.3.4.IV-e). Despite their assessment left little room for doubt, in the more recent literature various (and unsuccessful) attempts have been made (e.g. by Creton and colleagues[113,201,494,495]) to describe the tensile behavior of triblock TPEs with the R–P non-affine slip-tube model, and even with the Mooney–Rivlin equation. A reasonable description of the data was instead obtained by Watanabe and colleagues[164,222] by applying the Edwards–Vilgis slip-link model to the start-up extensional behavior of solutions of $(S–I–S)_p$–type multiblocks in *n*-tetradecane.

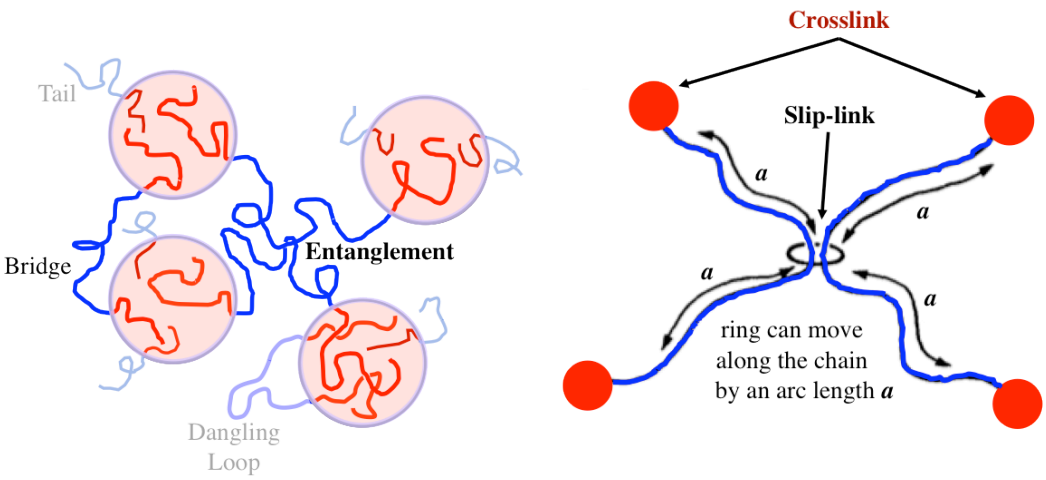

Figure 5.9. (left) Schematic illustration of an A–B–A (or A–B–A/A–B) microphase-segregated morphology, where chains are colored according to monomer type, with blue for type B and red for type A monomers. Shaded, spherical regions represent A microdomains. Entanglements are given the crude visual representation of local kinks between two neighbouring chains (cf. Chapter 2, §2.5 and Table 2.4), and are separated by an average distance *a* (i.e. the B tube SSL). Both the shape of the A microdomains and the entanglement density are chosen for simplicity. For the same reason, the drawing only shows B chains in bridge, dangling loop, or tail conformations (cf. Chapter 3, §3.3.4.IV-d and Figure 3.5). (right) Simplification of the real entanglement constraint in a *vulcanized rubber* according to the Edwards–Vilgis (E–V) slip-link model[83,84]. The presence of other entanglements or cross/endlinks (either physical or chemical) restricts the extent to which slip-links can slide independently along either of their connecting chains. Dangling loops and tails are not accounted for.

5.3.4.II-b The Edwards–Vilgis slip-link model

The concept of "slip-links" and some of their properties were first described by Graessley[27] in 1974. In 1977, Graessley and Pearson[496] demonstrated numerically that

"slip-links" yield uniaxial extension-compression behavior closely resembling the experimental observations, i.e. negative departures from neo-Hookean behavior in extension and nearly neo-Hookean behavior in compression.

In 1981, Ball et al.[83] derived the analytical expression for the *elastic energy density* W_e (= $\Delta A_e/V$, §5.3.1.I-a) associated with an ensemble of independent slip-link tetrahedra, and in 1986 Edwards and Vilgis[84] extended the model by including finite chain length effects (i.e. *non-Gaussian* conformation of network strands at sufficiently large elongation). The model, developed for vulcanized rubbers, assumes tetrafunctional cross/endlinks and entanglements that are thermally fluctuating around their mean position (like in the phantom network model[404,405], §5.3.1.I-a). In addition, (trapped) entanglements are viewed as "slip-links" that can slide along the chain primitive path by an arc length a (the tube SSL). The motion of junction points (cross/endlinks and entanglements) is therefore *non-affine*. The slip-link tetrahedron, and how it relates to the microstructure of microphase-segregated block copolymers, is schematically illustrated in Figure 5.9.

A detailed analysis of the E–V slip-link model is offered in Appendix H, §H.2.2. Such analysis was necessary because of the numerous typos that appear in the original papers of Ball et al.[83] and Edwards and Vilgis[84]. The 2014 *Macromolecules* review of Schlögl et al.[480] also contains an incorrect expression for the E–V slip-link model. In what follows, we briefly outline the main steps leading to the determination of the chemical and topological contributions to the reduced stress.

Elastic energy density

In the most general case, i.e. arbitrary deformation and both entanglement slippage and finite chain extensibility taken into account, the deformation-dependent part of W_e is[84]

$$W_e = \frac{1}{2} N_s kT \left\{ \sum_i \left[\frac{\left(1-\alpha^2\right)\left(1+\beta\right)\lambda_i^2}{\left(1-\alpha^2 I_1\right)\left(1+\beta\lambda_i^2\right)} + \ln\left(1+\beta\lambda_i^2\right) \right] + \ln\left(1-\alpha^2 I_1\right) \right\} \quad \text{slip-links} \quad (5.105)$$

where N_s is the *number density of elastically active slip-links*, α is the *finite extensibility parameter*, β is the *slippage parameter*, and I_1 is the first scalar invariant of the Finger/Green tensor (Eq. (5.6)a). The slippage parameter,[83]

$$0 \le \beta \le \infty \quad (5.106)$$

defines the permitted slip-link range along the strands: $\beta = 0$ corresponds to a cross/endlink, and $\beta \to \infty$ to an object whose deformation free energy depends only on volume changes, $\Delta A_e = N_s kT \cdot \ln(\lambda_1\lambda_2\lambda_3)$.[83,x] Therefore, the elastic energy density W_c associated with an ensemble of cross/endlinks is obtained[84] simply by setting $\beta = 0$ in Eq. (5.105),

$$W_c = \frac{1}{2} N_c kT \left\{ \sum_i \left[\frac{\left(1-\alpha^2\right)\lambda_i^2}{\left(1-\alpha^2 I_1\right)} \right] + \ln\left(1-\alpha^2 I_1\right) \right\} \quad \text{cross/endlinks} \quad (5.107)$$

where N_c is the *number density of elastically active cross/endlinks*. Since chemical and topological contributions are assumed to be *additive*, the total elastic energy density of the system is[83,84]

---

[x] The expression for ΔA_e in the limit for $\beta \to \infty$ can only be obtained by considering also the deformation-independent terms of W_e, not given in Eq. (5.105). See Vilgis and Erman[497].

$$W = W_c + W_e \tag{5.108}$$

The E–V slip-link model thus contains four parameters: N_c, N_s, α, and β. Notice that Eq. (5.107) with $\alpha = 0$ correctly reduces to the classical elastic energy density $W_c = (1/2)N_c kT \cdot I_1 = (1/2)G_0 \cdot I_1$, i.e. the deformation-dependent part of Eq. (5.14). To determine the domain of the finite extensibility parameter α, and how α relates to molecular characteristics, we need to examine the functional dependence of W_c.

By considering the singularity and sign of W_c at $\lambda = 1$, it follows that α must be restricted to the interval (§H.2.2)

$$0 \le \alpha < \frac{1}{3^{1/2}} \simeq 0.577 \tag{5.109}$$

The case $\alpha = 0$ corresponds to infinite chain extensibility, and therefore to the 1981 slip-link model of Ball et al.[83].

Relation between α and molecular characteristics

Under general deformation conditions, W_c becomes unbounded when I_1 reaches a critical value, $I_{1,\text{critical}}$, given by

$$1 - \alpha^2 I_{1,\text{critical}} = 0 \tag{5.110}$$

In uniaxial extension, this corresponds to a maximum elongation λ_{max} (cf. Eq. (5.8)a),

$$1 - \alpha^2 \left(\lambda_{max}^2 + \frac{2}{\lambda_{max}} \right) = 0 \tag{5.111}$$

If $\lambda_{max} \gg 2^{1/3} \simeq 1.26$, a condition usually met in practice, Eq. (5.111) simplifies to

$$\alpha \simeq \frac{1}{\lambda_{max}} \tag{5.112}$$

which gives the relation between the parameter α and the maximum (macroscopic) extensibility of the network, λ_{max}. A fundamental assumption of the E–V slip-link model is that the maximum stretch of the network is given by the maximum extensibility of the trapped entanglement strands therein[84], $\lambda_{max,e}$ (Eq. (5.75)). Thus,

$$\alpha \simeq \frac{1}{\lambda_{max,e}} = \frac{b_k}{a} \tag{5.113}$$

According to the results presented in Figure 2.3(b) and Table 2.5, the parameter α for linear flexible polymers should lie within the range 0.1–0.4. Indeed, the experimental investigations of Kilian and Vilgis[498,499] determined $\alpha \simeq 0.1$ for many commercial, unswollen rubbers.

Relation between β and molecular characteristics

In vulcanized rubbers, the slippage parameter β measures the amount of sliding of a typical (trapped) entanglement between two topologically neighbouring links (other entanglements or cross/endlinks). It is, however, a *relative* measure of the additional degree of freedom of entanglements compared to chemical cross/endlinks. In 1993, Vilgis and Erman[497] proposed an estimate of β based on molecular parameters. For a typical network monomer that is not adjacent to the cross/endlinks, the amplitude of the fluctuations is of the order of the tube SSL, a. If the system is unentangled (as in the affine and phantom network models), the transverse fluctuation of a network strand is of the order of the unperturbed strand size, R_g (the unperturbed mean-square mass-weighted distance of the monomers from their center of mass, or radius of gyration). According to Vilgis and Erman[497], β can therefore be estimated as

$$\beta \approx \frac{a^2}{R_g^2} \qquad \text{(slippage of } \textit{trapped} \text{ entanglements)} \qquad (5.114)$$

i.e. by the ratio of the square of the fluctuations in the constrained system to those in the unconstrained system. Since for Gaussian coils[23] $R_g^2 = (1/6)R^2$, and $R^2 = Za^2$ (Eqs. (2.2) and (3.1)), we may rewrite Eq. (5.114) as

$$\beta \approx \frac{6}{Z} \qquad \text{(slippage of } \textit{trapped} \text{ entanglements)} \qquad (5.115)$$

According to this argument, the slippage parameter for vulcanized rubbers should vary between 0 ($Z \to \infty$) and ≈ 6 ($Z = 1$) (cf. §4.3.2.II-c and Eq. (4.22)).

In the original model of Ball et al.[83] the estimate based on the replica formalism yielded $\beta \simeq 0.2$, but this cannot hold true for real networks[84]. For a crosslinked 92% *cis*-1,4 PI, Thirion and Weil[500] found that $\beta \simeq 0.4$ best described the experimental data. Of the same order of magnitude, $0.1 \leq \beta \leq 0.8$, were the best-fit results obtained by Urayama et al.[81,82] for endlinked poly(dimethylsiloxane) networks. In their investigations on $(S–I–S)_p$–type multiblocks, Watanabe and collaborators[164,222] assumed $\beta = 5$.

Chemical and topological contributions to the reduced stress

We obtained the chemical and topological contributions to the net tensile stress, $\sigma_E(\lambda)$, by applying Eq. (5.15) to Eqs. (5.105) and (5.107) (§H.2.2). The resulting reduced stress can be written as

$$\begin{aligned}\sigma_{\mathrm{E,red}}(\lambda;\theta,\alpha,\beta,G_0) &= \frac{G_0}{Q_\mathrm{c}(\alpha)+\theta\cdot Q_\mathrm{e}(\alpha,\beta)}\left(P_\mathrm{c}(\lambda;\alpha)+\theta\cdot P_\mathrm{e}(\lambda;\alpha,\beta)\right)\\ &= N_\mathrm{c}kT\cdot P_\mathrm{c}(\lambda;\alpha) \qquad +N_\mathrm{s}kT\cdot P_\mathrm{e}(\lambda;\alpha,\beta)\\ &= N_\mathrm{c}kT\cdot Q_\mathrm{c}(\alpha)\cdot Y_\mathrm{c}(\lambda;\alpha)+N_\mathrm{s}kT\cdot Q_\mathrm{e}(\alpha,\beta)\cdot Y_\mathrm{e}(\lambda;\alpha,\beta)\\ &= G_\mathrm{c}(N_\mathrm{c},\alpha)\cdot Y_\mathrm{c}(\lambda;\alpha) \quad +G_\mathrm{e}(N_\mathrm{s},\alpha,\beta)\cdot Y_\mathrm{e}(\lambda;\alpha,\beta)\end{aligned} \tag{5.116}$$

where $P_\mathrm{e}(\lambda;\alpha,\beta)$ is the *entanglement contribution*, $Q_\mathrm{e}(\alpha,\beta) \equiv P_\mathrm{e}(\lambda{=}1;\alpha,\beta)$ is the *initial entanglement contribution*, $Y_\mathrm{e}(\lambda;\alpha,\beta) \equiv P_\mathrm{e}(\lambda;\alpha,\beta)/Q_\mathrm{e}(\alpha,\beta)$ is the *normalized entanglement contribution*, and $\theta \equiv N_\mathrm{s}/N_\mathrm{c}$ is the *number density ratio* between slip-links and cross/endlinks; the chemical contributions are obtained from the entanglement contributions by setting $\beta = 0$: $P_\mathrm{c}(\lambda;\alpha) = P_\mathrm{e}(\lambda;\alpha,\beta{=}0)$, $Q_\mathrm{c}(\alpha) = Q_\mathrm{e}(\alpha,\beta{=}0)$, and $Y_\mathrm{c}(\lambda;\alpha) = Y_\mathrm{e}(\lambda;\alpha,\beta{=}0)$. Notice that Eq. (5.116)d is the necessary generalization of Eq. (5.97), since the E–V slip-link model predicts both the chemical and the topological contribution. Clearly, $Y_\mathrm{c}(\lambda;\alpha) = 1$ and $Y_\mathrm{e}(\lambda;\alpha,\beta) = 1$ at $\lambda = 1$ (by construction), so the requirement expressed by Eq. (5.21) is satisfied.

From Eqs. (5.116)c-d, the chemical and topological contributions to the initial shear modulus G_0 are given by

$$\begin{aligned}G_\mathrm{c}(N_\mathrm{c},\alpha) &= N_\mathrm{c}kT\cdot Q_\mathrm{c}(\alpha)\\ G_\mathrm{e}(N_\mathrm{s},\alpha,\beta) &= N_\mathrm{s}kT\cdot Q_\mathrm{e}(\alpha,\beta)\end{aligned} \tag{5.117}$$

If thermal fluctuations were neglected, the right-hand side of Eqs. (5.117) would be multiplied by 2 (according to the analyses of Chompff and Duiser[202] and Graessley[203,501]), so the number densities N_c and N_s would be reduced by 50%. The fraction of the initial shear modulus contributed by entanglements, ψ, and the relative magnitude of entanglement and endlink contributions, $\Omega = \psi/(1-\psi)$, are

$$\psi(\theta,\alpha,\beta)=\frac{\theta\cdot Q_{\mathrm{e}}(\alpha,\beta)}{Q_{\mathrm{c}}(\alpha)+\theta\cdot Q_{\mathrm{e}}(\alpha,\beta)}$$
$$\Omega(\theta,\alpha,\beta)=\theta\cdot\frac{Q_{\mathrm{e}}(\alpha,\beta)}{Q_{\mathrm{c}}(\alpha)} \tag{5.118}$$

The analytical expression for the entanglement contribution, $P_{\mathrm{e}}(\lambda;\alpha,\beta)$, is (§H.2.2)

$$P_{\mathrm{e}}(\lambda;\alpha,\beta)=P_{\mathrm{e},1}(\lambda;\alpha,\beta)+P_{\mathrm{e},2}(\lambda;\alpha,\beta)+P_{\mathrm{e},3}(\lambda;\alpha)+P_{\mathrm{e},4}(\lambda;\beta)$$

with

$$P_{\mathrm{e},1}(\lambda;\alpha,\beta)=\frac{\alpha^2\left(1-\alpha^2\right)(1+\beta)}{\left(1-I_1\alpha^2\right)^2}\left[\frac{\lambda^2}{1+\beta\lambda^2}+\frac{2}{\beta+\lambda}\right]$$
$$P_{\mathrm{e},2}(\lambda;\alpha,\beta)=\frac{\left(1-\alpha^2\right)(1+\beta)}{1-I_1\alpha^2}\left[\frac{\lambda}{\left(1+\beta\lambda^2\right)^2}-\frac{1}{(\beta+\lambda)^2}\right]\frac{1}{\lambda-\lambda^{-2}} \tag{5.119}$$
$$P_{\mathrm{e},3}(\lambda;\alpha)=-\frac{\alpha^2}{1-I_1\alpha^2}$$
$$P_{\mathrm{e},4}(\lambda;\beta)=\frac{\beta\lambda}{\left(1+\beta\lambda^2\right)(\beta+\lambda)}$$

while the initial entanglement contribution, $Q_{\mathrm{e}}(\alpha,\beta)$, is given by

$$\begin{aligned}Q_{\mathrm{e}}(\alpha,\beta)&=P_{\mathrm{e}}(\lambda=1;\alpha,\beta)\\&=\frac{1+2\alpha^2\left(-1+\beta+\beta^2\right)+\alpha^4(3+6\beta)}{\left(1-3\alpha^2\right)^2(1+\beta)^2}\end{aligned} \tag{5.120}$$

Therefore, the chemical contributions, $P_{\mathrm{c}}(\lambda;\alpha)$ and $Q_{\mathrm{c}}(\alpha)$, are

$$\begin{aligned}P_{\mathrm{c}}(\lambda;\alpha)&=P_{\mathrm{e}}(\lambda;\alpha,\beta=0)\\&=\frac{1-2\alpha^2+I_1\alpha^4}{\left(1-I_1\alpha^2\right)^2}\end{aligned} \tag{5.121}$$

and

$$\begin{aligned} Q_c(\alpha) &= P_e(\lambda = 1; \alpha, \beta = 0) \\ &= P_c(\lambda = 1; \alpha) \\ &= \frac{1 - 2\alpha^2 + 3\alpha^4}{\left(1 - 3\alpha^2\right)^2} \end{aligned} \tag{5.122}$$

If finite chain length effects are neglected ($\alpha = 0$),

$$P_e(\lambda; \alpha = 0, \beta) = \frac{\lambda^2}{(\beta + \lambda)\left(1 + \beta\lambda^2\right)}\left[\frac{(1+\beta)\left(1 - \beta^2\lambda\right)\lambda}{(\beta + \lambda)\left(1 + \beta\lambda^2\right)} + \beta\right] \tag{5.123}$$

$$Q_e(\alpha = 0, \beta) = \frac{1}{(1+\beta)^2} \tag{5.124}$$

$$P_c(\lambda; \alpha = 0) = 1 \tag{5.125}$$

$$Q_c(\alpha = 0) = 1 \tag{5.126}$$

Comparison with analytical expressions for $P_e(\lambda;\alpha,\beta)$, $Q_e(\alpha,\beta)$, and $Y_e(\lambda;\alpha,\beta)$ reported in the literature

In the original publication of Ball et al.[83], the expression for $Q_e(\alpha=0,\beta)$, equation (62) on page 1015, is incorrect. Typos are also present in the paper by Edwards and Vilgis[84]. Specifically, their expression for $P_e(\lambda;\alpha=0,\beta)$, on page 486, is missing $(1+\beta)$ in the numerator of the first and second term. In addition, equation (5.1) on page 491, giving the expression for $P_e(\lambda;\alpha,\beta)$, is incompatible with the elastic energy density and internally inconsistent with the equation for $P_c(\lambda;\alpha)$ ((5.3), on the same page) unless the second term is multiplied by $(1-\alpha^2)(1+\beta)$ (§H.2.2).

Equation (12) on page 2764 of Schlögl et al.[480] is also incorrect even though, ironically, the authors claim they are "correcting a typo in the original publication". In spite of such

claim, not only their expression for $Y_e(\lambda;\alpha=0,\beta)$ does not correct the original typo (which would have required multiplying by $(1+\beta)$ the numerator of their first and second term), but it is also missing a multiplicative common factor of $(1+\beta)^2$. As a result, their expression for $Y_e(\lambda;\alpha=0,\beta)$ is nothing more than the uncorrected equation for $P_e(\lambda;\alpha=0,\beta)$ given in the Edwards and Vilgis paper[84] (§H.2.2).

Our equations for $P_e(\lambda;\alpha,\beta)$, $Q_e(\alpha,\beta)$, and $Y_e(\lambda;\alpha,\beta)$, derived from the elastic energy density, are equivalent to the analytical expressions reported by Thirion and Well[500] and by Graessley[45] (for $Q_e(\alpha=0,\beta)$), and by Watanabe and co-workers[164,222] (§H.2.2).

Effect of model parameters on $P_e(\lambda;\alpha,\beta)$

The effect of the parameters α and β on the entanglement contribution, $P_e(\lambda;\alpha,\beta)$, is illustrated in Figure 5.10. When chains are assumed to be infinitely extensible, the entanglement contribution $P_e(\lambda;\alpha=0,\beta)$ is always lower than the neo-Hookean prediction, in both uniaxial extension and compression (Figure 5.10(top)). This is equivalent to the "*damping*" effect for polymer melts and solutions discussed in §5.3.1.II-b (Eq. (5.38)). For $\beta > 0$, *negative departures* from neo-Hookean behavior can be observed. In uniaxial extension, the initial slope decreases for $\beta > 0.2$, and tends to *zero* for $\beta > 6$ (in agreement with the analysis of Edwards and Vilgis[84]). For $\beta \geq 25$, $P_e(\lambda;\alpha=0,\beta)$ develops a *shallow minimum* (whose locus is approximately constant and located before $\lambda = 2$), and a *shallow maximum* (at $\lambda \geq 4$). This behavior is consistent with the qualitative observations of Thirion and Weil[500]. It is important to realize that such behavior is not exhibited when using the incorrect expressions for $P_e(\lambda;\alpha = 0,\beta)$ previously mentioned. Therefore, for

systems whose tensile response is described by large slippage parameters (such the multiblocks studied by Watanabe et al.[164,222] and our material, §5.3.4.IV), using the correct analytical expression for $P_e(\lambda;\alpha=0,\beta)$ becomes quantitatively relevant. As expected, $P_e(\lambda=1;\alpha=0,\beta)$ decreases with increasing β.

The cross/endlink contribution, $P_c(\lambda;\alpha) = P_e(\lambda;\alpha,\beta=0)$, exhibits *positive departures* from neo-Hookean behavior (cf. §5.3.1.II-b and Eq. (5.38)), and a local minimum at $\lambda = 1$ that increases with increasing α (Figure 5.10(middle)). In extension, $P_c(\lambda;\alpha)$ becomes unbounded at $\lambda = \lambda_{max} \simeq 1/\alpha$ (Eq. (5.112)). The lower panel of Figure 5.10 shows the combined effect of α and β on $P_e(\lambda;\alpha,\beta)$. Notice that, in this case, the locus of the local minimum is strongly dependent on the value of α (as opposed to the behavior shown in Figure 5.10(top)).

Effect of model parameters on $Q_e(\alpha,\beta)$

Figure 5.11 demonstrates the effect of the parameters α and β on the initial entanglement contribution, $Q_e(\alpha,\beta) = P_e(\lambda=1;\alpha,\beta)$. The general case is shown in Figure 5.11(top). $Q_e(\alpha,\beta)$ increases with increasing α or with decreasing β, as it should. We note that the condition $Q_e(\alpha,\beta) > 1$ is achieved for $\alpha > 0.39$ irrespective of the value of β. On the other hand, $Q_e(\alpha,\beta) < 1$ when $\alpha < 0.39$ and $\beta > 1$. When $\alpha = 0$, the initial entanglement contribution is about 10^{-2} for $\beta = 2$, and 10^{-4} for $\beta = 100$. This implies that large values of the slippage parameter, coupled with infinite chain extensibility, can significantly increase the number density of slip-links N_s compared to the number density of the actual entanglements in the system. From Eqs. (5.88)b and (5.117)b, $\xi_N \cdot \nu_{e,eff} =$

$N_s \cdot Q_e(\alpha,\beta)$. Therefore, if $Q_e(\alpha,\beta) \simeq 10^{-4}$, $N_s \simeq 10^4\ \xi_N \cdot \nu_{e,eff}$. A sharply different behavior is observed for the initial chemical contribution, $Q_c(\alpha) = Q_e(\alpha,\beta=0)$, in Figure 5.11(middle). Since $Q_c(\alpha) \simeq 1$ for $\alpha \leq 0.2$, the number density of cross/endlinks N_c is expected to be close to the number density of the actual cross/endlinks in the system (compare Eqs. (5.88)a and (5.117)a). Interestingly, $Q_e(\alpha,\beta)$ remains finite when topological constraints effectively disappear, $\beta \to \infty$, unless $\alpha = 0$ (Figure 5.11(bottom)).

Effect of model parameters on $Y_e(\lambda;\alpha,\beta)$

The effect of the parameters α and β on the normalized entanglement contribution, $Y_e(\lambda;\alpha,\beta) = P_e(\lambda;\alpha,\beta)/Q_e(\alpha,\beta)$, is shown in Figure 5.12. The overall behavior resembles the functional dependence of $P_e(\lambda;\alpha,\beta)$ in Figure 5.11. The normalized entanglement contribution remains always below the neo-Hookean prediction when $\alpha = 0$ (Figure 5.12(top)). The initial slope decreases with increasing β in the range $0 < \beta < 6$, and remains *constant* for $\beta \geq 6$. This corresponds to the *maximum degree of initial "damping"* allowed by the E–V slip-link model (cf. Eq. (5.104)b). For $\beta \geq 25$, $Y_e(\lambda;\alpha=0,\beta)$ develops a *well-defined minimum* (whose locus is approximately constant and located before $\lambda = 2$), and a *well-defined maximum* (at $\lambda \geq 4$). We stress again the fact that such behavior (local minimum followed by maximum) is suppressed when using the incorrect expression for $Y_e(\lambda;\alpha = 0,\beta)$ reported by Schlögl et al.[480]. Their qualitative and quantitative analyses of the E–V slip-link model is therefore erroneous.

The normalized cross/endlink contribution, $Y_c(\lambda;\alpha) = Y_e(\lambda;\alpha,\beta=0)$, exhibits *positive departures* from neo-Hookean behavior (cf. §5.3.1.II-b and Eq. (5.38)), and a local

minimum at $\lambda = 1$ (Figure 5.12(middle)). Mirroring the behavior of $P_c(\lambda;\alpha)$, $Y_c(\lambda;\alpha)$ becomes unbounded at $\lambda = \lambda_{max} \simeq 1/\alpha$ (Eq. (5.112)). The combined effect of α and β on $Y_e(\lambda;\alpha,\beta)$ is illustrated in Figure 5.12(bottom). Once again, the locus of the local minimum is strongly dependent on the value of α (in contrast with the behavior exhibited when $\alpha = 0$, Figure 5.12(top)).

Effect of model parameters on $S(\lambda;\theta,\alpha,\beta)$

Figures 5.13 and 5.14 reveal the effect of the parameters θ, α, and β on the dimensionless stress, $S(\lambda;\theta,\alpha,\beta)$. When $\alpha = 0$, Figure 5.13, the dimensionless stress never exceeds the neo-Hookean prediction (cf. §5.3.1.II-b and Eq. (5.38)). In addition, well-defined minima and maxima appear for $\theta \geq 10^3$ when $\beta = 25$, Figure 5.13(middle), and for $\theta \geq 10^4$ when $\beta = 100$, Figure 5.13(bottom). Once developed, the locus of both is independent of the value of θ. The locus of the minimum is also β-independent, and located before $\lambda = 2$.

When fitting experimental data to the E–V slip-link model, the analysis of the θ-dependence of the dimensionless stress is a prerequisite to discern whether meaningful results have been obtained. Notice that $S(\lambda;\theta,\alpha=0,\beta)$ becomes θ-independent for $\theta \geq 10^4$ when $\beta = 6$, Figure 5.13(top), for $\theta \geq 10^5$ when $\beta = 25$, Figure 5.13(middle), and for $\theta \geq 10^6$ when $\beta = 100$, Figure 5.13(bottom). As will be shown in §5.3.4.IV, the behavior in Figure 5.13 is compatible with our experimental data when $7 \leq \beta \leq 31$ and $\theta \simeq 10^5$.

The dimensionless stress exhibited by the E–V slip-link model when $\alpha = 0.05$ is shown in Figure 5.14. As anticipated in §5.3.1.II-b, finite chain extensibility in vulcanized

rubbers results in $S(\lambda;\theta,\alpha,\beta) > 1$ (hence $h(t,\lambda) > 1$), and causes $S(\lambda;\theta,\alpha,\beta)$ to diverge at sufficiently large elongations (when $\lambda = \lambda_{max} \simeq 1/\alpha$, (Eq. (5.112)).

Effect of model parameters on $\psi(\theta,\alpha,\beta)$

The effect of the parameters θ, α, and β on the fraction of the initial shear modulus contributed by entanglements, $\psi(\theta,\alpha,\beta)$, is elucidated in Figure 5.15. The sigmoidal shape of the curves yields characteristic dependences on the model parameters: $\psi(\theta,\alpha,\beta)$ increases with decreasing β (at fixed values of θ and α), and with increasing α (at fixed values of θ and β); if both $\psi(\theta,\alpha,\beta)$ and α are held constant, the number density ratio θ increases with increasing β. Notice that for $\theta \geq 10^4$, $\alpha = 0$, and $\beta < 100$, the initial shear modulus is largely dominated by topological constraints ($\psi(\theta,\alpha,\beta) > 0.9$ in the upper-right corner of Figure 5.15(top)).

Negative departures from neo-Hookean behavior for selected rubber elasticity models

The normalized entanglement contributions for selected rubber elasticity models from Figure 5.8(a) and for the E–V slip-link model with $\alpha = 0$ (infinite chain extensibility) are compared in Figure 5.16. Notice that the E–V slip-link model with small values of the slippage parameter (e.g. $\beta = 0.01$) reduces to neo-Hookean behavior at small strains. The initial departure from neo-Hookean behavior for the E–V slip-link model is similar to that of the modified Hooke's law and the R–P non-affine slip-tube model when $\beta = 0.2$, but for larger values of β it exceeds the prediction of all the other models.

Nonetheless, a sharp distinction remains with respect to materials exhibiting critical-gel-like behavior, for which $dY_e/d\lambda \to -\infty$ at $\lambda = 1$ (Eq. (5.104)). For such materials, the experimental tensile response, expressed as dimensionless stress, cannot be fitted to the prediction of rubber elasticity models. Use of the reduced stress, and therefore of the initial shear modulus G_0 as an additional fitting parameter, is necessary. A critical analysis of the G_0 values obtained from the fitting procedure thus requires an operational definition of initial modulus for critical-gel-like materials subjected to start-up extensional tests. This is the subject of the next section.

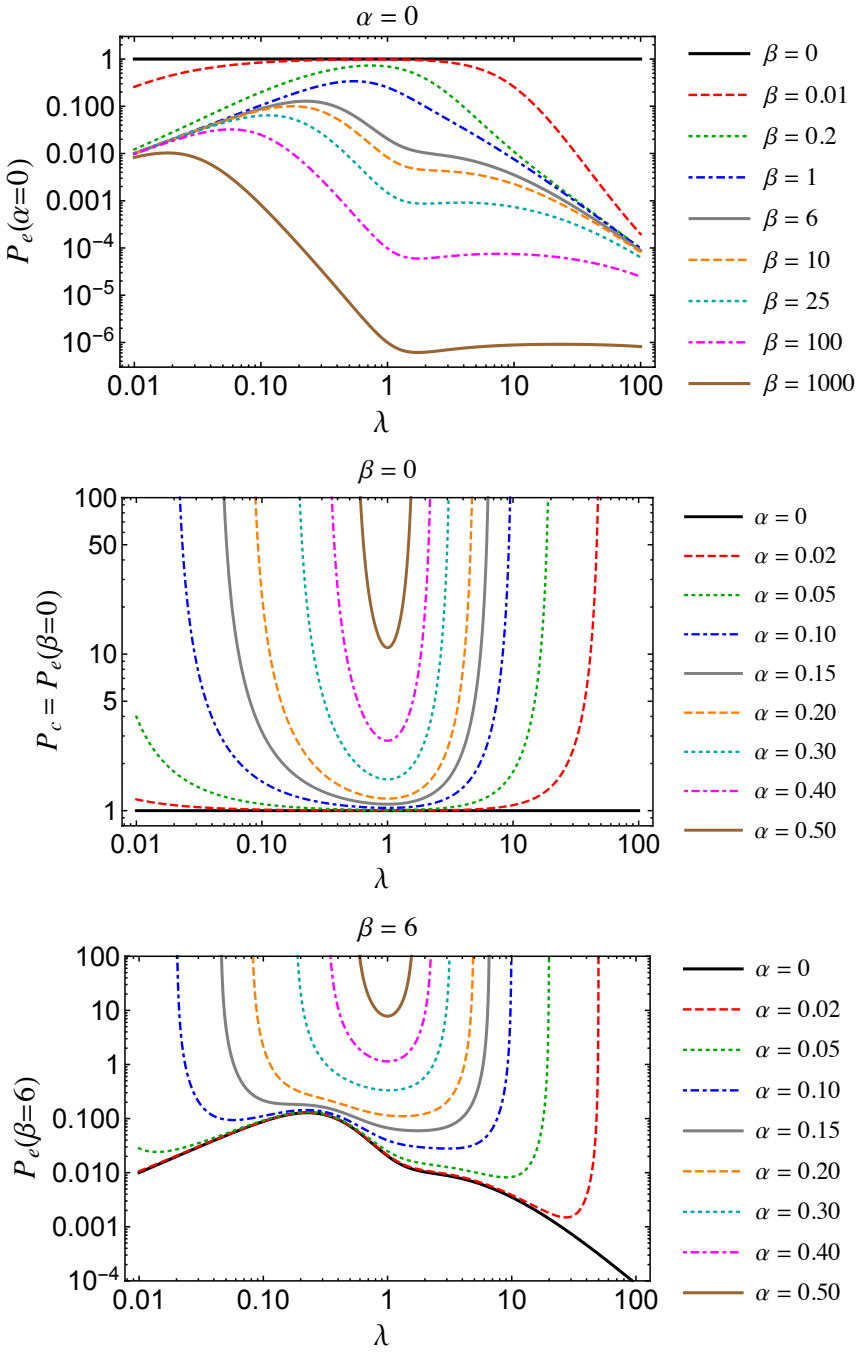

Figure 5.10. Entanglement contribution, $P_e(\lambda;\alpha,\beta)$, exhibited by the E–V slip-link model in uniaxial compression ($\lambda \leq 1$) and extension ($\lambda \geq 1$) for (top) $\alpha = 0$, (middle) $\beta = 0$, and (bottom) $\beta = 6$.

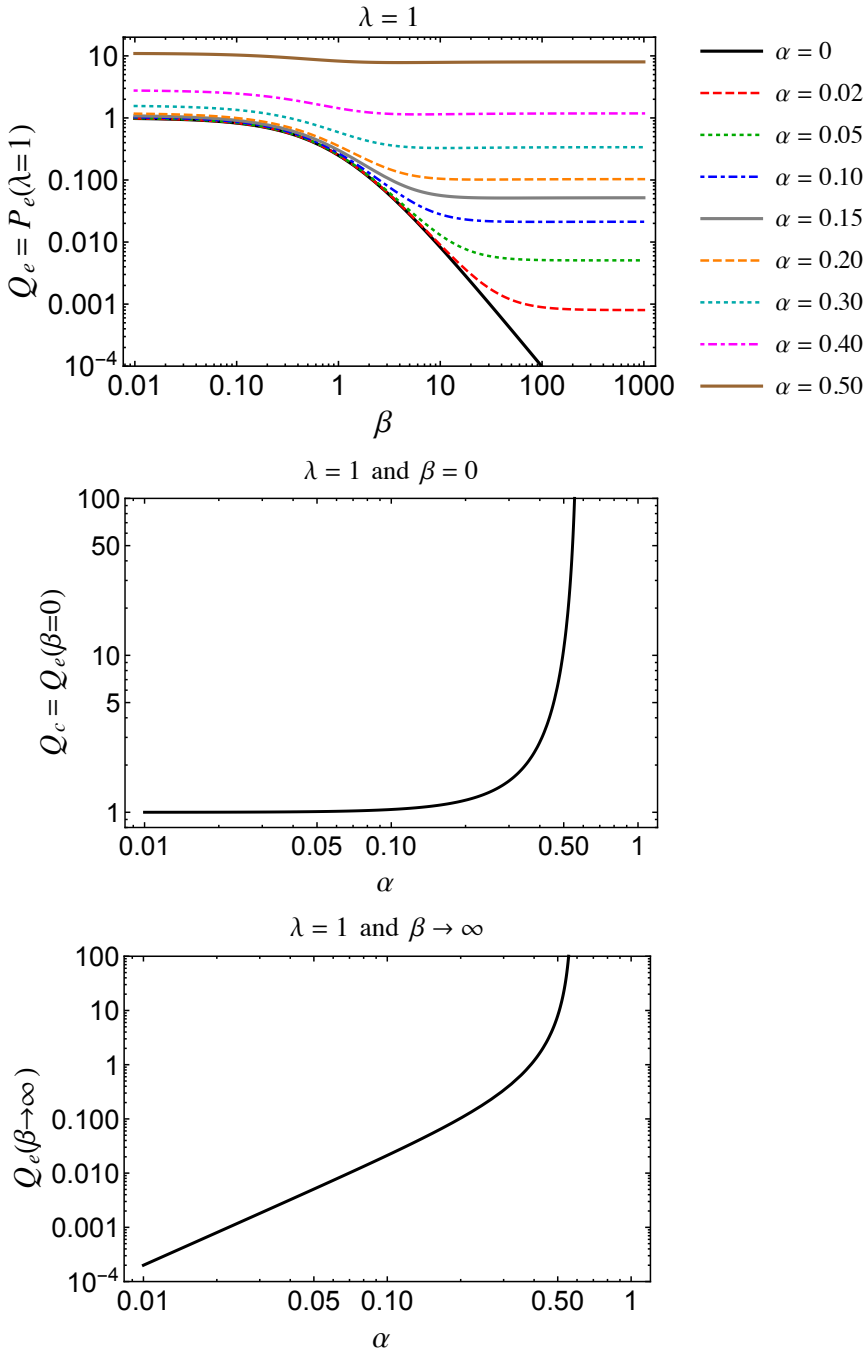

Figure 5.11. Initial entanglement contribution, $Q_e(\alpha,\beta) = P_e(\lambda=1;\alpha,\beta)$, exhibited by the E–V slip-link model for (top) general case, (middle) $\beta = 0$, and (bottom) $\beta \to \infty$.

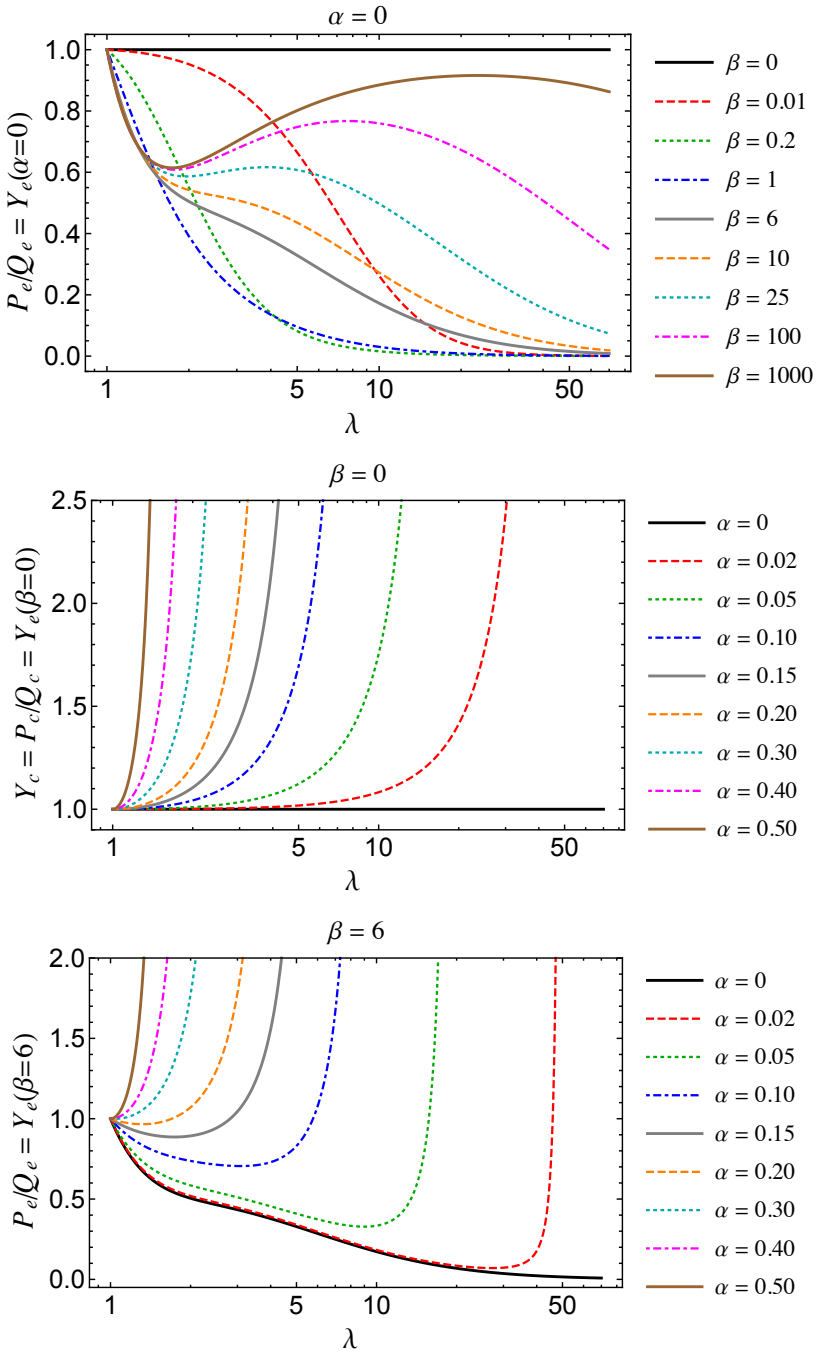

Figure 5.12. Normalized entanglement contribution, $Y_e(\lambda;\alpha,\beta) = P_e(\lambda;\alpha,\beta)/Q_e(\alpha,\beta)$, exhibited by the E–V slip-link model in uniaxial extension ($\lambda \geq 1$) for (top) $\alpha = 0$ – cf. Figure 5.8(a), (middle) $\beta = 0$, and (bottom) $\beta = 6$.

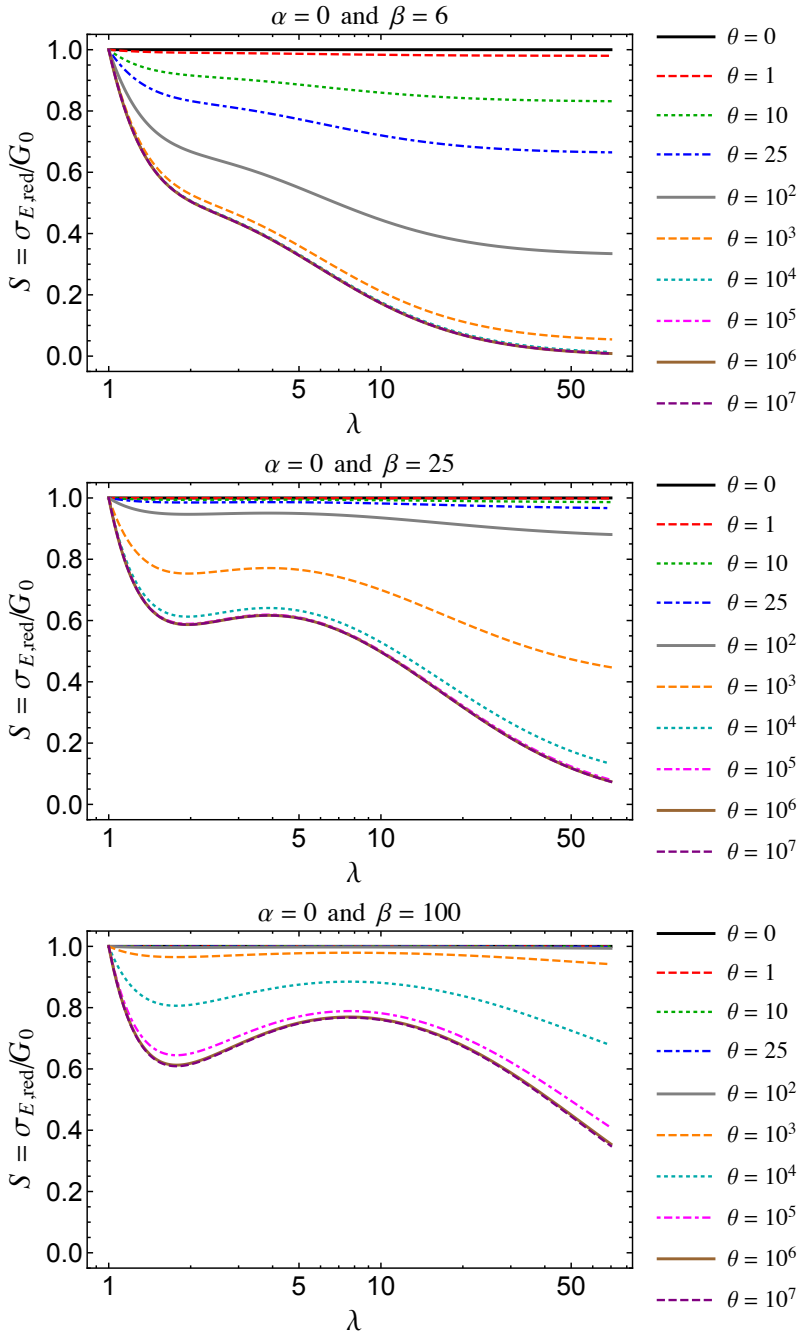

Figure 5.13. Dimensionless stress, $S(\lambda;\theta,\alpha,\beta)$, exhibited by the E–V slip-link model in uniaxial extension ($\lambda \geq 1$) for $\alpha = 0$ and (top) $\beta = 6$, (middle) $\beta = 25$, (bottom) $\beta = 100$.

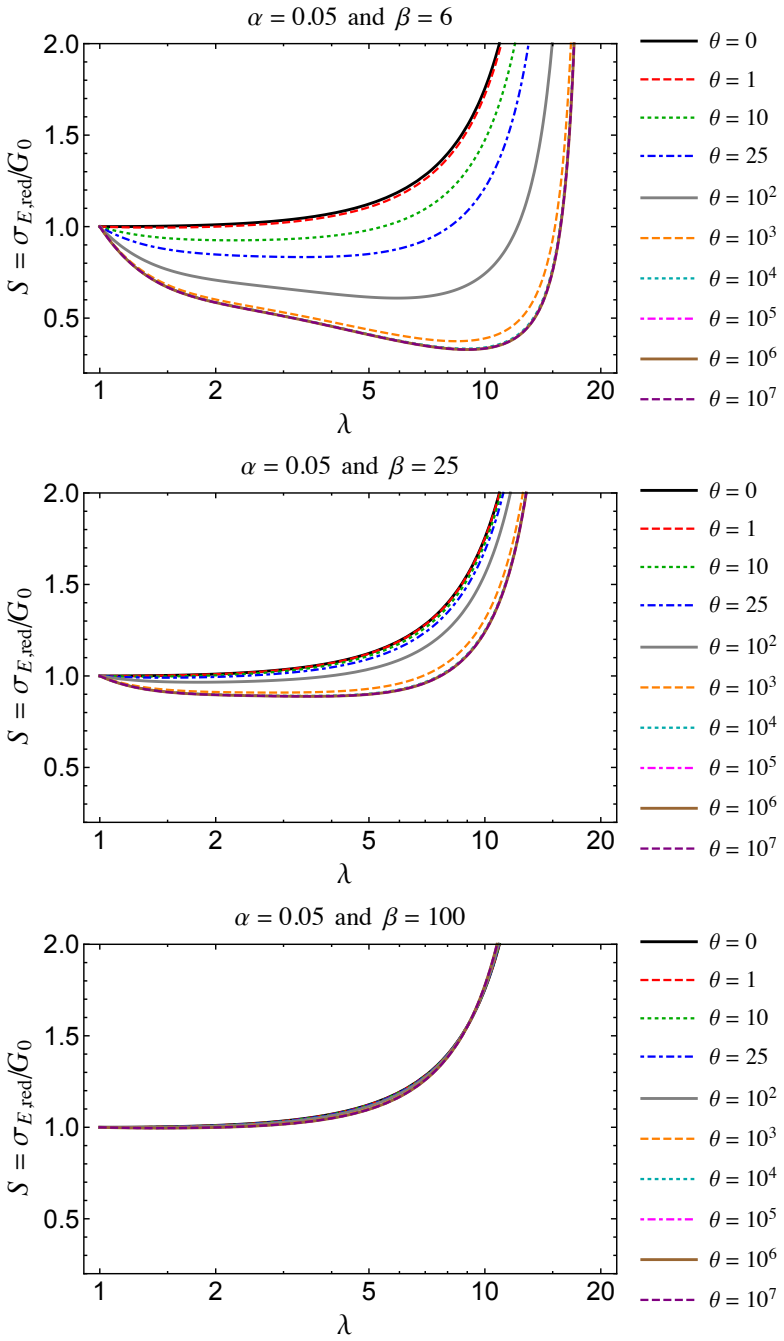

Figure 5.14. Dimensionless stress, $S(\lambda;\theta,\alpha,\beta)$, exhibited by the E–V slip-link model in uniaxial extension ($\lambda \geq 1$) for $\alpha = 0.05$ and (top) $\beta = 6$, (middle) $\beta = 25$, (bottom) $\beta = 100$.

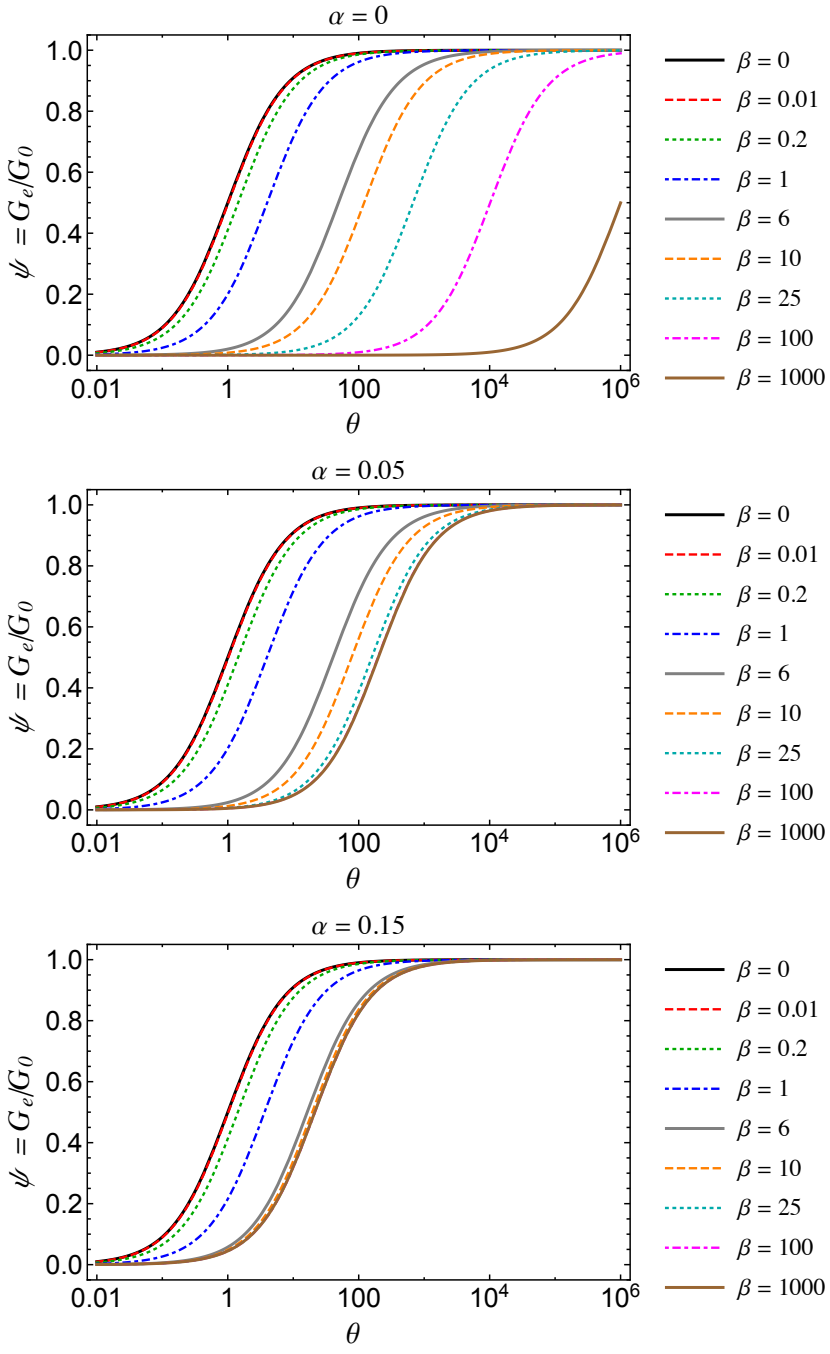

Figure 5.15. Fraction of the initial shear modulus G_0 contributed by entanglements, $\psi(\theta,\alpha,\beta)$, exhibited by the E–V slip-link model for (top) $\alpha = 0$, (middle) $\alpha = 0.05$, (bottom) $\alpha = 0.15$.

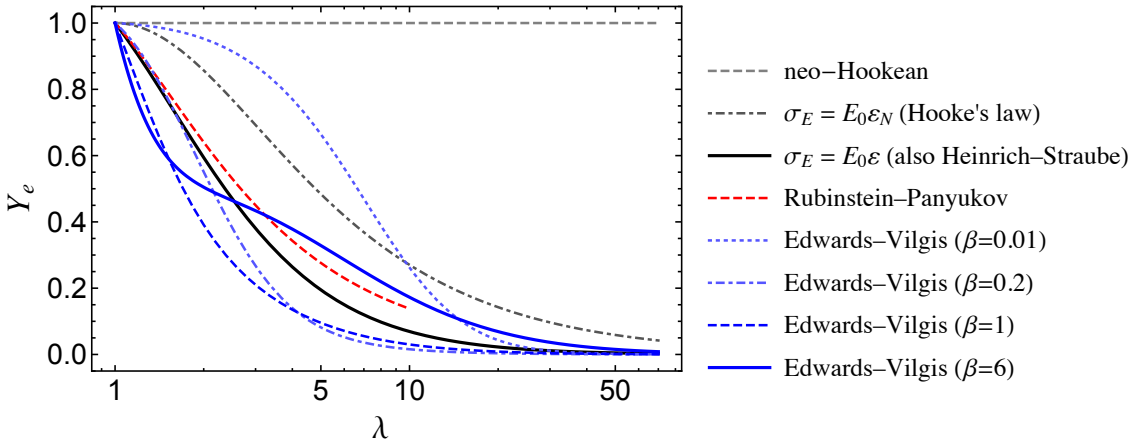

Figure 5.16. Normalized entanglement contribution, Y_e, for selected rubber elasticity models from Figure 5.8(a) and for the E–V slip-link model with $\alpha = 0$ (i.e. infinite chain extensibility). Notice that the E–V slip-link model with small values of the slippage parameter β (e.g. $\beta = 0.01$) reduces to neo-Hookean behavior at small strains. The initial departure from neo-Hookean behavior for the E–V slip-link model is similar to that of the modified Hooke's law and the R–P non-affine slip-tube model when $\beta = 0.2$, but for larger values of β it exceeds the prediction of all the other models. For $\beta \geq 6$, the initial slope for the E–V slip-link model remains unchanged, but an inflection point develops that is centered between $\lambda = 2$ and $\lambda = 3$ (cf. Figure 5.12(top)).

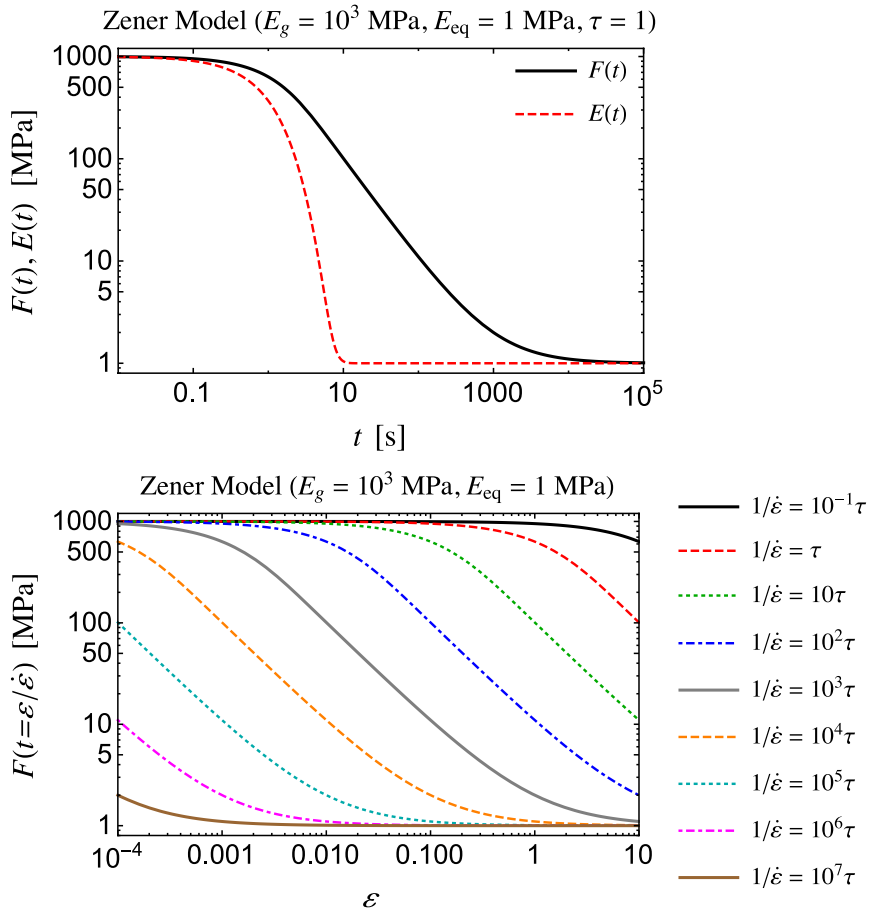

Figure 5.17. (a) Constant-strain-rate modulus, $F(t)$, and relaxation modulus, $E(t)$, for the simplest realistic model exhibiting *solid-like viscoelastic behavior*, i.e. the *3-parameter Maxwell model*[150] or *Zener model*[359] (cf. Appendix D, §D.4.3). The glassy and equilibrium moduli are (respectively) $F_g = E_g = 1$ GPa and $F_{eq} = E_{eq} = 1$ MPa, while the relaxation time is $\tau = 1$ s. (b) Strain dependence of the constant-strain-rate modulus over an experimentally accessible range of ε (cf. Figure 5.5(b)), for selected values of the rate of strain $\dot{\varepsilon}$. The initial extensional modulus or Young's modulus E_0 (by definition, equal to $F(t = \varepsilon / \dot{\varepsilon})$ in the limit for $\varepsilon \ll 1$) is always much greater than either $F(t = 1/\dot{\varepsilon})$ or $E(t = 1/\dot{\varepsilon})$, unless $1/\dot{\varepsilon} < \tau$ (e.g. $1/\dot{\varepsilon} = 10^{-1}\tau$) or $1/\dot{\varepsilon} \gg \tau$ (e.g. $1/\dot{\varepsilon} = 10^{7}\tau$).

5.3.4.III The initial modulus for viscoelastic materials in tensile tests at constant strain rate

The initial modulus for *elastic solids* was defined in §5.3.1.I-b, according to Eq. (5.19) (or, equivalently, Eq. (5.21)). For *viscoelastic solids* and for *critical-gel-like materials* subjected to start-up of steady uniaxial extension the mathematical definition of initial modulus must be slightly modified.

5.3.4.III-a Viscoelastic solids

Let us consider the simplest, yet realistic model exhibiting solid-like viscoelastic behavior, i.e. the 3-*parameter Maxwell model*[150] or *Zener model*[359] (Appendix D, Figure D.3(a) and §D.4.3). The relaxation modulus is (Eq. (D.61) and Table D.1)

$$\begin{cases} E(t) = Ee^{-t/\tau} + E_{\text{eq}} \\ \text{with} \\ E(0) = E + E_{\text{eq}} = E_{\text{g}} \\ E(\infty) = E_{\text{eq}} \end{cases} \tag{5.127}$$

where τ represents the relaxation time of the model, E is the relaxing modulus, E_{g} is the instantaneous or glassy modulus, and E_{eq} is the equilibrium modulus. From Eq. (D.26)c and Table D.1, the constant-strain-rate modulus is

$$\begin{cases} F(t) = \dfrac{E\tau}{t}\left(1 - e^{-t/\tau}\right) + E_{\text{eq}} \\ \text{with} \\ F(0) = E_{\text{g}} = F_{\text{g}} \\ F(\infty) = E_{\text{eq}} = F_{\text{eq}} \end{cases} \tag{5.128}$$

The behavior of $E(t)$ and $F(t)$ is illustrated in Figure 5.17(a), for a Zener model with $E_g = 1$ GPa, $E_{eq} = 1$ MPa, and $\tau = 1$ s.

Application of Eq. (5.19), coupled with Eqs. (5.61) and (5.65), gives

$$\begin{aligned} 3G_0 = E_0 &= \lim_{\varepsilon\to 0} \frac{\sigma^{+}_{E,NLVE}(\varepsilon,\dot{\varepsilon})}{\varepsilon} \\ &= \lim_{\varepsilon\to 0} F(t=\varepsilon/\dot{\varepsilon})\cdot\Lambda_F(\varepsilon,\dot{\varepsilon}) \\ &= \lim_{\varepsilon\to 0} F(t=\varepsilon/\dot{\varepsilon}) \\ &= \lim_{t\to 0} F(t) \\ &= F_g = E_g \end{aligned} \tag{5.129}$$

Thus, employing the definition of initial modulus for elastic solids renders E_0 equal to the glassy modulus E_g regardless of the characteristic relaxation time of the material, the applied rate of strain, and the experimental range of ε. This arises from the fact that, once $\dot{\varepsilon}$ is fixed, time and strain cannot be varied independently (cf. Eq. (5.52)). It is evident that the problem lies in letting ε go to zero.

This can be remedied by defining the initial modulus as the secant modulus in the limit for $\varepsilon \ll 1$, such that

$$\begin{aligned} 3G_0 = E_0 &= \lim_{\varepsilon\ll 1} \frac{\sigma^{+}_{E,NLVE}(\varepsilon,\dot{\varepsilon})}{\varepsilon} \\ &= \lim_{\varepsilon\ll 1} F(t=\varepsilon/\dot{\varepsilon})\cdot\Lambda_F(\varepsilon,\dot{\varepsilon}) \\ &= \lim_{\varepsilon\ll 1} F(t=\varepsilon/\dot{\varepsilon}) \\ &= \lim_{\varepsilon\ll 1}\left[\frac{E\tau\dot{\varepsilon}}{\varepsilon}\left(1-e^{-\varepsilon/\tau\dot{\varepsilon}}\right)+E_{eq}\right] \\ &= \begin{cases} \to E_g & \text{for } \varepsilon \ll \tau\dot{\varepsilon} \\ \to E_{eq} & \text{for } \quad \tau\dot{\varepsilon} \ll \varepsilon < \varepsilon_c \end{cases} \end{aligned} \tag{5.130}$$

where ε_c is the critical strain for the onset of nonlinear behavior. It is straightforward to show that the same result is obtained by considering the tangent modulus instead, $d\sigma^{+}_{E,NLVE}(\varepsilon,\dot{\varepsilon})/d\varepsilon$. Clearly, the definition of initial modulus according to Eq. (5.130) is consistent with experiments: depending on the relaxation time, the elongation rate, and the experimental range of ε, the initial slope of the stress-strain curve for viscoelastic solids can vary between E_g and E_{eq}.

Naively, one might assume that the initial modulus determined from tensile tests at a constant rate of strain $\dot{\varepsilon}$ should be given by the linear relaxation modulus $E(t)$ or the linear secant modulus $F(t)$ evaluated at $t = 1/\dot{\varepsilon}$. A comparison between Figure 5.17(a) and (b) shows that E_0 is always much greater than either $E(t = 1/\dot{\varepsilon})$ or $F(t = 1/\dot{\varepsilon})$, unless $1/\dot{\varepsilon} < \tau$ (e.g. $1/\dot{\varepsilon} = 10^{-1}\tau$) or $1/\dot{\varepsilon} \gg \tau$ (e.g. $1/\dot{\varepsilon} = 10^{7}\tau$). For the same reason, E_0 cannot be estimated by $E'(\omega = \dot{\varepsilon})$.

Notice that the foregoing discussion is independent of the specific model chosen to represent solid-like viscoelastic behavior. The arguments and results remain unchanged if the stress response functions, $E(t)$ and $F(t)$, are expressed in terms of a relaxation spectrum (Eqs. (D.87)b and (D.91)b, and Table D.1).

5.3.4.III-b Critical-gel-like materials

For materials exhibiting critical-gel-like behavior, $F(t\rightarrow 0) \rightarrow \infty$ and $F(t\rightarrow\infty) \rightarrow 0$ (Eq. (5.57)) prevent the use of Eq. (5.130). As an operational definition for initial modulus, we may therefore adopt the value of the secant modulus $F(t)$ evaluated at $t_0 = \varepsilon_0 / \dot{\varepsilon}$, where ε_0

represents the strain value of the first available data point satisfying the requirement $\varepsilon_0 \ll 1$, i.e.

$$\begin{aligned} 3G_0 = E_0 &= \lim_{\varepsilon \ll 1} \frac{\sigma^{+}_{\mathrm{E,NLVE}}(\varepsilon,\dot{\varepsilon})}{\varepsilon} \\ &= \lim_{\varepsilon \ll 1} F(t=\varepsilon/\dot{\varepsilon}) \cdot \Lambda_{\mathrm{F}}(\varepsilon,\dot{\varepsilon}) \\ &= \lim_{\varepsilon \ll 1} F(t=\varepsilon/\dot{\varepsilon}) \\ &= F(t_0 = \varepsilon_0/\dot{\varepsilon}) \\ &= F_0 \qquad \text{where } \varepsilon_0 \text{ is the first exp strain value} \ll 1 \end{aligned} \tag{5.131}$$

Applied to LIL50–12, F_0 is given by the first point of the LVE curves in Figure 5.5(b). Consistently with this approach, the characteristic frequency associated with each rate of strain $\dot{\varepsilon}$ can be calculated either as the reciprocal of t_0 or as the frequency ω_0 at which $E'(\omega_0) = E_0 = F_0$. We regard these alternatives as equivalent (they in fact yield similar frequency values), and choose the latter for present purposes. These results are summarized in Table 5.4.

Having established an operational definition for the initial modulus, we can now determine the relationship between the *dimensionless stress in tensile tests at constant strain rate*, $S_{\mathrm{F}}(\varepsilon,\dot{\varepsilon})$, and the step-strain extensional damping function, $h(t,\varepsilon)$, discussed in §5.3.1.II-c. From Eqs. (5.61) and (5.77),

$$\begin{aligned} \sigma^{+}_{\mathrm{E,NLVE}}(\varepsilon,\dot{\varepsilon}) &= F(t=\varepsilon/\dot{\varepsilon}) \cdot \Lambda_{\mathrm{F}}(\varepsilon,\dot{\varepsilon}) \cdot \varepsilon \\ &\simeq F(t=\varepsilon/\dot{\varepsilon}) \cdot h(t=\varepsilon/\dot{\varepsilon},\varepsilon) \cdot \frac{e^{2\varepsilon} - e^{-\varepsilon}}{3} \end{aligned} \tag{5.132}$$

therefore,

$$\frac{\sigma^{+}_{\mathrm{E,NLVE}}(\varepsilon,\dot{\varepsilon})}{G_0\left(e^{2\varepsilon}-e^{-\varepsilon}\right)} = S_{\mathrm{F}}(\varepsilon,\dot{\varepsilon}) \simeq \frac{F(t=\varepsilon/\dot{\varepsilon})}{F_0}\cdot h(t=\varepsilon/\dot{\varepsilon},\varepsilon) \tag{5.133}$$

where the ratio $F(t=\varepsilon/\dot{\varepsilon})/F_0 \le 1$ originates from *linear relaxation mechanisms*, while $h(t=\varepsilon/\dot{\varepsilon},\varepsilon)$ accounts for elastic (*strain softening/hardening*) and viscoelastic (*strain-induced relaxation*) nonlinear effects (cf. §5.3.1.II-b-c and §5.3.3.II-d-e).

Table 5.4. Initial shear modulus G_0 and characteristic frequency ω_0 associated with each rate of strain $\dot{\varepsilon}$, as deduced from the linear response.

$\dot{\varepsilon}$ [s^{-1}]	ε_0 [10^{-4}]	λ_0	$E_0 = F(t_0=\varepsilon_0/\dot{\varepsilon})$ [MPa]	$G_0 = E_0/3$ [MPa]	ω_0 [rad/s]
10^{-4}	1.58	1.0002	6.86	2.29	1
10^{-3}	2.00	1.0002	7.72	2.57	8
10^{-2}	2.55	1.0003	8.68	2.89	63
10^{-1}	3.49	1.0003	9.71	3.24	460
1	17.88	1.0018	10.09	3.36	899
10	28.78	1.0029	11.19	3.73	5583

5.3.4.IV Modeling the nonlinear elastic behavior with the Rubinstein–Panyukov non-affine slip-tube model and the Edwards–Vilgis slip-link model

Aided by a custom-built MATLAB® algorithm, we fitted the measured response at each rate of strain, expressed as *reduced stress* vs. *stretch ratio*, to the R–P non-affine slip-tube model and to the E–V slip-link model. For the former, we used Eqs. (5.97) and (5.103) with G_0 and ψ as fitting parameters; for the latter, we chose Eq. (5.116)a, which depends on α, β, θ, and G_0. The results, as well as the LVE predictions discussed in §5.3.3.I-a, are shown in Figures 5.18–20. Experimental data affected by systematic error at short times/small strains, such as those shown in Figure 5.19(b) in the proximity of $\lambda = 1$, were excluded from the fitting procedure.

The difference between the two models is heavily masked by plotting the results as *stress* vs. stretch ratio, and heightened when the *dimensionless stress* is considered instead (Figures 5.18 and 5.19). In the latter case, it is also possible to distinguish strain softening ($\lambda < 2$) and strain hardening behavior ($\lambda > 2$) as the experimental data fall slightly below and then rise significantly above the LVE curve (Figure 5.18(b)). As mentioned earlier, the infinite slope of the data at $\lambda = 1$ is the result of the power-law relaxation. Overall, the R–P non-affine slip-tube model is unable to capture the observed strain dependence of the stress, while the E–V slip-link model provides a reasonable description of the data even at the higher rates of strain (Figures 5.19(b) and 5.20). Notice that the strain and rate dependences of the dimensionless stress can be interpreted according to Eq. (5.133).

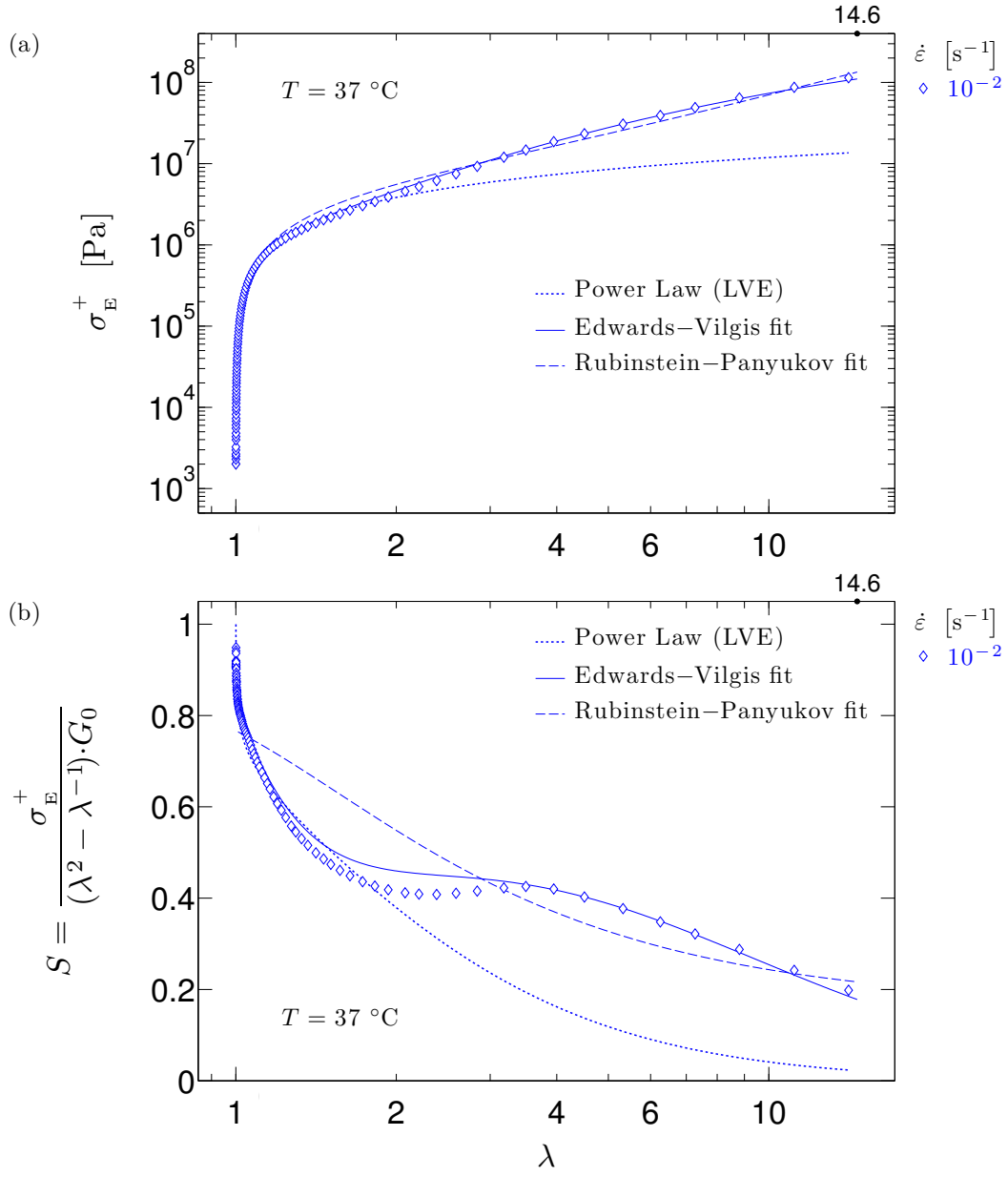

Figure 5.18. Comparison between the R–P non-affine slip-tube model and the E–V slip-link model for a rate of strain $\dot{\varepsilon} = 10^{-2}$ s^{-1}, in terms of elongational stress (a) and dimensionless stress (b) vs. stretch ratio. In each plot, the dotted line is the LVE prediction from the linear harmonic response modeled with a power-law relaxation spectrum (Figure 4.2). On the strain axes, the stretch ratio at rupture is shown.

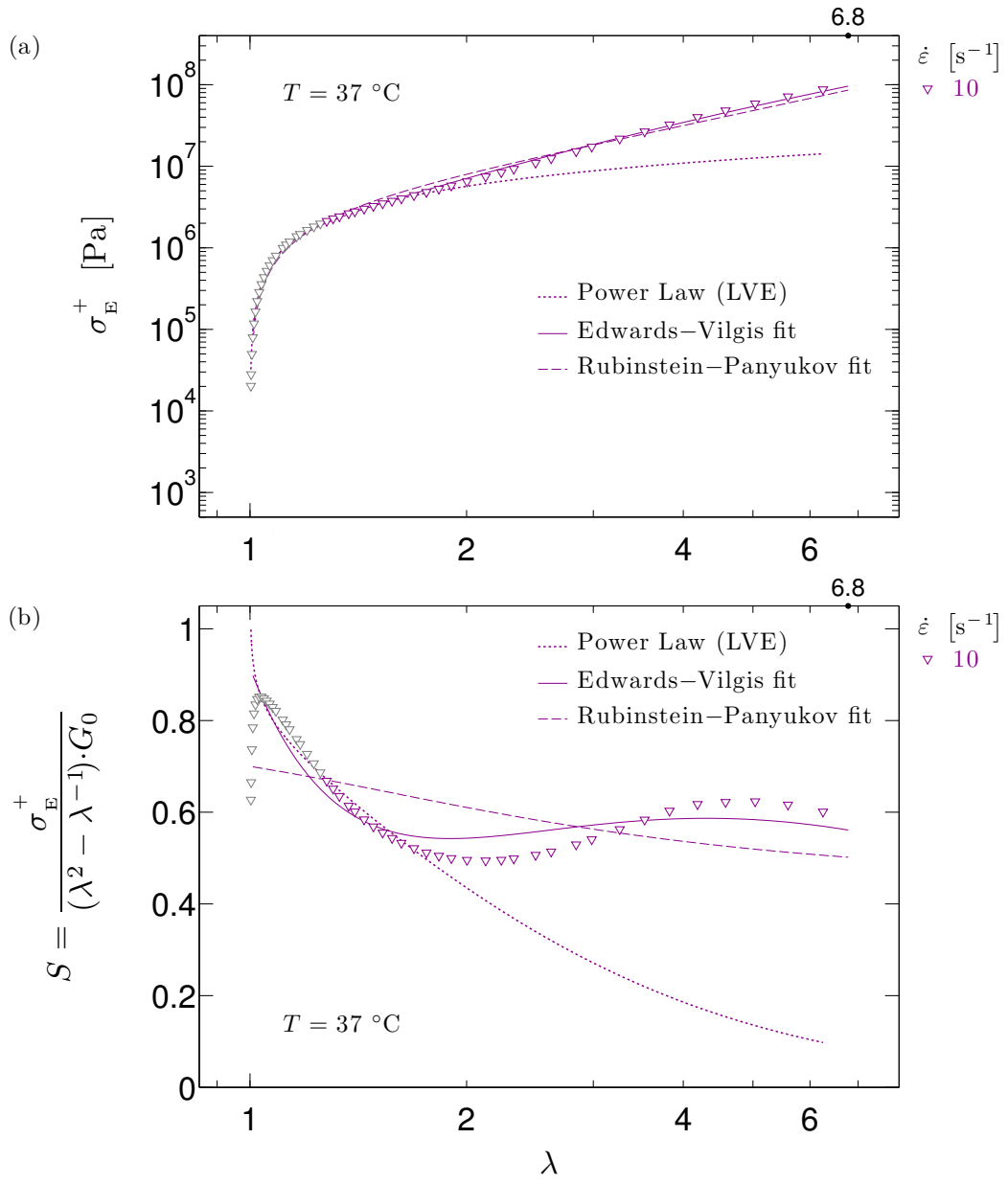

Figure 5.19. Comparison between the R–P non-affine slip-tube model and the E–V slip-link model for a rate of strain $\dot{\varepsilon} = 10$ s^{-1}, in terms of elongational stress (a) and dimensionless stress (b) vs. stretch ratio. In each plot, the dotted line is the LVE prediction from the linear harmonic response modeled with a power-law relaxation spectrum (Figure 4.2). On the strain axes, the stretch ratio at rupture is shown.

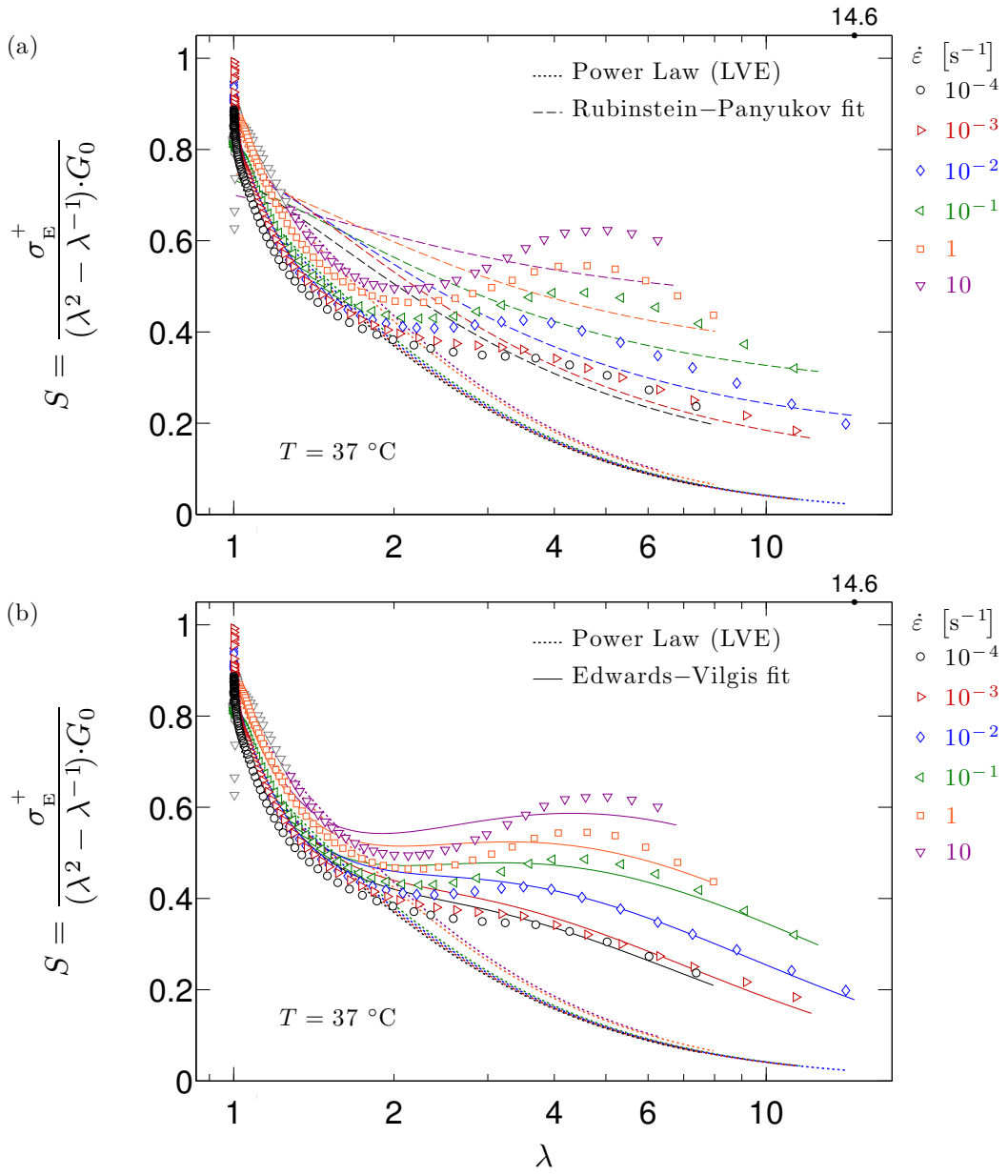

Figure 5.20. Comparison between the R–P non-affine slip-tube model (a) and the E–V slip-link model (b) for all the rates of strain employed. In each plot, the dotted lines are the LVE predictions from the linear harmonic response modeled with a power-law relaxation spectrum (Figure 4.2). On the strain axes, the maximum stretch ratio at rupture is shown (exhibited for $\dot{\varepsilon} = 10^{-2}$ s^{-1}).

5.3.4.IV-a Analysis of fitted and calculated parameters

The analysis of fitted and calculated parameters for the E–V slip-link model, which are summarized in Table 5.5, is enlightening. At all rates of strain, finite chain length effects were negligible and $\alpha = 0$. Thus, the E–V slip-link model effectively reduced to the original slip-link model of Ball et al.[83] with only three fitting parameters (β, θ, and G_0). If the macroscopic elongation of the network had been limited by the maximum extension of the trapped entanglement strands therein, α should have lain between about 0.13, b_k/a_{late}, and 0.16, b_k/a_{early} (Table 5.3 and §5.3.3.II-d). On the other hand, the full extension of the PI chain as a whole would have resulted in $\alpha \simeq 1/\lambda_{max,full} = b_k/R \simeq 0.05$ (Table 5.3). The zero value obtained for the finite chain extensibility parameter is consistent with the quantitative analysis of the model discussed in §5.3.4.II-b (cf. Figure 5.13(top) and (middle) and Figure 5.14(top)). Considering the proximity of the testing temperature to the glass transition of the microphase, lack of finite chain length effects coupled with negligible irreversible deformations (as judged by visual inspection of specimens after the test, cf. Figure 5.1) suggest *stress-induced pullout* of PLA chains from PLA domains and *deformation-assisted chain transfer* of the PLA blocks (§5.3.3.II-d).

The values of the slippage parameter β, ranging from about 7 to 31 and increasing with increasing rate of strain, are much larger than what is usually observed for vulcanized rubbers, and they exceed the prediction based on the estimate proposed by Vilgis and Erman[497]. For the PI block, $\beta \approx 6/Z$ would yield approximately 0.94 for tests performed at $\dot{\varepsilon} = 10^{-3}$ and 10^{-4} s^{-1} ($Z_I(1/\tau_{late}) \simeq 6.4$, Table 3.9), and about 0.65 at higher elongation

rates ($Z_I(1/2\tau_R) \simeq 9.25$, Table 3.9). Indeed, according to Eq. (5.115), the maximum value of β for undiluted PI would be observed for a PI melt with average molar mass $M_C \approx$ 12000 g/mol (Table 2.6). In this case, $Z_I = Z_{I,min}^{hI} \simeq 2.4$ (§4.3.2.II-c and Eq. (4.22)) and $\beta \approx 2.5$. A large value of β ($\beta = 5$ for $\dot{\varepsilon} = 3 \cdot 10^{-3}$ s^{-1}) was used by Watanabe and coworkers[164,222] to describe the tensile behavior of solutions of $(S–I–S)_p$–type multiblocks with a well-defined spherical morphology and in the vicinity of $T_{g,S}$. In this case, however, the system was diluted and $6/Z_I(\phi) \approx 3$. While the large values of slippage for our triblock may be tentatively attributed to the presence of a non-negligible fraction of *free-end-type midblocks* (or diblock impurities), the reason for the increased slippage with increasing elongation rate is, at present, unclear.

In view of the β range, the values obtained for the number density ratio θ are of the right order of magnitude, and therefore meaningful. When examining the effect of the model parameters on the dimensionless stress (§5.3.4.II-b), we observed that $S(\lambda;\theta,\alpha=0,\beta)$ becomes effectively θ-independent for $\theta \geq 10^4$ when $\beta = 6$, Figure 5.13(top), and for $\theta \geq 10^5$ when $\beta = 25$, Figure 5.13(middle).

The values of the initial shear modulus, G_0, are rather close to the estimates from the linear response (Table 5.4) and follow the predicted trend. Given the impossibility of the model to adequately describe the power-law stress response at very small strains, the agreement is more than satisfactory. The strain rate dependence of G_0 is largely driven by the entanglement contribution G_e which, in turn, is controlled by *linear relaxation mechanisms*: as the time scale decreases, an increasing number of free-end-type

midblocks remain entangled since star-like relaxation and reptation do not have enough time to occur. The analysis of the entanglement contribution in units of kT, G_e/kT, strongly corroborates this conclusion. At $\dot{\varepsilon} = 10\ s^{-1}$, the characteristic frequency, $\omega_0 \simeq 5583$ rad/s (Table 5.4), is essentially identical to the reciprocal of the path equilibration time, $1/2\tau_R \simeq 5400$ rad/s, and the value of G_e/kT, $7.94 \cdot 10^{26}/m^3$, is remarkably close to the LVE prediction, $7.72 \cdot 10^{26}/m^3$ (Eq. (5.88)b). In harmony with the proposed mechanism, G_e/kT decreases with decreasing strain rate. At $\dot{\varepsilon} = 10^{-4}\ s^{-1}$ and $\omega_0 \simeq 1$ rad/s (Table 5.4), the fitted value of $4.32 \cdot 10^{26}/m^3$ approaches the limiting value of $\approx 4.09 \cdot 10^{26}/m^3$ (Eq. (5.90) b) stemming solely from trapped entanglements at $\omega = 1/\tau_{late}$.

Similarly, the number density of slip-links, N_s, increases with an increase in rate of strain. The values of N_s, however, exceed the actual number of entanglements in the system by as much as three orders of magnitude. Whereas $N_s \simeq 8000 \cdot 10^{26}/m^3$ at $\dot{\varepsilon} = 10\ s^{-1}$, at this time scale the number density of entanglements is $\xi_N \cdot \mu_e(1/2\tau_R) \simeq 5 \cdot 10^{26}/m^3$ (since $\nu_e = (5/4)\nu_{e,eff}$ and $\mu_e = (1/2)\nu_e$, §3.3.4.IV-e). As explained in §5.3.4.II-b, this is the result of extremely low values of the initial entanglement contribution $Q_e(\alpha=0,\beta)$ as dictated by the slippage parameter (Eq. (5.117)b and Figure 5.11(top)).

The chemical contribution to the initial shear modulus, G_c/kT, provides further support to the hypothesis of stress-induced chain pullout. For deformations in the linear regime, the number density of PI strands terminated by endlinks, hence the chemical contribution, are essentially constant. In §5.3.4.I, we estimated $G_c'/kT \simeq 7.96 \cdot 10^{-1}\ 10^{26}/m^3$. Pullout of PLA chains in the nonlinear regime should be captured by the model through a reduced

number density of cross/endlinks $N_c = G_c/kT$ (since $Q_c(\alpha=0) = 1$, Eq. (5.117)a). In addition, we would expect the effect of chain pullout to become more severe at the lower elongation rates. Both of these expectations are met by the results of the fitting. Even at the highest elongation rate, $\dot{\varepsilon} = 10\ s^{-1}$, $G_c/kT \simeq 2.26 \cdot 10^{-2}\ 10^{26}/m^3$ is significantly lower than the endlink contribution in the material at rest. Combined with the apparent "infinite" chain extensibility ($\alpha = 0$), this result suggests the occurrence of PLA chain pullout at all the applied elongation rates. In turn, this explains why the relative entanglement contributions, ψ and Ω, are much higher than the upper limits admissible in the linear regime, $\psi_{max} = \psi(1/\tau_e) \simeq 0.92$ and $\Omega_{max} = \Omega(1/\tau_e) \simeq 12$ (§5.3.4.I).

The quantitative critical analysis of the E–V model parameters makes it easier to appreciate the inability of the R–P non-affine slip-tube model to correctly account for the observed elastic behavior. The R–P model parameters in Table 5.5 demonstrate that the model overestimates the chemical contribution (G_c/kT) for $\dot{\varepsilon} \geq 10^{-2}\ s^{-1}$, yields a strain rate dependence of the topological contribution that is at variance with the evolution of the network (notice that G_c/kT *increases* with decreasing elongation rate), and severely fails at the highest strain rate by predicting an initial shear modulus dominated by cross/endlinks ($\psi < 0.5$ and $\Omega < 1$).

5.3.4.IV-b Minimum static force to pull out a PLA chain from a PLA domain at 37 °C

Given the implications of the nonlinear elastic modeling, it is instructive to estimate the minimum static force required to pull out a PLA chain from a PLA domain at 37 °C. If stress-induced pullout occurred at all rates for strain, as the foregoing analysis suggested, then we may write

$$\sigma_{\text{pullout}} < \left[\sigma_{\text{N,max}}\right]_{\text{min}} \simeq 4.70 \text{ MPa} \tag{5.134}$$

where σ_{pullout} is the minimum static stress for chain pullout, and $\left[\sigma_{\text{N,max}}\right]_{\text{min}}$ is the minimum value of the peak nominal stress (exhibited for $\dot{\varepsilon} = 10^{-4}$ s^{-1}). Now, σ_{pullout} can be expressed as the minimum static force per PLA chain, f_{pullout}, multiplied by the areal density Σ of PI bridges and knotted-loops across a given plane in the matrix,

$$\sigma_{\text{pullout}} = f_{\text{pullout}} \cdot \Sigma < 4.70 \text{ MPa} \tag{5.135}$$

In turn, Σ is given by

$$\Sigma = \nu_{\text{c}} \cdot d \tag{5.136}$$

where $\nu_{\text{c}} \simeq 7.80 \cdot 10^{24}$ #strands/m^3 is the number density of PI strands terminated by PLA domains regardless of whether entanglements intervene (§5.3.4.I), and d is the average distance between PLA domains, which can be roughly approximated as the unperturbed end-to-end distance of the PI block, $R_{\text{I}} \simeq 17$ nm (at 25 °C, Table 3.3 – cf. §3.3.2 of Chapter 3, and Figure A.1(b) of Appendix A). Therefore,

$$f_{\text{pullout}} < 35 \text{ pN/PLA chain at } 37 \text{ °C} \tag{5.137}$$

and

$$\hat{f}_{\text{pullout}} < 0.2 \text{ pN/PLA monomer at } 37\ ^{\circ}\text{C} \tag{5.138}$$

The minimum static force to pull out a PS monomer from a glassy PS domain at room temperature was estimated by Washiyama et al.[502] at ≈ 6 pN/PS monomer. Hence, the upper bound for PLA at 37 °C seems reasonable.

Table 5.5. Parameters obtained by modeling the nonlinear elastic behavior of LIL50–12 at 37 °C with the *Rubinstein–Panyukov non-affine slip-tube model* (R–P) and the *Edwards–Vilgis slip-link model* (E–V).

$\dot{\varepsilon}$ [s^{-1}]					G_0 [MPa]	$\psi = G_e/G_0$	$\Omega = G_e/G_c$	G_c/kT [$10^{26}/m^3$]	G_e/kT [$10^{26}/m^3$]		
10^{-4}	R–P				1.70	0.8895	8.05	0.44	3.53		
10^{-3}					2.01	0.8856	7.74	0.54	4.15		
10^{-2}					2.22	0.7918	3.80	1.08	4.10		
10^{-1}					2.37	0.6431	1.80	1.98	3.57		
1					2.52	0.5598	1.27	2.59	3.29		
10					2.61	0.3556	0.55	3.93	2.17		
$\dot{\varepsilon}$ [s^{-1}]		α	β	$\theta = N_s/N_c$ [10^5]	G_0 [MPa]	$\psi = G_e/G_0$	$\Omega = G_e/G_c$	G_c/kT [$10^{26}/m^3$]	G_e/kT [$10^{26}/m^3$]	Q_e [10^{-3}]	N_s [$10^{26}/m^3$]
10^{-4}	E–V	0	7.28	1.62	1.85	0.9996	2359	$1.83 \cdot 10^{-3}$	4.32	14.6	296
10^{-3}		0	7.71	1.65	2.16	0.9995	2175	$2.32 \cdot 10^{-3}$	5.04	13.2	382
10^{-2}		0	11.48	1.79	2.41	0.9991	1146	$4.91 \cdot 10^{-3}$	5.63	6.4	878
10^{-1}		0	18.36	2.31	2.66	0.9984	615	$1.01 \cdot 10^{-2}$	6.20	2.7	2324
1		0	19.28	2.18	3.00	0.9981	531	$1.32 \cdot 10^{-2}$	6.99	2.4	2876
10		0	30.78	3.55	3.41	0.9972	352	$2.26 \cdot 10^{-2}$	7.94	1.0	8022

5.3.5 Ultimate Properties

So far, we have examined and modeled the tensile behavior of our triblock in the small- and large-strain regime (§5.3.3.I-a-b, §5.3.3.II-a-b, §5.3.4.IV), elucidated the role of *linear relaxation mechanisms* (§5.3.3.I-c, §5.3.3.II-d, §5.3.4.I, §5.3.4.III-b), and identified the elastic (*strain softening/hardening*) and viscoelastic (*strain-induced relaxation*) nonlinearities and their connection with network structure: namely, *entanglement slippage/chain stretching* (§5.3.3.II-d), and *viscoelastic deformation of the microphase* (§5.3.3.II-e). At large elongations, we have also inferred the occurrence of *stress-induced pullout* of PLA chains from PLA domains and *deformation-assisted chain transfer* of the PLA blocks (§5.3.3.II-d) from the modeling of the nonlinear elastic response (§5.3.4.IV-a-b). In this section, we analyze the ultimate properties of the material, i.e. the values of strain, stress, and time at the peak stress ($\varepsilon|_{\sigma_{max}}$, σ_{max}, and $t|_{\sigma_{max}}$) and at rupture (ε_b, σ_b, and t_b). Based on the molecular picture of the strain-induced structural changes gained thus far, we seek to infer the governing mechanism of rupture (§5.3.5.III), and to establish some quantitative correlations between limiting values of mechanical variables at the breaking point (§5.3.5.IV).

5.3.5.I Strain rate dependence of the limiting values of strain and stress

The influence of the elongation rate on the strain-at-maximum-stress, $\varepsilon|_{\sigma_{max}}$, and the strain-at-break, ε_b, is shown in Figure 5.21, while Figure 5.22 illustrates the corresponding effect on the maximum stress, σ_{max}, and the stress-at-break, σ_b.

Qualitatively, $\varepsilon\big|_{\sigma_{max}}$ and ε_b show a similar trend: they initially increase with increasing rate of strain, exhibit a local maximum at $\dot{\varepsilon} = 10^{-2}$ s^{-1}, and then decrease with $\dot{\varepsilon}$ at higher elongation rates. Notice that this behavior is reminiscent of zones III and IV in Figure 5.7. Overall, the average value of the strain-at-maximum-stress varies between 1.75 ($\lambda \simeq 5.8$) and 2.63 ($\lambda \simeq 13.9$), whereas the average value of the strain-at-break lies between 1.91 ($\lambda \simeq 6.8$) and 2.68 ($\lambda \simeq 14.6$). These average values are typical of commercial rubbers, for which the maximum elongation at break is frequently in the range 1.7–2.6 ($\lambda \simeq 5.5$–13.5).[451,498] When statistical fluctuations are taken into account, the elongation to break of the triblock never exceeds 2.92 ($\lambda \simeq 18.5$), effectively approaching the full-stretched length of the PI chain ($\varepsilon_{max,full} \simeq 2.95$, Table 5.3). In the low-strain-rate region ($10^{-4} \leq \dot{\varepsilon}/\text{s}^{-1} \leq 10^{-2}$), both $\varepsilon\big|_{\sigma_{max}}$ and ε_b increase in a power-law fashion and with a similar power-law exponent, respectively 0.056 and 0.054.

The rate of strain dependence of σ_{max} and σ_b (Figure 5.22) is somewhat analogous. In this case, however, the peak stress and the breaking stress pass through a maximum at $\dot{\varepsilon} = 10^{-1}$ s^{-1}. They vary, respectively, between 35±8 and 175±68 MPa, and between 1±0.6 and 98±45 MPa. For comparison, the maximum stress-at-break for cured rubbers is usually in the range 55–210 MPa.[447] For $\dot{\varepsilon} \leq 10^{-1}$ s^{-1}, the dependence of σ_{max} and σ_b on the strain rate can again be described by a power-law with comparable power-law exponents, respectively 0.259 and 0.271.

Since the ultimate properties depend, and strongly so, on the strain rate *there is no real* (constant) "*ultimate strain*" nor "*ultimate strength*" of triblock TPEs.[447,451-453] This feature

has often been neglected by the recent literature[92,113,164,201,222,392-394], despite being widely recognized and accounted for in the case of polymer melts[457-464,466], and also characteristic of vulcanized rubbers, as first shown by Smith more than 50 years ago[448] (cf. Figure 5.7). Indeed, characterizing the behavior at rupture by constant strain and stress values is questionable for *any* material at time scales when the effect of linear and nonlinear relaxations cannot be neglected.

5.3.5.II Assessing the validity of the data

As discussed in the Experimental Section, $\dot{\varepsilon} = 10\ s^{-1}$ is the maximum extension rate attainable by the EVF apparatus, and at this rate the manufacturer claims that a reliable torque signal is measured after 100 ms. Before dwelling into the analysis of the observed behavior, it is therefore worth assessing the validity of the data at the higher rates of strain, $\dot{\varepsilon}/s^{-1} = 1$ and 10. In particular, the value of the stress-to-break at $\dot{\varepsilon} = 10\ s^{-1}$ is suspicious. It is, on average, equal to the minimum tensile stress below which rupture does not occur in commercial (polydisperse) entangled melts[462,466] (Eq. (5.74)b). Taking into account sample variance, $\sigma_b(10\ s^{-1}) \simeq 0.4$ MPa is even close to the critical stress for the onset of rupture in monodisperse polymer melts[457,458,460-462], Eq. (5.74)a (§5.3.3.II-c).

Examining the behavior at the peak stress relative to that at rupture is helpful. As can be observed in Figure 5.23(a), the ratio of strain-at-maximum-stress to strain-at-break increases steadily with increasing strain rate before exhibiting a sudden decrease at $\dot{\varepsilon} = 10\ s^{-1}$. On the other hand, the ratio of maximum stress to stress-at-break (Figure 5.23(b))

remains essentially constant (centered roughly around 2) except for the abrupt increase at the maximum extension rate. The strain rate dependence of the ratio $\varepsilon|_{\sigma_{max}} / \varepsilon_b$ conforms to the expectation for a behavior that is predominantly elastic (zone III in Figure 5.7), i.e. the onset of non-uniform extension (or necking) and rupture tend to occur simultaneously[463,464] (§5.3.3.II-c); while the seemingly invariance of the ratio σ_{max}/σ_b is perhaps the result of a stress criterion for rupture. We therefore conclude that the ultimate properties measured at $\dot{\varepsilon} = 1\ s^{-1}$ are representative of the material response. The unusual behavior of the data at $\dot{\varepsilon} = 10\ s^{-1}$ can be attributed to instrument limitations, specifically to a time delay in recording the moment of rupture ($t_b \simeq 200$ ms), which would artificially increase and decrease respectively the value of ε_b and σ_b. Based on this analysis, the manufacturer's claim of obtaining reliable data after 100 ms at $\dot{\varepsilon} = 10\ s^{-1}$ seems to have been slightly too optimistic.

5.3.5.III Governing mechanism of rupture

In elastomeric materials, rupture involves three steps: (1) the formation of microcracks as a result of stress concentration near heterogeneities either within or on the surface of a specimen; (2) the enlargement of such cracks at a slow, but progressively increasing rate dependent on the dissipation of stored elastic energy through viscoelastic processes (*slow crack growth*); and (3) the development of an instability when a critical rupture condition is attained near or at the crack tip (*catastrophic propagation*).[503-508] High extensibility and

strength result not because microcracks do not develop but because their sustained growth is impeded.[451,452]

Prior to macroscopic rupture, beneficial processes that can dissipate considerable elastic energy in triblock TPEs include *cavitation* in the vicinity of the primary crack, and *orientation*, *deformation*, and *rupture of the microdomains* (cf. §5.3.2 and §5.3.3.II-d). Being of mesoscopic size and rather closely spaced, the domains play a key role in controlling the rupture process.[447,451-453] Not only can they promote cavitation, but they also must be disrupted before the crack's size can become sufficiently large to satisfy an instability criterion for the initiation of high speed crack propagation. By dissipating elastic energy through deformation and by acting as filler particles, domains can block, retard, or deflect growing cracks (causing them to follow a tortuous path).[447,451-453] Hence, the modulus of the microphase is mostly responsible for the values of strain and stress at rupture. This argument was put forth in 1969, by Morton et al.[509] to explain the change in ultimate strength among triblocks with different $T_{g,A}$'s, and by Smith[447] to justify the strain rate and temperature dependence of the ultimate tensile properties of an S–B–S triblock (S–B–S, Kraton® 101 30 wt%).

While *entanglement slippage* can also contribute to relieving the local stress concentration, it occurs quickly with respect to the time scales of the experiments (because it is associated with chain mobility in the rubbery phase, §5.3.3.II-d), and thus it cannot account for the dependence on elongation rate shown in Figures 5.21 and 5.22.

If the modulus of PLA is the parameter controlling the slow crack growth, then the elongation to break should be maximum when the domains are deformable enough so that the energy dissipated is large, while at the same time still able to act as filler particles that can promote cavitation and deflect growing cracks. In light of this postulated mechanism, the strain rate dependence of ε_b should be consistent with the *strain-induced relaxation* examined in §5.3.3.II-e. The results of Figure 5.6 indicate that, at large deformations, the PLA domains are essentially glassy on time scales $t \leq \approx 1$ s, and rubbery for $t \geq \approx 10^4$ s. The beneficial effect of PLA deformation should thus be minimum at the higher and lower rates of strain, where viscous dissipation and the effect of filler particles are reduced (respectively). Indeed, this is exactly what can be observed in Figure 5.21, in terms of both the strain-at-maximum-stress and the strain-at-break. In agreement with this argument, the maximum elongations occur at $\dot{\varepsilon} = 10^{-2}$ s^{-1}, which corresponds to the time scale where the PLA glass-rubber viscoelastic transition is approximately centered (Figure 5.6). By analogy with the behavior of monodisperse homopolymer melts and vulcanized rubbers shown in Figure 5.7, $\dot{\varepsilon}_{glass} \approx 10^{-2}$ s^{-1} sets the transition from a rubbery to a glassy response. For triblock TPEs, however, the rupture behavior is controlled by the viscoelasticity of the dispersed phase, not that of the matrix.

The accompanying increase in the ultimate stress with deformation rate arises naturally from the increase in the PLA modulus. To explain the decrease in the strain and continued increase in the stress from $\dot{\varepsilon} = 10^{-2}$ s^{-1} to $\dot{\varepsilon} = 10^{-1}$ s^{-1}, it may be postulated that PLA domains still undergoing ductile rupture have begun to loose their ability to

effectively dissipate elastic energy. At the higher strain rates, $\dot{\varepsilon}/\mathrm{s}^{-1} = 1$ and 10, the PLA domains, being harder and less ductile, rupture more nearly in a brittle fashion and the ultimate stress decreases.

We can conclude that the governing mechanism of rupture of LIL50–12 is the *ductile/fragile rupture of PLA domains*, and the rate-controlling step in the rupture process is the *strain-induced relaxation of PLA*. This, of course, should apply to any A–B–A triblocks under similar conditions, i.e. at service temperatures and strain rates at which strain-induced relaxation of the dispersed phase can occur. To the best of our knowledge, this is the first experimental evidence linking the strain rate dependence of triblock TPEs ultimate properties to the strain-induced glass-rubber transition of the domains.

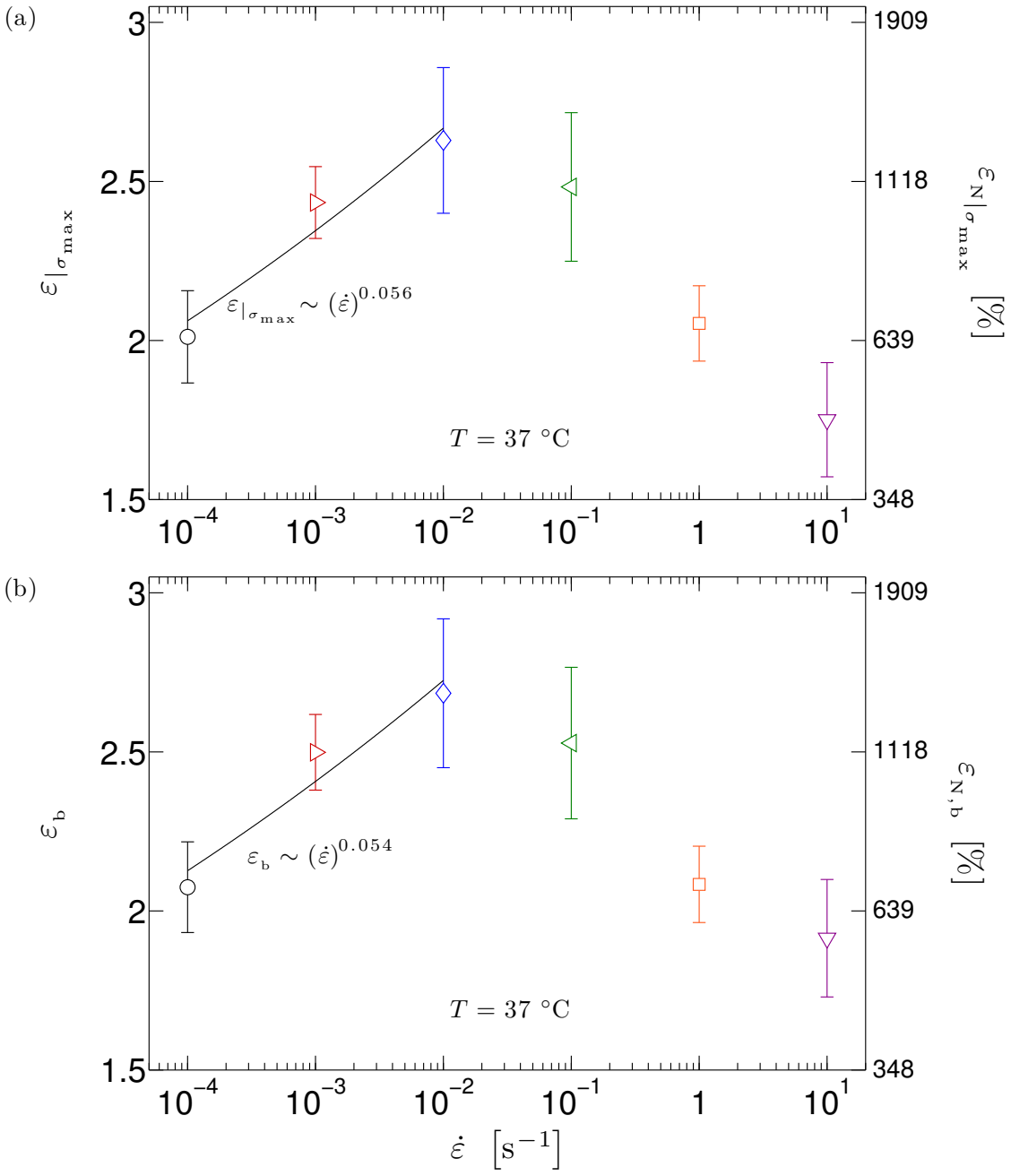

Figure 5.21. Rate of strain dependence of (a) the strain-at-maximum-stress and (b) the strain-at-break (cf. Figures 5.6 and 5.7).

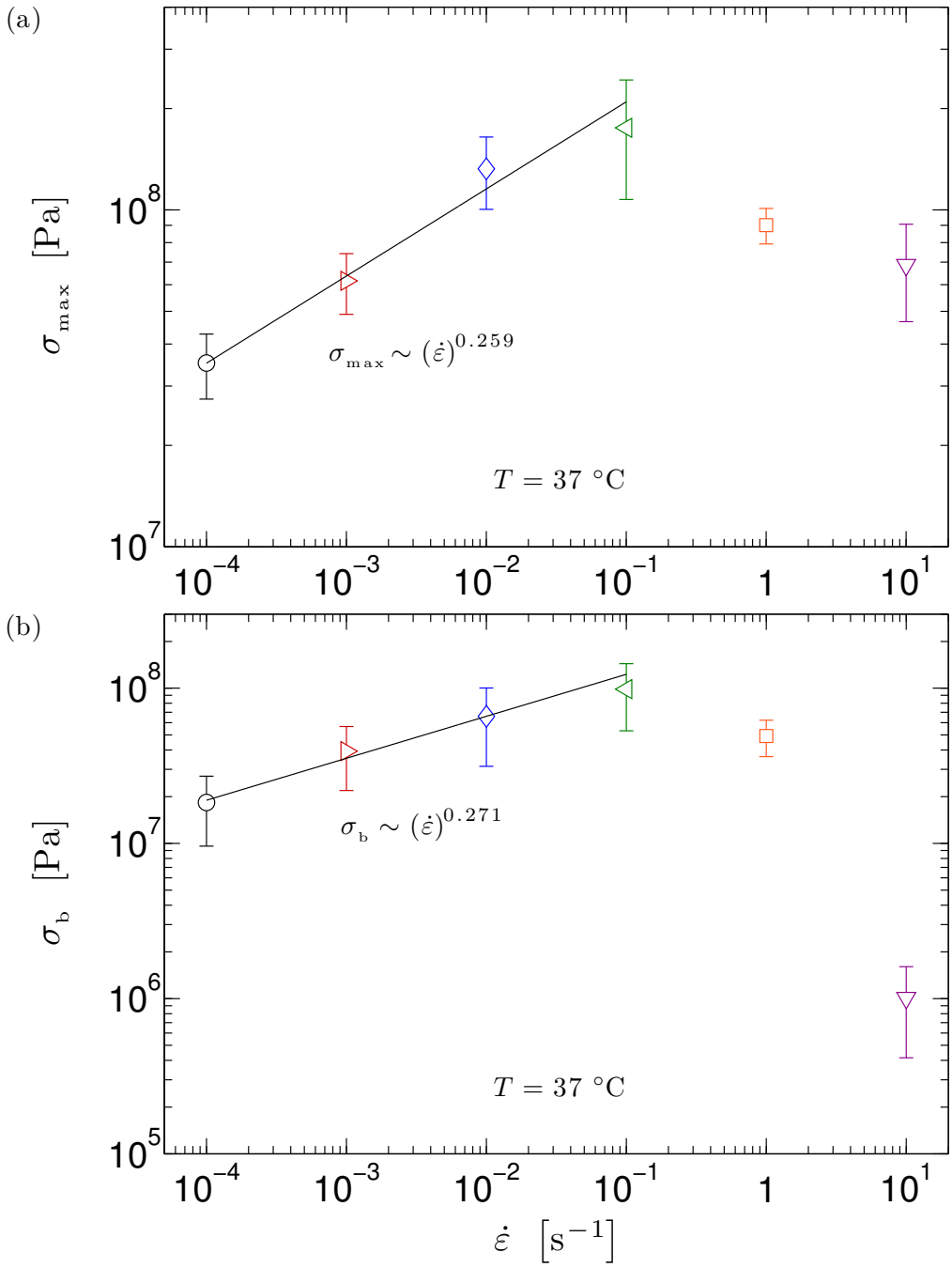

Figure 5.22. Rate of strain dependence of (a) the maximum stress and (b) the stress-at-break (cf. Figure 5.6).

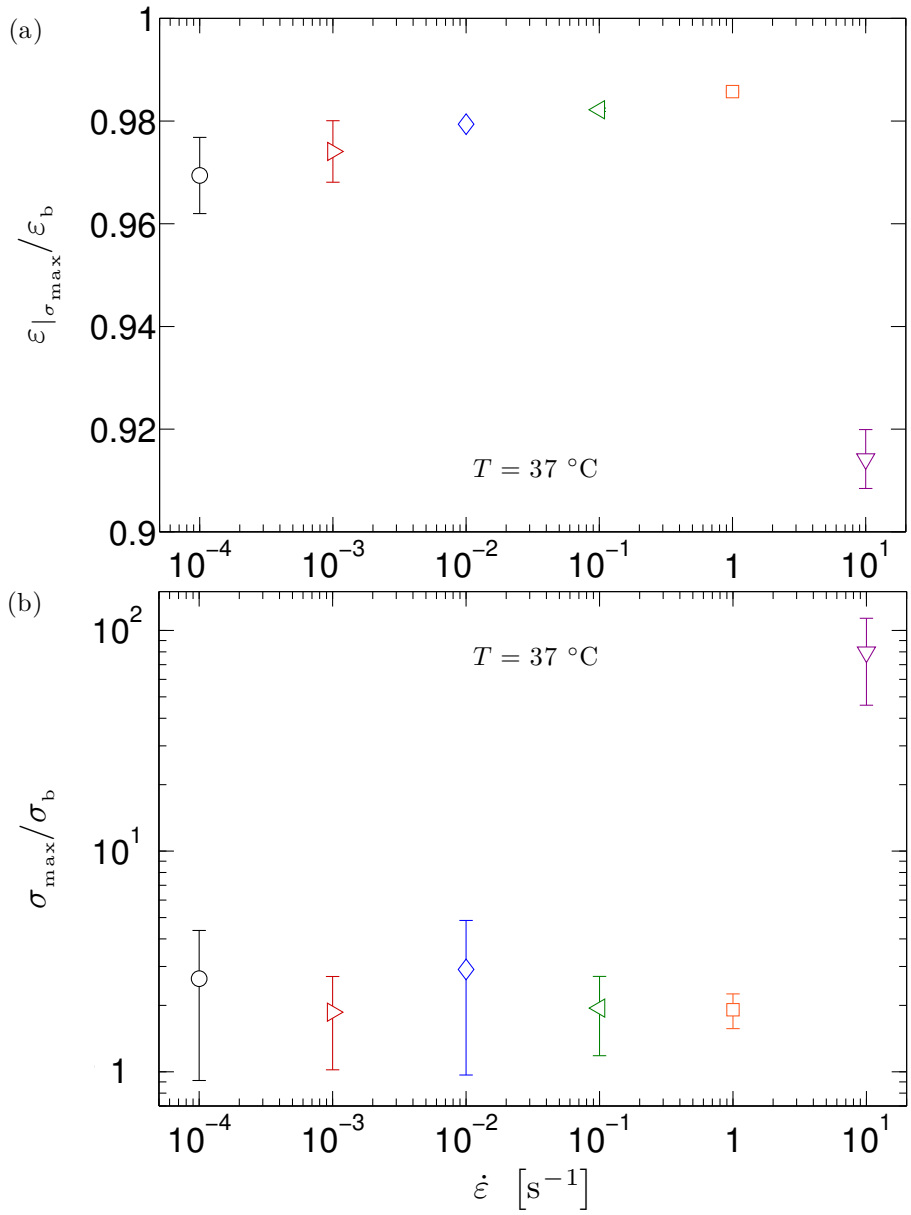

Figure 5.23. Rate of strain dependence of (a) the ratio of strain-at-maximum-stress to strain-at-break and (b) the ratio of maximum stress to stress-at-break. Since $\varepsilon|_{\sigma_{max}}$ and ε_b, as well as σ_{max} and σ_b, are correlated, data were not deduced from Figures 5.21 and 5.22. For each rate of strain, these ratios were determined for each test and then mean and sample variance were calculated.

5.3.5.IV Failure envelope

The ultimate properties of cured rubbers and triblock TPEs depend on (1) the structural characteristic of the polymeric network, and (2) the test conditions and (3) *type of test* under which rupture is observed. To separate these effects, in 1963 Smith[422] proposed the use of a "failure envelope", i.e. a plot of σ_b vs. ε_b. He was able to show that, as long as simple time-temperature superposition is applicable[448,449], the failure envelope is independent of strain rate and temperature (i.e. the test conditions), since either an increase in strain rate or a decrease in temperature merely shifts the rupture point in a counterclockwise direction around the envelope.[422,439,440,447] The ultimate properties of LIL50–12 are plotted in this fashion in Figure 5.24. Albeit simple time-temperature superposition does not apply for A–B–A triblocks near $T_{g,A}$ (§3.3.4.III-a and §4.3.2.I), the independence of the envelope on the elongation rate remains.

More importantly, Smith went on to show that the segment of a failure envelope that lies below the maximum elongation to break is nearly independent of stress-strain history prior to rupture (hence, of the test method). The envelope thus provides a useful *rupture criterion*, for it divides the stress-strain space into a metastable and an inaccessible region. Whenever the stress and strain approach those values prescribed by the envelope, rupture is likely to occur.[451,452] For instance, if a specimen of LIL50–12 were subjected to a constant extension $\varepsilon = 2.1$ (corresponding to the strain-at-break measured at $\dot{\varepsilon} = 10^{-4}$ s^{-1}, Figure 5.24(b)), *delayed rupture*[449] should occur when $\sigma \simeq 18\pm9$ MPa (even though

the stress decreases continuously prior to rupture). Extensional stress relaxation experiments conducted in the nonlinear regime confirmed this prediction.

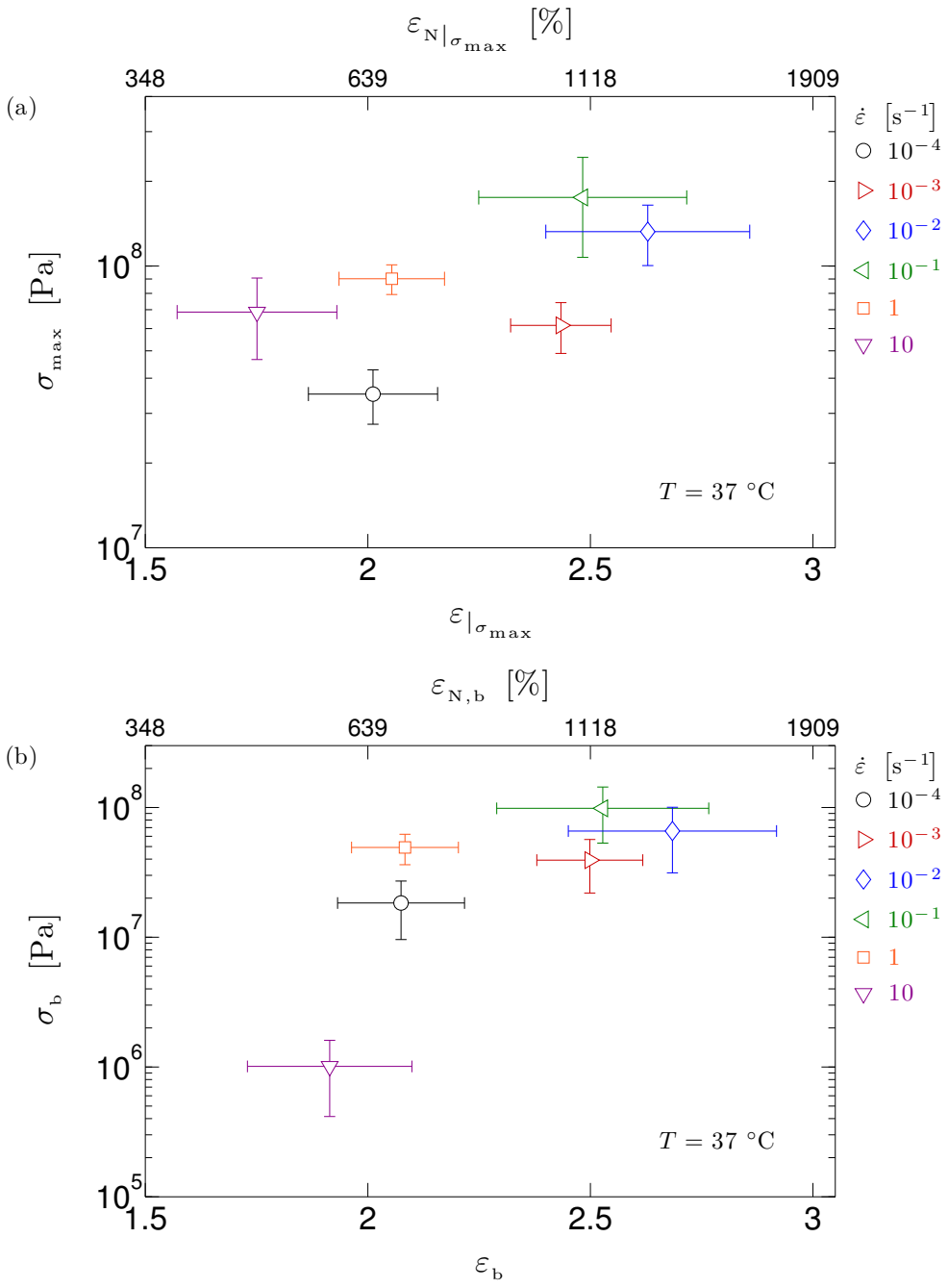

Figure 5.24. (a) Maximum stress vs. strain-at-maximum-stress. (b) Stress-at-break vs. strain-at-break (Smith's *failure envelope*[422]). In each plot, an increase in extension rate shifts the data point in a counterclockwise fashion around the envelope.

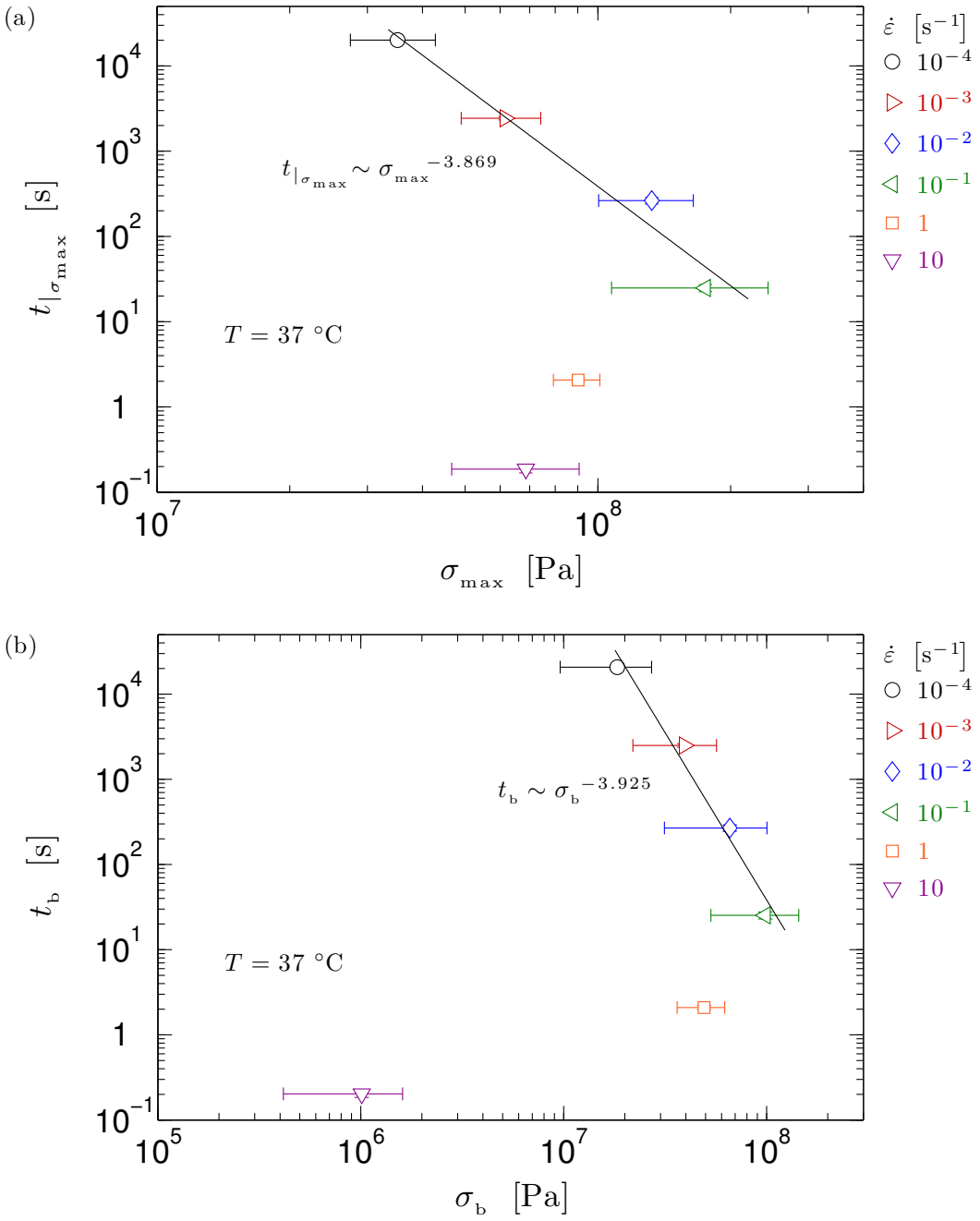

Figure 5.25. (a) Time-to-maximum-stress vs. maximum stress. (b) Time-to-break vs. stress-at-break.

5.3.5.V Durability and the Bailey criterion

When the ultimate properties of a material depend on the rate of strain its conditions of rupture are a consequence of its ''*durability*'' or time-to-break, t_b. For an arbitrary loading history $\sigma(t)$, the time-to-break t_b is expected to obey the so-called *Bailey criterion*[510]

$$\int_0^{t_b} \frac{1}{F[\sigma(t)]} dt = 1 \tag{5.139}$$

where $F(\cdot)$ is the dependence of time-to-break on stress in a constant stress experiment. Eq. (5.139) implies that rupture occurs because of damage accumulated during loading. First applied to metals[511], the Bailey criterion was later found applicable to polymer melts by Vinogradov and co-workers[457,458]. For both melts[457,458] and cured rubbers[451,462], $F(\cdot)$ is described by a power-law

$$t_b^{\sigma=const.} = K \cdot \sigma^{-n} \tag{5.140}$$

where K and n are empirical constants. Notice that with $F[\sigma(t)] = K \cdot \sigma^{-n}$, Eq. (5.139) correctly reduces to Eq. (5.140). In all cases investigated for different monodisperse polymer melts (including linear polyisoprenes and polybutadienes), it appeared that $n = 3.0$.[457-461] On the other hand, the exponent n for cured rubber varies from 3 to 12, increasing with growth of rigidity of the rubber.[451,462]

The dependence of time-to-maximum-stress, $t\big|_{\sigma_{max}}$, and time-to-break, t_b, on stress is illustrated in Figure 5.25. For $\dot{\varepsilon} \leq 10^{-1}$ s^{-1}, the functional form is a power-law with very similar exponents, 3.869 and 3.925 (respectively). In §5.3.3.II-b it was shown that the

stress response in the region $\varepsilon > 1$, which gives the main input into durability, could be modeled by a simple power-law expression, $\sigma^{+}_{\mathrm{E,NLVE}}(t,\dot{\varepsilon}) = A\cdot\left(\dot{\varepsilon}\right)^{c(\dot{\varepsilon})}\cdot t^{b(\dot{\varepsilon})}$ (Eq. (5.66)). Using this expression (or any other power-law dependence on time) in Eq. (5.139), it is straightforward to demonstrate that the same power-law exponent n must apply to both constant stress and constant strain rate experiments. We obtain,

$$t_{\mathrm{b}} = \frac{K\left[n\cdot b\left(\dot{\varepsilon}\right)+1\right]}{\left[\sigma^{+}_{\mathrm{E,NLVE}}\left(t_{\mathrm{b}},\dot{\varepsilon}\right)\right]^{n}} \tag{5.141}$$

Thus, the difference between $n = 3.0$ for linear polyisoprenes and $n \simeq 3.9$ for our material can be attributed to the impeded molecular motion of the PI blocks and the filler effect of the PLA domains.

From Eq. (5.141), it is possible to predict the dependence of ε_{b} and σ_{b} on the elongation rate. Neglecting the numerical prefactors,

$$\varepsilon_{\mathrm{b}} \sim \left(\dot{\varepsilon}\right)^{\frac{1+n(b-c)}{1+nb}} \tag{5.142}$$

and

$$\sigma_{\mathrm{b}} \sim \left(\dot{\varepsilon}\right)^{\frac{c}{1+nb}} \tag{5.143}$$

where b and c are average values to be calculated, over the relevant range of $\dot{\varepsilon}$, from the results shown in Table 5.2. Expressions analogous to Eqs. (5.141)–(5.143) hold for the values of time, strain, and stress at the peak stress. It follows that

$$\begin{aligned} \varepsilon\big|_{\sigma_{\max}} &\sim \left(\dot{\varepsilon}\right)^{0.063} \\ \sigma_{\max} &\sim \left(\dot{\varepsilon}\right)^{0.242} \end{aligned} \tag{5.144}$$

and

$$\begin{aligned} \varepsilon_{\mathrm{b}} &\sim \left(\dot{\varepsilon}\right)^{0.062} \\ \sigma_{\mathrm{b}} &\sim \left(\dot{\varepsilon}\right)^{0.239} \end{aligned} \tag{5.145}$$

Compared to the fitting results in Figure 5.25, the power-law exponents are slightly overestimated for $\varepsilon\big|_{\sigma_{\max}}$ (+12.5%) and ε_{b} (+14.8%), and underestimated for $\sigma_{\max}$ (–6.6%) and σ_{b} (–11.8%). Bearing in mind the approximations involved, as well as the statistical fluctuations of the data, the agreement is more than satisfactory.

5.4 Conclusions

Extensional deformations are relevant for the processing and often the end-use applications of A–B–A thermoplastic elastomers. At service temperatures ($T_{g,B} < T < T_{g,A}$), their nonlinear viscoelasticity is largely controlled by chain mobility of the B block and by deformation and rupture of A domains, regardless of the initial state of microstructural order.[391] For selecting or designing triblock TPEs that can meet the desired nonlinear rheological criteria in uniaxial extension, it is first necessary to determine how their large-strain behavior and ultimate properties are controlled by network structure and experimental conditions. Therefore, an adequate characterization of large deformation phenomena leading to macroscopic rupture requires that linear relaxation mechanisms, as well as elastic and viscoelastic nonlinearities, be identified and connected to molecular parameters. In the recent literature, however, both linear and nonlinear relaxations have often been neglected and the tensile behavior analyzed only in a framework appropriate for perfect elastic solids.[92,113,164,201,222,392,393,394] This oversimplified approach precludes the possibility of understanding the governing mechanism of rupture and predicting how ultimate properties will change under different experimental conditions.

In an effort to advance the current understanding of the tensile properties of triblock TPEs, we investigated the behavior of a microphase-segregated ($T_{ODT,SCFT} \simeq 290$ °C) A–B–A triblock at a service temperature approaching the T_g of the hard domains (§5.2.1). Testing specimens with similar orientation of microdomains were prepared by

compression molding (Chapter 3, §3.2.3), to characterize rheological properties of the thermoplastic elastomer under practical conditions[92,93] (§5.2.3). The response was measured in *start-up of steady uniaxial extension*, at several rates of (*true/Hencky*) *strain*[395] covering six orders of magnitude. Great care was taken to ensure that the initial stress response accurately represented the material linear behavior. To determine precision and obtain meaningful ultimate properties, each test was repeated between six and ten times. All specimens deformed uniformly up to rupture (i.e. without necking), and no slip was detected. Rupture always occurred towards the middle section of the gauge length (i.e. end effects were not observed) (§5.2.2). The analysis herein is independent from the specific choice of the constituent blocks.

The experimental data were processed in the MATLAB® environment. A program was developed to accomplish various tasks, which included the analysis of the instrument response at short times, the statistical treatment of the values of stress, strain, and time at the peak stress and at rupture, and the data averaging from repetitive tests. This allowed us to identify the sources of biased error (due to instrument limitations), and to minimize the unbiased error, which was associated with a random, small degree of anisotropy of the test specimens (§5.3.2).

To evaluate the reliability of our extensional data we compared the measured small-strain behavior with the linear response predicted by the Boltzmann superposition principle, using the relaxation spectrum inferred, in uniaxial extension, from small-amplitude oscillatory data (Chapter 4). In particular, the transient linear stress and

viscosity were calculated from the *constant-strain-rate* (or secant) *modulus* $F(t)$, in terms of the power-law exponent m and *quasi-property* P found from fits to the storage modulus $E'(\omega)$ (§5.3.3.I-a). Close agreement was observed with the LVE predictions, demonstrating the accuracy of both data sets. Furthermore, all transient viscosity data superposed at small strains and fit nicely on the predicted linear viscoelastic envelope, suggesting that sources of random error were effectively mitigated by the averaging process (§5.3.3.I-b). By highlighting the viscous character of the response, use of the secant modulus allowed us to clearly identify the effect of linear relaxation on tensile behavior. This is especially important for microphase-segregated triblocks, which often[110,111,112,447] exhibit a critical-gel-like response with small values of the power-law exponent m (§5.3.3.I-c).

The large-strain behavior was described in terms of the *nonlinear constant-strain-rate modulus* $F(t,\dot{\varepsilon})$. Factoring out the time dependence associated with the linear relaxation lead to the definition of $\Lambda_F(t,\dot{\varepsilon})$, which contained information about *all* the nonlinear effects that influenced the measured response at large strains (§5.3.3.II-a). While a steady-state was not attained even at the lowest applied strain rate (as expected), both *strain softening* ($\Lambda_F(\varepsilon,\dot{\varepsilon})<1$) and *strain hardening* ($\Lambda_F(\varepsilon,\dot{\varepsilon})>1$) behaviors were observed. In addition, the stress response in the region $\varepsilon > 1$ could be modeled by a simple power-law expression (§5.3.3.II-b).

As a first step to understanding the observed nonlinear response, we examined the expected start-up tensile behavior of an undiluted, monodisperse B melt with the same

molar mass as the midblock. To this end, we considered the regimes of behavior typical of homopolymer melts and vulcanized rubbers. We discussed the experimental requirement to achieve steady-state elongational flow, the strain and stress criteria for the onset of rupture, and the theoretical explanation (and necessary conditions) for strain softening/hardening given by tube models. By taking advantage of the discussion presented in Chapter 2, we related the maximum recoverable strain for melts and non-crystallizable rubbers to molecular characteristics of flexible polymer chains, namely to the maximum stretch ratio of a tube statistical segment, $\lambda_{max,e}$ (§5.3.3.II-c).

Based on the network structure at small and moderate strains and the available (linear and nonlinear) relaxation mechanisms, we attributed the onset of strain softening to *slippage of entanglements*, while the onset of strain hardening could be predicted from the nonlinear elastic behavior of an entanglement strand (§5.3.3.II-d). Both entanglement slippage and *chain stretching* represented *elastic nonlinearities*, i.e. elastic contributions to the nonlinear secant modulus $F(t,\dot{\varepsilon})$. They occurred at all the applied elongation rates, and each developed approximately at a constant strain. To separate elastic and *viscoelastic nonlinearities*, the experimental data were analyzed at constant values of strain. Exposing time and strain effects revealed how relaxation was affected by the increasing, macroscopic elongation. By exploiting the fractional modeling of the linear harmonic response presented in Chapter 4, we were able to assign the *strain-induced relaxation* observed at high strains to the glass-rubber transition of the microphase (§5.3.3.II-e).

Since the effects of time and strain were inherently intertwined, the nonlinear behavior could not be modeled by the classical constitutive equations for viscoelastic materials. We thus turned to rubber elasticity theories that could account for the observed elastic nonlinearities (entanglement slippage and chain stretching), namely the Rubinstein–Panyukov (R–P) non-affine slip-tube model[489,493] (§5.3.4.II-a) and the Edwards–Vilgis (E–V) slip-link model[83,84] (§5.3.4.II-b). A detailed analysis of the E–V slip-link model was performed, and the main steps leading to the determination of the chemical and topological contributions to the reduced stress were outlined. Such analysis was necessary because of the numerous typos that appear in the original papers of Ball et al.[83] and Edwards and Vilgis[84], as well as in a recent *Macromolecules* review of Schlögl et al.[480].

After establishing an operational definition of initial modulus for critical-gel-like materials subjected to start-up extensional tests, it was possible to determine the relationship between the dimensionless stress in tensile tests at constant strain rate, $S_F(\varepsilon,\dot{\varepsilon})$, and the step-strain extensional damping function, $h(t,\varepsilon)$ (§5.3.4.III-b). The difference between the two models was heavily masked by plotting the results as stress vs. stretch ratio, and heightened when the dimensionless stress was considered instead. Overall, the R–P non-affine slip-tube model was unable to capture the observed strain dependence of the stress, while the E–V slip-link model provided a reasonable description of the data even at the higher rates of strain (§5.3.4.IV). This was made even more apparent when the fitted parameters were compared with the predictions from the

linear response (§5.3.4.IV-a). The nonlinear elastic modeling suggested the occurrence of *stress-induced pullout* of A chains from A domains and *deformation-assisted chain transfer* of the A blocks, at all the applied rates of strain. In turn, this allowed us to estimate the minimum static force required to pull out an A chain from an A domain at the testing temperature (§5.3.4.IV-b).

Based on the molecular picture of the strain-induced structural changes gained from exposing time and strain effects, the governing mechanism of rupture could be unequivocally identified with *ductile/fragile rupture of A domains*, and the rate-controlling step in the rupture process with the *strain-induced relaxation of the microphase*. To the best of our knowledge, this is the first experimental evidence linking the strain rate dependence of ultimate properties of triblock TPEs to the strain-induced glass-rubber transition of the domains (§5.3.5.III). In addition, application of the *Bailey criterion* allowed us to quantitatively account for the deformation rate dependence of the ultimate properties in the regime of rubbery response (§5.3.5.IV).

Chapter 6

A Critical Gel Fluid with High Extensibility: The Rheology of Chewing Gum

Chewing gum provides an excellent everyday example of viscoelastic behavior, and understanding its rheological properties is important for application purposes. In this Chapter, we compare the rheological behavior of selected commercial chewing gums and bubble gums. Small amplitude oscillatory shear, shear creep, and steady shear demonstrate that both chewing and bubble gums behave like power-law critical gels in the linear regime. Nonlinear viscoelastic behavior is investigated using large amplitude oscillatory shear, shear creep, and start-up flows (in shear and uniaxial extension). Bubble gums show more pronounced strain hardening and greater stresses to break in start-up of steady uniaxial extension than chewing gums. We argue that this combination of rheological signatures is sufficient to provide a new robust definition of chewing gum that is independent of specific molecular composition. There are potentially many different formulations and design routes that can achieve this distinctive rheological fingerprint.[a]

---

[a] The majority of this work was published in "Martinetti et al. A Critical Gel Fluid with High Extensibility: The Rheology of Chewing Gum. *Journal of Rheology* **2014**, *58*, 821–838".

6.1 Introduction

Although ubiquitous in the field of food science, the term "gum" has various, and often conflicting, connotations. The Oxford dictionary defines gum as a "viscous secretion" from plants that "hardens upon drying yet is soluble in water". Examples of such exudate gums are gum arabic, guar gum, and locust bean gum. These materials are composed primarily of long chain polysaccharides and are used as food thickening or gelling agents[512,513]; however, their rheological effects vary wildly[514]. Xanthan gum is a similar thickening agent, yet it is not produced by a plant but by the bacterium *Xanthomonas campestris*[515]. Certain gelatin-based candies are referred to as "gums" such as gummy bears and wine gums. As opposed to the exudate gums, these substances are water insoluble, gel-like solids with smooth, bouncy textures. Modern day chewing gum is yet a different type of gum, designed as a pliable cud that releases flavorings and sweeteners in a controlled manner upon mastication. At the most general level, a gummy substance is one that is viscous or sticky. Thus, two materials both referred to as "gums" in the vernacular may host a wide range of differing rheological and physical properties, begging the question, "What is gum?"

To address this question, we focus on characterizing the mechanical properties of one subset of gum materials – chewing gum. Chewing gum provides an excellent everyday example of nonlinear viscoelastic behavior for which most individuals have both experience and physical intuition. The gum flows when being chewed or pulled slowly, stresses in it persist after the deformation has ceased, and some recoil occurs when it is

suddenly relieved of an externally imposed stress. The gum may also break when being blown into bubbles or pulled rapidly. Hence, understanding the rheological properties of chewing gums is important for application purposes.

To the best of our knowledge, no paper is found in the peer-reviewed literature regarding the rheological behavior of chewing gum. Only in a few patents do we find linear viscoelastic data[516-519]. Despite the fact that chewing involves large, complex, and unsteady deformations, no study has been published that characterizes chewing gum under these deformation regimes. The goals of this initial study are to compare the rheology of selected commercial chewing gums with bubble gums and to define the term "gum" based on its rheological properties. Henceforward, we will differentiate between "bubble" gums, those products specially designed for producing large, stable bubbles, from conventional "chewing" gums, those only meant for chewing.

In this Chapter, we outline the linear and nonlinear viscoelastic behavior of selected commercial chewing and bubble gums in shear and extension. The rheology of lab-scale gums with known formulations and a commercially available confectionary wax are included in Appendix G for easy comparison to similar everyday substances. Despite the heterogeneous and varied compositions of the chewing and bubble gums, all exhibit classic critical-gel-like behavior in the linear regime. Additionally, chewing gums can be differentiated from bubble gums based on the extent of strain hardening in the start-up of steady uniaxial extension. We argue that this unique rheological fingerprint is sufficient to define gum independently of a specific molecular formulation, and that similar

rheological definitions are applicable to any soft material where performance is dictated by rheology.

6.2 Experimental Section

6.2.1 Materials

The composition of a typical sugar-free chewing gum is shown in Figure 6.1. Although exact formulations may vary between products, commercially successful chewing and bubble gums consist of the same four basic ingredients: a gum base, sweeteners, flavorings, and softeners.[520,521] The gum base is the most complex element, composed of elastomers, resin plasticizers, texture fillers, waxes, fats, and emulsifiers.[522] The purpose of the gum base is to provide a suitable matrix for the flavorings as well as the water-soluble sweeteners and softeners that are extracted upon mastication. Simultaneously, the gum base must provide a pleasant chewing experience. The sweeteners and flavorings give chewing and bubble gum its taste, and softeners fine-tune the sensory feel. In this representative formulation, sweeteners represent 67 wt% of the chewing gum mass, gum base 25%, softeners 7%, and flavorings 1%. This particular gum base contains 13% by mass polyisobutylene (PIB), 10% rosin esters, 20% poly(vinyl acetate) (PVAc), 28% waxes, 25% filler, and 4% other materials. Note that all the aforementioned ingredients are food grade. We investigated four commercial chewing gums and four commercial bubble gums, the names of which are listed in Table 6.1.

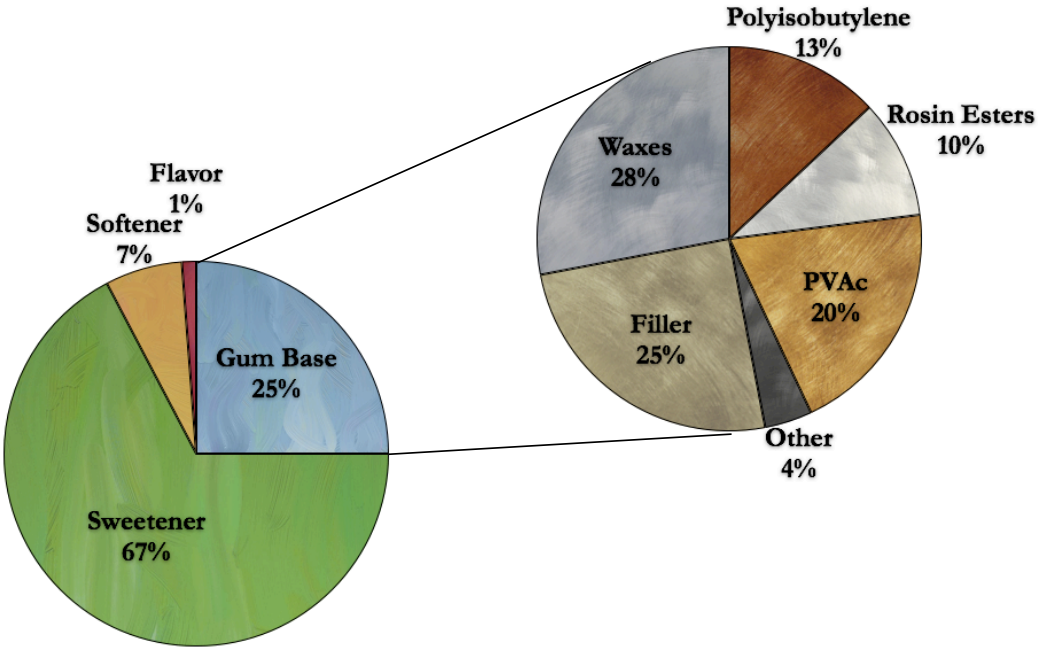

Figure 6.1. Typical sugar-free chewing gum formulation.[520,521] The four main ingredients by mass of chewing gum are sweeteners, the gum base, softeners, and flavorings. The gum base, in turn, is composed of polyisobutylene, rosin esters, poly(vinyl acetate), waxes, filler, and other ingredients.[522]

Table 6.1. Trade names for commercial chewing and bubble gums.

Sample	*Trade Name – Flavor*	*Sample*	*Trade Name – Flavor*
C1	Eclipse – Peppermint	B1	Hubba Bubba – Outrageous Original
C2	Winterfresh – N/A	B2	Hubba Bubba Bubble Tape – Awesome Original
C3	Trident White – Peppermint	B3	Trident – Bubble Gum
C4	Trident Soft – Peppermint	B4	BubbleYum – Original

6.2.2 Experiments

Based on general food rheology guidelines for chewing and specific studies on masticatory kinematics with chewing gum[523,524], we can identify the important deformation regimes associated with shear rates (10–100 s^{-1}), shear strains (1–10%), and shear stresses (> 10^4 Pa). For our rheological characterization, we targeted these regimes for shear tests and used them to estimate relevant rates and strains for extension tests.

Linear Viscoelastic Properties

In order to probe linear viscoelastic (LVE) properties, the gum samples were subjected to small strain deformations in oscillatory shear with an AR-G2 rheometer (TA Instruments, New Castle, DE). A 13 mm parallel plate was used for all LVE testing. The chewed gum cud was loaded on the bottom plate, and the top plate was lowered to make contact with the sample. A light pressure was maintained for several minutes as the gum cud was appropriately cut with a brass knife. Once the sample was properly shaped, it was immersed in distilled water to maintain hydration and regulate temperature. Heating was controlled via a Peltier plate. To identify the range of strains that give a linear viscoelastic response, isothermal strain sweeps were conducted at the highest and lowest frequencies of the subsequent frequency sweeps. Frequency sweeps were then performed at a strain within the linear regime. To identify thermal properties, a temperature ramp from 80 °C to 20 °C at a cooling rate of 1 °C/min was conducted at a frequency of 1 rad/s and at a strain within the linear regime.

Nonlinear Viscoelastic Behavior in Simple Shear

Behavior during start-up of steady shear was investigated with an ARES-G2 rheometer (TA Instruments) with an 8 mm, 0.1 radian cone and plate geometry. The tests were performed at a large range of shear rates (10^{-4} to 10^{2} s^{-1}). Large amplitude oscillatory shear measurements were strain-controlled with an 8 mm cone and plate on an ARES-G2 rheometer. The temperature was controlled via a recirculating water bath below the bottom plate. The strain sweeps were conducted at a given frequency to strains up to 100%. The maximum strain was limited by edge failure or slip, and the data was analyzed using MITlaos[525,526]. Shear creep and recovery experiments were performed with an 8 mm, 0.1 radian cone and plate on an AR-G2 rheometer. Upon loading, the temperature was raised to 37 °C, and a particular shear stress was applied for 100 s. The strain recovery was subsequently recorded for 1 hr. Edge failure limited the maximum shear stress to approximately 3000 Pa.

Nonlinear Viscoelastic Behavior in Uniaxial Extension

Uniaxial extension tests were conducted with an extensional viscosity fixture (EVF) (TA Instruments) on an ARES-G2 rheometer; this device operates with a counter-rotating dual drum geometry (Chapter 5, Figure 5.1). Gum cuds were pressed at room temperature in a 1 mm thick custom metal mold containing 21×5 mm rectangles. Teflon sheets were placed between the mold and exterior metal sheets to prevent adhesion and aid removal. Occasionally, dry ice was employed to lower the sample temperature in order to facilitate clean removal of the gum cud.

Samples were loaded onto the EVF and allowed to equilibrate at operational temperature for five minutes. The gum cuds were subsequently extended at a particular Hencky strain rate until failure occurred. At Hencky strains greater than about 4.3, the specimen overlapped itself (Chapter 5, §5.2.2), causing a slight step increase in the measured stress (see Figure 6.8). Nonetheless, this produced relatively small disturbances in the measurements and tests were carried past this point to estimate strain and stresses at break. At least five fresh gum samples were tested at each Hencky strain rate.

6.2.3 Testing Specimens

To simulate mouth chewing without the variability between human subjects, the following technique was developed. A gum sample was kneaded with hand pliers for 20 minutes in distilled water at room temperature. This hydrated the sample, removed soluble material, and allowed the gum cud mass to attain steady-state at roughly 40% of the original mass. Because the sample mass reached steady-state, we assume that the vast majority of the gum cud is composed of the insoluble gum base and flavorings and that any other residual components negligibly affect the rheology (the consistency of our results, as indicated by small error bars, supports this claim). The sample was then allowed to soak in distilled water for at least one hour at room temperature. All rheological tests were performed at 37 °C to correlate with physiological mouth temperature.

6.3 Results and Discussion

6.3.1 Thermal Characterization

Thermal characterization of the chewing and bubble gums demonstrate viscoelastic transitions near 37 °C. Figure 6.2 shows temperature dependent linear elastic (G') and loss (G'') moduli for a representative chewing gum, C1, and a representative bubble gum, B1 (Figure 6.2 and all subsequent figures have errors bars smaller than or equal to the data point markers, unless indicated otherwise). The modulus of C1 drops more than two orders of magnitude within a ten degree window from 30 to 40 °C. For B1, the temperature dependence of the elastic modulus shifts near 37 °C. The elastic modulus of both C1 and B1 remain relatively constant between 40 and 80 °C. To identify these thermal transitions, we performed differential scanning calorimetry (DSC) on representative chewing gum and bubble gum bases as well as on pure components of the gum bases, the results of which can be found in Appendix G (Figure G.1). The DSC curves confirm the presence of both crystallization and glass transitions near 37 °C, and their relative strengths depend on the exact composition of a particular gum base.

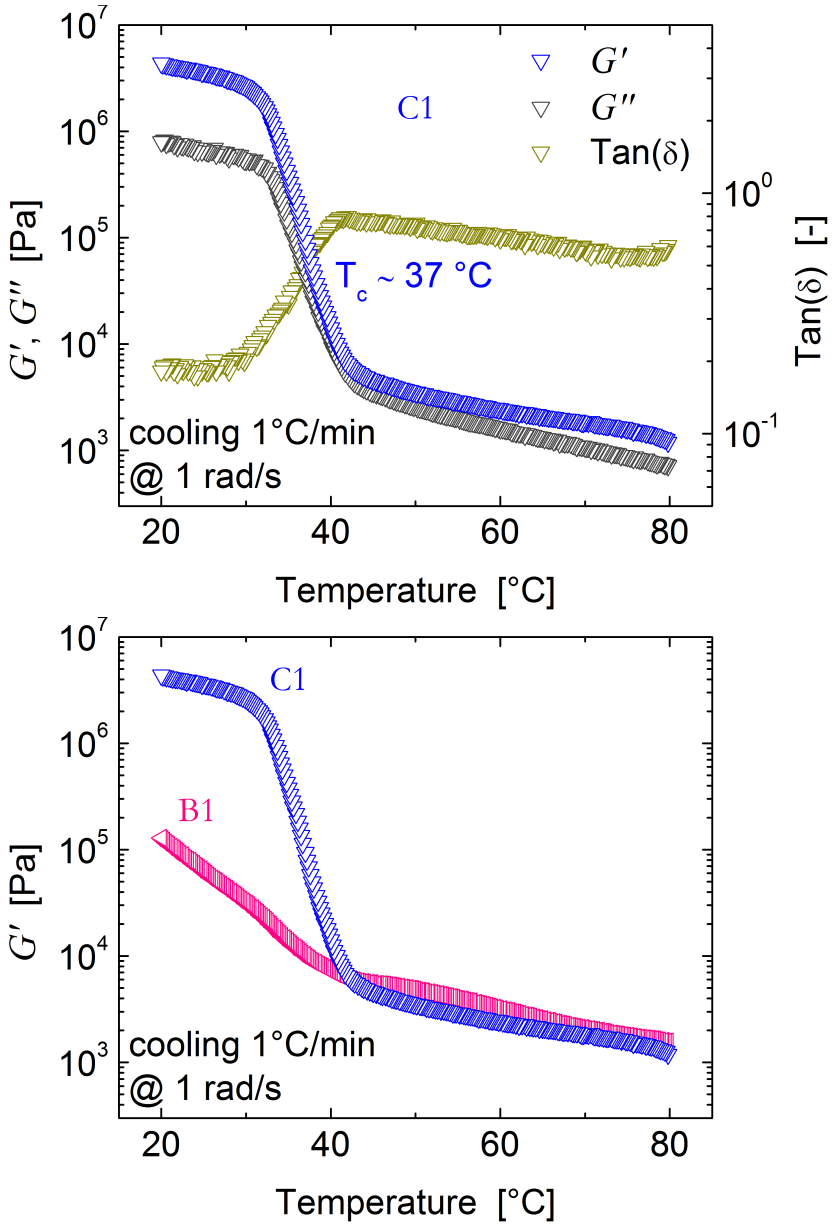

Figure 6.2. Storage and loss moduli versus temperature of representative chewing gum C1 and bubble gum B1 measured during small amplitude oscillation. These two samples and all other gums show a thermal transition near 37 °C. This transition is thought to be a combination of crystallization and glass transitions of gum base components.

6.3.2 Linear Viscoelastic Properties

Strain sweeps in small amplitude oscillatory shear (SAOS) demonstrate that the chewing gums have very low critical strains, $\gamma_{0,c}$, the strain at which the material begins to exhibit nonlinear behavior (Appendix G, Figure G.2). Here, the critical strain is defined as the strain at which the modulus deviates 10% from its original value. For representative chewing gum C1, the critical shear strain is 0.37% at a frequency of 0.05 rad/s and 0.07% at a frequency of 500 rad/s. A variety of other complex materials containing micron-size filler particles such as butter[527], reinforced polymer melts[528], and flour-water dough[529] also have critical strains on the order of 1% or lower. As opposed to polymer chains that can stretch to high strains and return to their original configuration, these filler particles can not withstand much deformation without losing memory of prior positions. Thus, we attribute the low critical strains of chewing gum to the relatively large percentage of filler and wax in the gum base formulations.

Frequency sweeps of gums C1 and B1 show a predominantly elastic response that follows power-law behavior (Figure 6.3(a)). The critical gel fit for C1 is shown in Figure 6.3(b). In our analysis, we fit the lower frequency data ($\omega < 10$ rad/s) for G' and used Chambon–Winter's critical gel model[289-292] (Table 4.1) to calculate G''. Although the critical gel model works well at these lower frequencies, both moduli deviate upwards as the crossover frequency is approached. We attribute this increase in modulus to additional Rouse-like modes[47], corresponding to the response of segmental building blocks of the material. Such Rouse-like contributions at high frequencies (or short time

scales) is well predicted by theory for entangled polymers[46], reversible networks[530], and cross-linked polymers[42] and they have been previously reported for a critical gel material, gluten dough[531,532]. For oscillatory shear, the Rouse model can be reduced to the following two equations (cf. Appendix D, Eq. (D.80), and Appendix E, Eqs. (E.1–2)),

$$\begin{aligned} G'(\omega) &= G_{\mathrm{R}} \sum_{p=1}^{S} \frac{\left(\omega\tau_{\mathrm{R}}/p^2\right)^2}{1+\left(\omega\tau_{\mathrm{R}}/p^2\right)^2} \\ G''(\omega) &= G_{\mathrm{R}} \sum_{p=1}^{S} \frac{\omega\tau_{\mathrm{R}}/p^2}{1+\left(\omega\tau_{\mathrm{R}}/p^2\right)^2} \end{aligned} \tag{6.1}$$

where G_{R} represents the *Rouse spectral strength*, and τ_{R} is the longest relaxation time of the model (called *the Rouse time* of the chain). To obtain the best combined estimate of the viscoelastic properties, we fit the Rouse model to the difference between the actual data and the critical gel fit. A summary of the fits for B1 and C1 is shown in Table 6.2.

The relatively high values of S and low values of m for C1 and B1 are consistent with a *stiff* gel; a soft gel has $0.5 < m < 1.0$ and an ideal gel is defined by $m = 0.5$.[319] Although m happens to be about equal for the two samples, the discrepancy in the other fitting parameters exposes differences in their compositions. The smaller value of S for B1 means that this particular bubble gum has a lower modulus than the chewing gum. Also, the larger G_{R} and smaller τ_{R} for B1 suggest the presence of smaller components that are able to relax stress faster. Regardless of these quantitative differences, C1, B1, and all the other gums we examined are qualitatively the same; that is, they behave as critical gels over a wide range of frequencies (Appendix G, Figure G.3).

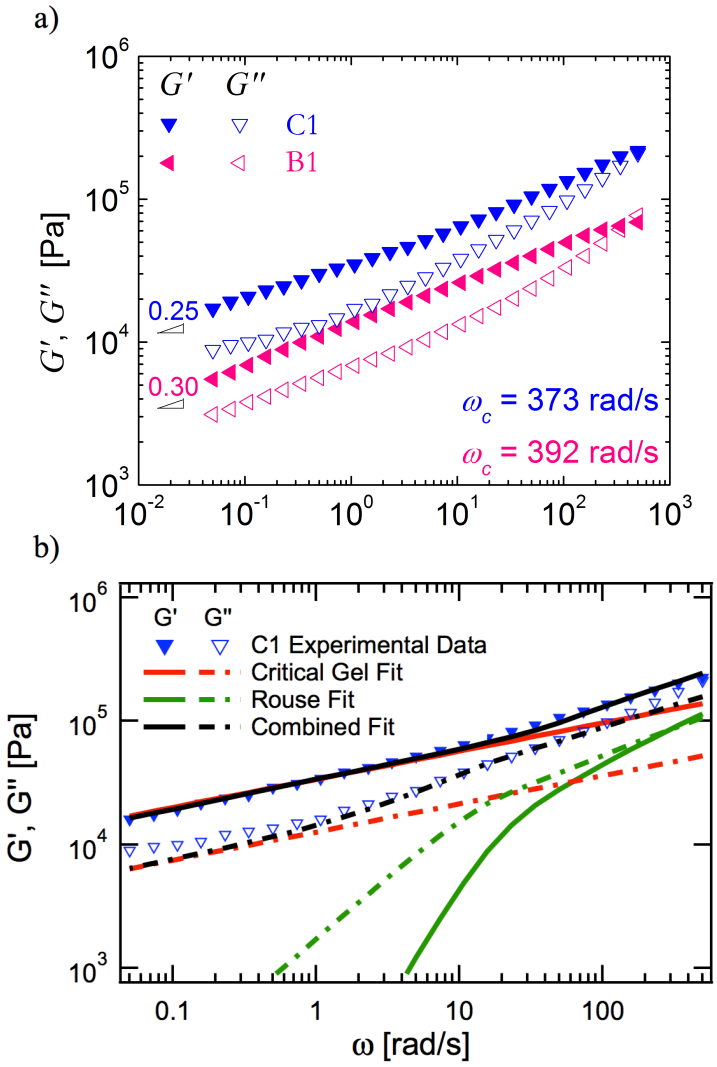

Figure 6.3. (a) Harmonic response of C1 and B1 measured during small amplitude oscillatory shear. Both moduli show a predominant elastic response and critical gel-like behavior. (b) Critical gel, Rouse, and combined fits of $G'(\omega)$ and $G''(\omega)$ for C1. The combined critical gel and Rouse model fits both moduli well over the full range of frequencies.

Table 6.2. Critical gel and Rouse model parameters for small amplitude oscillatory shear measurements of representative chewing and bubble gums. Standard deviations are included for parameters *S* and *m*.

Sample	*S* [Pa·s^m]	*m*	G_R [Pa]	τ_R [s]
C1	30100 ± 100	0.248 ± 0.003	24300	0.0440
B1	11700 ± 100	0.300 ± 0.001	501000	0.000114

6.3.3 Nonlinear Viscoelasticity

6.3.3.I Start-up of steady shear

In order to characterize chewing and bubble gums under large and unsteady deformations, we employ start-up of steady shear, a relatively simple rheological test to probe nonlinear viscoelastic behavior based on established theory[36]. For C1, the transient viscosity depends greatly on shear rate, as shown in Figure 6.4. The transient viscosity at a given time decreases with increasing shear rate, a common phenomenon in polymeric materials. Slight stress overshoots are present at 10^2 s^{-1}, the highest shear rate employed. Note that deviations for times < 0.05 s, marked with the dashed line in Figure 6.4(a), are ignored due to finite response times of the instrument, and similar designations have been made for subsequent transient tests. At a given shear rate, there are insignificant differences between chewing and bubbles gums (Appendix G, Figure G.5).

Here, we attempt to relate the start-up of steady shear behavior of C1 to the critical gel power-law fit extracted from SAOS. In the limit of linear viscoelasticity, the critical gel power-law model for start-up of steady shear can be expressed in the following manner[531]

$$\eta^{+}\left(\dot{\gamma}_0,\gamma\right)=S\cdot f(\dot{\gamma}_0)\cdot\Phi(\gamma)=S\cdot\dot{\gamma}_0^{m-1}\cdot\frac{\gamma^{1-m}}{1-m} \tag{6.2}$$

Factoring out the shear rate dependence $f(\dot{\gamma}_0)=\dot{\gamma}_0^{m-1}$ in Eq. (6.2) collapses the start-up of steady shear data to a single curve dependent only on strain, $S\cdot\Phi(\gamma)=S\cdot\gamma^{1-m}/(1-m)$. The results of this analysis are shown in Figure 6.4(b), using the *S* and *m* values derived from the power-law fit in SAOS. For strains < 0.1 and strain rates < 0.01 s^{-1}, the curves nearly fall onto a master curve. The critical gel power-law fit predicts the data well in this linear region, showing consistency between rheological tests. For larger strain rates and strains, however, large deviations occur. This demonstrates strong nonlinear behavior and network destruction with lower resistance to deformation, as all curves deviate below the critical gel power-law fit. (By network here and later we mean a weak interconnectivity between microstructures in the gums, for example waxes and fillers or entangled polymers, which can be disrupted by shear or extension.) With this start-up data, it is unclear if the network destruction corresponds to decreased elastic stored energy, viscous dissipation, or both. This can be clarified using creep recovery tests and especially nonlinear oscillatory measurements.

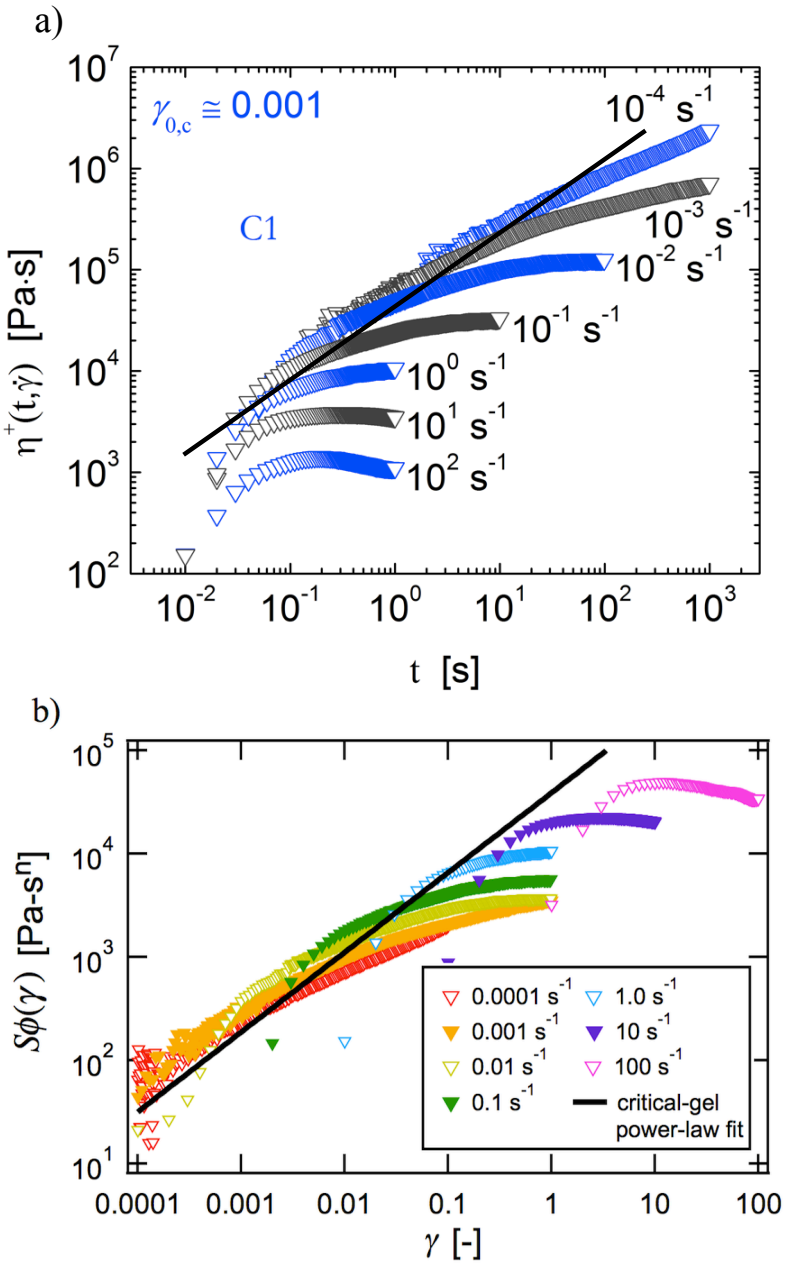

Figure 6.4. (a) Transient viscosity of C1 measured during start-up of steady shear. Note that a steady state could not be attained. (b) $S{\cdot}\Phi(\gamma)$ versus total strain, where $S{\cdot}\Phi(\gamma)$ is equal to the transient viscosity with the critical gel shear rate dependence, $\dot{\gamma}_0^{m-1}$, factored out. The data collapse onto a single curve for small strains, and this is accurately predicted by the critical gel power-law model.

6.3.3.II Shear creep

Creep is a particularly useful tool for understanding relaxation phenomena at longer time scales[533]. During a more conventional step strain experiment, the long relaxation times become obscured as the measured stresses decay. In a creep experiment, the constant stress allows for measureable strain responses at longer times. The results obtained from a creep test on C1 are shown in Figure 6.5. At lower stresses ($100 \leq \sigma/\text{Pa} \leq 600$), the shear compliance curves are nearly independent of shear stress, although some nonlinear softening can be observed. The dependence on shear stress becomes strikingly apparent at higher stresses (> 600 Pa). At 100 s, the compliance is still increasing for all stresses in Figure 6.5, and C1 exhibits a steady state for the lower stresses ($100 \leq \sigma/\text{Pa} \leq 600$). Such behavior can be captured by a standard linear liquid model such as the 4-parameter Voigt model or Burgers model (Appendix D, Eq. (D.70)). However, based on the previous results of SAOS and start-up of steady shear, it is likely that the lower stress data is more accurately captured with the critical gel model that reduces to the following equation in shear creep[531]

$$J(t) = \frac{1}{S \cdot \Gamma(1-m) \cdot \Gamma(1+m)} t^m \tag{6.3}$$

from which we obtain the values of $m = 0.42$ and $S = 21800$ Pa·s^m. This corresponds to a softer material (higher m, lower S) for the 100 Pa creep test compared to the small amplitude oscillatory shear results (see Table 6.2), consistent with being in the nonlinear regime and softening the network. Although nonlinear, the very good fit for $t > 40$ ms provides strong evidence that C1 behaves like a critical gel in shear creep at low stresses.

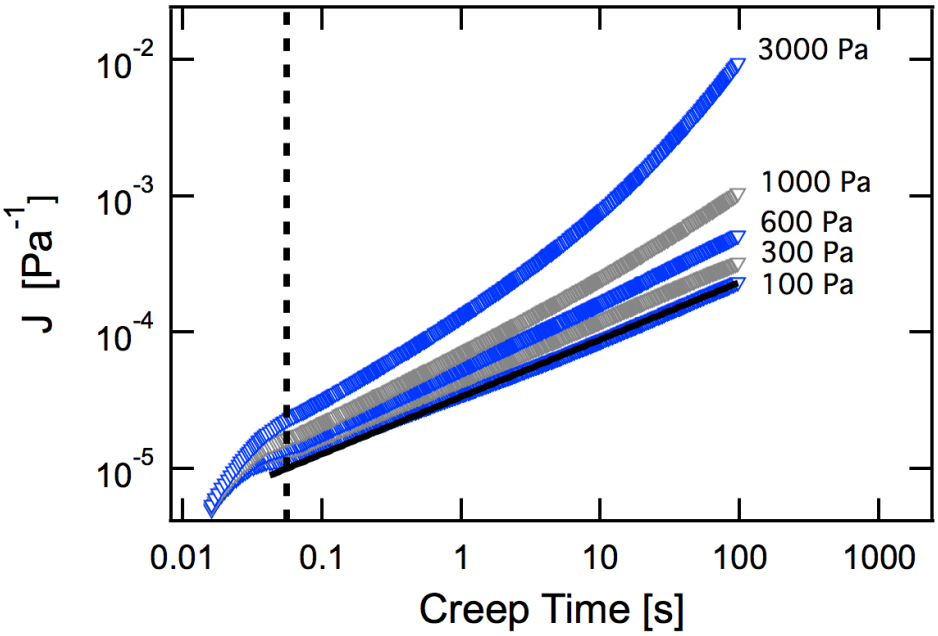

Figure 6.5. Compliance of C1 measured during shear creep at various shear stresses. A power-law model was fit to the 100 Pa curve, the curve most likely to be in the linear regime. Strong nonlinear behavior is readily apparent for the highest imposed stresses, 1000 and 3000 Pa. The data is ignored for times ≤ 40 ms due to the finite start-up time to attain the desired stress.

Close to the linear regime of stresses (≤ 600 Pa), all chewing and bubble gums show similar creep responses (Appendix G, Figure G.4). However, chewing and bubble gums can be distinguished by the fractional recovery upon the cessation of a large imposed shear stress as is shown in Figure 6.6. Here, fractional recovery is defined as γ_R/γ_M where γ_M is the measured strain after 100 s of deformation, marking the end of the creep test, and γ_R is the recovered strain after 100 s of zero shear stress. At low shear stresses (≤ 600

Pa), all chewing and bubble gums have similar fractional recoveries. However, for an imposed shear stress of 1000 Pa (marking the onset of the more dramatically nonlinear regime), there are substantial differences in the fractional recovery between chewing and bubble gums: chewing gums show 25–40% recovery whereas bubble gums show only 0–15%. With an imposed stress of 3000 Pa, none of the samples recover more than 5% of the original strain, masking the inherent differences in chewing and bubble gums.

This discrepancy in the fractional recovery of chewing gums versus bubble gums after a stress of 1000 Pa is consistent with the functionality of these commercial products. The ability for chewing or bubble gum to partially recover its original shape after being subjected to shear stresses is vital for proper sensory feel. This accounts for the relatively high fractional recoveries at smaller stresses. However, bubble gum has the additional task to form large, stable bubbles when blown at high shear stresses across the tongue. For the base of the bubble to maintain its shape and delay collapse, little to no fractional recovery is desired, such as those found at shear stresses of 1000 Pa. Chewing gum, not having this design limitation, naturally has a higher fractional recovery at this stage. At shear stresses as high as 3000 Pa all gums are strained to such a degree that even moderate fractional recoveries are impractical.

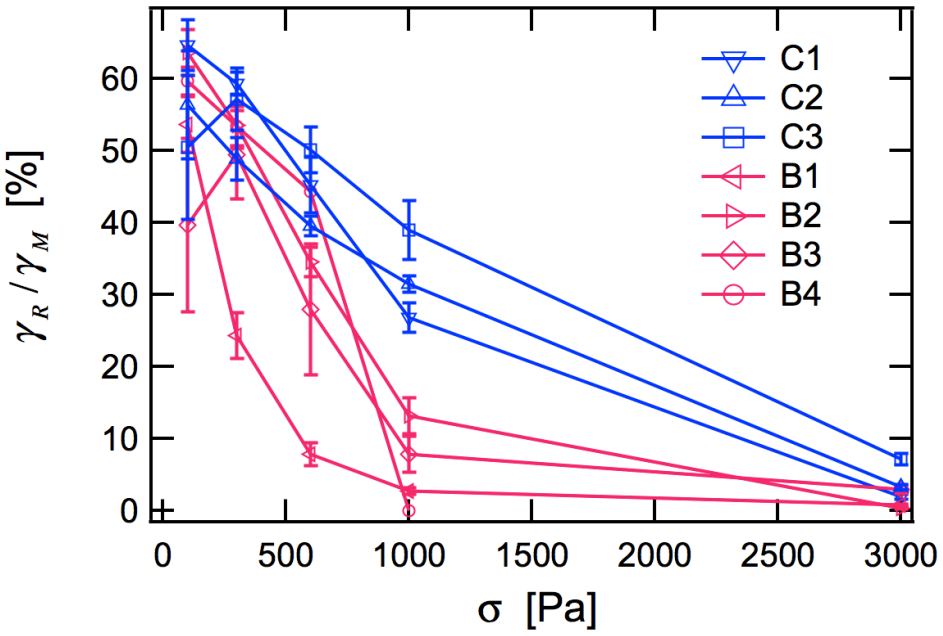

Figure 6.6. Shear creep fractional recovery at various shear stresses after 1 hour of recovery. At σ = 1000 Pa, chewing gums show significantly greater fractional recovery than bubble gums. This stress of 1000 Pa coincides with the transition to the more dramatically nonlinear regime.

6.3.3.III Large amplitude oscillatory shear (LAOS)

Transient viscosity and creep compliance reveal nonlinear shear network destruction of the gums studied here, but they do not distinguish between decreased elastic stored energy, viscous dissipation, or both. These measures based on step inputs combine elastic and viscous effects together. In contrast, large amplitude oscillatory shear (LAOS) can decompose the effects of nonlinear elastic energy storage and viscous energy dissipation, since the oscillatory protocol imposes strain and strain rate out of phase by exactly $\pi/2$

radians (i.e. in quadrature). Additionally, the smooth oscillatory conditions are less prone to experimental errors compared to abrupt step inputs. The resulting nonlinear oscillatory waveforms can be quantitatively described with a wide range of approaches; for a recent review on LAOS, see Hyun et al.[534]. Here, we examine the LAOS rheology of chewing and bubble gums with first-harmonic moduli (cycle-averaged measures), Lissajous curves, and the signs of leading order third-harmonic Chebyshev coefficients.[526]

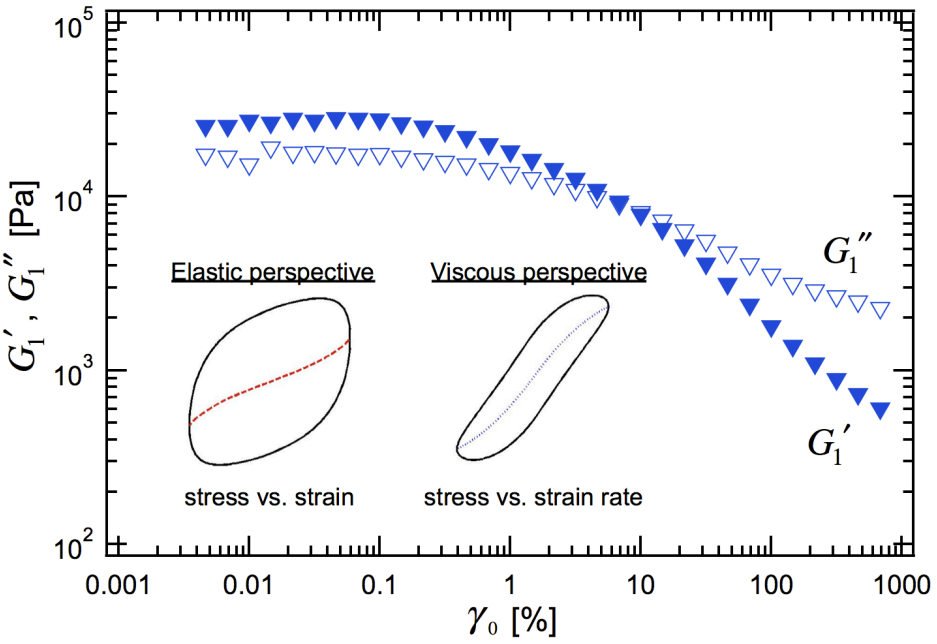

Figure 6.7. First harmonic average moduli of C1 measured during large amplitude oscillatory shear at ω = 1 rad/s. The relative values of G_1' and G_1'' change in the nonlinear viscoelastic regime. The insets are of the corresponding Lissajous curves at ω = 1 and γ_0 = 100%; left curve depicts stress vs. strain, right curve stress vs. strain rate. Interpretations of first-harmonics, Lissajous curves, and leading-order third-harmonic nonlinearities are described in the text.

Figure 6.7 shows the LAOS response of chewing gum C1 at the frequency $\omega = 1$ rad/s in terms of the first-harmonic (cycle-averaged) elastic and viscous moduli, G_1' and G_1''. To within experimental resolution, sample C1 shows a linear viscoelastic plateau at low strain amplitude below 0.1%, which is consistent with the low critical strains of these materials. As strain amplitude increases, the response shows a nonlinear, monotonic decrease of *both* elasticity and dissipation as the critical gel network is disrupted by large strain amplitude. We have recorded this qualitative behavior for all the gums listed in Table 6.1 (see Appendix G, Figure G.6). A monotonic decrease of both G_1' and G_1'' has been termed "Type 1" LAOS behavior by Hyun et al.[317], and can be found in a wide range of materials such as polymer melts, suspensions, and solutions. In the context of the linear viscoelastic critical gel network of the gums studied here, the decrease in elasticity G_1' indicates that the global (or average) network softening (e.g. due to disruption of network interactions) dominates any potential elastic stiffening (e.g. from the finitely extensible nonlinear elastic polymeric elements) which would otherwise increase G_1'.[526] The monotonic decrease in dissipation G_1'' is also noteworthy. Many yielding materials often show an initial strain-dependent *increase* and subsequent local maximum of G_1'', concomitant with monotonically decreasing G_1' (Type III behavior of Hyun et al.[317]). For the gum materials here, the microstructure also is yielding, but without a local maximum of G_1''.

The first-harmonic moduli G_1' and G_1'' are measures of *cycle-averaged* elasticity and dissipation; additional measures are required to fully characterize the nonlinear

oscillatory response. The full response is shown by the raw oscillatory stress waveforms, which can be represented as a function of time, or more physically as parametric curves (Lissajous curves) as a function of the input strain or strain rate. Representative Lissajous curves for chewing gum C1 are included in Figure 6.7 for $\omega = 1$ rad/s and $\gamma_0 = 100\%$, corresponding to one of the highest strains tested. The left Lissajous curve is normalized shear stress versus strain (the elastic perspective), with the dashed line showing the decomposed elastic stress, a single-valued function of stress versus strain defined by Cho et al.[535]. The right Lissajous curve is normalized shear stress versus strain rate (the viscous perspective), and the dotted line is the decomposed viscous stress, a single-valued function of stress versus strain rate. At this strain amplitude, the total stress curves are non-elliptical (and the decomposed stresses nonlinear), indicating that higher-harmonic nonlinearities are present. All gum materials tests showed qualitatively similar shapes to the Lissajous curves in Figure 6.7.

We interpret higher-harmonics to mean that local elastic energy storage and local viscous energy dissipation are changing through the deformation cycle (i.e. oscillating about the cycle-averaged values of the first-harmonics). The concavity of the decomposed stresses, represented at leading order by the signs of third-harmonic Chebyshev coefficients[526], indicate if these deviations are driven by locally high rates or high strains, as outlined by Ewoldt and Bharadwaj[536] (their Figure 7). In the context of the global elastic softening of G_1', the concavity of the decomposed elastic stress curve shows that the most extreme local softening occurs at locally large values of shear rate

(which occur at zero local strain, since they are out of phase). Quantitatively, this elastic concavity corresponds to positive third-harmonic Chebyshev coefficient $e_3 > 0$, and we interpret this as elastic softening driven by large strain rate, i.e. at this frequency, large strain rates are disrupting the elastic features of the critical gel network. Similarly, we find that the viscous features of the critical gel network are also disrupted by large strain rates. This conclusion is supported by the observation of decreasing G_1'' along with the negative leading-order viscous third-harmonic $v_3 < 0$; this appears visually in the Lissajous curve of decomposed viscous stress as negative concavity (curve bending down) in the domain of positive instantaneous strain rate.

These LAOS results indicate that, in simple shear deformation, the critical gel network is disrupted at large shear rates, decreasing the normalized elastic stored energy and viscous dissipated energy represented by G_1' and G_1''. However, extensional deformations may induce elastic or viscous hardening that dominates network disruption. This is examined in the following section with uniaxial extension tests.

6.3.3.IV Start-up of steady uniaxial extension

Uniaxial extension tests have been utilized primarily to characterize long-chain polymeric materials such as entangled homopolymer melts and solutions[537-539], dilute and semidilute polymeric solutions[540-542] and multiblock copolymers systems[222] in which the chain stretching mechanism, absent in most shear experiments, is of interest. Due to the large elongations attainable by chewing and bubble gum, steady uniaxial extension is

particularly relevant[543]. In order to apply constant rates of deformation, the gum samples were uniaxially stretched at a range of constant Hencky strain rates, $\dot{\varepsilon}$. The effect of $\dot{\varepsilon}$ on the extensional viscosity is quite dramatic (Figure 6.8). All gum samples investigated lacked a linear viscoelastic envelope, displayed extensional thinning for Hencky strains $\varepsilon \leq 1$, and failed between the grips before reaching a steady-state (no failure occurred outside the grips). At lower Hencky strain rates ($\dot{\varepsilon} \leq 0.10$ s^{-1}), sagging was observed, and the extensional viscosity showed a plateau before macroscopic failure. In contrast, at higher Hencky strain rates ($\dot{\varepsilon} \geq 0.25$ s^{-1}), the samples underwent necking (yet still appeared to deform uniformly) and demonstrated significant strain hardening leading up to the point of failure. These two distinct regimes suggest that different microstructures are relevant at different time scales. Figure 6.8 also shows representative photographs of chewing gum being stretched in the low and high Hencky strain rate regimes.

At lower $\dot{\varepsilon}$, the strain softening is indicative of the break-up of a brittle or fragile network. This network likely corresponds to the conglomeration of fillers and waxes that compose the bulk of the base. At higher $\dot{\varepsilon}$, the molecular origin of strain hardening could be due to a variety of mechanisms, including non-affine deformation of flexible polymers beyond the Gaussian statistical limit[544], strain-induced crystallization[545], or aggregation within colloidal gels[546].

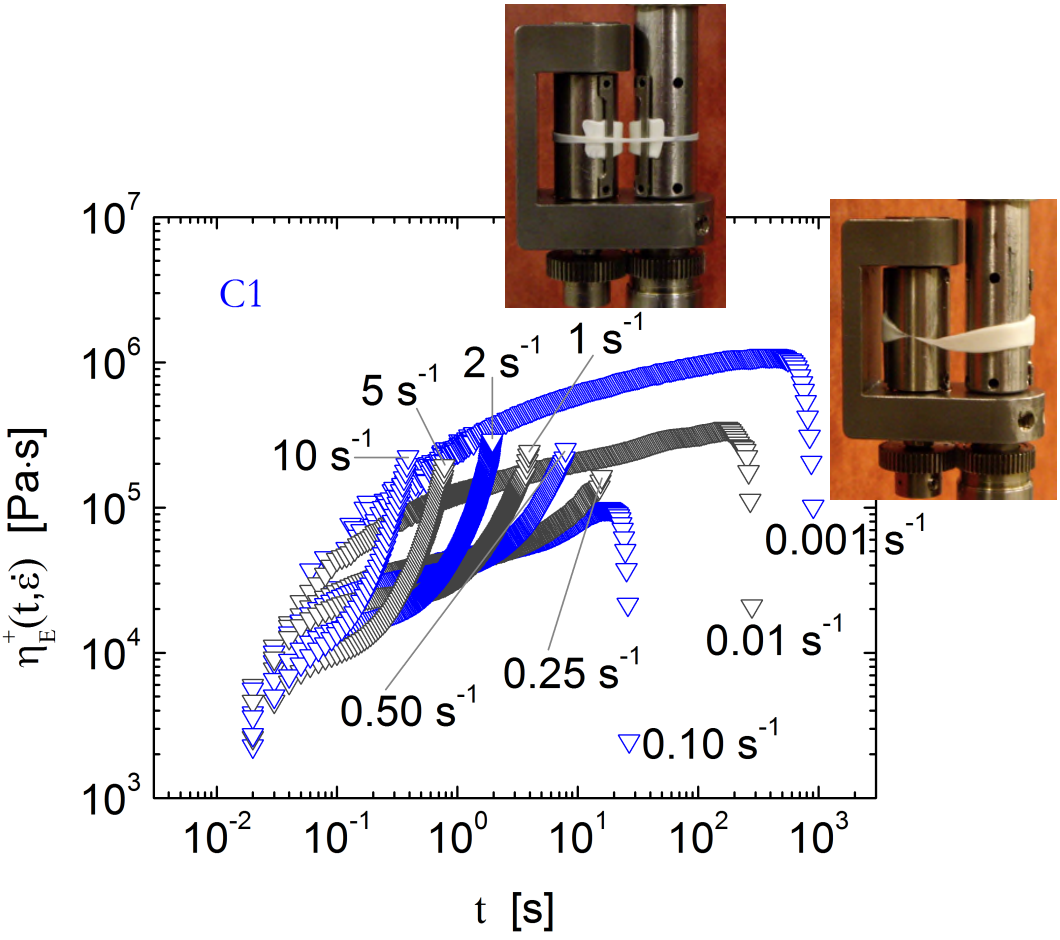

Figure 6.8. Results for start-up of steady uniaxial extension for C1 demonstrating the strong effect of strain rate on extensional behavior. The extensional viscosity plateaus before macroscopic failure at the lower Hencky strain rates ($\dot{\varepsilon} \leq 0.10$ s^{-1}) while strain hardening occurs at higher Hencky strain rates ($\dot{\varepsilon} \geq 0.25$ s^{-1}). The data has been cut off to exclude strains past the point of wrap-around. Also shown are representative photographs of the lower ($\dot{\varepsilon} \leq 0.10$ s^{-1}) and higher ($\dot{\varepsilon} \geq 0.25$ s^{-1}) Hencky strain rate regimes. Sagging was observed at the lower Hencky strain rates, while necking, yet uniform deformation, and wrap-around occurred at the higher Hencky strain rates.

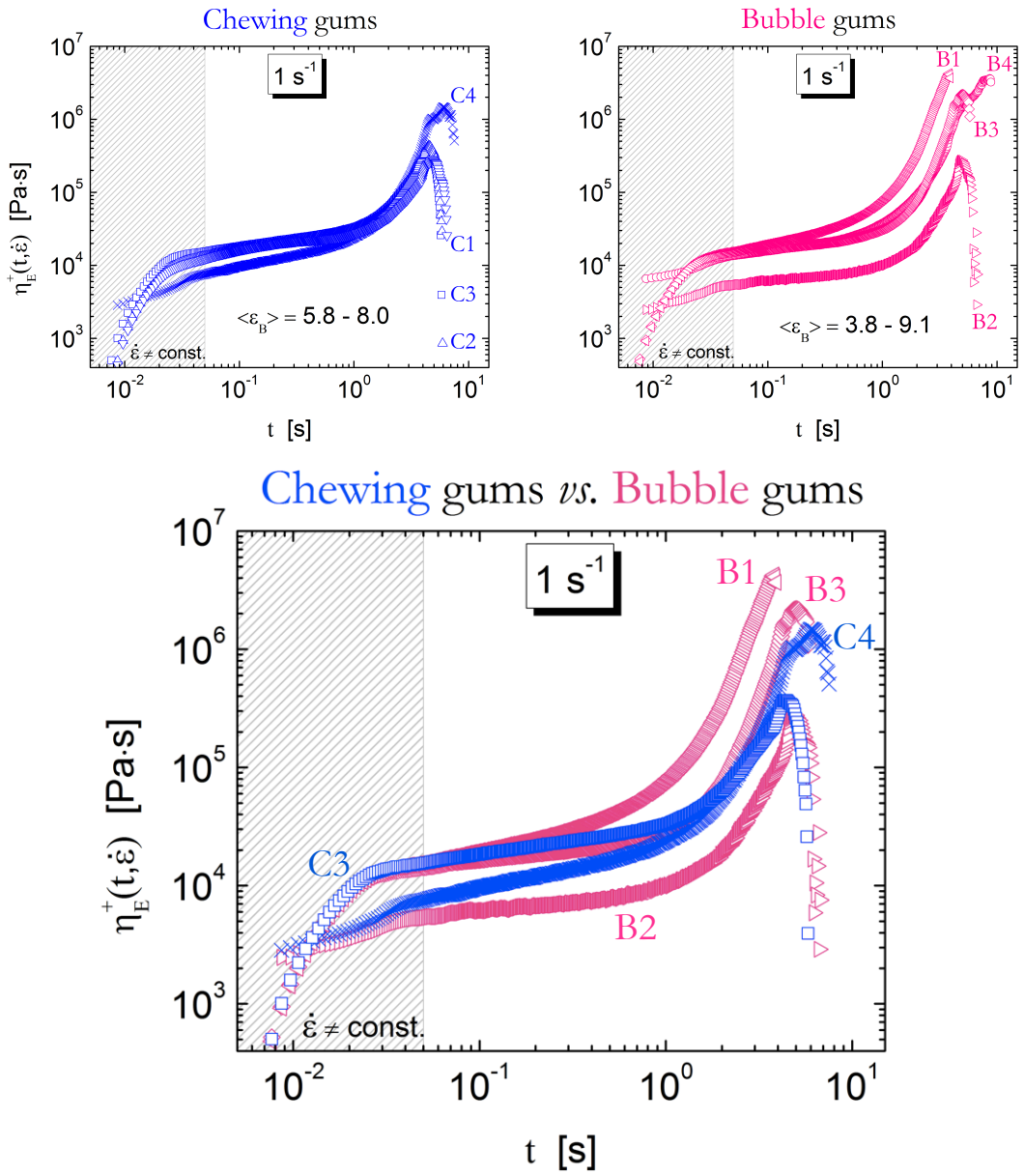

Figure 6.9. Chewing and bubble gum behavior during start-up of uniaxial extension at $\dot{\varepsilon} = 1\ s^{-1}$. The bubble gums, in general, are able to withstand greater extensional stresses and have more pronounced strain hardening. A notable exception to this trend is B2, the bubble gum tape.

We also found that start-up of steady uniaxial extension could be used to distinguish commercial chewing from bubble gums as shown in Figure 6.9. Subsequent tests were run at $\dot{\varepsilon} = 1\ s^{-1}$, since this Hencky strain rate is indicative of the type of deformations that gum undergoes during use. The linear response (low ε) is rather similar between chewing and bubble gums, but starker differences appear at large strains ($\varepsilon > 1$). Bubble gums typically sustained larger stresses and had more significant strain hardening than commercial chewing gums. To be quantitative, the peak extensional stresses of bubble gums were $> 2.0 \cdot 10^6$ Pa versus $\leq 2.0 \cdot 10^6$ Pa for chewing gums. The one exception was sample B2 with a maximum stress $\approx 3.0 \cdot 10^5$ Pa, reminiscent of a typical chewing gum. These findings are consistent with previous studies that found that extensional thickening stabilizes film blowing for polyethylene[547,548] and bubble blowing for bubble gum[543], a trait necessary for bubble gums but not chewing gums. A more quantitative comparison between uniaxial and biaxial extension for bubble gums was explored previously[543].

6.4 Conclusions

For the first time in the literature, a series of linear and nonlinear rheological tests have been conducted to characterize chewing gum at large, unsteady deformations, and we find that chewing and bubble gum share a distinct rheological profile unlike other classes of materials. To justify this claim, we compare our findings to similar materials of note. Polyisobutylene, a major polymeric component of chewing and bubble gum base, is an entangled melt with a plateau modulus of about 0.34 MPa at room temperature[20].

Although chewing and bubble gum have extensional strain hardening reminiscent of that of polyisobutylene, their dynamic responses do not demonstrate terminal behavior at low frequencies. Other filled elastomers, such as highly loaded clay nanocomposites[549], can exhibit qualitatively similar dynamic responses as chewing or bubble gum, yet there is no evidence of the Payne effect (marked by a local maximum of G'' in a strain sweep) in any commercial gum tested. Like chewing or bubble gum, wheat gluten[531] and poly(vinyl chloride) gels at the gel point[550] demonstrate critical gel behavior marked by power-law fits over the gamut of linear viscoelastic tests. However, these critical gels lack the substantial strain hardening in uniaxial extension inherent in all chewing and bubble gum tested. Only in chewing and bubble gums do we find power-law critical gel behavior in the linear regime coupled with such dramatic large strain extensional behavior.

From the rheology, one can glean information on the microstructure of chewing and bubble gum. Shear experiments demonstrate that chewing and bubble gum behave like a *firm* critical gel at small deformations. This result suggests the presence of a percolating network of various length scales throughout the chewing gum base. However, this network is rather fragile – the linear regime only encompasses the smallest shears and shear rates, and elastic and viscous softening dominate the strain response during large amplitude oscillatory shear. Another more robust network also exists, which produces the strain-hardening behavior during uniaxial extension. With these observations and knowledge of typical chewing gum ingredients, we can speculate on the links between ingredients and rheology. However, in designing for *performance*, the exact material

origins for the macroscopic behavior do not matter. We have shown that the unique rheological fingerprint is enough to define chewing gum, and a variety of compositions that give this rheological fingerprint will lead to the same product in terms of function. This design approach is common for complex microstructured products such as ice cream, paints, or alloys in which the structure-function framework, rather than specific materials, dictates desired properties and performance[551,552].

Additionally, rheology was used to differentiate between chewing gum products, namely conventional "chewing" gum and "bubble" gum, and to elucidate how certain deformations correlate with product function. Shear creep recovery experiments revealed that at moderate stresses, chewing gums recover a substantially larger percentage of imposed strain than bubble gums. We argued that this correlated with the need for bubble gum to retain strain after being spread across the tongue in order to sustain bubbles. Start-up of steady uniaxial extension showed that bubble gums withstood larger stresses before rupture. Since bubble gums are marketed to consumers for their propensity to form large bubbles, this finding is consistent with previous reports that extensional thickening stabilizes film blowing. In the future, it would be advantageous to explore the rheological response of a stress-controlled uniaxial or biaxial extension since these deformations are more reminiscent of how chewing or bubble gums are stretched during use; unfortunately, commercially available instruments with good temperature control to assess these types of deformations are not available at this time.

In the design of soft solids, rheology and performance are inherently linked. To ensure that these materials meet the necessary performance criteria, one must analyze the full, complex high-dimensional rheological signature including nonlinear deformations in both shear and extension. Our approach to characterizing chewing and bubble gum – correlating a unique rheological fingerprint and individual rheological responses to performance – is applicable to a wide range of materials including cosmetics, foods and adhesives. This systematic approach to product design, drawing on academic rigor and motivated by commercial viability and practical experience, forms a universal paradigm for the development of new technology.

Chapter 7

Ideas for Future Work

In harmony with the behavior of polymer networks with entangled dangling structures[185,186], in Chapter 3 we associated the observed low-frequency response of an A–B–A thermoplastic elastomer with arm retraction dynamics (stemming from single-free-end-type midblocks or perhaps from diblock impurities). As a stronger test of our conclusions, it would be interesting to examine the linear, rubbery behavior of an A–B–A with either polyethylene (PE) or poly(ethylene–*alt*–propylene) (PEP, i.e. hydrogenated 7% 3,4-PI) as midblock. Given the large negative temperature coefficient of chain dimensions of these polymer species[20,45,191,192], arm retraction dynamics would necessarily lead to thermo-rheological complexity[175,189,190]. Therefore, with a significant fraction of unsegregated A chains embedded in the matrix (e.g. as a result of A chains pullout at large deformations coupled with slow ordering kinetics), thermo-rheological complexity in the appropriate range of frequency and temperature (i.e. when interfacial relaxation does not intervene) would represent a more compelling evidence of star-like relaxation.

From our analysis, matrix dilution and partial segregation (either inherent or induced by chain pullout) emerge as powerful tools that can tune the ultimate properties of triblock- or multiblock-type networks. By taking advantage of matrix dilution and arm retraction dynamics, block polymer systems can be designed that meet the desired linear

and nonlinear extensional properties. For example, a precise control over the network architecture could be achieved by blending an A–B–C triblock terpolymer with an A–B diblock copolymer. Strong, unfavorable segment-segment interactions (e.g. χ_{AB}, χ_{AC} > 0.1) coupled with equilibrium self-assembly in the strong segregation regime would result in $x_b = 1$ ($x_l = x_f = 0$) for the triblock[233,234], whereas the entangled B tails of the diblock would provide the elastomeric network with retracting arms of known concentration. Varying the length and concentration of the B tails would then control the star-like relaxation as discussed in §3.3.4.IV-d.

By exploiting the model developed in Chapter 3 to describe the linear elastic behavior of A–B–A TPEs with glassy A domains, a simple relation was established between the measured power-law exponent *m* and the average number of tube segments per entangled B chain, $Z_B^{2m} = 5/4$. The agreement between the theoretical prediction (based merely on 1-D Rouse dynamics) and the value found from the power-law fit was remarkable (§4.3.2.II-c). This result deserves further investigation. It would be interesting to test the accuracy of our equation for other well-entangled A–B–A systems at temperatures close to the T_g of A, especially those with a large fraction of unsegregated chains or diblock impurities. Nevertheless, this first attempt at explaining the observed power-law exponent based on molecular structure can offer some guidance in the design of complex TPE-based materials that can mimic a specific self-similar behavior.

Although inadequate to represent the behavior of entangled A–B–A TPEs across $T_{g,A}$, the fractional Maxwell model[345] can potentially portray the double power-law relaxation

of lamellae-[103,105,246] and cylinder-forming[108,109] isotropic A–B and A–B–A block copolymers at temperatures above the glass transition of the higher T_g block and below the order-disorder transition (ODT). Furthermore, the FMM appears amenable to a quantitative description of the low-frequency response across the ODT, including the effect of composition fluctuations. To assess this hypothesis, a detailed comparison with experimental data is necessary and will be the subject of future work.

Bibliography

(1) Jamshidi, K.; Hyon, S. -H.; and Ikada, Y. Thermal Characterization of Polylactides. *Polymer* **1988**, *29*, 2229–2234.

(2) Joziasse, C. A.; Veenstra, H.; Grijpma, D. W.; and Pennings, A. J. On the Chain Stiffness of Poly(lactide)s. *Macromolecular Chemistry and Physics* **1996**, *197*, 2219–2229.

(3) Garlotta, D. A Literature Review of Poly(lactic acid). *Journal of Polymers and the Environment* **2001**, *9*, 63–84.

(4) Dorgan, J. R.; Janzen, J.; Clayton, M. P.; Hait, S. B.; and Knauss, D. M. Melt Rheology of Variable L-content Poly(lactic acid). *Journal of Rheology* **2005**, *49*, 607–619.

(5) Sinclair, R. G. The Case for Polylactic Acid As a Commodity Packaging Plastic. *Journal of Macromolecular Science, Part A: Pure and Applied Chemistry* **1996**, *33*, 585–597.

(6) Kulkarni, R. K.; Moore, E. G.; Hegyeli, A. F.; and Leonard, F. Biodegradable Poly(lactic acid) Polymers. *Journal of Biomedical Materials Research* **1971**, *5*, 169–181.

(7) Spenlehauer, G.; Vert, M.; Benoit, J. P.; and Boddaert, A. In Vitro and In Vivo Degradation of Poly(D,L-lactide/glycolide) Type Microspheres Made by Solvent Evaporation Method. *Biomaterials* **1989**, *10*, 557–563.

(8) Andrady, A. L. Biodegradability of Polymers. In *Physical Properties of Polymers Handbook*, 2nd ed.; Mark, J. E., Ed.; Springer: New York, 2007; pp 951–964.

(9) Anderson, K. S.; Schreck, K. M.; and Hillmyer, M. A. Toughening Polylactide. *Polymer Reviews* **2008**, *48*, 85–108.

(10) Lipinsky, E. S. and Sinclair, R. G. Is Lactic Acid a Commodity Chemical? *Chemical Engineering Progress* **1986**, *82*, 26–32.

(11) Suggs, L. J.; Moore, S. A.; and Mikos, A. G. Synthetic Biodegradable Polymers for Medical Applications. In *Physical Properties of Polymers Handbook*, 2nd ed.; Mark, J. E., Ed.; Springer: New York, 2007; pp 939–950.

(12) Ronca, G. Frequency Spectrum and Dynamic Correlations of Concentrated Polymer Liquids. *The Journal of Chemical Physics* **1983**, *79*, 1031–1043.

(13) Lin, Y. H. Number of Entanglement Strands Per Cubed Tube Diameter, a Fundamental Aspect of Topological Universality in Polymer Viscoelasticity. *Macromolecules* **1987**, *20*, 3080–3083.

(14) Kavassalis, T. A. and Noolandi, J. New View of Entanglements in Dense Polymer Systems. *Physical Review Letters* **1987**, *59*, 2674–2677.

(15) Kavassalis, T. A. and Noolandi, J. A New Theory of Entanglements and Dynamics in Dense Polymer Systems. *Macromolecules* **1988**, *21*, 2869–2879.

(16) Witten, T. A.; Milner, S. T.; and Wang, Z. G. In *Multiphase Macromolecular Systems*; Culbertson, B. M., Ed.; Plenum: New York, 1989.

(17) Fetters, L. J.; Lohse, D. J.; Richter, D.; Witten, T. A.; and Zirkel, A. Connection Between Polymer Molecular Weight, Density, Chain Dimensions, and Melt Viscoelastic Properties. *Macromolecules* **1994**, *27*, 4639–4647.

(18) Fetters, L. J.; Lohse, D. J.; Milner, S. T.; and Graessley, W. W. Packing Length Influence in Linear Polymer Melts on the Entanglement, Critical, and Reptation Molecular Weights. *Macromolecules* **1999**, *32*, 6847–6851.

(19) Fetters, L. J.; Lohse, D. J.; and Graessley, W. W. Chain Dimensions and Entanglement Spacings in Dense Macromolecular Systems. *Journal of Polymer Science Part B: Polymer Physics* **1999**, *37*, 1023–1033.

(20) Fetters, L. J.; Lohse, D. J.; and Colby, R. H. Chain Dimensions and Entanglement Spacings. In *Physical Properties of Polymers Handbook*, 2nd ed.; Mark, J. E., Ed.; Springer: New York, 2007; pp 447–454.

(21) Flory, P. J. *Statistical Mechanics of Chain Molecules,* 1st ed.; Wiley: New York; 1969.

(22) Rubinstein, M. and Colby, R. H. *Polymers Physics,* 1st ed.; Oxford University Press: New York; 2003; pp 7–12, 49–57, 212, 254–255, 265, 267, 281, 309, 312, 319–323, 330–334, 339, 362, 376–377, 379, 382–383.

(23) Hiemenz, P. C. and Lodge, T. P. *Polymer Chemistry,* 2nd ed.; CRC Press Taylor & Francis Group: Boca Raton, FL; 2007; pp 223–224, 227–228, 230–233, 241–242, 396–399, 409, 436, 479, 484, 491.

(24) Almdal, K.; Koppi, K. A.; Bates, F. S.; and Mortensen, K. Multiple Ordered Phases in a Block Copolymer Melt. *Macromolecules* **1992**, *25*, 1743–1751.

(25) Bates, F. S.; Schulz, M. F.; Khandpur, A. K.; Förster, S.; Rosedale, J. H.; Almdal, K.; and Mortensen, K. Fluctuations, Conformational Asymmetry and Block Copolymer Phase Behaviour. *Faraday Discussions* **1994**, *98*, 7–18.

(26) Bates, F. S.; Schulz, M. F.; Rosedale, J. H.; and Almdal, K. Correlation of Binary Polyolefin Phase Behavior with Statistical Segment Length Asymmetry. *Macromolecules* **1992**, *25*, 5547–5550.

(27) Graessley, W. W. The Entanglement Concept in Polymer Rheology. *Advances in Polymer Science* **1974**, *16*, 1–179.

(28) Dahlquist, C. A. In *Treatise on Adhesion and Adhesives*; Patrick, R. L., Ed.; Dekker: New York, 1969; p 244.

(29) Kirste, R. G.; Kruse, W. A.; and Ibel, K. Determination of the Conformation of Polymers in the Amorphous Solid State and in Concentrated Solution by Neutron Diffraction. *Polymer* **1975**, *16*, 120–124.

(30) Ho, J.; Govaert, L.; and Utz, M. Plastic Deformation of Glassy Polymers: Correlation Between Shear Activation Volume and Entanglement Density. *Macromolecules* **2003**, *36*, 7398–7404.

(31) Kausch, H. H. *Polymer Fracture,* 2nd ed.; Springer-Verlag: Berlin, Germany; 1987.

(32) Wu, S. Chain Structure, Phase Morphology, and Toughness Relationships in Polymers and Blends. *Polymer Engineering and Science* **1990**, *30*, 753–761.

(33) Wu, S. Control of Intrinsic Brittleness and Toughness of Polymers and Blends by Chemical Structure: A Review. *Polymer International* **1992**, *29*, 229–247.

(34) Mattice, W. L.; Helfer, C. A.; and Sokolov, A. P. Persistence Length and Finite Chain Length Effect on Characteristic Ratios. *Macromolecules* **2004**, *37*, 4711–4717.

(35) Larson, R. G.; Sridhar, T.; Leal, L. G.; McKinley, G. H.; Likhtman, A. E.; and McLeish, T. C. B. Definitions of Entanglement Spacing and Time Constants in the Tube Model. *Journal of Rheology* **2003**, *47*, 809–818.

(36) Dealy, J. M. and Larson, R. G. *Structure and Rheology of Molten Polymers: From Structure to Flow Behavior and Back Again,* 1st ed.; Carl Hanser Verlag: Munich, Germany; 2006; pp 8–11, 14, 99, 116–117, 132–134, 150, 154, 194–203, 208–209, 211, 214–216, 228–331, 341–342, 416–417.

(37) Odian, G. Stereochemistry of Polymerization. In *Principles of Polymerization*, 4th ed.; Wiley: Hoboken, New Jersey, 2004; pp 619–624, 689–694.

(38) Helfer, C. A. and Mattice, W. L. The Rotational Isomeric State Model. In *Physical Properties of Polymers Handbook*, 2nd ed.; Mark, J. E., Ed.; Springer: New York, 2007; pp 43–57.

(39) Anderson, K. S. and Hillmyer, M. A. Melt Chain Dimensions of Polylactide. *Macromolecules* **2004**, *37*, 1857–1862.

(40) Krishnamoorti, R.; Graessley, W. W.; Zirkel, A.; Richter, D.; Hadjichristidis, N.; Fetters, L. J.; and Lohse, D. J. Melt-State Polymer Chain Dimensions As a Function of Temperature. *Journal of Polymer Science Part B: Polymer Physics* **2002**, *40*, 1768–1776.

(41) Graessley, W. W. *Polymeric Liquids and Networks: Structure and Properties,* 1st ed.; Garland Science: New York; 2004; pp 125, 130–136, 441–451, 454, 458, 466, 479–480.

(42) Ferry, J. D. *Viscoelastic Properties of Polymers,* 3rd ed.; Wiley: New York; 1980; pp 24, 35–47, 60–61, 184–189, 225–227, 233–236, 240–247, 254, 256, 266–273, 276–289, 299, 304–312, 328–329, 345–348, 356–359, 369, 372–373, 408–411, 414–420, 426–427, 445, 557.

(43) Graessley, W. W. Entangled Linear, Branched and Network Polymer Systems – Molecular Theories. *Advances in Polymer Science* **1982**, *47*, 67–118.

(44) McLeish, T. C. B. Tube Theory of Entangled Polymer Dynamics. *Advances in Physics* **2002**, *51*, 1379–1527.

(45) Graessley, W. W. *Polymeric Liquids and Networks: Dynamics and Rheology,* 1st ed.; Garland Science: New York; 2008; pp 5, 24, 54, 145, 152–154, 420–429, 438–441, 462, 485–502, 520–527, 571, 579, 612, 661–663, 680.

(46) Doi, M. and Edwards, S. F. *The Theory of Polymer Dynamics,* 1st ed.; Oxford University Press: Oxford, U.K.; 1986; pp 115, 208, 233, 317, §6.4.4, §7.5.3.

(47) Rouse Jr, P. E. A Theory of the Linear Viscoelastic Properties of Dilute Solutions of Coiling Polymers. *The Journal of Chemical Physics* **1953**, *21*, 1272–1280.

(48) Bates, F. S.; Cohen, R. E.; and Berney, C. V. Small-Angle Neutron Scattering Determination of Macrolattice Structure in a Polystyrene–Polybutadiene Diblock Copolymer. *Macromolecules* **1982**, *15*, 589–592.

(49) Bates, F. S. and Hartney, M. A. Block Copolymers Near the Microphase Separation Transition. 3. Small-Angle Neutron Scattering Study of the Homogeneous Melt State. *Macromolecules* **1985**, *18*, 2478–2486.

(50) Wignall, G. D. and Bates, F. S. Absolute Calibration of Small-Angle Neutron Scattering Data. *Journal of Applied Crystallography* **1987**, *20*, 28–40.

(51) Bates, F. S. Small-Angle Neutron Scattering From Amorphous Polymers. *Journal of Applied Crystallography* **1988**, *21*, 681–691.

(52) Schindler, A. and Harper, D. Polylactide. II. Viscosity–Molecular Weight Relationships and Unperturbed Chain Dimensions. *Journal of Polymer Science: Polymer Chemistry Edition* **1979**, *17*, 2593–2599.

(53) Grijpma, D. W.; Penning, J. P.; and Pennings, A. J. Chain Entanglement, Mechanical Properties and Drawability of Poly(lactide). *Colloid and Polymer Science* **1994**, *272*, 1068–1081.

(54) Ren, J.; Urakawa, O.; and Adachi, K. Dielectric and Viscoelastic Studies of Segmental and Normal Mode Relaxations in Undiluted Poly(d,l-lactic acid). *Macromolecules* **2003**, *36*, 210–219.

(55) Kang, S.; Zhang, G.; Aou, K.; Hsu, S. L.; Stidham, H. D.; and Yang, X. An Analysis of Poly(lactic acid) with Varying Regio Regularity. *The Journal of Chemical Physics* **2003**, *118*, 3430–3436.

(56) Blomqvist, J. RIS Metropolis Monte Carlo Studies of Poly(L-lactic), Poly(L,D-lactic) and Polyglycolic Acids. *Polymer* **2001**, *42*, 3515–3521.

(57) Grijpma, D. W. and Pennings, A. J. Copolymers of L-lactide, 2. Mechanical Properties. *Macromolecular Chemistry and Physics* **1994**, *195*, 1649–1663.

(58) Kratky, O. and Porod, G. Röntgenuntersuchung Gelöster Fadenmoleküle. *Recueil Des Travaux Chimiques Des Pays-Bas* **1949**, *68*, 1106–1122.

(59) Aharoni, S. M. On Entanglements of Flexible and Rodlike Polymers. *Macromolecules* **1983**, *16*, 1722–1728.

(60) Aharoni, S. M. Correlations Between Chain Parameters and the Plateau Modulus of Polymers. *Macromolecules* **1986**, *19*, 426–434.

(61) Tonelli, A. E. and Flory, P. J. The Configurational Statistics of Random Poly(lactic acid) Chains. I. Experimental Results. *Macromolecules* **1969**, *2*, 225–227.

(62) Brant, D. A.; Tonelli, A. E.; and Flory, P. J. The Configurational Statistics of Random Poly(lactic acid) Chains. II. Theory. *Macromolecules* **1969**, *2*, 228–235.

(63) Wu, S. Predicting Chain Conformation and Entanglement of Polymers From Chemical Structure. *Polymer Engineering and Science* **1992**, *32*, 823–830.

(64) Doxastakis, M.; Mavrantzas, V. G.; and Theodorou, D. N. Atomistic Monte Carlo Simulation of *cis*-1,4 Polyisoprene Melts. I. Single Temperature End-Bridging Monte Carlo Simulations. *The Journal of Chemical Physics* **2001**, *115*, 11339–11351.

(65) Faller, R.; Müller-Plathe, F.; Doxastakis, M.; and Theodorou, D. Local Structure and Dynamics of *trans*-Polyisoprene Oligomers. *Macromolecules* **2001**, *34*, 1436–1448.

(66) Sasanuma, Y.; Asai, S.; and Kumagai, R. Conformational Characteristics and Configurational Properties of Poly(ethylene oxide–*alt*–ethylene sulfide). *Macromolecules* **2007**, *40*, 3488–3497.

(67) Heymans, N. A Novel Look at Models for Polymer Entanglement. *Macromolecules* **2000**, *33*, 4226–4234.

(68) Richter, D.; Farago, B.; Butera, R.; Fetters, L. J.; Huang, J. S.; and Ewen, B. On the Origins of Entanglement Constraints. *Macromolecules* **1993**, *26*, 795–804.

(69) Orwoll, R. A. Densities, Coefficients of Thermal Expansion, and Compressibilities of Amorphous Polymers. In *Physical Properties of Polymers Handbook*, 2nd ed.; Mark, J. E., Ed.; Springer: New York, 2007; pp 93–101.

(70) Wu, S. Chain Structure and Entanglement. *Journal of Polymer Science Part B: Polymer Physics* **1989**, *27*, 723–741.

(71) Witzke, D. R. Introduction to Properties, Engineering, and Prospects of Polylactide Polymers. Ph.D. Thesis, Michigan State University, 1997.

(72) Zhao, J.; Hahn, S. F.; Hucul, D. A.; and Meunier, D. M. Thermal and Viscoelastic Behavior of Hydrogenated Polystyrene. *Macromolecules* **2001**, *34*, 1737–1741.

(73) Graessley, W. W. and Edwards, S. F. Entanglement Interactions in Polymers and the Chain Contour Concentration. *Polymer* **1981**, *22*, 1329–1334.

(74) Helfand, E. and Sapse, A. M. Theory of Unsymmetric Polymer–Polymer Interfaces. *The Journal of Chemical Physics* **1975**, *62*, 1327–1331.

(75) Graessley, W. W. Some Phenomenological Consequences of the Doi–Edwards Theory of Viscoelasticity. *Journal of Polymer Science: Polymer Physics Edition* **1980**, *18*, 27–34.

(76) Marvin, R. S. and Oser, H. A Model for the Viscoelastic Behavior of Rubberlike Polymers Including Entanglements Effects. *Journal of Research of the National Bureau of Standards – B. Mathematics and Mathematical Physics* **1962**, *66B*, 171–180.

(77) Oser, H. and Marvin, R. S. Effect of Molecular Weight on Viscoelastic Properties of Polymers As Predicted by a Molecular Theory. *Journal of Research of the National Bureau of Standards – B. Mathematics and Mathematical Physics* **1963**, *67B*, 87–90.

(78) Chompff, A. J. and Prins, W. Viscoelasticity of Networks Consisting of Crosslinked or Entangled Macromolecules. II. Verification of the Theory for Entanglement Networks. *The Journal of Chemical Physics* **1968**, *48*, 235–243.

(79) Raju, V. R.; Menezes, E. V.; Marin, G.; Graessley, W. W.; and Fetters, L. J. Concentration and Molecular Weight Dependence of Viscoelastic Properties in Linear and Star Polymers. *Macromolecules* **1981**, *14*, 1668–1676.

(80) Kawamura, T.; Urayama, K.; and Kohjiya, S. Multiaxial Deformations of End-Linked Poly(dimethylsiloxane) Networks. 1. Phenomenological Approach to Strain Energy Density Function. *Macromolecules* **2001**, *34*, 8252–8260.

(81) Urayama, K.; Kawamura, T.; and Kohjiya, S. Multiaxial Deformations of End-Linked Poly(dimethylsiloxane) Networks. 2. Experimental Tests of Molecular Entanglement Models of Rubber Elasticity. *Macromolecules* **2001**, *34*, 8261–8269.

(82) Urayama, K.; Kawamura, T.; and Kohjiya, S. Multiaxial Deformations of End-Linked Poly(dimethylsiloxane) Networks. 4. Further Assessment of the Slip-Link Model for Chain-Entanglement Effect on Rubber Elasticity. *The Journal of Chemical Physics* **2003**, *118*, 5658–5664.

(83) Ball, R. C.; Doi, M.; Edwards, S. F.; and Warner, M. Elasticity of Entangled Networks. *Polymer* **1981**, *22*, 1010–1018.

(84) Edwards, S. F. and Vilgis, T. The Effect of Entanglements in Rubber Elasticity. *Polymer* **1986**, *27*, 483–492.

(85) Bueche, F. Viscosity, Self-Diffusion, and Allied Effects in Solid Polymers. *The Journal of Chemical Physics* **1952**, *20*, 1959–1964.

(86) Ferry, J. D.; Landel, R. F.; and Williams, M. L. Extensions of the Rouse Theory of Viscoelastic Properties to Undiluted Linear Polymers. *Journal of Applied Physics* **1955**, *26*, 359–362.

(87) Bueche, F. *Physical Properties of Polymers,* 1st ed.; Wiley: New York; 1962.

(88) Doi, M. Explanation for the 3.4-Power Law for Viscosity of Polymeric Liquids on the Basis of the Tube Model. *Journal of Polymer Science Part C: Polymer Letters* **1981**, *19*, 265–273.

(89) Doi, M. Explanation for the 3.4-Power Law for Viscosity of Polymeric Liquids on the Basis of the Tube Model. *Journal of Polymer Science: Polymer Physics Edition* **1983**, *21*, 667–684.

(90) Berry, G. C. and Fox, T. G. The Viscosity of Polymers and Their Concentrated Solutions. *Advances in Polymer Science* **1968**, *5*, 261–357.

(91) Holden, G. Thermoplastic Elastomers. In *Kirk-Othmer Encyclopedia of Chemical Technology*; Wiley Online Library, 2000; pp 1–23.

(92) Holden, G.; Kricheldorf, H. R.; and Quirk, R. P. *Thermoplastic Elastomers,* 3rd ed.; Hanser Gardner; 2004.

(93) Costa, F. R.; Dutta, N. K.; Choudhury, N. R.; and Bhowmick, A. K. Thermoplastic Elastomers. In *Current Topics in Elastomers Research*; CRC Press, 2009; pp 101–164.

(94) Bates, F. S. and Fredrickson, G. H. Block Copolymer Thermodynamics: Theory and Experiment. *Annual Reviews of Physical Chemistry* **1990**, *41*, 525–557.

(95) Bates, F. S. Polymer–Polymer Phase Behavior. *Science* **1991**, *251*, 898–905.

(96) Bates, F. S. and Fredrickson, G. H. Block Copolymers–Designer Soft Materials. *Physics Today* **1999**, *52*, 32–38.

(97) Matsen, M. W. The Standard Gaussian Model for Block Copolymer Melts. *Journal of Physics: Condensed Matter* **2002**, *14*, R21–R47.

(98) Fredrickson, G. H. and Bates, F. S. Dynamics of Block Copolymers: Theory and Experiment. *Annual Reviews of Materials Science* **1996**, *26*, 501–550.

(99) Castelletto, V. and Hamley, I. W. Block Copolymer Melts. In *Physical Properties of Polymers Handbook*, 2nd ed.; Mark, J. E., Ed.; Springer: New York, 2007; pp 641–652.

(100) Honeker, C. C. and Thomas, E. L. Impact of Morphological Orientation in Determining Mechanical Properties in Triblock Copolymer Systems. *Chemistry of Materials* **1996**, *8*, 1702–1714.

(101) Kossuth, M. B.; Morse, D. C.; and Bates, F. S. Viscoelastic Behavior of Cubic Phases in Block Copolymer Melts. *Journal of Rheology* **1999**, *43*, 167–196.

(102) Balsara, N. P.; Dai, H. J.; Watanabe, H.; Sato, T.; and Osaki, K. Influence of Defect Density on the Rheology of Ordered Block Copolymers. *Macromolecules* **1996**, *29*, 3507–3510.

(103) Rosedale, J. H. and Bates, F. S. Rheology of Ordered and Disordered Symmetric Poly(ethylenepropylene)–Poly(ethylethylene) Diblock Copolymers. *Macromolecules* **1990**, *23*, 2329–2338.

(104) Kawasaki, K. and Onuki, A. Dynamics and Rheology of Diblock Copolymers Quenched Into Microphase-Separated States. *Physical Review A* **1990**, *42*, 3664–3666.

(105) Gehlsen, M. D.; Almdal, K.; and Bates, F. S. Order-Disorder Transition: Diblock Versus Triblock Copolymers. *Macromolecules* **1992**, *25*, 939–943.

(106) Rubinstein, M. and Obukhov, S. P. Power-Law-Like Stress Relaxation of Block Copolymers: Disentanglement Regimes. *Macromolecules* **1993**, *26*, 1740–1750.

(107) Schulz, M. F.; Bates, F. S.; Almdal, K.; and Mortensen, K. Epitaxial Relationship for Hexagonal-to-Cubic Phase Transition in a Book Copolymer Mixture. *Physical Review Letters* **1994**, *73*, 86–91.

(108) Zhao, J.; Majumdar, B.; Schulz, M. F.; Bates, F. S.; Almdal, K.; Mortensen, K.; Hajduk, D. A.; and Gruner, S. M. Phase Behavior of Pure Diblocks and Binary Diblock Blends of Poly(ethylene)–Poly(ethylethylene). *Macromolecules* **1996**, *29*, 1204–1215.

(109) Ryu, C. Y.; Lee, M. S.; Hajduk, D. A.; and Lodge, T. P. Structure and Viscoelasticity of Matched Asymmetric Diblock and Triblock Copolymers in the Cylinder and Sphere Microstructures. *Journal of Polymer Science Part B: Polymer Physics* **1997**, *35*, 2811–2823.

(110) Bard, J. K. and Chung, C. I. Modeling the Elastic Behavior of Poly(styrene–*b*–butadiene–*b*–styrene) Block Copolymers. In *Thermoplastic Elastomers*, 1st ed.; Legge, N. R.; Holden, G.; and Schroeder, H. E., Ed.; Carl Hanser Verlag: Munich, Germany, 1987; pp 303–323.

(111) Daniel, C. and Hamley, I. W. Extensional and Shear Rheometry of Oriented Triblock Copolymers. *Rheologica Acta* **2000**, *39*, 191–200.

(112) Hotta, A.; Clarke, . M.; and Terentjev, . M. Stress Relaxation in Transient Networks of Symmetric Triblock Styrene–Isoprene–Styrene Copolymer. *Macromolecules* **2002**, *35*, 271–277.

(113) Roos, A. and Creton, C. Effect of the Presence of Diblock Copolymer on the Nonlinear Elastic and Viscoelastic Properties of Elastomeric Triblock Copolymers. *Macromolecules* **2005**, *38*, 7807–7818.

(114) Tong, J. -D. and Jerôme, R. Dependence of the Ultimate Tensile Strength of Thermoplastic Elastomers of the Triblock Type on the Molecular Weight Between Chain Entanglements of the Central Block. *Macromolecules* **2000**, *33*, 1479–1481.

(115) Schmidt, S. C. and Hillmyer, M. A. Synthesis and Characterization of Model Polyisoprene–Polylactide Diblock Copolymers. *Macromolecules* **1999**, *32*, 4794–4801.

(116) Lee, S. Structure and Dynamics of Block Copolymer Based Soft Materials. Ph.D. Thesis, University of Minnesota, 2011; pp 139, 146, 180.

(117) Daniel, C.; Hamley, I. W.; and Mortensen, K. Effect of Planar Extension on the Structure and Mechanical Properties of Polystyrene–Poly(ethylene–*co*–butylene)–Polystyrene Triblock Copolymers. *Polymer* **2000**, *41*, 9239–9247.

(118) Kholodovych, V. and Welsh, W. J. Thermal-Oxidative Stability and Degradation of Polymers. In *Physical Properties of Polymers Handbook*, 2nd ed.; Mark, J. E., Ed.; Springer: New York, 2007; pp 927–938.

(119) Khan, S. A. and Larson, R. G. Step Planar Extension of Polymer Melts Using a Lubricated Channel. *Rheologica Acta* **1991**, *30*, 1–6.

(120) Plazek, D. J. and Ngai, K. L. The Glass Temperature. In *Physical Properties of Polymers Handbook*, 2nd ed.; Mark, J. E., Ed.; Springer: New York, 2007; pp 187–215.

(121) Matsen, M. W. and Thompson, R. B. Equilibrium Behavior of Symmetric ABA Triblock Copolymer Melts. *The Journal of Chemical Physics* **1999**, *111*, 7139–7146.

(122) Watanabe, H. Viscoelasticity and Dynamics of Entangled Polymers. *Progress in Polymer Science* **1999**, *24*, 1253–1403.

(123) Kraus, G.; Childers, C. W.; and Gruver, J. T. Properties of Random and Block Copolymers of Butadiene and Styrene. I. Dynamic Properties and Glassy Transition Temperatures. *Journal of Applied Polymer Science* **1967**, *11*, 1581–1591.

(124) Kaplan, D. and Tschoegl, N. W. Time-Temperature Superposition in Two-Phase Polyblends. *Polymer Engineering and Science* **1974**, *14*, 43–49.

(125) Colby, R. H. Breakdown of Time-Temperature Superposition in Miscible Polymer Blends. *Polymer* **1989**, *30*, 1275–1278.

(126) Lim, C. K.; Cohen, R. E.; and Tschoegl, N. W. Time-Temperature Superposition in Block Copolymers. *Advances in Chemistry Series* **1971**, *99*, 397–417.

(127) Fesko, D. G. and Tschoegl, N. W. Time-Temperature Superposition in Thermorheologically Complex Materials. *Journal of Polymer Science Part C: Polymer Symposia* **1971**, *35*, 51–69.

(128) Fesko, D. G. and Tschoegl, N. W. Time-Temperature Superposition in Styrene/Butadiene/Styrene Block Copolymers. *International Journal of Polymeric Materials* **1974**, *3*, 51–79.

(129) Cohen, R. E. and Tschoegl, N. W. Comparison of the Dynamic Mechanical Properties of Two Styrene–Butadiene–Styrene Triblock Copolymers with 1,2- and 1,4-Polybutadiene Center Blocks. *Transactions of the Society of Rheology* **1976**, *20*, 153–169.

(130) Schwarzl, F. and Staverman, A. J. Time-Temperature Dependence of Linear Viscoelastic Behavior. *Journal of Applied Physics* **1952**, *23*, 838–843.

(131) Plazek, D. J. Temperature Dependence of the Viscoelastic Behavior of Polystyrene. *The Journal of Physical Chemistry* **1965**, *69*, 3480–3487.

(132) Plazek, D. J. 1995 Bingham Medal Address: Oh, Thermorheological Simplicity, Wherefore Art Thou? *Journal of Rheology* **1996**, *40*, 987–1014.

(133) Ngai, K. L. and Plazek, D. J. Temperature Dependences of the Viscoelastic Response of Polymer Systems. In *Physical Properties of Polymers Handbook*, 2nd ed.; Mark, J. E., Ed.; Springer: New York, 2007; pp 455–478.

(134) Gotro, J. T. and Graessley, W. W. Model Hydrocarbon Polymers: Rheological Properties of Linear Polyisoprenes and Hydrogenated Polyisoprenes. *Macromolecules* **1984**, *17*, 2767–2775.

(135) Sato, T.; Watanabe, H.; and Osaki, K. Rheological and Dielectric Behavior of a Styrene–Isoprene–Styrene Triblock Copolymer in *n*-Tetradecane. 1. Rubbery-Plastic-Viscous Transition. *Macromolecules* **1996**, *29*, 6231–6239.

(136) Watanabe, H.; Sato, T.; Osaki, K.; Yao, M. -L.; and Yamagishi, A. Rheological and Dielectric Behavior of a Styrene–Isoprene–Styrene Triblock Copolymer in Selective Solvents. 2. Contribution of Loop-Type Middle Blocks to Elasticity and Plasticity. *Macromolecules* **1997**, *30*, 5877–5892.

(137) Leonardi, F.; Derail, C.; and Marin, G. Some Applications of Molecular Rheology: Polymer Formulation and Molecular Design. *Journal of Non-Newtonian Fluid Mechanics* **2005**, *128*, 50–61.

(138) Williams, M. L.; Landel, R. F.; and Ferry, J. D. The Temperature Dependence of Relaxation Mechanisms in Amorphous Polymers and Other Glass-forming Liquids. *Journal of the American Chemical Society* **1955**, *77*, 3701–3707.

(139) Klopffer, M. -H.; Bokobza, L.; and Monnerie, L. Effect of Vinyl Content on the Viscoelastic Properties of Polybutadienes and Polyisoprenes – Monomeric Friction Coefficient. *Polymer* **1998**, *39*, 3445–3449.

(140) Chapman, B. R.; Hamersky, M. W.; Milhaupt, J. M.; Kostelecky, C.; Lodge, T. P.; von Meerwall, E. D.; and Smith, S. D. Structure and Dynamics of Disordered

Tetrablock Copolymers: Composition and Temperature Dependence of Local Friction. *Macromolecules* **1998**, *31*, 4562–4573.

(141) Doolittle, A. K. Studies in Newtonian Flow. I. The Dependence of the Viscosity of Liquids on Temperature. *Journal of Applied Physics* **1951**, *22*, 1031–1035.

(142) Doolittle, A. K. Studies in Newtonian Flow. II. The Dependence of the Viscosity of Liquids on Free-Space. *Journal of Applied Physics* **1951**, *22*, 1471–1475.

(143) Doolittle, A. K. Studies in Newtonian Flow. III. The Dependence of the Viscosity of Liquids on Molecular Weight and Free Space (in Homologous Series). *Journal of Applied Physics* **1952**, *23*, 236–239.

(144) Vogel, H. The Law of the Relation Between the Viscosity of Liquids and the Temperature. *Physikalische Zeitschrift* **1921**, *22*, 645–646.

(145) Bero, C. A. and Plazek, D. J. Volume-Dependent Rate Processes in An Epoxy Resin. *Journal of Polymer Science Part B: Polymer Physics* **1991**, *29*, 39–47.

(146) Plazek, D. J. and Ngai, K. L. Correlation of Polymer Segmental Chain Dynamics with Temperature-Dependent Time-Scale Shifts. *Macromolecules* **1991**, *24*, 1222–1224.

(147) Roovers, J. and Toporowski, P. M. Microheterogeneity in Miscible Blends of 1,2-Polybutadiene and 1,4-Polyisoprene. *Macromolecules* **1992**, *25*, 3454–3461.

(148) Payne, A. R. In *Rheology of Elastomers*, 1st ed.; Mason, P. and Wookey, N., Ed.; Pergamon Press: London, 1958.

(149) Mark, J. E. *Polymer Data Handbook,* Mark, J. E., Ed.; Oxford University Press: New York; 1998.

(150) Tschoegl, N. W. *The Phenomenological Theory of Linear Viscoelastic Behavior: An Introduction,* 1st ed.; Springer-Verlag: Berlin, Germany; 1989; pp 55–66, 93, 127, 158–224, 229–237, 350, 509, 520–531, 539–540, 574–580.

(151) He, C.; Wood-Adams, P.; and Dealy, J. M. Broad Frequency Range Characterization of Molten Polymers. *Journal of Rheology* **2004**, *48*, 711–724.

(152) Honerkamp, J. and Weese, J. A Nonlinear Regularization Method for the Calculation of Relaxation Spectra. *Rheologica Acta* **1993**, *32*, 65–73.

(153) Davies, A. R. and Anderssen, R. S. Sampling Localization in Determining the Relaxation Spectrum. *Journal of Non-Newtonian Fluid Mechanics* **1997**, *73*, 163–179.

(154) Cohen, R. E. and Tschoegl, N. W. Dynamic Mechanical Properties of Block Copolymer Blends–A Study of the Effects of Terminal Chains in Elastomeric Materials: 2. Forced Oscillation Measurements. *International Journal of Polymeric Materials* **1973**, *2*, 205–223.

(155) Chasset, R. and Thirion, P. *Physics of Non-Crystalline Solids, Proceedings of the International Conference* **1965**, 345–359.

(156) Langley, N. R. and Ferry, J. D. Dynamic Mechanical Properties of Cross-Linked Rubbers. VI. Poly(dimethylsiloxane) Networks. *Macromolecules* **1968**, *1*, 353–358.

(157) Doi, M. Basic Principle in the Viscoelasticity of Polymeric Liquids. *Journal of Non-Newtonian Fluid Mechanics* **1987**, *23*, 151–162.

(158) Dickie, R. A. and Ferry, J. D. Dynamic Mechanical Properties of Cross-Linked Rubbers. III. Dicumyl Peroxide Vulcanizates of Natural Rubber. *The Journal of Physical Chemistry* **1966**, *70*, 2594–2600.

(159) Osaki, K.; Inoue, T.; Uematsu, T.; and Yamashita, Y. Evaluation Methods of the Longest Rouse Relaxation Time of An Entangled Polymer in a Semidilute Solution. *Journal of Polymer Science Part B: Polymer Physics* **2001**, *39*, 1704–1712.

(160) Matsen, M. W. and Schick, M. Lamellar Phase of a Symmetric Triblock Copolymer. *Macromolecules* **1994**, *27*, 187–192.

(161) Matsen, M. W. Bridging and Looping in Multiblock Copolymer Melts. *The Journal of Chemical Physics* **1995**, *102*, 3884–3887.

(162) Watanabe, H. Slow Dielectric Relaxation of a Styrene–Isoprene–Styrene Triblock Copolymer with Dipole Inversion in the Middle Block: A Challenge to a Loop/Bridge Problem. *Macromolecules* **1995**, *28*, 5006–5011.

(163) Watanabe, H.; Sato, T.; and Osaki, K. Concentration Dependence of Loop Fraction in Styrene–Isoprene–Styrene Triblock Copolymer Solutions and Corresponding Changes in Equilibrium Elasticity. *Macromolecules* **2000**, *33*, 2545–2550.

(164) Watanabe, H.; Matsumiya, Y.; Sawada, T.; and Iwamoto, T. Rheological and Dielectric Behavior of Dipole-Inverted $(SIS)_p$-Type Multiblock Copolymers: Estimates of Bridge/Loop Fractions for Respective I Blocks and Effect of Loops on High Extensibility of Bridges. *Macromolecules* **2007**, *40*, 6885–6897.

(165) Watanabe, H. Personal communication, **2011**.

(166) De Gennes, P. G. Coherent Scattering by One Reptating Chain. *Journal De Physique* **1981**, *42*, 735–740.

(167) Milner, S. T. and McLeish, T. C. B. Reptation and Contour-Length Fluctuations in Melts of Linear Polymers. *Physical Review Letters* **1998**, *81*, 725–728.

(168) Milner, S. T. and McLeish, T. C. B. Parameter-Free Theory for Stress Relaxation in Star Polymer Melts. *Macromolecules* **1997**, *30*, 2159–2166.

(169) De Gennes, P. G. Reptation of Stars. *Journal De Physique* **1975**, *36*, 1199–1203.

(170) De Gennes, P. G. Dynamics of Entangled Polymer Solutions. I. The Rouse Model. *Macromolecules* **1976**, *9*, 587–593.

(171) Colby, R. H. and Rubinstein, M. Two-Parameter Scaling for Polymers in Θ Solvents. *Macromolecules* **1990**, *23*, 2753–2757.

(172) Marrucci, G. Relaxation by Reptation and Tube Enlargement: A Model for Polydisperse Polymers. *Journal of Polymer Science: Polymer Physics Edition* **1985**, *23*, 159–177.

(173) Ball, R. C. and McLeish, T. C. B. Dynamic Dilution and the Viscosity of Star Polymer Melts. *Macromolecules* **1989**, *22*, 1911–1913.

(174) Pearson, D. S. and Helfand, E. Viscoelastic Properties of Star-Shaped Polymers. *Macromolecules* **1984**, *17*, 888–895.

(175) Fetters, L. J.; Kiss, A. D.; Pearson, D. S.; Quack, G. F.; and Vitus, F. J. Rheological Behavior of Star-Shaped Polymers. *Macromolecules* **1993**, *26*, 647–654.

(176) Sato, T.; Watanabe, H.; Osaki, K.; and Yao, M. -L. Relaxation of Spherical Micellar Systems of Styrene–Isoprene Diblock Copolymers. 1. Linear Viscoelastic and Dielectric Behavior. *Macromolecules* **1996**, *29*, 3881–3889.

(177) Watanabe, H.; Sato, T.; and Osaki, K. Viscoelastic Relaxation of Styrene–Butadiene Diblock Copolymer Micellar Systems. 1. Behavior in a Nonentangling, Short Polybutadiene Matrix. *Macromolecules* **1996**, *29*, 104–112.

(178) Watanabe, H.; Sato, T.; and Osaki, K. Viscoelastic Relaxation of Styrene–Butadiene Diblock Copolymer Micellar Systems. 2. Behavior in Entangling, Long Polybutadiene Matrices. *Macromolecules* **1996**, *29*, 113–118.

(179) Watanabe, H. Rheology of Diblock Copolymer Micellar Systems. *Acta Polymerica* **1997**, *48*, 215–233.

(180) Watanabe, H.; Yao, M. -L.; Sato, T.; and Osaki, K. Non-Newtonian Flow Behavior of Diblock Copolymer Micelles: Shear-Thinning in a Nonentangling Matrix. *Macromolecules* **1997**, *30*, 5905–5912.

(181) Watanabe, H.; Sato, T.; Osaki, K.; Hamersky, M. W.; Chapman, B. R.; and Lodge, T. P. Diffusion and Viscoelasticity of Copolymer Micelles in a Homopolymer Matrix. *Macromolecules* **1998**, *31*, 3740–3742.

(182) Watanabe, H. Nonlinear Rheology of Diblock Copolymer Micellar Dispersion: A Review of Recent Findings. *Journal of Non-Newtonian Fluid Mechanics* **1999**, *82*, 315–329.

(183) Kan, H. -C.; Ferry, J. D.; and Fetters, L. J. Rubber Networks Containing Unattached Macromolecules. 5. Stress Relaxation in Styrene–Butadiene–Styrene Block Copolymer with Unattached Linear and Star Polybutadienes. *Macromolecules* **1980**, *13*, 1571–1577.

(184) De Gennes, P. G. Reptation of a Polymer Chain in the Presence of Fixed Obstacles. *The Journal of Chemical Physics* **1971**, *55*, 572–579.

(185) Curro, J. G. and Pincus, P. A Theoretical Basis for Viscoelastic Relaxation of Elastomers in the Long-Time Limit. *Macromolecules* **1983**, *16*, 559–562.

(186) Curro, J. G.; Pearson, D. S.; and Helfand, E. Viscoelasticity of Randomly Crosslinked Polymer Networks. Relaxation of Dangling Chains. *Macromolecules* **1985**, *18*, 1157–1162.

(187) Raju, V. R.; Rachapudy, H.; and Graessley, W. W. Properties of Amorphous and Crystallizable Hydrocarbon Polymers. IV. Melt Rheology of Linear and Star-Branched Hydrogenated Polybutadiene. *Journal of Polymer Science: Polymer Physics Edition* **1979**, *17*, 1223–1235.

(188) Graessley, W. W. and Raju, V. R. Some Rheological Properties of Solutions and Blends of Hydrogenated Polybutadiene. *Journal of Polymer Science: Polymer Symposium* **1984**, *71*, 77–93.

(189) Carella, J. M.; Gotro, J. T.; and Graessley, W. W. Thermorheological Effects of Long-Chain Branching in Entangled Polymer Melts. *Macromolecules* **1986**, *19*, 659–667.

(190) Milner, S. T. and McLeish, T. C. B. Arm-Length Dependence of Stress Relaxation in Star Polymer Melts. *Macromolecules* **1998**, *31*, 7479–7482.

(191) Graessley, W. W. Effect of Long Branches on the Temperature Dependence of Viscoelastic Properties in Polymer Melts. *Macromolecules* **1982**, *15*, 1164–1167.

(192) Levine, A. J. and Milner, S. T. Star Polymers and the Failure of Time-Temperature Superposition. *Macromolecules* **1998**, *31*, 8623–8637.

(193) Green, M. S. and Tobolsky, A. V. A New Approach to the Theory of Relaxing Polymeric Media. *The Journal of Chemical Physics* **1946**, *14*, 80–92.

(194) Tobolsky, A. V.; Carlson, D. W.; and Indictor, N. Rubber Elasticity and Chain Configuration. *Journal of Polymer Science* **1961**, *54*, 175–192.

(195) Meier, D. J. Theory of the Morphology of Block Copolymers. *Polymer Preprints (American Chemical Society, Division of Polymer Chemistry)* **1970**, *11*, 400–405.

(196) Meier, D. J. Network Statistics of Block Copolymers and Filled Elastomers: Swelling Equilibria. *Applied Polymer Symposia* **1974**, *24*, 67–81.

(197) Gaylord, R. J. and Lohse, D. J. Block Copolymer Deformation. *Polymer Engineering and Science* **1978**, *18*, 359–365.

(198) Gaylord, R. J. Molecular Theories of the Interdomain Contribution to the Deformation of Multiple Domain Polymeric Systems. *Advances in Chemistry Series* **1979**, *176*, 231–236.

(199) Kuhn, W. Relationship Between Molecular Size, Static Molecular Shape and Elastic Characteristics of High Polymer Materials. *Kolloid-Zeitschrift* **1936**, *76*, 258–271.

(200) Richards, R. W. and Welsh, G. Deformation of Matrix Macromolecules in a Uniaxially Extended Styrene–Isoprene–Styrene Linear Triblock Copolymer. *European Polymer Journal* **1995**, *31*, 1197–1206.

(201) Daoulas, K. C.; Theodorou, D. N.; Roos, A.; and Creton, C. Experimental and Self-Consistent-Field Theoretical Study of Styrene Block Copolymer Self-Adhesive Materials. *Macromolecules* **2004**, *37*, 5093–5109.

(202) Chompff, A. J. and Duiser, J. A. Viscoelasticity of Networks Consisting of Crosslinked or Entangled Macromolecules. I. Normal Modes and Mechanical Spectra. *The Journal of Chemical Physics* **1966**, *45*, 1505–1514.

(203) Graessley, W. W. Statistical Mechanics of Random Coil Networks. *Macromolecules* **1975**, *8*, 186–190.

(204) Ronca, G. and Allegra, G. An Approach to Rubber Elasticity with Internal Constraints. *The Journal of Chemical Physics* **1975**, *63*, 4990–4997.

(205) Flory, P. J. Theory of Elasticity of Polymer Networks. The Effect of Local Constraints on Junctions. *The Journal of Chemical Physics* **1977**, *66*, 5720–5729.

(206) Dossin, L. M. and Graessley, W. W. Rubber Elasticity of Well-Characterized Polybutadiene Networks. *Macromolecules* **1979**, *12*, 123–130.

(207) Pearson, D. S. and Graessley, W. W. Elastic Properties of Well-Characterized Ethylene–Propylene Copolymer Networks. *Macromolecules* **1980**, *13*, 1001–1009.

(208) Langley, N. R. Elastically Effective Strand Density in Polymer Networks. *Macromolecules* **1968**, *1*, 348–352.

(209) Langley, N. R. and Polmanteer, K. E. Relation of Elastic Modulus to Crosslink and Entanglement Concentrations in Rubber Networks. *Journal of Polymer Science: Polymer Physics Edition* **1974**, *12*, 1023–1034.

(210) Gottlieb, M.; Macosko, C. W.; Benjamin, G. S.; Meyers, K. O.; and Merrill, E. W. Equilibrium Modulus of Model Poly(dimethylsiloxane) Networks. *Macromolecules* **1981**, *14*, 1039–1046.

(211) Patel, S. K.; Malone, S.; Cohen, C.; Gillmor, J. R.; and Colby, R. H. Elastic Modulus and Equilibrium Swelling of Poly(dimethylsiloxane) Networks. *Macromolecules* **1992**, *25*, 5241–5251.

(212) Duering, E. R.; Kremer, K.; and Grest, G. S. Structure and Relaxation of End-Linked Polymer Networks. *The Journal of Chemical Physics* **1994**, *101*, 8169–8192.

(213) Everaers, R. and Kremer, K. Topological Interactions in Model Polymer Networks. *Physical Review E* **1996**, *53*, R37–R40.

(214) Everaers, R. Entanglement Effects in Defect-Free Model Polymer Networks. *New Journal of Physics* **1999**, *1*, 12.1–12.54.

(215) Gilra, N.; Cohen, C.; and Panagiotopoulos, A. Z. A Monte Carlo Study of the Structural Properties of End-Linked Polymer Networks. *The Journal of Chemical Physics* **2000**, *112*, 6910–6916.

(216) Grest, G. S.; Pütz, M.; Everaers, R.; and Kremer, K. Stress–Strain Relation of Entangled Polymer Networks. *Journal of Non-Crystalline Solids* **2000**, *274*, 139–146.

(217) van der Poel, C. On the Rheology of Concentrated Dispersions. *Rheologica Acta* **1958**, *1*, 198–205.

(218) Smith, J. C. Experimental Values for the Elastic Constants of a Particulate-Filled Glassy Polymer. *Journal of Research of the National Bureau of Standards – A. Physics and Chemistry* **1976**, *80A*, 45–49.

(219) Smith, J. C. The Elastic Constants of a Particulate-Filled Glassy Polymer: Comparison of Experimental Values with Theoretical Predictions. *Polymer Engineering and Science* **1976**, *16*, 394–399.

(220) Scanlan, J. The Effect of Network Flaws on the Elastic Properties of Vulcanizates. *Journal of Polymer Science* **1960**, *43*, 501–508.

(221) Case, L. C. Branching in Polymers. I. Network Defects. *Journal of Polymer Science* **1960**, *45*, 397–404.

(222) Matsumiya, Y.; Watanabe, H.; Takano, A.; and Takahashi, Y. Uniaxial Extensional Behavior of $(SIS)_p$-Type Multiblock Copolymer Systems: Structural Origin of High Extensibility. *Macromolecules* **2013**, *46*, 2681–2695.

(223) Guth, E. Theory of Filler Reinforcement. *Journal of Applied Physics* **1945**, *16*, 20–25.

(224) Fox, T. G. Influence of Diluent and of Copolymer Composition on the Glass Temperature of a Polymer System. *Bull. Am. Phys. Soc.* **1956**, *1*, 1–123.

(225) Couchman, P. R. and Karasz, F. E. A Classical Thermodynamic Discussion of the Effect of Composition on Glass-Transition Temperatures. *Macromolecules* **1978**, *11*, 117–119.

(226) Couchman, P. R. Compositional Variation of Glass-Transition Temperatures. 2. Application of the Thermodynamic Theory to Compatible Polymer Blends. *Macromolecules* **1978**, *11*, 1156–1161.

(227) Couchman, P. R. Compositional Variation of Glass-Transition Temperatures. 7. Copolymers. *Macromolecules* **1982**, *15*, 770–773.

(228) Couchman, P. R. Composition-Dependent Glass-Transition Temperatures and Copolymers. *Nature* **1982**, *298*, 729–730.

(229) Macosko, C. W. and Miller, D. R. A New Derivation of Average Molecular Weights of Nonlinear Polymers. *Macromolecules* **1976**, *9*, 199–206.

(230) Miller, D. R. and Macosko, C. W. A New Derivation of Post Gel Properties of Network Polymers. *Macromolecules* **1976**, *9*, 206–211.

(231) Meyers, K. O.; Bye, M. L.; and Merrill, E. W. Model Silicone Elastomer Networks of High Juction Functionality: Synthesis, Tensile Behavior, Swelling Behavior, and Comparison with Molecular Theories of Rubber Elasticity. *Macromolecules* **1980**, *13*, 1045–1053.

(232) Graessley, W. W. and Roovers, J. Melt Rheology of Four-Arm and Six-Arm Star Polystyrenes. *Macromolecules* **1979**, *12*, 959–965.

(233) Takano, A.; Kamaya, I.; Takahashi, Y.; and Matsushita, Y. Effect of Loop/Bridge Conformation Ratio on Elastic Properties of the Sphere-Forming ABA Triblock Copolymers: Preparation of Samples and Determination of Loop/Bridge Ratio. *Macromolecules* **2005**, *38*, 9718–9723.

(234) Takahashi, Y.; Song, Y.; Nemoto, N.; Takano, A.; Akazawa, Y.; and Matsushita, Y. Effect of Loop/Bridge Conformation Ratio on Elastic Properties of the Sphere-Forming ABA Triblock Copolymers Under Uniaxial Elongation. *Macromolecules* **2005**, *38*, 9724–9729.

(235) Watanabe, H.; Kotaka, T.; Hashimoto, T.; Shibayama, M.; and Kawai, H. Rheological and Morphological Behavior of Styrene–Butadiene Diblock Copolymer Solutions in Selective Solvents. *Journal of Rheology* **1982**, *26*, 153–179.

(236) Watanabe, H. and Kotaka, T. Rheology of Styrene–Butadiene Diblock Copolymers Dissolved in Selective Solvent: Dependence on Molecular Dimension. *Polymer Journal* **1982**, *14*, 739–747.

(237) Watanabe, H. and Kotaka, T. Rheology of Ternary Mixtures of Styrene–Butadiene Diblock Copolymer, Homopolybutadiene, and *n*-Tetradecane. *Journal of Rheology* **1983**, *27*, 223–240.

(238) Watanabe, H.; Kuwahara, S.; and Kotaka, T. Rheology of Styrene–Butadiene–Styrene Triblock Copolymer in *n*-Tetradecane Systems. *Journal of Rheology* **1984**, *28*, 393–409.

(239) Watanabe, H.; Kanaya, T.; and Takahashi, Y. Equilibrium Elasticity of Diblock Copolymer Micellar Lattice. *Macromolecules* **2001**, *34*, 662–665.

(240) Watanabe, H.; Matsumiya, Y.; Kanaya, T.; and Takahashi, Y. Rheology and Structure of a Butadiene–Styrene Diblock Copolymer in Dibutyl Phthalate: Role of Concentration Fluctuation in Disruption and Reformation of Micellar Lattice. *Macromolecules* **2001**, *34*, 6742–6755.

(241) Tan, H.; Watanabe, H.; Matsumiya, Y.; Kanaya, T.; and Takahashi, Y. Shear-Induced Disruption and Recovery of Microphase-Separated Network Structure of a BSB Triblock Copolymer in Dibutyl Phthalate. *Macromolecules* **2003**, *36*, 2886–2893.

(242) Matsumiya, Y.; Matsumoto, M.; Watanabe, H.; Kanaya, T.; and Takahashi, Y. Nonlinear Rheology and Structural Changes of $(BS)_n$ Multiblock Copolymers Under Shear Flow. *Macromolecules* **2007**, *40*, 3724–3732.

(243) Helfand, E. and Wasserman, Z. R. Block Copolymer Theory. 4. Narrow Interphase Approximation. *Macromolecules* **1976**, *9*, 879–888.

(244) Hashimoto, T.; Shibayama, M.; and Kawai, H. Domain-Boundary Structure of Styrene–Isoprene Block Copolymer Films Cast From Solution. 4. Molecular-Weight Dependence of Lamellar Microdomains. *Macromolecules* **1980**, *13*, 1237–1247.

(245) Hadziioannou, G. and Skoulios, A. Molecular Weight Dependence of Lamellar Structure in Styrene/Isoprene Two- and Three-Block Copolymers. *Macromolecules* **1982**, *15*, 258–262.

(246) Bates, F. S. Block Copolymers Near the Microphase Separation Transition. 2. Linear Dynamic Mechanical Properties. *Macromolecules* **1984**, *17*, 2607–2613.

(247) Abetz, V. and Simon, P. F. W. Phase Behaviour and Morphologies of Block Copolymers. In *Block Copolymers I*; Springer-Verlag: Berlin, Germany, 2005; pp 125–212.

(248) Lynd, N. A.; Meuler, A. J.; and Hillmyer, M. A. Polydispersity and Block Copolymer Self-Assembly. *Progress in Polymer Science* **2008**, *33*, 875–893.

(249) Meuler, A. J.; Ellison, C. J.; Hillmyer, M. A.; and Bates, F. S. Polydispersity-Induced Stabilization of the Core-Shell Gyroid. *Macromolecules* **2008**, *41*, 6272–6275.

(250) Meuler, A. J.; Ellison, C. J.; Qin, J.; Evans, C. M.; Hillmyer, M. A.; and Bates, F. S. Polydispersity Effects in Poly(isoprene–*b*–styrene–*b*–ethylene oxide) Triblock Terpolymers. *The Journal of Chemical Physics* **2009**, *130*, 234903.

(251) Bouchaud, J. -P. and Georges, A. Anomalous Diffusion in Disordered Media: Statistical Mechanisms, Models and Physical Applications. *Physics Reports* **1990**, *195*, 127–293.

(252) Metzler, R. and Klafter, J. The Random Walk's Guide to Anomalous Diffusion: A Fractional Dynamics Approach. *Physics Reports* **2000**, *339*, 1–77.

(253) Mandelbrot, B. B. How Long Is the Coast of Britain? Statistical Self-Similarity and Fractional Dimension. *Science* **1967**, *156*, 636–638.

(254) Mandelbrot, B. B. and Van Ness, J. W. Fractional Brownian Motions, Fractional Noises and Applications. *SIAM Review* **1968**, *10*, 422–437.

(255) Mandelbrot, B. B. *The Fractal Geometry of Nature,* Freeman: New York; 1983.

(256) Mandelbrot, B. B.; Passoja, D. E.; and Paullay, A. J. Fractal Character of Fracture Surfaces of Metals. *Nature* **1984**, *308*, 721–722.

(257) Mandelbrot, B. B. Self-Affine Fractals and Fractal Dimension. *Physica Scripta* **1985**, *32*, 257–260.

(258) Falconer, K. *Fractal Geometry: Mathematical Foundations and Applications,* 3rd ed.; Wiley: Chichester, UK; 2013.

(259) Stanley, H. E. and Meakin, P. Multifractal Phenomena in Physics and Chemistry. *Nature* **1988**, *335*, 405–409.

(260) Metzler, R.; Klafter, J.; and Sokolov, I. M. Anomalous Transport in External Fields: Continuous Time Random Walks and Fractional Diffusion Equations Extended. *Physical Review E* **1998**, *58*, 1621–1633.

(261) Metzler, R.; Barkai, E.; and Klafter, J. Anomalous Diffusion and Relaxation Close to Thermal Equilibrium: A Fractional Fokker–Planck Equation Approach. *Physical Review Letters* **1999**, *82*, 3563–3567.

(262) Metzler, R. and Klafter, J. From Stretched Exponential to Inverse Power-Law: Fractional Dynamics, Cole–Cole Relaxation Processes, and Beyond. *Journal of Non-Crystalline Solids* **2002**, *305*, 81–87.

(263) Metzler, R. and Klafter, J. The Restaurant at the End of the Random Walk: Recent Developments in the Description of Anomalous Transport by Fractional Dynamics. *Journal of Physics A: Mathematical and General* **2004**, *37*, R161–R208.

(264) Parisi, G. On Complexity. *Measures of Complexity, Lecture Notes in Physics* **1988**, *314*, 22–27.

(265) Takayama, H. Cooperative Dynamics in Complex Physical Systems. *Proceedings of the Second Yukawa International Symposium, Kyoto, Japan* **1989**, *43*.

*(*266) Winter, H. H. Gel Point. In *Encyclopedia of Polymer Science and Technology*; Wiley Online Library, 2002; pp 132–145.

(267) Tobolsky, A. V. Elastoviscous Properties of Polyisobutylene. VI. Relation Between Stress Relaxation Modulus and Dynamic Modulus. *Journal of the American Chemical Society* **1952**, *74*, 3786–3788.

(268) Tobolsky, A. V. and Catsiff, E. Elastoviscous Properties of Polyisobutylene (and Other Amorphous Polymers) From Stress–Relaxation Studies. IX. A Summary of Results. *Journal of Polymer Science* **1956**, *19*, 111–121.

(269) Larson, R. G. Constitutive Relationships for Polymeric Materials with Power-Law Distributions of Relaxation Times. *Rheologica Acta* **1985**, *24*, 327–334.

(270) Baumgaertel, M.; Schausberger, A.; and Winter, H. H. The Relaxation of Polymers with Linear Flexible Chains of Uniform Length. *Rheologica Acta* **1990**, *29*, 400–408.

(271) Baumgaertel, M.; De Rosa, M. E.; Machado, J.; Masse, M.; and Winter, H. H. The Relaxation Time Spectrum of Nearly Monodisperse Polybutadiene Melts. *Rheologica Acta* **1992**, *31*, 75–82.

(272) Roovers, J. and Graessley, W. W. Melt Rheology of Some Model Comb Polystyrenes. *Macromolecules* **1981**, *14*, 766–773.

(273) Roovers, J. Melt Rheology of H-Shaped Polystyrenes. *Macromolecules* **1984**, *17*, 1196–1200.

(274) Friedrich, C. Rheological Material Functions for Associating Comb-Shaped or H-Shaped Polymers: A Fractional Calculus Approach. *Philosophical Magazine Letters* **1992**, *66*, 287–292.

(275) Friedrich, C. and Braun, H. Linear Viscoelastic Behaviour of Complex Polymeric Materials: A Fractional Mode Representation. *Colloid and Polymer Science* **1994**, *272*, 1536–1546.

(276) Friedrich, C.; Braun, H.; and Weese, J. Determination of Relaxation Time Spectra by Analytical Inversion Using a Linear Viscoelastic Model with Fractional Derivatives. *Polymer Engineering and Science* **1995**, *35*, 1661–1669.

(277) McLeish, T. C. B.; Allgaier, J.; Bick, . K.; Bishko, G.; Biswas, P.; Blackwell, R.; Blottière, B.; Clarke, N.; Gibbs, B.; Groves, . J.; Hakiki, A.; Heenan, . K.; Johnson, . M.; Kant, R.; Read, . J.; and Young, . N. Dynamics of Entangled H-Polymers: Theory, Rheology, and Neutron-Scattering. *Macromolecules* **1999**, *32*, 6734–6758.

(278) García-Franco, C. A.; Srinivas, S.; Lohse, D. J.; and Brant, P. Similarities Between Gelation and Long Chain Branching Viscoelastic Behavior. *Macromolecules* **2001**, *34*, 3115–3117.

(279) Bailly, C.; Stephenne, V.; Muchtar, Z.; Schappacher, M.; and Deffieux, A. Linear Viscoelastic Behavior of Densely Grafted Poly(chloroethyl vinyl ether)–*g*–Polystyrene Combs in the Melt. *Journal of Rheology* **2003**, *47*, 821–827.

(280) Kapnistos, M.; Lang, M.; Vlassopoulos, D.; Pyckhout-Hintzen, W.; Richter, D.; Cho, D.; Chang, T.; and Rubinstein, M. Unexpected Power-Law Stress Relaxation of Entangled Ring Polymers. *Nature Materials* **2008**, *7*, 997–1002.

(281) Stadler, R.; de Lucca Freitas, L.; Krieger, V.; and Klotz, S. Influence of the Phase Separation on the Linear Viscoelastic Properties of a Polystyrene–Poly(vinyl methyl ether) Blend. *Polymer* **1988**, *29*, 1643–1647.

(282) Mani, S.; Malone, M. F.; and Winter, H. H. Influence of Phase Separation on the Linear Viscoelastic Behavior of a Miscible Polymer Blend. *Journal of Rheology* **1992**, *36*, 1625–1649.

(283) Sailer, C. and Handge, . A. Melt Viscosity, Elasticity, and Morphology of Reactively Compatibilized Polyamide 6/Styrene–Acrylonitrile Blends in Shear and Elongation. *Macromolecules* **2007**, *40*, 2019–2028.

(284) Handge, U. A.; Buschnakowski, M.; and Michler, G. H. Deformation and Alignment of Lamellae in Melt Extension of Blends of a Styrene–Butadiene Block Copolymer with Polystyrene. *Journal of Applied Polymer Science* **2009**, *112*, 1319–1329.

(285) Bagley, R. L. and Torvik, P. J. A Theoretical Basis for the Application of Fractional Calculus to Viscoelasticity. *Journal of Rheology* **1983**, *27*, 201–210.

(286) Bagley, R. L. and Torvik, P. J. On the Fractional Calculus Model of Viscoelastic Behavior. *Journal of Rheology* **1986**, *30*, 133–155.

(287) Cates, M. E. Brownian Dynamics of Self-Similar Macromolecules. *Journal De Physique* **1985**, *46*, 1059–1077.

(288) Muthukumar, M. Dynamics of Polymeric Fractals. *The Journal of Chemical Physics* **1985**, *83*, 3161–3168.

(289) Chambon, F. and Winter, H. H. Stopping of Crosslinking Reaction in a PDMS Polymer at the Gel Point. *Polymer Bulletin* **1985**, *13*, 499–503.

(290) Winter, H. H. and Chambon, F. Analysis of Linear Viscoelasticity of a Crosslinking Polymer at the Gel Point. *Journal of Rheology* **1986**, *30*, 367–382.

(291) Chambon, F.; Petrovic, Z. S.; MacKnight, W. J.; and Winter, H. H. Rheology of Model Polyurethanes at the Gel Point. *Macromolecules* **1986**, *19*, 2146–2149.

(292) Chambon, F. and Winter, H. H. Linear Viscoelasticity at the Gel Point of a Crosslinking PDMS with Imbalanced Stoichiometry. *Journal of Rheology* **1987**, *31*, 683–697.

(293) Scanlan, J. C. and Winter, H. H. Composition Dependence of the Viscoelasticity of End-Linked Poly(dimethylsiloxane) at the Gel Point. *Macromolecules* **1991**, *24*, 47–54.

(294) Izuka, A.; Winter, H. H.; and Hashimoto, T. Molecular Weight Dependence of Viscoelasticity of Polycaprolactone Critical Gels. *Macromolecules* **1992**, *25*, 2422–2428.

(295) Masuda, T.; Nakajima, A.; Kitamura, M.; Aoki, Y.; Yamauchi, N.; and Yoshioka, A. Viscoelastic Properties of Rubber-Modified Polymeric Materials at Elevated Temperatures. *Pure and Applied Chemistry* **1984**, *56*, 1457–1475.

(296) Metzler, R.; Schick, W.; Kilian, H. -G.; and Nonnenmacher, T. F. Relaxation in Filled Polymers: A Fractional Calculus Approach. *The Journal of Chemical Physics* **1995**, *103*, 7180–7186.

(297) Fetters, L. J.; Graessley, W. W.; Hadjichristidis, N.; Kiss, A. D.; Pearson, D. S.; and Younghouse, L. B. Association Behavior of End-Functionalized Polymers. 2. Melt Rheology of Polyisoprenes with Carboxylate, Amine, and Zwitterion End Groups. *Macromolecules* **1988**, *21*, 1644–1653.

(298) Stadler, R. and De Lucca Freitas, L. Relaxation Behavior of Linear Polymer Chains with Statistically Distributed Functional Groups. *Macromolecules* **1989**, *22*, 714–719.

(299) Lin, Y. G.; Mallin, D. T.; Chien, J. C. W.; and Winter, H. H. Dynamic Mechanical Measurement of Crystallization-Induced Gelation in Thermoplastic Elastomeric Poly(propylene). *Macromolecules* **1991**, *24*, 850–854.

(300) Khan, S. A.; Schnepper, C. A.; and Armstrong, R. C. Foam Rheology: III. Measurement of Shear Flow Properties. *Journal of Rheology* **1988**, *32*, 69–92.

(301) Colby, R. H.; Gillmor, J. R.; Galli, G.; Laus, M.; Ober, C. K.; and Hall, E. Linear Viscoelasticity of Side Chain Liquid Crystal Polymer. *Liquid Crystals* **1993**, *13*, 233–245.

(302) Ketz Jr, R. J.; Prud'homme, R. K.; and Graessley, W. W. Rheology of Concentrated Microgel Solutions. *Rheologica Acta* **1988**, *27*, 531–539.

(303) Antonietti, M.; Bremser, W.; and Schmidt, M. Microgels: Model Polymers for the Crosslinked State. *Macromolecules* **1990**, *23*, 3796–3805.

(304) Sollich, P.; Lequeux, F.; Hébraud, P.; and Cates, M. E. Rheology of Soft Glassy Materials. *Physical Review Letters* **1997**, *78*, 2020–2023.

(305) Sollich, P. Rheological Constitutive Equation for a Model of Soft Glassy Materials. *Physical Review E* **1998**, *58*, 738–759.

(306) Metzner, A. B. Rheology of Suspensions in Polymeric Liquids. *Journal of Rheology* **1985**, *29*, 739–775.

(307) Mason, T. G. and Weitz, D. A. Linear Viscoelasticity of Colloidal Hard Sphere Suspensions Near the Glass Transition. *Physical Review Letters* **1995**, *75*, 2770–2773.

(308) Martinetti, L.; Mannion, A. M.; Voje Jr, W. E.; Xie, R.; Ewoldt, R. H.; Morgret, L. D.; Bates, F. S.; and Macosko, C. W. A Critical Gel Fluid with High Extensibility: The Rheology of Chewing Gum. *Journal of Rheology* **2014**, *58*, 821–838.

(309) Caputo, M. and Mainardi, F. Linear Models of Dissipation in Anelastic Solids. *La Rivista Del Nuovo Cimento Della Societá Italiana Di Fisica* **1971**, *1*, 161–198.

(310) Richert, R. and Blumen, A. *Disorder Effects on Relaxational Processes: Glasses, Polymers, Proteins,* 1st ed.; Springer-Verlag: Berlin; 1994.

(311) Mainardi, F. Fractional Relaxation in Anelastic Solids. *Journal of Alloys and Compounds* **1994**, *211/212*, 534–538.

(312) Glöckle, W. G. and Nonnenmacher, T. F. A Fractional Calculus Approach to Self-Similar Protein Dynamics. *Biophysical Journal* **1995**, *68*, 46–53.

(313) Cole, K. S. and Cole, R. H. Dispersion and Absorption in Dielectrics I. Alternating Current Characteristics. *The Journal of Chemical Physics* **1941**, *9*, 341–351.

(314) Soskey, P. R. and Winter, H. H. Large Step Shear Strain Experiments with Parallel-Disk Rotational Rheometers. *Journal of Rheology* **1984**, *28*, 625–645.

(315) Nutting, P. G. A New General Law of Deformation. *Journal of the Franklin Institute* **1921**, *191*, 679–685.

(316) Nutting, P. G. A Study of Elastic Viscous Deformation. *Proc. Amer. Soc. Test. Mater.* **1921**, *21*, 1162–1171.

(317) Hyun, K.; Kim, S. H.; Ahn, K. H.; and Lee, S. J. Large Amplitude Oscillatory Shear As a Way to Classify the Complex Fluids. *Journal of Non-Newtonian Fluid Mechanics* **2002**, *107*, 51–65.

(318) Scott Blair, G. W.; Veinoglou, B. C.; and Caffyn, J. E. Limitations of the Newtonian Time Scale in Relation to Non-Equilibrium Rheological States and a Theory of Quasi-Properties. *Proceedings of the Royal Society of London. Series A: Mathematical and Physical Sciences* **1947**, *189*, 69–87.

(319) Winter, H. H. and Mours, M. Rheology of Polymers Near Liquid-Solid Transitions. *Advances in Polymer Science* **1997**, *134*, 165–234.

(320) Stauffer, D.; Coniglio, A.; and Adam, M. Gelation and Critical Phenomena. *Advances in Polymer Science* **1982**, *44*, 103–158.

(321) Martin, J. E. and Adolf, D. The Sol-Gel Transition in Chemical Gels. *Annual Review of Physical Chemistry* **1991**, *42*, 311–339.

(322) Flory, P. J. Molecular Size Distribution in Three Dimensional Polymers. I. Gelation. *J Am Chem Soc* **1941**, *63*, 3083–3090.

(323) Flory, P. J. Molecular Size Distribution in Three Dimensional Polymers. II. Trifunctional Branching Units. *J Am Chem Soc* **1941**, *63*, 3091–3096.

(324) Flory, P. J. Molecular Size Distribution in Three Dimensional Polymers. III. Tetrafunctional Branching Units. *J Am Chem Soc* **1941**, *63*, 3096–3100.

(325) Flory, P. J. *Principles of Polymer Chemistry,* 1st ed.; Cornell University Press: Ithaca, New York; 1953.

(326) Stockmayer, W. H. Theory of Molecular Size Distribution and Gel Formation in Branched-Chain Polymers. *The Journal of Chemical Physics* **1943**, *11*, 45–55.

(327) Stockmayer, W. H. Theory of Molecular Size Distribution and Gel Formation in Branched Polymers II. General Cross Linking. *The Journal of Chemical Physics* **1944**, *12*, 125–131.

(328) De Gennes, P. G. *Scaling Concepts in Polymer Physics,* 1st ed.; Cornell University Press: Ithaca, NY; 1979.

(329) Stanley, H. E. *Introduction to Phase Transitions and Critical Phenomena,* New York: Oxford University Press; 1987.

(330) Winter, H. H. Transient Networks. Evolution of Rheology During Chemical Gelation. *Progress in Colloid and Polymer Science* **1987**, *75*, 104–110.

(331) Vilgis, T. A. and Winter, H. H. Mechanical Selfsimilarity of Polymers During Chemical Gelation. *Colloid and Polymer Science* **1988**, *266*, 494–500.

(332) Kramers, H. A. *Estratto Dagli Atti Del Congresso Internazionale di Fisica, Como* **1927**, 545.

(333) Kronig, R. L. On the Theory of Dispersion of X-Rays. *Journal of the Optical Society of America* **1926**, *12*, 547–556.

(334) Friedrich, C. and Heymann, L. Extension of a Model for Crosslinking Polymer at the Gel Point. *Journal of Rheology* **1988**, *32*, 235–241.

(335) Friedrich, C.; Heymann, L.; and Berger, H. -R. Evolution of Time Constants During Sol-Gel Transition. *Rheologica Acta* **1989**, *28*, 535–539.

(336) Jaishankar, A. and McKinley, G. H. Power-Law Rheology in the Bulk and at the Interface: Quasi-Properties and Fractional Constitutive Equations. *Proceedings of the Royal Society of London. Series A: Mathematical, Physical and Engineering Sciences* **2013**, *469*, 20120284.

(337) Velankar, S. S. and Giles, D. How Do I Know If My Phase Angles Are Correct? *Rheology Bulletin* **2007**, *76*, 8–20.

(338) Muthukumar, M. and Winter, H. H. Fractal Dimension of a Crosslinking Polymer at the Gel Point. *Macromolecules* **1986**, *19*, 1284–1285.

(339) Muthukumar, M. Screening Effect on Viscoelasticity Near the Gel Point. *Macromolecules* **1989**, *22*, 4656–4658.

(340) Bird, R. B.; Armstrong, R. C.; and Hassager, O. *Dynamics of Polymeric Liquids: Fluid Mechanics,* 2nd ed.; Wiley: New York; 1987.

(341) Spanier, J. and Oldham, K. B. *The Fractional Calculus: Theory and Applications of Differentiation and Integration to Arbitrary Order,* 1st ed.; Academic Press: New York; 1974.

(342) Koeller, R. C. Applications of Fractional Calculus to the Theory of Viscoelasticity. *Journal of Applied Mechanics* **1984**, *51*, 299–307.

(343) Schiessel, H. and Blumen, A. Hierarchical Analogues to Fractional Relaxation Equations. *Journal of Physics A: Mathematical and General* **1993**, *26*, 5057–5069.

(344) Heymans, N. and Bauwens, J. -C. Fractal Rheological Models and Fractional Differential Equations for Viscoelastic Behavior. *Rheologica Acta* **1994**, *33*, 210–219.

(345) Schiessel, H.; Metzler, R.; Blumen, A.; and Nonnenmacher, T. F. Generalized Viscoelastic Models: Their Fractional Equations with Solutions. *Journal of Physics A: Mathematical and General* **1995**, *28*, 6567–6584.

(346) Kollmannsberger, P. and Fabry, B. Linear and Nonlinear Rheology of Living Cells. *Annual Review of Materials Research* **2011**, *41*, 75–97.

(347) Podlubny, I. Geometric and Physical Interpretation of Fractional Integration and Fractional Differentiation. *ArXiv Preprint Math/0110241* **2001.**

(348) Glöckle, W. G. and Nonnenmacher, T. F. Fractional Integral Operators and Fox Functions in the Theory of Viscoelasticity. *Macromolecules* **1991**, *24*, 6426–6434.

(349) Friedrich, C. Relaxation and Retardation Functions of the Maxwell Model with Fractional Derivatives. *Rheologica Acta* **1991**, *30*, 151–158.

(350) Friedrich, C. Relaxation Functions of Rheological Constitutive Equations with Fractional Derivatives: Thermodynamical Constraints. In *Rheological Modelling: Thermodynamical and Statistical Approaches, Lecture Notes in Physics*; Casas-Vazquez, J. and Jou, D., Ed.; Springer: Berlin, 1991; pp 321–330.

(351) Friedrich, C. Mechanical Stress Relaxation in Polymers: Fractional Integral Model Versus Fractional Differential Model. *Journal of Non-Newtonian Fluid Mechanics* **1993**, *46*, 307–314.

(352) Glöckle, W. G. and Nonnenmacher, T. F. Fractional Relaxation and the Time-Temperature Superposition Principle. *Rheologica Acta* **1994**, *33*, 337–343.

(353) Beris, A. N. and Edwards, B. J. On the Admissibility Criteria for Linear Viscoelasticity Kernels. *Rheologica Acta* **1993**, *32*, 505–510.

(354) Heymans, N. Hierarchical Models for Viscoelasticity: Dynamic Behaviour in the Linear Range. *Rheologica Acta* **1996**, *35*, 508–519.

(355) Lion, A. On the Thermodynamics of Fractional Damping Elements. *Continuum Mechanics and Thermodynamics* **1997**, *9*, 83–96.

(356) Friedrich, C.; Schiessel, H.; and Blumen, A. Constitutive Behavior Modeling and Fractional Derivatives. In *Rheology Series, Advances in the Flow and Rheology of Non-Newtonian Fluids Part A*; Siginer, D. A.; De Kee, D.; and Chhabra, R. P., Ed.; Elsevier, 1999; pp 429–466.

(357) Maxwell, J. C. On the Dynamical Theory of Gases. *Philosophical Transactions of the Royal Society of London* **1867**, *157*, 49–88.

(358) Voigt, W. Ueber Innere Reibung Fester Körper, Insbesondere Der Metalle. *Annalen Der Physik* **1892**, *283*, 671–693.

(359) Ward, I. M. *Mechanical Properties of Solid Polymers,* 2nd ed.; Wiley: Chichester, U.K.; 1983.

(360) Carpinteri, A. *Structural Mechanics: A Unified Approach,* 1st ed.; Taylor & Francis: London; 1997.

(361) Heymans, N. and Podlubny, I. Physical Interpretation of Initial Conditions for Fractional Differential Equations with Riemann–Liouville Fractional Derivatives. *Rheologica Acta* **2006**, *45*, 765–771.

(362) Heymans, N. Constitutive Equations for Polymer Viscoelasticity Derived From Hierarchical Models in Cases of Failure of Time-Temperature Superposition. *Signal Processing* **2003**, *83*, 2345–2357.

(363) Gross, B. and Fuoss, R. M. Ladder Structures for Representation of Viscoelastic Systems. *Journal of Polymer Science* **1956**, *19*, 39–50.

(364) Gross, B. Ladder Structures for Representation of Viscoelastic Systems. II. *Journal of Polymer Science* **1956**, *20*, 123–131.

(365) Marvin, R. S. and Oser, H. A Model for the Viscoelastic Behavior of Rubberlike Polymers Including Entanglements Effects. *Journal of Research of the National Bureau of Standards – B. Mathematics and Mathematical Physics* **1962**, *66B*, 171–180.

(366) Friedrich, C. and Braun, H. Generalized Cole–Cole Behavior and Its Rheological Relevance. *Rheologica Acta* **1992**, *31*, 309–322.

(367) Wiman, A. Über Den Fundamentalsatz in Der Teorie Der Funktionen $E_\alpha(x)$. *Acta Mathematica* **1905**, *29*, 191–201.

(368) Wiman, A. Über Die Nullstellen Der Funktionen $E_\alpha(x)$. *Acta Mathematica* **1905**, *29*, 217–234.

(369) Erdélyi, A.; Magnus, W.; Oberhettinger, F.; Tricomi, F. G.; and Bateman, H. *Higher Transcendental Functions. Vol. 3,* New York: McGraw-Hill; 1955.

(370) Dzherbashyan, M. M. *Integral Transforms and Representations of Functions in the Complex Plane,* Nauka, Moscow; 1966.

(371) Haubold, H. J.; Mathai, A. M.; and Saxena, R. K. Mittag-Leffler Functions and Their Applications. *Journal of Applied Mathematics* **2011**, *2011*, 1–51.

(372) Mittag-Leffler, G. M. Une Généralisation De L'Intégrale De Laplace–Abel. *Comptes Rendus De L'Academie Des Sciences* **1903**, *137*, 537–539.

(373) Mittag-Leffler, G. M. Sur La Nouvelle Fonction $E_\alpha(x)$. *Comptes Rendus De L'Academie Des Sciences* **1903**, *137*, 554–558.

(374) Chamberlin, R. V.; Mozurkewich, G.; and Orbach, R. Time Decay of the Remanent Magnetization in Spin-Glasses. *Physical Review Letters* **1984**, *52*, 867–870.

(375) Cardona, M.; Chamberlin, R. V.; and Marx, W. The History of the Stretched Exponential Function. *Annalen Der Physik* **2007**, *16*, 842–845.

(376) Kohlrausch, R. Theorie Des Elektrischen Rückstandes in Der Leidener Flasche. *Annalen Der Physik Und Chemie* **1854**, *167*, 179–214.

(377) Kohlrausch, F. Ueber Die Elastische Nachwirkung Bei Der Torsion. *Annalen Der Physik Und Chemie* **1863**, *195*, 337–368.

(378) Williams, G. and Watts, D. C. Non-Symmetrical Dielectric Relaxation Behaviour Arising From a Simple Empirical Decay Function. *Transactions of the Faraday Society* **1970**, *66*, 80–85.

(379) Weibull, W. A Statistical Distribution Function of Wide Applicability. *Journal of Applied Mechanics* **1951**, *18*, 293–297.

(380) Scott Blair, G. W. A New Criterion for Expressing the 'Intensity of Firmness' of Soft Bodies. *Nature* **1943**, *152*, 412.

(381) Scott Blair, G. W. The Role of Psychophysics in Rheology. *Journal of Colloid Science* **1947**, *2*, 21–32.

(382) Reiner, M. *Deformation, Strain and Flow: An Elementary Introduction to Rheology,* 3rd ed.; H. K. Lewis: London; 1969.

(383) Gemant, A. A Method of Analyzing Experimental Results Obtained From Elasto-Viscous Bodies. *Physics* **1936**, *7*, 311–317.

(384) Gemant, A. XLV. On Fractional Differentials. *The London, Edinburgh, and Dublin Philosophical Magazine and Journal of Science* **1938**, *25*, 540–549.

(385) Schiessel, H. and Blumen, A. Mesoscopic Pictures of the Sol-Gel Transition: Ladder Models and Fractal Networks. *Macromolecules* **1995**, *28*, 4013–4019.

(386) Liu, C.; He, J.; Ruymbeke, E. V.; Keunings, R.; and Bailly, C. Evaluation of Different Methods for the Determination of the Plateau Modulus and the Entanglement Molecular Weight. *Polymer* **2006**, *47*, 4461–4479.

(387) Sanders, J. F.; Ferry, J. D.; and Valentine, R. H. Viscoelastic Properties of 1,2-Polybutadiene. Comparison with Natural Rubber and Other Elastomers. *Journal of Polymer Science Part A-2: Polymer Physics* **1968**, *6*, 967–980.

(388) Mancke, R. G. and Ferry, J. D. Dynamic Mechanical Properties of Cross-Linked Rubbers. IV. Dicumyl Peroxide Vulcanizates of Styrene–Butadiene Rubber. *Transactions of the Society of Rheology* **1968**, *12*, 335–350.

(389) Plazek, D. J. and O'Rourke, V. M. Viscoelastic Behavior of Low Molecular Weight Polystyrene. *Journal of Polymer Science Part A-2: Polymer Physics* **1971**, *9*, 209–243.

(390) Marvin, R. S. A New Approximate Conversion Method for Relating Stress Relaxation and Dynamic Modulus. *Physical Review* **1952**, *86*, 644–644.

(391) Pakula, T.; Saijo, K.; Kawai, H.; and Hashimoto, T. Deformation Behavior of Styrene–Butadiene–Styrene Triblock Copolymer with Cylindrical Morphology. *Macromolecules* **1985**, *18*, 1294–1302.

(392) Morton, M. Structure-Property Relations in Amorphous and Crystallizable ABA Triblock Copolymers. *Rubber Chemistry and Technology* **1983**, *56*, 1096–1110.

(393) Frick, E. M.; Zalusky, A. S.; and Hillmyer, M. A. Characterization of Polylactide–*b*–Polyisoprene–*b*–Polylactide Thermoplastic Elastomers. *Biomacromolecules* **2003**, *4*, 216–223.

(394) Martello, M. T. and Hillmyer, M. A. Polylactide–Poly(6-methyl-ε-caprolactone)–Polylactide Thermoplastic Elastomers. *Macromolecules* **2011**, *44*, 8537–8545.

(395) Hencky, H. Die Bewegungsgleichungen Beim Nichtstationären Fließen Plastischer Massen. *Annalen Der Angewandten Mathematischen Mechanik* **1925**, *5*, 144–146.

(396) Rivlin, R. S. Large Elastic Deformations of Isotropic Materials. IV. Further Developments of the General Theory. *Philosophical Transactions of the Royal Society of London. Series A: Mathematical, Physical and Engineering Sciences* **1948**, *241*, 379–397.

(397) Rivlin, R. S. and Saunders, D. W. Large Elastic Deformations of Isotropic Materials. VII. Experiments on the Deformation of Rubber. *Philosophical Transactions of the Royal Society of London. Series A: Mathematical, Physical and Engineering Sciences* **1951**, *243*, 251–288.

(398) Rivlin, R. S. In *Rheology: Theory and Applications, Vol. 1*; Eirich, F. R., Ed.; Academic Press: New York, 1956; pp 761.

(399) Mooney, M. A Theory of Large Elastic Deformation. *Journal of Applied Physics* **1940**, *11*, 582–592.

(400) Macosko, C. W. *Rheology: Principles, Measurements, and Applications,* 1st ed.; Wiley-VCH: New York; 1994.

(401) Wall, F. T. Statistical Thermodynamics of Rubber. *The Journal of Chemical Physics* **1942**, *10*, 132–134.

(402) Wall, F. T. Statistical Thermodynamics of Rubber. II. *The Journal of Chemical Physics* **1942**, *10*, 485–488.

(403) Treloar, L. R. G. The Elasticity of a Network of Long-Chain Molecules. I.. *Transactions of the Faraday Society* **1943**, *39*, 36–41.

(404) James, H. M. and Guth, E. Theory of the Elastic Properties of Rubber. *The Journal of Chemical Physics* **1943**, *11*, 455–481.

(405) Flory, P. J. and Rehner Jr, J. Statistical Mechanics of Cross-Linked Polymer Networks I. Rubberlike Elasticity. *The Journal of Chemical Physics* **1943**, *11*, 512–520.

(406) Wagner, M. H. and Schaeffer, J. Rubbers and Polymer Melts: Universal Aspects of Nonlinear Stress-Strain Relations. *Journal of Rheology* **1993**, *37*, 643–661.

(407) Lodge, A. S. A Classification of Constitutive Equations Based on Stress Relaxation Predictions for the Single-Jump Shear Strain Experiment. *Journal of Non-Newtonian Fluid Mechanics* **1984**, *14*, 67–83.

(408) Rivlin, R. S. and Sawyers, K. N. Nonlinear Continuum Mechanics of Viscoelastic Fluids. *Annual Review of Fluid Mechanics* **1971**, *3*, 117–146.

(409) Tanner, R. I. From A to (BK) Z in Constitutive Relations. *Journal of Rheology* **1988**, *32*, 673–702.

(410) Kaye, A. Note No. 134, College of Aeronautics, Cranfield, U.K., 1962.

(411) Bernstein, B.; Kearsley, E. A.; and Zapas, L. J. A Study of Stress Relaxation with Finite Strain. *Transactions of the Society of Rheology* **1963**, *7*, 391–410.

(412) Einaga, Y.; Osaki, K.; Kurata, M.; Kimura, S. -I.; and Tamura, M. Stress Relaxation of Polymer Solutions Under Large Strain. *Polymer Journal* **1971**, *2*, 550–552.

(413) Osaki, K.; Nishizawa, K.; and Kurata, M. Material Time Constant Characterizing the Nonlinear Viscoelasticity of Entangled Polymeric Systems. *Macromolecules* **1982**, *15*, 1068–1071.

(414) Osaki, K. On the Damping Function of Shear Relaxation Modulus for Entangled Polymers. *Rheologica Acta* **1993**, *32*, 429–437.

(415) Archer, L. A. Separability Criteria for Entangled Polymer Liquids. *Journal of Rheology* **1999**, *43*, 1555–1571.

(416) Sanchez-Reyes, J. and Archer, L. A. Step Shear Dynamics of Entangled Polymer Liquids. *Macromolecules* **2002**, *35*, 5194–5202.

(417) Inoue, T.; Uematsu, T.; Yamashita, Y.; and Osaki, K. Significance of the Longest Rouse Relaxation Time in the Stress Relaxation Process at Large Deformation of Entangled Polymer Solutions. *Macromolecules* **2002**, *35*, 4718–4724.

(418) Tobolsky, A. V. and Andrews, R. D. Systems Manifesting Superposed Elastic and Viscous Behavior. *The Journal of Chemical Physics* **1945**, *13*, 3–27.

(419) Andrews, R. D.; Hofman-Bang, N.; and Tobolsky, A. V. Elastoviscous Properties of Polyisobutylene. I. Relaxation of Stress in Whole Polymer of Different Molecular Weights at Elevated Temperatures. *Journal of Polymer Science* **1948**, *3*, 669–692.

(420) Guth, E.; Wack, P. E.; and Anthony, R. L. Significance of the Equation of State for Rubber. *Journal of Applied Physics* **1946**, *17*, 347–351.

(421) Smith, T. L. Nonlinear Viscoelastic Response of Amorphous Elastomers to Constant Strain Rates. *Transactions of the Society of Rheology* **1962**, *6*, 61–80.

(422) Smith, T. L. Ultimate Tensile Properties of Elastomers. I. Characterization by a Time and Temperature Independent Failure Envelope. *Journal of Polymer Science Part A: General Papers* **1963**, *1*, 3597–3615.

(423) White, J. L. and Tokita, N. An Additive Functional Theory of Viscoelastic Deformation with Application to Amorphous Polymers, Solutions and Vulcanizates. *Journal of the Physical Society of Japan* **1967**, *22*, 719–724.

(424) Zapas, L. J. and Phillips, J. C. Simple Shearing Flows in Polyisobutylene Solutions. *Journal of Research of the National Bureau of Standards – A. Physics and Chemistry* **1970**, *75A*, 33–40.

(425) Wagner, M. H. Analysis of Time-Dependent Non-Linear Stress-Growth Data for Shear and Elongational Flow of a Low-Density Branched Polyethylene Melt. *Rheologica Acta* **1976**, *15*, 136–142.

(426) Lodge, A. S. *Elastic Liquids: An Introductory Vector Treatment of Finite-Strain Polymer Rheology,* 1st.; Academic Press: New York; 1964.

(427) Rolón-Garrido, V. H. and Wagner, M. H. The Damping Function in Rheology. *Rheologica Acta* **2009**, *48*, 245–284.

(428) Wagner, M. H. and Meissner, J. Network Disentanglement and Time-Dependent Flow Behaviour of Polymer Melts. *Die Makromolekulare Chemie* **1980**, *181*, 1533–1550.

(429) Isono, Y. and Ferry, J. D. Stress Relaxation and Differential Dynamic Modulus of Polyisobutylene in Large Shearing Deformations. *Journal of Rheology* **1985**, *29*, 273–280.

(430) Graessley, W. W. Molecular Entanglement Theory of Flow Behavior in Amorphous Polymers. *The Journal of Chemical Physics* **1965**, *43*, 2696–2703.

(431) Marrucci, G. Dynamics of Entanglements: A Nonlinear Model Consistent with the Cox–Merz Rule. *Journal of Non-Newtonian Fluid Mechanics* **1996**, *62*, 279–289.

(432) Mead, D. W.; Larson, R. G.; and Doi, M. A Molecular Theory for Fast Flows of Entangled Polymers. *Macromolecules* **1998**, *31*, 7895–7914.

(433) Marrucci, G. and Grizzuti, N. Fast Flows of Concentrated Polymers: Predictions of the Tube Model on Chain Stretching. *Gazzetta Chimica Italiana* **1988**, *118*, 179–185.

(434) Pearson, D. S.; Kiss, A. D.; Fetters, L. J.; and Doi, M. Flow-Induced Birefringence of Concentrated Polyisoprene Solutions. *Journal of Rheology* **1989**, *33*, 517–535.

(435) Pearson, D. S.; Herbolzheimer, E.; Grizzuti, N.; and Marrucci, G. Transient Behavior of Entangled Polymers at High Shear Rates. *Journal of Polymer Science Part B: Polymer Physics* **1991**, *29*, 1589–1597.

(436) Marrucci, G. and Grizzuti, N. The Free Energy Function of the Doi–Edwards Theory: Analysis of the Instabilities in Stress Relaxation. *Journal of Rheology* **1983**, *27*, 433–450.

(437) Dealy, J. M. Official Nomenclature for Material Functions Describing the Response of a Viscoelastic Fluid to Various Shearing and Extensional Deformations. *Journal of Rheology* **1995**, *39*, 253–265.

(438) Halpin, . C. Nonlinear Rubberlike Viscoelasticity—A Molecular Approach. *Journal of Applied Physics* **1965**, *36*, 2975–2982.

(439) Smith, T. L. and Frederick, . E. Ultimate Tensile Properties of Elastomers. IV. Dependence of the Failure Envelope, Maximum Extensibility, and Equilibrium Stress-Strain Curve on Network Characteristics. *Journal of Applied Physics* **1965**, *36*, 2996–3005.

(440) Smith, T. L. and Dickie, R. A. Effect of Finite Extensibility on the Viscoelastic Properties of a Styrene–Butadiene Rubber Vulcanizate in Simple Tensile Deformations Up to Rupture. *Journal of Polymer Science Part A-2: Polymer Physics* **1969**, *7*, 635–658.

(441) Keller, A.; Pedemonte, E.; and Willmouth, F. M. Macro-Lattice From Segregated Amorphous Phases of a Three Block Copolymer. *Nature* **1970**, *225*, 538–539.

(442) Hamley, I. W. Structure and Flow Behaviour of Block Copolymers. *Journal of Physics: Condensed Matter* **2001**, *13*, R643–R671.

(443) Tarasov, S. G.; Tsvankin, D. Y.; and Godovskii, Y. K. The Structural Changes During the Deformation of Orientated and Isotropic Butadiene–Styrene Block Copolymers. *Polymer Science USSR* **1978**, *20*, 1728–1739.

(444) Honeker, C. C.; Thomas, E. L.; Albalak, R. J.; Hajduk, D. A.; Gruner, S. M.; and Capel, M. C. Perpendicular Deformation of a Near-Single-Crystal Triblock Copolymer

with a Cylindrical Morphology. 1. Synchrotron SAXS. *Macromolecules* **2000**, *33*, 9395–9406.

(445) Honeker, C. C. and Thomas, E. L. Perpendicular Deformation of a Near-Single-Crystal Triblock Copolymer with a Cylindrical Morphology. 2. TEM. *Macromolecules* **2000**, *33*, 9407–9417.

(446) Folkes, M. J. and Keller, A. The Birefringence and Mechanical Properties of a 'Single Crystal' from a Three-Block Copolymer. *Polymer* **1971**, *12*, 222–236.

(447) Smith, T. L. and Dickie, R. A. Viscoelastic and Ultimate Tensile Properties of Styrene–Butadiene–Styrene Block Copolymers. *Journal of Polymer Science Part C* **1969**, *26*, 163–187.

(448) Smith, T. L. Dependence of the Ultimate Properties of a GR-S Rubber on Strain Rate and Temperature. *Journal of Polymer Science* **1958**, *32*, 99–113.

(449) Smith, T. L. and Stedry, P. J. Time and Temperature Dependence of the Ultimate Properties of an SBR Rubber at Constant Elongations. *Journal of Applied Physics* **1960**, *31*, 1892–1898.

(450) Smith, T. L. Ultimate Tensile Properties of Elastomers. II. Comparison of Failure Envelopes of Unfilled Vulcanizates. *Journal of Applied Physics* **1964**, *35*, 27–32.

(451) Smith, T. L. Strength and Extensibility of Elastomers. In *Rheology: Theory and Applications, Vol. 5*; Eirich, F. R., Ed.; Academic Press: New York, 1969; pp 127–221.

(452) Smith, T. L. Strength of Elastomers. A Perspective. *Rubber Chemistry and Technology* **1978**, *51*, 225–252.

(453) Smith, T. L. Tensile Strength of Polyurethane and Other Elastomeric Block Copolymers. *Journal of Polymer Science: Polymer Physics Edition* **1974**, *12*, 1825–1848.

(454) Dealy, J. M. Do Polymeric Liquids Exhibit Strain Hardening? *Journal of Rheology* **1990**, *34*, 1133–1147.

(455) Wagner, M. H.; Bastian, H.; Hachmann, P.; Meissner, J.; Kurzbeck, S.; Münstedt, H.; and Langouche, F. The Strain-Hardening Behaviour of Linear and Long-

Chain-Branched Polyolefin Melts in Extensional Flows. *Rheologica Acta* **2000**, *39*, 97–109.

(456) *Atlas of Stress-Strain Curves,* ASM International: Materials Park, OH; 2002.

(457) Vinogradov, G. V.; Malkin, A. Y.; and Volosevitch, V. V. Some Fundamental Problems in Viscoelastic Behavior of Polymers in Shear and Extension. *Applied Polymer Symposium* **1975**, *27*, 47–59.

(458) Vinogradov, G. V.; Volosevitch, V. V.; Shatalov, V. P.; and Yudin, V. P. Flow, High-Elastic (Recoverable) Deformation, and Rupture of Uncured High Molecular Weight Linear Polymers in Uniaxial Extension. *Journal of Polymer Science: Polymer Physics Edition* **1975**, *13*, 1721–1735.

(459) Vinogradov, G. V. Viscoelasticity and Fracture Phenomenon in Uniaxial Extension of High-Molecular Linear Polymers. *Rheologica Acta* **1975**, *14*, 942–954.

(460) Malkin, A. Y. and Vinogradov, G. V. Fracture of Polymers in the Visco-Fluid State on Stretching. Review. *Polymer Science U.S.S.R.* **1985**, *27*, 245–257.

(461) Vinogradov, G. V. and Malkin, A. Y. *Rheology of Polymers: Viscoelasticity and Flow of Polymers,* Springer Berlin Heidelberg: Berlin; 2013.

(462) Malkin, A. Y. and Petrie, C. J. S. Some Conditions for Rupture of Polymer Liquids in Extension. *Journal of Rheology* **1997**, *41*, 1–25.

(463) Onogi, S.; Matsumoto, T.; and Kamei, E. Effects of Molecular Weight and Its Distribution on Fractural Behavior of Polystyrene. *Polymer Journal* **1972**, *3*, 531–537.

(464) Kamei, E. and Onogi, S. Extensional and Fractural Properties of Monodisperse Polystyrenes at Elevated Temperatures. *Applied Polymer Symposium* **1975**, *27*, 19–46.

(465) Petrie, C. J. S. *Elongational Flows: Aspects of the Behaviour of Model Elasticoviscous Fluids,* Pitman: London; 1979.

(466) Cogswell, F. N. Polymer Melt Rheology During Elongational Flow. *Applied Polymer Symposium* **1975**, *27*, 1–18.

(467) Marrucci, G. and Ianniruberto, G. Interchain Pressure Effect in Extensional Flows of Entangled Polymer Melts. *Macromolecules* **2004**, *37*, 3934–3942.

(468) McLeish, T. C. B. and Larson, R. G. Molecular Constitutive Equations for a Class of Branched Polymers: The Pom-Pom Polymer. *Journal of Rheology* **1998**, *42*, 81–110.

(469) Van der Hoff, B. M. E. and Buckler, E. J. Transient Changes in Topology and Energy on Extension of Polybutadiene Networks. *Journal of Macromolecular Science (Chemistry)* **1967**, *1*, 747–788.

(470) Meier, D. J. The Deformation of Block Copolymers and Filled Systems. *IUPAC 28th Macromol. Symp.* **1982**, p 698.

(471) Kovacs, A. J. Bulk Creep and Recovery in Systems with Viscosity Dependent Upon Free Volume. *Transactions of the Society of Rheology* **1961**, *5*, 285–296.

(472) Kovacs, A. J.; Stratton, R. A.; and Ferry, J. D. Dynamic Mechanical Properties of Polyvinyl Acetate in Shear in the Glass Transition Temperature Range. *The Journal of Physical Chemistry* **1963**, *67*, 152–161.

(473) Kovacs, A. J. Transition Vitreuse Dans Les Polymères Amorphes. Etude Phénoménologique. *Advances in Polymer Science* **1964**, *3*, 394–507.

(474) Kovacs, A. J.; Aklonis, J. J.; Hutchinson, J. M.; and Ramos, A. R. Isobaric Volume and Enthalpy Recovery of Glasses. II. A Transparent Multiparameter Theory. *Journal of Polymer Science: Polymer Physics Edition* **1979**, *17*, 1097–1162.

(475) Struik, L. C. E. Volume Relaxation in Polymers. *Rheologica Acta* **1966**, *5*, 303–311.

(476) Struik, L. C. E. Physical Aging in Amorphous Glassy Polymers. *Annals of the New York Academy of Sciences* **1976**, *279*, 78–85.

(477) Struik, L. C. E. Physical Aging in Amorphous Polymers and Other Materials. Ph.D. Thesis, Delft University of Technology, 1977.

(478) Tschoegl, N. W.; Knauss, W. G.; and Emri, I. Poisson's Ratio in Linear Viscoelasticity–a Critical Review. *Mechanics of Time-Dependent Materials* **2002**, *6*, 3–51.

(479) Ferry, J. D. and Stratton, R. A. The Free Volume Interpretation of the Dependence of Viscosities and Viscoelastic Relaxation Times on Concentration, Pressure, and Tensile Strain. *Kolloid-Zeitschrift* **1960**, *171*, 107–111.

(480) Schlögl, S.; Trutschel, M. -L.; Chassé, W.; Riess, G.; and Saalwächter, K. Entanglement Effects in Elastomers: Macroscopic vs Microscopic Properties. *Macromolecules* **2014**, *47*, 2759–2773.

(481) Mark, J. E. The Constants $2C_1$ and $2C_2$ in Phenomenological Elasticity Theory and Their Dependence on Experimental Variables. *Rubber Chemistry and Technology* **1975**, *48*, 495–512.

(482) Price, C. and Wolf, F. -P. Thermodynamics of Rubber Elasticity [and Discussion]. *Proceedings of the Royal Society of London. Series A: Mathematical, Physical and Engineering Sciences* **1976**, *351*, 331–350.

(483) Allen, G.; Charlesby, A.; Tabor, D.; and Welding, G. N. The Molecular Basis of Rubber Elasticity [and Discussion]. *Proceedings of the Royal Society of London. Series A: Mathematical, Physical and Engineering Sciences* **1976**, *351*, 381–396.

(484) Ferry, J. D. and Kan, H. -C. Interpretation of Deviations From Neo-Hookean Elasticity by a Two-Network Model with Crosslinks and Trapped Entanglements. *Rubber Chemistry and Technology* **1978**, *51*, 731–737.

(485) Heinrich, G.; Straube, E.; and Helmis, G. Rubber Elasticity of Polymer Networks: Theories. *Advances in Polymer Science* **1988**, *85*, 33–87.

(486) Heinrich, G. and Straube, E. On the Strength and Deformation Dependence of the Tube-Like Topological Constraints of Polymer Networks, Melts and Concentrated Solutions. I. The Polymer Network Case. *Acta Polymerica* **1983**, *34*, 589–594.

(487) Marrucci, G. A Mechanical Model for Rubbers Containing Entanglements. *Rheologica Acta* **1979**, *18*, 193–198.

(488) Marrucci, G. Rubber Elasticity Theory. A Network of Entangled Chains. *Macromolecules* **1981**, *14*, 434–442.

(489) Rubinstein, M. and Panyukov, S. Nonaffine Deformation and Elasticity of Polymer Networks. *Macromolecules* **1997**, *30*, 8036–8044.

(490) Erman, B. and Flory, P. J. Theory of Elasticity of Polymer Networks. II. The Effect of Geometric Constraints on Junctions. *The Journal of Chemical Physics* **1978**, *68*, 5363–5368.

(491) Flory, P. J. Molecular Theory of Rubber Elasticity. *Polymer* **1979**, *20*, 1317–1320.

(492) Flory, P. J. and Erman, B. Theory of Elasticity of Polymer Networks. 3. *Macromolecules* **1982**, *15*, 800–806.

(493) Rubinstein, M. and Panyukov, S. Elasticity of Polymer Networks. *Macromolecules* **2002**, *35*, 6670–6686.

(494) Roos, A. and Creton, C. Linear Viscoelasticity and Non-Linear Elasticity of Block Copolymer Blends Used As Soft Adhesives. *Macromolecular Symposia* **2004**, *214*, 147–156.

(495) Creton, C.; Roos, A.; and Chiche, A. Effect of the Diblock Content on the Adhesive and Deformation Properties of PSAs Based on Styrenic Block Copolymers. In *Adhesion – Current Research and Application*; Wiley-VCH Verlag, 2006; pp 337–363.

(496) Graessley, W. W. and Pearson, D. S. Stress-Strain Behavior in Polymer Networks Containing Nonlocalized Junctions. *The Journal of Chemical Physics* **1977**, *66*, 3363–3370.

(497) Vilgis, T. A. and Erman, B. Comparison of the Constrained Junction and the Slip-Link Models of Rubber Elasticity. *Macromolecules* **1993**, *26*, 6657–6659.

(498) Kilian, H. -G. and Vilgis, T. Fundamental Aspects of Rubber-Elasticity in Real Networks. *Colloid and Polymer Science* **1984**, *262*, 15–21.

(499) Vilgis, T. A. and Kilian, H. -G. The Van Der Waals-Network – a Phenomenological Approach to Dense Networks. *Polymer* **1984**, *25*, 71–74.

(500) Thirion, P. and Weil, T. Assessment of the Sliding Link Model of Chain Entanglement in Polymer Networks. *Polymer* **1984**, *25*, 609–614.

(501) Graessley, W. W. Elasticity and Chain Dimensions in Gaussian Networks. *Macromolecules* **1975**, *8*, 865–868.

(502) Washiyama, J.; Kramer, E. J.; and Hui, C. Y. Fracture Mechanisms of Polymer Interfaces Reinforced with Block Copolymers: Transition From Chain Pullout to Crazing. *Macromolecules* **1993**, *26*, 2928–2934.

(503) Knauss, W. G. Rupture Phenomena in Viscoelastic Materials. Ph.D. Thesis, California Institute of Technology, 1963.

(504) Bueche, F. and Halpin, J. C. Molecular Theory for the Tensile Strength of Gum Elastomers. *Journal of Applied Physics* **1964**, *35*, 36–41.

(505) Halpin, J. C. Fracture of Amorphous Polymeric Solids: Time to Break. *Journal of Applied Physics* **1964**, *35*, 3133–3141.

(506) Halpin, J. C. and Bueche, F. Fracture of Amorphous Polymeric Solids: Reinforcement. *Journal of Applied Physics* **1964**, *35*, 3142–3149.

(507) Halpin, J. C. Molecular View of Fracture in Amorphous Elastomers. *Rubber Chemistry and Technology* **1965**, *38*, 1007–1038.

(508) Halpin, J. C. and Polley, H. W. Observations on the Fracture of Viscoelastic Bodies. *Journal of Composite Materials* **1967**, *1*, 64–81.

(509) Morton, M.; McGrath, J. E.; and Juliano, P. C. Structure-Property Relationships for Styrene–Diene Thermoplastic Elastomers. *Journal of Polymer Science Part C* **1969**, *26*, 99–115.

(510) Bailey, J. *The Glass Industry* **1939**, *20*, 94.

(511) Eirich, F. R. and Smith, T. L. Molecular Mechanical Aspects of the Isothermal Rupture of Elastomers. In *Fracture: an Advanced Treatise*; Liebowitz, H., Ed.; Academic Press: New York, 1972; pp 104–469.

(512) Doublier, J. L. and Launay, B. Rheology of Galactomannan Solutions: Comparative Study of Guar Gum and Locust Bean Gum. *Journal of Texture Studies* **1981**, *12*, 151–172.

(513) Sanchez, C.; Renard, D.; Robert, P.; Schmitt, C.; and Lefebvre, J. Structure and Rheological Properties of Acacia Gum Dispersions. *Food Hydrocolloids* **2002**, *16*, 257–267.

(514) Yaseen, E. I.; Herald, T. J.; Aramouni, F. M.; and Alavi, S. Rheological Properties of Selected Gum Solutions. *Food Research International* **2005**, *38*, 111–119.

(515) Whitcomb, P. J. and Macosko, C. W. Rheology of Xanthan Gum. *Journal of Rheology* **1978**, *22*, 493–505.

(516) Andersen, L.; Wittorff, H.; Storey, R.; and Isaksen, A. Degradable Elastomers for Chewing Gum Base. *U.S. Patent 0156949* **2004.**

(517) Andersen, L.; Wittorff, H.; and Storey, R. Biodegradable Chewing Gum and Method of Manufacturing Such Chewing Gum. *U.S. Patent 0130250* **2008.**

(518) Morgret, L. D.; Haas, M. S.; Xia, X.; Hillmyer, M. A.; Martello, M. T.; Macosko, C.; Martinetti, L.; Bates, F. S.; Lee, S.; Bunczek, M.; and Greenberg, M. T. Chewing Gum Compositions. *U.S. Patent 048508* **2010.**

(519) Phillips, D.; Morgret, L. D.; Xia, X.; and Shen, C. Chewing Gums Having Improved Removability Based on Linear Viscoelastic Shear Rheology. *U.S. Patent 0269924* **2010.**

(520) Mestres, J. Modern Chewing Gum. In *Formulation and production of chewing and bubble gums*; Fritz, D., Ed.; Kennedy's Books: Loughton, Essex, 2006; pp 47–74.

(521) Fritz, D. Gum Formulation. In *Formulation and production of chewing and bubble gums*; Fritz, D., Ed.; Kennedy's Books: Loughton, Essex, 2006; pp 239–252.

(522) Estruch, R. A. Gum Base. In *Formulation and production of chewing and bubble gums*; Fritz, D., Ed.; Kennedy's Books: Loughton, Essex, 2006; pp 93–118.

(523) Steffe, J. F. *Rheological Methods in Food Process Engineering,* Freeman Press: East Lansing, MI; 1992.

(524) Anderson, K.; Throckmorton, G. S.; Buschang, P. H.; and Hayasaki, H. The Effects of Bolus Hardness on Masticatory Kinematics. *Journal of Oral Rehabilitation* **2002**, *29*, 689–696.

(525) Ewoldt, R. H.; Winter, P.; and McKinley, G. H. *MITlaos Version 2.1 Beta for MATLAB,* self-published: Cambridge, MA; 2007.

(526) Ewoldt, R. H.; Hosoi, A. E.; and McKinley, G. H. New Measures for Characterizing Nonlinear Viscoelasticity in Large Amplitude Oscillatory Shear. *Journal of Rheology* **2008**, *52*, 1427–1458.

(527) Rohm, H. and Weidinger, K. -H. Rheological Behaviour of Butter at Small Deformations. *Journal of Texture Studies* **1993**, *24*, 157–172.

(528) Aranguren, M. I.; Mora, E.; DeGroot Jr, J. V.; and Macosko, C. W. Effect of Reinforcing Fillers on the Rheology of Polymer Melts. *Journal of Rheology* **1992**, *36*, 1165–1182.

(529) Phan-Thien, N. and Safari-Ardi, M. Linear Viscoelastic Properties of Flour–Water Doughs at Different Water Concentrations. *Journal of Non-Newtonian Fluid Mechanics* **1998**, *74*, 137–150.

(530) Leibler, L.; Rubinstein, M.; and Colby, R. H. Dynamics of Reversible Networks. *Macromolecules* **1991**, *24*, 4701–4707.

(531) Ng, T. S. and McKinley, G. H. Power Law Gels at Finite Strains: The Nonlinear Rheology of Gluten Gels. *Journal of Rheology* **2008**, *52*, 417–449.

(532) Ng, T. S.; McKinley, G. H.; and Ewoldt, R. H. Large Amplitude Oscillatory Shear Flow of Gluten Dough: A Model Power-Law Gel. *Journal of Rheology* **2011**, *55*, 627–654.

(533) Lefebvre, J.; Pruska-Kedzior, A.; Kedzior, Z.; and Lavenant, L. A Phenomenological Analysis of Wheat Gluten Viscoelastic Response in Retardation and in Dynamic Experiments Over a Large Time Scale. *Journal of Cereal Science* **2003**, *38*, 257–267.

(534) Hyun, K.; Wilhelm, M.; Klein, C. O.; Cho, K. S.; Nam, J. G.; Ahn, K. H.; Lee, S. J.; Ewoldt, R. H.; and McKinley, G. H. A Review of Nonlinear Oscillatory Shear Tests: Analysis and Application of Large Amplitude Oscillatory Shear (LAOS). *Progress in Polymer Science* **2011**, *36*, 1697–1753.

(535) Cho, K. S.; Hyun, K.; Ahn, K. H.; and Lee, S. J. A Geometrical Interpretation of Large Amplitude Oscillatory Shear Response. *Journal of Rheology* **2005**, *49*, 747–758.

(536) Ewoldt, R. H. and Bharadwaj, N. A. Low-Dimensional Intrinsic Material Functions for Nonlinear Viscoelasticity. *Rheologica Acta* **2013**, *52*, 201–219.

(537) Bhattacharjee, P. K.; Oberhauser, J. P.; McKinley, G. H.; Leal, L. G.; and Sridhar, T. Extensional Rheometry of Entangled Solutions. *Macromolecules* **2002**, *35*, 10131–10148.

(538) Bach, A.; Almdal, K.; Rasmussen, H. K.; and Hassager, O. Elongational Viscosity of Narrow Molar Mass Distribution Polystyrene. *Macromolecules* **2003**, *36*, 5174–5179.

(539) Sentmanat, M.; Wang, B. N.; and McKinley, G. H. Measuring the Transient Extensional Rheology of Polyethylene Melts Using the SER Universal Testing Platform. *Journal of Rheology* **2005**, *49*, 585–606.

(540) Spiegelberg, S. H. and McKinley, G. H. Stress Relaxation and Elastic Decohesion of Viscoelastic Polymer Solutions in Extensional Flow. *Journal of Non-Newtonian Fluid Mechanics* **1996**, *67*, 49–76.

(541) McKinley, G. H. and Sridhar, T. Filament-Stretching Rheometry of Complex Fluids. *Annual Review of Fluid Mechanics* **2002**, *34*, 375–415.

(542) Clasen, C.; Plog, J. P.; Kulicke, W. -M.; Owens, M.; Macosko, C.; Scriven, L. E.; Verani, M.; and McKinley, G. H. How Dilute Are Dilute Solutions in Extensional Flows? *Journal of Rheology* **2006**, *50*, 849–881.

(543) Morgret, L. D. Science-Based Design of High-Performance Bubblegum. Ph.D. Thesis, Northwestern University, 2005.

(544) Treloar, L. R. G. *The Physics of Rubber Elasticity,* 3rd ed.; Clarendon Press: Oxford, U.K.; 2005.

(545) Mark, J. E. The Effect of Strain-Induced Crystallization on the Ultimate Properties of An Elastomeric Polymer Network. *Polymer Engineering and Science* **1979**, *19*, 409–413.

(546) Gisler, T.; Ball, R. C.; and Weitz, D. A. Strain Hardening of Fractal Colloidal Gels. *Physical Review Letters* **1999**, *82*, 1064.

(547) Fleissner, M. Elongational Flow of HDPE Samples and Bubble Instability in Film Blowing. *International Polymer Processing* **1988**, *2*, 229–233.

(548) Field, G. J.; Micic, P.; and Bhattacharya, S. N. Melt Strength and Film Bubble Instability of LLDPE/LDPE Blends. *Polymer International* **1999**, *48*, 461–466.

(549) Cassagnau, P. Melt Rheology of Organoclay and Fumed Silica Nanocomposites. *Polymer* **2008**, *49*, 2183–2196.

(550) Watanabe, H.; Sato, T.; Osaki, K.; Aoki, Y.; Li, L.; Kakiuchi, M.; and Yao, M. -L. Rheological Images of Poly(vinyl chloride) Gels. 4. Nonlinear Behavior in a Critical Gel State. *Macromolecules* **1998**, *31*, 4198–4204.

(551) Olson, G. B. Designing a New Material World. *Science* **2000**, *288*, 993–998.

(552) Cussler, E. L. and Moggridge, G. D. *Chemical Product Design,* 1st ed.; Cambridge University Press: Cambridge; New York; 2001.

(553) Frick, E. M. and Hillmyer, M. A. Synthesis and Characterization of Polylactide–*block*–Polyisoprene–*block*–Polylactide Triblock Copolymers: New Thermoplastic Elastomers Containing Biodegradable Segments. *Macromolecular Rapid Communications* **2000**, *21*, 1317–1322.

(554) Richardson, W. S. and Sacher, A. Infrared Examination of Various Polyisoprenes. *Journal of Polymer Science* **1953**, *10*, 353–370.

(555) Tanaka, Y.; Takeuchi, Y.; Kobayashi, M.; and Tadokoro, H. Characterization of Diene Polymers. I. Infrared and NMR Studies: Nonadditive Behavior of Characteristic Infrared Bands. *Journal of Polymer Science Part A-2: Polymer Physics* **1971**, *9*, 43–57.

(556) Gibbs, J. H. and DiMarzio, E. A. Nature of the Glass Transition and the Glassy State. *The Journal of Chemical Physics* **1958**, *28*, 373–383.

(557) Fox Jr, T. G. and Flory, P. J. Second-Order Transition Temperatures and Related Properties of Polystyrene. I. Influence of Molecular Weight. *Journal of Applied Physics* **1950**, *21*, 581–591.

(558) Abdel-Goad, M.; Pyckhout-Hintzen, W.; Kahle, S.; Allgaier, J.; Richter, D.; and Fetters, L. J. Rheological Properties of 1,4-Polyisoprene Over a Large Molecular Weight Range. *Macromolecules* **2004**, *37*, 8135–8144.

(559) Boyer, R. F. Dependence of T_g (K) on the Product of the Cohesive Energy Density (CED) and Chain Stiffness Parameter C_∞. *Macromolecules* **1992**, *25*, 5326–5330.

(560) Hoff, E. A. W.; Robinson, D. W.; and Willbourn, A. H. Relation Between the Structure of Polymers and Their Dynamic Mechanical and Electrical Properties. Part II. Glassy State Mechanical Dispersions in Acrylic Polymers. *Journal of Polymer Science* **1955**, *18*, 161–176.

(561) Gradshteyn, I. S. and Ryzhik, I. M. *Table of Integrals, Series, and Products,* Jeffrey, A. and Zwillinger, D., Ed.; 7th ed.; Academic Press: Burlington, MA; 2007.

(562) Olver, F. W. J.; Lozier, D. W.; Boisvert, R. F.; and Clark, C. W. *NIST Handbook of Mathematical Functions,* Olver, F. W. J.; Lozier, D. W.; Boisvert, R. F.; and Clark, C. W., Ed.; Cambridge University Press: New York; 2010.

(563) Olver, F. W. J.; Lozier, D. W.; Boisvert, R. F.; and Clark, C. W. *NIST Digital Library of Mathematical Functions. http://dlmf.nist.gov/,* Release 1.0.9 of 2014-08-29. Online Companion to (564).

*(*564) Mittag-Leffler, G. M. Sur La Représentation Analytique Dune Branche Uniforme Dune Fonction Monogène: Cinquième Note. *Acta Mathematica* **1905**, *29*, 101–181.

(565) Paris, R. B. Exponential Asymptotics of the Mittag–Leffler Function. *Proceedings of the Royal Society of London. Series A: Mathematical, Physical and Engineering Sciences* **2002**, *458*, 3041–3052.

(566) Weisstein, E. W. *From MathWorld – A Wolfram Web Resource. http://mathworld.wolfram.com/.*

*(*567) Podlubny, I. Mittag-Leffler Function. *MATLAB Central File Exchange. Http://www.mathworks.com/matlabcentral/fileexchange/8738-mittag-leffler-function.* Retrieved Sept 12, 2012.

(568) Podlubny, I. Fitting Data Using the Mittag-Leffler Function. *MATLAB Central File Exchange. Http://www.mathworks.com/matlabcentral/fileexchange/32170-fitting-data-using-the-mittag-leffler-function*. Retrieved Sept 12, 2012.

(569) Findley, W. N.; Lai, J. S.; and Onaran, K. *Creep and Relaxation of Nonlinear Viscoelastic Materials,* 2nd ed.; Dover: New York; 1989.

(570) Zimm, B. H. Dynamics of Polymer Molecules in Dilute Solution: Viscoelasticity, Flow Birefringence and Dielectric Loss. *The Journal of Chemical Physics* **1956**, *24*, 269–278.

(571) Leibniz, G. W. Letter From Hanover, Germany, September 30, 1695 to G. A. L"Hospital. *Leibnizen Mathematische Schriften* **1849**, *2*, 301–302.

(572) Debye, P. J. W. *Polar Molecules,* The Chemical Catalog Company, Inc.: New York; 1929.

(573) Zener, C. Internal Friction in Solids. I. Theory of Internal Friction in Reeds. *Physical Review* **1937**, *52*, 230.

(574) Zener, C. Internal Friction in Solids II. General Theory of Thermoelastic Internal Friction. *Physical Review* **1938**, *53*, 90.

(575) Hughes, B. D. *Random Walks and Random Environments,* Clarendon Press: Oxford; 1995.

(576) Vlad, M. O.; Metzler, R.; Nonnenmacher, T. F.; and Mackey, M. C. Universality Classes for Asymptotic Behavior of Relaxation Processes in Systems with Dynamical Disorder: Dynamical Generalizations of Stretched Exponential. *Journal of Mathematical Physics* **1996**, *37*, 2279–2306.

(577) Kobeko, P.; Kuvshinsky, E.; and Gurevitch, G. Elasticity of Amorphous Bodies. *Tech. Phys. USSR* **1937**, *4*, 622.

(578) Shlesinger, M. F.; Zaslavsky, G. M.; and Klafter, J. Strange Kinetics. *Nature* **1993**, *363*, 31–37.

(579) Klafter, J.; Shlesinger, M. F.; and Zumofen, G. Beyond Brownian Motion. *Physics Today* **1996**, *49*, 33–39.

(580) Pusey, P. N. Brownian Motion Goes Ballistic. *Science* **2011**, *332*, 802–803.

(581) Risken, H. *The Fokker–Planck Equation: Methods of Solution and Applications,* 2nd ed.; Springer-Verlag: Berlin; 1989.

(582) Einstein, A. Zur Theorie Der Brownschen Bewegung. *Annalen Der Physik* **1906**, *324*, 371–381.

(583) Wilson, K. G. Problems in Physics with Many Scales of Length. *Scientific American* **1979**, *241*, 158–179.

(584) Wilson, K. G. The Renormalization Group and Critical Phenomena. *Reviews of Modern Physics* **1983**, *55*, 583–600.

(585) Morton, M. *Advances in Chemistry Series* **1971**, *99*, 490.

(586) Adhikari, R.; Henning, S.; and Michler, G. H. Importance of Molecular Coupling for Mechanical Performance of Block Copolymer Compounds. *Macromolecular Symposia* **2010**, *294*, 55–66.

Appendix A

Synthesis, Molecular and Morphological Characterization, Differential Scanning Calorimetry, and Isochronal Viscoelastic Measurements

In this Appendix, synthesis, molecular and morphological characterization, differential scanning calorimetry, and isochronal viscoelastic measurements of the A–B–A thermoplastic elastomer investigated in Chapters 3, 4, and 5 are presented and discussed. Furthermore, a subtle phenomenon that can significantly bias extensional measurements in the proximity of glass transitions is examined.

A.1 Experimental Section

A.1.1 **Synthesis** (work performed by Sangwoo Lee)

The L–I–L triblock copolymer was synthesized following an established protocol[115,553] and kindly provided by Sangwoo Lee. The α,ω-dihydroxyl polyisoprene block (HO-PI-OH) was anionically polymerized in anhydrous cyclohexane (CHX) using a 3-triisopropylsilyloxy-1-propyllithium (TIPSOPrLi) protected initiator, while a triethylaluminum (AlEt3) catalyst was chosen for the polymerization of the poly(D,L-lactide) endblocks. The adopted synthetic scheme[553] yields model (i.e. narrow

polydispersities) materials free of diblock and homopolymer contaminations. The resulting triblock copolymer was precipitated in methanol to remove (ionic) impurities, freeze-dried from a benzene solution, and stored in a deep freezer until use.

A.1.2 Molecular Characterization (work performed by Sangwoo Lee)

Number-average molar mass and block composition (Chapter 3, Table 3.1) were assessed using proton nuclear magnetic resonance (^{1}H NMR) spectroscopy (Varian Inova 500), and size exclusion chromatography (SEC) (Hewlett-Packard 1100, using chloroform eluent) was performed to determine the polydispersity of the triblock copolymer. The distribution of chemical microstructures of the isoprene midblock (Chapter 3, Figure 3.1 and Table 3.1) was obtained by infrared and ^{1}H NMR measurements using well-known procedures[554,555].

A.1.3 Morphological Characterization (work performed by Sangwoo Lee)

The morphology of the L–I–L triblock copolymer, hereafter referred to as LIL50–12, was characterized using small-angle X-ray scattering (SAXS) and transmission electron microscopy (TEM) techniques. Specimens used for the SAXS data were prepared by pressure molding (radial flow) at 100 °C. SAXS experiments were conducted at Argonne National Laboratories (Argonne, IL) in Sector 5-ID-D maintained by the Dow–Northwestern–DuPont Collaborative Access Team (DND-CAT). The detector was a Mar CCD area detector with a 165 mm diameter, the sample to detector distance was 3.97 m, and the X-ray wavelength was 0.73 Å. Scattering data were collected at room

temperature, and azimuthally integrated to the one-dimensional form of intensity versus scattering wave vector, $q = (4\pi/\lambda)\cdot\sin(\theta/2)$, where λ and θ are the radiation wavelength and the scattering angle, respectively. Projected images of the triblock copolymer were obtained using TEM. Thin slices (≈ 70 nm) were prepared using a Reichert UltraCut S Ultramicrotome (Leica) at –80 °C, and contrast between the PI and PLA blocks was achieved by exposing samples to vapor from a 4% aqueous solution of osmium tetroxide (OsO_4) for approximately 10 min at room temperature. Micrographs were acquired at room temperature using a FEI Tecnai G^2 F30 field emission gun TEM operating at 300 kV and equipped with a Gatan 4k × 4k pixels Ultrascan CCD camera.

A.1.4 Calorimetry

Differential scanning calorimetry (DSC) was conducted on a TA Instruments Q-1000 to identify the presence of glass and/or crystalline transitions, and the following measurement protocol was employed. Samples, loaded at room temperature in hermetically sealed aluminum pans, were heated to 200 °C (above any suspected glass/melting transition) at 20 °C/min and held at this temperature for 2 min to erase memory of past thermal and mechanical histories. Samples were then cooled to –100 °C (below the PI glass transition, $T_g \approx$ –65 °C) at 10 °C/min, and a second heating scan to 200 °C at the same ramp rate begun immediately. Glass transitions were reported upon the second heating cycle, extracting the values of T_g from the inflection points of the thermal trace.

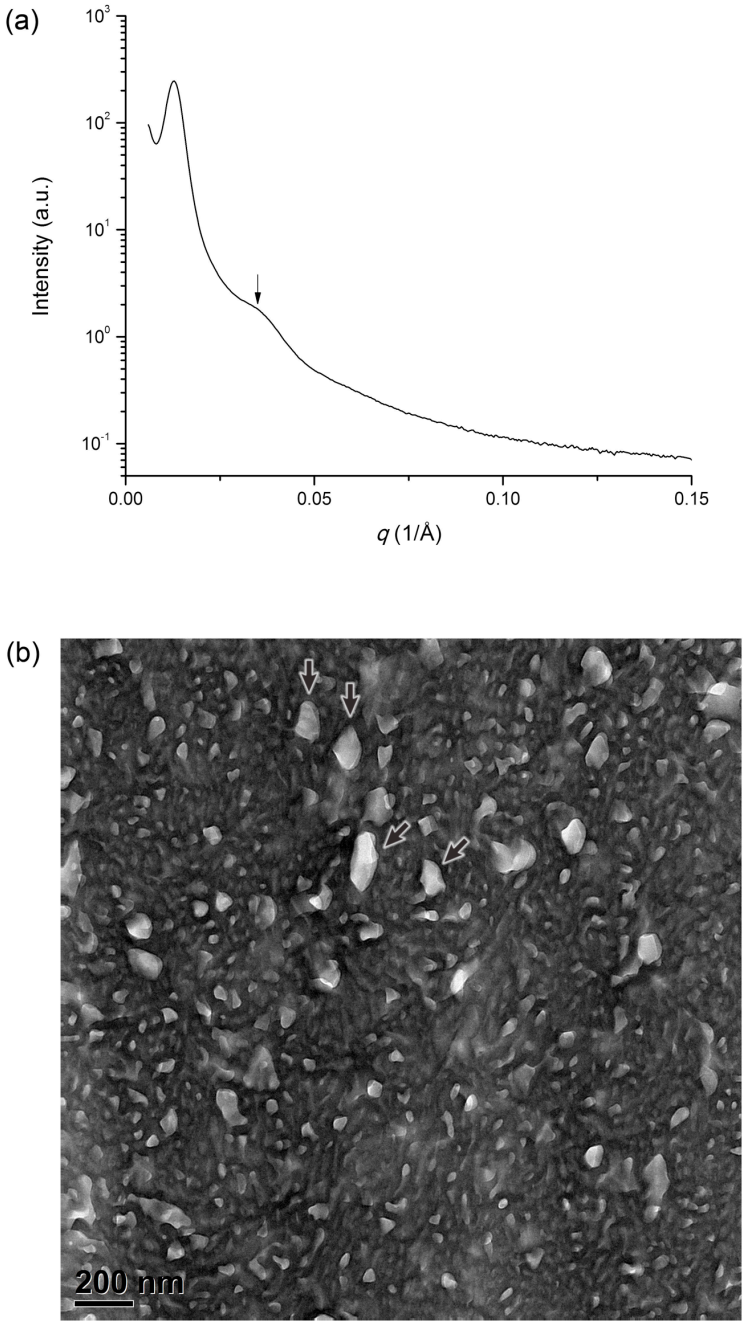

Figure A.1. (a) SAXS pattern and (b) representative TEM micrograph obtained from LIL50–12 (samples prepared by pressure molding and *radial* hydrodynamic flow).

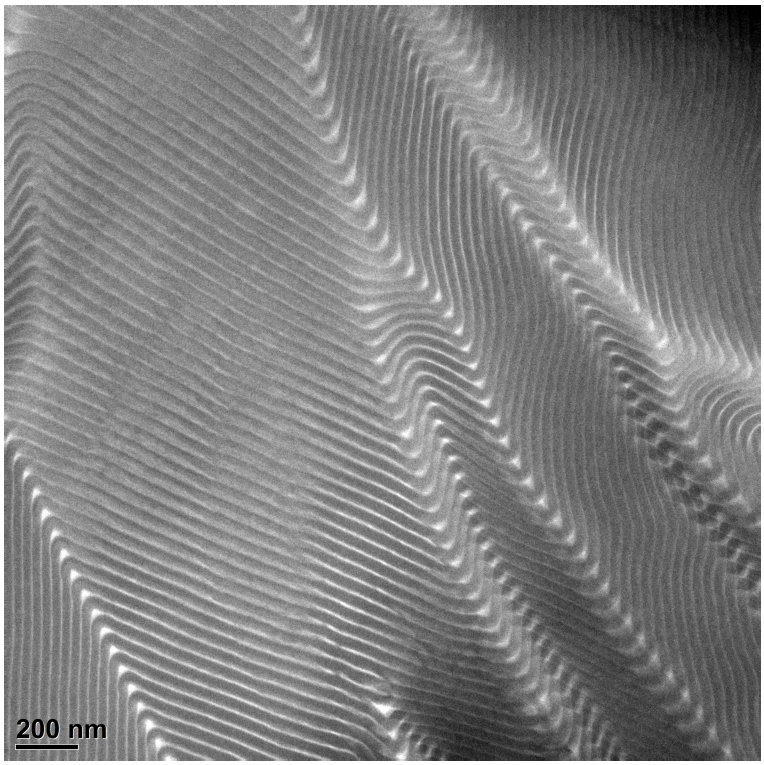

Figure A.2. Representative TEM micrograph obtained from LIL50–12 (samples prepared by solvent casting).

A.2 Results and Discussion

A.2.1 Morphology

The SAXS pattern of LIL50–12 is compatible with a lack of periodically ordered microdomains and long-range order (Figure A.1(a)). This interpretation is further supported by the TEM micrograph (Figure A.1(b)), displaying irregularly shaped microphase-segregated PLA domains (white regions) embedded in a PI-rich matrix. The domains size can be roughly estimated with the assumptions of spherical geometry, by

taking the shoulder feature marked by the arrow in Figure A.1(a) as the first maximum of the spherical form factor ($qR_s = 5.8$, where R_s is the sphere radius). This gives $R_s \approx 16$ nm, which is approximately 4 times larger than the radius of gyration of the unperturbed PLA block at 25 °C, $R_{g,L} \simeq 3.70$ nm (Chapter 3, Table 3.3), and thus suggests highly stretched PLA chains (consistent with the strong state of segregation of the system, $\chi\hat{N}$ (25 °C) $\simeq$ 436). Specimens used for SAXS and TEM were prepared using a different pressing procedure than specimens used for rheology. The pressure and thermal histories were almost identical ($P \approx 20$ atm, $T = 100$ °C, time ≈ 3–5 min), final sample thickness was similar as well (≈ 0.5 mm), but the imposed hydrodynamic flow was different: *radial* and *planar extension*-like (Chapter 3, §3.2.3), respectively. We do not believe this made any significant difference in terms of segregation and the attainment of thermodynamic equilibrium. However, it may have caused the irregularly shaped PLA domains to have different orientation and aspect ratio distributions.

In specimens prepared by solvent casting, TEM micrographs revealed the presence of cylindrical PLA domains (Figure A.2), in agreement with both the theoretical prediction for monodisperse and compositionally symmetric A–B–A triblock copolymers[121] and the strong segregation regime of the experimental I–L phase diagram[116] at this composition, $f_A = 0.25$.

A.2.2 Calorimetry

As expected from the mixed-microstructures of the PI and PLA blocks, no evidence of crystallinity was found from the thermal (DSC) analysis. The material appeared to be completely amorphous, and exhibited two second-order-like transitions consistent with a biphasic system comprised of PI-rich (T_g = –59.8 °C) and PLA-rich (T_g = 50.7 °C) domains.

It is informative to compare these block glass transitions with those that would be exhibited by the corresponding pure homopolymers. To this goal, the roles played by the chemical microstructure and the molar mass need to be considered. For undiluted PI, backbone and sidegroups flexibility depend on the distribution of configurational isomers. Accordingly, dilatometry experiments in the literature have shown that the glass transition of the homopolymer can range from about –70 °C for 100% *cis*-1,4 PI to about –58 °C for PI with all isomers in *trans*-1,4 configuration.[120] Therefore, PIs with mixed-microstructure will display a T_g somewhere in this range, as confirmed for example by the results of Gotro and Graessley[134], who measured (by DSC, extrapolating to zero heating rate) T_g = –67 °C for a 74% *cis*/18% *trans*/8% 3,4 polyisoprene. The PI glass transitions discussed thus far refer to homopolymer chains sufficiently long that the effect of their molar mass (M_n) can be neglected. The influence of chain length can be

understood in terms of free volume arguments, and it is usually[556,a] well-described by the equation proposed in 1950 by Fox and Flory[557], $T_g(M_n) = T_g(M_n \rightarrow \infty) - A/M_n$, where A is an empirical parameter related to the excess molar free volume associated with chain ends (acting as internal plasticizers). For a 1,4-PI, Abdel-Goad et al.[558] established $T_g(M_n \rightarrow \infty) = -66$ °C and $A = 18500$ deg·g/mol. Although the PI they studied does not match the distribution of configurational isomers of our PI blocks, both materials are the result of a prevalent (≃ 93%) 1,4 head-to-tail addition. Hence, based on their value of A and the length of our midblocks ($M_{n,I}$ = 49800 g/mol – Chapter 3, Table 3.1), it is plausible to assume that the glass transition temperature measured in our DSC experiment (–59.8 °C) was not affected by the PI molar mass and is close to the value at saturation (i.e. $T_g(M_n \rightarrow \infty) \approx -59.8$ °C). Considering the relative fractions of configurational isomers of the PI block (46.5% *cis*/46.5% *trans*/7% 3,4 – Chapter 3, Table 3.1) and the results reported by Gotro and Graessley[134] and Plazek and Ngai[120], we would expect, for a compositionally pure PI matrix, a glass transition probably in the neighborhood of –64 °C[224,b]. We then conclude that the increased PI-block glass transition with respect to a pure PI homopolymer is most likely to be attributed to partial inclusion of PLA chains in

---

[a] Deviations can occur at very low molar masses where the theory of Gibbs and DiMarzio[556], which concentrates on the conformational entropy, does a better job at fitting the experimental data.

[b] An estimate can be obtained by applying the Fox equation[224], $1/T_g = w_1/T_{g,1} + w_2/T_{g,,2}$, to a polyisoprene chain comprised of *cis*-1,4 (T_g = –70 °C) and *trans*-1,4 (T_g = –58 °C) configurational isomers.

the PI-rich microphase (i.e. despite the strong driving force towards segregation, $\chi\hat{N}$(25 °C) ≃ 436, a fraction of endblocks may still dwell outside PLA microdomains).

The tacticity of polylactides has a mild effect on their glass transition temperatures, and literature reports tend to agree on both the $T_g(M_n \rightarrow \infty)$ and A values determined from similar DSC measurements (at 10 °C/min heating rate). The glass transition at infinite molar mass has been shown to slightly decrease from 58–63 °C (0% D) to 54–57 °C (50% D) with decreasing stereo-regularity (i.e. increasing D content).[1,2,4] The underlying cause of this minor dependence from optical composition remains, however, unsettled. Although it is believed that both cohesive energy density (CED) and chain flexibility (C_∞) generally affect the T_g [120,559,c], some authors[2] hypothesized the latter to be the governing factor in the case of polylactides. Using the values reported by Jamshidi et al.[1], $T_g(M_n \rightarrow \infty)$ = 57 °C and A = 73000 deg·g/mol, application of the Fox–Flory equation[557] to the PLA block ($M_{n,L}$ = 11650 g/mol – Chapter 3, Table 3.1) predicts a glass transition of 50.7 °C, in excellent agreement with our DSC measurement. This analysis seems to suggest that LIL50–12 consists of nearly pure PLA domains embedded in a PI-rich matrix.

One additional comment is worth making. Since these glass transition temperatures were measured on heating after cooling (at the same rate) from above T_g, they emanate

---

[c] In semi-crystalline polymers, such as PDLA and PLLA, the T_g can also increase or decrease with the degree of crystallinity depending on the relative densities of the amorphous and crystalline phases.[120]

from a non-equilibrium condition and are more appropriately designated as *fictive temperatures*, T_f.[120]

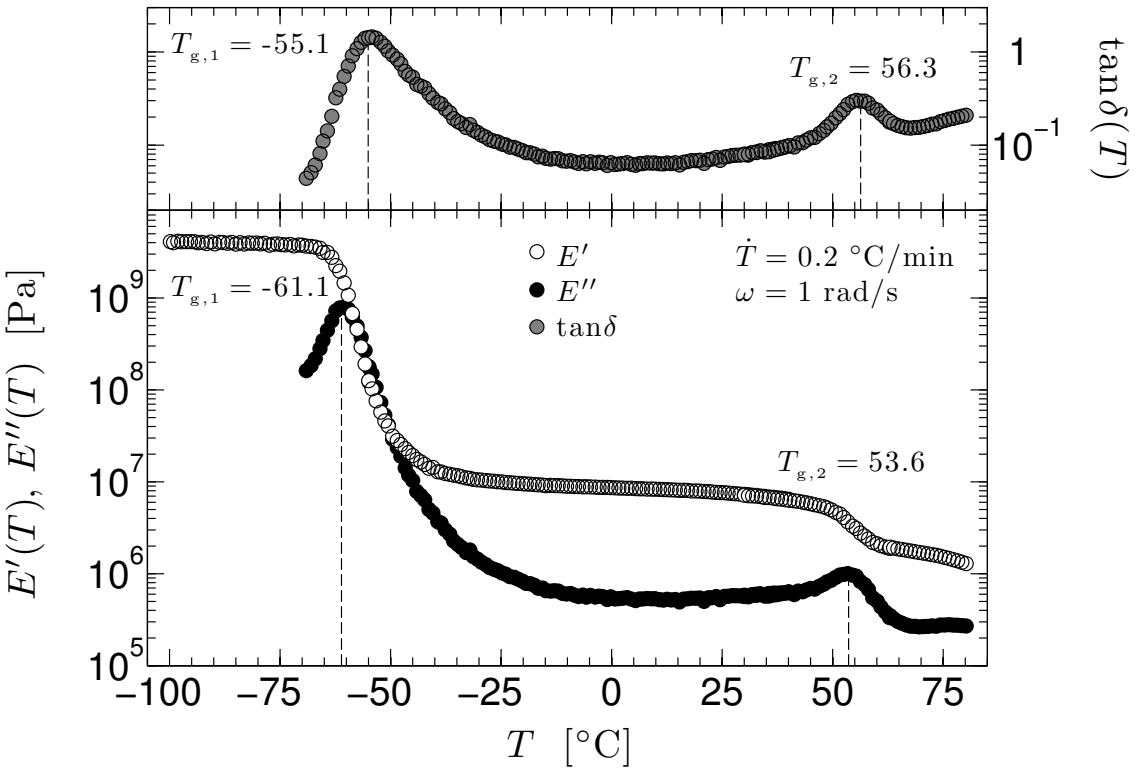

Figure A.3. Representative data of isochronal temperature ramp experiments performed on LIL50–12 at the angular frequency of 1 rad/s, upon cooling and heating at 0.2 °C/min.

A.2.3 Rheology

A.2.3.I Thermal behavior

The biphasic nature of the thermoplastic elastomer is evident in Figure A.3, which shows the results of two consecutive isochronal temperature ramps (on cooling from 80 °C and then heating, at 0.2 °C/min) conducted at a frequency of 1 rad/s.[d] The microphase-segregation of LIL50–12 is manifested in the appearance of two separate glass transitions[123] stemming from the PI-rich matrix and the embedded PLA domains, which thereby set the lower and upper bound (respectively) of the TPE service temperatures. Each microphase reveals its primary α relaxation[560] by a sudden change in the energy stored ($E'(T)$) and a local maximum in dissipation ($E''(T)$, $\tan\delta(T)$) over a relatively narrow (≈ 10–15 degrees) temperature span. Remarkably, no hysteresis is observed between the cooling and heating isochronal scans, indicating thermal as well as apparent dynamic equilibrium. It must be remembered, however, that while the block copolymer microstructure lacks thermodynamic equilibrium over the entire temperature window, voluminal equilibrium of the microphases is also lost below their respective T_g's. As usual, the locus of the loss modulus peak is close to the onset of the transition in the storage modulus, whereas the maximum in loss tangent roughly corresponds to the inflection point in $E'(T)$. We use the former to assign temperature values to the glass transitions ($T_{g,I}$ = –61.1 °C, $T_{g,L}$ = 53.6 °C) and note that these values are close to the

---

[d] Below –70 °C, the data of the loss functions are noisy and not reported for a more convenient plot.

fictive temperatures established by DSC ($T_{f,I}$ = –59.8 °C, $T_{f,L}$ = 50.7 °C). Considering the significant differences between the two experiments (i.e. quantities being measured, rates of temperature change, and sample thermal histories), this similarity seems to be fortuitous at best. Contrary to the DSC analysis, qualitative and semi-quantitative inspection of the curves in Figure A.3 yields some information about the topological structure of LIL50–12 and the associated dynamics.

A.2.3.I-a Thermal behavior for $T < T_{g,B}$

Below the glass transition of the entangled PI-rich matrix, all conformational rearrangements of polymer chain backbones are extremely slow and limited to local molecular motions that are oblivious of topological constraints (e.g. bending and stretching of chemical bonds, rotation of methyl groups, crankshaft and kink motions). As expected, the slight temperature dependence of the storage modulus in this region is indicative of enthalpic elasticity[22,23,42]. The material thus behaves like a linear elastic solid ($E'(\omega) \simeq const. = E_g$ and $E''(\omega) \to 0$) with a glassy modulus $E_g \simeq E'$(–100 °C, 1 rad/s) = 4 GPa. Since LIL50–12 is comprised for the most part (75 v%) of polyisoprene, it is instructive to compare its glassy modulus with that of pure PI homopolymer. Rubinstein and Colby[22] report for undiluted 1,4-PI a value of the shear glassy modulus $G_{g,PI}$ = 1.5 GPa. For isotropic viscoelastic materials, linear harmonic responses in shear and uniaxial extension can be interconverted through[150] $E^*(\omega) = 2[1+\mu^*(\omega)]G^*(\omega)$, which generally requires knowledge of the frequency-dependent Poisson's ratio, $\mu^*(\omega)$. However, in the

glassy state ($\omega \to \infty$, $t \to 0$) the imaginary component of $\mu^*(\omega)$ vanishes and Poisson's ratio can be approximated by a real constant, μ_g, which is often[42,150] around 1/3. We can then estimate the extensional glassy modulus of 1,4-PI as $E_{g,PI} = 2(1+\mu_g)G_{g,PI} \simeq (8/3)G_{g,PI}$ = 4 GPa, in excellent agreement with the measured E_g of LIL50–12. Implicit in the above calculation has been the use of the time-temperature superposition (TTS) principle. In composite systems like microphase-segregated block copolymers, its quantitative application (in simple form) is limited to a specific range of frequencies and temperatures[105,127,128] (Chapter 3, §3.3.4.III). Nevertheless, the underlying principle of corresponding states still holds that low-temperature properties (e.g. E_g) correspond to high-frequency ($\omega \to \infty$) or short-time ($t \to 0$) behavior.

A.2.3.I-b Thermal behavior for $T_{g,B} < T < T_{g,A}$

With increasing temperature, the entangled PI-rich matrix undergoes a transition from glass-like to rubber-like consistency as segmental motions of the PI chains governed by the monomeric friction coefficient ($\zeta_{0,PI}$) become progressively "unfrozen". This acceleration of the rate of structural rearrangement (at length scales comparable to the statistical size of the PI monomer, b_I(0 °C) ≃ 0.6 nm – Chapter 3, Table 3.3) becomes evident in the measurements by a drop in $E'(T)$ and a rapid increase in both $E''(T)$ and tan$\delta(T)$ when the related relaxation processes of the PI backbones can occur within 1 s

(i.e. the reciprocal of the applied angular frequency)[23,e]. As normally observed in amorphous polymers[42], the loss tangent in the transition zone is in the neighborhood of $\tan\delta(T) \approx 1$. While the increase in the loss functions reflects a dissipative mechanism previously not available at lower temperatures, their subsequent drop is the signature of a network structure that temporarily impedes further relaxation[42]. The presence of a polymeric network is also suggested by the relative magnitudes of the dynamic moduli ($E''(T) < E'(T)$) and their weak temperature dependence, based on the behavior commonly seen in entangled or lightly crosslinked polymers[42].

The width of the transition, measured by the sharpness of the loss tangent peak, is known to correlate with the steepness of the relaxation spectrum in the transition zone.[42] Consequently, the relatively broad region of temperature scale (≈ 45 degrees) associated with $T_{g,I}$ indicates a relatively broad distribution of segmental relaxation times. Since the molecular characterization of LIL50–12 showed nearly monodisperse blocks, this might be explained by partial inclusion of PLA chains in the PI matrix. This hypothesis is in agreement with the conclusions drawn from the analysis of the DSC measurements. The extent of the transition on the temperature scale is also affected by the rate of change of the segmental relaxation times in this region.[42] Application of the Williams-Landel-Ferry (WLF) equation[138] shows that (Chapter 3, §3.3.4.III-b), in close proximity to $T_{g,I}$, the PI segmental relaxation times decrease by about a factor of 10 for each 3.6 degrees increase

---

[e] For comparison, the same relaxation processes occur within ≈ 7 ns at 0 °C (Chapter 3, Table 3.8).

in temperature.[45] Incidentally, this also implies that the locus of the loss functions peak would shift by about 3.6 degrees with a change in time scale (i.e. heating/cooling rate) of a factor of 10.[42]

The range of magnitudes of the storage modulus across $T_{g,I}$ (≈ 4 GPa – 10 MPa) is controlled by the density of network junctions, and in particular it would narrow with increasing density of physical or chemical constraints.[42] In analogy with the analysis of the glassy response, we can compare the plateau modulus of LIL50–12 (E_N) with that of a pure and entangled PI matrix ($E^0_{N,PI}$). The storage modulus of LIL50–12 remains rather flat over a wide temperature range (≈ 80 degrees), and we can select E'(0 °C, 1 rad/s) = 8.65 MPa ≈ E_N(0 °C) as representative of the rubbery plateau response. An accurate determination of the plateau modulus of LIL50–12 at 0 °C requires a detailed assessment of the associated dynamics and, in particular, knowledge of the path equilibration time at this temperature, $2\tau_R$(0 °C) (Chapter 3, §3.3.4.IV-d). This is discussed in Chapter 3, and for the present purpose we use the above value as an approximation. However, albeit the time scale of the isochronal measurement (1 s) overestimates $2\tau_R$(0 °C) by about 2 orders of magnitude (Chapter 3, Table 3.8), the more precise value of E_N(0 °C) (9.4 MPa) only adds merit to the following analysis. For undiluted 1,4-PI (7% 3,4), the shear plateau modulus is $G^0_{N,PI}$ = 0.35 MPa at 25 °C (Chapter 3, Table 3.4). In the equilibrium state ($\omega \to 0$, $t \to \infty$), the imaginary component of $\mu^*(\omega)$ vanishes and Poisson's ratio can again be approximated by a real constant, μ_{eq}. Under this condition, materials are often termed "incompressible" or "soft elastic" as they tend to display a bulk modulus K_{eq}

much greater than the shear modulus G_{eq}, causing the change in volume to become negligible in comparison with the change in shape and Poisson's ratio to approach the "ideal" value of 1/2.[42,150] Therefore, we can calculate the extensional plateau modulus of 1,4-PI at 25 °C as $E^0_{N,PI} = 2(1+\mu_{eq})\,G^0_{N,PI} \simeq 3G^0_{N,PI} = 1.05$ MPa. Taking into account the mild temperature dependence of entropic elasticity ($\sim \rho T$) gives $E^0_{N,PI}(0\ °C) = 0.98$ MPa, which is about 9 times smaller than the estimated $E_N(0\ °C)$ of LIL50–12 (cf. Chapter 3, §3.3.4.IV-e). Clearly, the material does not behave simply like an entangled PI-rich matrix. This large difference is attributed to the additional network junctions arising from the anchoring effect (physical endlinking) of the glassy PLA domains on the PI chain ends. While the augmented number of network junctions is analogous to what would result from increasing the entanglement density or inducing chemical crosslinking in the PI matrix, the major contribution to the increase of the PI plateau modulus comes from the filler effect of the PLA domains (acting as pseudo-rigid occupiers of space just like filler particles) (cf. Chapter 3, §3.3.4.IV-e).

An additional feature emerges by closer examination of the behavior of LIL50–12 at service temperatures ($T_{g,I} < T < T_{g,L}$) shown in Figure A.3. The temperature dependence of the storage modulus associated with entropic elasticity of the PI chains is concealed by the labile character of the network junctions (both PI entanglements and PLA domains), which become less effective with increasing temperature. Above $T_{g,I}$, the material thus regains its viscoelastic character (i.e. frequency-dependent moduli $E'(\omega)$ and $E''(\omega)$), and at service temperatures behaves similarly to a filled and entangled PI-rich rubber.

A.2.3.I-c Thermal behavior for $T > T_{g,A}$

As the temperature is increased still further, segmental motions of the PLA chains governed by the monomeric friction coefficient ($\zeta_{0,PLA}$) accelerate and eventually can relax the stress within 1 s over length scales comparable to the statistical size of the PLA monomer (b_L(25 °C) ≃ 0.7 nm – Chapter 3, Table 3.3). As a result of this additional dissipative mechanism, the storage modulus drops to a lower level while the loss functions increase and tan$\delta(T)$ falls again within the range (≈ 0.2–3) usually observed in amorphous polymers in the transition zone[42]. The following decrease of $E''(T)$ and tan$\delta(T)$, coupled with the relative magnitudes of the dynamic moduli ($E''(T) < E'(T)$), are unequivocal manifestations of a network structure that persists after the PLA domains have lost their glass-like consistency (hence, their ability to act as space-filling physical endlinks for the PI chains). In principle, this behavior could result from topological constraints in either microphase (or both). However, considering that the PLA chains are only slightly entangled ($M_n/M_C \approx 1.4$, $Z \simeq 3.7$ – Chapter 3, §3.3.3 and Table 3.4), we attribute this polymeric network mainly to the entangled PI-rich matrix. This conclusion can be further supported by comparing the pseudo-equilibrium plateau modulus of LIL50–12 (E_N^0) with that of an entangled PI homopolymer, at a temperature well above the PLA block glass transition. For this purpose, we can consider the response of the material at 80 °C, E'(80 °C, 1 rad/s) = 1.30 MPa, as an approximation of its pseudo-

equilibrium plateau modulus at the same temperature[f] (i.e. $E_N^0(80\ °C) \approx 1.30$ MPa). Following the same arguments as before, we calculate the extensional pseudo-equilibrium plateau modulus of undiluted 1,4-PI at 80 °C as $E_{N,PI}^0 = 1.20$ MPa. Bearing in mind the approximations involved in this analysis, these results suggest that the viscoelastic response of LIL50–12 above $T_{g,L}$ (and at a time scale of 1 s) is primarily due to the entangled PI-rich microphase[g].

Moreover, by examining the sharpness of the loss tangent peak associated with $T_{g,L}$, the width of this transition appears relatively narrow (spanning about 20 degrees on the temperature scale). This observation is consistent with the hypothesis that nearly monodisperse PLA chains (as evidenced by the molecular characterization) have microphase-segregated into almost pure PLA domains (as expected by the strong segregation of LIL50–12), which would hence exhibit a fairly narrow distribution of segmental relaxation times. This hypothesis is further corroborated by the DSC results, as previously discussed.

---

[f] At 0 °C, $2\tau_R$ is about 7.6 ms (Chapter 3, Table 3.8). Therefore, at 80 °C the time scale of the isochronal measurement (1 s) greatly overestimates $2\tau_R$.

[g] At temperatures above both T_g's and at *low enough* frequencies (i.e. large time and length scales) the underlying state of order becomes the dominant factor that dictates the viscoelastic response of block copolymer TPEs.[98,101,103,105,107-109] The frequency (1 rad/s) of the isochronal measurement falls within the time scales of entanglement-dominated dynamics (Chapter 3, §3.1.2 and §3.3.4.III).

A.2.3.II The effect of extensional strains near T_g

A subtle phenomenon that can significantly bias extensional measurements in the proximity of glass transitions is noteworthy. When a material is subjected to an extensional deformation both its shape and volume are affected. Polymeric systems can usually be treated as if they were "incompressible" (i.e. $\mu^*(\omega) \simeq \mu_{eq} \simeq 1/2$) over a wide range of time and temperature scales as mentioned earlier. However, when a polymer approaches glass-like consistency its Poisson's ratio decreases (i.e. $\mu^*(\omega) \simeq \mu < 1/2$) and lateral contractions (or expansions, in compression) cause a non-negligible change in volume. This behavior is of course exacerbated at or below the glass transition when Poisson's ratio assumes its minimum value ($\mu_g \simeq 1/3$). When a glass-like polymer is tested in uniaxial extension, a portion of its volume increase determines an expansion of free volume. Although a rather vaguely defined concept, the free volume is widely believed in polymer science to be the main parameter controlling (at any temperature) the rate of molecular mobility and the associated transport phenomena (e.g. diffusion).[42] Consequently, an expansion of free volume upon application of an extensional strain will inevitably produce an acceleration of all relaxation times[h]. Ferry[42] estimated that, near or below T_g, an extensional strain of just 1% causes about a 90% acceleration of the segmental relaxation times (i.e. a shift of about one logarithmic decade on the time scale). Following his approach, we assessed the magnitude of this phenomenon in our

---

[h] This is the underlying cause of the intrinsic strong nonlinearity of polymers bulk viscoelasticity.

measurements, which amounts to an acceleration of the PI segmental relaxation times of about 4% in the region below –60 °C (0.03% strain amplitude – Chapter 3, §3.2.2) and less than about 10% in the region from –60 °C to –50 °C (0.07% strain amplitude – Chapter 3, §3.2.2). Although measurements around the PLA glass transition were conducted with a larger strain amplitude (0.5%), it is reasonable to assume that the rubbery PI-rich matrix took up the vast majority of the macroscopically applied strain, thus causing no change in the PLA segmental relaxation times.

Appendix B

Integral Transforms

This Appendix attempts a short review of the integral transforms used or referenced to in the main body and other Appendices of this dissertation. It should by no means be considered an exposition of the subject; it is meant to serve simply as an introduction to the notation used and as a handy reference. Theorems and formulae are stated without proof, in the form in which they are applicable in the context of the dissertation. The following material is largely based on the work of Tschoegl[150], Gradshteyn and Ryzhik[561], and Olver et al.[562,563].

B.1 Introduction

Suppose $f(t)$ is a real- or complex-valued function and s is a real or complex parameter. Then $F(s)$ an *integral transform* of $f(t)$ if:[150]

$$F(s) = \int_0^\infty f(t)K(t,s)dt \qquad t,s \in \mathbb{R} \vee \mathbb{C} \tag{B.1}$$

and $F(s)$ exists. The given function $f(t)$ is called the *source function*, s is the *transform variable*, $K(t,s)$ is the *kernel function*, and $F(s)$ is the *image function*.

B.2 The Laplace Transform

B.2.1 Definition

The (one-sided or unilateral) *Laplace transform* of a real-valued function $f(t)$ defined on $[0, \infty)$ is:[150,561-563]

$$\overline{f}(s) = \int_0^{\infty} f(t) e^{-st}\, dt \qquad t \in \mathbb{R},\ s \in \mathbb{C},\ \mathrm{Re}(s) > 0 \tag{B.2}$$

Alternative notations are $\mathcal{L}[f(t);\, s]$, $\mathcal{L}[f(t)]$, or $\mathcal{L}\, f(t)$. The *source function* $f(t)$ and the *image function* $\overline{f}(s)$ are said to be in the *time domain* and in the *complex domain*, respectively.[150]

B.2.2 Inversion

The *inverse Laplace transform* is:[150,561-563]

$$f(t) = \frac{1}{2\pi i} \int_{c-i\infty}^{c+i\infty} \overline{f}(s) e^{+st}\, ds \qquad t, c \in \mathbb{R},\ s \in \mathbb{C} \tag{B.3}$$

where c is a real constant that exceeds the real part of all the singularities of $\overline{f}(s)$. Alternative notations are $\mathcal{L}^{-1}\left[\overline{f}(s);\, t\right]$, $\mathcal{L}^{-1}\left[\overline{f}(s)\right]$, or $\mathcal{L}^{-1}\,\overline{f}(s)$.

B.2.3 Properties

Linearity:[150,561-563]

$$\mathcal{L}\left[af(t) + bg(t)\right] = a\overline{f}(s) + b\overline{g}(s) \tag{B.4}$$

Translation:[150,561-563]

$$\begin{aligned} &\mathcal{L}\, f(t)h(t) = \overline{f}(s) \\ &\mathcal{L}\, f(t-t')h(t-t') = \overline{f}(s)e^{-t's} \\ &\mathcal{L}\, f(t)e^{-at} = \overline{f}(s+a) \end{aligned} \tag{B.5}$$

where $h(t)$ denotes the Heaviside unit step function.

Real differentiation:[150,561-563]

$$\begin{aligned}
&\mathcal{L}\ \frac{d}{dt}f(t) = s\overline{f}(s) - f(0)\\
&\mathcal{L}\ \frac{d^2}{dt^2}f(t) = s^2\overline{f}(s) - sf(0) - f'(0)\\
&\dots\\
&\mathcal{L}\ \frac{d^n}{dt^n}f(t) = s^n\overline{f}(s) - s^{n-1}f(0) - s^{n-2}f'(0) - \dots - f^{(n-1)}(0)
\end{aligned} \tag{B.6}$$

with[150]

$$\mathcal{L}^{-1}\ s\overline{f}(s) = \frac{df(t)}{dt} + f(0)\delta(t) \tag{B.7}$$

Real integration:[150,561-563]

$$\begin{aligned}
&\mathcal{L}\ \int_0^t f(u)\,du = \frac{\overline{f}(s)}{s}\\
&\left.\begin{aligned}
&\mathcal{L}\ \int_0^t\int_0^v f(u)\,du\,dv\\
&\mathcal{L}\ \int_0^t uf(t-u)\,du\\
&\mathcal{L}\ \int_0^t (t-u)f(u)\,du
\end{aligned}\right\} = \frac{\overline{f}(s)}{s^2}\\
&\dots
\end{aligned} \tag{B.8}$$

Therefore, for *zero initial conditions* $f(0) = f'(0) = \dots = f^{(n-1)} = 0$,

$$\mathcal{L}\ \frac{d^n}{dt^n}f(t) = s^n\overline{f}(s) \qquad n \in \mathbb{Z} \tag{B.9}$$

where d^n/dt^n denotes the ordinary n^{th} order derivative or the ordinary n^{th} order integral (i.e. Cauchy's multiple integral) depending on whether $n > 0$ or $n < 0$, respectively.

The *Laplace convolution* $(f * g)$ of two functions $f(t)$ and $g(t)$ defined on $[0, \infty)$ is:[561-563]

$$\begin{aligned}(f*g)(t) &= \int_0^t f(t-u)g(u)\,du \\ &= \int_0^t f(t)g(t-u)\,du \\ &= (g*f)(t)\end{aligned} \tag{B.10}$$

then[150,561-563]

$$\mathcal{L}\ (f*g)(t) = \overline{f}(s)\overline{g}(s) \tag{B.11}$$

and[150]

$$\left.\begin{array}{l}\mathcal{L}\left[f(0)g(t)+\int_0^t \frac{df(u)}{du}g(t-u)\,du\right] \\ \mathcal{L}\left[f(0)g(t)+\int_0^t \frac{df(t-u)}{d(t-u)}g(u)\,du\right] \\ \mathcal{L}\left[f(t)g(0)+\int_0^t f(t-u)\frac{dg(u)}{du}\,du\right] \\ \mathcal{L}\left[f(t)g(0)+\int_0^t f(u)\frac{dg(t-u)}{d(t-u)}\,du\right]\end{array}\right\} = s\overline{f}(s)\overline{g}(s) \tag{B.12}$$

Initial value theorem:[150]

$$\lim_{t\to 0} f(t) = \lim_{s\to\infty} s\overline{f}(s) = f(0) \tag{B.13}$$

Final value theorem:[150]

$$\lim_{t\to\infty} f(t) = \lim_{s\to 0} s\overline{f}(s) = f(\infty) \tag{B.14}$$

B.2.4 Laplace Transform Pairs

The Laplace transform pairs relevant to this dissertation are contained in Table B.1. When referenced, they will be identified as LTP followed by the number under which they are listed below.

Table B.1. Laplace transform pairs.[150,371,561]

$f(t)$	$\bar{f}(s)$	No.
$\delta(t-a)$	$\exp(-as)$	(1)
$h(t-a)$	$\frac{1}{s}\exp(-as)$	(2)
$p(t-a)$	$\frac{1}{s^2}\exp(-as)$	(3)
$t^n \exp(at)$	$\frac{\Gamma(n+1)}{(s-a)^{n+1}}$ for $n>-1$	(4)
$\exp(-t/a)$	$\frac{a}{1+as}$	(5)
$1-\exp(-t/a)$	$\frac{1}{s(1+as)}$	(6)
$[1-\exp(-t/a)]/t$	$\ln(1+1/as)$	(7)
$\delta(t)-a^{-1}\exp(-t/a)$	$\frac{as}{1+as}$	(8)
$\exp[(a+ib)t]$	$\frac{1}{(s-a)-ib}$	(9)
$\sin(at)$	$\frac{a}{s^2+a^2}$	(10)
$\cos(at)$	$\frac{s}{s^2+a^2}$	(11)
$\gamma(m, t/a)\, t^{-m}$	$s^{m-1}\mathrm{B}_{\mathrm{T}}(m, 1-m; 1/as)$	(12)
$t^{b-1}E_{a,b}(ct^a)$	$\frac{1}{s^b(1-cs^{-a})}$	(13)

$\delta(t)$ is the delta (or unit impulse) function, $h(t)$ is the Heaviside unit step function, and $p(t)$ is the slope function (Appendix D); $\Gamma(m)$ is the complete gamma function, $\gamma(m, x)$ is the lower incomplete gamma function, $\mathrm{B}_{\mathrm{T}}(p, q; x)$ is the incomplete beta function, and $E_{a,b}(x)$ is the generalized Mittag-Leffler function (Appendix C).

B.3 The Fourier Transform

B.3.1 Definition

The (one-sided or unilateral) *Fourier transform* of a real-valued function $f(t)$ defined on $[0, \infty)$ is:[150]

$$f^*(\omega) = \int_0^\infty f(t) e^{-i\omega t}\, dt \qquad t, \omega \in \mathbb{R} \tag{B.15}$$

Alternative notations are $\mathcal{F}[f(t); i\omega]$, $\mathcal{F}[f(t)]$, or $\mathcal{F}\, f(t)$. Separating the real and imaginary part of $e^{-i\omega t}$ we may further define:[150]

$$f^*(\omega) = f'(\omega) - if''(\omega) \tag{B.16}$$

where

$$f'(\omega) = \int_0^\infty f(t) \cos(\omega t)\, dt \qquad t, \omega \in \mathbb{R} \tag{B.17}$$

is the *Fourier cosine transform* (also denoted as $\mathcal{F}_c[f(t); \omega]$, $\mathcal{F}_c[f(t)]$, or $\mathcal{F}_c f(t)$), and

$$f''(\omega) = \int_0^\infty f(t) \sin(\omega t)\, dt \qquad t, \omega \in \mathbb{R} \tag{B.18}$$

is the *Fourier sine transform* (also denoted as $\mathcal{F}_s[f(t); \omega]$, $\mathcal{F}_s[f(t)]$, or $\mathcal{F}_s f(t)$). The image functions $f^*(\omega)$, $f'(\omega)$, and $f''(\omega)$ are said to be in the *frequency domain*.[150] From Eqs. (B.2) and (B.15), it follows that the Laplace transform may be considered to be a Fourier transform of a function which has been multiplied by the *integrating factor* $\exp[\mathrm{Re}(s)t]$ to insure convergence of the integral. Conversely, the Fourier transform may be regarded as a Laplace transform in which the transform variable s is purely imaginary.[150]

B.3.2 Inversion

The *inverse Fourier transform* is:[150]

$$f(t) = \frac{1}{2\pi} \int_{-\infty}^{+\infty} f^*(\omega) e^{+i\omega t}\, d\omega \qquad t, \omega \in \mathbb{R} \tag{B.19}$$

where the normalization constants in front of the integrals (in Eqs. (B.15) and (B.19)) can take any form as long as their product is $1/2\pi$.[150] Alternative notations are $\mathcal{F}^{-1}[f^*(\omega); t]$, $\mathcal{F}^{-1}[f^*(\omega)]$, or $\mathcal{F}^{-1}\, f^*(\omega)$. A special situation arises when the corresponding Laplace transform $\overline{f}(s)$ is a rational algebraic function. In this case, it is possible to show that[150]

$$\begin{aligned} f(t) &= \frac{2}{\pi} \int_0^{\infty} f'(\omega) \cos(\omega t)\, d\omega \\ &= \frac{2}{\pi} \int_0^{\infty} f''(\omega) \sin(\omega t)\, d\omega \end{aligned} \tag{B.20}$$

B.4 The Generalized Fourier Transform

B.4.1 Definition

The (one-sided or unilateral) *generalized Fourier transform* of a real-valued function $f(t)$ defined on $[0, \infty)$ is:[150]

$$\begin{aligned} f^*(\omega) &= \lim_{\mathrm{Re}(s) \to 0} \int_0^{\infty} f(t) e^{-st}\, dt \qquad t \in \mathbb{R},\ s \in \mathbb{C},\ \mathrm{Im}(s) = \omega \\ &= \overline{f}(s)\Big|_{s = i\omega} \end{aligned} \tag{B.21}$$

Thus, the generalized Fourier transform is obtained by replacing the transform variable s of the Laplace transform by its imaginary part $i\omega$.

B.5 The Stieltjes Transform

B.5.1 Definition

The *Stieltjes transform* of a real-valued function $f(t)$ is:[150,562,563]

$$\tilde{f}(s) = \int_0^\infty \frac{f(t)}{s+t} dt \qquad t \in \mathbb{R},\ s \in \mathbb{C},\ \mathrm{Re}(s) > 0 \tag{B.22}$$

Alternative notations are $\mathcal{S}[f(t);\ s]$, $\mathcal{S}[f(t)]$, or $\mathcal{S}\ f(t)$. If the integral converges, then it converges uniformly in any compact domain in the complex plane not containing any point of the interval $(-\infty, 0]$. In this case, $\mathcal{S}[f(t);\ s]$ represents an analytic function in the s-plane cut along the negative real axis.[562,563] Let s be:

$$\begin{aligned} s &= -x \pm iy \qquad x, y \in \mathbb{R}^+ \\ &= |s| \exp(\pm i\theta) \end{aligned} \tag{B.23}$$

with

$$\begin{aligned} |s| &= \left(x^2 + y^2\right)^{1/2} \\ \theta &= \pi - \arctan(y/x) \end{aligned} \tag{B.24}$$

Then,

$$\frac{1}{s} = z \exp(\mp i\theta) \tag{B.25}$$

with

$$z = |s|^{-1} \tag{B.26}$$

The value of $\tilde{f}(s)$ on the negative real axis will therefore depend on whether the cut is approached from above or below[150], i.e. whether we take the limit

$$\lim_{y \to 0} \tilde{f}(-x + iy) = \lim_{y \to 0^+} \tilde{f}(-x + iy) \tag{B.27}$$

or the limit

$$\lim_{y\to 0} \tilde{f}(-x-iy) = \lim_{y\to 0^-} \tilde{f}(-x+iy) \tag{B.28}$$

The difference between the two limits (i.e. the *jump* between the two Riemann surfaces joined at the cut) can be used to invert the transform.[150]

B.5.2 Inversion

The *inverse Stieltjes transform* is:[150]

$$\begin{aligned} f(t) &= \frac{1}{2\pi i} \lim_{y\to 0} \left[\tilde{f}(-t-iy) - \tilde{f}(-t+iy) \right] \qquad t \in \mathbb{R}^+ \\ &= \mp \frac{1}{\pi} \lim_{y\to 0} \left[\operatorname{Im} \tilde{f}(-t \pm iy) \right] \end{aligned} \tag{B.29}$$

with

$$\lim_{y\to 0} \left(-t \pm iy \right) = t \exp\left(\pm i\pi \right) \tag{B.30}$$

from Eqs. (B.23) and (B.24). Alternative notations are $\mathcal{S}^{-1}\left[\tilde{f}(s);\, t \right]$, $\mathcal{S}^{-1}\left[\tilde{f}(s) \right]$, or $\mathcal{S}^{-1}\ \tilde{f}(s)$.

B.5.3 Properties

The Stieltjes transform is an iterated Laplace transform, i.e.[150,562,563]

$$\mathcal{S}\, f(t) = \mathcal{L}\ \mathcal{L}\, f(t) \tag{B.31}$$

Appendix C

Special Functions

This Appendix attempts a short review of the special functions used or referenced to in the main body and other Appendices of this dissertation. It should by no means be considered an exposition of the subject; it is meant to serve simply as an introduction to the notation used and as a handy reference. Formulae are stated without proof, in the form in which they are applicable in the context of the dissertation. The following material is largely based on the work of Mittag-Leffler[372,373,564], Wiman[367,368], Erdélyi et al.[369], Dzherbashyan[370], Spanier and Oldham[341], Tschoegl[150], Paris[565], Gradshteyn and Ryzhik[561], Olver et al.[562,563], Haubold et al.[371], and Weisstein[566].

C.1 Gamma Function

C.1.1 Definition

The (complete) *gamma function* $\Gamma(s)$ is an extension of the factorial to complex (s) or real (m = Re(s)) arguments. It can be defined as an integral transformation (Euler's integral of the second kind):[341,561-563,566]

$$\Gamma(s) \equiv \int_0^\infty u^{s-1} e^{-u}\, du \qquad s \in \mathbb{C},\ \mathrm{Re}(s) > 0 \tag{C.1}$$

It is implemented in MATLAB® as *gamma*(m), and in Mathematica® as *Gamma*[s].

C.1.2 Properties

Recurrence:[562,563]

$$\Gamma(s+1) = s\Gamma(s) \tag{C.2}$$

$$\Gamma(n+1) = n! \qquad n \in \{0\} \bigcup \mathbb{Z}^+ \tag{C.3}$$

Reflection:[562,563]

$$\begin{aligned}
\Gamma(s)\Gamma(1-s) &= \frac{\pi}{\sin(\pi s)} && s \neq \pm k \quad \wedge k \in \mathbb{Z} \\
\Gamma\left(\frac{s}{2}\right)\Gamma\left(1-\frac{s}{2}\right) &= \frac{\pi}{\sin\left(\pi s/2\right)} && s \neq \pm 2k \quad \wedge k \in \mathbb{Z} \\
\Gamma\left(\frac{1}{2}+s\right)\Gamma\left(\frac{1}{2}-s\right) &= \frac{\pi}{\cos(\pi s)} && s \neq \pm\left(k+\frac{1}{2}\right) \quad \wedge k \in \mathbb{Z} \\
\Gamma\left(\frac{1}{2}+\frac{s}{2}\right)\Gamma\left(\frac{1}{2}-\frac{s}{2}\right) &= \frac{\pi}{\cos\left(\pi s/2\right)} && s \neq \pm(2k+1) \quad \wedge k \in \mathbb{Z}
\end{aligned} \tag{C.4}$$

Notice that Eqs. (C.4)c-d follow directly from Eq. (C.4)a, since $\Gamma(1/2 - s) = \Gamma[1 - (1/2 + s)]$ and $\sin(u \pm v) = \sin(u)\cos(v) \pm \cos(u)\sin(v)$.

C.2 Incomplete Gamma Functions

C.2.1 Definitions

The complete gamma function $\Gamma(s)$ can be generalized to the *lower incomplete gamma function* $\gamma(s, x)$ and *upper incomplete gamma function* $\Gamma(s, x)$ as:[561-563]

$$\gamma(s,x) \equiv \int_0^x u^{s-1}e^{-u}\,du \qquad s,x \in \mathbb{C},\ \mathrm{Re}(s) > 0 \tag{C.5}$$

$$\Gamma(s,x) \equiv \int_x^\infty u^{s-1}e^{-u}\,du \qquad s,x \in \mathbb{C} \tag{C.6}$$

In MATLAB®, the normalized lower incomplete gamma function $P(m, x) \equiv \gamma(m, x) / \Gamma(m)$ is implemented as *gammainc*(x, m) or *gammainc*(x, m, '*lower*'), while the normalized upper incomplete gamma function $Q(m, x) \equiv \Gamma(m, x) / \Gamma(m)$ is implemented as *gammainc*(x, m, '*upper*'); in either case, m and x must be real numbers. In Mathematica®, the lower incomplete gamma function $\gamma(s, x)$ is implemented as *Gamma*[s, 0, x], while the upper incomplete gamma function $\Gamma(s, x)$ is implemented as *Gamma*[s, 0, x]; in either case, s and x can be complex numbers.

C.2.2 Properties

Limits:

$$\begin{aligned} \lim_{x\to\infty}\gamma(s,x) &= \lim_{x\to 0}\Gamma(s,x) = \Gamma(s) \\ \lim_{x\to 0}\gamma(s,x) &= \lim_{x\to\infty}\Gamma(s,x) = 0 \end{aligned} \tag{C.7}$$

Identity:[562,563]

$$\gamma(s,x)+\Gamma(s,x)=\Gamma(s) \qquad s\neq 0,-1,-2,\ldots \tag{C.8}$$

Recurrence:[561-563]

$$\begin{aligned} \gamma(s+1,x) &= s\gamma(s,x)-x^s e^{-x} \\ \Gamma(s+1,x) &= s\Gamma(s,x)+x^s e^{-x} \end{aligned} \tag{C.9}$$

Derivative (obtained via integration by parts):[561-563]

$$\frac{d}{dx}\gamma(s,x) = -\frac{d}{dx}\Gamma(s,x) = x^{s-1}e^{-x} \tag{C.10}$$

C.3 Beta Function

C.3.1 Definition

The (complete) *beta function* B(p, q) is defined by the beta integral (Euler's integral of the first kind):[341,561-563,566]

$$\begin{aligned} \mathrm{B}(p,q) &= \int_0^1 u^{p-1}(1-u)^{q-1}\,du \\ &= \int_0^\infty \frac{u^{p-1}}{(1+u)^{p+q}}\,du \\ &= \frac{\Gamma(p)\Gamma(q)}{\Gamma(p+q)} \qquad p,q\in\mathbb{C},\ \mathrm{Re}(p),\mathrm{Re}(q)>0 \end{aligned} \tag{C.11}$$

where the second integral representation is obtained with a change of variable ($y = u/(1-u)$). The complete beta function is implemented in MATLAB® as *beta*(p, q), for real arguments, and in Mathematica® as *Beta*[p, q], for real or complex arguments.

C.4 Incomplete Beta Functions

C.4.1 Definitions

The complete beta function B(p, q) defined by the beta integral (Eq. (C.11)a) can be generalized to the *incomplete beta function* B(p, q; x) as:[561-563,566]

$$\begin{aligned} \mathrm{B}(p,q;x) &= \int_0^x u^{p-1}(1-u)^{q-1}\,du \qquad p,q\in\mathbb{C},\ \mathrm{Re}(p),\mathrm{Re}(q)>0 \\ &\qquad\qquad\qquad\qquad\qquad\qquad x\in\mathbb{R},\ 0\le x\le 1 \end{aligned} \tag{C.12}$$

The alternative definition used by Tschoegl[150] (given on page 348 of his book):

$$\mathrm{B_T}(p,q;x)=\int_0^x \frac{u^{p-1}}{(1+u)^{p+q}}\,du \qquad p,q\in\mathbb{C},\ \mathrm{Re}(p),\mathrm{Re}(q)>0 \qquad x\in\mathbb{R},\ 0\le x\le 1 \tag{C.13}$$

is based on the second integral representation of B(p, q), Eq. (C.11)b. The two definitions are related by:

$$\begin{aligned}\mathrm{B}(p,q;x)&=\mathrm{B_T}\left(p,q;\frac{x}{1-x}\right)\\ \mathrm{B_T}(p,q;x)&=\mathrm{B}\left(p,q;\frac{x}{1+x}\right)\end{aligned} \tag{C.14}$$

In MATLAB®, the normalized incomplete beta function $I(p, q; x) \equiv \mathrm{B}(p, q; x) / \mathrm{B}(p, q)$ is implemented as *betainc*(x, p, q) or *betainc*(x, p, q, '*lower*'), for real arguments p and q. In Mathematica®, the incomplete beta function B(p, q; x) is implemented as *Beta*[x, p, q], for real or complex arguments p and q.

C.4.2 Properties

Limits:

$$\begin{aligned}\lim_{x\to 1}\mathrm{B}(p,q;x)&=\lim_{x\to\infty}\mathrm{B_T}(p,q;x)=\mathrm{B}(p,q)\\ \lim_{x\to 0}\mathrm{B}(p,q;x)&=\lim_{x\to 0}\mathrm{B_T}(p,q;x)=0\end{aligned} \tag{C.15}$$

Derivative:[566]

$$\frac{d}{dx}\mathrm{B}(p,q;x)=x^{p-1}(1-x)^{q-1} \tag{C.16}$$

C.5 Ordinary Mittag-Leffler Function

C.5.1 Definition

The *ordinary* (or one-parameter) *Mittag-Leffler function*[372,373,564] (MLF) $E_a(s)$ is an entire function of order $1/a$ (i.e. a complex function that is analytic at all finite points of the complex plane)[369] defined by the series:[369-371]

$$E_a(s) = \sum_{k=0}^{\infty} \frac{s^k}{\Gamma(ak+1)} \qquad s,a \in \mathbb{C},\ \mathrm{Re}(a) > 0 \tag{C.17}$$

It follows from Eq. (C.17) that the ordinary Mittag-Leffler function is a generalization of the exponential function e^s, which is obtained as a special case for $a = 1$.

For real argument x and $a \in (0, 1)$, $E_a(-x^a)$ is a positive and strictly monotonically decreasing function that interpolates between an initial stretched exponential[374,375] pattern – often referred to as the Kohlrausch–Williams–Watts (KWW) law[376-378] or the Weibull distribution[379] – and a terminal inverse power-law decay – often referred to as the Nutting law[315,316,318,380-382] –, both of index a (cf. Eq. (C.20)).

It is implemented in Mathematica® as *MittagLefflerE*[a, s]. In MATLAB®, the MLF can be calculated with the routine developed by Podlubny in 2012.[567,568]

C.5.2 Properties

Some special cases include:[371]

$$\begin{aligned} &E_0(s) = \frac{1}{1-s} \qquad |s| < 1 \\ &E_{1/2}\left(\pm s^{1/2}\right) = e^s\left[1 + \operatorname{erf}\left(\pm s^{1/2}\right)\right] = e^s \operatorname{erfc}\left(\mp s^{1/2}\right) \\ &E_1(s) = e^s \\ &E_2(s) = \cosh\left(s^{1/2}\right) \\ &E_2\left(-s^2\right) = \cos(s) \end{aligned} \tag{C.18}$$

where erf and erfc denote the error function and the complimentary error function, and cosh denotes the hyperbolic cosine.

Limiting behaviors include:[369,565]

$$E_a(x) \sim \frac{1}{a}\exp\left(x^{1/a}\right) - \mathrm{O}\left(x^{-1}\right) \qquad x,a \in \mathbb{R},\ x \to \infty,\ 0 < a < 2 \tag{C.19}$$

and[252,369]

$$\begin{aligned} &E_a\left(-x^a\right) \sim \exp\left(-\frac{x^a}{\Gamma(1+a)}\right) \qquad x,a \in \mathbb{R},\ x \to 0,\ 0 < a < 1 \\ &E_a\left(-x^a\right) \sim \frac{1}{\Gamma(1-a)}\frac{1}{x^a} \qquad x,a \in \mathbb{R},\ x \to \infty,\ 0 < a < 1 \end{aligned} \tag{C.20}$$

C.6 Generalized Mittag-Leffler Function

C.6.1 Definition

The *generalized* (or two-parameter) *Mittag-Leffler function*[367,368] (GMLF) $E_{a,b}(s)$ is an entire function of order[369] $1/a$ defined by the series:[369-371]

$$E_{a,b}(s)=\sum_{k=0}^{\infty}\frac{s^k}{\Gamma(ak+b)} \qquad s,a,b\in\mathbb{C},\ \mathrm{Re}(a),\mathrm{Re}(b)>0 \tag{C.21}$$

The generalized Mittag-Leffler function can be represented in terms of Fox *H*-functions.[348] For $b = 1$, the MLF is recovered (Eq. (C.22)a). It is implemented in Mathematica® as *MittagLefflerE*[a, b, s]. In MATLAB®, the GMLF can be calculated with the routine developed by Podlubny in 2012.[567,568]

C.5.2 Properties

Some special cases include:[371]

$$\begin{aligned} E_{a,1}(s)&=E_a(s)\\ E_{1,2}(s)&=\frac{e^s-1}{s}\\ E_{2,2}(s)&=\frac{\sinh(s^{1/2})}{s^{1/2}} \end{aligned} \tag{C.22}$$

where sinh denotes the hyperbolic sine.

Recurrence:[371,565]

$$\begin{aligned} E_{a,b}(s)&=\frac{1}{s}E_{a,b-a}(s)-\frac{1}{s\cdot\Gamma(b-a)}\\ E_{a,b}(s)&=sE_{a,b+a}(s)+\frac{1}{\Gamma(b)} \end{aligned} \tag{C.23}$$

Identities:[349,369,371]

$$\begin{aligned} E_a(-x) &= E_{2a}\left(x^2\right) - x \cdot E_{2a,1+a}\left(x^2\right) \\ E_{a,b}(-x) &= E_{2a,b}\left(x^2\right) - x \cdot E_{2a,b+a}\left(x^2\right) \end{aligned} \tag{C.24}$$

Limiting behaviors include:[369,371]

$$E_{a,b}(x) \sim \frac{1}{a} x^{(1-b)/a} \exp\left(x^{1/a}\right) - \mathrm{O}\left(x^{-1}\right) \qquad x,a,b \in \mathbb{R},\ x \to \infty,\ 0 < a < 2 \tag{C.25}$$

and[366,369]

$$\begin{aligned} E_{a,a}(-x) &\sim \frac{a}{\Gamma(1-a)} \frac{1}{x^2} && x,a \in \mathbb{R},\ x \to \infty,\ 0 < a < 1 \\ E_{a,b}(-x) &\sim \frac{1}{\Gamma(b-a)} \frac{1}{x} && x,a,b \in \mathbb{R},\ x \to \infty,\ 0 < a < 1,\ a < b \end{aligned} \tag{C.26}$$

Appendix D

Linear Viscoelastic Functions

This Appendix attempts a short review of the linear viscoelastic functions used in the main body and other Appendices of this dissertation. It should by no means be considered an exposition of the subject; it is meant to serve simply as an introduction to the notation used and as a handy reference. Formulae are generally stated without proof, in the form in which they are applicable in the context of the dissertation. The following material is largely based on the work of Tschoegl[150].

D.1 Introduction

In this Appendix we will be concerned with *linear*, *time-dependent* stresses or strains. Here, we will disregard the tensorial character of stress and strain, and will consider a time-dependent scalar stress $\sigma(t)$ and a time-dependent scalar strain $\varepsilon(t)$. Without loss of generality, we will assume these functions to be defined on $[0, \infty)$ and with *zero initial conditions* (Appendix B, §B.2.3). Accordingly, we will consider the state in which the material is at $t = 0$ to be the *reference state* in which it is free of the effects of any prior stress or strain history. For viscoelastic solids, this reference state corresponds to the *undeformed state*. The functions $\sigma(t)$ and $\varepsilon(t)$ represent the infinitesimal shear stress and strain (respectively) in *simple shear*, and the infinitesimal tensile stress and strain

(respectively) in *uniaxial extension*.[a] Linear viscoelastic functions will be first defined in simple shear. The notation adopted in uniaxial extension will be subsequently introduced.

D.2 Linear Viscoelastic Behavior

In the limit of infinitesimal deformation, viscoelastic behavior of an isotropic material can be described by a *linear* ordinary differential equation with *constant* coefficients

$$\sum_{n=0} u_n \frac{d^n \sigma(t)}{dt^n} = \sum_{m=0} q_m \frac{d^m \varepsilon(t)}{dt^m} \tag{D.1}$$

where u_n and q_m are the constant coefficients. Laplace transformation of Eq. (D.1) gives, for *zero initial conditions* (cf. Appendix B, §B.2.3),

$$\overline{u}(s)\overline{\sigma}(s) = \overline{q}(s)\overline{\varepsilon}(s) \tag{D.2}$$

where $\overline{\sigma}(s)$ and $\overline{\varepsilon}(s)$ are the *stress* and *strain transforms*, respectively, and

$$\begin{aligned} \overline{u}(s) &= \sum_{n=0} u_n s^n \\ \overline{q}(s) &= \sum_{m=0} q_m s^m \end{aligned} \tag{D.3}$$

---

[a] Based on the definition of the *infinitesimal strain tensor* adopted by Tschoegl[150], the scalar strain component in *simple shear* equals half of the (traditionally defined) shear strain γ. In *uniaxial extension*, the scalar strain component equals ε_N, where ε_N denotes the nominal/engineering strain. Since the true/Hencky strain is defined as $\varepsilon \equiv \ln(L/L_0) = \ln(\lambda) = \ln(\varepsilon_N + 1)$ – where L and L_0 stand for the deformed and undeformed length (respectively), and λ is the elongation ratio – in the limit of infinitesimal uniaxial deformation the scalar strain component and the Hencky strain coincide. Note that the infinitesimal strain tensor is often defined (e.g. Ferry[42], Bird et al.[340], and Graessley[45]) as twice the tensor used by Tschoegl; in this case, the scalar strain component in simple shear equals the shear strain γ, while in uniaxial extension is $2\varepsilon_N \simeq 2\varepsilon$.

are polynomials in the transform variable s. From Eqs. (D.2) and (D.3), we obtain *Hooke's laws in the complex plane*

$$\begin{aligned}\bar{\sigma}(s) &= \bar{Q}(s)\bar{\varepsilon}(s)\\ \bar{\varepsilon}(s) &= \bar{U}(s)\bar{\sigma}(s)\end{aligned} \tag{D.4}$$

with

$$\bar{Q}(s)\bar{U}(s) = 1 \tag{D.5}$$

where $\bar{Q}(s) = \bar{q}(s)/\bar{u}(s)$ and $\bar{U}(s) = \bar{u}(s)/\bar{q}(s)$ are the *operational shear relaxance* and *retardance* (respectively). In Eq. (D.4)a, strain is the *excitation* and stress is the *response*; in Eq. (D.4)b, their role is reversed. Based on their definitions, the *operational shear respondances* $\bar{Q}(s)$ and $\bar{U}(s)$ are rational algebraic functions in the transform variable s (cf. Appendix B, §B.3.2).

Inverse Laplace transformation of Eqs. (D.4) and (D.5) in the *time domain* leads to the *Boltzmann superposition integrals* (Laplace convolutions – cf. Appendix B, Eqs. (B.10) and (B.11), and Table B.1, LTP (1))

$$\begin{aligned}\sigma(t) &= \int_0^t Q(t-u)\varepsilon(u)\,du = \int_0^t Q(u)\varepsilon(t-u)\,du\\ \varepsilon(t) &= \int_0^t U(t-u)\sigma(u)\,du = \int_0^t U(u)\sigma(t-u)\,du\end{aligned} \tag{D.6}$$

and

$$\int_0^t Q(t-u)U(u)\,du = \int_0^t Q(u)U(t-u)\,du = \delta(t) \tag{D.7}$$

where $\delta(t)$ denotes the delta (or unit impulse) function, t signifies the *present time*, and – in Eqs. $(D.6)_1$ and $(D.7)_1$ – u is the *historic time*, and $t–u$ is the *elapsed time*[b]. The real-valued shear relaxance $Q(t)$ and retardance $U(t)$ represent the material response (to unit impulses of strain and stress, respectively – §D.3.1) and are termed *material* or *memory functions*. For instance, Eq. (D.6)a implies that the stress at the present time t is a linear superposition of all strains applied at historic times u multiplied by the values of the material function corresponding to the time intervals $(t–u)$ which have elapsed since imposition of the respective strain. The response to *unit standard* stress or strain *excitations* (i.e. impulse, step, slope, or harmonic excitations) defines a characteristic material response function.

---

[b] Since we chose the state at $t = 0$ as the *reference state*, the *historic time* u ranges from 0 to t, and the *elapsed time* $w = t–u$ ranges over the same interval extending *forward* from u to t. This is the view-point adopted here following Tschoegl's approach (see pages 40, 67, and 660 of his book[150]). An alternative view-point is often used (e.g. by Ferry[42], Bird et al.[340], Dealy and Larson[36], and Graessley[45]) when dealing with viscoelastic *liquids* (this is the view-point of *fluid mechanics*). In this case, the historic time u ranges from $–\infty$ to t, the elapsed time $s = t–u$ ranges over the closed interval $[0, \infty]$ extending *backward* from the present time t into the indefinite past, and the strain is defined as the strain at time u referred to the strain at the present time t, i.e. $\varepsilon_t(s) \equiv \varepsilon(u) – \varepsilon(t) = \varepsilon(t–s) – \varepsilon(t)$. In other words, the strain at present time t, $\varepsilon(t)$, serves as the reference state, and the liquid is considered as having been in motion for an indefinite period of time in the past before any observation is made. The associated memory function is defined as $m(t–u) \equiv dG(t–u)/du$ (Ferry[42] p 7, Bird et al.[340] p 263, Dealy and Larson[36] p 335, and Graessley[45] p 119). Note that, in this case, $G(\infty) = G_{eq} = 0$.

D.3 Material Response Functions

D.3.1 The Impulse Response Functions

Strain excitation

Let the excitation be an *impulsive strain* of strength $\hat{\varepsilon}_0$, i.e.

$$\begin{aligned} \varepsilon(t) &= \hat{\varepsilon}_0 \delta(t) \\ \bar{\varepsilon}(s) &= \hat{\varepsilon}_0 \end{aligned} \tag{D.8}$$

where $\delta(t)$ is the delta (or unit impulse) function and $\mathcal{L}\ \delta(t) = 1$ (cf. Appendix B, Table B.1, LTP (1)). Then, from Eq. (D.4)a, the characteristic material response function (in the complex and time domains) is

$$\begin{aligned} \bar{Q}(s) &= \frac{\bar{\sigma}(s)}{\hat{\varepsilon}_0} \\ Q(t) &= \frac{\sigma(t)}{\hat{\varepsilon}_0} \end{aligned} \tag{D.9}$$

Stress excitation

Similarly, when the excitation is an *impulsive stress* of strength $\hat{\sigma}_0$, i.e.

$$\begin{aligned} \sigma(t) &= \hat{\sigma}_0 \delta(t) \\ \bar{\sigma}(s) &= \hat{\sigma}_0 \end{aligned} \tag{D.10}$$

from Eq. (D.4)b the characteristic material response function (in the complex and time domains) is

$$\begin{aligned} \bar{U}(s) &= \frac{\bar{\varepsilon}(s)}{\hat{\sigma}_0} \\ U(t) &= \frac{\varepsilon(t)}{\hat{\sigma}_0} \end{aligned} \tag{D.11}$$

D.3.2 The Step Response Functions

Strain excitation

Let the excitation be a *step of strain* of height ε_0, i.e.

$$\begin{aligned} \varepsilon(t) &= \varepsilon_0 h(t) \\ \bar{\varepsilon}(s) &= \varepsilon_0 \frac{1}{s} \end{aligned} \tag{D.12}$$

where $h(t)$ is the Heaviside unit step function, with $\delta(t) = dh(t)/dt$ and $\mathcal{L}\, h(t) = 1/s$ (cf. Appendix B, Table B.1, LTP (2); note that the value $h(0)$ is arbitrary and does not affect the Laplace transform of $h(t)$). Then, from Eq. (D.4)a, the characteristic material response function (in the complex and time domains – cf. Appendix B, Eq. (B.8)a) is

$$\begin{aligned} \bar{G}(s) &\equiv \frac{\bar{\sigma}(s)}{\varepsilon_0} = \frac{\bar{Q}(s)}{s} \\ G(t) &= \frac{\sigma(t)}{\varepsilon_0} = \int_0^t Q(u)\,du \end{aligned} \tag{D.13}$$

where $G(t)$ is termed the *shear relaxation modulus*. It follows from Eq. (D.13)a that (cf. Appendix B, Eq. (B.7))

$$\begin{aligned} \bar{Q}(s) &= s\bar{G}(s) \\ Q(t) &= \frac{dG(t)}{dt} + G(0)\delta(t) \end{aligned} \tag{D.14}$$

where $G_g \equiv G(0)$ is the *glassy* or *instantaneous shear modulus* (cf. footnote [b]). Moreover, combining Eqs. (D.4)a and (D.14)a and making use of $\varepsilon(0) = h(0) = 0$ lead to (cf. Appendix B, Eq. (B.12))

$$\bar{\sigma}(s) = s\bar{G}(s)\bar{\varepsilon}(s)$$

$$\sigma(t) = \begin{cases} G_g\varepsilon(t) + \int_0^t \dfrac{dG(u)}{du}\varepsilon(t-u)du \\ G_g\varepsilon(t) + \int_0^t \dfrac{dG(t-u)}{d(t-u)}\varepsilon(u)du \\ \int_0^t G(t-u)\dfrac{d\varepsilon(u)}{du}du \\ \int_0^t G(u)\dfrac{d\varepsilon(t-u)}{d(t-u)}du \end{cases} \tag{D.15}$$

Stress excitation

Similarly, when the excitation is a *step of stress* of height σ_0, i.e.

$$\begin{aligned} \sigma(t) &= \sigma_0 h(t) \\ \bar{\sigma}(s) &= \sigma_0 \frac{1}{s} \end{aligned} \tag{D.16}$$

from Eq. (D.4)b the characteristic material response function (in the complex and time domains – cf. Appendix B, Eq. (B.8)a) is

$$\begin{aligned} \bar{J}(s) &\equiv \frac{\bar{\varepsilon}(s)}{\sigma_0} = \frac{\bar{U}(s)}{s} \\ J(t) &= \frac{\varepsilon(t)}{\sigma_0} = \int_0^t U(u)du \end{aligned} \tag{D.17}$$

where $J(t)$ is termed the *shear creep compliance*. It follows from Eq. (D.17)a that (cf. Appendix B, Eq. (B.7))

$$\begin{aligned} \bar{U}(s) &= s\bar{J}(s) \\ U(t) &= \frac{dJ(t)}{dt} + J(0)\delta(t) \end{aligned} \tag{D.18}$$

where $J_g \equiv J(0)$ is the *glassy* or *instantaneous shear compliance*. Moreover, combining Eqs. (D.4)b and (D.18)a and making use of $\sigma(0) = h(0) = 0$ lead to (cf. Appendix B, Eq. (B.12))

$$\bar{\varepsilon}(s) = s\bar{J}(s)\bar{\sigma}(s)$$

$$\varepsilon(t) = \begin{cases} J_g\sigma(t) + \int_0^t \dfrac{dJ(u)}{du}\sigma(t-u)\,du \\ J_g\sigma(t) + \int_0^t \dfrac{dJ(t-u)}{d(t-u)}\sigma(u)\,du \\ \int_0^t J(t-u)\dfrac{d\sigma(u)}{du}\,du \\ \int_0^t J(u)\dfrac{d\sigma(t-u)}{d(t-u)}\,du \end{cases} \tag{D.19}$$

It follows from Eqs. (D.5), (D.14)a, and (D.18)a that (cf. Appendix B, Eqs. (B.10) and (B.11), and Appendix C, Eq. (C.3))

$$\bar{G}(s)\bar{J}(s) = \frac{1}{s^2}$$

$$\int_0^t G(t-u)J(u)\,du = \int_0^t G(u)J(t-u)\,du = t \tag{D.20}$$

where we have made use of $\mathcal{L}^{-1}\ \Gamma(n)/s^n = t^{n-1}$ (cf. Appendix B, Table B.1, LTP (4)). Furthermore, it is possible to show that

$$G(t)J(t) \le 1 \tag{D.21}$$

the equality holding only in the limit as $t \to 0$ or $t \to \infty$.

D.3.3 The Slope Response Functions

Strain excitation

Let the excitation be a *constant rate of strain* $\dot{\varepsilon}_0$, i.e.

$$\begin{aligned} \varepsilon(t) &= \dot{\varepsilon}_0 p(t) = \dot{\varepsilon}_0 t \cdot h(t) \\ \overline{\varepsilon}(s) &= \dot{\varepsilon}_0 \frac{1}{s^2} \end{aligned} \tag{D.22}$$

where $p(t) = t \cdot h(t) = \int_0^t h(u)\,du$ is the slope function and $\mathcal{L}\, p(t) = 1/s^2$ (cf. Appendix B, Table B.1, LTP (3)). Then, from Eq. (D.4)a, the characteristic material response function (in the complex and time domains – cf. Appendix B, Eq. (B.8)) is

$$\begin{aligned} \overline{\eta}(s) &\equiv \frac{\overline{\sigma}(s)}{\dot{\varepsilon}_0} = \frac{\overline{Q}(s)}{s^2} = \frac{\overline{G}(s)}{s} \\ \eta(t) &= \frac{\sigma(t)}{\dot{\varepsilon}_0} = \int_0^t \int_0^v Q(u)\,du\,dv = \int_0^t G(u)\,du \end{aligned} \tag{D.23}$$

where $\eta(t)$ is termed the *transient shear viscosity*. The *steady-state shear viscosity* is defined by

$$\eta_0 = \lim_{t \to \infty} \eta(t) = \int_0^\infty G(u)\,du \tag{D.24}$$

It follows from Eq. (D.23)a that (cf. Appendix B, Eq. (B.7))

$$\begin{aligned} \overline{G}(s) &= s\overline{\eta}(s) \\ G(t) &= \frac{d\eta(t)}{dt} + \eta(0)\delta(t) \end{aligned} \tag{D.25}$$

where $\eta(0) = 0$. In experiments at constant rate of strain, another material response function is the *constant-strain-rate* or *secant modulus*, $R(t)$, defined by Smith[421] as:

$$\begin{aligned} R(t) \equiv \frac{\sigma(t)}{\varepsilon(t)} &= \frac{\sigma(t)}{\dot{\varepsilon}_0 t} \\ &= \frac{\eta(t)}{t} \\ &= \frac{1}{t}\int_0^t G(u)\,du \end{aligned} \tag{D.26}$$

Multiplication of both sides of Eq. (D.26) by t and differentiation yields

$$R(t)\left[1+\frac{d\log R(t)}{d\log t}\right] = G(t) \tag{D.27}$$

where we have made use of the identity $\log_a f(x) = \log_b f(x) \,/\, \log_b a$ (hence, Eq. (D.27) holds for any base of the logarithm). In the complex domain[150]

$$\bar{R}(s) = \mathcal{L}\ \frac{\eta(t)}{t} = \int_s^\infty \bar{\eta}(x)\,dx \tag{D.28}$$

Stress excitation

Similarly, when the excitation is a *constant rate of stress* $\dot{\sigma}_0$, i.e.

$$\begin{aligned} \sigma(t) &= \dot{\sigma}_0 p(t) = \dot{\sigma}_0 t \cdot h(t) \\ \bar{\sigma}(s) &= \dot{\sigma}_0 \frac{1}{s^2} \end{aligned} \tag{D.29}$$

from Eq. (D.4)b the characteristic material response function (in the complex and time domains – cf. Appendix B, Eq. (B.8)) is

$$\begin{aligned} \bar{\chi}(s) &\equiv \frac{\bar{\varepsilon}(s)}{\dot{\sigma}_0} = \frac{\bar{U}(s)}{s^2} = \frac{\bar{J}(s)}{s} \\ \chi(t) &= \frac{\varepsilon(t)}{\dot{\sigma}_0} = \int_0^t \int_0^v U(u)\,du\,dv = \int_0^t J(u)\,du \end{aligned} \tag{D.30}$$

It follows from Eq. (D.30)a that (cf. Appendix B, Eq. (B.7))

$$\begin{aligned} \overline{J}(s) &= s\overline{\chi}(s) \\ J(t) &= \frac{d\chi(t)}{dt} + \chi(0)\delta(t) \end{aligned} \tag{D.31}$$

where $\chi(0) = 0$.

Combining Eqs. (D.5), (D.14)a, (D.18)a, (D.25)a, and (D.31)a leads to (cf. Appendix B, Eqs. (B.10) and (B.11), and Appendix C, Eq. (C.3))

$$\begin{aligned} \overline{\eta}(s)\overline{\chi}(s) &= \frac{1}{s^4} \\ \int_0^t \eta(t-u)\chi(u)\,du &= \int_0^t \eta(u)\chi(t-u)\,du = \frac{t^3}{6} \end{aligned} \tag{D.32}$$

where we have made use of $\mathcal{L}^{-1}\,\Gamma(n)/s^n = t^{n-1}$ (cf. Appendix B, Table B.1, LTP (4)).

D.3.4 The Harmonic Response Functions

Strain excitation

Let the excitation be a *generalized harmonic strain* of amplitude ε_0 and radian frequency ω, i.e. (cf. Appendix B, Table B.1, LTP (9))

$$\begin{aligned} \varepsilon(t) &= \varepsilon(\omega) = \varepsilon_0 \exp(i\omega t) \\ \bar{\varepsilon}(s) &= \frac{\varepsilon_0}{s - i\omega} \end{aligned} \tag{D.33}$$

Then, from Eq. (D.4)a, by decomposition into partial fractions the characteristic material response function at *steady-state* (in the frequency domain) is

$$\begin{aligned} G^*(\omega) \equiv \frac{\sigma_{ss}(\omega)}{\varepsilon(\omega)} &= \bar{Q}(s)\big|_{s=i\omega} = \int_0^\infty Q(u) e^{-i\omega u}\, du \\ &= \tilde{G}(\omega)\exp\left[i\delta(\omega)\right] \\ &= G'(\omega) + iG''(\omega) \end{aligned} \tag{D.34}$$

where $\sigma_{ss}(\omega)$ represents the *generalized harmonic stress response at steady-state*, $G^*(\omega)$ is termed the *complex shear modulus*, $\tilde{G}(\omega)$ is the *absolute shear modulus*, $\delta(\omega) \in [0, \pi/2]$ is the *loss angle* (i.e. the phase angle between stress and strain), $G'(\omega)$ is the *storage shear modulus*, and $G''(\omega)$ is the *loss shear modulus*. It follows from Eq. (D.34)a that the complex shear modulus $G^*(\omega)$ is the *generalized Fourier transform* of the shear relaxance $Q(t)$ (cf. Appendix B, Eq. (B.21)). Since $\bar{Q}(s) = s\bar{G}(s)$ (Eq. (D.14)a), Eq. (D.34)a may be rewritten as

$$\begin{aligned} G^*(\omega) &= \left[s\bar{G}(s) \right]_{s=i\omega} \\ &= i\omega \cdot \mathcal{F}\ G(t) \\ &= i\omega \cdot \int_0^\infty G(u) e^{-i\omega u}\, du \end{aligned} \tag{D.35}$$

i.e. the complex shear modulus $G^*(\omega)$ is the $i\omega$-multiplied *generalized Fourier transform* of the shear relaxation modulus $G(t)$.

It is often useful to define a *complex shear viscosity* $\eta^*(\omega)$ as the response of the sinusoidal steady-state stress $\sigma_{ss}(\omega)$ to the *sinusoidal steady-state rate of strain* $\dot{\varepsilon}(\omega) = i\omega \cdot \varepsilon(\omega)$, i.e.

$$\begin{aligned} \eta^*(\omega) \equiv \frac{\sigma_{ss}(\omega)}{\dot{\varepsilon}(\omega)} &= \left[\frac{\bar{Q}(s)}{s} \right]_{s=i\omega} = \bar{G}(s)\Big|_{s=i\omega} = \int_0^\infty G(u) e^{-i\omega u}\, du \\ &= \frac{G^*(\omega)}{i\omega} \\ &= \tilde{\eta}(\omega) \exp\left[-i\Theta(\omega) \right] \\ &= \eta'(\omega) - i\eta''(\omega) \end{aligned} \tag{D.36}$$

where $\tilde{\eta}(\omega) = \tilde{G}(\omega)/\omega$ is the *absolute shear viscosity*, $\Theta(\omega) = \pi/2 - \delta(\omega)$ is the *storage angle* (i.e. the phase angle between stress and rate of strain), $\eta'(\omega) = G''(\omega)/\omega$ is the *loss shear viscosity*, and $\eta''(\omega) = G'(\omega)/\omega$ is the *storage shear viscosity*.[c] It follows from Eq. (D.36)a that the complex shear viscosity $\eta^*(\omega)$ is the *generalized Fourier transform* of the shear relaxation modulus $G(t)$ (cf. Appendix B, Eq. (B.21)). Since $\bar{G}(s) = s\bar{\eta}(s)$ (Eq. (D.25)a), Eq. (D.36)a may be rewritten as

---

[c] Recall that $i = \exp(i\pi/2)$.

$$\begin{aligned}\eta^*(\omega) &= \left[s\bar{\eta}(s)\right]_{s=i\omega} \\ &= i\omega \cdot \mathcal{F}\ \eta(t) \\ &= i\omega \cdot \int_0^\infty \eta(u) e^{-i\omega u}\, du\end{aligned} \tag{D.37}$$

i.e. the complex shear viscosity $\eta^*(\omega)$ is the $i\omega$-multiplied *generalized Fourier transform* of the transient shear viscosity $\eta(t)$.

Stress excitation

In a completely analogous fashion, when the excitation is a *generalized harmonic stress* of amplitude σ_0 and radian frequency ω, i.e.

$$\begin{aligned}\sigma(t) &= \sigma(\omega) = \sigma_0 \exp(i\omega t) \\ \bar{\sigma}(s) &= \frac{\sigma_0}{s - i\omega}\end{aligned} \tag{D.38}$$

Then, from Eq. (D.4)b, by decomposition into partial fractions the characteristic material response function at *steady-state* (in the frequency domain) is

$$\begin{aligned}J^*(\omega) \equiv \frac{\varepsilon_{ss}(\omega)}{\sigma(\omega)} &= \bar{U}(s)\Big|_{s=i\omega} = \int_0^\infty U(u) e^{-i\omega u}\, du \\ &= \tilde{J}(\omega)\exp\left[-i\delta(\omega)\right] \\ &= J'(\omega) - iJ''(\omega)\end{aligned} \tag{D.39}$$

where $\varepsilon_{ss}(\omega)$ represents the *generalized harmonic strain response at steady-state*, $J^*(\omega)$ is termed the *complex shear compliance*, $\tilde{J}(\omega)$ is the *absolute shear compliance*, $J'(\omega)$ is the *storage shear compliance*, and $J''(\omega)$ is the *loss shear compliance*. It follows from Eq. (D.39)a that the complex shear compliance $J^*(\omega)$ is the *generalized Fourier transform* of the shear retardance $U(t)$. Since $\bar{U}(s) = s\bar{J}(s)$ (Eq. (D.18)a), Eq. (D.39)a may be rewritten as

$$\begin{aligned} J^*(\omega) &= \left[s\bar{J}(s) \right]_{s=i\omega} \\ &= i\omega \cdot \mathcal{F}\ J(t) \\ &= i\omega \cdot \int_0^\infty J(u) e^{-i\omega u}\, du \end{aligned} \tag{D.40}$$

i.e. the complex shear compliance $J^*(\omega)$ is the $i\omega$-multiplied *generalized Fourier transform* of the shear creep compliance $J(t)$.

We may similarly define $\chi^*(\omega)$ as the response of the sinusoidal steady-state strain $\varepsilon_{ss}(\omega)$ to the *sinusoidal steady-state rate of stress* $\dot{\sigma}(\omega) = i\omega \cdot \sigma(\omega)$, i.e.

$$\begin{aligned} \chi^*(\omega) \equiv \frac{\varepsilon_{ss}(\omega)}{\dot{\sigma}(\omega)} &= \left[\frac{\bar{U}(s)}{s} \right]_{s=i\omega} = \bar{J}(s)\Big|_{s=i\omega} = \int_0^\infty J(u) e^{-i\omega u}\, du \\ &= \frac{J^*(\omega)}{i\omega} \\ &= \tilde{\chi}(\omega) \exp\left[i\left(\Theta(\omega) + \pi \right) \right] \end{aligned} \tag{D.41}$$

It follows from Eq. (D.41)a that $\chi^*(\omega)$ is the *generalized Fourier transform* of the shear creep compliance $J(t)$. Since $\bar{J}(s) = s\bar{\chi}(s)$ (Eq. (D.31)a), Eq. (D.41)a may be rewritten as

$$\begin{aligned} \chi^*(\omega) &= \left[s\bar{\chi}(s) \right]_{s=i\omega} \\ &= i\omega \cdot \mathcal{F}\ \chi(t) \\ &= i\omega \cdot \int_0^\infty \chi(u) e^{-i\omega u}\, du \end{aligned} \tag{D.42}$$

i.e. $\chi^*(\omega)$ is the $i\omega$-multiplied *generalized Fourier transform* of $\chi(t)$.

Moreover, Eqs. (D.5), (D.34), and (D.39) lead to

$$\begin{aligned} G^*(\omega) J^*(\omega) &= 1 \\ \tilde{G}(\omega) \tilde{J}(\omega) &= 1 \end{aligned} \tag{D.43}$$

and

$$\frac{G''(\omega)}{G'(\omega)} = \frac{J''(\omega)}{J'(\omega)} = \tan\delta(\omega) \tag{D.44}$$

where $\tan\delta(\omega)$ is called the *loss tangent*. Since $\tan\delta(\omega)$ is the ratio of two moduli, the loss angle $\delta(\omega)$ is always positive. Therefore, the stress always reaches its peak value earlier than the strain, i.e. the *stress leads the strain*. Conversely, the *strain lags the stress*. Note that Eqs. (D.43)b and (D.44) require the minus sign in Eqs. (D.39)b-c.

Theoretical interconversion between time- and frequency-dependent stress response functions

Since the Fourier transform of a constant a is $\mathcal{F}\ a = a/i\omega$ (cf. Appendix B, Table B.1, LTP (2)), we may rewrite Eq. (D.35)b as

$$\begin{aligned} G^*(\omega) - G_{eq} &= i\omega \cdot \mathcal{F}\left[G(t) - G_{eq}\right] \\ &= i\omega \cdot \left\{\mathcal{F}_c\left[G(t) - G_{eq}\right] - i\mathcal{F}_s\left[G(t) - G_{eq}\right]\right\} \end{aligned} \tag{D.45}$$

where G_{eq} is the *equilibrium shear modulus*, and we have decomposed the generalized Fourier transform in the corresponding cosine and sine transforms according to Eq. (B.16) of Appendix B. Inserting in the left-hand side of Eq. (D.45) the definition of $G^*(\omega)$ given by Eq. (D.34)c and rearranging yield

$$\begin{aligned} G'(\omega) - G_{eq} &= \omega \cdot \mathcal{F}_s\left[G(t) - G_{eq}\right] \\ &= \omega \cdot \int_0^\infty \left[G(t) - G_{eq}\right] \sin(\omega t)\, dt \end{aligned} \tag{D.46}$$

and

$$\begin{aligned} G''(\omega) &= \omega \cdot \mathcal{F}_{\mathrm{c}}\left[G(t) - G_{\mathrm{eq}} \right] \\ &= \omega \cdot \int_0^{\infty} \left[G(t) - G_{\mathrm{eq}} \right] \cos(\omega t)\, dt \end{aligned} \tag{D.47}$$

where we have used the definitions of the Fourier cosine and sine transforms (Appendix B, Eqs. (B.17) and (B.18)).

The Laplace transform of $[G(t) - G_{\mathrm{eq}}]$, $\left[\bar{Q}(s) - G_{\mathrm{eq}} \right] / s$, is a rational algebraic function in the transform variable s (cf. §D.2). Therefore, based on Eqs. (B.19) and (B.20) of Appendix B, we may write

$$\begin{aligned} G(t) - G_{\mathrm{eq}} &= \frac{1}{2\pi} \int_{-\infty}^{+\infty} \mathcal{F}\left[G(t) - G_{\mathrm{eq}} \right] e^{+i\omega t}\, d\omega \\ &= \frac{2}{\pi} \int_0^{\infty} \mathcal{F}_{\mathrm{c}}\left[G(t) - G_{\mathrm{eq}} \right] \cos(\omega t)\, d\omega \\ &= \frac{2}{\pi} \int_0^{\infty} \mathcal{F}_{\mathrm{s}}\left[G(t) - G_{\mathrm{eq}} \right] \sin(\omega t)\, d\omega \end{aligned} \tag{D.48}$$

Substituting Eqs. (D.45)a, (D.46)a, and (D.47)a into Eq. (D.48) leads to

$$\begin{aligned} G(t) - G_{\mathrm{eq}} &= \frac{1}{2\pi} \int_{-\infty}^{+\infty} \frac{G^*(\omega) - G_{\mathrm{eq}}}{i\omega}\, e^{+i\omega t}\, d\omega \\ &= \frac{2}{\pi} \int_0^{\infty} \frac{G''(\omega)}{\omega} \cos(\omega t)\, d\omega \\ &= \frac{2}{\pi} \int_0^{\infty} \frac{G'(\omega) - G_{\mathrm{eq}}}{\omega} \sin(\omega t)\, d\omega \end{aligned} \tag{D.49}$$

Taking the limit for $t \to 0$ in Eq. (D.49)b yields

$$G_g - G_{eq} = \frac{2}{\pi}\int_0^{\infty}\frac{G''(\omega)}{\omega}d\omega = \frac{2}{\pi}\int_{-\infty}^{+\infty}G''(\omega)d\ln\omega$$
$$= \frac{2}{\pi}\int_0^{\infty}\frac{G''(1/\tau)}{\tau}d\tau = \frac{2}{\pi}\int_{-\infty}^{+\infty}G''(1/\tau)d\ln\tau \qquad \text{(D.50)}$$

where $\omega = 1/\tau$. The domain of integration in Eq. (D.50)a can be restricted to integrate over a relatively isolated maximum in $G''(\omega)$, thereby obtaining the contribution to G_g from the particular class of relaxation mechanism it represents.[42] Eq. (D.50)b is useful in connection with the spectral response functions discussed in §D.5 (cf. Eqs. (D.95), (D.98)c or (D.118)). It is also worth mentioning that

$$G'(1/t) > G(t) \qquad \text{(D.51)}$$

at all times, and $G'(1/t) \simeq G(t)$ when $G(t)$ is changing very slowly (see discussion on page 41 of Ferry's book[42]). Eq. (D.51) is obtained by subtracting Eq. (D.87)b from Eq. (D.89)b with $\omega = 1/t$, and noticing that the resulting integral is always positive.[390]

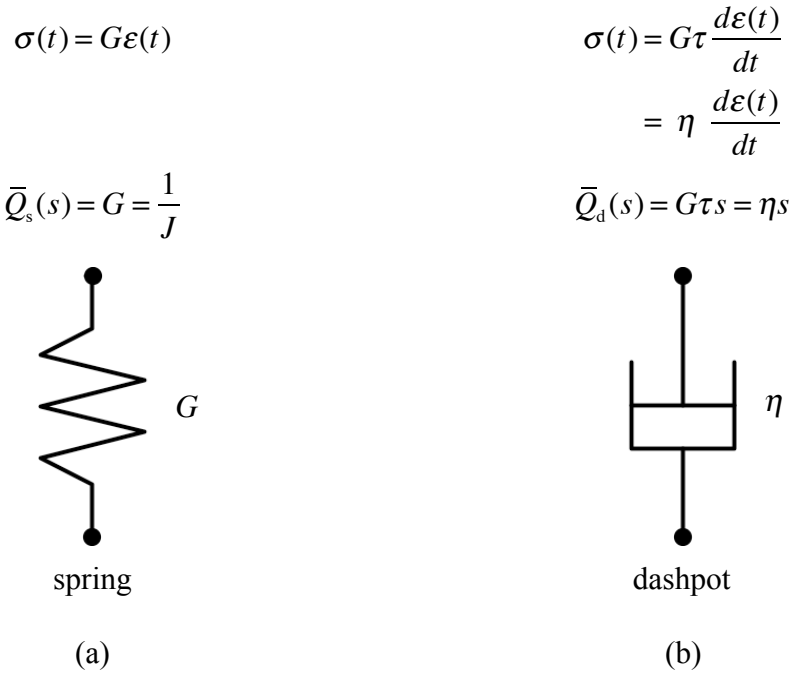

Figure D.1. Model representation, operational shear relaxance, and constitutive equation of purely elastic (a) and purely viscous (b) linear behavior.

D.4 Standard Series-Parallel Models

D.4.1 Basic Units: Spring and Dashpot

Mechanical models furnish a convenient way of modeling the response of linear viscoelastic materials. In these models, the underlying physical system is replaced by idealized counterparts of its actual constitutive elements. Specifically, it is customary to use the symbol of a *spring* (Figure D.1(a)) to represent storage of potential energy, and the symbol of a *dashpot* (Figure D.1(b)) to represent dissipation of mechanical energy. It

is further assumed that the spring behaves as a *Hookean* (i.e. *linear*) *solid with negligible mass* and shear modulus G, thereby obeying the constitutive equation (cf. Eq. (D.1))

$$\sigma(t) = G\varepsilon(t) \qquad \text{spring} \tag{D.52}$$

which, upon Laplace transformation, yields the operational shear relaxance (cf. Eqs. (D.2)–(D.5))

$$\bar{Q}_{\mathrm{s}}(s) = G = \frac{1}{J} = \frac{1}{\bar{U}_{\mathrm{s}}(s)} \tag{D.53}$$

where $J = 1/G$ is the corresponding shear compliance (cf. Eq. (D.21) for $t \to 0$). The spring is therefore the idealized mechanical element exhibiting *purely elastic linear behavior*, and it is fully defined by the single parameter G. Conversely, the dashpot is assumed to behave as a *Newtonian* (i.e. *linear*) *liquid with negligible mass* and shear viscosity $\eta = G\tau$ (τ being a characteristic retardation time), thereby obeying the constitutive equation (cf. Eq. (D.1))

$$\sigma(t) = G\tau \frac{d\varepsilon(t)}{dt} \qquad \text{dashpot} \tag{D.54}$$

which, upon Laplace transformation, yields the operational shear relaxance (cf. Eqs. (D.2)–(D.5))

$$\bar{Q}_{\mathrm{d}}(s) = G\tau s = \eta s = \frac{1}{\bar{U}_{\mathrm{d}}(s)} \tag{D.55}$$

The dashpot is thus the idealized mechanical element exhibiting *purely viscous linear behavior*, and it is fully defined by the single parameter η.

Springs and dashpots are the basic units of classical mechanical models. When arranged in series and/or parallel combinations, the corresponding models are referred to

as *series-parallel models*. In a series combination, the strains are additive and the same stress acts through all of the elements. In a parallel combination, all elements see the same strain and the stresses in the elements are additive. Hence, series-parallel models obey the *combination rules* that *retardances add in series* and *relaxances add in parallel*.

$$\bar{Q}_{\mathrm{M}}(s) = \frac{G\tau s}{1+\tau s} \qquad \bar{U}_{\mathrm{V}}(s) = \frac{J}{1+\tau s}$$

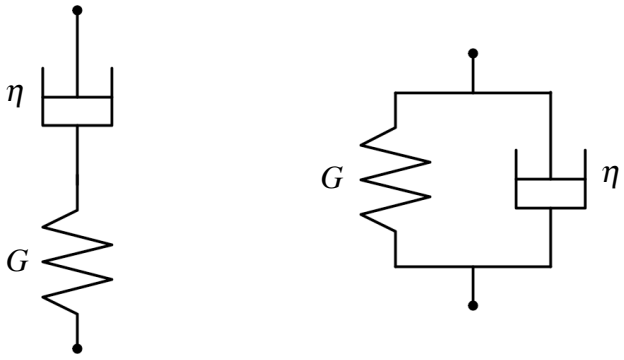

Maxwell model (M) Voigt model (V)

(a) (b)

Figure D.2. (a) The (2-parameter) Maxwell model (M), and its operational shear relaxance $\bar{Q}_{\mathrm{M}}(s)$. (b) The (2-parameter) Voigt model (V), and its operational shear retardance $\bar{U}_{\mathrm{V}}(s)$.

D.4.2 Building Blocks: the Maxwell (M) and Voigt (V) Models

The series combination of a spring and a dashpot is commonly referred to as the Maxwell model[357] (Figure D.2(a)). It follows from the combination rule and Eq. (D.5) that

$$\begin{aligned} \bar{U}_{\mathrm{M}}(s) &= \bar{U}_{\mathrm{s}}(s) + \bar{U}_{\mathrm{d}}(s) \\ \bar{Q}_{\mathrm{M}}(s) &= \frac{G\tau s}{1+\tau s} \end{aligned} \tag{D.56}$$

where $\tau = G/\eta$ represents the *relaxation time* of the model. Substitution of Eq. (D.56)b in Eq. (D.4)a and inverse Laplace transformation lead to the constitutive equation of the Maxwell model in the time domain

$$\sigma(t) + \tau \frac{d\sigma(t)}{dt} = G\tau \frac{d\varepsilon(t)}{dt} \qquad \text{Maxwell model (M)} \tag{D.57}$$

The parallel combination of a spring and a dashpot is commonly referred to as the Voigt model[358] (Figure D.2(b)). It follows from the combination rule and Eq. (D.5) that

$$\begin{aligned} \bar{Q}_{\mathrm{V}}(s) &= \bar{Q}_{\mathrm{s}}(s) + \bar{Q}_{\mathrm{d}}(s) \\ \bar{U}_{\mathrm{V}}(s) &= \frac{J}{1+\tau s} \end{aligned} \tag{D.58}$$

where $\tau = G/\eta$ represents the *retardation time* of the model. Substitution of Eq. (D.58)b in Eq. (D.4)b and inverse Laplace transformation lead to the constitutive equation of the Voigt model in the time domain

$$\sigma(t) = G\varepsilon(t) + G\tau \frac{d\varepsilon(t)}{dt} \qquad \text{Voigt model (V)} \tag{D.59}$$

It is straightforward to show that the Maxwell model is capable of expressing stress relaxation but not strain retardation (i.e. creep); the reverse is true for the Voigt model.

Thus, neither model can satisfactorily represent viscoelastic behavior. They are, however, the basic building blocks out of which more complex models can be constructed. An adequate model of *solid-like* (i.e. $G_{eq} > 0$ and $\eta_0 \rightarrow \infty$) linear viscoelastic behavior requires a minimum of three elements (two springs and one dashpot), while *liquid-like* (i.e. $G_{eq} = 0$ and η_0 finite) behavior must be modeled by no less than four elements (two springs and two dashpots). Because of the combination rules, 3- and 4-parameter models are constructed by adding to a Maxwell model in parallel (*Maxwell models*) and to a Voigt model in series (*Voigt models*). Moreover, physically meaningful behavior requires a finite instantaneous modulus G_g (i.e. a non-vanishing instantaneous compliance $J_g = 1/G_g$); series-parallel models that exhibit such behavior are called *standard* and will be discussed in the next section.

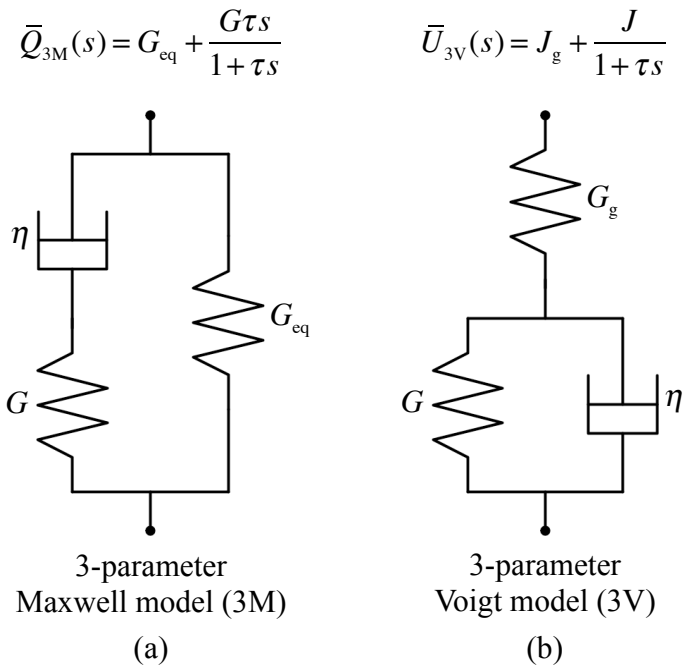

Figure D.3. The models of the *standard linear solid* (i.e. G_g finite, $G_{eq} > 0$, and $\eta_0 \to \infty$). (a) The 3-parameter Maxwell model (3M) or Zener model, and its operational shear relaxance $\bar{Q}_{3M}(s)$. (b) The 3-parameter Voigt model (3V) or Poynting–Thomson model, and its operational shear retardance $\bar{U}_{3V}(s)$.

D.4.3 The Models of the Standard Linear Solid

3-parameter Maxwell model (3M) or Zener model

In Figure D.3(a) it is shown the model obtained by adding a spring in parallel to a Maxwell model, usually called the *standard 3-parameter Maxwell model* (3M)[150] or the *Zener model*[359]. It follows from the combination rule that

$$\begin{aligned}\bar{Q}_{3M}(s) &= \bar{Q}_s(s) + \bar{Q}_M(s) \\ &= G_{eq} + \frac{G\tau s}{1+\tau s} \\ &= \frac{G_{eq} + G_g \tau s}{1+\tau s}\end{aligned} \tag{D.60}$$

where $\tau = G/\eta$ represents the *relaxation time* of the model. Inserting Eq. (D.60)b into Eqs. (D.13)a and (D.23)a, and inverting into the time domain yield (cf. Appendix B, Table B.1, LTP (5) and (6))

$$\begin{aligned}G_{3M}(t) &= G_{eq} + Ge^{-t/\tau} \\ \eta_{3M}(t) &= G_{eq}t + G\tau\left(1 - e^{-t/\tau}\right)\end{aligned} \tag{D.61}$$

where $G_{3M}(0) = G_g = G_{eq} + G$ is the *instantaneous* (or glassy) *shear modulus*, G is called the *relaxing shear modulus*, and $G_{3M}(t \to \infty) = G_{eq}$ is the *equilibrium shear modulus*. Notice that $\eta_{3M}(0) = 0$, and

$$\lim_{t\to\infty} \eta_{3M}(t) = \eta_{3M,0} \to \infty \tag{D.62}$$

3-parameter Voigt model (3V) or Poynting–Thomson model

In Figure D.3(b) it is shown the model obtained by adding a spring in series to a Voigt model, usually called the *standard 3-parameter Voigt model* (3V)[150] or the *Poynting–Thomson model*[359]. It follows from the combination rule that

$$\begin{aligned}\bar{U}_{3V}(s) &= \bar{U}_s(s) + \bar{U}_V(s) \\ &= J_g + \frac{J}{1+\tau s}\end{aligned} \tag{D.63}$$

where $\tau = G/\eta$ represents the *retardation time* of the model. Inserting Eq. (D.63)b into Eq. (D.17)a and inverting into the time domain yield (cf. Appendix B, Table B.1, LTP (6))

$$J_{3V}(t) = J_g + J\left(1 - e^{-t/\tau}\right) \tag{D.64}$$

where $J_{3V}(0) = J_g = 1/G_g$ is the *instantaneous* (or glassy) *shear compliance*, J is called the *retarded* or *delayed shear compliance*, and $J_{3V}(t \to \infty) = J_g + J = J_{eq} = 1/G_{eq}$ is the *equilibrium shear compliance*.

The behavior of the two models (3M and 3V) is qualitatively identical, and it can be made quantitatively identical with the proper choice of the numerical values of their parameters. Thus, they are *conjugate models* (i.e. they respond identically to the same excitation). Substitution of Eq. (D.60)b in Eq. (D.4)a, or of Eq. (D.63)b in Eq. (D.4)b, followed by inverse Laplace transformation leads to the constitutive equation of the *standard linear solid* (i.e. G_g finite, $G_{eq} > 0$, and $\eta_0 \to \infty$) in the time domain

$$\sigma(t) + \tau \frac{d\sigma(t)}{dt} = G_{eq}\varepsilon(t) + G_g \tau \frac{d\varepsilon(t)}{dt} \qquad \text{Standard Linear Solid} \tag{D.65}$$

D.4.4 The Models of the Standard Linear Liquid

4-parameter Maxwell model (4M)

In Figure D.4(a) it is shown the model obtained by adding two Maxwell models in parallel, usually called the *standard* 4*-parameter Maxwell model* (4M)[150]. It follows from the combination rule that

$$\begin{aligned} \bar{Q}_{4M}(s) &= \bar{Q}_{M_1}(s) + \bar{Q}_{M_2}(s) \\ &= \frac{G_1\tau_1 s}{1+\tau_1 s} + \frac{G_2\tau_2 s}{1+\tau_2 s} \end{aligned} \tag{D.66}$$

where $\tau_1 = G_1/\eta_1$ and $\tau_2 = G_2/\eta_2$ represent the two *relaxation times* of the model.

$$\bar{Q}_{4M}(s) = \frac{G_1\tau_1 s}{1+\tau_1 s} + \frac{G_2\tau_2 s}{1+\tau_2 s} \qquad \bar{U}_{4V}(s) = J_g + \frac{J}{1+\tau s} + \frac{1}{\eta_0 s}$$

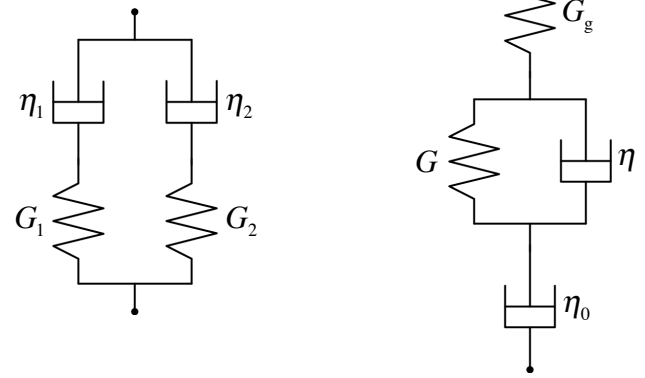

4-parameter Maxwell model (4M) (a)

4-parameter Voigt model (4V) (b)

Figure D.4. The models of the *standard linear liquid* (i.e. G_g finite, $G_{eq} = 0$, and η_0 finite). (a) The 4-parameter Maxwell model (4M), and its operational shear relaxance $\bar{Q}_{4M}(s)$. (b) The 4-parameter Voigt model (4V) or Burgers model, and its operational shear retardance $\bar{U}_{4V}(s)$.

Inserting Eq. (D.66)b into Eqs. (D.13)a and (D.23)a, and inverting into the time domain yield (cf. Appendix B, Table B.1, LTP (5) and (6))

$$\begin{aligned} G_{4M}(t) &= G_1 e^{-t/\tau_1} + G_2 e^{-t/\tau_2} \\ \eta_{4M}(t) &= G_1\tau_1\left(1-e^{-t/\tau_1}\right) + G_2\tau_2\left(1-e^{-t/\tau_2}\right) \end{aligned} \tag{D.67}$$

where $G_{4M}(0) = G_g = G_1 + G_2$ is the *instantaneous* (or glassy) *shear modulus*. Notice that $G_{4M}(t \to \infty) = G_{eq} = 0$, $\eta_{4M}(0) = 0$, and

$$\lim_{t\to\infty}\eta_{4\mathrm{M}}(t)=\eta_{4\mathrm{M},0}=G_1\tau_1+G_2\tau_2=\eta_1+\eta_2 \tag{D.68}$$

4-parameter Voigt model (4V) or Burgers model

In Figure D.4(b) it is shown the model obtained by adding a spring and a dashpot in series to a Voigt model, usually called the *standard* 4*-parameter Voigt model* (4V)[150] or the *Burgers model*[569]. It follows from the combination rule that

$$\begin{aligned}\bar{U}_{4\mathrm{V}}(s)&=\bar{U}_{\mathrm{s}}(s)+\bar{U}_{\mathrm{V}}(s)+\bar{U}_{\mathrm{d}}(s)\\&=J_{\mathrm{g}}+\frac{J}{1+\tau s}+\frac{1}{\eta_0 s}\end{aligned} \tag{D.69}$$

where $\tau = G/\eta$ represents the *retardation time* and η_0 the *steady-state shear viscosity* of the model (i.e. $\eta_{4\mathrm{V}}(t \to \infty) = \eta_{4\mathrm{V},0} = \eta_0$). Inserting Eq. (D.69)b into Eq. (D.17)a and inverting into the time domain yield (cf. Appendix B, Table B.1, LTP (3) and (6))

$$J_{4\mathrm{V}}(t)=J_{\mathrm{g}}+J\left(1-e^{-t/\tau}\right)+\frac{t}{\eta_0} \tag{D.70}$$

where $J_{4\mathrm{V}}(0) = J_{\mathrm{g}} = 1/G_{\mathrm{g}}$ is the *instantaneous* (or glassy) *shear compliance*, and J is the *retarded* or *delayed shear compliance*. At long times, $J_{4\mathrm{V}}(t) - t/\eta_0$ approaches a limiting value

$$\lim_{t\to\infty}\left[J_{4\mathrm{V}}(t)-\frac{t}{\eta_0}\right]=J_{\mathrm{g}}+J=J_{\mathrm{eq}}^0 \tag{D.71}$$

Therefore, J_{eq}^0 is called the *steady-state shear compliance*, and $G_{\mathrm{eq}}^0=1/J_{\mathrm{eq}}^0$ is the corresponding *steady-state shear modulus*.

As can be seen from Eqs. (D.61), (D.64), (D.67), and (D.70), the separation of the response into a purely elastic, viscoelastic, and (if it is present) a purely viscous

contribution is characteristic of the *retardance* (i.e. the *Voigt models*); in the *Maxwell models* the three contributions are not separated into additive terms.

The behavior of the two models (4M and 4V) is again qualitatively identical, and it can be made quantitatively identical with the proper choice of the numerical values of their parameters. Thus, they are *conjugate models*. Substitution of Eq. (D.66)b in Eq. (D.4)a, or of Eq. (D.69)b in Eq. (D.4)b, followed by inverse Laplace transformation leads to the constitutive equation of the *standard linear liquid* (i.e. G_g finite, $G_{eq} = 0$, and η_0 finite) in the time domain (cf. Eq. (D.1))

$$\sigma(t) + u_1 \frac{d\sigma(t)}{dt} + u_2 \frac{d^2\sigma(t)}{dt^2} = q_0 \varepsilon(t) + q_2 \frac{d^2\varepsilon(t)}{dt^2} \qquad \text{Standard Linear Liquid} \quad \text{(D.72)}$$

with

$$\begin{aligned} u_1 &= \tau_1 + \tau_2 \\ u_2 &= \tau_1 \tau_2 \\ q_0 &= G_1 \tau_1 + G_2 \tau_2 \\ q_2 &= \left(G_1 + G_2\right) \tau_1 \tau_2 \end{aligned} \qquad \text{(D.73)}$$

D.4.5 The Generalized (Standard) Series-Parallel Models

The standard 3- and 4-parameter series-parallel models allow one to gain insight into the physical meaning of typical viscoelastic phenomena as stress relaxation, strain retardation (i.e. creep), instantaneous and equilibrium modulus and compliance, steady-state modulus and compliance, steady-state viscosity, and concepts such as relaxation and retardation time. Generally, however, an accurate representation of the behavior of most

viscoelastic materials requires series-parallel models with a large (or even infinite) number of springs and dashpots.

It is convenient to introduce a notation that will allow us to treat solid-like and liquid-like behavior simultaneously. Following Tschoegl's approach, we use braces around the parameters (or their subscripts or superscripts) which must be either present or absent depending on whether or not the model exhibits steady-state flow (i.e. liquid-like behavior).

The generalized (standard) Maxwell model

By adding further Maxwell models (Figure D.2(a)) in parallel to the standard 3-parameter Maxwell model (Figure D.3(a)) we obtain the operational shear relaxance of the *generalized* (standard) *Maxwell model* (cf. Eq. (D.60)b)

$$\bar{Q}(s) = \left\{G_{\mathrm{eq}}\right\} + \sum_{n=1}^{N} \frac{G_{\mathrm{n}}\tau_{\mathrm{n}}s}{1+\tau_{\mathrm{n}}s} \tag{D.74}$$

where the braces around the first term indicate that this term must be present for the model to exhibit solid-like behavior. Since Eq. (D.74) implies a *discrete* (or *line*) *distribution of relaxation times* τ_{n}'s, each modulus G_{n} represents the *relaxation* (or *spectral*) *strength* at $t = \tau_{\mathrm{n}}$. The *discrete relaxation spectrum* corresponding to Eq. (D.74) is

$$H(\tau) = \sum_{n=1}^{N} G_{\mathrm{n}}\tau_{\mathrm{n}}\delta\left(\tau - \tau_{\mathrm{n}}\right) \tag{D.75}$$

Accordingly, Eq. (D.61) translates into a Prony or Dirichlet series for the shear relaxation modulus

$$G(t) = \left\{G_{\text{eq}}\right\} + \sum_{n=1}^{N} G_{\text{n}} e^{-t/\tau_{\text{n}}} \tag{D.76}$$

with

$$G_{\text{g}} = \left\{G_{\text{eq}}\right\} + \sum_{n=1}^{N} G_{\text{n}} \tag{D.77}$$

while the transient shear viscosity becomes

$$\begin{aligned}
\eta(t) &= \left\{G_{\text{eq}} t\right\} + \sum_{n=1}^{N} G_{\text{n}} \tau_{\text{n}} \left(1 - e^{-t/\tau_{\text{n}}}\right) \\
&= \left\{G_{\text{eq}} t\right\} + \sum_{n=1}^{N} G_{\text{n}} \tau_{\text{n}} - \sum_{n=1}^{N} G_{\text{n}} \tau_{\text{n}} e^{-t/\tau_{n}} \\
&= \left\{G_{\text{eq}} t\right\} + \sum_{n=1}^{N} \eta_{\text{n}} \quad - \sum_{n=1}^{N} \eta_{\text{n}} e^{-t/\tau_{\text{n}}} \\
&= \left\{G_{\text{eq}} t\right\} + \eta_{\{0\}} \quad - \sum_{n=1}^{N} \eta_{\text{n}} e^{-t/\tau_{\text{n}}}
\end{aligned} \tag{D.78}$$

with (cf. Eqs. (D.24) and (D.68))

$$\begin{aligned}
\lim_{t\to\infty} \left[\eta(t) - \left\{G_{\text{eq}} t\right\}\right] &= \eta_{\{0\}} \\
&= \sum_{n=1}^{N} \eta_{\text{n}} = \sum_{n=1}^{N} G_{\text{n}} \tau_{\text{n}}
\end{aligned} \tag{D.79}$$

Thus, $\eta_{\{0\}}$ is the sum of the shear viscosities of all dashpots. When the behavior is solid-like, the sum does not represent the steady-state shear viscosity (which diverges) and is then written simply as η. When the behavior is liquid-like, the braces are omitted because the sum of the viscosities is then the steady-state shear viscosity η_0.

Inserting Eq. (D.74) into Eq. (D.34), or Eq. (D.76) into Eq. (D.35), leads to

$$
\begin{aligned}
G^*(\omega) &= \left\{G_{\text{eq}}\right\} + \sum_{n=1}^{N} \frac{G_{\text{n}} \cdot i\omega\tau_{\text{n}}}{1 + i\omega\tau_{\text{n}}} \\
G'(\omega) &= \left\{G_{\text{eq}}\right\} + \sum_{n=1}^{N} \frac{G_{\text{n}} \left(\omega\tau_{\text{n}}\right)^2}{1 + \left(\omega\tau_{\text{n}}\right)^2} \\
G''(\omega) &= \sum_{n=1}^{N} \frac{G_{\text{n}}\omega\tau_{\text{n}}}{1 + \left(\omega\tau_{\text{n}}\right)^2}
\end{aligned}
\tag{D.80}
$$

The generalized (standard) Voigt model

By adding further Voigt models (Figure D.2(b)) in series to the standard 4-parameter Voigt model (Figure D.4(b)) we obtain the operational shear retardance of the *generalized* (standard) *Voigt model* (cf. Eq. (D.69)b)

$$
\bar{U}(s) = J_{\text{g}} + \sum_{n=1}^{N} \frac{J_{\text{n}}}{1 + \tau_{\text{n}} s} + \left\{\frac{1}{\eta_0 s}\right\} \tag{D.81}
$$

where the braces around the last term indicate that this term must be absent for the model to exhibit solid-like behavior. Since Eq. (D.81) implies a *discrete* (or *line*) *distribution of retardation times* τ_{n}'s, each compliance J_{n} represents the *retardation* (or *spectral*) *strength* at $t = \tau_{\text{n}}$. The *discrete retardation spectrum*, $L(\tau)$, is analogous to Eq. (D.75). Accordingly, the shear creep compliance given by Eq. (D.70) becomes

$$
\begin{aligned}
J(t) &= J_{\text{g}} + \sum_{n=1}^{N} J_{\text{n}} \left(1 - e^{-t/\tau_{\text{n}}}\right) + \left\{\frac{t}{\eta_0}\right\} \\
&= J_{\text{g}} + \sum_{n=1}^{N} J_{\text{n}} - \sum_{n=1}^{N} J_{\text{n}} e^{-t/\tau_{\text{n}}} + \left\{\frac{t}{\eta_0}\right\} \\
&= J_{\text{eq}}^{\{0\}} - \sum_{n=1}^{N} J_{\text{n}} e^{-t/\tau_{\text{n}}} + \left\{\frac{t}{\eta_0}\right\}
\end{aligned}
\tag{D.82}
$$

with (cf. Eq. (D.71))

$$\lim_{t\to\infty}\left[J(t)-\left\{\frac{t}{\eta_0}\right\}\right]=J_{\text{eq}}^{\{0\}}$$
$$=J_{\text{g}}+\sum_{n=1}^{N}J_{\text{n}} \tag{D.83}$$

Thus, $J_{\text{eq}}^{\{0\}}$ is the equilibrium shear compliance J_{eq} when the behavior is solid-like, and the steady-state shear compliance J_{eq}^{0} when the behavior is liquid-like.

Inserting Eq. (D.81) into Eq. (D.39), or Eq. (D.82) into Eq. (D.40), leads to

$$\begin{aligned}
J^*(\omega)&=J_{\text{g}}+\sum_{n=1}^{N}\frac{J_{\text{n}}}{1+i\omega\tau_{\text{n}}}+\left\{\frac{1}{i\omega\eta_0}\right\}\\
J'(\omega)&=J_{\text{g}}+\sum_{n=1}^{N}\frac{J_{\text{n}}}{1+\left(\omega\tau_{\text{n}}\right)^2}\\
J''(\omega)&=\sum_{n=1}^{N}\frac{J_{\text{n}}\omega\tau_{\text{n}}}{1+\left(\omega\tau_{\text{n}}\right)^2}+\left\{\frac{1}{\omega\eta_0}\right\}
\end{aligned} \tag{D.84}$$

The generalized Maxwell and Voigt models we have just discussed contain N Maxwell and Voigt submodels (respectively). It is generally useful to let N approach infinity. In this case, to retain the standard character of the models (i.e. finite instantaneous modulus G_{g} and non-vanishing instantaneous compliance $J_{\text{g}} = 1/G_{\text{g}}$) the distributions of moduli and compliances must be bounded (cf. Eqs. (D.77) and (D.83)b), i.e.

$$\sum_{n=1}^{\infty}G_{\text{n}}=G_{\text{g}}-\left\{G_{\text{eq}}\right\}$$
$$\sum_{n=1}^{\infty}J_{\text{n}}=J_{\text{eq}}^{\{0\}}-J_{\text{g}} \tag{D.85}$$

The generalized Maxwell and Voigt models with $N \to \infty$ and subjected to the restriction of Eq. (D.85) are called *canonical models*.

D.5 Spectral Response Functions

The stress response functions $\bar{Q}(s)$, $G(t)$, $\eta(t)$, and $G^*(\omega)$ – given respectively by Eqs. (D.74), (D.76), (D.78), and (D.80) – and the strain response functions $\bar{U}(s)$, $J(t)$, and $J^*(\omega)$ – given respectively by Eqs. (D.81), (D.82), and (D.84) – were written in terms of *discrete spectral distributions* of relaxation and retardation times, respectively (cf. Eq. (D.75)). When N is very large, the relaxation or retardation times become so closely spaced that the sum of the discrete contributions may be replaced by the integral over appropriate continuous functions, i.e. the *continuous spectral distributions* or *spectral response functions*. Material response functions written in terms of continuous spectral distributions are said to be expressed in the *canonical representation* if they are the continuous analogs of the discrete forms associated with the canonical models (cf. Eq. (D.85)).

Relaxation spectrum

The canonical representation of the stress response functions is based on the extension of Eq. (D.74) to the continuous limit, i.e.

$$\begin{aligned}\bar{Q}(s) &= \left\{G_{\mathrm{eq}}\right\} + \sum_{n=1}^{N} \frac{G_{\mathrm{n}}\tau_{\mathrm{n}}s}{1+\tau_{\mathrm{n}}s} \\ &= \left\{G_{\mathrm{eq}}\right\} + \int_{0}^{\infty} \hat{Q}(\tau)\frac{\tau s}{1+\tau s}d\tau \\ &= \left\{G_{\mathrm{eq}}\right\} + \int_{-\infty}^{+\infty} H(\tau)\frac{\tau s}{1+\tau s}d\ln\tau\end{aligned} \tag{D.86}$$

where $\hat{Q}(\tau)$ is the continuous distribution of relaxation times (having the same dimensions as $Q(t)$, i.e. Pa/s), and $H(\tau)=\tau\cdot\hat{Q}(\tau)$ is the continuous distribution of shear moduli (with dimension of Pa) and is called the *shear relaxation spectrum*. Using Eq. (D.86), Eqs. (D.76), (D.78), and (D.80) become

$$\begin{aligned}\frac{\bar{Q}(s)}{s}=\bar{G}(s)&=\left\{\frac{G_{\text{eq}}}{s}\right\}+\int_{-\infty}^{+\infty}H(\tau)\frac{\tau}{1+\tau s}d\ln\tau\\ G(t)&=\left\{G_{\text{eq}}\right\}+\int_{-\infty}^{+\infty}H(\tau)e^{-t/\tau}\,d\ln\tau\end{aligned}\tag{D.87}$$

$$\begin{aligned}\frac{\bar{Q}(s)}{s^2}=\bar{\eta}(s)&=\left\{\frac{G_{\text{eq}}}{s^2}\right\}+\int_{-\infty}^{+\infty}H(\tau)\frac{\tau}{s(1+\tau s)}d\ln\tau\\ \eta(t)&=\left\{G_{\text{eq}}t\right\}+\int_{-\infty}^{+\infty}\tau H(\tau)\left(1-e^{-t/\tau}\right)d\ln\tau\end{aligned}\tag{D.88}$$

$$\begin{aligned}\bar{Q}(s)\big|_{s=i\omega}=G^*(\omega)&=\left\{G_{\text{eq}}\right\}+\int_{-\infty}^{+\infty}H(\tau)\frac{i\omega\tau}{1+i\omega\tau}d\ln\tau\\ G'(\omega)&=\left\{G_{\text{eq}}\right\}+\int_{-\infty}^{+\infty}H(\tau)\frac{(\omega\tau)^2}{1+(\omega\tau)^2}d\ln\tau\\ G''(\omega)&=\int_{-\infty}^{+\infty}H(\tau)\frac{\omega\tau}{1+(\omega\tau)^2}d\ln\tau\end{aligned}\tag{D.89}$$

while the complex shear viscosity $\eta^*(\omega)$ follows from Eq. (D.36) as

$$\begin{aligned}\frac{G^*(\omega)}{i\omega}=\eta^*(\omega)&=\left\{\frac{G_{\text{eq}}}{i\omega}\right\}+\int_{-\infty}^{+\infty}H(\tau)\frac{\tau}{1+i\omega\tau}d\ln\tau\\ \frac{G''(\omega)}{\omega}=\eta'(\omega)&=\int_{-\infty}^{+\infty}H(\tau)\frac{\tau}{1+(\omega\tau)^2}d\ln\tau\\ \frac{G'(\omega)}{\omega}=\eta''(\omega)&=\left\{\frac{G_{\text{eq}}}{\omega}\right\}+\int_{-\infty}^{+\infty}H(\tau)\frac{\omega\tau^2}{1+(\omega\tau)^2}d\ln\tau\end{aligned}\tag{D.90}$$

The constant-strain-rate modulus, $R(t)$, is obtained from Eqs. (D.26) and (D.28) as

$$\int_s^{\infty} \bar{\eta}(x)dx = \bar{R}(s) = \left\{\frac{G_{\text{eq}}}{s}\right\} + \int_{-\infty}^{+\infty} \tau H(\tau) \ln\left(1 + \frac{1}{\tau s}\right) d\ln\tau$$
$$\frac{\eta(t)}{t} = R(t) = \left\{G_{\text{eq}}\right\} + \frac{1}{t}\int_{-\infty}^{+\infty} \tau H(\tau)\left(1 - e^{-t/\tau}\right) d\ln\tau \tag{D.91}$$

where we have made use of LTP (7) (Appendix B, Table B.1).

Retardation spectrum

In a completely analogous fashion, the canonical representation of the strain response functions is based on the extension of Eq. (D.81) to the continuous limit, i.e.

$$\begin{aligned}\bar{U}(s) &= J_{\text{g}} + \sum_{n=1}^{N} \frac{J_{\text{n}}}{1+\tau_{\text{n}} s} + \left\{\frac{1}{\eta_0 s}\right\} \\ &= J_{\text{g}} + \int_0^{\infty} \hat{U}(\tau)\frac{1}{1+\tau s} d\tau + \left\{\frac{1}{\eta_0 s}\right\} \\ &= J_{\text{g}} + \int_{-\infty}^{+\infty} L(\tau)\frac{1}{1+\tau s} d\ln\tau + \left\{\frac{1}{\eta_0 s}\right\}\end{aligned} \tag{D.92}$$

where $\hat{U}(\tau)$ is the continuous distribution of retardation times (having the same dimensions as $U(t)$, i.e. 1/Pa·s), and $L(\tau) = \tau \cdot \hat{U}(\tau)$ is the continuous distribution of shear compliances (with dimension of 1/Pa) and is called the *shear retardation spectrum*. Using Eq. (D.92), Eqs. (D.82) and (D.84) become

$$\frac{\bar{U}(s)}{s} = \bar{J}(s) = \frac{J_{\text{g}}}{s} + \int_{-\infty}^{+\infty} L(\tau)\frac{1}{s(1+\tau s)} d\ln\tau + \left\{\frac{1}{\eta_0 s^2}\right\}$$
$$J(t) = J_{\text{g}} + \int_{-\infty}^{+\infty} L(\tau)\left(1 - e^{-t/\tau}\right) d\ln\tau + \left\{\frac{t}{\eta_0}\right\} \tag{D.93}$$

$$\bar{U}(s)\Big|_{s=i\omega} = J^*(\omega) = J_g + \int_{-\infty}^{+\infty} L(\tau)\frac{1}{1+i\omega\tau}d\ln\tau \quad + \left\{\frac{1}{i\omega\eta_0}\right\}$$

$$J'(\omega) \;= J_g + \int_{-\infty}^{+\infty} L(\tau)\frac{1}{1+(\omega\tau)^2}d\ln\tau \tag{D.94}$$

$$J''(\omega) = \qquad \int_{-\infty}^{+\infty} L(\tau)\frac{\omega\tau}{1+(\omega\tau)^2}d\ln\tau + \left\{\frac{1}{\omega\eta_0}\right\}$$

Thus, linear experimental responses of isotropic materials can be described by time-independent *viscoelastic constants* (associated with purely elastic or viscous behavior) – i.e. G_g, $\{G_{eq}\}$, J_g, $J_{eq}^{\{0\}}$, and $\eta_{\{0\}}$ – coupled with *integral transforms* (Appendix B, Eq. (B.1)) *of spectral response functions* (governing the viscoelastic behavior) – i.e. $H(\tau)$ and $L(\tau)$. Furthermore, it follows from Eqs. (D.87)–(D.94) that the material response functions are all *functionals*, i.e. every given value of a response function (e.g. $G(t_0)$) depends on all values of the spectral function (e.g. $H(\tau)$) over its entire domain of definition from $\tau = 0$ to $\tau \to \infty$.

Obviously, the spectral response functions cannot be obtained directly by any experiment. They must be extracted mathematically from Eqs. (D.87)–(D.94). The integrals involving $H(\tau)$ and $L(\tau)$ are Fredholm integral equations of the first kind. In principle, they can be solved explicitly for $H(\tau)$ or $L(\tau)$, but it is a mathematically "ill-posed" problem (because small perturbations in the experimental data can lead to arbitrarily large perturbations in the spectrum).

When the spectra are slowly changing functions of τ, they can be estimated by processes of differentiation of the experimental data. In particular, since the step response

functions (Eqs. (D.87) and (D.93)) are essentially Laplace transforms of the spectra (cf. Appendix B, §B.2), approximations to the spectra can be obtained by approximate inversion of the Laplace transform on the real time axis. Similarly, since the harmonic response functions (Eqs. (D.89) and (D.94)) are essentially Stieltjes transform of the spectra (cf. Appendix B, §B.5), approximations to the spectra can be obtained by approximate inversion of the Stieltjes transform on the real time axis. Approximations to the spectra include, to the zeroth order

$$H_0(\tau) = \frac{2}{\pi} G''(1/\tau) \tag{D.95}$$

and to the first order

$$\begin{aligned} H_1(\tau) &= \left. \frac{dG'(\omega)}{d\ln\omega} \right|_{\omega=1/\tau} \\ H_1(\tau) &= -\left. \frac{dG(t)}{d\ln t} \right|_{t=\tau} \end{aligned} \tag{D.96}$$

D.5.1 The Viscoelastic Constants

We now examine the relationships between the viscoelastic constants and the spectral response functions. While discussing the standard series-parallel models we mentioned that the following equations always hold (cf. Eqs. (D.21) and (D.71))

$$\begin{aligned} G_g J_g &= 1 \\ G_{eq}^{\{0\}} J_{eq}^{\{0\}} &= 1 \end{aligned} \tag{D.97}$$

Using the definitions of the viscoelastic constants (§D.3.2, Eqs. (D.24), (D.61), (D.64), (D.71), (D.79), and (D.83)), the *limit value theorems* of the Laplace transform (Appendix

B, §B.2.3), and Eqs. (D.86)c, (D.87)b, (D.88)b, (D.89)b, (D.90)b, (D.92)c, (D.93)b, and (D.94)b, we obtain

$$\begin{aligned} G_{\mathrm{g}} &= \lim_{t\to 0} G(t) = \lim_{s\to\infty} s\bar{G}(s) = \lim_{s\to\infty} \bar{Q}(s) \\ &= \lim_{\omega\to\infty} G'(\omega) \\ &= \left\{G_{\mathrm{eq}}\right\} + \int_{-\infty}^{+\infty} H(\tau)\, d\ln\tau \end{aligned} \tag{D.98}$$

$$\begin{aligned} G_{\mathrm{eq}} &= \lim_{t\to\infty} G(t) = \lim_{s\to 0} s\bar{G}(s) = \lim_{s\to 0} \bar{Q}(s) \\ &= \lim_{\omega\to 0} G'(\omega) \end{aligned} \tag{D.99}$$

$$\begin{aligned} J_{\mathrm{g}} &= \lim_{t\to 0} J(t) = \lim_{s\to\infty} s\bar{J}(s) = \lim_{s\to\infty} \bar{U}(s) \\ &= \lim_{\omega\to\infty} J'(\omega) \end{aligned} \tag{D.100}$$

$$\begin{aligned} J_{\mathrm{eq}}^{\{0\}} &= \lim_{t\to\infty}\left[J(t) - \left\{\frac{t}{\eta_0}\right\}\right] = \lim_{s\to 0}\left[s\bar{J}(s) - \left\{\frac{1}{\eta_0 s}\right\}\right] = \lim_{s\to 0}\left[\bar{U}(s) - \left\{\frac{1}{\eta_0 s}\right\}\right] \\ &= \lim_{\omega\to 0} J'(\omega) \\ &= J_{\mathrm{g}} + \int_{-\infty}^{+\infty} L(\tau)\, d\ln\tau \end{aligned} \tag{D.101}$$

$$\begin{aligned} \eta_{\{0\}} &= \lim_{t\to\infty}\left[\eta(t) - \left\{G_{\mathrm{eq}} t\right\}\right] = \lim_{s\to 0}\left[s\bar{\eta}(s) - \left\{\frac{G_{\mathrm{eq}}}{s}\right\}\right] \\ &= \lim_{\omega\to 0} \eta'(\omega) \\ &= \lim_{\omega\to 0} \frac{G''(\omega)}{\omega} \\ &= \int_{-\infty}^{+\infty} \tau H(\tau)\, d\ln\tau \end{aligned} \tag{D.102}$$

Thus, the *initial value theorem* (Appendix B, Eq. (B.13)) allows one to ascertain, from the operational respondances $\bar{Q}(s)$ and $\bar{U}(s)$, whether or not the model is standard. Conversely, the *final value theorem* (Appendix B, Eq. (B.14)) permits the distinction

between solid-like and liquid-like behavior. We also notice that the zeroth order approximation to $H(\tau)$, Eq. (D.95), may be suggested by a comparison of Eq. (D.50)b with Eq. (D.98)c.

Terminal behavior of linear viscoelastic *solids*

Based on Eqs. (D.99)b and (D.102)b-c, the *terminal behavior* (i.e. for $\omega \to 0$) of a linear viscoelastic *solid* is described by

$$\begin{aligned} \eta'(\omega \to 0) &= \eta \\ \eta''(\omega \to 0) &= G_{\text{eq}} \cdot \frac{1}{\omega} \end{aligned} \tag{D.103}$$

$$\begin{aligned} G'(\omega \to 0) &= G_{\text{eq}} \\ G''(\omega \to 0) &= \eta \cdot \omega \end{aligned} \tag{D.104}$$

where η represents the integral of all viscous contributions (Eq. (D.102)d), not the steady-state viscosity (cf. Eq. (D.79)). Notice that η may or may not be finite (vide infra).

Terminal behavior of linear viscoelastic *liquids*

It is useful to derive from Eq. (D.101)b the expression applicable to viscoelastic *liquids*, i.e. J_{eq}^0. It follows from Eqs. (D.43)a, (D.89)b-c, and (D.102)d that

$$\begin{aligned} J_{\text{eq}}^{\{0\}} &= \lim_{\omega \to 0} J'(\omega) \\ &= \lim_{\omega \to 0} \frac{G'(\omega)}{\left[G'(\omega)\right]^2 + \left[G''(\omega)\right]^2} \\ &= \begin{cases} \dfrac{\int_{-\infty}^{+\infty} \tau^2 H(\tau)\, d\ln\tau}{\left(\eta_0\right)^2} = J_{\text{eq}}^0 & \text{for } \textit{liquid - like} \text{ behavior} \\ \dfrac{1}{G_{\text{eq}}} = J_{\text{eq}} & \text{for } \textit{solid - like} \text{ behavior} \end{cases} \end{aligned} \tag{D.105}$$

Therefore, combining Eqs. (D.90)c and (D.105)c yields

$$\begin{aligned} J_{\text{eq}}^{0} &= \frac{1}{\left(\eta_0\right)^2} \lim_{\omega \to 0} \frac{\eta''(\omega)}{\omega} \\ &= \frac{1}{\left(\eta_0\right)^2} \lim_{\omega \to 0} \frac{G'(\omega)}{\omega^2} \end{aligned} \tag{D.106}$$

Moreover, it follows from Eqs. (D.46), (D.106)b, and de L'Hospital's rule that

$$J_{\text{eq}}^{0} = \frac{1}{\left(\eta_0\right)^2} \int_0^\infty G(t) t \, dt \tag{D.107}$$

Based on Eqs. (D.102)b-c and (D.106), the *terminal behavior* of a linear viscoelastic *liquid* obeys the general limiting laws

$$\begin{aligned} \eta'(\omega \to 0) &= \eta_0 \\ \eta''(\omega \to 0) &= \eta_0^2 J_{\text{eq}}^{0} \cdot \omega \end{aligned} \tag{D.108}$$

$$\begin{aligned} G'(\omega \to 0) &= \eta_0^2 J_{\text{eq}}^{0} \cdot \omega^2 \\ G''(\omega \to 0) &= \eta_0 \cdot \omega \end{aligned} \tag{D.109}$$

The intersection of these limiting laws defines a frequency

$$\omega_{\text{w}} = \frac{1}{\eta_0 J_{\text{eq}}^{0}} \tag{D.110}$$

that can serve as a *characteristic relaxation rate* for viscoelastic liquids.[232,272] Its reciprocal

$$\tau_{\text{w}} = \eta_0 J_{\text{eq}}^{0} \tag{D.111}$$

can serve as a *characteristic relaxation time* for viscoelastic liquids.[389] The reason for the subscript "w" in Eqs. (D.110) and (D.111) will become clear in the next section.

Let us suppose that the viscoelastic behavior of a material is well-described by the generalized Maxwell model discussed in §D.4.5, and let τ_1 be the *longest relaxation time* of the model, i.e. $\tau_1 = \max\left\{\tau_n\right\}_{n=1}^{N}$. Then, by inserting Eq. (D.76) into Eqs. (D.24) and (D.107), it is straightforward to show that[22]

$$\begin{aligned} \eta_0 &\approx G(\tau_1)\tau_1 \\ J_{eq}^0 &\approx \frac{1}{G(\tau_1)} \end{aligned} \tag{D.112}$$

therefore[22,340]

$$\tau_1 \approx \tau_w \tag{D.113}$$

D.5.2 Moments of the Spectral Response Functions

The n^{th} moment about the origin of a continuous distribution $P(x)$ defined on $[0, \infty)$ is given by

$$\left\langle x^n \right\rangle = \frac{\int_0^\infty x^n P(x)\,dx}{\int_0^\infty P(x)\,dx} \tag{D.114}$$

The first moment about the origin is called the *mean* and is denoted by $\overline{x}$: it determines the *location* of the distribution along the axis of x. Higher moments are particularly useful when computed about the mean rather than the origin, i.e.

$$\left\langle \left(x-\overline{x}\right)^n \right\rangle = \frac{\int_0^\infty \left(x-\overline{x}\right)^n P(x)\,dx}{\int_0^\infty P(x)\,dx} \tag{D.115}$$

The second moment about the mean is called the *variance* and is denoted by σ^2. The square root, σ, is the *standard deviation*. This is a measure of the *spread*, or *breadth*, of the distribution. The equation for the variance is

$$\begin{aligned}\left\langle (x-\overline{x})^2 \right\rangle &= \frac{\int_0^\infty (x-\overline{x})^2 P(x)\,dx}{\int_0^\infty P(x)\,dx} \\ &= \left\langle x^2 \right\rangle - \overline{x}^2 \\ &= (\mathrm{PDI}-1)\overline{x}^2 \\ &= \sigma^2\end{aligned} \tag{D.116}$$

where PDI is the *polydispersity index*, defined as

$$\mathrm{PDI} = \frac{\left\langle x^2 \right\rangle}{\overline{x}^2} \tag{D.117}$$

The third moment about the mean, when normalized through division by σ^3, is called the *skewness*, and is a measure of the *asymmetry* of the distribution.

Average relaxation times

Let $P(x)$ be the continuous distribution of relaxation times $\hat{Q}(\tau)$. It follows from Eq. (D.98)c and the identity $H(\tau) = \tau \cdot \hat{Q}(\tau)$ that

$$\int_0^\infty \hat{Q}(\tau)\,d\tau = \int_{-\infty}^{+\infty} H(\tau)\,d\ln\tau = G_g - \left\{G_{eq}\right\} \tag{D.118}$$

Notice that Eq. (D.118) is the continuous analog of Eq. (D.85)a. Using Eqs. (D.102)d, (D.114), and (D.118), the first moment about the origin (i.e. the mean of the distribution) is given by

$$\begin{aligned}\langle\tau\rangle &= \frac{\int_0^{\infty}\tau\hat{Q}(\tau)d\tau}{\int_0^{\infty}\hat{Q}(\tau)d\tau} = \frac{\int_{-\infty}^{+\infty}\tau H(\tau)d\ln\tau}{\int_{-\infty}^{+\infty}H(\tau)d\ln\tau} \\ &= \frac{\eta_{\{0\}}}{G_g - \{G_{eq}\}} \\ &= \tau_n\end{aligned} \tag{D.119}$$

It is called the *number-average relaxation time* and denoted by τ_n, in analogy with the moments of the distribution of molar masses in a polymer chain.[27,45] It is clear from Eq. (D.119)b that τ_n is always finite for viscoelastic liquids. For viscoelastic solids, $\eta_{\{0\}}$ (hence, τ_n) may or may not be finite depending on the shape of $H(\tau)$ and how fast it goes to zero for $\tau \to \infty$ (see, e.g., the comment on page 65 of Ferry's book[42]). It is straightforward to show that for materials (such as critical gels) characterized by a power-law distribution of relaxation times[150], i.e. $H(\tau) \sim \tau^{-m}$ on the interval $[\tau_{min}, \infty)$, $\eta_{\{0\}} \to \infty$ for $m < 1$ (Appendix E, §E.3).

For viscoelastic *liquids*, it is possible to compute the second moment about the origin. From Eqs. (D.105)c (D.114), and (D.118), we obtain

$$\begin{aligned}\langle\tau^2\rangle &= \frac{\int_0^{\infty}\tau^2\hat{Q}(\tau)d\tau}{\int_0^{\infty}\hat{Q}(\tau)d\tau} = \frac{\int_{-\infty}^{+\infty}\tau^2 H(\tau)d\ln\tau}{\int_{-\infty}^{+\infty}H(\tau)d\ln\tau} \\ &= \frac{(\eta_0)^2 J_{eq}^0}{G_g} \\ &= \tau_n\tau_w\end{aligned} \tag{D.120}$$

where τ_w is defined as

$$\tau_w = \frac{\int_0^\infty \tau^2 \hat{Q}(\tau) d\tau}{\int_0^\infty \tau \hat{Q}(\tau) d\tau} = \frac{\int_{-\infty}^{+\infty} \tau^2 H(\tau) d\ln\tau}{\int_{-\infty}^{+\infty} \tau H(\tau) d\ln\tau} = \eta_0 J_{eq}^0 \tag{D.121}$$

and called the *weight-average relaxation time*[27,45] (cf. Eq. (D.111)). Therefore, average relaxation times are calculated as ratios of successive moments of the relaxation spectrum $H(\tau)$. Their ratio, i.e. the *polydispersity index of relaxation times*,

$$\frac{\tau_w}{\tau_n} = \text{PDI} = J_{eq}^0 G_g \tag{D.122}$$

is a dimensionless measure of the *spread* of the distribution[27,45] (cf. Eqs. (D.116) and (D.117). Average retardation times and spread of $L(\tau)$ can be found in a similar manner.

The relaxation spectrum for polymeric materials generally consists of two or more dispersions (a dispersion being a collection of related relaxation processes[45]). Thus, τ_n and τ_w can be applied to the entire (unresolved) distribution of relaxation times or to each individual dispersion (in this case, the lower and upper integration limits in Eqs. (D.119) and (D.121) extend over the range of the resolved individual dispersions).[45]

If a dispersion were described by a single Maxwell model (Figure D.2(a)), then $\tau_w/\tau_n = 1$. This follows directly from Eqs. (D.76) with $G_{eq} = 0$, $N = 1$, and $G_1 = G_g$, Eq. (D.112) and Eq. (D.122). Hence, the value of τ_w/τ_n measures the *deviation from a single exponential relaxation*.

Average relaxation times in the terminal region of viscoelastic *liquids*

Highly entangled systems, especially those of narrow molar mass distribution, are characterized by a terminal dispersion at long times (terminal region) which is more or less isolated from the more rapid processes. Because η_0 and J_{eq}^0 depend on weighted averages over $H(\tau)$ (Eqs. (D.102)d and (D.105)c), their values are controlled almost completely by the terminal processes. Furthermore, the shear plateau modulus G_N^0 represents the initial modulus for the terminal region. Thus, from Eqs. (D.119), (D.121), and (D.122), we can define *average relaxation times* and *spectral width for the terminal region* as[27,45]

$$\begin{aligned} \tau_n &= \frac{\eta_0}{G_N^0} \\ \tau_w &= \eta_0 J_{eq}^0 \\ \frac{\tau_w}{\tau_n} &= J_{eq}^0 G_N^0 \end{aligned} \tag{D.123}$$

As opposed to the plateau modulus G_N^0, the steady-state compliance J_{eq}^0 is very sensitive to large-scale structural features such as molar mass distribution and long-chain branching.[45] As a result, the product $J_{eq}^0 G_N^0$ increases as the molar mass distribution becomes broader.[27]

Experiments on melts and solutions of nearly monodisperse and well-entangled *linear* chains have shown that the product $J_{eq}^0 G_N^0$ is insensitive to both concentration and chain molar mass M, and[27,45,79]

$$J_{\mathrm{eq}}^{0}G_{\mathrm{N}}^{0} \approx 2.5 \qquad \text{for } Z = \frac{M}{M_{\mathrm{e}}^{\mathrm{G}}} >\approx 7 \qquad \text{linear polymers (exp)} \qquad \text{(D.124)}$$

By contrast, the tube model proposed by Doi and Edwards[46] for an entangled, monodisperse linear polymer predicts

$$J_{\mathrm{eq}}^{0}G_{\mathrm{N}}^{0} = \frac{6}{5} \qquad \text{linear polymers (theory)} \qquad \text{(D.125)}$$

which reflects the nearly-exponential relaxation modulus predicted by this model.

Assembled data on melts and solutions of nearly monodisperse and well-entangled *star* chains have shown that the product $J_{\mathrm{eq}}^{0}G_{\mathrm{N}}^{0}$ depends on both concentration and arm molar mass M_{a} as[174]

$$J_{\mathrm{eq}}^{0}G_{\mathrm{N}}^{0} \approx 0.5Z_{\mathrm{a}} \qquad \text{with } Z_{\mathrm{a}} = \frac{M_{\mathrm{a}}}{M_{\mathrm{e}}^{\mathrm{G}}} \qquad \text{star polymers (exp)} \qquad \text{(D.126)}$$

For star-shaped polymers, the tube model theory with no constraint release (i.e. no dynamic dilution, $\alpha = 0$ – cf. Chapter 3, Eq. (3.21)) proposed by Pearson and Helfand[174] predicts

$$J_{\mathrm{eq}}^{0}G_{\mathrm{N}}^{0} = \frac{3}{2}Z_{\mathrm{a}} \qquad \text{with } \alpha = 0 \qquad \text{star polymers (theory)} \qquad \text{(D.127)}$$

while the theory developed by Ball and McLeish[173] for $\alpha = 1$ gives

$$J_{\mathrm{eq}}^{0}G_{\mathrm{N}}^{0} = \frac{3}{4}Z_{\mathrm{a}} \qquad \text{with } \alpha = 1 \qquad \text{star polymers (theory)} \qquad \text{(D.128)}$$

D.6 Linear Viscoelastic Functions and Constants in Uniaxial Extension

The discussion so far has been limited to linear viscoelastic behavior in simple shear. All of the equations in the previous sections remain valid when a material is subjected to *uniaxial extension* (see, however, footnote [a] at the beginning of §D.2 for the meaning of $\varepsilon(t)$). Material response functions, spectral response functions, and viscoelastic constants are identified by the term *stretched*, *tensile*, *elongational*, or *extensional* (rather than shear), and are assigned the symbols shown in Table D.1.

Table D.1. Symbols for linear viscoelastic functions and constants in *simple shear* and *uniaxial extension*.

		Mode of Deformation	
Excitation	*Quantity*	*Simple Shear*	*Uniaxial Extension*
Strain	Relaxation Spectrum	$H(\tau)$	$H_E(\tau)$
	Distribution of Relaxation Times	$\hat{Q}(\tau)$	$\hat{Y}(\tau)$
	Relaxance (Memory Function)	$Q(t)$	$Y(t)$
	Relaxation Modulus	$G(t)$	$E(t)$
	Instantaneous Modulus	G_g	E_g
	Equilibrium Modulus	G_{eq}	E_{eq}
	Transient Viscosity	$\eta(t)$	$\eta_E(t)$
	Steady-State Viscosity	η_0	$\eta_{E,0}$
	Constant-Strain-Rate Modulus	$R(t)$	$F(t)$
	Complex Modulus	$G^*(\omega)$	$E^*(\omega)$
	Storage Modulus	$G'(\omega)$	$E'(\omega)$
	Loss Modulus	$G''(\omega)$	$E''(\omega)$
	Complex Viscosity	$\eta^*(\omega)$	$\eta_E^*(\omega)$
	Storage Viscosity	$\eta'(\omega)$	$\eta_E'(\omega)$
	Loss Viscosity	$\eta''(\omega)$	$\eta_E''(\omega)$
Stress	Retardation Spectrum	$L(\tau)$	$L_D(\tau)$
	Distribution of Retardation Times	$\hat{U}(\tau)$	$\hat{L}(\tau)$
	Retardance (Memory Function)	$U(t)$	$L(t)$
	Creep Compliance	$J(t)$	$D(t)$
	Instantaneous Compliance	J_g	D_g
	Equilibrium Compliance	J_{eq}	D_{eq}
	Steady-State Compliance	J_{eq}^0	D_{eq}^0
	Complex Compliance	$J^*(\omega)$	$D^*(\omega)$
	Storage Compliance	$J'(\omega)$	$D'(\omega)$
	Loss Compliance	$J''(\omega)$	$D''(\omega)$

Appendix E

Wedge Relaxation Spectrum, Power-Law Relaxation Spectrum, and Chambon–Winter's Critical Gel Model

This Appendix is concerned with the modeling of the relaxation spectrum through power-laws, via wedge and power-law distributions, as well as Chambon–Winter's critical gel model. For the first time in literature, we obtain the analytical expression of the transient viscosity for the wedge distribution. The following material is relevant to Chapter 3 (cf. the Bueche–Ferry law), and especially to Chapters 4, 5, 6, and Appendix F.

E.1 Introduction

Molecular theories of the viscoelastic behavior of polymers predict *discrete* distributions of relaxation times. For instance, from a statistical mechanical analysis of the behavior of monodisperse linear polymer chains in dilute solutions Rouse[47] derived a relaxation spectrum (i.e. moduli distribution) of the form (cf. Appendix D, Eq. (D.75))

$$H^{\text{Rouse}}(\tau) = G\sum_{p=1}^{S}\tau_{\text{p}}\delta(\tau-\tau_{\text{p}}) \tag{E.1}$$

with[42] (cf. Chapter 3, Eq. (3.14), and end of §3.3.4.IV-c)

$$\begin{aligned} &\tau \text{ large } \textit{enough}\text{, i.e. away from the glassy relaxation modes} \\ &G = \frac{\rho RT}{M} \\ &\tau_p = \frac{\tau_1}{p^2} \qquad \text{for large } S \\ &\tau_1 = \tau_R = \frac{1}{6\pi^2}\frac{\zeta_0 b^2}{kT}N^2 \end{aligned} \tag{E.2}$$

where $\delta(\tau - \tau_p)$ denotes the Dirac delta function centered at the relaxation time $\tau = \tau_p$, and τ_1 represents the longest relaxation time of the model (called the Rouse time of the chain). The *Rouse spectrum*, Eqs. (E.1) and (E.2), is a *non-standard* (i.e. $G(0) = G_g = 1/J_g \rightarrow \infty$, Appendix D, §D.4.2) discrete distribution[150], equivalent to a *generalized Maxwell model* with $G_n = G$ (cf. Appendix D, Eq. (D.75)) or, alternatively, to the ladder model of springs and dashpots introduced in 1956 by Gross[363,364] and in 1962 by Marvin[365]. In the customary limit of $S \rightarrow \infty$, the *Gross–Marvin ladder model* yields the material response functions of the Rouse distribution in closed form.[150,363-365] Over a certain range of τ_p's, the relaxation times are so closely spaced that the discrete Rouse spectrum can be approximated by a *continuous* distribution function of the power-law-type, i.e. $H^{Rouse}(\tau) \sim \tau^{-1/2}$ (cf. Chapter 3, Figure 3.4(b), Eq. (3.15), and the Bueche–Ferry law). As pointed out by Larson[269], the power-law character of the continuous Rouse spectrum is a consequence of equally-weighted relaxation times (i.e. $G_n = G$). Thus, a similar state of play holds for the continuous *Zimm spectrum*[570], $H^{Zimm}(\tau) \sim \tau^{-2/3}$, but not for the *Doi–Edwards spectrum*[46].

In §D.5 of Appendix D, continuous spectral distributions were introduced in a similar fashion: the description of experimentally observed viscoelastic behavior by series-

parallel models generally requires a very large (practically infinite) number of Maxwell or Voigt submodels whose respondances times are so closely spaced that resolution becomes impossible.

Here, we are concerned with *mathematical models* that represent the general shape of observed relaxation and retardation spectra by simple continuous functions. In particular, we will discuss approximations to the relaxation spectrum through *power-laws*, as described by the *wedge distribution* (w), and its progressively simplified versions, i.e. the *power-law distribution* (p), and *Chambon–Winter's critical gel model* (cg). Stress relaxing in a power-law fashion is an expression of *mechanical self-similarity*, i.e. it is the same at all scales of observations (in analogy with geometrical self-similarity[253-258]). Thus, self-similar dynamics is often called "*scale invariant*", "*scale free*", "*fractal*", or "*fractional*" (Appendix F).

In what follows, we will adopt the notation appropriate for *uniaxial extension* (Appendix D, Table D.1); however, for the extensional relaxation spectrum $H_E(\tau)$, the transient extensional viscosity $\eta_E(t)$, the steady-state extensional viscosity $\eta_{E,0}$, and the extensional stress $\sigma_E(t)$ we will drop the subscript "E" and only use the subscript "w", "p", or "cg" depending on whether the spectrum is represented by the wedge distribution, the power-law distribution, or Chambon–Winter's critical gel model (respectively).

E.2 The Wedge Distribution of Relaxation Times

The wedge distribution is based on the experimental observation that a plot of log $H(\tau)$ vs. log τ often yields, over a restricted range of τ, a straight line with a negative slope m (e.g. Chapter 3, Figure 3.4(b); Chapter 4, Figures 4.2(b), 4.5(b), and 4.7(b)), i.e.

$$-\frac{d\log H(\tau)}{d\log\tau} = m > 0 \tag{E.3}$$

Thus, the *wedge distribution* (w) *of relaxation times*, $\hat{Y}_{\mathrm{w}}(\tau) = H_{\mathrm{w}}(\tau)/\tau$, is defined by the *relaxation spectrum*[150,267]

$$H_{\mathrm{w}}(\tau) = \begin{cases} H_0 \cdot \left(\dfrac{\tau}{\tau_0}\right)^{-m} & \text{for } \tau \in \left[\tau_{\min}, \tau_{\max}\right] \\ 0 & \text{elsewhere} \end{cases} \tag{E.4}$$

The value of the constant H_0 (which has dimensions of Pa) can be expressed in terms of $\tau_{\min}$, $\tau_{\max}$, and the viscoelastic constants through the normalization condition (Appendix D, Eq. (D.113)). In keeping with the notation introduced in Appendix D, §D.4.5, we will use braces around the parameters (or their subscripts or superscripts) which must be either present or absent depending on whether or not the model exhibits steady-state flow (i.e. liquid-like behavior).

Let ΔE be

$$\Delta E = E_{\mathrm{g}} - \left\{E_{\mathrm{eq}}\right\} \tag{E.5}$$

then the normalization condition

$$\Delta E = \int_{-\infty}^{+\infty} H_{\mathrm{w}}(\tau)\, d\ln\tau = \int_{\tau_{\min}}^{\tau_{\max}} \frac{H_{\mathrm{w}}(\tau)}{\tau}\, d\tau = H_0 \left(\tau_0\right)^m \int_{\tau_{\min}}^{\tau_{\max}} \tau^{-m-1}\, d\tau \tag{E.6}$$

yields

$$H_0 = \frac{\Delta E \cdot m}{\left[1-\left(\frac{\tau_{\min}}{\tau_{\max}}\right)^m\right]}\left(\frac{\tau_0}{\tau_{\min}}\right)^{-m} = H_{\mathrm{w},0}\left(\frac{\tau_0}{\tau_{\min}}\right)^{-m} \tag{E.7}$$

with the new constant $H_{\mathrm{w},0}$ defined as

$$H_{\mathrm{w},0} = \frac{\Delta E \cdot m}{\left[1-\left(\frac{\tau_{\min}}{\tau_{\max}}\right)^m\right]} \tag{E.8}$$

Hence, we may rewrite Eq. (E.4) as

$$H_{\mathrm{w}}(\tau) = \begin{cases} \dfrac{\Delta E \cdot m}{\left[1-\left(\frac{\tau_{\min}}{\tau_{\max}}\right)^m\right]}\left(\dfrac{\tau}{\tau_{\min}}\right)^{-m} = H_{\mathrm{w},0}\left(\tau_{\min}\right)^m \tau^{-m} & \text{for } \tau \in \left[\tau_{\min}, \tau_{\max}\right] \\ 0 & \text{elsewhere} \end{cases} \tag{E.9}$$

To find the *operational extensional relaxance* for the wedge distribution, $\bar{Y}_{\mathrm{w}}(s)$ (Appendix D, Table D.1), we substitute Eq. (E.9) into Eq. (D.85)c. This gives

$$\bar{Y}_{\mathrm{w}}(s) = \left\{E_{\mathrm{eq}}\right\} + H_{\mathrm{w},0}\left(\tau_{\min} s\right)^m \int_{\tau_{\min} s}^{\tau_{\max} s} \frac{(\tau s)^{-m}}{1+\tau s} d(\tau s) \tag{E.10}$$

which, with the change of variable $\tau s = 1/x$, yields[150]

$$\begin{aligned} \bar{Y}_{\mathrm{w}}(s) &= \left\{E_{\mathrm{eq}}\right\} + H_{\mathrm{w},0}\left(\tau_{\min} s\right)^m \left[\mathrm{B}_{\mathrm{T}}\left(m, 1-m; \frac{1}{\tau_{\min} s}\right) - \mathrm{B}_{\mathrm{T}}\left(m, 1-m; \frac{1}{\tau_{\max} s}\right)\right] \\ &= \left\{E_{\mathrm{eq}}\right\} + H_{\mathrm{w},0}\left(\tau_{\min} s\right)^m \left[\mathrm{B}\left(m, 1-m; \frac{1}{1+\tau_{\min} s}\right) - \mathrm{B}\left(m, 1-m; \frac{1}{1+\tau_{\max} s}\right)\right] \end{aligned} \tag{E.11}$$

$$\text{for } 0 < m < 1$$

where $B(p, q; x)$ and $B_T(p, q; x)$ are the incomplete beta functions defined in Appendix C, §C.4, and we have made use of Eq. (C.14) (notice that the definition of the incomplete beta functions henceforth restricts the validity of this treatment to $0 < m < 1$).

From $\overline{Y}(s) = s\overline{E}(s)$ (Eq. (D.14)a) and LTP (12) (Appendix B, Table B.1), the *extensional relaxation modulus* for the wedge distribution, $E_w(t)$, is given by[150]

$$E_w(t) = \left\{E_{eq}\right\} + H_{w,0}\left(\tau_{min}\right)^m t^{-m}\left[\gamma\left(m, \frac{t}{\tau_{min}}\right) - \gamma\left(m, \frac{t}{\tau_{max}}\right)\right] \tag{E.12}$$

where $\gamma(m, x)$ is the lower incomplete gamma function defined in Appendix C, §C.2. The relaxation modulus for the wedge distribution is a monotonic decreasing function, i.e. $E_w(t_1) < E_w(t_2)$ for $t_1 > t_2$. It mimics the transition from one plateau at short times ($E_w(t) \to E_g$ for $t \ll \tau_{min}$) to another plateau at long times ($E_w(t) \to E_{eq}$ for $t \gg \tau_{max}$) through a power-law ($E_w(t) \sim t^{-m}$ for $\tau_{min} \ll t \ll \tau_{max}$). Thus, we may call $E_w(t)$ a function of the Z-type, because its shape resembles that of a Z that has been stretched out by pulling its two ends in opposite directions. Eqs. (E.11)a and (E.12) are derived for simple shear on pages 347–348 of Tschoegl's book[150].

The *transient extensional viscosity* for the wedge distribution, $\eta_w(t)$, can be computed from $\overline{\eta}_E(s) = \overline{E}(s)/s$ (Eq. (D.25)a) and inverse Laplace transformation, or directly in the time domain through Eq. (D.23)b, i.e. by integrating Eq. (E.12)

$$\begin{aligned}\eta_w(t) &= \int_0^t E_w(u)\,du \\ &= \left\{E_{eq}t\right\} + H_{w,0}\left(\tau_{min}\right)^m \int_0^t u^{-m}\left[\gamma\left(m, \frac{u}{\tau_{min}}\right) - \gamma\left(m, \frac{u}{\tau_{max}}\right)\right]du\end{aligned} \tag{E.13}$$

The integral

$$\int_0^t u^{-m}\gamma\left(m,\frac{u}{a}\right)du \tag{E.14}$$

can be calculated with a change of variable, $u/a = x$, followed by integration by parts and the use of Eq. (C.10)

$$\frac{d}{dx}\gamma(m,x) = x^{m-1}e^{-x} \tag{E.15}$$

We obtain

$$\begin{aligned}\int_0^t u^{-m}\gamma\left(m,\frac{u}{a}\right)du &= a^{1-m}\int_0^{t/a} x^{-m}\gamma(m,x)\,dx \\ &= a^{1-m}\left\{\left[\frac{x^{1-m}}{1-m}\gamma(m,x)\right]_0^{t/a} - \frac{1}{1-m}\int_0^{t/a} x^{1-m}x^{m-1}e^{-x}\,dx\right\} \\ &= \frac{a^{1-m}}{1-m}\left[\left(\frac{t}{a}\right)^{1-m}\gamma\left(m,\frac{t}{a}\right) + e^{-t/a} - 1\right]\end{aligned} \tag{E.16}$$

hence

$$\begin{aligned}\eta_{\mathrm{w}}(t) = \left\{E_{\mathrm{eq}}t\right\} + \frac{H_{\mathrm{w},0}\left(\tau_{\min}\right)^m}{1-m}\Bigg\{&t^{1-m}\left[\gamma\left(m,\frac{t}{\tau_{\min}}\right) - \gamma\left(m,\frac{t}{\tau_{\max}}\right)\right] \\ &+\left(\tau_{\min}\right)^{1-m}\left(e^{-t/\tau_{\min}} - 1\right) \\ &-\left(\tau_{\max}\right)^{1-m}\left(e^{-t/\tau_{\max}} - 1\right)\Bigg\}\end{aligned} \tag{E.17}$$

We are not aware of published work providing the analytical expression of the transient viscosity for the wedge distribution, Eq. (E.17). To check the validity of Eq. (E.17) we may use Eq. (D.100) and calculate the viscoelastic constant $\eta_{\{0\},\mathrm{w}}$

$$\begin{aligned}\eta_{\{0\},\mathrm{w}} &= \lim_{t\to\infty}\left[\eta_{\mathrm{w}}(t)-\left\{E_{\mathrm{eq}}t\right\}\right] \\ &= \int_{-\infty}^{+\infty}\tau H_{\mathrm{w}}(\tau)\,d\ln\tau\end{aligned} \tag{E.18}$$

Inserting Eq. (E.9) into Eq. (E.18)b gives

$$\begin{aligned}\eta_{\{0\},\mathrm{w}} &= \int_{\tau_{\min}}^{\tau_{\max}} H_{\mathrm{w}}(\tau)\,d\tau \\ &= H_{\mathrm{w},0}\left(\tau_{\min}\right)^{m}\int_{\tau_{\min}}^{\tau_{\max}}\tau^{-m}\,d\tau \\ &= \frac{H_{\mathrm{w},0}\left(\tau_{\min}\right)^{m}}{1-m}\left[\left(\tau_{\max}\right)^{1-m}-\left(\tau_{\min}\right)^{1-m}\right] \\ &= \Delta E\,\frac{m}{1-m}\,\frac{\left(\tau_{\max}\right)^{1-m}-\left(\tau_{\min}\right)^{1-m}}{\left(\tau_{\min}\right)^{-m}-\left(\tau_{\max}\right)^{-m}}\end{aligned} \tag{E.19}$$

On the other hand, combining Eqs. (E.17) and (E.18)a results in

$$\begin{aligned}\eta_{\{0\},\mathrm{w}} = \frac{H_{\mathrm{w},0}\left(\tau_{\min}\right)^{m}}{1-m}\lim_{t\to\infty}\Bigg\{ & t^{1-m}\left[\gamma\left(m,\frac{t}{\tau_{\min}}\right)-\gamma\left(m,\frac{t}{\tau_{\max}}\right)\right] \\ & +\left(\tau_{\min}\right)^{1-m}\left(e^{-t/\tau_{\min}}-1\right) \\ & -\left(\tau_{\max}\right)^{1-m}\left(e^{-t/\tau_{\max}}-1\right)\Bigg\}\end{aligned} \tag{E.20}$$

The exponentials in Eq. (E.20) vanish, while the limit

$$\lim_{t\to\infty} t^{1-m}\left[\gamma\left(m,\frac{t}{\tau_{\min}}\right)-\gamma\left(m,\frac{t}{\tau_{\max}}\right)\right] \tag{E.21}$$

can be calculated by applying De L'Hospital's rule (because $\gamma(m, \infty) = \Gamma(m)$, Appendix C, Eq. (C.7)a) with

$$\frac{d}{dx}\gamma\left(m,\frac{x}{a}\right) = x^{m-1}a^{-m}e^{-x/a} \tag{E.22}$$

which follows directly from Eq. (E.15). This gives

$$\begin{aligned}\lim_{t\to\infty} t^{1-m}\left[\gamma\left(m,\frac{t}{\tau_{\min}}\right)-\gamma\left(m,\frac{t}{\tau_{\max}}\right)\right] &= \lim_{t\to\infty}\frac{t^{m-1}\left[\left(\tau_{\min}\right)^{-m}e^{-t/\tau_{\min}}-\left(\tau_{\max}\right)^{-m}e^{-t/\tau_{\max}}\right]}{(m-1)t^{m-2}} \\ &= \lim_{t\to\infty}\frac{1}{m-1}\left[\frac{t}{\left(\tau_{\min}\right)^{m}e^{t/\tau_{\min}}}-\frac{t}{\left(\tau_{\max}\right)^{m}e^{t/\tau_{\max}}}\right] \\ &= 0\end{aligned} \tag{E.23}$$

By using this result in Eq. (E.20), the expression for $\eta_{\{0\},\mathrm{w}}$ given by Eq. (E.19) is recovered. Notice that, with $E_{\mathrm{eq}} = 0$ (i.e. $\Delta E = E_{\mathrm{g}}$), Eq. (E.19) represents the *steady-state extensional viscosity* for the wedge distribution, $\eta_{0,\mathrm{w}}$.

The *complex extensional modulus*, $E^{*}_{\mathrm{w}}(\omega)$, follows from the operational relaxance as $E^{*}_{\mathrm{w}}(\omega) = \bar{Y}_{\mathrm{w}}(s)\big|_{s=i\omega}$ (Appendix D, Eq. (D.34)). Separation of the real and imaginary parts yields[150]

$$\begin{aligned}E'_{\mathrm{w}}(\omega) &= \left\{E_{\mathrm{eq}}\right\}+\frac{H_{\mathrm{w},0}}{2}\left(\tau_{\min}\omega\right)^{m}\left[\mathrm{B}_{\mathrm{T}}\left(\frac{m}{2},1-\frac{m}{2};\frac{1}{\omega^{2}\tau_{\min}^{2}}\right)-\mathrm{B}_{\mathrm{T}}\left(\frac{m}{2},1-\frac{m}{2};\frac{1}{\omega^{2}\tau_{\max}^{2}}\right)\right] \\ &= \left\{E_{\mathrm{eq}}\right\}+\frac{H_{\mathrm{w},0}}{2}\left(\tau_{\min}\omega\right)^{m}\left[\mathrm{B}\left(\frac{m}{2},1-\frac{m}{2};\frac{1}{1+\omega^{2}\tau_{\min}^{2}}\right)-\mathrm{B}\left(\frac{m}{2},1-\frac{m}{2};\frac{1}{1+\omega^{2}\tau_{\max}^{2}}\right)\right]\end{aligned} \tag{E.24}$$

and

$$\begin{aligned}E''_{\mathrm{w}}(\omega) &= \frac{H_{\mathrm{w},0}}{2}\left(\tau_{\min}\omega\right)^{m}\left[\mathrm{B}_{\mathrm{T}}\left(\frac{1}{2}+\frac{m}{2},\frac{1}{2}-\frac{m}{2};\frac{1}{\omega^{2}\tau_{\min}^{2}}\right)-\mathrm{B}_{\mathrm{T}}\left(\frac{1}{2}+\frac{m}{2},\frac{1}{2}-\frac{m}{2};\frac{1}{\omega^{2}\tau_{\max}^{2}}\right)\right] \\ &= \frac{H_{\mathrm{w},0}}{2}\left(\tau_{\min}\omega\right)^{m}\left[\mathrm{B}\left(\frac{1}{2}+\frac{m}{2},\frac{1}{2}-\frac{m}{2};\frac{1}{1+\omega^{2}\tau_{\min}^{2}}\right)-\mathrm{B}\left(\frac{1}{2}+\frac{m}{2},\frac{1}{2}-\frac{m}{2};\frac{1}{1+\omega^{2}\tau_{\max}^{2}}\right)\right]\end{aligned} \tag{E.25}$$

Eqs. (E.24)a and (E.25)a are derived for simple shear on page 348 of Tschoegl's book[150].

It is worth mentioning that the model obtained from the wedge distribution is a *standard* model, i.e. it possesses a finite instantaneous modulus $E_w(0) = E_g$. This is in contrast, for instance, with the non-standard behavior (i.e. $E(0) \rightarrow \infty$) exhibited by the Rouse distribution (Eqs. (E.1) and (E.2)), the power-law distribution, and Chambon–Winter's critical gel model (vide infra). To show that Eq. (E.12) is the equation of a standard model, we must show that $E_w(0) = E_g$; since $\gamma(m, 0) = 0$ (Appendix C, Eq. (C.7)b), the proof is obtained by applying De L'Hospital's rule and using Eq. (E.22).

Since the wedge relaxation spectrum yields a standard model, it gives a physically reasonable description of linear viscoelastic behavior at short times, i.e. relaxation times that include the transition to *glassy behavior*. As a result, the wedge relaxation spectrum was proposed in 1952 by Tobolsky[267,268] to model the glass-rubber viscoelastic transition of polyisobutylene. Furthermore, by examining the long-time behavior of the wedge distribution it is clear (from Eqs. (E.12), (E.17), and (E.20)) that this mathematical model applies equally well to viscoelastic *solids* (defined by a non-zero equilibrium modulus, $E_{eq} > 0$, and a diverging steady-state viscosity, $\eta_0 \rightarrow \infty$) and viscoelastic *liquids* (defined by a vanishing equilibrium modulus, $E_{eq} = 0$, and a finite steady state viscosity, $\eta_0 < \infty$).

The results for the wedge distribution are summarized in Table E.1.

Table E.1. Material response functions for the *wedge distribution* (w) of relaxation times. Notice that this model describes *glassy behavior* (i.e. $E(0) = E_g$), and applies equally well to viscoelastic *solids* (i.e. $E_{eq} > 0$ and $\eta_0 \to \infty$) and viscoelastic *liquids* (i.e. $E_{eq} = 0$ and $\eta_0 < \infty$).

$$\Delta E = E_g - \left\{E_{eq}\right\}$$

$$H_{w,0} = \frac{\Delta E \cdot m}{\left[1-\left(\tau_{min}/\tau_{max}\right)^m\right]}$$

$$H_w(\tau) = \begin{cases} H_{w,0}\left(\tau_{min}\right)^m \tau^{-m} & \text{for } \tau \in \left[\tau_{min},\tau_{max}\right] \text{ and } m \in (0,1) \\ 0 & \text{elsewhere} \end{cases}$$

$$E_w(t) = \left\{E_{eq}\right\} + H_{w,0}\left(\tau_{min}\right)^m t^{-m}\left[\gamma\left(m,t/\tau_{min}\right) - \gamma\left(m,t/\tau_{max}\right)\right]$$

$$\lim_{t\to 0} E_w(t) = E_g \qquad \text{i.e. standard model}$$

$$\eta_w(t) = \left\{E_{eq}t\right\} + \frac{H_{w,0}\left(\tau_{min}\right)^m}{1-m}\left\{t^{1-m}\left[\gamma\left(m,t/\tau_{min}\right) - \gamma\left(m,t/\tau_{max}\right)\right] + \left(\tau_{min}\right)^{1-m}\left(e^{-t/\tau_{min}} - 1\right) - \left(\tau_{max}\right)^{1-m}\left(e^{-t/\tau_{max}} - 1\right)\right\}$$

$$\eta_{\{0\},w} = \Delta E \frac{m}{1-m}\frac{\left(\tau_{max}\right)^{1-m} - \left(\tau_{min}\right)^{1-m}}{\left(\tau_{min}\right)^{-m} - \left(\tau_{max}\right)^{-m}}$$

$$E'_w(\omega) = \left\{E_{eq}\right\} + \frac{H_{w,0}}{2}\left(\tau_{min}\omega\right)^m\left[\mathrm{B}\left(\frac{m}{2},1-\frac{m}{2};\frac{1}{1+\omega^2\tau_{min}^2}\right) - \mathrm{B}\left(\frac{m}{2},1-\frac{m}{2};\frac{1}{1+\omega^2\tau_{max}^2}\right)\right]$$

$$E''_w(\omega) = \frac{H_{w,0}}{2}\left(\tau_{min}\omega\right)^m\left[\mathrm{B}\left(\frac{1}{2}+\frac{m}{2},\frac{1}{2}-\frac{m}{2};\frac{1}{1+\omega^2\tau_{min}^2}\right) - \mathrm{B}\left(\frac{1}{2}+\frac{m}{2},\frac{1}{2}-\frac{m}{2};\frac{1}{1+\omega^2\tau_{max}^2}\right)\right]$$

E.3 The Power-Law Distribution of Relaxation Times

The power-law distribution of relaxation times is a simplified version of the wedge distribution. Specifically, it is based on the assumptions that[150]

1) $\tau_{\min} > 0$, but very small, i.e. $t/\tau_{\min} \gg 1$, $\omega\tau_{\min} \ll 1$, and $\tau_{\min} s \ll 1$

2) $\tau_{\max} \to \infty$

With these assumptions, the ratio $\tau_{\min}/\tau_{\max}$ in Eq. (E.9) vanishes and the *power-law* (p) *relaxation spectrum*, $H_{\mathrm{p}}(\tau)$, is

$$H_{\mathrm{p}}(\tau) = \begin{cases} \Delta E \cdot m \left(\tau_{\min}\right)^{m} \tau^{-m} = H_{\mathrm{p},0} \left(\tau_{\min}\right)^{m} \tau^{-m} = P \cdot m \cdot \tau^{-m} & \text{for } \tau \in \left[\tau_{\min}, \infty\right) \\ 0 & \text{for } \tau < \tau_{\min} \end{cases} \tag{E.26}$$

with

$$H_{\mathrm{p},0} = \Delta E \cdot m \tag{E.27}$$

and the new constant P defined as

$$P = \Delta E \cdot \left(\tau_{\min}\right)^{m} \tag{E.28}$$

Notice that while $H_{\mathrm{p},0}$ has again the dimensions of a modulus, the dimensions of P are Pa·s^{m}. As will be discussed in Appendix F, P is a *quasi-property*[318] related to the fractional dynamics of the system.

The *operational extensional relaxance* for the power-law distribution, $\bar{Y}_{\mathrm{p}}(s)$, follows from Eq. (E.11) with (cf. Appendix C, Eqs. (C.11) and (C.15)a)

$$\lim_{\tau_{\min} s \ll 1} \mathrm{B}\left(m, 1-m; \frac{1}{1+\tau_{\min} s} \right) = \mathrm{B}(m, 1-m)$$
$$= \frac{\Gamma(m)\Gamma(1-m)}{\Gamma(1)} \tag{E.29}$$
$$= \Gamma(m)\Gamma(1-m)$$

and (cf. Appendix C, Eq. (C.15)b)

$$\lim_{\tau_{\max} \to \infty} \mathrm{B}\left(m, 1-m; \frac{1}{1+\tau_{\max} s} \right) = 0 \tag{E.30}$$

yielding

$$\bar{Y}_{\mathrm{p}}(s) = \left\{ E_{\mathrm{eq}} \right\} + P \cdot m\Gamma(m)\Gamma(1-m) \cdot s^m$$
$$= \left\{ E_{\mathrm{eq}} \right\} + P \cdot \Gamma(1+m)\Gamma(1-m) \cdot s^m \tag{E.31}$$
$$= \left\{ E_{\mathrm{eq}} \right\} + P \cdot \frac{\pi m}{\sin(\pi m)} \cdot s^m$$

where $\Gamma(m)$ is the complete gamma function defined in Appendix C, §C.1, and we have used Eqs. (C.2) and (C.4)a (recall that $0 < m < 1$, Eq. (E.11)).

Similarly, the *extensional relaxation modulus* for the power-law distribution, $E_{\mathrm{p}}(t)$, is given by Eq. (E.12) with (cf. Appendix C, Eq. (C.7)a)

$$\lim_{t/\tau_{\min} \gg 1} \gamma\left(m, \frac{t}{\tau_{\min}} \right) \simeq \lim_{t/\tau_{\min} \to \infty} \gamma\left(m, \frac{t}{\tau_{\min}} \right) = \Gamma(m) \tag{E.32}$$

and (cf. Appendix C, Eq. (C.7)b)

$$\lim_{t/\tau_{\max} \to 0} \gamma\left(m, \frac{t}{\tau_{\max}} \right) = 0 \tag{E.33}$$

yielding

$$\begin{aligned} E_{\mathrm{p}}(t) &= \left\{E_{\mathrm{eq}}\right\} + P \cdot m\Gamma(m) \cdot t^{-m} \\ &= \left\{E_{\mathrm{eq}}\right\} + P \cdot \Gamma(1+m) \cdot t^{-m} \end{aligned} \tag{E.34}$$

Clearly, the model obtained with a power-law spectrum is a *non-standard* model, since

$$\lim_{t\to 0} E_{\mathrm{p}}(t) = \lim_{s\to\infty} \overline{Y}_{\mathrm{p}}(s) = \infty \tag{E.35}$$

If $E_{\mathrm{eq}} > 0$, the relaxation modulus for the power-law distribution mimics the transition from a power-law behavior ($E_{\mathrm{p}}(t) \sim t^{-m}$) to a plateau at long times ($E_{\mathrm{p}}(t) \to E_{\mathrm{eq}}$ for $t \to \infty$).

Integration of Eq. (E.34) gives the *transient extensional viscosity* for the power-law distribution, $\eta_{\mathrm{p}}(t)$,

$$\eta_{\mathrm{p}}(t) = \left\{E_{\mathrm{eq}} t\right\} + P \cdot \frac{\Gamma(1+m)}{1-m} \cdot t^{1-m} \tag{E.36}$$

It follows from Eq. (E.36), or Eq. (E.19), that this model does not exhibit steady-state flow, because

$$\eta_{0,\mathrm{p}} = \lim_{t\to\infty} \eta_{\mathrm{p}}(t) = \lim_{\substack{t/\tau_{\min}\gg 1 \\ \tau_{\max}\to\infty}} \eta_{0,\mathrm{w}} = \infty \tag{E.37}$$

and the viscoelastic constant $\eta_{\{0\},\mathrm{p}}$ diverges as well

$$\eta_{\{0\},\mathrm{p}} = \lim_{t\to\infty} \left[\eta_{\mathrm{p}}(t) - \left\{E_{\mathrm{eq}} t\right\}\right] = \lim_{\substack{t/\tau_{\min}\gg 1 \\ \tau_{\max}\to\infty}} \eta_{\{0\},\mathrm{w}} = \infty \tag{E.38}$$

Eq. (E.36) can also be obtained from Eq. (E.17) in the limit for $t/\tau_{\min} \gg 1$ and $\tau_{\max} \to \infty$. Since

$$\lim_{t/\tau_{\min}\gg 1} \left(\tau_{\min}\right)^{1-m} \left(e^{-t/\tau_{\min}} - 1\right) \simeq \lim_{\tau_{\min}\to 0} \left(\tau_{\min}\right)^{1-m} \left(e^{-t/\tau_{\min}} - 1\right) = 0 \tag{E.39}$$

and

$$\begin{aligned}\lim_{\tau_{\max}\to\infty}\left(\tau_{\max}\right)^{1-m}\left(e^{-t/\tau_{\max}}-1\right) &= \lim_{\tau_{\max}\to\infty}\frac{e^{-t/\tau_{\max}}-1}{\left(\tau_{\max}\right)^{m-1}} \\ &= \lim_{\tau_{\max}\to\infty}\frac{t\cdot e^{-t/\tau_{\max}}}{\left(\tau_{\max}\right)^{2}\left(m-1\right)\left(\tau_{\max}\right)^{m-2}} \\ &= \lim_{\tau_{\max}\to\infty}\frac{t\cdot e^{-t/\tau_{\max}}}{\left(m-1\right)\left(\tau_{\max}\right)^{m}} \\ &= 0\end{aligned} \tag{E.40}$$

we obtain

$$\begin{aligned}\lim_{\substack{t/\tau_{\min}\gg 1\\ \tau_{\max}\to\infty}}\eta_{\mathrm{w}}(t) &= \left\{E_{\mathrm{eq}}t\right\}+\frac{H_{\mathrm{p},0}\left(\tau_{\min}\right)^{m}}{1-m}\Gamma(m)\cdot t^{1-m} \\ &= \left\{E_{\mathrm{eq}}t\right\}+\Delta E\left(\tau_{\min}\right)^{m}\frac{m}{1-m}\Gamma(m)\cdot t^{1-m} \\ &= \left\{E_{\mathrm{eq}}t\right\}+P\cdot\frac{\Gamma(1+m)}{1-m}\cdot t^{1-m} \\ &= \eta_{\mathrm{p}}(t)\end{aligned} \tag{E.41}$$

The *constant-strain-rate extensional modulus* for the power-law distribution, $F_{\mathrm{p}}(t) = \eta_{\mathrm{p}}(t)/t$ (Appendix D, Eqs. (D.26), (D.91)b, and Table D.1), is therefore

$$\begin{aligned}F_{\mathrm{p}}(t) &= \frac{\sigma_{\mathrm{p}}(t)}{\varepsilon(t)} = \frac{\sigma_{\mathrm{p}}(t)}{\dot{\varepsilon}_0 t} \\ &= \left\{E_{\mathrm{eq}}\right\}+P\cdot\frac{\Gamma(1+m)}{1-m}\cdot t^{-m}\end{aligned} \tag{E.42}$$

corresponding to a (*constant-strain-rate*) *extensional stress*

$$\sigma_{\mathrm{p}}(t) = \left\{E_{\mathrm{eq}}\dot{\varepsilon}_0 t\right\}+P\cdot\frac{\Gamma(1+m)}{1-m}\cdot\dot{\varepsilon}_0\cdot t^{1-m} \tag{E.43}$$

as a function of the time t, or

$$\sigma_{\mathrm{p}}(\varepsilon) = \left\{E_{\mathrm{eq}}\varepsilon\right\}+P\cdot\frac{\Gamma(1+m)}{1-m}\cdot\left(\dot{\varepsilon}_0\right)^{m}\cdot\varepsilon^{1-m} \tag{E.44}$$

as a function of the strain $\varepsilon = \varepsilon(t) = \dot{\varepsilon}_0 t$.

Notice that the relaxation modulus, $E_p(t)$, and the constant-strain-rate modulus, $F_p(t)$, are similar in magnitude and share the same time dependence, i.e. they both decay as $\sim t^{-m}$ (being related to each other by Eq. (D.27) of Appendix D). As will be discussed in Appendix F (see also Chapter 4), power-law relaxation patterns are a universal feature of *complex systems*. Simple systems, on the other hand, usually obey the classical exponential relaxation predicted by the Maxwell models (i.e. a single exponential decay or a superposition of exponentials – Appendix D, Eq. (D.76)).

It is also evident from Eqs. (E.36), (E.43), and (E.44) that, for small values of m, the power-law distribution approaches a linear time dependence of the transient viscosity, $\eta_p(t) \sim t$, and linear time and strain dependencies of the stress, $\sigma_p(t) \sim t$ and $\sigma_p(\varepsilon) \sim \varepsilon$.

The *complex extensional modulus* for the power-law distribution, $E_p^*(\omega)$, follows from the operational relaxance as $E_p^*(\omega) = \bar{Y}_p(s)\big|_{s=i\omega}$ (Appendix D, Eq. (D.34)),

$$\begin{aligned} E_p^*(\omega) &= \left\{E_{eq}\right\} + P \cdot \frac{\pi m}{\sin(\pi m)} \cdot (i\omega)^m \\ &= \left\{E_{eq}\right\} + P \cdot \frac{\pi m}{\sin(\pi m)} \cdot e^{i\frac{\pi m}{2}} \cdot \omega^m \end{aligned} \tag{E.45}$$

Separation of the real and imaginary parts yields

$$\begin{aligned} E_p'(\omega) &= \left\{E_{eq}\right\} + P \cdot \frac{\pi m/2}{\sin(\pi m/2)} \cdot \omega^m \\ E_p''(\omega) &= \qquad\quad P \cdot \frac{\pi m/2}{\cos(\pi m/2)} \cdot \omega^m \end{aligned} \tag{E.46}$$

with

$$\tan\delta_{p}(\omega)=\frac{\tan\left(\pi m/2\right)}{1+\left\{\dfrac{E_{eq}}{P}\dfrac{\sin\left(\pi m/2\right)}{\pi m/2}\omega^{-m}\right\}} \tag{E.47}$$

As expected, Eqs. (E.24) and (E.25) reduce to Eq. (E.46)a-b in the limit for $t/\tau_{min} \gg 1$ and $\tau_{max} \rightarrow \infty$. The proof entails the use of equations analogous to Eqs. (E.29) and (E.30), coupled with Eqs. (C.4)b and (C.4)d.

It follows from Eqs. (E.31), (E.34), (E.36), and (E.42)–(E.47) that all the material response functions of the power-law distribution depend on the quasi-property P and a numerical coefficient containing m and/or its gamma-function-related values (cf. Appendix C, Eqs. (C.2) and (C.4)).

Since the power-law relaxation spectrum yields a non-standard model, it cannot be used to describe linear viscoelastic behavior in the glassy region of relaxation times. Furthermore, by examining the long-time behavior of the power-law distribution it is clear (from Eqs. (E.34), and (E.36)–(E.38)) that this mathematical model cannot be applied to viscoelastic liquids, which require a finite steady-state viscosity, $\eta_0 < \infty$, coupled with a zero equilibrium modulus, $E_{eq} = 0$. The power-law relaxation spectrum, as defined by Eq. (E.26), always exhibits a diverging steady-state viscosity, $\eta_0 \rightarrow \infty$. As a result, this model is able to describe the (terminal) behavior of viscoelastic *solids* (i.e. $E_{eq} > 0$ and $\eta_0 \rightarrow \infty$), or *critical gels* (defined by a vanishing equilibrium modulus, $E_{eq} = 0$, and a diverging steady-state viscosity, $\eta_0 \rightarrow \infty$)[320,321].

Indeed, a relaxation modulus of the form described by Eq. (E.34) with $E_{eq} > 0$, i.e.

$$E(t) = E_{\text{eq}}\left[1+\left(t/\tau_{\text{m}}\right)^{-m}\right] \qquad \text{with } 0 < m < 1 \tag{E.48}$$

was proposed in 1965 by Chasset and Thirion[155] to model the long-time relaxation behavior of rubber networks with entangled dangling structures (i.e. lightly crosslinked polymers). A molecular interpretation of the so-called *Chasset–Thirion equation* was later provided by Curro and co-workers[185,186], in terms of arm retraction[169] of the dangling strands (cf. Chapter 3, §3.3.4.IV-d and footnote [qq]).

The power-law spectrum for critical gels will be further discussed in the next section.

The results for the power-law distribution are summarized in Table E.2.

Table E.2. Material response functions for the *power-law distribution* (p) of relaxation times. Notice that this model cannot describe glassy behavior (because $E(0) \to \infty$), and can only be applied to viscoelastic *solids* (i.e. $E_{eq} > 0$ and $\eta_0 \to \infty$) or *critical gels* (i.e. $E_{eq} = 0$ and $\eta_0 \to \infty$).

$$\Delta E = E_g - \left\{E_{eq}\right\}$$

$$H_{p,0} = \Delta E \cdot m \qquad P = \Delta E \cdot \left(\tau_{min}\right)^m$$

$$H_p(\tau) = \begin{cases} H_{p,0}\left(\tau_{min}\right)^m \tau^{-m} = P \cdot m \cdot \tau^{-m} & \text{for } \tau \in \left[\tau_{min}, \infty\right) \text{ and } m \in (0,1) \\ 0 & \text{for } \tau < \tau_{min} \end{cases}$$

$$E_p(t) = \left\{E_{eq}\right\} + P \cdot \Gamma(1+m) \cdot t^{-m}$$

$$\lim_{t \to 0} E_p(t) = \infty$$

$$\eta_p(t) = \left\{E_{eq} t\right\} + P \cdot \frac{\Gamma(1+m)}{1-m} \cdot t^{1-m}$$

$$\eta_{\{0\},p} = \eta_{0,p} = \infty$$

$$F_p(t) = \left\{E_{eq}\right\} + P \cdot \frac{\Gamma(1+m)}{1-m} \cdot t^{-m}$$

$$\sigma_p(t) = \left\{E_{eq} \dot{\varepsilon}_0 t\right\} + P \cdot \frac{\Gamma(1+m)}{1-m} \cdot \dot{\varepsilon}_0 \cdot t^{1-m}$$

$$\sigma_p(\varepsilon) = \left\{E_{eq} \varepsilon\right\} + P \cdot \frac{\Gamma(1+m)}{1-m} \cdot \left(\dot{\varepsilon}_0\right)^m \cdot \varepsilon^{1-m}$$

$$E'_p(\omega) = \left\{E_{eq}\right\} + P \cdot \frac{\pi m/2}{\sin\left(\pi m/2\right)} \cdot \omega^m$$

$$E''_p(\omega) = \qquad P \cdot \frac{\pi m/2}{\cos\left(\pi m/2\right)} \cdot \omega^m$$

$$\tan\delta_p(\omega) = \frac{\tan\left(\pi m/2\right)}{1 + \left\{\dfrac{E_{eq}}{P} \dfrac{\sin\left(\pi m/2\right)}{\pi m/2} \omega^{-m}\right\}}$$

E.3.1 Chambon–Winter's Critical Gel Model

The Gel Point

For polymeric materials, the *gel point* marks the transition from liquid-like (i.e. $E_{eq} = 0$ and $\eta_0 < \infty$) to solid-like (i.e. $E_{eq} > 0$ and $\eta_0 \to \infty$) behavior, i.e. it represents a *liquid-solid viscoelastic transition* (LST). As a result, a polymer at the gel point does not yet possess an equilibrium modulus ($E_{eq} = 0$) but already exhibits a divergent longest relaxation time ($\tau_1 \to \infty$), hence (cf. Appendix D, Eqs. (D.108), (D.109)a, (D.110), and (D.118)) a divergent steady-state viscosity ($\eta_0 \to \infty$).[320,321] This LST is caused by a growth of *connectivity*, which correlates molecular motion over larger and larger distances. The spatial extent of this connectivity, i.e. the z-average cluster size R_z, is the *correlation length*.[320,321] At the gel point, the correlation length diverges. To some extent, the gel point is thus analogous to the Curie point for appearance of spontaneous magnetization, or to the vapor-liquid critical point in thermodynamics.[320,321]

The definition of gel point in terms of the equilibrium mechanical properties E_{eq} and η_0 dates back to the classical mean-field theory of Flory[322-325] and Stockmayer[326,327], developed for chemically crosslinked polymers (*chemical gels*). The term *physical gels* is used when the LST occurs via physical linking. Since a polymer at the gel point is in a *critical state* [320,328,329], the name *critical gel* was proposed by Winter and Vilgis[330,331] to distinguish it from the various materials that are commonly called gels.

The Chambon–Winter Spectrum

In a series of papers[289-292] published between 1985 and 1987, Chambon and Winter hypothesized a power-law frequency-dependent complex modulus to model the (terminal) linear viscoelastic behavior of chemical gels at the gel point. The equations they used are similar to Eqs. (E.46) with $E_{eq} = 0$. In the polymer literature, their model is often referred to as the Chambon–Winter spectrum[266,319]. However, rather than assuming a power-law spectrum and deriving the corresponding material response functions accordingly, Chambon and Winter introduced a power-law complex modulus, $G^*(\omega) \sim (i\omega)^m$, as a means to interpret their experimental data and then applied the Kramers[332]–Kronig[333] relations to check for internal consistency. Furthermore, a relaxation spectrum of the power-law-type was first suggested (more than three decades earlier) by Tobolsky[267,268] in the form of the wedge distribution (§E.2). The term *Chambon–Winter's critical gel model* (cg) seems, therefore, more appropriate.

The Chambon–Winter's critical gel model can be obtained from the wedge distribution by assuming that

1) $\tau_{min} > 0$, but very small, i.e. $t/\tau_{min} \gg 1$, $\omega\tau_{min} \ll 1$, and $\tau_{min}s \ll 1$

2) $\tau_{max} \to \infty$

3) $E_{eq} = 0$

and by replacing E_g with some characteristic modulus E associated with the lower time limit τ_{min} (due to glass transition or entanglement effects) of self-similar dynamics. The

phenomenological approach proposed by Chambon and Winter gave the relaxation modulus as

$$E_{cg}(t) = S \cdot t^{-m} \qquad \text{with } 0 < m < 1 \tag{E.49}$$

where S, which has dimensions of Pa·s^m, was called the *gel strength*. Notice that Eq. (E.49) follows from the Chasset–Thirion[155] equation (Eq. (E.48)) on the assumption that $E_{eq} = 0$. Later investigations[293,294,334,335] concluded that $S = E_{eq}(\tau_{min})^m$, where E_{eq} is the equilibrium modulus of the fully crosslinked material[334,335] and $E_{eq}\tau_{min}$ is the steady-state viscosity of the precursor molecule (building block of the chemical gel)[293,294]. Accordingly, a large value of S (i.e. strong gel) is always associated with a small value of m.[266,319] A comparison of Eq. (E.34) with $E_{eq} = 0$ and Eq. (E.49) leads to the relation between the quasi-property P defined earlier and the gel strength S,

$$P \cdot \Gamma(1+m) = S \tag{E.50}$$

The expressions for the Chambon–Winter critical gel model thus follow directly from the results of the previous section, combined with Eqs. (C.2) and (C.4)a of Appendix C. They are summarized in Table E.3.

Table E.3. Material response functions for the *Chambon–Winter critical gel model* (cg).

$$P = E \cdot \left(\tau_{\min}\right)^{m} \qquad P \cdot \Gamma(1+m) = S$$

$$H_{\mathrm{cg}}(\tau) = \begin{cases} P \cdot m \cdot \tau^{-m} = \dfrac{S}{\Gamma(m)} \cdot \tau^{-m} & \text{for } \tau \in \left[\tau_{\min}, \infty\right) \text{ and } m \in (0,1) \\ 0 & \text{for } \tau < \tau_{\min} \end{cases}$$

$$E_{\mathrm{cg}}(t) = P \cdot \Gamma(1+m) \cdot t^{-m} = S \cdot t^{-m}$$

$$\eta_{\mathrm{cg}}(t) = P \cdot \frac{\Gamma(1+m)}{1-m} \cdot t^{1-m} = \frac{S}{1-m} \cdot t^{1-m}$$

$$F_{\mathrm{cg}}(t) = P \cdot \frac{\Gamma(1+m)}{1-m} \cdot t^{-m} = \frac{S}{1-m} \cdot t^{-m}$$

$$\sigma_{\mathrm{cg}}(t) = P \cdot \frac{\Gamma(1+m)}{1-m} \cdot \dot{\varepsilon}_0 \cdot t^{1-m} = \frac{S}{1-m} \cdot \dot{\varepsilon}_0 \cdot t^{1-m}$$

$$\sigma_{\mathrm{cg}}(\varepsilon) = P \cdot \frac{\Gamma(1+m)}{1-m} \cdot \left(\dot{\varepsilon}_0\right)^{m} \cdot \varepsilon^{1-m} = \frac{S}{1-m} \cdot \left(\dot{\varepsilon}_0\right)^{m} \cdot \varepsilon^{1-m}$$

$$E'_{\mathrm{cg}}(\omega) = P \cdot \frac{\pi m/2}{\sin\left(\pi m/2\right)} \cdot \omega^{m} = S \cdot \Gamma(1-m) \cdot \cos\left(\pi m/2\right) \cdot \omega^{m}$$

$$E''_{\mathrm{cg}}(\omega) = P \cdot \frac{\pi m/2}{\cos\left(\pi m/2\right)} \cdot \omega^{m} == S \cdot \Gamma(1-m) \cdot \sin\left(\pi m/2\right) \cdot \omega^{m}$$

$$\tan\delta_{\mathrm{cg}}(\omega) = \tan\left(\pi m/2\right)$$

Appendix F

Fractional Calculus and Fractional Dynamics

This Appendix attempts a short introduction to the formalism and properties of fractional operators, and to the molecular origins of fractional dynamics and quasi-properties in complex systems. The connection between diffusion and relaxation is examined, in terms of the Fokker–Planck equation and its fractional generalization. It is not an exposition of the subject; rather, it is meant to serve simply as a presentation of the notation used in the main body of this dissertation and as a handy reference. Formulae are generally stated without proof, in the form in which they are applicable in the context of the dissertation. The following material is relevant to Chapter 3 (§3.3.4.IV-d), and especially to Chapter 4 and Appendix E.

F.1 Introduction

Power-law relaxation patterns are by no means unique to homopolymers undergoing the glass-rubber transition[267,268], to lightly crosslinked rubbers[155], or to chemical gels at the gel point[289-294] (Appendix E). Within the realm of polymer science, they are characteristic to numerous systems, including linear entangled homopolymers (both polydisperse[269] and monodisperse[270,271]), branched polymers with star-, H-, or comb-like topologies[44,272-279], ring polymers[280], polymer blends[276,281-284], rubbers[285,286], and polymer fractals[287,288]; in the class of physical gels, examples include filled polymers[295,296], associating

polymers[275,297,298], crystallizing polymers[299], foams[300], liquid crystalline polymers[301], microgel dispersions[302,303], soft glassy materials[304,305], suspensions[306,307], chewing gum[308], and microphase-segregated block copolymers both above[98,101,103-109,246,284,587] and below[110-113] the glass transition temperature of the higher T_g block (cf. Chapter 3, Figure 3.4, and Chapter 4, Figure 4.2).

Being the result of long-range spatial or temporal correlations, self-similar dynamics is not even a prerogative of polymeric materials. Rocks, metals, inorganic glasses[309-311], and proteins[310,312] have been found to exhibit power-law relaxations. In fact, self-similar dynamics has been predicted and observed in various disciplines including physics, chemistry, engineering, geology, biology, economy, meteorology, astrophysics and others.[252,263]

In analogy with geometrical self-similarity[253-258], self-similar dynamics is often called "*scale invariant*", "*scale free*", "*fractal*", or "*fractional*". Indeed, the mathematical description of self-similar dynamics naturally leads to the so-called *fractional calculus*.

The formalism and properties of fractional operators will be introduced in §F.2. The molecular origins of self-similar dynamics and quasi-properties, as well as the connection between diffusion and relaxation, will be briefly examined in §F.3.

F.2 Fractional Calculus

The concept of differentiation and integration to non-integer order dates back to Leibniz, who prophetically wrote, in a letter to de L'Hospital[571] in 1695, "Thus it follows that $d^{1/2}x$ will be equal to $x\sqrt[2]{dx:x}$, an apparent paradox, from which one day useful consequences will be drawn". While not a new mathematical concept, it was only in 1936 that fractional calculus was first applied in the field of rheology by Gemant[383,384]. Today, virtually no area of classical analysis has been left untouched by fractional calculus.[341]

In the *Riemann–Liouville formalism*, the *fractional* (*differintegral*) *operator* ${}_{t_0}D_t^{\alpha}$ is defined for any real number α as[341]

$$ {}_{t_0}D_t^{\alpha} f(t) = \begin{cases} \dfrac{1}{\Gamma(-\alpha)} \displaystyle\int_{t_0}^{t} (t-u)^{-\alpha-1} f(u)\,du & \text{for } \alpha \in \mathbb{R},\ \alpha < 0 \\ f(t) & \text{for } \alpha = 0 \\ \dfrac{d^n}{dt^n}\left[{}_{t_0}D_t^{\alpha-n} f(t) \right] = \dfrac{1}{\Gamma(n-\alpha)} \dfrac{d^n}{dt^n} \displaystyle\int_{t_0}^{t} (t-u)^{n-\alpha-1} f(u)\,du & \text{for } \alpha \in \mathbb{R},\ \alpha > 0 \end{cases} \tag{F.1} $$

with n being the smallest positive integer larger than or equal to α, i.e.

$$ n \geq \alpha > n-1, \quad \text{and } n \in \mathbb{Z}^+ \tag{F.2} $$

where $\Gamma(\cdot)$ is the complete gamma function defined in Appendix C (§C.1), and d^n/dt^n represents the ordinary n-fold derivative. When α is negative, Eq. (F.1)a defines the operation of *fractional integration* to non-integer order α; for positive values of α, Eqs. (F.1)c and (F.2) define the operation of *fractional differentiation* to non-integer order α.

For integer values of α, the fractional operator ${}_{t_0}D_t^{\alpha}$ reduces to the ordinary integration and ordinary differentiation. If $\alpha = -n$, it follows from Eq. (F.1)a that

$$ {}_{t_0}D_t^{-n} f(t) = \frac{1}{\Gamma(n)} \int_{t_0}^{t} (t-u)^{n-1} f(u)\,du \qquad \text{for } n \in \mathbb{Z}^+ \tag{F.3} $$

which corresponds to the ordinary n-fold integral, i.e. Cauchy's multiple integral. If $\alpha = n$, Eqs. (F.1)b-c and (F.2) give

$$ {}_{t_0}D_t^{n} f(t) = \frac{d^n}{dt^n}\left[{}_{t_0}D_t^{0} f(t) \right] = \frac{d^n}{dt^n} f(t) \qquad \text{for } n \in \mathbb{Z}^+ \tag{F.4} $$

which corresponds to the ordinary n-fold derivative.

Linearity

As a direct result of its definition, the fractional operator ${}_{t_0}D_t^{\alpha}$ is a *linear* operator, i.e.[341]

$$ {}_{t_0}D_t^{\alpha}\left[f(t) + g(t) \right] = {}_{t_0}D_t^{\alpha} f(t) + {}_{t_0}D_t^{\alpha} g(t) \tag{F.5} $$

Composition rule

In general[341],

$$ {}_{t_0}D_t^{\alpha}\, {}_{t_0}D_t^{\beta} f(t) \neq {}_{t_0}D_t^{\alpha+\beta} f(t) \tag{F.6} $$

The simple *composition rule*,

$$ {}_{t_0}D_t^{\alpha}\, {}_{t_0}D_t^{\beta} f(t) = {}_{t_0}D_t^{\alpha+\beta} f(t) \tag{F.7} $$

only holds if $\beta < 0$, or if $\beta < 1$ and $f(t)$ is bounded at $t = t_0$.[341]

Two important properties of the fractional operator ${}_{t_0}D_t^{\alpha}$, which find direct application in linear viscoelasticity, are the fractional differintegral of the function $f(t) = (t - t_0)^p$, and the Laplace transform of ${}_{0}D_t^{\alpha}$.

Fractional differintegral of $f(t) = (t - t_0)^p$

It can be shown that ${}_{t_0}D_t^{\alpha}$ is a map relating power-laws of different indices, i.e.[341]

$$ {}_{t_0}D_t^{\alpha}\left(t-t_0\right)^p = \frac{\Gamma(1+p)}{\Gamma(1+p-\alpha)}\cdot\left(t-t_0\right)^{p-\alpha} \qquad \text{for } p>-1 \tag{F.8} $$

This formula, which suggests tight relations between fractional differintegrals and fractal geometry dimensions, formed the basis of the concept of fractional differentiation as developed by Gemant[383,384], and later by Scott Blair et al.[318]. Notice that Eq. (F.8) is the generalization of the ordinary *n*-fold derivative of $(t - t_0)^p$,

$$ \frac{d^n}{dt^n}\left(t-t_0\right)^p = \frac{\Gamma(1+p)}{\Gamma(1+p-n)}\cdot\left(t-t_0\right)^{p-n} \qquad n\in\{0\}\bigcup\mathbb{Z}^+ \tag{F.9} $$

An interesting consequence of Eq. (F.8) is the non-vanishing fractional differintegral of a constant[341],

$$ {}_{t_0}D_t^{\alpha}c = \frac{c}{\Gamma(1-\alpha)}\cdot\left(t-t_0\right)^{-\alpha} \tag{F.10} $$

Laplace transform of $ {}_0D_t^{\alpha}$

In the description of linear viscoelastic behavior we can always assume, without loss of generality[150], that the infinitesimal stress $\sigma(t)$ and strain $\varepsilon(t)$ are defined on $[0, \infty)$ and with *zero initial conditions* (cf. Appendix B, §B.2.3, and Appendix D, §D.1). Restricting our attention to the domain $t > 0$ allows us to choose the lower limit of integration $t_0 = 0$, i.e. the fractional operator becomes ${}_0D_t^{\alpha}$. We seek the Laplace transform of ${}_0D_t^{\alpha}$. For zero initial conditions, the Laplace transform of the ordinary n^{th} order derivative or the ordinary n^{th} order integral is (Appendix B, Eq. (B.9))

$$ \mathcal{L}\ \frac{d^n}{dt^n}f(t) = s^n\overline{f}(s) \qquad n\in\mathbb{Z} \tag{F.11} $$

It is easy to show that Eq. (F.11) generalizes to include non-integer α by the simple extension[341]

$$\mathcal{L}\ {}_0D_t^{\alpha} f(t) = s^{\alpha}\overline{f}(s) \qquad \alpha \in \mathbb{R} \tag{F.12}$$

In proving Eq. (F.12), we first consider $\alpha < 0$, so that the definition of Eq. (F.1)a may be adopted. It follows from Eq. (B.10) that Eq. (F.1)a is a Laplace convolution

$${}_0D_t^{\alpha} f(t) = \frac{t^{-\alpha-1}}{\Gamma(-\alpha)} * f(t) \qquad \alpha < 0 \tag{F.13}$$

Therefore, application of Eq. (B.11) and LTP (4) (Appendix B, Table B.1) gives

$$\begin{aligned} \mathcal{L}\ {}_0D_t^{\alpha} f(t) &= \mathcal{L}\left[\frac{t^{-\alpha-1}}{\Gamma(-\alpha)}\right]\mathcal{L} f(t) \\ &= s^{\alpha}\overline{f}(s) \qquad \alpha < 0 \end{aligned} \tag{F.14}$$

For non-integer $\alpha > 0$, we use the definition of ${}_0D_t^{\alpha}$ expressed by Eqs. (F.1)c and (F.2),

$$\mathcal{L}\ {}_0D_t^{\alpha} f(t) = \mathcal{L}\ \frac{d^n}{dt^n}\left[{}_0D_t^{\alpha-n} f(t)\right] \qquad \alpha > 0,\ n \geq \alpha > n-1,\ n \in \mathbb{Z}^+ \tag{F.15}$$

Now, application of Eq. (F.11) leads to

$$\mathcal{L}\ {}_0D_t^{\alpha} f(t) = s^n \mathcal{L}\ {}_0D_t^{\alpha-n} f(t) \qquad \alpha > 0,\ n \geq \alpha > n-1,\ n \in \mathbb{Z}^+ \tag{F.16}$$

Since $\alpha - n < 0$, we may then apply Eq. (F.14) and obtain

$$\begin{aligned} \mathcal{L}\ {}_0D_t^{\alpha} f(t) &= s^n s^{\alpha-n}\overline{f}(s) \\ &= s^{\alpha}\overline{f}(s) \qquad \alpha > 0 \end{aligned} \tag{F.17}$$

The Laplace transformation of the fractional operator, Eq. (F.12), is particularly useful as it transforms linear differential or integral equations to non-integer order (the so-called *extraordinary differential equations*)[341] into polynomials in the transform variable s.

Solutions to extraordinary differential equations are thus accomplished through the use of Eq. (F.12).

When the lower limit of integration is zero (e.g. in the application to linear viscoelasticity), we can use a more compact notation for the fractional operator,

$$ {}_0D_t^{\alpha} f(t) \equiv \frac{d^{\alpha}}{dt^{\alpha}} f(t) \qquad \alpha \in \mathbb{R} \tag{F.18} $$

F.2.1 Fractional Derivatives and Power-Law Spectra

It is important to realize that fractional calculus arises naturally when dealing with materials that exhibit a power-law spectrum. Let us consider the fractional derivative ${}_0D_t^{\alpha}$ with $t_0 = 0$ and $\alpha \in (0, 1)$, hence $n = 1$ (from Eq. (F.2)). It follows from Eq. (F.1)c that

$$ \begin{aligned} {}_0D_t^{\alpha} f(t) &= \frac{d}{dt}\left[{}_0D_t^{\alpha-1} f(t) \right] \\ &= \frac{1}{\Gamma(1-\alpha)} \frac{d}{dt} \int_{t_0}^{t} (t-u)^{-\alpha} f(u)\, du \\ &= \frac{1}{\Gamma(1-\alpha)} \frac{d}{dt} \int_{0}^{t} u^{-\alpha} f(t-u)\, du \\ &= \frac{1}{\Gamma(1-\alpha)} \left\{ \int_0^t u^{-\alpha} \frac{\partial}{\partial t} f(t-u)\, du + t^{-\alpha} \underbrace{f(0)}_{0} \right\} \\ &= \frac{1}{\Gamma(1-\alpha)} \int_0^t u^{-\alpha} \frac{df(t-u)}{d(t-u)} du \qquad \text{with } 0 < \alpha < 1 \end{aligned} \tag{F.19} $$

where we have used the relation[588]

$$\frac{d}{dt}\int_0^t \phi(t,u)\,du = \int_0^t \frac{\partial}{\partial t}\phi(t,u)\,du + \phi(t,t) \tag{F.20}$$

and we have assumed $f(0) = 0$.

Let us now suppose that the material under study exhibits critical gel behavior upon application of a step strain, i.e. (Appendix E, Eq. (E.49))

$$E_{cg}(t) = S \cdot t^{-m} \qquad \text{with } 0 < m < 1 \tag{F.21}$$

then, the stress $\sigma_{cg}(t)$ follows from the Boltzmann superposition integrals (cf. Appendix D, Eqs. (D.6)a and (D.15)d) as

$$\begin{aligned}
\sigma_{cg}(t) &= \int_0^t E_{cg}(u)\frac{d\varepsilon(t-u)}{d(t-u)}\,du \\
&= S\int_0^t u^{-m}\frac{d\varepsilon(t-u)}{d(t-u)}\,du \\
&= S\cdot\Gamma(1-m)\cdot\frac{1}{\Gamma(1-m)}\int_0^t u^{-m}\frac{d\varepsilon(t-u)}{d(t-u)}\,du \qquad \text{with } 0 < m < 1
\end{aligned} \tag{F.22}$$

The last term on the right-hand side of Eq. (F.22) coincides with Eq. (F.19)e, and therefore represents the fractional derivative of $\varepsilon(t)$ to non-integer order m,

$$\sigma_{cg}(t) = S\cdot\Gamma(1-m)\cdot {}_0D_t^m\varepsilon(t) \qquad \text{with } 0 < m < 1 \tag{F.23}$$

In Chapter 4, it is shown that $S\cdot\Gamma(1 - m)$ is the parameter associated with a fractional mechanical element called the "*spring-pot*" (cf. Chapter 4, Figure 4.3, Eqs. (4.25) and (4.45), and Table 4.1).

F.3 Fractional Dynamics

F.3.1 Simple Systems and Classical Behavior

In simple systems, relaxation processes are described in terms of the classical *exponential Maxwell–Debye*[357,572] pattern

$$\phi(t) = \phi_0 \exp\left(-t/\tau\right) \tag{F.24}$$

Thus, the relaxation function $\phi(t)$ possesses the *characteristic time scale* τ and fulfills the standard relaxation equation

$$\begin{aligned} &\frac{d}{dt}\phi(t) = -\frac{1}{\tau}\phi(t) \\ &\phi(0) = \phi_0 \end{aligned} \tag{F.25}$$

In a rather general perspective, relaxation theory can be based on the diffusion of defects in the system under consideration.[573,574] Diffusion processes in simple systems follow Gaussian statistics, and therefore Fick's second law describes the related transport behavior. As a direct consequence of the *central limit theorem* and the Markovian nature of the underlying stochastic process[575], the mean-square displacement exhibits a linear time dependence characteristic of *Brownian motion*,

$$\left\langle x^2(t)\right\rangle \sim D \cdot t \tag{F.26}$$

where D is the *diffusion coefficient* (with dimensions of L^2T^{-1}).

F.3.2 Complex Systems and Anomalous Behavior

Complex systems are characterized by (i) a large diversity of elementary units, (ii) strong interactions between the units, and (iii) anomalous (i.e. non-classical) time evolution.[264,265]

Relaxation processes in complex systems are governed by a large variety of characteristic times, and can often be described[150,576] in terms of a *stretched exponential*[374,375] pattern, usually referred to as the Kohlrausch–Williams–Watts (KWW) law[376-378] or the Weibull distribution[379],

$$\phi(t) = \phi_0 \exp\left[-\left(t/\tau\right)^{\alpha}\right] \qquad \text{with } 0 < \alpha < 1 \tag{F.27}$$

or[150] by *asymptotic power-laws* such as the Cole–Cole[313] function

$$\phi(t) = \phi_0 \frac{1}{1+\left(t/\tau\right)^{\alpha}} \qquad \text{with } \alpha > 0 \tag{F.28}$$

or the Kobeko[577] function (known in dielectrics as the Cole–Davidson function)

$$\phi(t) = \phi_0 \frac{1}{\left(1+t/\tau\right)^{\alpha}} \qquad \text{with } \alpha > 0 \tag{F.29}$$

which show the long-time inverse power-law decay of the Nutting law[315,316,318,380-382]

$$\phi(t) = \phi_0 \frac{1}{\left(t/\tau\right)^{\alpha}} \qquad \text{with } \alpha > 0 \tag{F.30}$$

Relaxation patterns intermediate between a stretched exponential and the Nutting law have also been observed.[348]

Similarly, diffusion processes in various complex systems usually no longer follow Gaussian statistics, and thus Fick's second law fails to describe the related transport

behavior. In particular, one observes a non-linear growth of the mean-square displacement in the course of time, often of the power-law-type[578,579]

$$\left\langle x^2(t)\right\rangle \sim D_\alpha \cdot t^\alpha \qquad \text{with } \alpha > 0 \tag{F.31}$$

where D_α is the *generalized diffusion coefficient* (with dimensions of $L^2T^{-\alpha}$)[251,252,261]. In contrast to Brownian diffusion, anomalous diffusion is non-universal as it involves a parameter, α, which is related to the order of the fractional derivative (vide infra). Anomalous diffusion described by Eq. (F.31) is connected with the breakdown of the central limit theorem, caused by either broad distributions or long-range correlations. In such situations, the *Levy–Gnedenko generalized central limit theorem* applies.[251]

Depending on the value of the anomalous diffusion exponent α in Eq. (F.31), three different regimes of diffusion can be distinguished: *subdiffusion* ($0 < \alpha < 1$), *Brownian* or *normal diffusion* ($\alpha = 1$), and *superdiffusion* ($\alpha > 1$). Within the domain of superdiffusion, $\alpha = 2$ is usually referred to as *ballistic diffusion*.[580]

In polymeric systems, Rouse dynamics[47] and local reptation (i.e. Rouse motion of a chain confined to a tube)[46,89,166] are well-known examples of subdiffusive behavior (Chapter 3, §3.3.4.IV-d). Brownian motion is achieved, for instance, in polymer melts beyond their tube disengagement time. [46]

F.3.3 The Fokker–Planck Equation

Let us consider the (one-dimensional) relaxation of an excitation undergoing *Brownian diffusion* in the presence of an external potential field $V(x)$. In the standard Markovian model, it is assumed that the probability density function $P(x, t)$ to find a given excitation at position x at time t follows the *Fokker–Planck equation* (FPE)[581]

$$\frac{\partial}{\partial t}P(x,t)=\left[\frac{\partial}{\partial x}\frac{V'(x)}{\zeta}+D\frac{\partial^2}{\partial x^2}\right]P(x,t) \qquad \text{(FPE)} \tag{F.32}$$

where $F(x) = -V'(x)$ is the external force field, ζ is the (molecular or Stokes) *friction coefficient* (with dimensions of MT^{-1}), D is the (tracer) *diffusion coefficient* (with dimensions of $\mathrm{L}^2\mathrm{T}^{-1}$), and ζ and D satisfy the *Einstein–Stokes–Smoluchowski relation*[575,582]

$$D=\frac{k_\mathrm{B}T}{\zeta} \tag{F.33}$$

where k_B is Boltzmann's constant, and T is the absolute temperature.

In the force-free limit, the FPE reduces to the classical *diffusion equation* (DE), i.e. *Fick's second law*

$$\frac{\partial}{\partial t}P(x,t)=D\frac{\partial^2}{\partial x^2}P(x,t) \qquad \text{(DE)} \tag{F.34}$$

As a consequence of the central limit theorem, for the impulsive initial condition $P(x, 0) = \delta(x)$ the solution of the DE is Gaussian, $P(x, t) = (4\pi Dt)^{-1/2}\cdot\exp[-x^2/(4Dt)]$, and the time evolution of the mean-square displacement is given by[252]

$$\left\langle x^2(t)\right\rangle = 2D\cdot t \tag{F.35}$$

Consequently, a relaxation function $\phi(t)$ can be defined which is connected to the temporal decay of a given mode k, through[252,262]

$$\phi(t) \equiv P^*(k,t) = \exp\left(-Dk^2 t\right) \tag{F.36}$$

where $P^*(k, t)$ is the two-sided Fourier transform of $P(x, t)$ defined as (cf. Appendix B, Eq. (B.15))

$$P^*(k,t) = \int_{-\infty}^{+\infty} P(x,t) e^{ikx}\, dx \tag{F.37}$$

Eq. (F.36) describes the temporal *exponential* relaxation of a macroscopic excitation, for a fixed wavenumber k.

F.3.4 The Fractional Fokker–Planck Equation

Let us now consider generalizations of Eqs. (F.32)–(F.36) for systems which exhibit self-similar dynamics. For the description of *subdiffusion* in the presence of an external potential field $V(x)$ Metzler and co-workers[252,261] have introduced a fractional extension of the FPE, namely the *fractional Fokker–Planck equation* (FFPE)

$$\frac{\partial}{\partial t} P(x,t) = {}_0D_t^{1-\alpha} \left[\frac{\partial}{\partial x} \frac{V'(x)}{\zeta_\alpha} + D_\alpha \frac{\partial^2}{\partial x^2} \right] P(x,t) \qquad \text{with } 0 < \alpha \le 1 \quad \text{(FFPE)} \tag{F.38}$$

where ${}_0D_t^{1-\alpha}$ is the fractional derivative (to non-integer order $1–\alpha$) discussed in §F.2, ζ_α is the *generalized friction coefficient* (with dimensions of $\mathrm{MT}^{\alpha-2}$), D_α is the *generalized diffusion coefficient* (with dimensions of $\mathrm{L}^2\mathrm{T}^{-\alpha}$), and ζ_α and D_α satisfy the *generalized Einstein–Stokes–Smoluchowski relation*[251,252,261]

$$D_\alpha = \frac{k_B T}{\zeta_\alpha} \tag{F.39}$$

For $\alpha = 1$, Eq. (F.38) reduces to the standard FPE (Eq. (F.32)).

In the force-free limit, the FFPE yields the *fractional diffusion equation* (FDE)

$$\frac{\partial}{\partial t} P(x,t) = {}_0D_t^{1-\alpha} D_\alpha \frac{\partial^2}{\partial x^2} P(x,t) \qquad \text{with } 0 < \alpha \le 1 \quad (\text{FDE}) \tag{F.40}$$

The solution $P(x, t)$ of the FDE is not Gaussian. A closed-form solution can be found in terms of Fox H-functions.[252,261] Furthermore, the time evolution of the mean-square displacement obtained from Eq. (F.40) describes subdiffusion[252,261]

$$\left\langle x^2(t) \right\rangle = \frac{2D_\alpha}{\Gamma(1+\alpha)} \cdot t^\alpha \qquad \text{with } 0 < \alpha \le 1 \tag{F.41}$$

i.e. the random walker spreads less efficiently than a Brownian random walker. Notice that Eq. (F.41) reduces to Brownian diffusion for $\alpha = 1$ (since $\Gamma(2) = 1$, Appendix C, Eq. (C.3)). Single modes of the FDE decay according to the *Mittag-Leffler pattern*[252,261]

$$\phi(t) \equiv P^*(k,t) = E_\alpha\left(-D_\alpha k^2 t^\alpha\right) \qquad \text{with } 0 < \alpha \le 1 \tag{F.42}$$

where $E_\alpha(x)$ is the one-parameter Mittag-Leffler function[369-373,564] defined in Appendix C, §C.5. For $\alpha \in (0, 1)$, $E_\alpha(-x^\alpha)$ is a positive and strictly monotonically decreasing function that interpolates between an initial stretched exponential (Eq. (F.27)) and a terminal inverse power-law decay (Eq. (F.30)), both of index α (cf. Appendix C, Eq. (C.20)). For $\alpha = 1$, $E_\alpha(x)$ reduces to the exponential function (Appendix C, Eq. (C.18)c) and the classical relaxation pattern of Eq. (F.36) is recovered.

Therefore, transport dynamics in systems governed by subdiffusion and non-exponential relaxations can be described by the fractional generalization of the Fokker–Planck equation.

F.3.5 On the Molecular Origins of Fractional Dynamics and Quasi-Properties

Fractional dynamics in complex systems is a natural consequence of molecular processes with a certain statistics. In 1983, Bagley and Torvik[285] were able to demonstrate that the Rouse[47] theory is compatible with a fractional differential equation of order 1/2. More generally, the fractional Fokker–Planck equation (Eq. (F.38)) can be derived from a continuous time random walk scheme, and it can be shown to be connected to a *multiple trapping process* with broad waiting time distribution.[252] Continuous time random walks are often used in the description of dynamically hindered or glassy systems where the jumping particles and the traps are assumed to be packages of free volume and dynamical restrictions like entanglements (respectively). Thereby fractional kinetic equations such as Eq. (F.38) are related to the stochastic behavior on a microscopic level.

The multiple trapping model underlying Eq. (F.38) describes a diffusing particle that can get occasionally trapped at a given space point, and only be released after a given (random) waiting time. After release, the particle diffuses until it gets trapped again, and so on.[261] The slow relaxation manifested in the Mittag-Leffler decay (Eq. (F.42)) is therefore directly related to these waiting times, whose characteristic scale diverges.[252,260-262] In the system under consideration, there might be a combination of different diffusion

processes each with its own *internal time scale*, i.e. a different value of the exponent α. The combined relaxation process may therefore be composed of two or more individual Mittag-Leffler patterns, giving rise to more elaborate relaxation decays.[262]

Quasi-properties, such as the generalized diffusion coefficient D_α, are a direct consequence of fractional (i.e. self-similar) dynamics. They differ from material to material in the dimensions of mass M, length L, and time T, depending on the power α. As first suggested by Scott Blair et al.[318] in 1947, quasi-properties are numerical measures of a *dynamic process* rather than of an equilibrium state. Building on the ideas introduced by Scott Blair and co-workers[318], in 2001 Podlubny[347] proposed a physical and geometrical interpretation of fractional operators as converting between an *external/laboratory Newtonian time scale* (with regularly spaced intervals) and an *internal/material time scale* (with irregularly spaced intervals). It is the different character of these time scales that gives quasi-properties non-integer dimensions in M, L, and T.[318]

Self-similar dynamics is characterized by lack of a characteristic time scale or, equivalently, by the coexistence in a self-similar manner of a great number of internal time scales. Physical systems with a large variety of time and/or length scales are widespread in nature. As briefly mentioned in Appendix E (§E.3.1), a comparable situation is known from thermodynamic systems at the vapor-liquid critical point and for the appearance of spontaneous magnetization below the Curie point, where the correlation length diverges. In the renormalization group theory invented by Wilson[583,584],

the divergence of the correlation length is mathematically treated by assuming a composition of subsystems with a special coupling constant. Each of these subsystems is comprised of sub-subsystems with another coupling constant and so forth. A change of the scale leads to the same behavior apart from the renormalization of the coupling constant.[583,584]

Just like the shapes of objects in nature are in general better described in the language of fractal geometry[253-258] rather than by Euclidian geometry, fractional calculus should be regarded as a mathematical construct that captures the main features of the dynamics in complex systems.

Appendix G

The Rheology of Chewing Gum:

Supplemental Material

This Appendix contains material that is supplementary to Chapter 6, for linear and nonlinear viscoelastic behavior in shear and extension of additional chewing gums, bubble gums, lab-scale gums, and waxes.

G.1 Materials

The formulations for three lab-scale gums are indicated in Table G.1. These were created in order to directly compare the rheological fingerprint of commercial chewing and bubble gum with materials of known compositions. Additionally, a commercially available confectionary wax, Wack-o-wax Mr. Stache (available at http://shop.tootsie.com), was utilized for certain studies and is referred to as "W".

Table G.1. Formulations of lab-scale gums (in wt%).

Sample	*Base*	*Calcium Carbonate*	*Sorbitol*	*Glycerine*	*Medium Chain Triglycerides*	*Flavorings*
V1	40	–	57	3	–	–
V2	30	10	55	3	–	2
V3	30	5	55	3	5	2

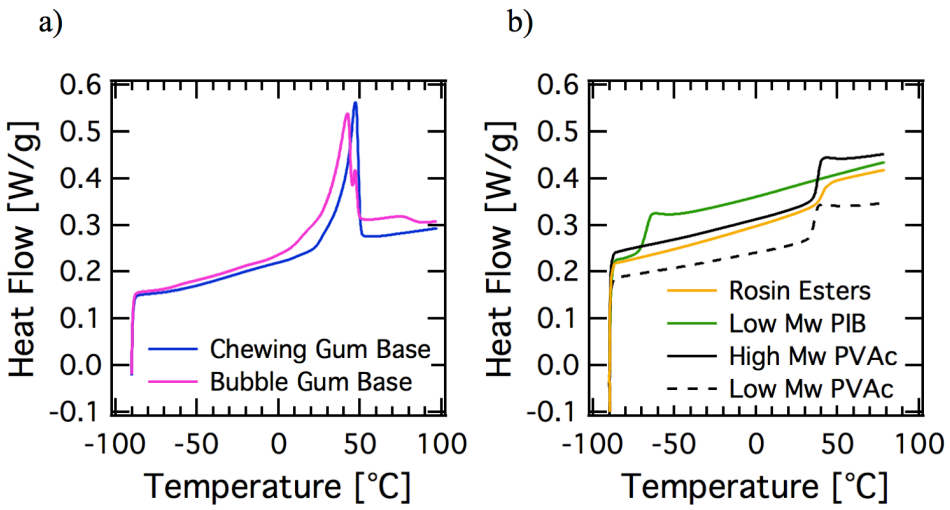

Figure G.1. Differential scanning calorimetry (DSC) curves upon second heating at a ramp rate of 10 °C/min for (a) a chewing gum base and a bubble gum base and (b) low molar mass poly(isobutylene) (PIB), low and high molar mass poly(vinyl acetate) (PVAc), and rosin esters. The gum bases show thermal transitions between 30 °C and 40 °C that appear predominately crystalline, while the PVAc and rosin esters show glass transitions in this same temperature window.

G.2 Results

G.2.1 Thermal Characterization

Thermal analysis was conducted on two representative gum bases – a chewing gum base and a bubble gum base – using a Thermal Analysis Q1000 DSC (TA Instruments). The DSC traces upon second heating at a ramp rate of 10 °C/min are shown in Figure G.1(a), confirming the presence of a thermal transition between 30 °C and 40 °C that appears mostly crystalline. We also performed DSC on some of the pure components of the gum bases such as poly(isobutylene), low and high molar mass poly(vinyl acetate)

(PVAc), and rosin esters, the traces of which are shown in Figure G.1(b). For the PVAc and rosin esters, a clear glass transition temperature can be seen in this same temperature window between 30 °C and 40 °C.

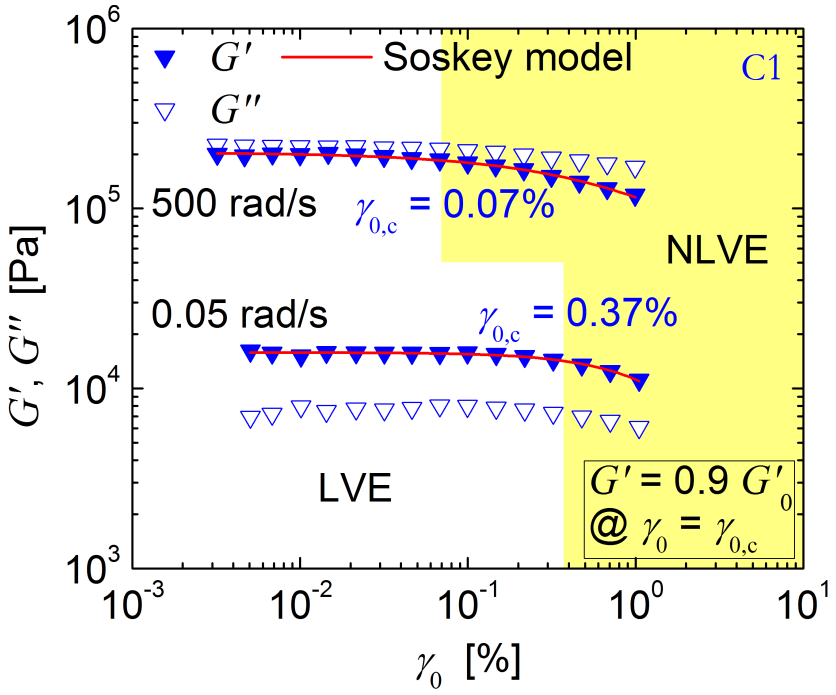

Figure G.2. Storage and loss moduli for chewing gum C1 measured during small amplitude oscillatory shear. The critical strain is defined as the strain at which G' decreases by 10%. At both low and high frequencies, the critical strain was found to be $< 0.5\%$.

G.2.2 Linear Viscoelasticity

Strain sweeps of chewing and bubble gums were conducted at frequencies of 0.05 rad/s and 500 rad/s to target the low and high frequency regimes, respectively. The results for

C1 are shown in Figure G.2. In the low frequency regime, C1 demonstrated a higher critical strain (0.37%) than in the high frequency regime (0.07%), although in both frequency regimes the linear region is rather small as discussed in Chapter 6.

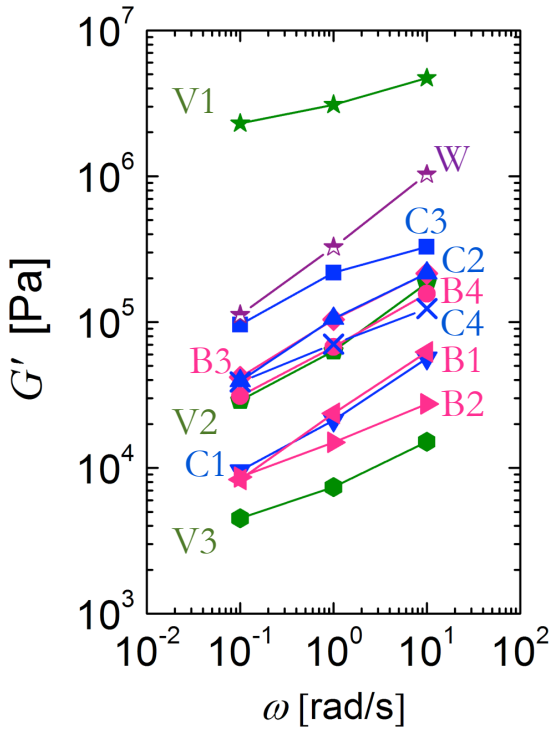

Figure G.3. Storage modulus versus frequency for chewing gums, bubble gums, lab-scale gums, and wax.

The elastic moduli of all chewing gums, bubble gums, lab-scale gums, and the wax at three different frequencies are shown in Figure G.3. These data were obtained during LAOS tests at strains that were well within the linear region; hence, only three data points

per sample were collected. Although somewhat sparse, these data demonstrate two key features: 1) at a given frequency, the elastic modulus deviates by over an order of magnitude between commercial products without large deviations in sensory feel or performance and 2) all samples behave like critical gels.

Finally, Figure G.4 demonstrates that in shear creep conducted over 100 s at a stress of 100 Pa all chewing and bubble gums show similar responses. Further testing must be done to verify these are in the linear regime.

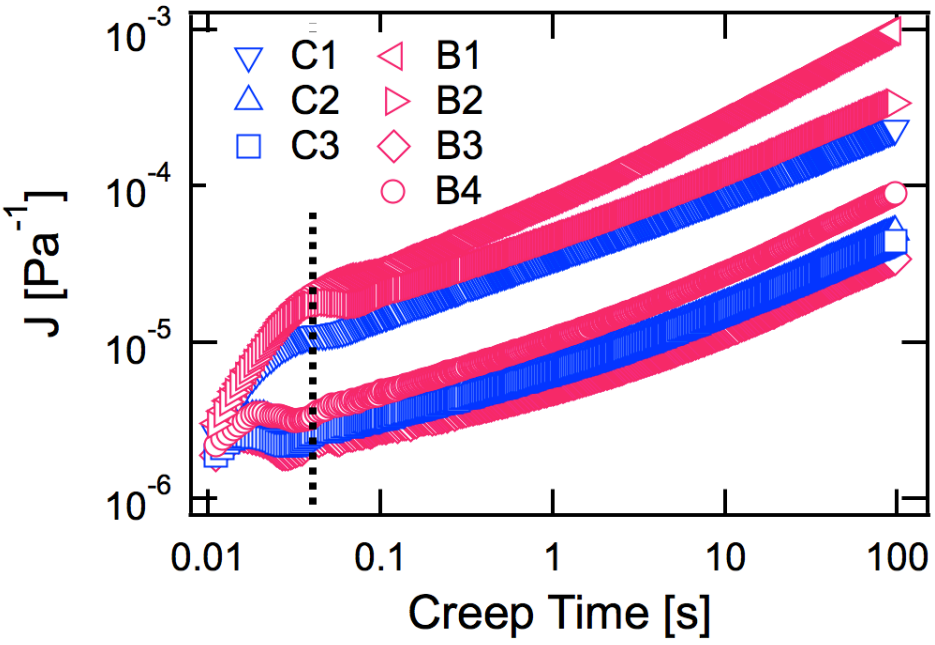

Figure G.4. Shear creep results of chewing and bubble gums at a stress of 100 Pa showing critical gel-like behavior for all samples. Inconsistencies at times < 0.04 s (denoted by the dotted line) are attributed to finite start-up time of the instrument.

G.2.3 Nonlinear Viscoelasticity

Here we provide supplementary results to compare chewing gums, bubble gums, lab-scale gums, and a commercial wax in a series of rheological tests that probe nonlinearity in shear and extension. Figure G.5 shows results for start-up of steady shear at a constant shear rate of 1.732 s^{-1} for all samples but V3. Once a constant strain rate is achieved, all chewing and bubble gums have relatively constant viscosities, ranging from 1000 to 6000 Pa·s, until the point of edge failure. Conversely, the lab-scale gums and wax demonstrate higher viscosities (> 8000 Pa·s), and the viscosities of V1 and W decrease with time. The latter observation is attributed to both yielding and slip.

Figure G.6 shows the LAOS response of all chewing gums, bubble gums, lab-scale gums, and the wax at the frequency $\omega = 1$ rad/s in terms of the first-harmonic (cycle-averaged) complex modulus, $\left|G_1^*\right|$. As noted in Chapter 6, all samples show a nonlinear, monotonic decrease of *both* elasticity and dissipation, but we only plot $\left|G_1^*\right|$ for the sake of simplicity.

The start-up of steady uniaxial extension was deemed a key attribute in differentiating between chewing and bubble gums. Chewing gums failed at extensional stresses $\leq 2.0 \cdot 10^6$ Pa while most bubble gums withstood higher stresses ($> 2.0 \cdot 10^6$ Pa) with similar strains at break. Additionally, both chewing and bubble gums strain hardened leading up to the failure point. The responses of V1, V2, and W are shown in Figure G.7 for comparison. Sample V1 shows qualitatively similar extensional behavior to the chewing and bubble gums with strain hardening and a high strain at break. Conversely,

W yielded almost immediately, strain softened, and broke at a Hencky strain of ≈ 0.4. V2 showed a combination of these two behaviors – yielding and strain softening at lower strains, yet strain hardening close to a large strain at break ($\varepsilon \sim 5.4$).

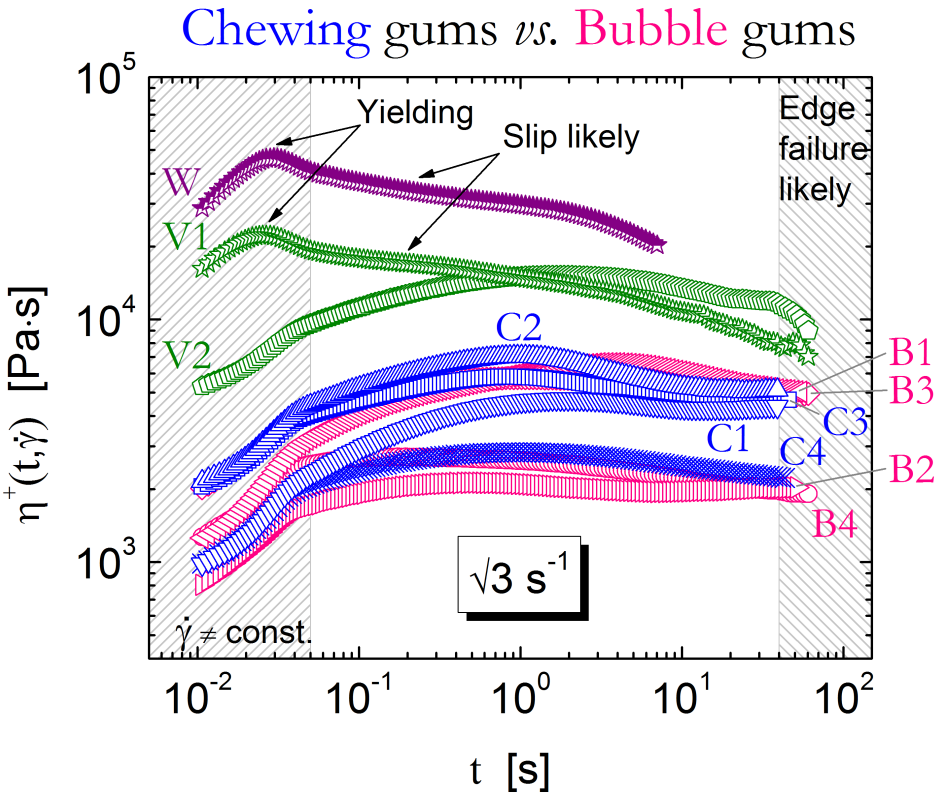

Figure G.5. Transient shear viscosity measured during start-up of steady shear for chewing gums, bubble gums, lab scale gums, and wax at a Hencky strain rate of 1.732 s^{-1}. Experimental concerns included yielding, slip, and edge failure.

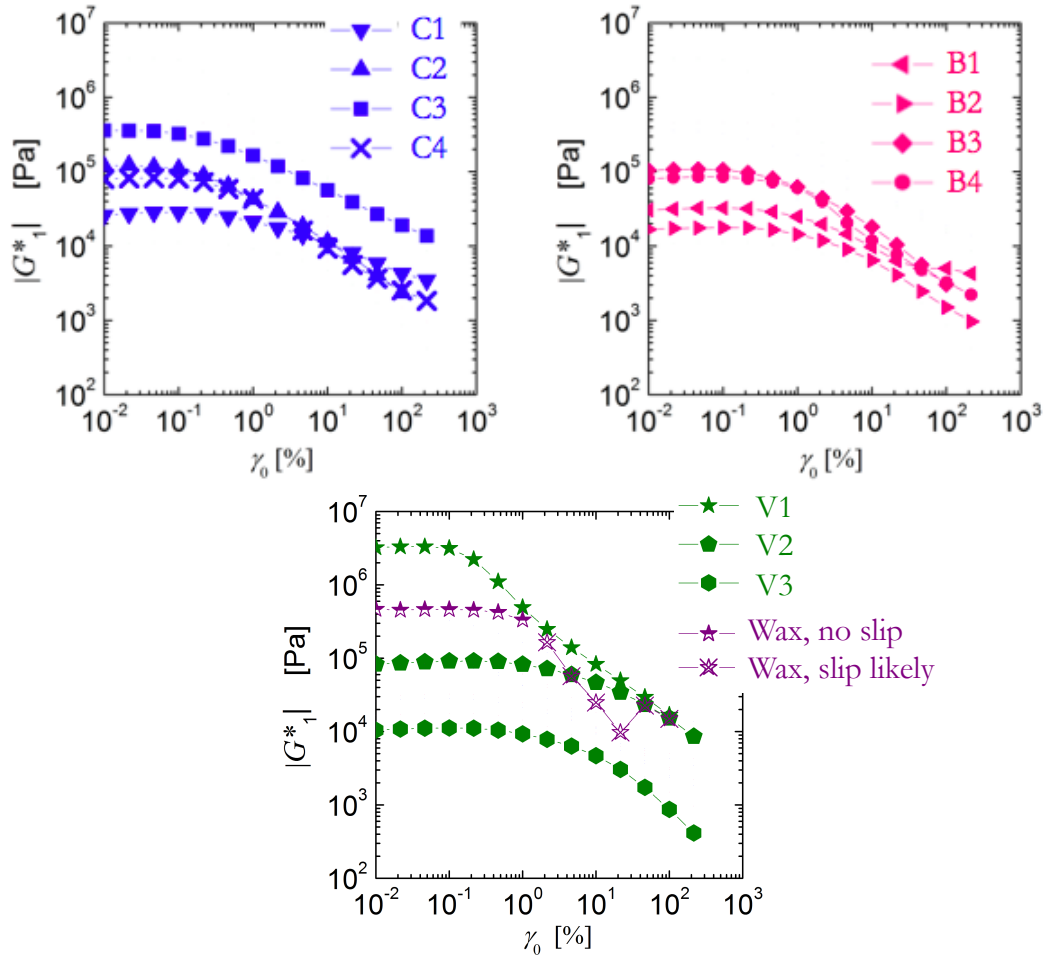

Figure G.6. First harmonic average moduli for chewing gums, bubble gums, lab-scale gums and wax measured during large amplitude oscillatory shear. The relative values of $|G_1^*|$ change in the nonlinear viscoelastic regime.

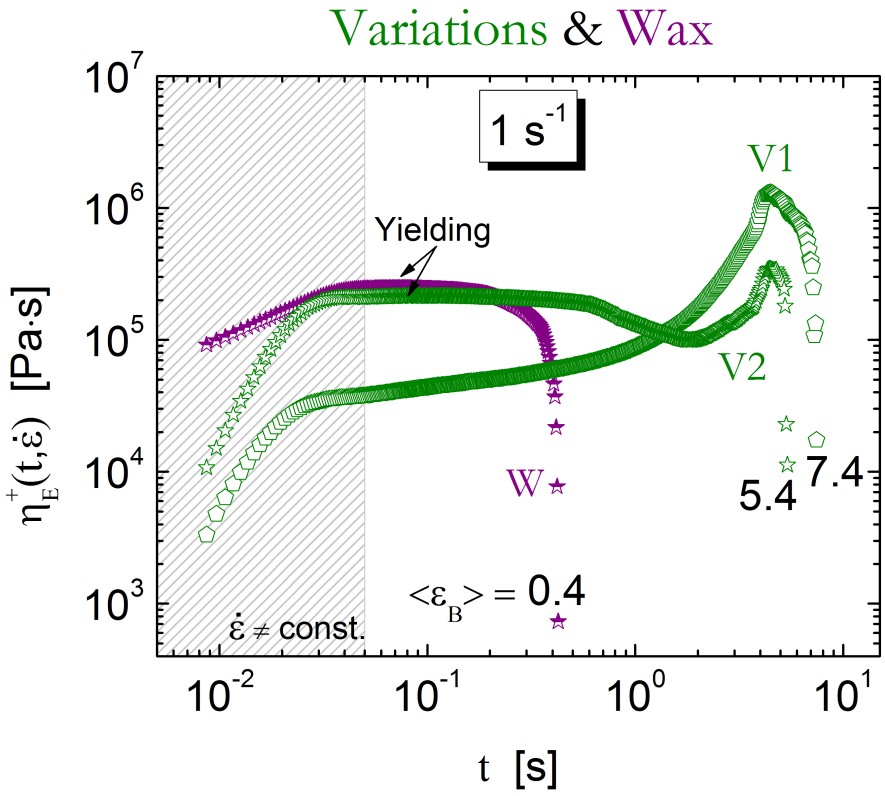

Figure G.7. Transient extensional viscosity measured during start-up of steady uniaxial extension for lab scale gums and wax at a Hencky strain rate of 1 s^{-1}. The lab scale gums and waxes show distinct behavior from the chewing and bubble gums.

Appendix H

Mathematica and MATLAB Code

This Appendix contains examples of the Mathematica® (Version 10.0, Wolfram Research, Inc.) and MATLAB® (Release 2011a, Version 7.12, The MathWorks, Inc.) scripts encoding algorithms used in this dissertation. Full source code is given only for the routines implemented in Mathematica. The data presented in Chapters 2 to 5 were analyzed, modeled, and visualized in the MATLAB environment. To this end, automated routines were developed which amount to more than 40k lines of code. The MATLAB scripts provided here are brief excerpts of the programs developed for this research, partially describing some of the key algorithms. The following material is particularly relevant to Chapters 3 (§3.3.4.IV-e), 4, and 5.

H.1 Introduction

The algorithms provided in the next sections were developed to accomplish various tasks, such as: differentiation and integration of the viscoelastic functions of the fractional Maxwell model[345] (§H.2.1), determination of the analytical expression of the Edwards–Vilgis[84] slip-link model[a] (§H.2.2), modeling the linear elastic behavior of A–B–A melts (§H.3.3), and fitting experimental data to the fractional Maxwell model[345] (§H.3.4).

---

[a] Equations given in the original papers[83,84] and in a recent *Macromolecules* review[480] contain some typos.

H.2 Mathematica Code

H.2.1 Fractional Maxwell Model

This algorithm enables the calculation of the plateau modulus of the fractional Maxwell model[345] (Chapter 4, §4.3.2.III-a), following the determination of the model parameters (§H.3.4).

```
(* ------------------------------------------------------------------ *)
(* Model Parameters, from MATLAB *)

V = 4.3182*10^10;
α = 0.75643;
W = 6.8621*10^6;
β = 0.054796;

(* Relaxation Time (tau_FMM) *)
(* Relaxation Frequency (1/tau_FMM) *)
(* Characteristic Modulus (E_FMM,0) *)

τo = (V/W)^(1/(α - β));
ωo = 1/τo;
Eo = V/τo^α;
ScientificForm[τo, 2]
ScientificForm[Eo, 3]
 2.6*10^5
 3.47*10^6

(* ------------------------------------------------------------------ *)
(* Functions Definition *)

a0 = Sin[Pi*α];
b0 = Sin[Pi*β];
c0 = Cos[Pi*(β - α)];
a1 = Cos[Pi*(α/2)];
b1 = Cos[Pi*(β/2)];
a2 = Sin[Pi*(α/2)];
b2 = Sin[Pi*(β/2)];
c12 = Cos[Pi*((α - β)/2)];

Num0 = (a0 + b0*(τ/τo)^(β - α))/(τ/τo)^α;
Den0 = 1 + 2*c0*(τ/τo)^(β - α) + (τ/τo)^(2*(β - α));
Num1 = a1*(ω*τo)^α + b1*(ω*τo)^(2*α - β);
Num2 = a2*(ω*τo)^α + b2*(ω*τo)^(2*α - β);
Den12 = 1 + 2*c12*(ω*τo)^(α - β) + (ω*τo)^(2*(α - β));
```

```
HFunc[τ_] := (Eo/Pi)*((a0 + b0*(τ/τo)^(β - α))/
        ((τ/τo)^α*(1 + 2*c0*(τ/τo)^(β - α) + (τ/τo)^(2*(β - α)))))

EstorFunc[ω_] := Eo*((a1*(ω*τo)^α + b1*(ω*τo)^(2*α - β))/
        (1 + 2*c12*(ω*τo)^(α - β) + (ω*τo)^(2*(α - β))))

ElossFunc[ω_] := Eo*((a2*(ω*τo)^α + b2*(ω*τo)^(2*α - β))/
        (1 + 2*c12*(ω*τo)^(α - β) + (ω*τo)^(2*(α - β))))

EFunc[t_] := (Eo*MittagLefflerE[α - β, 1 - β, -(t/τo)^(α - β)])/
     (t/τo)^β

f[ω_] := ElossFunc[ω];
Eq[ω_] := ElossFunc[ω]/10^6;
LogLinearPlot[Eq[ω], {ω, 1/10^6, 1/10^2}];

z = τ/τo;
Num0 = (a0 + b0*z^(β - α))/z^α;
Den0 = 1 + 2*c0*z^(β - α) + z^(2*(β - α));
H = (Eo/Pi)*(Num0/Den0);

x = ω*τo;
Num2 = a2*x^α + b2*x^(2*α - β);
Den12 = 1 + 2*c12*x^(α - β) + x^(2*(α - β));
Eloss = Eo*(Num2/Den12);

(* ------------------------------------------------------------------- *)
(* Characteristic Times at which the asymptotic behaviors of
   the Relaxation Spectrum,
   the Relaxation Modulus, and
   the Storage Modulus intersect *)

τstar = τo*(a0/b0)^(1/(α - β));
ScientificForm[τstar, 2]

tstar = τo*(Gamma[1 - β]/Gamma[1 - α])^(1/(α - β));
ScientificForm[tstar, 2]

invωstar = τo*(a1/b1)^(1/(α - β));
ScientificForm[invωstar, 2]
 1.9*10^6
 4.2*10^4
 6.4*10^4

(* Ratios Relaxation Time / Characteristic Times *)

ScientificForm[τo/τstar, 2]
ScientificForm[τo/tstar, 2]
ScientificForm[τo/invωstar, 2]
 1.4*10^-1
 6.2
```

```
 4.1

(* ------------------------------------------------------------------ *)
(* Relaxation Modulus at Relaxation Time *)

ScientificForm[EFunc[τo], 3]
 1.28*10^6

(* ------------------------------------------------------------------ *)
(* Storage Modulus at Relaxation Frequency *)

ScientificForm[EstorFunc[1/τo], 3]
 1.63*10^6

(* ------------------------------------------------------------------ *)
(* Find Local Minimum and Maximum of Relaxation Spectrum
   (2 equivalent methods) *)

dHdτ = D[H, τ];
Factor[dHdτ];

Eq[τ_] := Derivative[1][HFunc][τ];
Eq[τ];
FindRoot[Eq[τ] == 0, {τ, 1000}]
FindRoot[Eq[τ] == 0, {τ, τo}]
LogLinearPlot[Eq[τ], {τ, 1*10^2, 1*10^7}];
 {τ->696.22}
 {τ->217851.}

(* Peak in Relaxation Spectrum *)

τHMIN = 700;
τHMAX = 220000;
ScientificForm[HFunc[τHMAX], 3]
 1.19*10^6

(* ------------------------------------------------------------------ *)
(* Find Crossover Frequency and Crossover Modulus *)

FindRoot[EstorFunc[ω] == ElossFunc[ω], {ω, ωo}]
 {ω->1.89982*10^-6}

OmegaCross = ω /. {ω -> 1.89982*10^-6};
ECross = EstorFunc[ω] /. {ω -> 1.89982*10^-6};
ScientificForm[1/OmegaCross, 2]
ScientificForm[ECross, 3]
 5.3*10^5
 1.04*10^6
```

```
(* ------------------------------------------------------------------ *)
(* Find Local Maximum of Loss Modulus (2 equivalent methods) *)

dElossdω = D[Eloss, ω];
Factor[dElossdω];

Eq[ω_] := Factor[dElossdω];
Eq[ω];
FindRoot[Eq[ω] == 0, {ω, ωo}];

Eq[ω_] := Derivative[1][ElossFunc][ω]/10^9;
Eq[ω];
FindRoot[Eq[ω] == 0, {ω, 1/10^6}]
LogLinearPlot[Eq[ω], {ω, 1/10^6, 1/10^2}];
 {ω->5.69937*10^-6}

OmegaElossMAX = 5.7/10^6;
ScientificForm[1/OmegaElossMAX, 2]
 1.8*10^5

(* Peak in Loss Modulus *)

ElossMAX = ElossFunc[OmegaElossMAX];
ScientificForm[ElossMAX, 3]
 1.24*10^6

(* ------------------------------------------------------------------ *)
(* 5 Ways of Calculating the Plateau Modulus *)
(* ------------------------------------------------------------------ *)

(* Plateau Modulus from Peak in Loss Modulus *)
(* Relationship established by RAJU et al. (1981) M 14:1668 *)

PlateauModulusRAJU = 3.56*ElossMAX;
ScientificForm[PlateauModulusRAJU, 2]
 4.4*10^6

(* Relationship established by
   MARVIN and OSER (1962) J.RES.NAT.BUR.STAND. 66B:171
   OSER and MARVIN (1963) J.RES.NAT.BUR.STAND. 67B:87 *)

PlateauModulusMARVINandOSER = 4.83*ElossMAX;
ScientificForm[PlateauModulusMARVINandOSER, 2]
 6.*10^6

(* Plateau Modulus from Storage Modulus *)
(* Method proposed by JANZEN in DEALY and LARSON (2006) p 150 *)

PlateauModulusJANZEN = EstorFunc[1/τHMIN];
ScientificForm[PlateauModulusJANZEN, 2]
 4.7*10^6
```

```
(* Plateau Modulus from Integration of Relaxation Spectrum/tau *)
(* Method proposed by CHOMPFF and PRINS (1968) JCP 48:235 *)

PlateauModulusCHOMPFFandPRINS = NIntegrate[HFunc[τ]/τ,
       {τ, τHMIN, Infinity}];
ScientificForm[PlateauModulusCHOMPFFandPRINS, 2]
 4.7*10^6

(* Plateau Modulus from
   Integration of Loss Modulus/omega + Extrapolation *)
(* Method proposed by FERRY (1980) pp 70—71, 372—375 *)

(* Find Inflection Point in Loss Modulus, on a log axis *)

Eq[ω_] := ((f[ω] - ω*Derivative[1][f][ω])*Derivative[1][f][ω] +
          ω*f[ω]*Derivative[2][f][ω])/10^16;
FindRoot[Eq[ω] == 0, {ω, 1/10^5}]
LogLinearPlot[Eq[ω], {ω, 1/10^6, 1/10^2}];
 {ω->0.000041188}

(* Find Slope at Inflection Point in Loss Modulus, on a log axis *)

Eq[ω_] := ω*(Derivative[1][f][ω]/f[ω]);
ω0 = 0.000041;
Eq[ω0]
 -0.275158
(* first integrand: Loss Modulus/omega *)
Eq1[ω_] := (2/Pi)*(f[ω]/ω);
(* second integrand: Power-Law Extrapolation/omega *)
intercept = 53885; (* value found using MATLAB *)
slope = -0.275;
Eq2[ω_] := (2/Pi)*(intercept*ω^(slope - 1));
(* numerical integration *)
E1 = NIntegrate[Eq1[ω], {ω, 0, ω0}]
E2 = NIntegrate[Eq2[ω], {ω, ω0, Infinity}]
 3.36949*10^6
 2.00678*10^6

PlateauModulusFERRY = E1 + E2;
ScientificForm[PlateauModulusFERRY, 2]
 5.4*10^6
```

H.2.2 Edwards–Vilgis Slip-Link Model

This algorithm yields the correct analytical expression of the crosslink and entanglement contributions for the Edwards–Vilgis[84] slip-link model (Chapter 5). It was developed after noticing some typos in the original papers[83,84]. A recent review article[480] published in *Macromolecules* in 2014 contains a typo as well (vide infra).

```
(* Analysis of the Edwards–Vilgis SLIP-LINK model *)

(* ------------------------------------------------------------------ *)
(* PAPERS *)

(* Ball, Doi, Edwards, Warner (1981) Polymer 22:1010
   Thirion and Weil (1984) Polymer 25:609
   Edwards and Vilgis (1986) Polymer 27:483
   Vilgis and Erman (1993) Macromolecules 26:6657
   Watanabe et al. (2007) Macromolecules 40:6885
   Schlogl et al. (2014) Macromolecules 47:2759 *)

(* ------------------------------------------------------------------ *)
(* LEGEND *)

(* k = Boltzmann's constant
   T = absolute temperature *)

(* νc      = # density of elastically active strands from CROSSLINKS
   μc = Nc = # density of elastically active junctions/CROSSLINKS *)

(* ENTANGLEMENTS viewed as SLIP-LINKS *)
(* νe      = # density of elastically active strands from ENTANGLEMENTS
   μe = Ns = # density of elastically active junctions/ENTANGLEMENTS *)

(* fc = CROSSLINK functionality
   fe = ENTANGLEMENT functionality *)

(* Go = initial shear modulus, i.e. Go = G(λ=1)
   Eo = initial extensional modulus = 3*Go *)

(* A = Helmholtz free energy
   V = volume *)
(* W = elastic energy density = ΔA/V *)

(* λ   = macroscopic stretch ratio *)
(* sm  = strain measure (based on true stress)           = λ^2-λ^-1 *)
(* smN = strain measure (based on nominal stress) = sm/λ = λ-λ^-2 *)
(* I1  = first invariant of the Finger/Green tensor      = λ^2+2λ^-1 *)
```

```
(* σ  = true extensional stress = λ*σN *)
(* σN = nominal/engineering extensional stress *)

(* σ/sm      = reduced extensional stress = (λ*σN)/sm = σN/smN *)
(* σ/(sm*Go) = dimensionless extensional stress = S *)

(* α = finite extensibility parameter ≃ 1/λmax - vide infra *)
(* the E–V model assumes λmax = λmax,e = a/bk *)
(* α = 0, λmax = ∞, infinite extensibility,
                    gives the Ball et al. (1981) results
   α < 1/(3^(1/2)), due to the singularity of W - vide infra *)

(* β = slippage parameter *)
(* Vilgis and Erman estimate β as β = (a/Rg)^2 = 6*(a/R)^2 = 6/Z *)
(* β = 0, SLIP-LINK/ENTANGLEMENT behaves as a CROSSLINK
   β = ∞, no constraint *)
(* NOTE: with Vilgis and Erman's estimate, βmax = 6 since Zmin = 1 *)

(* ------------------------------------------------------------------- *)
(* ------------------------------------------------------------------- *)
(* ------------------------------------------------------------------- *)
(* Basic DEFINITIONS and ASSUMPTIONS *)

(* Assume: Uniaxial Extension-Compression along x, λ = L/Lo
           Constant Volume, λxλyλz = 1 *)
λx=λ;
λy=λ^(-1/2);
λz=λ^(-1/2);

(* Strain measure (based on true stress) *)
sm=λ^2-λ^-1;
(* Strain measure (based on nominal stress) *)
smN=sm/λ;smN=Simplify[smN];
(* First invariant of the Finger/Green tensor *)
I1=(λx^2+λy^2+λz^2);

(* Assume: CROSSLINKS and ENTANGLEMENTS are tetrafunctional *)
fc=4;
fe=4;

(* Relation between ν and μ *)
(* μ = 2*ν/f, Rubinstein–Colby (2004) p. 263 *)
νc=Nc*fc/2;
νe=Ns*fe/2;

(* Assume EQUILIBRIUM: Go = Geq *)
(* AFFINE network
   Geq_AFFINE = ν*k*T *)
(* PHANTOM network, i.e. thermal fluctuactions around mean positions
   Geq_PHANTOM = ((f-2)/f)*ν*k*T *)
```

```
(* If AFFINE network, then *)
(* Initial shear modulus from CROSSLINKS *)
GcAFFINE=νc*k*T
(* Initial shear modulus from ENTANGLEMENTS *)
GeAFFINE=νe*k*T
 2 k Nc T
 2 k Ns T

(* If PHANTOM network, then *)
(* Initial shear modulus from CROSSLINKS *)
GcPHANTOM=((fc-2)/fc)*νc*k*T
(* Initial shear modulus from ENTANGLEMENTS *)
GePHANTOM=((fe-2)/fe)*νe*k*T
 k Nc T
 k Ns T

(* ---------------------------------------------------------------- *)
(* ---------------------------------------------------------------- *)
(* ---------------------------------------------------------------- *)
(* Contribution from CROSSLINKS *)

(* Elastic energy density from CROSSLINKS *)
(* KEY POINT: this is only the deformation dependent part *)

prefactorC=(1/2)*Nc*k*T;
alphaterm=(1-α^2);
logtermα=Log[1-I1*α^2];

Wc=prefactorC*(((I1*alphaterm)/(1-I1*α^2))+logtermα);
Wc=FullSimplify[Wc]

Wcα0=Limit[Wc,α->0]

 1/2 k Nc T (((-1+α^2) (2+λ^3))/(-λ+α^2 (2+λ^3))+Log[1-(α^2 (2+λ^3))/λ])
 (k Nc T (2+λ^3))/(2 λ)

(* Let's consider Wc(λ=1) *)
Wcλ1=Wc/.λ->1

 1/2 k Nc T ((3 (-1+α^2))/(-1+3 α^2)+Log[1-3 α^2])

(* Find domain of α *)
(* need to consider singularity and sign of Wc, for λ=1 *)
term1=(1-I1*α^2);
term2=(Wc/(Nc*k*T));
Reduce[term1>0&&λ==1&&α>0,α,Reals]
Reduce[term1>0&&term2>0&&λ==1&&α>0,α,Reals]

 λ==1&&0<α<1/√3
 λ==1&&0<α<1/√3
```

```
(* Define domain of α *)
αdomain=ImplicitRegion[α>0&&α<(1/√3),{α}];

(* Find λ at which (1-I1*α^2), hence Wc, diverges *)
(* critical λ in COMPRESSION, i.e. λmin *)
Reduce[term1==0&&λ>0&&λ<1&&{α}∈αdomain,λ,Reals]
(* critical λ in EXTENSION, i.e. λmax *)
Reduce[term1==0&&λ>0&&λ>1&&{α}∈αdomain,λ,Reals]

 0<α<1/&&λ==Root[2 α^2-#1+α^2 #1^3&,2]
 0<α<1/&&λ==Root[2 α^2-#1+α^2 #1^3&,3]

(* Define critical λ in COMPRESSION, i.e. λmin *)
λcriticalCOMP[α_]:=Root[2 α^2-#1+α^2 #1^3&,2];
(* Define critical λ in EXTENSION, i.e. λmax *)
λcriticalEXT[α_]:=Root[2 α^2-#1+α^2 #1^3&,3];

(* KEY POINT: in EXTENSION, λmax ≃ 1/α *)
(* since I1    = λ^2+2*λ^-1 *)
(*       I1max = λmax^2+2*λmax^-1 ≃ λmax^2, for λmax >> 2^(1/3)≃1.26 *)
(* therefore, (1-I1max*α^2)=0 *)
(*            can be approximated by (1-λmax^2*α^2)=0 *)
(*            yielding λmax ≃ 1/α *)

(* Extensional stress from CROSSLINKS *)
σc=λ*D[Wc,λ];σc=FullSimplify[σc];
σcα0=Limit[σc,α->0];

(* Initial shear modulus from CROSSLINKS *)
Gc=(1/3)*Limit[σc/(λ-1),λ->1]
(* COMMENTS: *)
(* 1) Gc is not simply Nc*k*T, it depends on α too *)
(*    Gc = Nc*k*T*Qc, with Qc=Qc(α) *)
(* 2) to get the AFFINE network result, multiply by 2 *)

Gcα0=Limit[Gc,α->0]
(* COMMENTS: *)
(* 1) Gc is that of a PHANTOM network, Nc*k*T *)
(*    Gc = Nc*k*T*Qc, with Qc=1 *)
(* 2) to get the AFFINE network result, multiply by 2 *)

 (k Nc T (1-2 α^2+3 α^4))/(1-3 α^2)^2
 k Nc T

(* ---------------------------------------------------------------- *)
(* ---------------------------------------------------------------- *)
(* ---------------------------------------------------------------- *)
(* Contribution from ENTANGLEMENTS *)

(* Elastic energy density from ENTANGLEMENTS *)
(* KEY POINT: this is only the deformation dependent part *)
```

```
prefactorS=(1/2)*Ns*k*T;
termx=((λx^2)*(1+β))/(1+β*λx^2);
termy=((λy^2)*(1+β))/(1+β*λy^2);
termz=((λz^2)*(1+β))/(1+β*λz^2);
logtermx=Log[(1+β*λx^2)];
logtermy=Log[(1+β*λy^2)];
logtermz=Log[(1+β*λz^2)];
termxα=((1-α^2)*(1+β)*λx^2)/((1-I1*α^2)*(1+β*λx^2));
termyα=((1-α^2)*(1+β)*λy^2)/((1-I1*α^2)*(1+β*λy^2));
termzα=((1-α^2)*(1+β)*λz^2)/((1-I1*α^2)*(1+β*λz^2));

We=
prefactorS*(termxα+termyα+termzα+logtermx+logtermy+logtermz+logtermα);
We=FullSimplify[We]

(* Limits *)
Weα0=Limit[We,α->0]
Weβ0=Limit[We,β->0];
Weα0β0=Limit[Weα0,β->0];

(* verify that Weβ0 = Wc *)
Simplify[(Weβ0/Wc)*(Nc/Ns)]===1
(* verify that Weα0β0 = Wcα0 *)
Simplify[(Weα0β0/Wcα0)*(Nc/Ns)]===1

 1/2 k Ns T (((-1+α^2) (1+β) λ (2+3 β λ^2+λ^3))/((β+λ) (1+β λ^2) (-λ+α^2
(2+λ^3)))+2 Log[(β+λ)/λ]+Log[1+β λ^2]+Log[1-(α^2 (2+λ^3))/λ])
 1/2 k Ns T (((1+β) (2+3 β λ^2+λ^3))/((β+λ) (1+β λ^2))+2 Log[(β+λ)/λ]+Log[1+β
λ^2])
 True
 True

(* Extensional stress from ENTANGLEMENTS *)
σe=λ*D[We,λ];σe=FullSimplify[σe];

(* Limits *)
σeα0=Limit[σe,α->0];
σeβ0=Limit[σe,β->0];
σeα0β0=Limit[σeα0,β->0];

(* verify that σeβ0 = σc *)
Simplify[(σeβ0/σc)*(Nc/Ns)]===1
(* verify that σeα0β0 = σcα0 *)
Simplify[(σeα0β0/σcα0)*(Nc/Ns)]===1
 True
 True

(* Initial shear modulus from ENTANGLEMENTS *)
Ge=(1/3)*Limit[σe/(λ-1),λ->1]
(* COMMENTS: *)
(* 1) Ge is not simply Ns*k*T, it depends on α and β too *)
```

```
(*    Ge = Ns*k*T*Qe, with Qe=Qe(α,β) *)
(* 2) to get the AFFINE network result, multiply by 2 *)

Geα0=Limit[Ge,α->0]
(* COMMENTS: *)
(* 1) Ge is not simply Ns*k*T, it depends on β too *)
(*    Ge = Ns*k*T*Qe, with Qe=Qe(β) *)
(* 2) to get the AFFINE network result, multiply by 2 *)

 (k Ns T (1+α^4 (3+6 β)+2 α^2 (-1+β+β^2)))/((1-3 α^2)^2 (1+β)^2)
 (k Ns T)/(1+β)^2

(* Limits *)
Geβ∞=Limit[Ge,β->∞]
(* COMMENTS:
   for β⟶∞, Ge is small but not zero if α≠0 *)
Geα0β∞=Limit[Geα0,β->∞]

 (2 k Ns T α^2)/(1-3 α^2)^2
 0

(* ---------------------------------------------------------------- *)
(* ---------------------------------------------------------------- *)
(* ---------------------------------------------------------------- *)
(* CROSSLINKS + ENTANGLEMENTS, final results *)
(* ---------------------------------------------------------------- *)
(* ---------------------------------------------------------------- *)
(* ---------------------------------------------------------------- *)

(* ---------------------------------------------------------------- *)
(* Elastic energy density *)
(* KEY POINT: this is only the deformation dependent part *)

W=Wc+We;
W=Collect[FullSimplify[W],{Nc,Ns}];

Wα0=Limit[W,α->0];
Wα0=Collect[FullSimplify[Wα0],{Nc,Ns}];

(* ---------------------------------------------------------------- *)
(* Extensional stress *)

σ=λ*D[W,λ];
σ=Collect[FullSimplify[σ],{Nc,Ns}];

σα0=Limit[σ,α->0];
σα0=Collect[FullSimplify[σα0],{Nc,Ns}];

(* verify additivity *)
σ2=σc+σe;σ/σ2===1
 True
```

```
(* ------------------------------------------------------------------ *)
(* Initial shear modulus *)

(* Go = Nc*k*T*Qc(α) + Ns*k*T*Qe(α,β) *)
Go=(1/3)*Limit[σ/(λ-1),λ->1];
Go=Collect[Go,{Nc,Ns}]

(* Go = Nc*k*T + Ns*k*T*Qe(β) *)
Goα0=Limit[Go,α->0];
Goα0=Collect[Goα0,{Nc,Ns}]

(* verify additivity *)
Go2=Gc+Ge;
Go/Go2===1

 (k Nc T (1-2 α^2+3 α^4))/(1-3 α^2)^2+(k Ns T (1+α^4 (3+6 β)+2 α^2 (-
1+β+β^2)))/((1-3 α^2)^2 (1+β)^2)
 k Nc T+(k Ns T)/(1+β)^2
 True

(* Limits *)
Goβ0=Limit[Go,β->0];Goβ0=Collect[Goβ0,{Nc,Ns}]
Goβ∞=Limit[Go,β->∞];Goβ∞=Collect[Goβ∞,{Nc,Ns}]
(* COMMENTS:
   albeit weakly, for β⟶∞ Go depends on Ns too if α≠0 *)
Goα0β0=Limit[Goα0,β->0]
Goα0β∞=Limit[Goα0,β->∞]

 (k Nc T (1-2 α^2+3 α^4))/(1-3 α^2)^2+(k Ns T (1-2 α^2+3 α^4))/(1-3 α^2)^2
 (2 k Ns T α^2)/(1-3 α^2)^2+(k Nc T (1-2 α^2+3 α^4))/(1-3 α^2)^2
 k (Nc+Ns) T
 k Nc T

(* ------------------------------------------------------------------ *)
(* Fraction of Go contributed by ENTANGLEMENTS *)
ψ=Simplify[Ge/Go]
ψα0=Limit[ψ,α->0]

 (Ns (1+α^4 (3+6 β)+2 α^2 (-1+β+β^2)))/(Nc (1-2 α^2+3 α^4) (1+β)^2+Ns (1+α^4 (3+6
β)+2 α^2 (-1+β+β^2)))
 Ns/(Ns+Nc (1+β)^2)

(* Limits *)
ψβ0=Limit[ψ,β->0]
ψβ∞=Limit[ψ,β->∞]
(* COMMENTS:
   for β⟶∞, ψ is small but not zero if α≠0 *)
ψα0β0=Limit[ψα0,β->0]
ψα0β∞=Limit[ψα0,β->∞]
 Ns/(Nc+Ns)
 (2 Ns α^2)/(Nc-2 Nc α^2+2 Ns α^2+3 Nc α^4)
```

```
 Ns/(Nc+Ns)
 0

(* ------------------------------------------------------------------ *)
(* Reduced extensional stress *)
(* NOTE: σRED = σ/sm = σN/smN *)

(* σRED = Gc*Yc(λ;α)           + Ge*Ye(λ;α,β)
        = Nc*k*T*Qc(α)*Yc(λ;α) + Ns*k*T*Qe(α,β)*Ye(λ;α,β)
        = Nc*k*T*Pc(λ;α)       + Ns*k*T*Pe(λ;α,β) *)
σRED=σ/sm;
σRED=Collect[FullSimplify[σRED],{Nc,Ns}];

(* σRED = Gc     + Ge*Ye(λ;β)
        = Nc*k*T + Ns*k*T*Qe(β)*Ye(λ;β)
        = Nc*k*T + Ns*k*T*Pe(λ;β) *)
σREDα0=Limit[σRED,α->0];
σREDα0=Collect[FullSimplify[σREDα0],{Nc,Ns}];

(* ------------------------------------------------------------------ *)
(* σRED = Gc*Yc(λ;α)           + Ge*Ye(λ;α,β)
        = Nc*k*T*Qc(α)*Yc(λ;α) + Ns*k*T*Qe(α,β)*Ye(λ;α,β)
        = Nc*k*T*Pc(λ;α)       + Ns*k*T*Pe(λ;α,β) *)

(* σRED(λ⟶1) = Go = Gc + Ge *)

(* S = σRED/Go = (Gc/Go)*Yc + (Ge/Go)*Ye
               = (1-ψ)*Yc   + ψ*Ye *)

(* ------------------------------------------------------------------ *)
(* Pc: CROSSLINK contribution *)
Pc=FullSimplify[Coefficient[σRED,(Nc*k*T)]]
Pcα0=Limit[Pc,α->0]

 (λ (λ-2 α^2 λ+α^4 (2+λ^3)))/(λ-α^2 (2+λ^3))^2
 1

(* Qc: CROSSLINK contribution at λ=1 *)
Qc=Simplify[Limit[Pc,λ->1]]
Qcα0=Simplify[Limit[Pcα0,λ->1]]

 (1-2 α^2+3 α^4)/(1-3 α^2)^2
 1

(* Yc: Normalized CROSSLINK contribution *)
Yc=FullSimplify[Pc/Qc]
Ycα0=FullSimplify[Pcα0/Qcα0]

 ((1-3 α^2)^2 λ (λ-2 α^2 λ+α^4 (2+λ^3)))/((1-2 α^2+3 α^4) (λ-α^2 (2+λ^3))^2)
 1
```

```
(* Verify that Yc=1 for λ=1 *)
(Yc/.λ->1)===1
(Ycα0/.λ->1)===1
 True
 True

(* ------------------------------------------------------------------------ *)
(* Pe: ENTANGLEMENT contribution *)
Pe=FullSimplify[Coefficient[σRED,(Ns*k*T)]]
Peα0=Limit[Pe,α->0]

(* Limits for β⟶0 *)
Peβ0=Limit[Pe,β->0];
Peα0β0=Limit[Peα0,β->0];

(* verify that Peβ0 = Pc *)
Simplify[(Peβ0/Pc)]===1
(* verify that Peα0β0 = Pcα0 *)
Simplify[(Peα0β0/Pcα0)]===1

 (λ (α^2 λ ((2-3 β) β-6 β λ+(-2+β (-1+β (7+β))) λ^2+β (6+(-3+β) β) λ^3+β (-4+β^2
(3+2 β)) λ^4+β^2 (5+β) λ^5+(1-2 β) β λ^6)+λ^2 (λ+2 β λ+β^2 (1+(-1+λ) λ^2))+α^4 (λ^2
(2+λ^3)+β^4 λ^4 (2-3 λ+λ^3)+2 β λ (3+2 λ^3+λ^6)+β^3 λ^2 (8-7 λ+7 λ^3-5 λ^4+3 λ^6)+β^2 (6-2
λ+10 λ^3-6 λ^4+6 λ^6-λ^7+2 λ^9))))/((β+λ)^2 (1+β λ^2)^2 (λ-α^2 (2+λ^3))^2)
 (λ (λ+2 β λ+β^2 (1-λ^2+λ^3)))/((β+λ)^2 (1+β λ^2)^2)
 True
 True

(* Qe: ENTANGLEMENT contribution at λ=1 *)
Qe=Simplify[Limit[Pe,λ->1]]
Qeα0=Simplify[Limit[Peα0,λ->1]]

(* Limits for β⟶0 *)
Qeβ0=Limit[Qe,β->0];
Qeα0β0=Limit[Qeα0,β->0];

(* verify that Qeβ0 = Qc *)
Simplify[(Qeβ0/Qc)]===1
(* verify that Qeα0β0 = Qcα0 *)
Simplify[(Qeα0β0/Qcα0)]===1

 (1+α^4 (3+6 β)+2 α^2 (-1+β+β^2))/((1-3 α^2)^2 (1+β)^2)
 1/(1+β)^2
 True
 True

(* Ye: Normalized ENTANGLEMENT contribution *)
Ye=FullSimplify[Pe/Qe]
Yeα0=FullSimplify[Peα0/Qeα0]
```

```
(* Limits for β⟶0 *)
Yeβ0=Limit[Ye,β->0];
Yeα0β0=Limit[Yeα0,β->0];

(* verify that Yeβ0 = Yc *)
Simplify[(Yeβ0/Yc)]===1
(* verify that Yeα0β0 = Ycα0 *)
Simplify[(Yeα0β0/Ycα0)]===1

 ((1-3 α^2)^2 (1+β)^2 λ (α^2 λ ((2-3 β) β-6 β λ+(-2+β (-1+β (7+β))) λ^2+β (6+(-
3+β) β) λ^3+β (-4+β^2 (3+2 β)) λ^4+β^2 (5+β) λ^5+(1-2 β) β λ^6)+λ^2 (λ+2 β λ+β^2 (1+(-
1+λ) λ^2))+α^4 (λ^2 (2+λ^3)+β^4 λ^4 (2-3 λ+λ^3)+2 β λ (3+2 λ^3+λ^6)+β^3 λ^2 (8-7 λ+7 λ^3-5
λ^4+3 λ^6)+β^2 (6-2 λ+10 λ^3-6 λ^4+6 λ^6-λ^7+2 λ^9))))/((1+α^4 (3+6 β)+2 α^2 (-1+β+β^2))
(β+λ)^2 (1+β λ^2)^2 (λ-α^2 (2+λ^3))^2)
 ((1+β)^2 λ (λ+2 β λ+β^2 (1+(-1+λ) λ^2)))/((β+λ)^2 (1+β λ^2)^2)
 True
 True

(* ---------------------------------------------------------------------- *)
(* ---------------------------------------------------------------------- *)
(* ---------------------------------------------------------------------- *)
(* Compare Ye, for α = 0,
   with analytical expressions from LITERATURE *)
(* ---------------------------------------------------------------------- *)
(* ---------------------------------------------------------------------- *)
(* ---------------------------------------------------------------------- *)

(* σRED = Gc     + Ge*Ye(λ;β)
        = Nc*k*T + Ns*k*T*Qe(β)*Ye(λ;β)
        = Nc*k*T + Ns*k*T*Pe(λ;β) *)

(* ---------------------------------------------------------------------- *)
(* Eq.(10.60) given by Graessley (2004) at p. 523 *)
Yeα0Graessley=((1+β)^2*λ)/((β+λ)*(1+β*λ^2))*(((1+β)*(1-
λ*β^2)*λ)/((β+λ)*(1+β*λ^2))+β);
(* verify whether Yeα0Graessley = Yeα0 *)
Simplify[Yeα0Graessley/Yeα0]===1
(* ⟶ OK *)
 True

(* ---------------------------------------------------------------------- *)
(* Yeα0 deduced from Thirion and Weil (1984) Polymer 25:609 *)
(* Specifically, from the Eq. (4) at p. 609 *)
(* NOTE: their t is σ *)
Peα0TW=λ^2/(λ^2+λ+1)*(1/(β+λ)^2+(λ+1)/(λ*(1+β*λ^2)^2));
Qeα0TW=Limit[Peα0TW,λ->1]
Yeα0TW=Peα0TW/Qeα0TW;
Yeα0TW=FullSimplify[Yeα0TW];
(* ⟶ OK *)
 1/(1+β)^2
```

```
(* verify whether Peα0TW = Peα0 *)
FullSimplify[Peα0TW/Peα0]===1
(* verify whether Qeα0TW = Qeα0 *)
FullSimplify[Qeα0TW/Qeα0]===1
(* verify whether Yeα0TW = Yeα0 *)
FullSimplify[Yeα0TW/Yeα0]===1
(* ⟶ OK *)
 True
 True
 True

(* ------------------------------------------------------------------ *)
(* Yeα0 deduced from Edwards and Vilgis (1986) Polymer 27:483 *)
(* Specifically, from the Eq. given at p. 486
                      and Eq. (5.1) at p. 491 with α = 0 *)
(* NOTE: their f is σN and their D is smN *)
Peα0EV=(λ/(smN*(1+β*λ^2)^2)-1/(smN*(β+λ)^2)+(β*λ)/((1+β*λ^2)*(β+λ)));
Qeα0EV=Limit[Peα0EV,λ->1]
Yeα0EV=Peα0EV/Qeα0EV;
Yeα0EV=FullSimplify[Yeα0EV];
(* ⟶ INCORRECT *)
 (1+β^2)/(1+β)^3

(* verify whether Peα0EV = Peα0 *)
FullSimplify[Peα0EV/Peα0]===1
(* verify whether Qeα0EV = Qeα0 *)
FullSimplify[Qeα0EV/Qeα0]===1
(* verify whether Yeα0EV = Yeα0 *)
FullSimplify[Yeα0EV/Yeα0]===1
(* ⟶ INCORRECT *)
 False
 False
 False

(* TYPOS in Edwards and Vilgis (1986) Polymer 27:483 *)
(* To be consistent with W, Peα0EV should have (1+β)
   in the numerator of the first and second term *)
Peα0EVcorrected=((λ*(1+β))/(smN*(1+β*λ^2)^2)-
(1+β)/(smN*(β+λ)^2)+(β*λ)/((1+β*λ^2)*(β+λ)));
Qeα0EVcorrected=Limit[Peα0EVcorrected,λ->1]
Yeα0EVcorrected=Peα0EVcorrected/Qeα0EVcorrected;
Yeα0EVcorrected=FullSimplify[Yeα0EVcorrected];
(* ⟶ OK *)
 1/(1+β)^2

(* verify whether Peα0EV = Peα0 *)
FullSimplify[Peα0EVcorrected/Peα0]===1
(* verify whether Qeα0EV = Qeα0 *)
FullSimplify[Qeα0EVcorrected/Qeα0]===1
(* verify whether Yeα0EV = Yeα0 *)
```

```
FullSimplify[Yeα0EVcorrected/Yeα0]===1
(* ⟶ OK *)
 True
 True
 True

(* ------------------------------------------------------------------- *)
(* Eq.(12) given by Schlogl et al. (2014) Macromolecules 47:2759 *)
(* NOTE: their D is smN *)
Yeα0Schlogl=λ/(smN*(1+β*λ^2)^2)-1/(smN*(β+λ)^2)+(β*λ)/((1+β*λ^2)*(β+λ));
Yeα0Schlogl=FullSimplify[Yeα0Schlogl];
(* verify whether Yeα0Schlogl = Yeα0 *)
FullSimplify[Yeα0Schlogl/Yeα0]===1
(* ⟶ INCORRECT *)
 False

(* ERROR # 1
   Eq. (12) is taken from the original paper of Edwards and Vilgis,
   which should have (1+β) in the numerator of first and second term *)
(* ERROR # 2
   since Ge = (Ns*k*T)/((1+β)^2), need to multiply by (1+β)^2 *)
Yeα0Schloglcorrected=((λ*(1+β))/(smN*(1+β*λ^2)^2)-
(1+β)/(smN*(β+λ)^2)+(β*λ)/((1+β*λ^2)*(β+λ)))*(1+β)^2;
Yeα0Schloglcorrected=FullSimplify[Yeα0Schloglcorrected];
(* verify whether Yeα0Schloglcorrected = Yeα0 *)
FullSimplify[Yeα0Schloglcorrected/Yeα0]===1
(* ⟶ OK *)
 True

(* ------------------------------------------------------------------- *)
(* ------------------------------------------------------------------- *)
(* ------------------------------------------------------------------- *)
(* Compare Ye, for α ≠ 0,
   with analytical expressions from LITERATURE *)
(* ------------------------------------------------------------------- *)
(* ------------------------------------------------------------------- *)
(* ------------------------------------------------------------------- *)

(* σRED = Gc*Yc(λ;α)            + Ge*Ye(λ;α,β)
        = Nc*k*T*Qc(α)*Yc(λ;α) + Ns*k*T*Qe(α,β)*Ye(λ;α,β)
        = Nc*k*T*Pc(λ;α)       + Ns*k*T*Pe(λ;α,β) *)

(* ------------------------------------------------------------------- *)
(* Ye deduced from Edwards and Vilgis (1986) Polymer 27:483 *)
(* NOTE: their f is σN, their D is smN, and their ϕ is I1 *)

(* Pe from Eq. (5.1) at p. 491 *)
Pe1EV=(α^2*(1-α^2)*(1+β))/(1-I1*α^2)^2*(λ^2/(1+β*λ^2)+2/(β+λ));
Pe2EV=1/(1-I1*α^2)*(λ/(1+β*λ^2)^2-1/(β+λ)^2)*1/(λ-λ^-2);
Pe3EV=-(α^2/(1-I1*α^2));
Pe4EV=(β*λ)/((1+β*λ^2)*(β+λ));
```

```
PeEV=Pe1EV+Pe2EV+Pe3EV+Pe4EV;

(* Pc from Eq. (5.3) at p. 491 *)
PcEV=(1-α^2)/(1-I1*α^2)^2-α^2/(1-I1*α^2);

(* Limits *)
PeEVα0=Limit[PeEV,α->0];
PeEVβ0=Limit[PeEV,β->0];

(* verify that PeEV(α=0) = Peα0EVcorrected (see above) *)
Simplify[PeEVα0/Peα0EVcorrected]===1
(* ⟶ INCORRECT *)
(* verify that PeEV(β=0) = PcEV, internal consistency *)
Simplify[PeEVβ0/PcEV]===1
(* ⟶ INCORRECT, this PeEV is INCONSISTENT with PcEV *)
 False
 False

(* TYPOS in Edwards and Vilgis (1986) Polymer 27:483 *)
(* To be consistent with W and with PcEV, PeEV should have (1-α^2)*(1+β)
   in the numerator of Pe2EV *)
Pe2EVcorrected=((1-α^2)*(1+β))/(1-I1*α^2)*(λ/(1+β*λ^2)^2-1/(β+λ)^2)*1/(λ-λ^-2);
PeEVcorrected=Pe1EV+Pe2EVcorrected+Pe3EV+Pe4EV;

(* Limits *)
PeEVα0=Limit[PeEVcorrected,α->0];
PeEVβ0=Limit[PeEVcorrected,β->0];

(* verify that PeEV(α=0) = Peα0EVcorrected (see above) *)
Simplify[PeEVα0/Peα0EVcorrected]===1
(* verify that PeEV(β=0) = PcEV, internal consistency *)
Simplify[PeEVβ0/PcEV]===1
(* ⟶ OK *)
 True
 True

(* verify that PeEVcorrected = Pe *)
Simplify[PeEVcorrected/Pe]===1
(* verify that PcEV = Pc *)
Simplify[PcEV/Pc]===1
(* ⟶ OK *)
 True
 True

QeEVcorrected=Limit[PeEVcorrected,λ->1];
YeEVcorrected=PeEVcorrected/QeEVcorrected;
YeEVcorrected=FullSimplify[YeEVcorrected];
(* verify that QeEVcorrected = Qe *)
Simplify[QeEVcorrected/Qe]===1
(* verify that YeEVcorrected = Ye *)
Simplify[YeEVcorrected/Ye]===1
```

```
(* ⟶ OK *)
 True
 True

(* ---------------------------------------------------------------------- *)
(* Ye deduced from Watanabe et al. (2007) Macromolecules 40:6885 *)

(* Pe from equations given in Appendix A *)
Pe1Watanabe=(α^2*(1-α^2)*(1+β))/(1-I1*α^2)^2*(λ^2/(1+β*λ^2)+2/(β+λ));
Pe2Watanabe=((1-α^2)*(1+β))/(1-I1*α^2)*(λ/(1+β*λ^2)^2-1/(β+λ)^2)*1/(λ-λ^-2);
Pe3Watanabe=-(α^2/(1-I1*α^2));
Pe4Watanabe=(β*λ)/((1+β*λ^2)*(β+λ));
PeWatanabe=Pe1Watanabe+Pe2Watanabe+Pe3Watanabe+Pe4Watanabe;

(* Pc from equations given in Appendix A *)
PcWatanabe=(1-2*α^2+I1*α^4)/(1-I1*α^2)^2;

(* Limits *)
PeWatanabeα0=Limit[PeWatanabe,α->0];
PeWatanabeβ0=Limit[PeWatanabe,β->0];

(* verify that PeWatanabe(β=0) = PcWatanabe, internal consistency *)
Simplify[PeWatanabeβ0/PcWatanabe]===1
 True

(* verify that PeWatanabe = Pe *)
Simplify[PeWatanabe/Pe]===1
(* verify that PcWatanabe = Pc *)
Simplify[PcWatanabe/Pc]===1
(* ⟶ OK *)
 True
 True

QeWatanabe=Limit[PeWatanabe,λ->1];
YeWatanabe=PeWatanabe/QeWatanabe;
YeWatanabe=FullSimplify[YeWatanabe];
(* verify that QeWatanabe = Qe *)
Simplify[QeWatanabe/Qe]===1
(* verify that YeWatanabe = Ye *)
Simplify[YeWatanabe/Ye]===1
(* ⟶ OK *)
 True
 True
```

H.3 MATLAB Code

H.3.1 How to Import Experimental Data

This script illustrates how to import experimental data into MATLAB. Raw data given as "txt" files are first saved as "mat" files, and later stored in matrix arrays for calculations and plotting.

```
function Import_Txt_FREQ_Sweep()

    clc;
    clear all;

    type = 'FREQsweep';

    all       = strcat('*', type, '*.txt');
    list_txt  = dir(all);
    list_mat  = list_txt;
    num_files = length(list_txt);
    mydata    = cell(num_files, 1);

    for k = 1:num_files
      mydata{k} = importdata(list_txt(k).name);
      a_frequency       = mydata{k}.data(:,3);
      b_storage_modulus = mydata{k}.data(:,4);
      c_loss_modulus    = mydata{k}.data(:,5);
      list_mat(k).name  = regexprep(list_txt(k).name, '.txt', '.mat');
      save(list_mat(k).name, 'a_frequency', ...
                             'b_storage_modulus', 'c_loss_modulus');
      clear('a_frequency', 'b_storage_modulus', 'c_loss_modulus');
    end

    list_name = strcat('List_', type);
    save(list_name, 'list_mat');

end

...

test_name = 'FREQsweep';
list_name = strcat('List_', test_name, '.mat');

List = load(list_name);                  % load list of mat files %
max_num_files = length(List.list_mat);   % total number of mat files %

npts = zeros(1, max_num_files);

max_num_datapoints = 0;
```

```
for k = 1:max_num_files

    File = load(List.list_mat(k).name);   % load mat file %
    X_exp_data = File.a_frequency;        % assign experimental data %

    npts(1,k) = length(X_exp_data);
    if npts(1,k) > max_num_datapoints
        max_num_datapoints = npts(1,k);
    end
end

x  = zeros(max_num_datapoints, max_num_files);
y1 = zeros(max_num_datapoints, max_num_files);
y2 = zeros(max_num_datapoints, max_num_files);
y3 = zeros(max_num_datapoints, max_num_files);
y4 = zeros(max_num_datapoints, max_num_files);

for k = 1:max_num_files

    File = load(List.list_mat(k).name);
    lim = npts(1,k);

    x(1:lim,k)  = File.a_frequency;        % assign experimental data %
    y1(1:lim,k) = File.b_storage_modulus;  % assign experimental data %
    y2(1:lim,k) = File.c_loss_modulus;     % assign experimental data %
    y3(1:lim,k) = tan(atan2(y2(1:lim,k), y1(1:lim,k)));
    y4(1:lim,k) = abs(complex(y1(1:lim,k), y2(1:lim,k)));
end

x(x==0)   = NaN;
y1(y1==0) = NaN;
y2(y2==0) = NaN;

% varargout = NoDuplicateData(Xdata, Ydata, ...
%                             tol_target_min)

nodupl_npts = zeros(1, max_num_files);

max_num_datapoints = 0;
for k = 1:max_num_files

    noduplX = NoDuplicateData(x(:,k), x(:,k));
    nodupl_npts(1,k) = length(noduplX);

    if nodupl_npts(1,k) > max_num_datapoints
        max_num_datapoints = nodupl_npts(1,k);
    end
end

nodupl_x  = zeros(max_num_datapoints, max_num_files);
nodupl_y1 = zeros(max_num_datapoints, max_num_files);
nodupl_y2 = zeros(max_num_datapoints, max_num_files);
nodupl_y3 = zeros(max_num_datapoints, max_num_files);
```

```
nodupl_y4 = zeros(max_num_datapoints, max_num_files);

for k = 1:max_num_files

    lim = nodupl_npts(1,k);

    [nodupl_x(1:lim,k), nodupl_y1(1:lim,k)] = ...
                          NoDuplicateData(x(:,k), y1(:,k));
    nodupl_y2(1:lim,k) = NoDuplicateData(x(:,k), y2(:,k));
    nodupl_y3(1:lim,k) = tan(atan2(nodupl_y2(1:lim,k), ...
                                   nodupl_y1(1:lim,k)));
    nodupl_y4(1:lim,k) = abs(complex(nodupl_y1(1:lim,k), ...
                                     nodupl_y2(1:lim,k)));
end

nodupl_x(nodupl_x==0)   = NaN;
nodupl_y1(nodupl_y1==0) = NaN;
nodupl_y2(nodupl_y2==0) = NaN;
nodupl_y3(nodupl_y3==0) = NaN;
```

H.3.2 Basic Functions

These functions were developed to handle experimental data and numerical outputs.

```
% ------------------------------------------------------------------- %
% ROUND, CEIL, or FLOOR input data
% according to the chosen # of fractional digits
% ------------------------------------------------------------------- %

function out = RoundData(data, digits, type)

    if nargin < 3
        type = 'round';
    end

    if size(data, 2) > 1
        data = data';
    end

    length_data = length(data);
    ones_vector = ones(length_data, 1);

    floor_log10_data = floor(log10(abs(data)));
    floor_log10_data(floor_log10_data == -Inf) = 0;

    exponent = - digits .* ones_vector;

    for k = 1:length_data
        if exponent(k) > floor_log10_data(k)
            exponent(k) = floor_log10_data(k);
        end
    end

    divide_by = 10.^exponent;

    if strcmpi(type, 'round')
        out = round(data ./ divide_by) .* divide_by;
    elseif strcmpi(type, 'ceil')
        out = ceil(data ./ divide_by) .* divide_by;
    elseif strcmpi(type, 'floor')
        out = floor(data ./ divide_by) .* divide_by;
    end

end

% ******************************************************************* %
```

```
% ------------------------------------------------------------------- %
% Creates a vector with components spaced on a linear or log scale
% ------------------------------------------------------------------- %

function out = SpaceX(X_data_or_limits, ...
                      spacing,          ...
                      pts_per_decade)

    if nargin < 3
        pts_per_decade = 6;
    end
    if nargin < 2
        spacing = 'log';
    end

    XdataMin = min(X_data_or_limits);
    XdataMax = max(X_data_or_limits);

    log10_XdataMin = log10(XdataMin);
    log10_XdataMax = log10(XdataMax);

    if strcmpi(spacing, 'log')
        num_decades_log = log10_XdataMax - log10_XdataMin;
        pts_log         = round(pts_per_decade * num_decades_log);
        logspaceX = logspace(log10_XdataMin, log10_XdataMax, pts_log)';
        out = logspaceX;
    elseif strcmpi(spacing, 'lin')
        num_decades_lin = (XdataMax - XdataMin) / 10;
        pts_lin         = round(pts_per_decade * num_decades_lin);
        linspaceX       = linspace(XdataMin, XdataMax, pts_lin)';
        out = linspaceX;
    end

end

% ******************************************************************* %

% ------------------------------------------------------------------- %
% Finds specific data from an experimental data set
% to within the specified tolerance
% ------------------------------------------------------------------- %

function indices_target = FindExpData(exp_data, target, ...
                                      relation,         ...
                                      tol_target_min,   ...
                                      tol_target)

    if nargin < 5
        tol_target = 0.50;   % 0.50 = 50 percent %
    end
    if nargin < 4
        tol_target_min = 0.10;   % 0.1 =  10 percent %
    end
```

```
if nargin < 3
    relation = '=';
end

offset = 1;
if target == 0
    exp_data = exp_data + offset;
    target   = target   + offset;
end

indices_target = [0, 0];   % set length(indices_target) = 2 %

if strcmpi(relation, '=')      || ...
   strcmpi(relation, 'equal')  || ...
   strcmpi(relation, 'equalto')
    while length(indices_target) > 1
        indices_target = ...
            find( abs((exp_data - target)./target) <= tol_target );
        if (tol_target <= tol_target_min) && ...
           (length(indices_target) >= 2)
            indices_target = indices_target(1);
        else
            tol_target = tol_target * 0.99;
        end
    end
end

if strcmpi(relation, '>')          || ...
   strcmpi(relation, 'greater')    || ...
   strcmpi(relation, 'greaterthan')
    while length(indices_target) > 1
        indices_target =                        ...
            find( ((exp_data - target) > 0) & ...
                (abs((exp_data - target)./target) <= tol_target) );
        if (tol_target <= tol_target_min) && ...
           (length(indices_target) >= 2)
            indices_target = indices_target(1);
        else
            tol_target = tol_target * 0.99;
        end
    end
end

if strcmpi(relation, '>=')                   || ...
   strcmpi(relation, '=>')                   || ...
   strcmpi(relation, 'greaterorequal')       || ...
   strcmpi(relation, 'equalorgreater')       || ...
   strcmpi(relation, 'greaterthanorequalto') || ...
   strcmpi(relation, 'equaltoorgreaterthan')
    while length(indices_target) > 1
        indices_target =                        ...
            find( ((exp_data - target) >= 0) & ...
                (abs((exp_data - target)./target) <= tol_target) );
```

```
            if (tol_target <= tol_target_min) && ...
               (length(indices_target) >= 2)
                indices_target = indices_target(1);
            else
                tol_target = tol_target * 0.99;
            end
        end
    end

    if strcmpi(relation, '<')       || ...
       strcmpi(relation, 'less')    || ...
       strcmpi(relation, 'lessthan')
        while length(indices_target) > 1
            indices_target =                        ...
                find( ((exp_data - target) < 0) & ...
                    (abs((exp_data - target)./target) <= tol_target) );
            if (tol_target <= tol_target_min) && ...
               (length(indices_target) >= 2)
                indices_target = indices_target(1);
            else
                tol_target = tol_target * 0.99;
            end
        end
    end

    if strcmpi(relation, '<=')                || ...
       strcmpi(relation, '=<')                || ...
       strcmpi(relation, 'lessorequal')       || ...
       strcmpi(relation, 'equalorless')       || ...
       strcmpi(relation, 'lessthanorequalto') || ...
       strcmpi(relation, 'equaltoorlessthan')
        while length(indices_target) > 1
            indices_target =                         ...
                find( ((exp_data - target) <= 0) & ...
                    (abs((exp_data - target)./target) <= tol_target) );
            if (tol_target <= tol_target_min) && ...
               (length(indices_target) >= 2)
                indices_target = indices_target(1);
            else
                tol_target = tol_target * 0.99;
            end
        end
    end

end

% ********************************************************************** %
```

```
% ------------------------------------------------------------------- %
% Eliminates duplicate data in an experimental data set
% ------------------------------------------------------------------- %

function varargout = NoDuplicateData(Xdata, Ydata, ...
                                     tol_target_min)

    if nargin < 3
        tol_target_min = 0.001;   % 0.001 =  0.1 percent %
    end

    pts = length(Xdata);
    subset_Xdata = zeros(pts, 1);
    subset_Ydata = zeros(pts, 1);
    j = 1;

    for k = 1:pts

        indices_target = ...
                    FindExpData(Xdata, Xdata(k), '=', tol_target_min);

        if ~isempty(indices_target) && ...
            isempty(find(subset_Xdata == Xdata(indices_target), 1))
            subset_Xdata(j) = Xdata(indices_target);
            subset_Ydata(j) = Ydata(indices_target);
            j = j + 1;
        end
    end

    if isempty(find(subset_Xdata == 0, 1))
        reduced_pts = pts;
    else
        reduced_pts = find(subset_Xdata == 0, 1) - 1;
    end
    reduced_Xdata = subset_Xdata(1:reduced_pts);
    reduced_Ydata = subset_Ydata(1:reduced_pts);

    if nargout == 2
        varargout(1) = {reduced_Xdata};
        varargout(2) = {reduced_Ydata};
    elseif nargout == 1
        varargout(1) = {reduced_Ydata};
    end

end

% ******************************************************************* %
```

```
% ------------------------------------------------------------------- %
% Reduces the experimental data set on a linear or log scale
% to the specified number of points per decade
% ------------------------------------------------------------------- %

function varargout = ReduceData(Xdata, Ydata,   ...
                                spacing,        ...
                                pts_per_decade, ...
                                tol_target_min, ...
                                Xdata_limits)

    if nargin < 6 || isempty(Xdata_limits)
        XdataMin = min(Xdata);
        XdataMax = max(Xdata);
    else
        XdataMin = min(Xdata_limits);
        XdataMax = max(Xdata_limits);
    end
    if nargin < 5
        tol_target_min = 0.01;
    end
    if nargin < 4
        pts_per_decade = 6;
    end
    if nargin < 3
        spacing = 'log';
    end

    log10_XdataMin = log10(XdataMin);
    log10_XdataMax = log10(XdataMax);

    if strcmpi(spacing, 'log')
        num_decades_log = log10_XdataMax - log10_XdataMin;
        max_pts_log     = round(pts_per_decade * num_decades_log);
        logspaceX       = ...
                logspace(log10_XdataMin, log10_XdataMax, max_pts_log)';
        max_pts = max_pts_log;
        spaceX = logspaceX;
    elseif strcmpi(spacing, 'lin')
        num_decades_lin = (XdataMax - XdataMin) / 10;
        max_pts_lin     = round(pts_per_decade * num_decades_lin);
        linspaceX       = linspace(XdataMin, XdataMax, max_pts_lin)';
        max_pts = max_pts_lin;
        spaceX = linspaceX;
    end

    subset_Xdata = zeros(max_pts, 1);
    subset_Ydata = zeros(max_pts, 1);
    j = 1;
    for k = 1:max_pts

        indices_target = ...
                    FindExpData(Xdata, spaceX(k), '=', tol_target_min);
```

```
        if k == 1
            if ~isempty(indices_target) && ...
                isempty(find(subset_Xdata == Xdata(indices_target), 1))

                subset_Xdata(j) = Xdata(indices_target);
                subset_Ydata(j) = Ydata(indices_target);
                j = j + 1;
            end
        else
            if ~isempty(indices_target) && ...
                isempty(find(subset_Xdata == Xdata(indices_target), 1))
&& ...
                abs(Xdata(indices_target) - spaceX(k)) < ...
                abs(Xdata(indices_target) - spaceX(k-1))

                subset_Xdata(j) = Xdata(indices_target);
                subset_Ydata(j) = Ydata(indices_target);
                j = j + 1;
            end
        end
    end

    if isempty(find(subset_Xdata == 0, 1))
        reduced_pts = max_pts;
    else
        reduced_pts = find(subset_Xdata == 0, 1) - 1;
    end
    reduced_Xdata = subset_Xdata(1:reduced_pts);
    reduced_Ydata = subset_Ydata(1:reduced_pts);

    if nargout == 2
        varargout(1) = {reduced_Xdata};
        varargout(2) = {reduced_Ydata};
    elseif nargout == 1
        varargout(1) = {reduced_Ydata};
    end

end
```

H.3.3 Modeling the Linear Elastic Behavior of A–B–A Melts

What follows is part of the algorithm implemented to model the linear elastic behavior of A–B–A melts in the pseudo-plateau region and up to the entanglement time τ_e (Chapter 3, §3.3.4.IV-e).

```
% ------------------------------------------------------------------- %
%
% If solve_system == 1
% (it only applies to an A-B-A MELT)
%
% it calculates the FILLER EFFECT at 1/tau_e and 1/2tauR
%        and the FRACTION OF MIDBLOCK CHAINS B WITH AT LEAST 1 FREE END
% i.e. [xi_tau_e, xi_plateau, xf]
% based on experimental values of Gprime
%                                  at 1/tau_e, 1/2tauR, and omega->0
% i.e. [Gprime_inv_tau_e_exp, G_plateau_exp, G_equilibrium_exp]
%
% If solve_system == 1 && matrix_composition_from_DSC == 1
%
% it also calculates the composition of the matrix, B + UNSEGREGATED A,
% (w_A_matrix_DSC and x_A_un_DSC) based on the Tg's
%
% ------------------------------------------------------------------- %
%
% Define a SYSTEM of 3 EQUATIONS
%
% Gprime_inv_tau_e - (G_c +       G_e_TeONE    + G_Cubic) = 0;
% G_plateau        - (G_c + (4/5)*G_e_TeONE    + G_Cubic) = 0;
% G_equilibrium    - (G_c + (4/5)*G_e_TeONE*Te + G_Cubic) = 0;
%
% with 3 UNKNOWNS: xi_tau_e, xi_plateau, xf
%
% to this end, we need to set xd = 0 (OK for long B, i.e. Z_hB >> 1)
%              use alpha as a known parameter
%              and assume xi_plateau = xi_equilibrium (reasonable)
%
% ------------------------------------------------------------------- %

...

function out = G_SYSTEM(unknowns, parameters)

    xi_tau_e_var   = unknowns(1);
    xi_plateau_var = unknowns(2);
    xf_var         = unknowns(3);

    alpha_par            = parameters(1);
    phi_B_matrix_par     = parameters(2);
```

```
    Gprime_inv_tau_e_par = parameters(3);
    G_plateau_par        = parameters(4);
    G_equilibrium_par    = parameters(5);

    xd_var = 0;

    G_Cubic_value         = G_Cubic_FUNC(alpha_par);

    G_c_tau_e_value       = G_c_FUNC(xi_tau_e_var,   ...
                                     xd_var, xf_var, phi_B_matrix_par);
    G_c_plateau_value     = G_c_FUNC(xi_plateau_var, ...
                                     xd_var, xf_var, phi_B_matrix_par);
    G_c_equilibrium_value = G_c_plateau_value;

    Te_value              = Te_FUNC(xd_var, xf_var);

    G_e_tau_e_value       =         G_e_TeONE_FUNC(xi_tau_e_var, ...
                                                   xd_var,       ...
                                                   phi_B_matrix_par);
    G_e_plateau_value     = (4/5) * G_e_TeONE_FUNC(xi_plateau_var, ...
                                                   xd_var,         ...
                                                   phi_B_matrix_par);
    G_e_equilibrium_value = G_e_plateau_value * Te_value;

    Gprime_inv_tau_e_value = G_c_tau_e_value + ...
                             G_e_tau_e_value + ...
                             G_Cubic_value;
    G_plateau_value        = G_c_plateau_value + ...
                             G_e_plateau_value + ...
                             G_Cubic_value;
    G_equilibrium_value    = G_c_equilibrium_value + ...
                             G_e_equilibrium_value + ...
                             G_Cubic_value;

    out(1,1) = Gprime_inv_tau_e_par - Gprime_inv_tau_e_value;
    out(2,1) = G_plateau_par        - G_plateau_value;
    out(3,1) = G_equilibrium_par    - G_equilibrium_value;

end

% ------------------------------------------------------------------- %

...

if (solve_system == 1) && (proceed == 1)

    INPUT_data = INPUT_SystemData;
    if ~isequal(size(INPUT_data), [3,1])
        INPUT_data = INPUT_data';
    end

    INPUT_guess = INPUT_SystemGuesses;
    if ~isequal(size(INPUT_guess), [3,1])
```

```
    INPUT_guess = INPUT_guess';
end

% ------------------------------------------------------------- %

% NOTE: for "PAPERS calculations", MATRIX = B + S
%       for "SYSTEM calculations", MATRIX = B + UNSEGREGATED A

tolerance = 1e-6;   % in percent

delta   = inf;
counter = 0;

while (delta > tolerance)

    if counter == 0
        % to start, assume MATRIX = B
        % (i.e. x_A_un = 0, w_A_matrix = 0)
        old_w_A_matrix = 0;
    else
        % to continue, consider MATRIX = B + UNSEGREGATED A
        % using the last estimate of w_A_matrix
        old_w_A_matrix = new_w_A_matrix;
    end

    % ---------------------------------- %

    % Calculate phi_B_matrix
    % MATRIX = B + UNSEGREGATED A

    Xdata  = old_w_A_matrix;
    XXdata = [rho_B, rho_A];

    phi_B_matrix_2 = Block_B_Volume_Fraction_Matrix(Xdata, XXdata);
    conc_B_matrix  = phi_B_matrix_2 .* rho_B;   % kg/m3

    % nu of block B in matrix
    nu_B_matrix = phi_B_matrix_2 .* nu_B_hB;

    % ---------------------------------- %

    % B Molar Mass Between Entanglements (Graessley-Fetters def.)

    Xdata   = Me_hB;
    XX1data = phi_B_matrix_2;
    XX2data = xd;

    Me_B = Me_B_func(Xdata, XX1data, XX2data);

    % ---------------------------------- %
```

```
% Is B Entangled ?

M_Me_B = M_B ./ Me_B;

Is_B_Entangled = M_Me_B;
Is_B_Entangled(Is_B_Entangled <  Critical_M_Me) = 0;
Is_B_Entangled(Is_B_Entangled >= Critical_M_Me) = 1;

Z_hB = Is_B_Entangled .* (M_B / Me_hB);
Z_B  = Is_B_Entangled .* (M_B ./ Me_B);

% ---------------------------------- %

% Solve SYSTEM to find xi_tau_e, xi_plateau, and xf

data  = INPUT_data;
guess = INPUT_guess;

parameters = [alpha; phi_B_matrix_2; data];

TolFun  = TolFunCoeff * min(data);
options = optimset('Display', 'off',   ...
                   'MaxIter', MaxIter, ...
                   'TolFun',  TolFun,  ...
                   'TolX',    TolX);

[results, fval, exitflag, output] =                          ...
                     fsolve(@(unknowns)                      ...
                            G_SYSTEM(unknowns, parameters), ...
                            guess,                           ...
                            options);

xi_tau_e_result   = results(1);
xi_plateau_result = results(2);
xf_result         = results(3);

% ---------------------------------- %

% Based on xf, calculate Te (Langley Trapping Factor)

Te_result = Te_FUNC(0, xf_result);

% ---------------------------------- %

% Based on xf, calculate x_A_un (fraction of A UNSEGREGATED)
%
% NOTE:
% the total # of A chains is twice the total # of B chains
% hence
% if all B chains belonging to xf had both ends free
% then x_A_un = xf
% if all B chains belonging to xf had only one end free
% then x_A_un = xf/2
```

```
    x_A_un_MIN     = xf_result / 2;
    x_A_un_MAX     = xf_result;

    x_A_un_AVERAGE = xf_result / sqrt(2);

    % ---------------------------------- %

    % Based on x_A_un, calculate a new value for w_A_matrix

    % Which value of x_A_un to use ?
    % 3 options:
    %x_A_un_to_use = x_A_un_MIN;
    %x_A_un_to_use = x_A_un_MAX;
    x_A_un_to_use = x_A_un_AVERAGE;

    var1  = x_A_un_to_use;
    var3  = w_A;
    data  = [var1, var3];
    guess = old_w_A_matrix;

    TolFun  = TolFunCoeff * min(data);
    options = optimset('Display', 'off',   ...
                       'MaxIter', MaxIter, ...
                       'TolFun',  TolFun,  ...
                       'TolX',    TolX);

    new_w_A_matrix = fsolve(@(var2)                       ...
                            x_A_un_EQ(var1, var2, var3), ...
                            guess,                       ...
                            options);

    % ---------------------------------- %

    % since the starting value of old_w_A_matrix is zero
    % need to shift both by a constant before calculating delta
    old_w_A_matrix_plus1 = old_w_A_matrix + 1;
    new_w_A_matrix_plus1 = new_w_A_matrix + 1;

    delta = 100 *                                          ...
            (abs(new_w_A_matrix_plus1 - old_w_A_matrix_plus1) ...
             / old_w_A_matrix_plus1);

    counter = counter + 1;

end

% ------------------------------------------------------------- %

% Since xf has been determined, and xd = 0 is assumed,
% xbk = (xb + xk) can be calculated
%
% xd = 0 (assumption)
```

```
    xf  = xf_result;
    xbk = 1 - xd - xf;

    % ------------------------------------------------------------- %

    if matrix_composition_from_DSC == 1

        % Use the Fox equation to find the composition of the matrix

        var2  = Tg_matrix;
        var3  = Tg_hA;
        var4  = Tg_hB;
        data  = 1 ./ [var3, var4];
        guess = 0;

        TolFun  = TolFunCoeff * min(data);
        options = optimset('Display', 'off',   ...
                           'MaxIter', MaxIter, ...
                           'TolFun',  TolFun,  ...
                           'TolX',    TolX);

        result_fsolve = fsolve(@(var1)                          ...
                               Fox_EQ(var1, var2, var3, var4), ...
                               guess,                          ...
                               options);

        w_A_matrix_DSC = result_fsolve;

        % Based on this composition, find x_A_un

        var2  = w_A_matrix_DSC;
        var3  = w_A;
        data  = [var2, var3];
        guess = 0;

        TolFun  = TolFunCoeff * min(data);
        options = optimset('Display', 'off',   ...
                           'MaxIter', MaxIter, ...
                           'TolFun',  TolFun,  ...
                           'TolX',    TolX);

        result_fsolve = fsolve(@(var1)                       ...
                               x_A_un_EQ(var1, var2, var3), ...
                               guess,                       ...
                               options);

        x_A_un_DSC = result_fsolve;

    end

    % ---------------------------------- %

end
```

H.3.4 Fractional Maxwell Model

What follows is part of the algorithm implemented to fit experimental data to the fractional Maxwell model (Chapter 4, §4.3.2.III-a).

```
% ------------------------------------------------------------------- %
% FMM = Fractional Maxwell Model %
% Friedrich RA (1991); Schiessel et al. JPA (1995) %
% 0 <= beta < alpha <= 1 %
% ------------------------------------------------------------------- %

% Functions definition

% Relaxation Time %
function out = CharTime_FMM_func(param)

    alpha = param(1);
    beta  = param(2);
    V     = param(3);
    W     = param(4);

    out = (V / W)^(1/(alpha - beta));
end

% Characteristic Modulus %
function out = CharModulus_FMM_func(param)

    alpha = param(1);
    beta  = param(2);
    V     = param(3);
    W     = param(4);

    out = V * ((V / W)^(alpha/(beta - alpha)));
end

% Relaxation Spectrum, H %
function out = SpectrumH_FMM_func(param, Xdata)

    alpha = param(1);
    beta  = param(2);
    V     = param(3);
    W     = param(4);
    tau   = Xdata;

    CharTime    = CharTime_FMM_func([alpha, beta, V, W]);
    CharModulus = CharModulus_FMM_func([alpha, beta, V, W]);

    z = tau / CharTime;

    num = sin(pi*alpha) + sin(pi*beta)*(z.^(beta-alpha));
```

```
    den = 1 + 2*cos(pi*(beta-alpha))*(z.^(beta-alpha)) + ...
                                     (z.^(2*(beta-alpha)));

    out = (CharModulus * z.^(-alpha) .* num) ./ (pi * den);
end

% Storage Modulus, E' %
function out = Storage_FMM_func(param, Xdata)

    alpha = param(1);
    beta  = param(2);
    V     = param(3);
    W     = param(4);
    omega = Xdata;

    storage_num_1 = ...
             ((W*omega.^beta).^2).*(V*omega.^alpha).*cos(pi*0.5*alpha);
    storage_num_2 = ...
             ((V*omega.^alpha).^2).*(W*omega.^beta).*cos(pi*0.5*beta);

    storage_num   = storage_num_1 + storage_num_2;

    den_1         = (V*omega.^alpha).^2;
    den_2         = (W*omega.^beta).^2;
    den_3         = 2*(V*omega.^alpha).*(W*omega.^beta).*...
                    cos(pi*0.5*(alpha-beta));

    den           = den_1 + den_2 + den_3;

    out           = storage_num ./ den;
end

% Loss Modulus, E'' %
function out = Loss_FMM_func(param, Xdata)

    alpha = param(1);
    beta  = param(2);
    V     = param(3);
    W     = param(4);
    omega = Xdata;

    loss_num_1 = ...
             ((W*omega.^beta).^2).*(V*omega.^alpha).*sin(pi*0.5*alpha);
    loss_num_2 = ...
             ((V*omega.^alpha).^2).*(W*omega.^beta).*sin(pi*0.5*beta);

    loss_num   = loss_num_1 + loss_num_2;

    den_1      = (V*omega.^alpha).^2;
    den_2      = (W*omega.^beta).^2;
    den_3      = 2*(V*omega.^alpha).*(W*omega.^beta).*...
                 cos(pi*0.5*(alpha-beta));
```

```
    den        = den_1 + den_2 + den_3;

    out        = loss_num ./ den;
end

function out = Fit_FMM_func(param, Xdata)

    alpha = param(1);
    beta  = param(2);
    V     = param(3);
    W     = param(4);
    omega = Xdata;

    out(:,1) = Storage_FMM_func([alpha, beta, V, W], omega);
    out(:,2) = Loss_FMM_func([alpha, beta, V, W], omega);
end

% ------------------------------------------------------------------- %

% Create cell of struct arrays, cell of row vectors, and matrix %
% that store goodness of fit results & fit results %

num_rows           = max_num_files;
num_parameters_FMM = 4;

% --- FMM, Fitting both the Storage AND the Loss Modulus --- %

% cell of struct arrays %
struct_array = struct('resnorm', [],    ...
                      'exitflag', [],   ...
                      'output_message', []);
gof_FMM    = cell(num_rows, 1);
gof_FMM(:) = {struct_array};

% matrix that stores fitting parameters %
matrix_fit_FMM_param = zeros(num_rows, num_parameters_FMM);
matrix_fit_FMM_param(matrix_fit_FMM_param == 0) = NaN;

% matrix that stores CharModulus and CharTime %
matrix_fit_FMM_mt = zeros(num_rows, 2);
matrix_fit_FMM_mt(matrix_fit_FMM_mt == 0) = NaN;

% matrix that stores H, E', and E'' at CharTime %
matrix_fit_FMM_charmoduli = zeros(num_rows, 3);
matrix_fit_FMM_charmoduli(matrix_fit_FMM_charmoduli == 0) = NaN;

% matrix that stores E'=E'' at Crossover, 1/Crossover, and Crossover %
matrix_fit_FMM_crossover = zeros(num_rows, 3);
matrix_fit_FMM_crossover(matrix_fit_FMM_crossover == 0) = NaN;
```

```
% cell of struct arrays %
struct_array = struct('omega', [],           ...
                      'storage_modulus', [], ...
                      'loss_modulus', []);
fit_results_FMM    = cell(num_rows, 1);
fit_results_FMM(:) = {struct_array};

% ------------------------------------------------------------------- %

...

if (proceed_fit_Y1 == 1) && (proceed_fit_Y2 == 1)

    lower_index = max(lower_index_Y1, lower_index_Y2);
    upper_index = min(upper_index_Y1, upper_index_Y2);

    X_data  =  nodupl_x(lower_index:upper_index,k);
    Y1_data = nodupl_y1(lower_index:upper_index,k);
    Y2_data = nodupl_y2(lower_index:upper_index,k);

    TolFun = TolFunCoeff * min([Y1_data; Y2_data]);

    % --- Parameters Guesses --- %

    X_data_temp  =  nodupl_x(:,k);
    Y1_data_temp = nodupl_y1(:,k);
    Y2_data_temp = nodupl_y2(:,k);

    index_omegazero      = find(X_data_temp == min(X_data_temp));
    index_omegainfinity  = find(X_data_temp == max(X_data_temp));

    X_data_omegazero     = X_data_temp(index_omegazero);
    X_data_omegainfinity = X_data_temp(index_omegainfinity);

    Y1_data_omegazero     = Y1_data_temp(index_omegazero);
    Y1_data_omegainfinity = Y1_data_temp(index_omegainfinity);

    Y2_data_omegazero     = Y2_data_temp(index_omegazero);
    Y2_data_omegainfinity = Y2_data_temp(index_omegainfinity);

    V1_guess = Y1_data_omegazero * ...
    (((X_data_omegazero^alpha_guess)*cos(pi*0.5*alpha_guess))^-1);

    W1_guess = Y1_data_omegainfinity * ...
    (((X_data_omegainfinity^beta_guess)*cos(pi*0.5*beta_guess))^-1);

    V2_guess = Y2_data_omegazero * ...
    (((X_data_omegazero^alpha_guess)*sin(pi*0.5*alpha_guess))^-1);

    W2_guess = Y2_data_omegainfinity * ...
    (((X_data_omegainfinity^beta_guess)*sin(pi*0.5*beta_guess))^-1);
```

```
V_guess = mean([V1_guess, V2_guess]);
W_guess = mean([W1_guess, W2_guess]);

% --- Parameters Limits ---- %

V1_lower = (factor^-1) *           ...
            min(Y1_data_omegazero, ...
                Y1_data_omegazero/X_data_omegazero);
V1_upper =  factor *               ...
            max(Y1_data_omegazero, ...
                Y1_data_omegazero/X_data_omegazero);

V2_lower = (factor^-1) *           ...
            min(Y2_data_omegazero, ...
                Y2_data_omegazero/X_data_omegazero);
V2_upper =  factor *               ...
            max(Y2_data_omegazero, ...
                Y2_data_omegazero/X_data_omegazero);

V_lower = mean([V1_lower, V2_lower]);
V_upper = mean([V1_upper, V2_upper]);

W1_lower = (factor^-1) *               ...
            min(Y1_data_omegainfinity, ...
                Y1_data_omegainfinity/X_data_omegainfinity);
W1_upper =  factor *                   ...
            max(Y1_data_omegainfinity, ...
                Y1_data_omegainfinity/X_data_omegainfinity);

W2_lower = (factor^-1) *               ...
            min(Y2_data_omegainfinity, ...
                Y2_data_omegainfinity/X_data_omegainfinity);
W2_upper =  factor *                   ...
            max(Y2_data_omegainfinity, ...
                Y2_data_omegainfinity/X_data_omegainfinity);

W_lower = mean([W1_lower, W2_lower]);
W_upper = mean([W1_upper, W2_upper]);

% ------------------------------------------------------------ %

function_handle  = @Fit_FMM_func;

Parameters_Guess = [alpha_guess, beta_guess, V_guess, W_guess];
Parameters_Lower = [alpha_lower, beta_lower, V_lower, W_lower];
Parameters_Upper = [alpha_upper, beta_upper, V_upper, W_upper];

% ------------------------------------------------ %
```

```
options = optimset('Diagnostics', 'off',       ...
                   'Display', 'off',        ... % 'notify-detailed'
                   'MaxFunEvals', MaxFunEvals, ...
                   'MaxIter', MaxIter,         ...
                   'TolFun', TolFun,           ...
                   'TolX', TolX);

[Parameters_Fit, resnorm, ~, exitflag, output] = ...
lsqcurvefit(function_handle, Parameters_Guess,   ...
            X_data, [Y1_data, Y2_data],          ...
            Parameters_Lower, Parameters_Upper, options);

matrix_fit_FMM_param(k, :) = Parameters_Fit;

matrix_fit_FMM_mt(k, 1) = ...
            CharModulus_FMM_func(Parameters_Fit);
time_temp = CharTime_FMM_func(Parameters_Fit);
matrix_fit_FMM_mt(k, 2) = time_temp;

H_temp     = SpectrumH_FMM_func(Parameters_Fit, time_temp);
Estor_temp = Storage_FMM_func(Parameters_Fit, 1/time_temp);
Eloss_temp = Loss_FMM_func(Parameters_Fit, 1/time_temp);

matrix_fit_FMM_charmoduli(k, 1) = H_temp;
matrix_fit_FMM_charmoduli(k, 2) = Estor_temp;
matrix_fit_FMM_charmoduli(k, 3) = Eloss_temp;

freq_temp = Crossover_FMM_func(Parameters_Fit);
if isreal(freq_temp)

    Estor_temp = Storage_FMM_func(Parameters_Fit, freq_temp);
    matrix_fit_FMM_crossover(k, 1) = Estor_temp;
    matrix_fit_FMM_crossover(k, 2) = 1/freq_temp;
    matrix_fit_FMM_crossover(k, 3) = freq_temp;
end

gof_FMM{k}.resnorm        = resnorm;
gof_FMM{k}.exitflag       = exitflag;
gof_FMM{k}.output_message = output.message;

% ------------------------------------------------ %

X_fit_limits(1) = max([min(X_fit_Y1_limits), ...
                       min(X_fit_Y2_limits)]);
X_fit_limits(2) = min([max(X_fit_Y1_limits), ...
                       max(X_fit_Y2_limits)]);

if isnan(X_fit_limits)
    X_data_or_limits = X_data;
else
    X_data_or_limits = X_fit_limits;
end
```

```
    omega_vector = SpaceX(X_data_or_limits, ...
                          spacing, pts_per_decade);

    % ------------------------------------------------ %

    [output_fit] = Fit_FMM_func(Parameters_Fit, omega_vector);

    storage_modulus_vector = output_fit(:,1);
    loss_modulus_vector    = output_fit(:,2);

    % ------------------------------------------------ %

    fit_results_FMM{k}.omega           = omega_vector;
    fit_results_FMM{k}.storage_modulus = storage_modulus_vector;
    fit_results_FMM{k}.loss_modulus    = loss_modulus_vector;

end
```

Appendix I

Experimental Results on the Extensional Behavior of $(A–B–A)_n$/B–A Blends

The materials used in this study are binary and ternary blends prepared from moderate molar mass A–B–A and $(B–A)_n$ block copolymers and low molar mass B–A diblocks. The pure components, listed in Table I.1 and synthesized by Sangwoo Lee and Mark Martello, were blended by a solvent-casting procedure using chloroform. The viscoelastic behavior was probed in uniaxial extension, using a TA Instruments ARES-G2 rheometer equipped with the extensional viscosity fixture (EVF – Chapter 5, §5.2.2 and Figure 5.1). Specimens were prepared as described in §3.2.3 and §5.2.3, and tested in start-up of steady uniaxial extension at 37 °C and $\dot{\varepsilon} = 1\ s^{-1}$. To determine precision and obtain meaningful ultimate properties, each test was repeated between five and eight times. The experimental data were processed in the MATLAB® environment as discussed in §5.3.2.

Table I.1. Molecular characteristics of A–B–A, B–A, and $(B–A)_n$ block copolymers, with A = poly(D,L-lactide) (L), and B = polyisoprene (I), poly(6-methyl-ε-caprolactone) (6M), and poly(ε-decalactone) (D).

Sample		$M_{n,B}$ [a)] [g/mol]	$M_{n,A}$ [a)] [g/mol]	f_A [b)]	$T_{g,A}$ [c)] [°C]	Morphology [d)]
L–I–L (50–12)		49800	11650	0.25	51	–
I–L (4–1)	e)	4000	1000	0.16	2	disordered
I–L (4–4)		4000	4000	0.41	37	LAM
L–I–L (62–17)		62000	17000	0.28	55	–
I–L (4–1.5)	e)	4000	1500	0.20	11	BCC
I–L (4–3)		4000	3000	0.34	39	HEX
L–6M–L (98–33)	f)	98000	33000	0.33	53	HEX
6M–L (9–5.5)		9000	5500	0.35	42	HEX
L–D–L (100–18)		100000	18000	0.21	51	–
D–L (9.6–6)	f)	9600	5900	0.33	43	–
$[(D–L)\ (8.7–4.4)]_{12}$		8700	4400	0.31	42	–

a) Number-average molar masses of the individual blocks, determined by ^{1}H NMR spectroscopy.

b) Volume fraction of poly(D,L-lactide) at 25 °C, calculated using pure component densities.

c) Glass transition of the L block, determined by DSC.

d) Determined by small-angle X-ray scattering (SAXS) and transmission electron microscopy (TEM).

e) Synthesis, molecular, and morphological characterization performed by Sangwoo Lee.

f) Synthesis, molecular, and morphological characterization performed by Mark Martello.

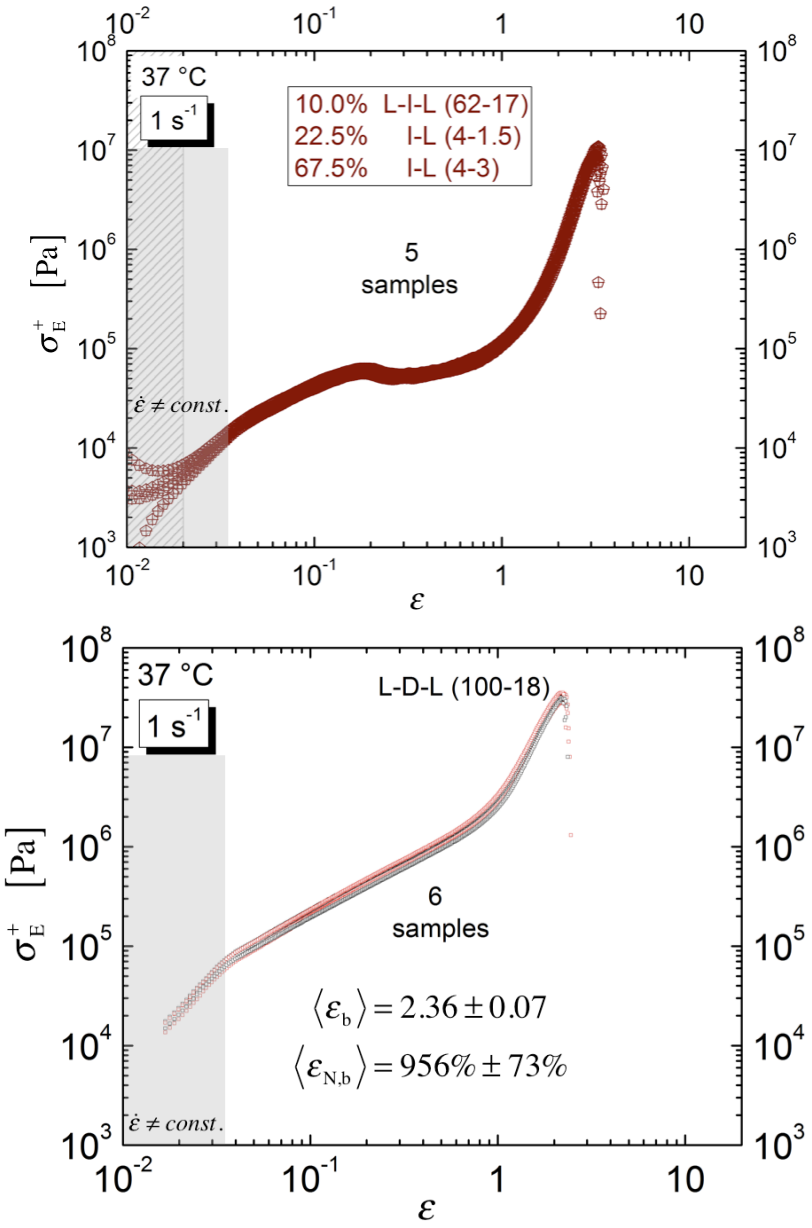

Figure I.1. Examples of data reproducibility.

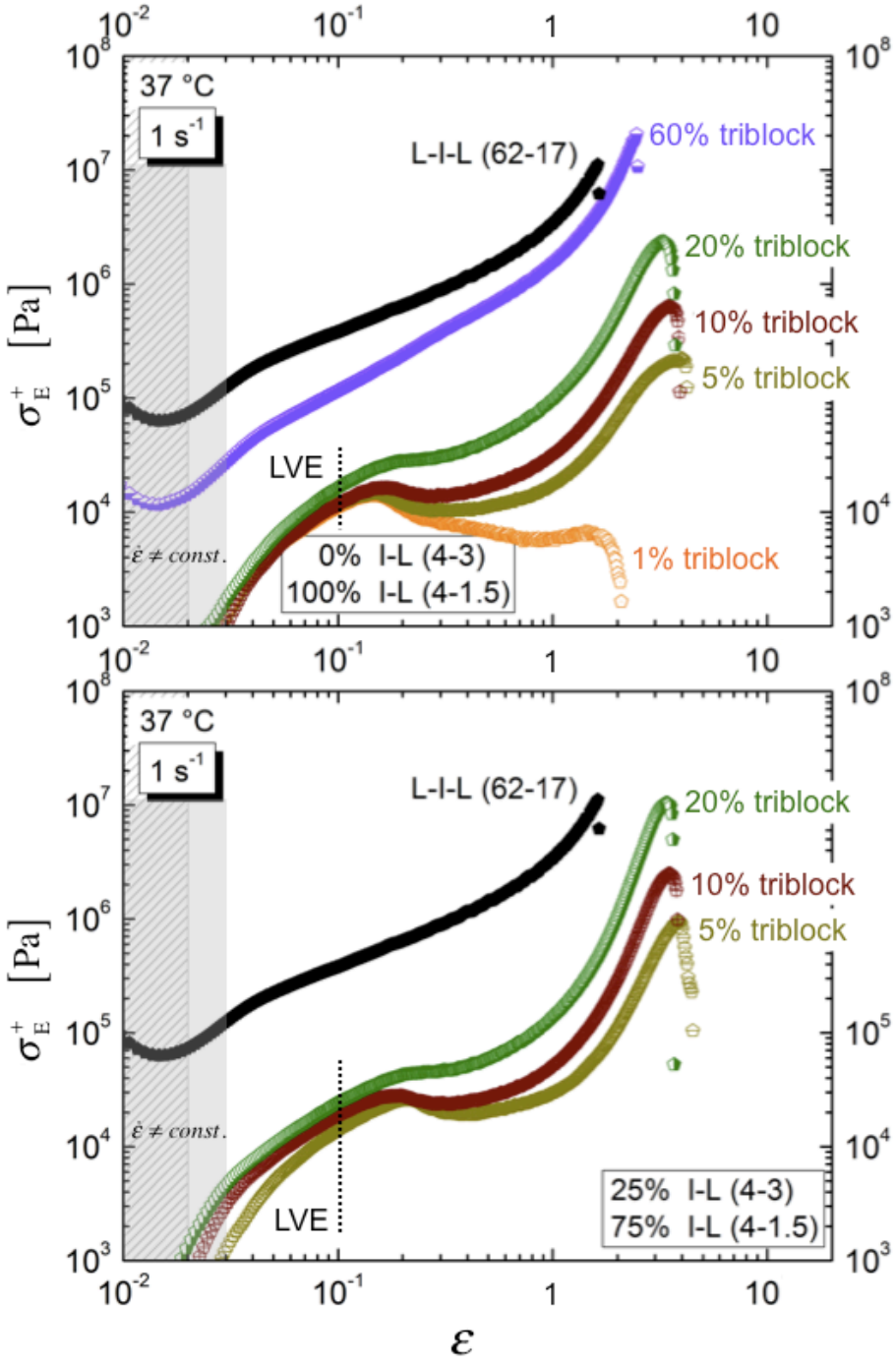

Figure I.2. (*cont.*)

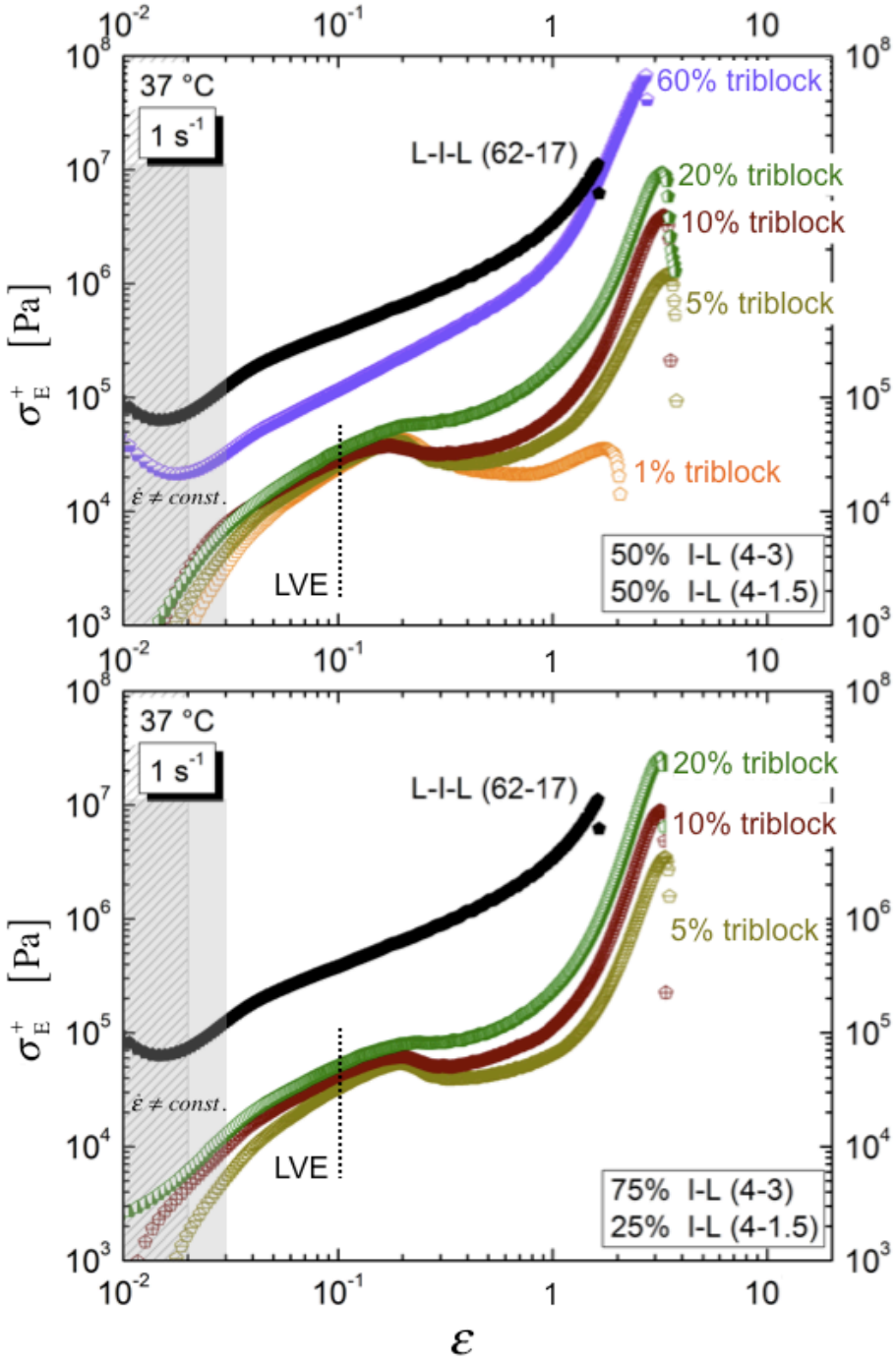

Figure I.2. (*cont.*)

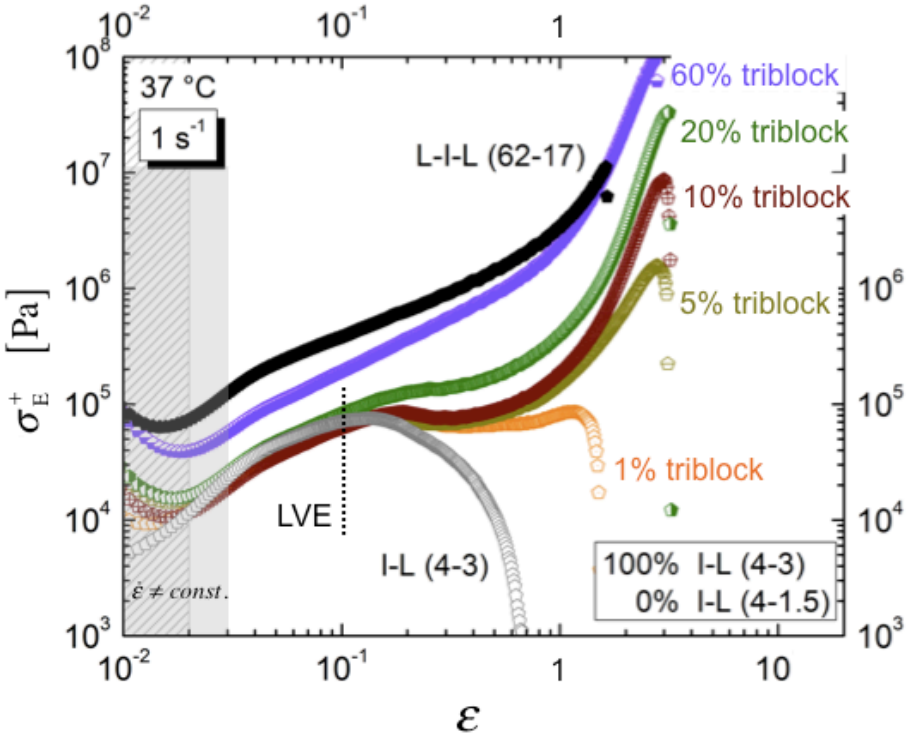

Figure I.2. Elongational stress vs. strain for the system L–I–L (62–17) / I–L (4–1.5) / I–L (4–3). In each plot, the ratio between the two diblocks is constant. The nonlinear behavior of the diblock system is drastically modified by adding just 1 wt% of triblock. The linear response remains essentially unchanged while the strain hardening behavior is more pronounced with increasing triblock content up to 20 wt%. Notice that the ultimate properties (stress- and strain-at-break) of some of these blends (especially those with 60 wt% of triblock) are improved with respect to the pure thermoplastic elastomer (cf. Figures I.3 and I.4). This behavior – attributed to a decrease in the glass transition temperature of the hard domains (consistently with the governing mechanism of rupture discussed in Chapter 5) – is at variance with several studies in the literature that claim[92,453] or show[113,201,494,495,585,586] a detrimental effect on the ultimate properties of TPEs upon addition of diblocks.

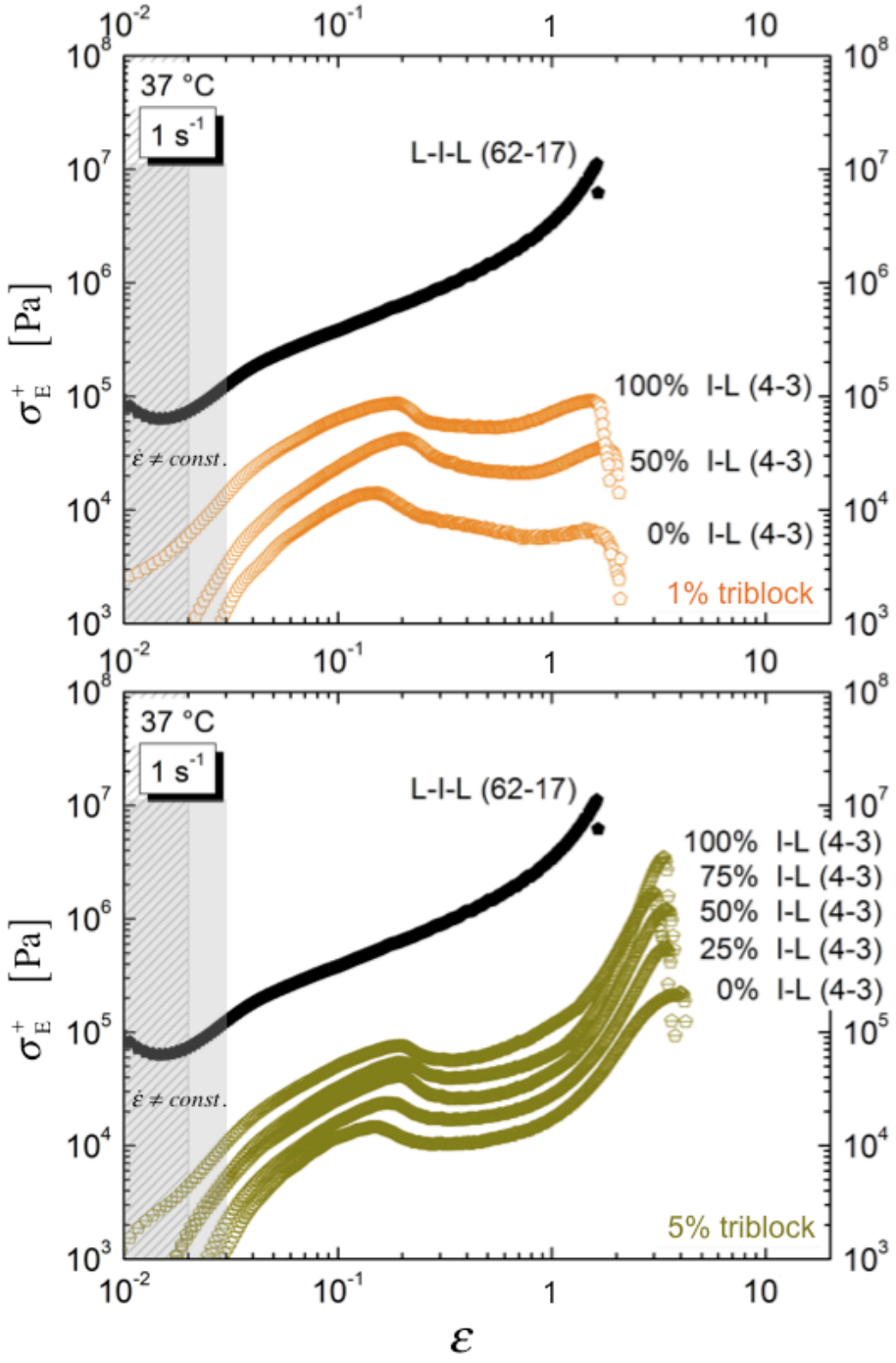

Figure I.3. (*cont.*)

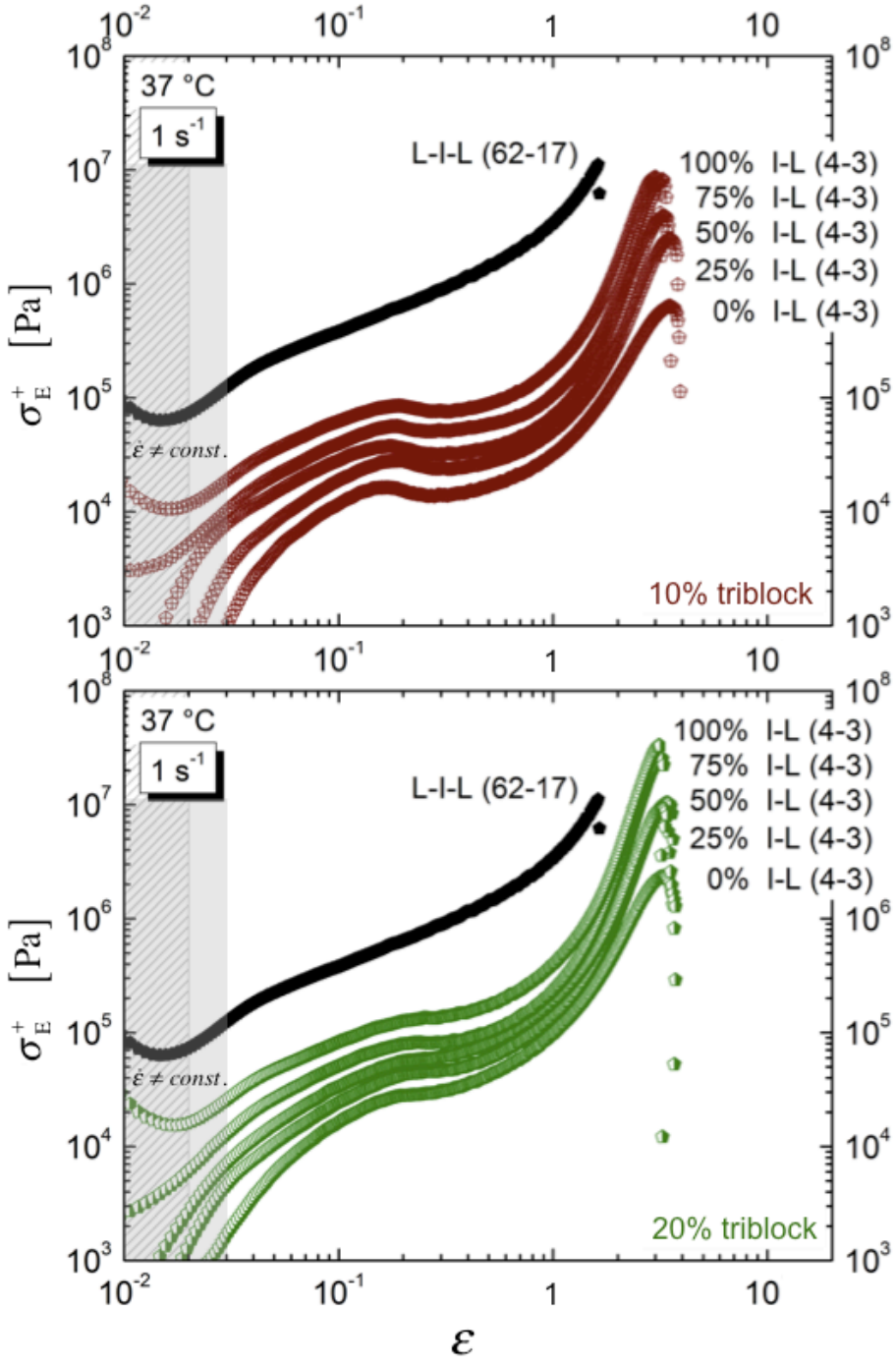

Figure I.3. (*cont.*)

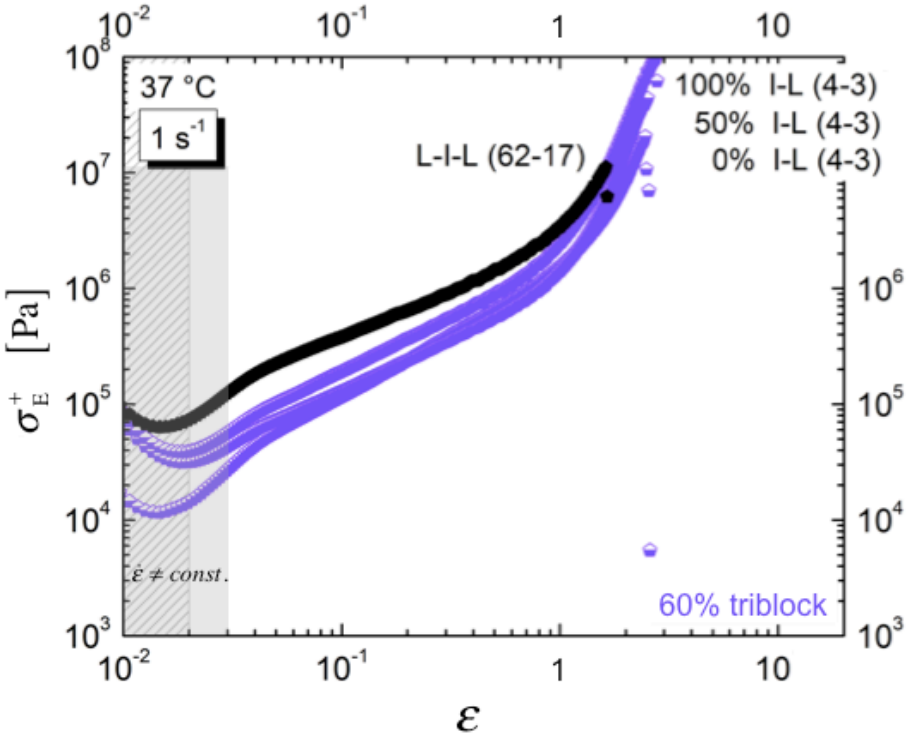

Figure I.3. Elongational stress vs. strain for the system L–I–L (62–17) / I–L (4–1.5) / I–L (4–3). In each plot, the triblock content is constant. The system exhibits an overall increase in stress with increasing I–L (4–3) content (due to an increase in $T_{g,L}$). Notice that the ultimate properties (stress- and strain-at-break) of some of these blends (especially those with 60 wt% of triblock) are improved with respect to the pure thermoplastic elastomer (cf. Figures I.2 and I.4). This behavior – attributed to a decrease in the glass transition temperature of the hard domains (consistently with the governing mechanism of rupture discussed in Chapter 5) – is at variance with several studies in the literature that claim[92,453] or show[113,201,494,495,585,586] a detrimental effect on the ultimate properties of TPEs upon addition of diblocks.

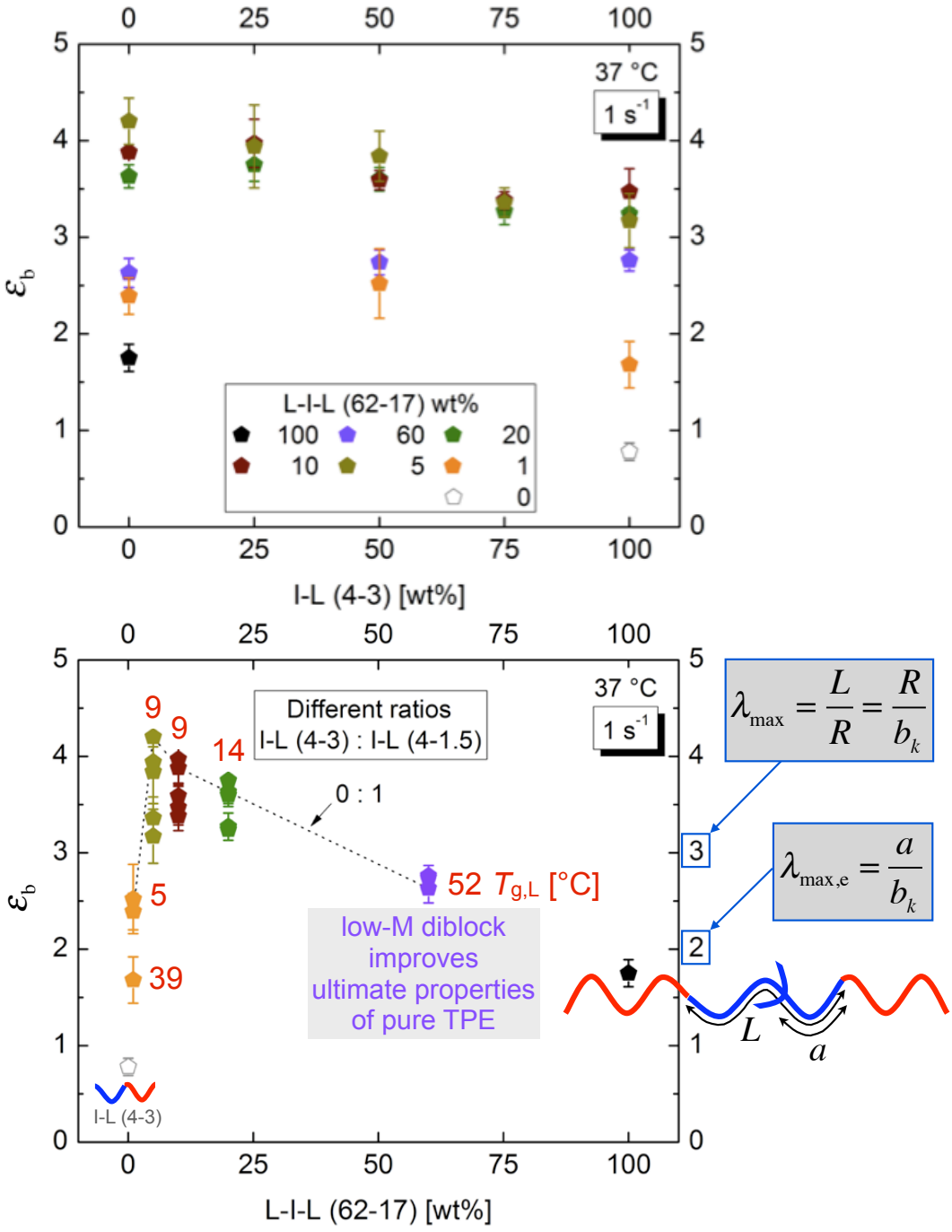

Figure I.4. Strain-at-break as a function of composition for the system L–I–L (62–17) / I–L (4–1.5) / I–L (4–3). The highest extensibilities are exhibited at the lowest triblock content (5 and 10 wt%) and for I–L (4–1.5) / I–L (4–3) ratios of 1:0, 3:1, and 1:1.

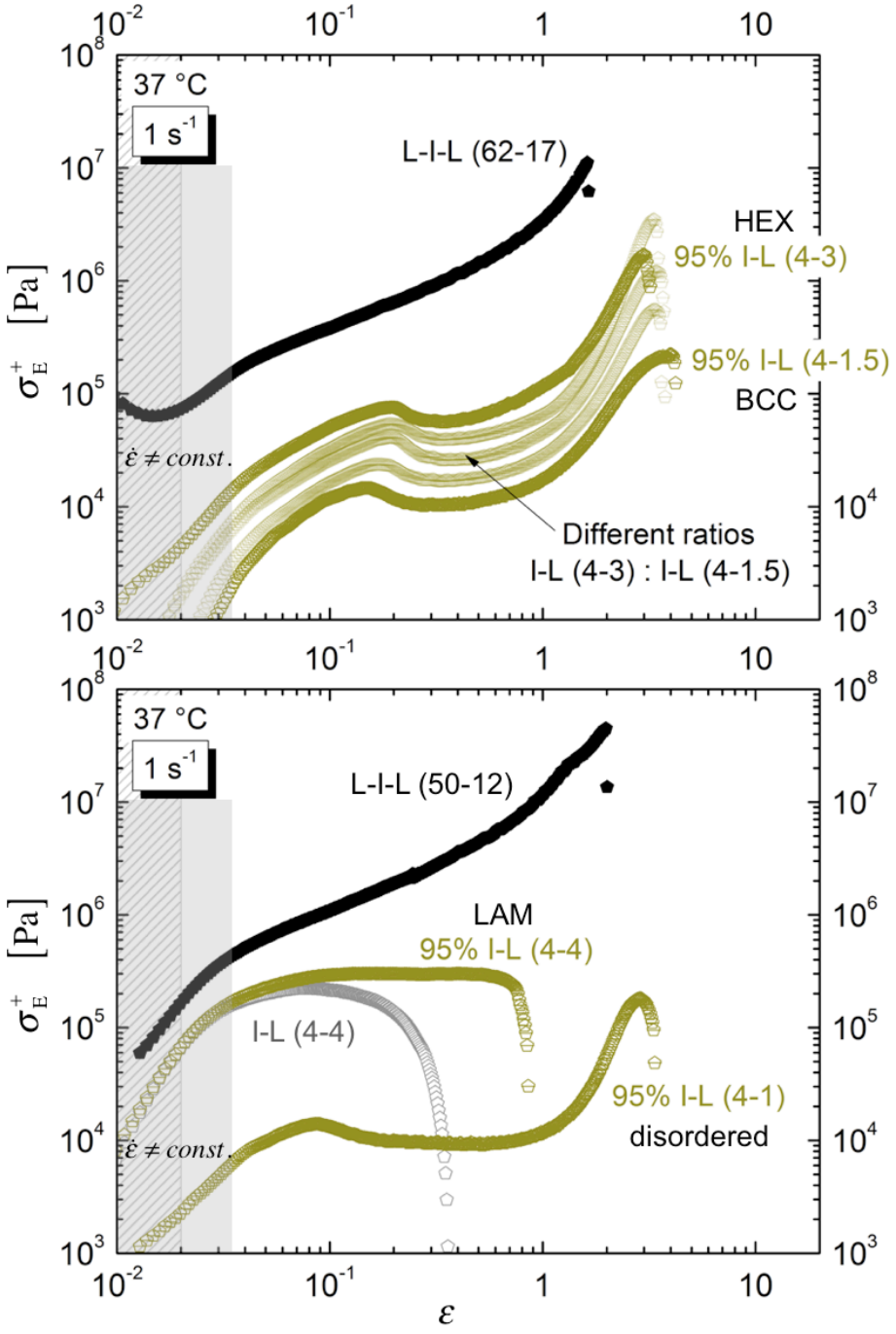

Figure I.5. Elongational stress vs. strain for the systems (upper) L–I–L (62–17) / I–L (4–1.5) / I–L (4–3), and (lower) L–I–L (50–12) / I–L (4–1) and L–I–L (50–12) / I–L (4–4), at 5 wt% of triblock content. Shown in each plot is the morphology of the pure diblocks.

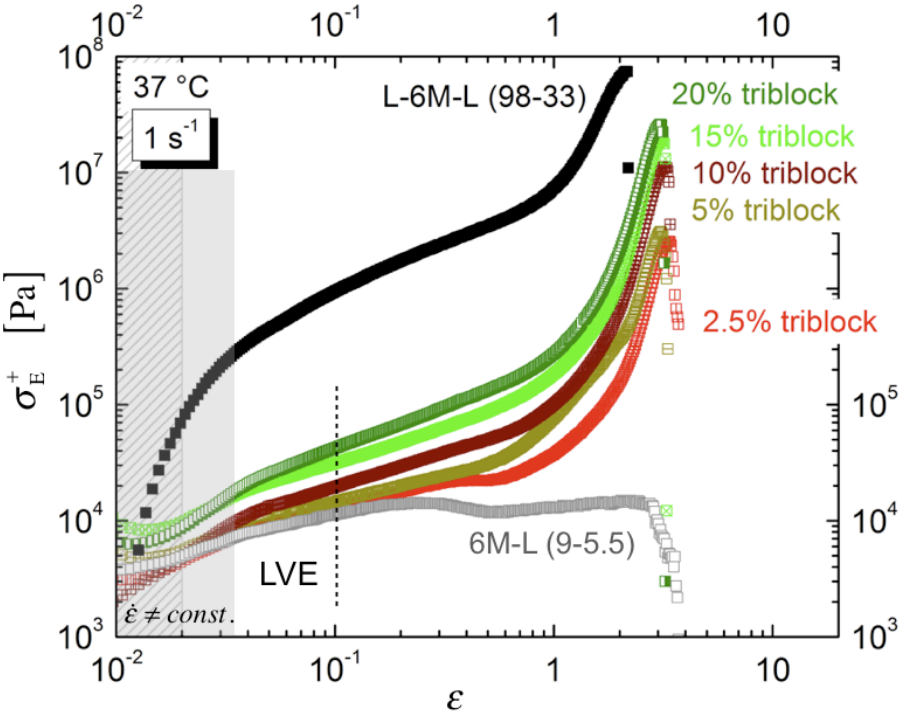

Figure I.6. Elongational stress vs. strain for the system L–6M–L (98–33) / 6M–L (9–5.5). Similarly to Figure I.2, the nonlinear behavior of the diblock is drastically modified by adding just 2.5 wt% of triblock. In contrast with the behavior exhibited by the L–I–L / I–L system, increasing the triblock content affects both the linear and nonlinear response.

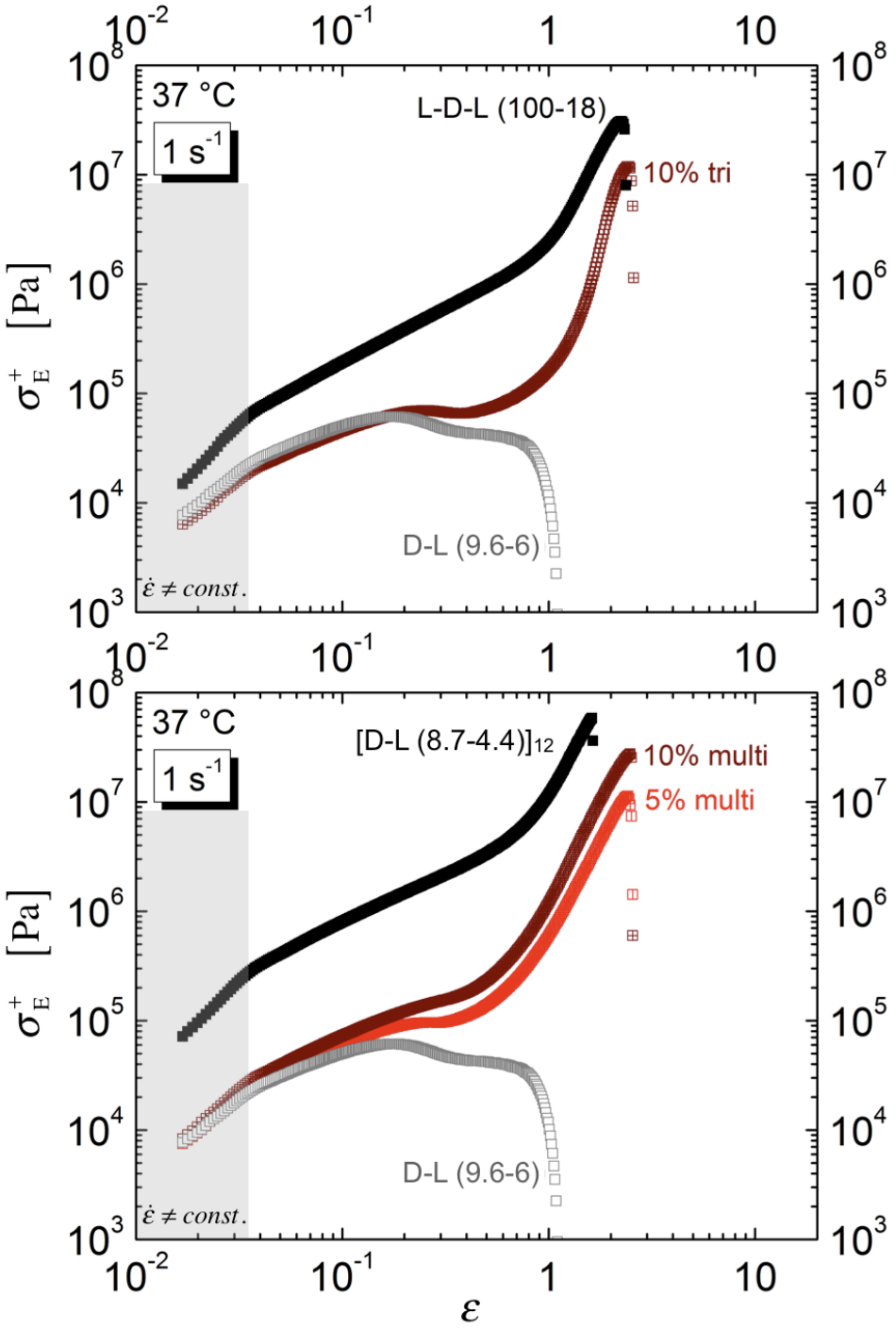

Figure I.7. Elongational stress vs. strain for the systems (upper) L–D–L (100–18) / D–L (9.6–6), and (lower) $[D–L\ (8.7–4.4)]_{12}$ / D–L (9.6–6).